Mechanics of Fast Force Recovery in striated muscles

M. Caruel

To cite this version:

M. Caruel. Mechanics of Fast Force Recovery in striated muscles. Solid mechanics [physics.class-ph]. Ecole Polytechnique X, 2011. English. NNT : . pastel-00668301

HAL Id: pastel-00668301
https://pastel.hal.science/pastel-00668301

Submitted on 9 Feb 2012

Thèse de doctorat de l'École Polytechnique

Spécialité : Mécanique

présentée par

Matthieu Caruel

Mechanics of fast force recovery in striated muscles

préparée

au Laboratoire de Mécanique des Solides (CNRS UMR 7649)

Soutenue le 11 Octobre 2011 devant le jury composé de

Jean-Marc Allain	Co-encadrant
Dominique Chapelle	Rapporteur
Jean-François Joanny	Président
Karsten Kruse	Rapporteur
Patrick Le-Tallec	Examinateur
Massimo Reconditi	Examinateur
Ken Sekimoto	Examinateur
Lev Truskinovsky	Directeur de thèse

Florebo quocumque ferar

Remerciements

J'adresse mes remerciements au Laboratoire de Mécanique des Solides et à ses directeurs successifs Bernard Halphen et Patrick Le-Tallec. J'associe l'École doctorale de l'École Polytechnique qui m'a permis d'écrire cette thèse dans d'excellentes conditions. Aussi ai-je pu effectuer un séjour de deux mois à Florence dans le groupe du Pr. Lombardi et assister à la conférence de la Société de Biophysique aux USA.

Je remercie chaleureusement Lev Truskinovsky pour son accompagnement durant cette aventure sur la "route du savoir". Sa pugnacité et ses multiples questionnements m'ont permis de toujours approfondir mes recherches.

Cette thèse est également le fruit d'interactions riches avec Jean-Marc Allain. Son sens physique et sa motivation ont été des alliés de choix pour la réalisation de ce projet. Je le remercie pour sa présence et ses conseils avisés.

Je tiens a remercier mes rapporteurs Dominique Chapelle et Karsten Kruse ainsi que les membres de mon jury, Jean-François Joanny, Patrick Le Tallec, Massimo Reconditi et Ken Sekimoto, pour les discussions intéressantes que j'ai pu avoir avec chacun et pour l'attention qu'ils ont portée à mon travail en particulier dans la relecture du manuscrit.

Le passage vers la bio-mécanique opéré pendant ces années aurait été impossible sans la contribution de Vincenzo Lombardi et de toute l'équipe du Laboratoire de Physiologie Florence qui m'ont accepté parmi eux au printemps 2010 : Marco Linari, Gabriella Piazzesi, Massimo Reconditi, Elisabetta, Marco, Luca e Luca, Pasquale sans oublier Mario. Je les remercie d'avoir partagé avec moi leurs connaissances extraordinaires de la contraction musculaire dans une ambiance toujours chaleureuse.

J'ai également eu la chance de rencontrer Tony Lelièvre et de travailler avec lui au cours de cette dernière année. Merci pour ces longues heures, très appréciées, passées à élaborer l'ébauche du modèle équivalent. J'espère que ce travail se poursuivra.

A mes très estimés collègues de thèse, Raman et Pierre, je tiens à dire toute ma reconnaissance. Ils m'ont beaucoup apporté et avant tout, leur amitié. Rien de plus agréable et stimulant que de travailler avec ses amis.

A toute l'équipe du LMS et en particulier Alexandra, Christiane et Christian j'adresse un grand Merci pour leurs compétences et leur soutien dans les diverses démarches administratives et soucis informatiques.

Ils n'ont pas nécessairement contribué directement à mon travail de thèse ; néanmoins je n'aurais pas autant progressé au saxophone sans le concours du LMS jazz band. Merci donc à Eva, Nicolas, Mathieu, Marc, Anders, Gérard, Raman, Gauthier et Camille pour ces midis funk. J'associe les thésards du LMS qui créent l'ambiance unique de ce laboratoire.

Merci à Jérôme pour son soutien scolaire.

J'adresse mes remerciements à mes parents pour leur soutien et leurs encouragements ainsi qu'à mes amis et à mes proches.

Enfin, un vibrant Merci à Laëtitia pour avoir été là chaque jour.

Contents

Introduction

Muscles perform various functions in living organisms: they control the volume of hollow organs, pump blood and drive body locomotion. Different types of muscle are specialized for different tasks. In this Thesis, we are focusing on *skeletal muscles*.

Although the mechanism of contraction is basically the same for all types of muscles, skeletal or striated muscles are probably the most natural object to study the *general principles* of muscle contraction. First, striated muscles are geometrically simple because of their mostly one-dimensional arrangement. Second, skeletal muscle fibers have an almost crystalline microstructure, allowing one to use X-ray diffraction techniques to measure displacements at the nano-meter scale. Most importantly, this structural simplicity makes adequate even the models with *minimal geometrical complexity*.

In this Thesis we attempt to answer two fundamental questions of muscle mechanics originating from experimental observations and not yet explained satisfactorily by the existing theories. These question are:

1. *Explain the pronounced difference in the rate of mechanical response of striated muscles in soft and hard devices (Edman and Curtin, 2001; Piazzesi et al., 2002a, 2007).*
2. *Explain the well documented heterogeneity of half sarcomere lengths observed in the broad physiologically relevant range (Rassier and Pavlov, 2010; Telley et al., 2006b).*

While answering these specific questions we had to deal with a much more general question which we formulate as follows:

3. *Is the power-stroke a purely mechanical phenomenon or does it require ATP the hydrolysis for its functioning ?*

We recall that at the microscale, skeletal muscles can be viewed as an assembly of parallel fibers. Each fiber has a striated structure originating from the series arrangement of sarcomeres. The sarcomere is a generic contractile unit of every muscle (not only skeletal muscles): it contains two types of filaments, actin and myosin. Actin is a helical fiber with periodic arrangement of attachment sites. The myosin filament is a bundle of motor proteins (myosin II) that are connected to a backbone and point out towards the surrounding actin filaments. Actin and myosin interaction is ultimately responsible for muscle contraction.

Myosin consumes energy which is released during ATP hydrolysis. This allows it: to attach to the actin filament to form what is called a *cross-bridge* (step 1), to generate an incremental force called the *power-stroke* (step 2), to detach form the actin filament (step 3) and finally to 'recharge' the power-stroke mechanism (step 4). By cyclically going through those four steps known as the Lymn–Taylor cycle, the myosin motors pull on actin filaments, generating the shortening of the sarcomere and thereby producing a macroscopic force.

The main goal of this Thesis is to understand the inner mechanical working of the power-stroke mechanism (step 2). While the whole Lymn-Taylor cycle requires ATP supply, the power-stroke is believed by many to be taking place at such short time scales (milliseconds) that it can be considered as a *mostly mechanical phenomenon* which is not rate limited by the ATP delivery/kinetics. In this sense, the power-stroke is the perfect object to be studied by means of mechanics. In view of the small sizes of the 'mechanical parts' involved (nanometers), the classical mechanical picture should be of course augmented by taking temperature induced fluctuations into account.

Power-stroke has been thoroughly studied experimentally through the transient responses of single muscle fibers to fast loadings. In this Thesis, we contribute to the rationalization of the results of these mechanical experiments and also propose new experimental set-ups.

On the modeling side, muscle contraction is usually associated with a set of chemical reactions among a finite number of states (detached pre-power-stroke ↔ attached pre-power-stroke ↔ attached post-power-stroke ↔ detached post-power-stroke, etc ...). The response of the system strongly depends on the transition rates characterizing these reactions. To match experimental data, some researchers find it necessary to introduce more and more chemical states which they interpret as 'sub-strokes'. While these new states are usually not clearly linked to specific chemical species, the additional chemical constants (which are actually functions of the mechanical variables in the case of muscle) bring new curve fitting possibilities.

In this Thesis we abandon the phenomenological path of chemo-mechanical models and pursue an approach based on a consistent mechanical modeling of the power-stroke mechanism. More specifically, instead of a set of discrete states, we consider a continuum of states and replace the phenomenological assumptions regarding rate functions by the study of stochastic dynamics in a multi-dimensional energy landscape. This approach has the advantage of capturing the mechanical response of the sarcomere lattice within a framework based on a small set of parameters rather than a set of fitting functions. One outcome of our model is a mechanical interpretation of the rate constants in the conventional chemo-mechanical models of the power-stroke, in terms of mechanical and anatomical characteristics of actin and myosin fibers.

Our main result is a quantitative model of a half-sarcomere which is in full agreement with experiments. We consider the attached myosin heads as a set of parallel bi-stable springs with a non-convex bi-quadratic potential responsible for the conformational change. Following experimental evidence, we incorporate into the model, the linear elasticity of myofilaments (actin and myosin filaments) which introduces a mean-field type interaction between the cross-bridges and generates collective effects. We find that the model with just 8 parameters (!) reproduces rather well the experimental data on fast force recovery after shortening, including the mysterious difference in time scales of mechanical experiments in hard and soft devices (imposed displacement and imposed force known in muscle as load clamp/isotonic and length clamp/ isometric settings). Our model also reinforces the opinion that the power-stroke mechanism is characterized by negative stiffness and operates in an inherently unstable regime. We show that this instability leads to highly inhomogeneous response of a multi-sarcomere chain which is in agreement with the growing experimental evidence.

In a separate development, we have proposed a way to rigorously replace the stochastic dynamics of many (~ 300) interacting cross-bridges by an effective stochastic dynamics of a single point in a one-dimensional configurational space. Such model reduction allows one to construct effective algorithms dealing with stochastic evolution of a chain of interacting sarcomeres paving the way towards building an adequate model of a whole muscle fiber.

The manuscript is organized as follows:

Chapter 1 contains a brief account of basic muscle anatomy and physiology. In particular, we review the mechanism of muscle contraction and discuss mechanical experiments that contributed to the understanding of the cross-bridge behaviour.

Chapter 2 is focused on the modeling of the power-stroke viewed as a sub-system of a more general contractile machinery. After a review of the previous theoretical and experimental work we summarize the proposed model and introduce the main non dimensional parameters.

In Chapters 3–5, we present a study of the mechanical response of our model system in hard and soft device loadings.

First, in Chapter 3, we neglect the effects of temperature and present an account of local and global minima of the mechanical energy of the system. At this stage, the crucial difference between the behaviours in hard and soft devices is revealed and linked to the presence of the mean field elastic interaction between different cross-bridges.

In Chapter 4, the temperature is added to the picture. We perform the analytical computation of the free energy and study the detailed structure of both the isotherms and the adiabats.

The kinetic response of a half-sarcomere to ramp loadings is studied in Chapter 5 where we simulate numerically a large system of stochastic ordinary differential equations. The study of the characteristic rates in different loading conditions shows the phenomenon of ‘kinetic trapping’ which we link to the presence of the mean field interaction among the cross-bridges. We show that this phenomenon is more pronounced in soft device than in hard device (in accordance with experiments).

In Chapter 6 we develop a reduced version of our model, with only one collective variable. We show that such a simplified model still allows us to capture rather well the mechanical transients exhibited by the original model.

In Chapter 7, we perform some benchmark simulations of the mechanical response of a half-sarcomere by using a realistic set of parameters. We first show in detail how the parameters can be extracted from the experimental data. Based on the quantitative comparison of the theory with experiments, we conclude that, at ambient temperatures, a single half sarcomere behaves as a ‘cold system’ which is characterized by negative stiffness and is inherently unstable. We propose several mechanisms of active stabilization requiring continuous energy supply. In the same Chapter, we also briefly discuss the role of strain inhomogeneity inside individual half-sarcomere and study additional mechanisms that may get involved during stretching (second head, detachment)

Finally in Chapter 8, we study the collective behaviour of a chain of half-sarcomeres connected in series. We find that the response is markedly non affine. In contrast to the behaviour of a single half-sarcomere, the whole chain exhibits small but positive effective stiffness and operates in a stable regime.

The last Chapter contains our conclusions.

Chapter 1

Basic muscle anatomy and physiology

To understand the mechanics of muscle contraction and to interpret the experiments carried out on muscle proteins and muscle fibers, it is natural to first turn to the basics of muscle anatomy and physiology. After the principles of muscle contraction are clarified, we present some typical mechanical experiments revealing the inner working of single molecules involved in active force generation.

Contents

1.1 The background

In this section, we introduce the basic anatomical and physiological concepts that are necessary to understand this manuscript (Alberts et al., 2008; Tortora and Derrikson, 2009).

1.1.1 Muscles in human organism

Muscles are contractile tissues, that play a variety of roles in living organisms. The most visible one is to allow motion of the body by either exerting forces on joints or pulling on the environmental surfaces. More precisely, muscle tissue accomplishes at least 4 different tasks in the human body:

1. It produces movement by coordinated displacements of the bones. The most important example is locomotion.
2. It stabilizes a posture through continuous contraction. For example, neck muscles are constantly contracting in order to keep the position of the head of a standing up person.
3. It regulates organs volume. In particular, sphincters prevent leakage from hollow organs such as the stomach or the bladder.
4. It displaces substances in the organism. For instance, repeated contractions of cardiac muscle pump the blood while muscle tissues around blood vessels regulate the flow rate.

Muscles are highly specialized in order to accomplish different tasks. One distinguishes 3 families of muscles which differ essentially by their regulation processes and by the spatial organization of their constitutive fibers.

Smooth muscles are mostly present in digestive organs, around blood vessels, along air ways, and even in erector muscles of hair. Smooth muscle cells are elongated ellipsoids of 30 to 200 μm long. Inside each cell the contracting fibers are arranged almost randomly so the contraction is close to being isotropic. Smooth muscle are autorythmic: they contract without stimulation by the central nervous system and are instead activated by local electric signals.

Cardiac muscles are found only in the heart and are also autorythmic. Their fibers are 50 to 100 μm long and 14 μm wide. The organization of the fibers is less isotropic than in smooth muscles but still one finds there connected fibers constituting a ramified network which, during contraction, exerts an isotropic stress.

Skeletal muscles are the main elements of body locomotion. They are fixed to the bones by tendons. Skeletal fibers are long, non ramified cells (from 100 μm to 30 cm long and 10 μm to 100 μm wide) that confer a preferred orientation to the muscle. Skeletal muscles elongate and apply stress in a uni-dimensional manner. Their contraction is faster than for other types of muscle and is directly triggered by the central nervous system.

In the present work, we focus on single muscle fibers. As we shall see in the following sections, the muscle fiber is highly organized, almost crystalline, which facilitates both observation and modeling. However, the principles of active force generation revealed by the study of skeletal muscles, remain valid for other muscle types as well.

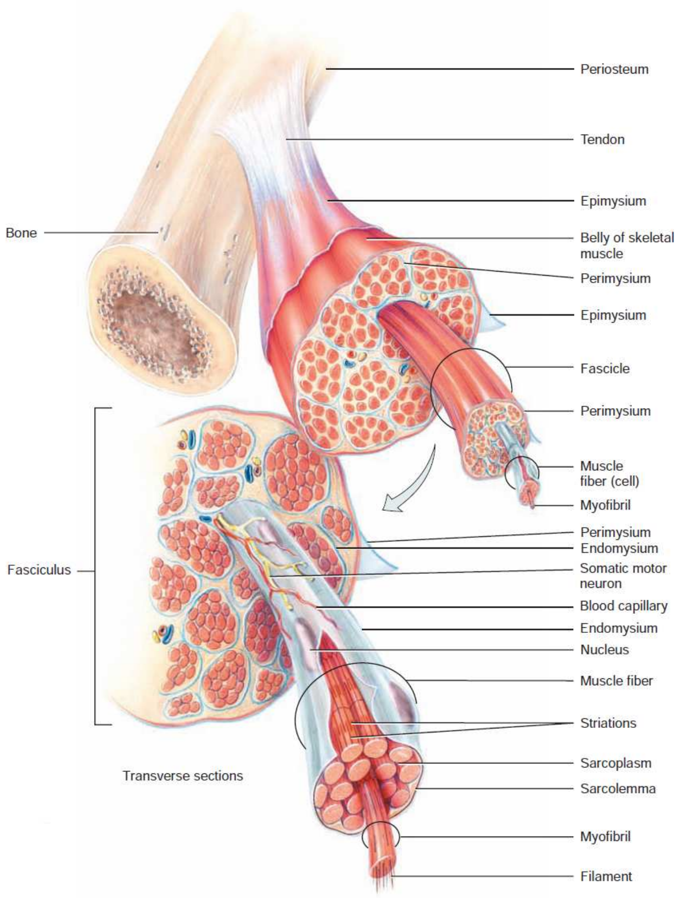

Fig. 1.1 – Representation of a skeletal muscle and its multiscale organization. Muscle is an ensemble of fascicles. Each fascicle contains muscle cells. Muscle cells are also called fibers. They span the whole fiber length. Each fiber is composed of myofibrils; each one being a crystalline array of interdigitated filaments. Adapted from Tortora and Derrikson (2009).

1.1.2 Anatomy of a skeletal muscle

Fascicles and muscle fibers

A skeletal muscle is a multiscale tissue (see Fig.1.1). Typically, a human skeletal muscle is a few cm long and less that 5 cm wide. We can distinguish, in a transversal cut, bundles of about 1 mm diameter called the fascicles. Each fascicle contains 10 to 100 parallel muscle fibers. A muscle fiber is a multi-nuclei cell that spans the whole length of the tissue (see Fig.1.2). Muscle cells do not divide and their number does not change during the adult life. Their cytoplasm contains hundreds of 2 μm wide myofibrils that are covered by a network of tubes called the transverse tubules whose role is to deliver the chemicals that trigger the contraction (see section 1.1.3 and Fig.1.9).

The sarcomere

Under the transmission electron microscope, one can see that myofibrils exhibit, along their longitudinal axis, a very regular succession of dark an light bands. These striations are present in both skeletal and cardiac muscle fibers justify the term: *striated muscles*. Dark and light bands are due to periodic succession of contractile units called *sarcomeres* (Fig. 1.3). Each sarcomere is about 50 nm wide and 2.4 μm long so the region between

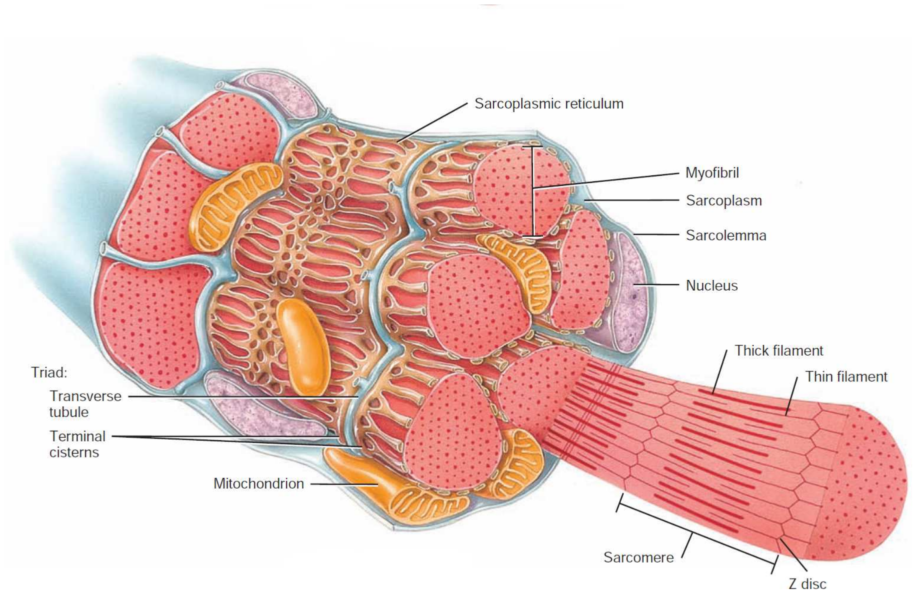

Fig. 1.2 – **Detailed representation of a muscle fiber**. Adapted from Tortora and Derrikson (2009).

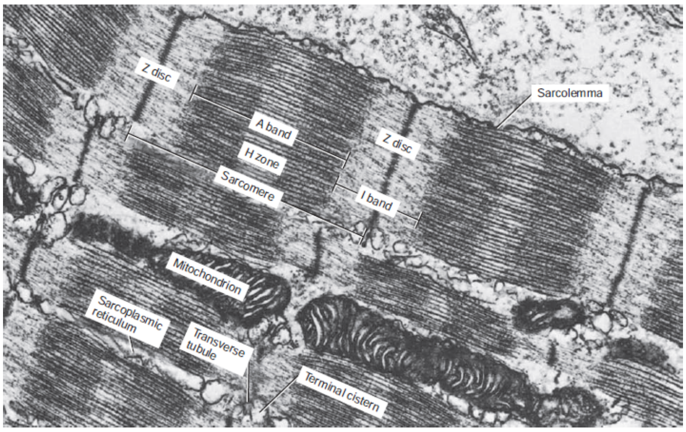

Fig. 1.3 – **Transmission electron micrograph of a myofibril**. Each sarcomere is about 2.1μm long. Adapted from Tortora and Derrikson (2009).

the two light bands is in fact a parallel arrangement of $\sim$1000 sarcomeres. Note that a 10 cm muscle fiber contains about 10^{15} sarcomeres with $\sim 10^9$ sarcomeres in the cross section and $\sim 10^6$ sarcomeres along the length.

The fibrous aspect of the sarcomere is the consequence of the presence of interdigitated myofilaments: the actin (or thin) and myosin (or thick) filaments, that can overlap and cross-link. The myosin filament is an assembly of molecular motors (the myosins) that can bind to the actin filament to form *cross-bridges*. We specify the structure of the thick and thin filaments in the next paragraph.

In Fig.1.3 we show the striated structure of myofibrils in more details. One can easily identify:

- The darker A–band spans the region where, in the sarcomere, the actin and myosin filaments overlap. In the middle of the A–band, the H–zone corresponds to bare segments of thick filaments where there are no myosin motors. The M–line, where different thick filaments are cross-linked, is located in the center of the A–band.
- The I–band is brighter and corresponds to a zone where there are no thick filaments

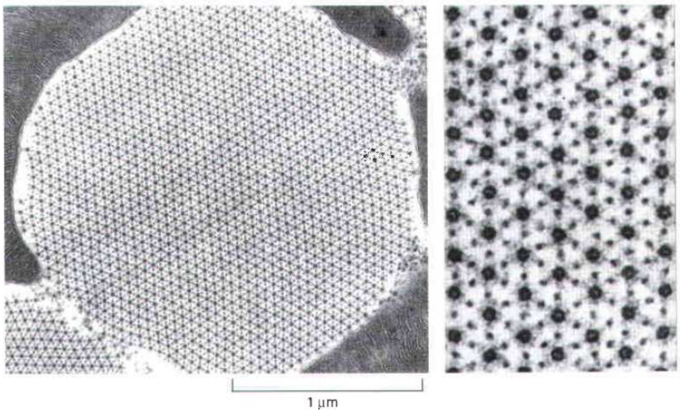

Fig. 1.4 – **Cross section electron micrograph of an insect myofibril**. See the almost crystalline hexagonal alternation of thick (darker spots) and thin filaments (lighter spots). From Alberts et al. (2008).

	diameter	cross-section	relative quantity	per muscle
thin filaments	8 nm	50 nm^2	3000/myofibril	100.10^9/muscle
thick filaments	10 nm.	80 nm^2	1500/myofibril	50.10^9/muscle
myofibril	2 μm	3 μm^2	700/fiber	35.10^6/muscle
fiber	50 μm	2000 μm^2	500/fascicle	50000/muscle
fascicle	1 mm	1 mm^2	100/muscle	

Tab. 1.1 – **Main anatomic components of a muscle with their characteristic scale**. From Tortora and Derrikson (2009).

overlapping the actin filaments. The Z–disk that separates two adjacent sarcomeres is located in the middle of the I–band.

In the cross section of the myofibril (see Fig.1.4), the alternation of thick and thin filaments (thick filaments form darker spots on the micrograph) forms an almost perfect hexagonal lattice. In Tab.1.1, we summarize the main elements that constitute the muscle fiber together with their characteristic size and their quantities.

Myofilaments and molecular motors

We now turn to the structure of actin and myosin filaments:

- The actin filament (also called thin filament) is 8 nm wide and 1 μm long. It is a double helix built with polymerized actin monomers as one can see in Fig.1.6 and Fig.1.9. Each actin monomer has a 5 nm diameter and the helix has a periodicity of about 36 nm. The actin monomers are surrounded by a proteins called tropomyosins are activated in the presence of calcium ions. When activated, tropomyosin flips and reveals the actin monomers to which the surrounding myosin can bind; otherwise, the actin monomers remain hidden and unable to bind myosin (see Sec.1.1.3).
- The myosin filament (thick filament) is an arrangement of ∼300 myosin II molecules. The ensemble of myosins is a triple helix with a myosin head projected every 14.5 nm (Fig.1.6B).

Myosin II is a molecular motor: an enzyme that is able to convert the chemical energy carried by the ATP [1] into mechanical work. In the presence of ATP it undergoes time-periodic

---

[1] Adenosine triphosphate

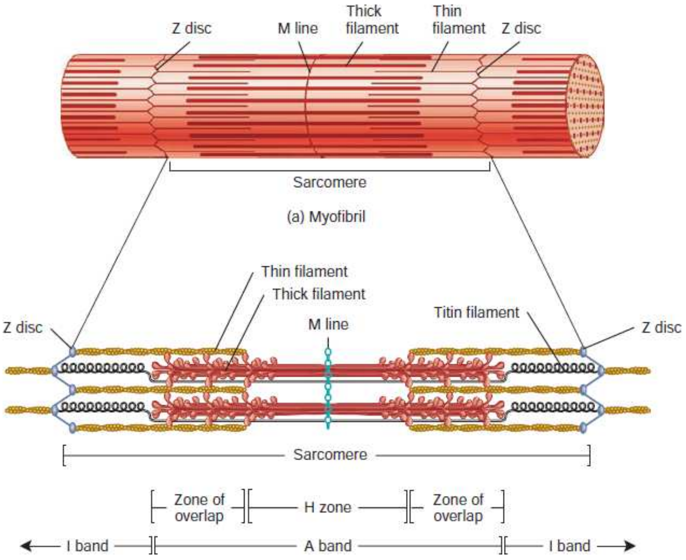

Fig. 1.5 – Schematic representation of a sarcomere. From Tortora and Derrikson (2009)

conformational changes in the vicinity of the actin filament to which it successively attaches and detaches (see section 1.8). This protein has 2 globular heads (S1) whose tails are assembled in a helix (see Fig. 1.6 A). In the sarcomere, the tails of different myosins are packed together and constitute the backbone of the thick filament from which all the 300 heads project outward towards the surrounding actin filaments (see Fig. 1.6 B). The part of the tail that points out of the thick filament backbone is called S2 and the part inside the thick filament is called the light meromyosin (LMM, Craig and Woodhead, 2006). Together, S1 and S2 segments are called the heavy meromyosin (HMM). The fine structure of myosin S1 will be discussed in Sec.2.1 where we focus on the power-stroke proper.

There exists a large variety of molecular motors. Each family of motor accomplish specific tasks in the living organisms. For example, in the cytoplasm of cells, kinesins and dyneins are molecular motors that carry vesicles along the microtubules. Molecular motors can be classified in two families (for a more detailed introduction to molecular motors we refer to Howard (2001) and references therein):

- Processive motors act individually in the living environment. The time the motor spends attached to the filament (not necessarily actin) is large compared to the time it spends detached (high duty ratio). Those motors have two *legs* and *walk* on the filament. Myosin V and Kinesin I are examples of such proteins.
- Non-processive motors act in a collective fashion like *rowers* (while processive motors are sometimes called *porters*). The attached time to the filament is small compared to the detached time, so the motors spend a small fraction of time performing the work (low *duty ratio*). Myosin II responsible for muscles contraction belongs to this second category.

So far, we have not mention yet another sarcomere protein: titin. This giant molecule (the biggest in the organism), spanning the whole sarcomere length and anchored on the Z-disks (see Fig.1.5), contributes to passive elasticity of the muscle and allows the muscle to preserve its integrity when the latter is stretched beyond the overlap between actin and myosin fibers (Leonard et al., 2010).

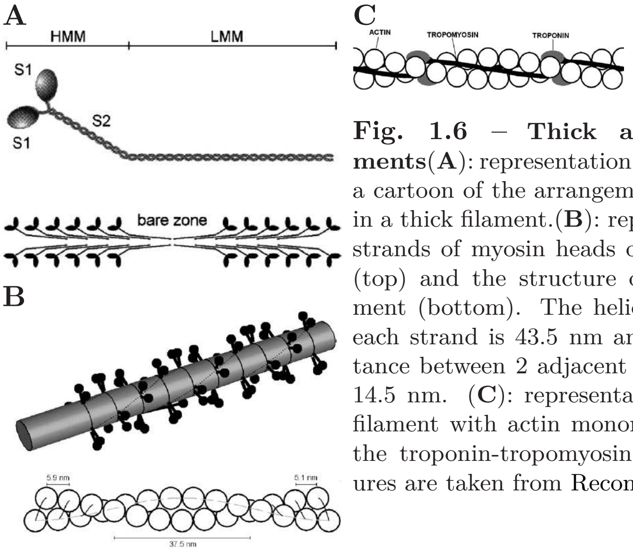

Fig. 1.6 – Thick and thin filaments(A): representation of myosin II and a cartoon of the arrangement of myosin II in a thick filament.(**B**): representation of 3 strands of myosin heads on the backbone (top) and the structure of an actin filament (bottom). The helical repetition of each strand is 43.5 nm and the axial distance between 2 adjacent myosin heads is 14.5 nm. (**C**): representation of the thin filament with actin monomers covered by the troponin-tropomyosin complex. Figures are taken from Reconditi (2006).

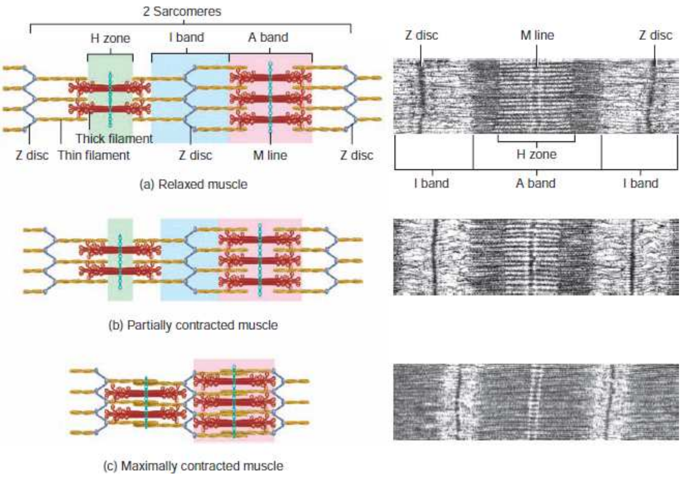

Fig. 1.7 – Muscle contraction at the scale of the sarcomere. On the left column: a cartoon representing the sliding of the filaments during contraction. On the left column: an electron myograph of a contracting sarcomere. The width of the A band (dark) remains constant while the I band (white) shortens. From Tortora and Derrikson (2009)

1.1.3 Physiology of muscle contraction

The sliding filament theory

The basics of the sliding filament theory were developed by A.F Huxley and H.E Huxley in the 1950's. The improvement of electron microscopy and X-ray diffraction techniques allowed them to observe the structure of the dark and light bands in muscle myofibrils during fiber contraction (Hanson and Huxley, 1953; Huxley and Niedergerke, 1954). The first contraction mechanism was proposed in a famous article by A.F. Huxley (Huxley, 1957). Huxley argued that muscle contraction is due to a periodic attachment of the cross-bridges between the myosin filaments and the actin filaments (see also Huxley, 1953). The individual attachment phase lasts few tens of millisecond during which the muscle develops force. The maximum force developed during contraction depends on the sarcomere length as we will explain in section 1.2.2.

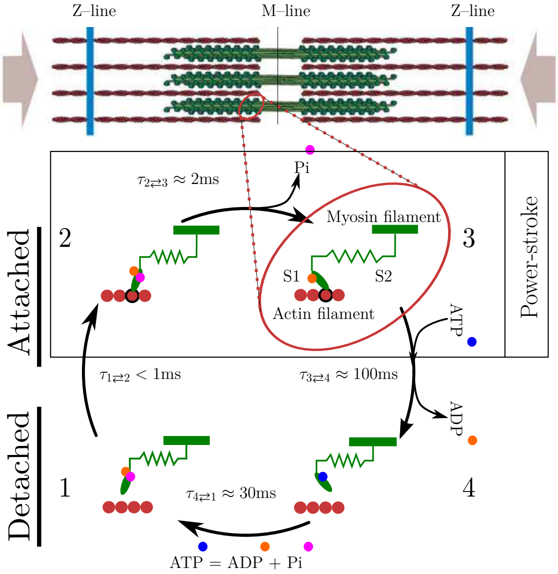

Fig. 1.8 – **Representation of the Lymn–Taylor cycle** with for each step an indication of the characteristic time ms

Molecular mechanism of muscle contraction

As we have already mentioned, filament sliding is induced by the periodic attachment and detachment between the myosin heads and the actin binding sites. In 1971, R.W. Lymn and E.W. Taylor proposed a chemo-mechanical scheme that establishes quantitative relation between the conformational change of myosin head and the ATP splitting (Lymn and Taylor, 1971). Although their proposed cycle has been updated many times since, it remains a reference in the field and has the advantage of representing the inner mechanism of muscle contraction in its simplest form (Fortune et al., 1991; Kawai and Halvorson, 1991; Linari et al., 2010; Smith et al., 2008; White and Taylor, 1976).

The Lymn–Taylor cycle has 4 steps (see Fig.1.8):

- **1→2: Attachment.** The myosin head is first detached from actin in a pre-power-stroke configuration. ATP is in its hydrolyzed form ADP+Pi[2] which has high affinity to actin binding sites. Then, the binding site is open, the myosin heads ends up attached to the actin filament.
- **2→3: Power-stroke** is a conformational change during which the myosin head executes a rotation around the binding site which corresponds to a displacement increment of a few nm towards the Z–line. This movement stretches the elastic tail connecting the head to the backbone and thus generates a force of a few pN. During the power-stroke, phosphate (Pi) is released (Linari et al., 2010)
- **3→4: Detachment** occurs after the power-stroke while the myosin head still remains in its post-power-stroke state. Detachment coincides with the release of ADP (the second hydrolysis product that has low affinity to the attached state) and recruitment of a fresh ATP molecule.
- **4→1: ATP Hydrolysis** provides the energy to recharge the power-stroke mechanism. The myosin head is now searching for the next binding site to restart the cycle.

Each ATP molecule provides $\sim$100 zJ[3] which is equivalent to $\sim$25 $k_b\theta$ ($1k_b\theta \sim 4$ zJ)

---

[2] ADP: Adenosine DiPhosphate; Pi: Phosphate

[3] z stands for *zepta* $= 10^{-21}$

at room temperature. Here, k_b is the Boltzmann constant ($k_b = 1.381.10^{-23}$J.K^{-1}) and θ is the absolute temperature in K.

The characteristic times indicated in Fig.1.8 are obtained from (Linari et al., 2010; Lymn and Taylor, 1971) and correspond to experiments made with actin and myosin in solution. These experiments clearly show that the different steps of the cycle have different time scales. On the one hand, the fastest steps are the attachment of the myosin head S1 to actin ($1 \rightleftarrows 2$) and the conformational change ($2 \rightleftarrows 3$): both last a few ms. On the other hand, the detachment and the hydrolysis of ATP occur, in solution, on a much slower time scale (≈ 100 ms).

Above conclusions based on experiments in solutions have to be considered very carefully when dealing with actual reactions inside the sarcomere:

- In solution, the different molecular motors are not mechanically coupled to a loading device. So those rates do not take into account the effect of the stress in the fiber which clearly influences the kinetics of muscle contraction (Bigland and Lippold, 1954; Edman, 1988; Hill, 1938; Huxley and Simmons, 1971).
- The chemical cycle does not take into account the geometry of the system (*steric effects*). Thus, in solution, the attachment is as a very fast step as soon as the myosin is in its hydrolyzed state. Indeed, if the concentration of actin is sufficiently high, there is a high probability for the myosin to find a binding site. In the muscle, as the binding sites on the actin filament are separated by a distance of 36 nm (Howard, 2001), the hydrolyzed myosin head may stay detached if there is no binding site near its position. Hence, the attachment rate is likely to be slower in the fiber than in solution.

The control mechanisms

The control of skeletal muscle contraction is by itself a broad and active field of research and we only mention here the basic ideas explaining how the Lymn–Taylor cycle is activated and controlled.

A detailed scheme of the regulation loop is presented on Fig.1.9. Activation reduces to the conversion of an electric signal from the moto-neuron (there can be many axon terminals along the same muscle fiber) into an action potential (a depolarization of the fiber membrane). The signal travels along the transverse tubule (see Fig.1.2) and triggers the release of calcium ions Ca^{2+} from sarcoplasmic reticulum into the sarcoplasm. As we explained earlier (see section 1.1), actin filament are covered by tropomyosin, a protein with two conformations controlled by Ca^{2+}. In the presence of Ca^{2+}, tropomyosin flips and allows myosin heads to bind to the actin filaments (see Fig.1.9).

Without continuous electric stimulation, the depolarization of the membrane cannot be maintained and the calcium ions are pumped back into the sarcoplasmic reticulum. As a result the muscle relaxes as tropomyosin flips back into its inactivated conformation.

The degree of activation is controlled not by the intensity of the action potential but by the frequency of the stimulation, each action potential being an ‘1 or 0’ trigger. A single action potential generate a *twitch* that lasts ~ 50 ms, during which the fiber contracts and then relaxes (see Fig.1.10A and B(a)). A low frequency stimulation (*i.e.* $30 \sim 40$ Hz in human) generates a so called *unfused tetanus* where the successive twitches are summed but remain distinguishable (see Fig.1.10B(b) and (c)). At sufficiently high frequency (~ 100Hz in human), the twitches merge and become undistinguishable and the force raises up to a level called *fused tetanus* (see Fig.1.10B(d)).

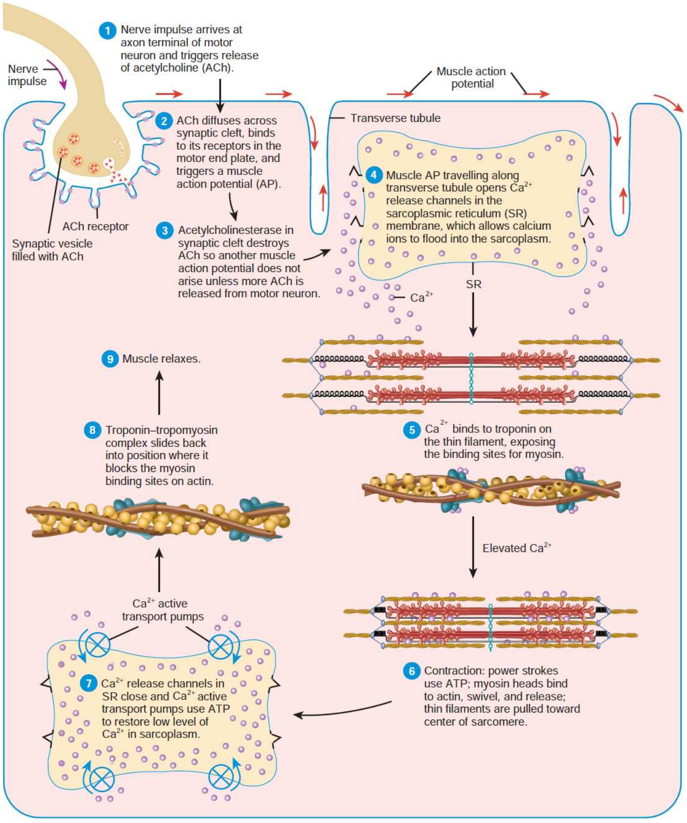

Fig. 1.9 – Summary of the events of contraction and relaxation in a skeletal muscle fiber. A crucial role is played by calcium ions that allow the attachment of myosin heads to actin. From Tortora and Derrikson (2009)

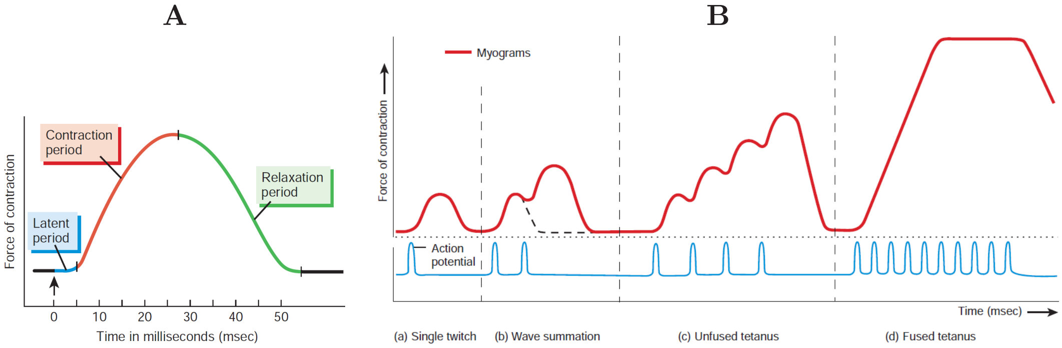

Fig. 1.10 – Electric stimulation triggering muscle contraction. (**A**) Electromyogram (force *vs* time) showing the contraction following a single stimulation (single twitch). (**B**) Twitches summation towards a fused tetanus. From Tortora and Derrikson (2009).

1.2 Mechanical experiments

In this section we briefly review mechanical experiments carried out on muscle fibers. However, we leave the experiments specifically focused on the power-stroke mechanism for the next Chapter.

1.2.1 Typical experimental set-up

The classical experimental set-up allows one to realize length clamp and force clamp experiments on a single fiber (diameter $\sim 100\mu$m) with a feedback control on the sarcomere length (Ford et al., 1977; Piazzesi et al., 1992)

After the fiber is carefully dissected from the animal (usually *sartorius* or *psoas* muscles of the leg from frog or rabbit), it is mounted between a loudspeaker motor that can apply controlled displacements and a capacitance force transducer. The total fiber length is a few mm. The muscle fiber has to be kept in an appropriate solution (called Ringer's solution) containing mainly: NaCl, KCl, $CaCl_2$ and ATP. An optical set-up (Huxley et al., 1981), called *striation follower*, can detect the displacement of sarcomere dark and light bands by means of an array of photodiodes. Two laser beams are pointed on two spots on the fiber separated by 1 mm. The segment between the spots contains about 500 sarcomeres. Under the assumption of the homogeneous sarcomere length distribution between the spots, the length change per sarcomere is deduced from counting the striation entering and leaving the segment during the time of experiment. The resolution is 1μs in time and 1 nm in length. The signal from the optical system enters a feedback loop that allows one to indirectly control the sarcomere length by moving the extremities of the fiber (*length clamp mode*). An alternative is to use the signal from the force transducer in the feedback loop and apply the appropriate displacements on the fiber. This is the way to maintain the force at the desired value (*force clamp mode*).

Some experiments are carried out on intact fibers that need to be electrically stimulated in order to contract. However, typical experiments are performed on skinned fibers (where the cell membrane is removed by chemical agents) offering the possibility to directly control the chemical environment of the myofibrils (for instance, the calcium concentration, see Sec.7.1.3). In that case, the contraction is triggered by the temperature increments instead of electrical impulses (Coupland et al., 2001; Linari et al., 2004).

1.2.2 Muscle fiber experiments

Isometric contraction

We introduced, in section 1.1.3, the notion of *fused tetanus* where the muscle generates its maximal force called the tetanic or isometric force. The isometric force varies with the imposed sarcomere length (sl) (see Fig.1.11). The resulting curve 'tension *vs* elongation' is not obtained by a quasi-static stretching as for classical material. Instead, each point corresponds to a different tetanic stimulation at a given sarcomere length. As it is shown by Fig.1.11A, the isometric force is directly linked to the degree of filaments overlap in each sarcomere. The maximal isometric tension is reached for $2 < sl < 2.5$ μm, which is the physiological regime of muscle contraction. At such sarcomere lengths, all myosin heads are facing an actin filament (full overlap). If $sl < 2$ μm, the isometric tension starts to decrease with sarcomere length even though filaments are in full overlap: when a sarcomere is too short, the internal geometrical structure of the sarcomere is perturbed due to steric reasons (filament buckling, bad attachments conditions, frustration, ...). After $sl > 2.5\mu$m,

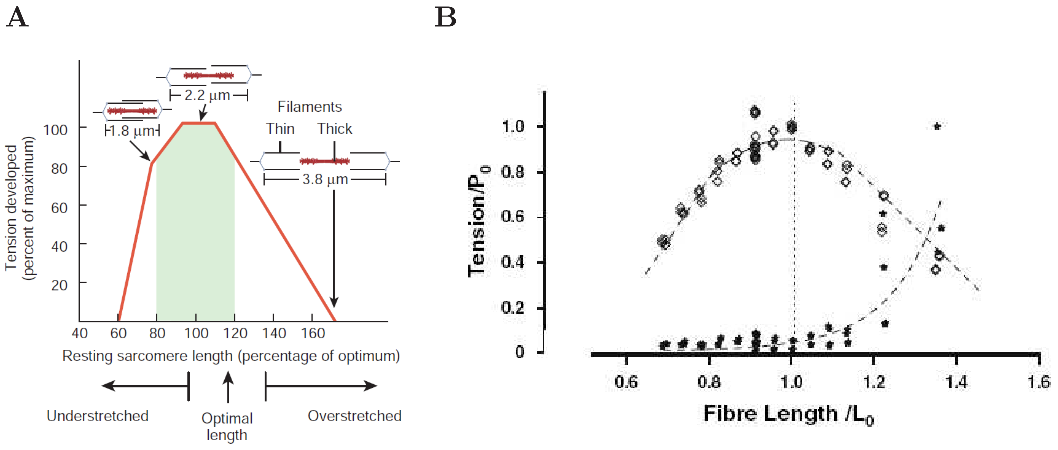

Fig. 1.11 – Tension *vs* sarcomere length relation. (**A**): scheme indicating the relation between the isometric tension and the degree of filament overlap (from Tortora and Derrikson, 2009). The tension reaches a plateau for an optimal filament overlap ($2 < sl < 2.5$ μm). On the ascending limb ($sl < 2$ μm), the tension generation is less efficient for steric reasons. On the descending limb ($sl > 2.5$ μm), the tension decreases as the degree of overlap decreases with sl, instabilities starts to develop. (**B**) Data from rat flexor *allucis brevis* from (Roots et al., 2007). (◇): isometric tension obtained for various sarcomere lengths. (*): tension *vs* strain curve obtained with a relaxed muscle showing an hyperelastic behavior.

the degree of overlap decreases progressively with sl (*descending limb*). In some sarcomeres, the overlap may be lost completely leading to the phenomenon called 'sarcomere popping'. The behavior of the muscle fiber on the descending limb has been studied experimentally by W. Herzog and co-authors (Rassier and Herzog, 2005; Rassier et al., 2003b; Walcott and Herzog, 2008). Most recent experiments (Leonard et al., 2010) imply the role of titin responsible the particular behavior of muscle fibers in this range. A theoretical explanation of popping instability was proposed in (Novak and Truskinovsky, 2002).

In addition to the isometric tension, Fig.1.11B shows how the 'passive tension', obtained during a quasi-static stretching of a non-activated muscle, depends on sarcomere length (Roots et al., 2007). This purely mechanical response is usually interpreted as hyperelastic behavior with a considerable (exponential) increase in stiffness at large deformation. In the physiological regimes (corresponding to the plateau on Fig.1.11), we observe that the contribution of those passive structures is negligible.

Force-velocity relation

Force-velocity relation is one of the main experimental result in muscle mechanics. It is actively discussed since the early 20th century. Even now many models of muscle contraction implement the hyperbolic law derived by A.V. Hill in (Hill, 1938) (see for instance the work of D. Chapelle and co-workers in Bestel et al., 2001; Chapelle et al., 2001). A non-trivial hyperbolic force-velocity relation is a crucial property of active materials. It is shown by A. Asnacios *et al.* that a single cell exhibits a force-velocity relation comparable to the one observed in full muscles (Mitrossilis et al., 2009).

Experimentally, the force-velocity relation is obtained as follows (Piazzesi et al., 2002a, 2007):

First, the muscle fiber is stimulated under isometric conditions till it reaches the tetanus force T_0. From this point the control device is switched to force clamp mode and a force step is applied. As a consequence, the fiber shortens.

After three transient phases, the shortening ends up in a steady state regime (marked

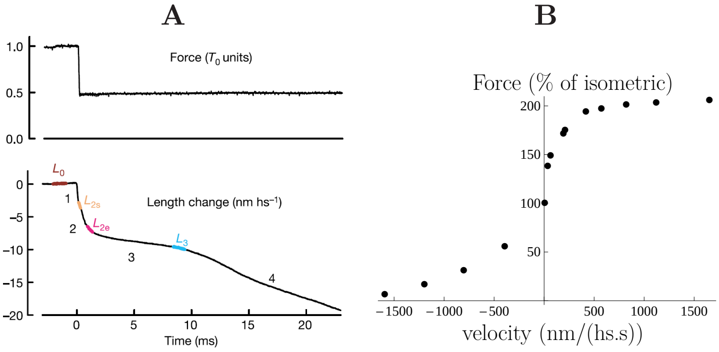

Fig. 1.12 – **Force velocity relation**.(**A**), from (Reconditi et al., 2004). Upper trace: force change normalized to the isometric tension T_0. Lower trace: length change in nm per half-sarcomere (nm/hs). Transients phases 1 and 2 reveal the fast process occurring at the scale of the cross-bridges (see Sec.2.2). Phase 3 represents the onset of attachment detachment process and phase 4 is a steady state regime with shortening at constant velocity (from Reconditi et al., 2004). (**B**): the constant velocity attained in phase 4 *vs* the normalized force (T/T_0). In shortening we recognize the hyperbolic force-velocity relation described in (Hill, 1938). The force for which the velocity is equal to 0 is called the *stall force* . For low stretching ($T/T_0 < 120\%$), muscle 'resists' the applied force before the velocity diverges ($T/T_0 > 120\%$, destruction of the fiber). Data are compiled from (Ford et al., 1985) (for shortening) and (Lombardi and Piazzesi, 1990) (for lengthening).

as phase 4 on Fig.1.12A) and it is at this stage that the velocity corresponding to the given force is extracted. The intermediate phases 1&2 reflect the fast processes (detailed in section 2.2) occurring at the scale of the cross-bridges before the attachment-detachment process starts getting involved (Huxley and Simmons, 1971). Phase 3 reflects the onset of the attachment–detachment process, characterized by the first detachments of cross-bridges (Reconditi et al., 2004).

Fig.1.12B shows the force-velocity relation characterizing the typical frog muscles (Ford et al., 1985; Lombardi and Piazzesi, 1990). In the shortening regime (negative velocities), the muscle acts against the applied load and the dependence of the velocity on the force follows an almost hyperbolic relation (Hill, 1938). The shortening velocity progressively decreases as the force rises up to the *stall force* where the velocity is equal to zero. In the stretching regime (positive velocities), the velocity remains close to zero until the force reaches about 120% of the stall force and then diverges at the point where the force reaches $\sim$ 200% of isometric force (yield) leading to the destruction of the fiber (Katz, 1939). The precise shape of the force velocity curve around the stall force is in fact poorly known because it is probably exhibiting a short region of negative slope, with two velocity regimes existing for the same imposed force. The experimental study of these regimes are complicated by oscillations at different scales (Edman, 1988; Fabiato and Fabiato, 1978; Placais et al., 2009).

The strong asymmetry of the response in shortening and stretching protocols suggests that the behavior of muscles is different in these two regimes. Shortening is a physiological regime: muscle displaces a load and plays the role of a motor. Stretching is a more rare regime in which the structural integrity of the muscle is threatened if the load is too high. For moderate stretching loads, the muscle can 'resist' by keeping the velocity close to zero and in this regime it plays the role of a damper (Lindstedt et al., 2001). It might be that the internal mechanisms operating in those two regimes are rather different which allows them to perform successfully these two different tasks.

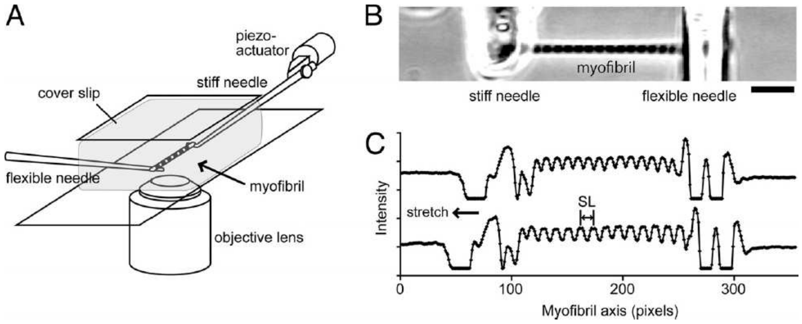

Fig. 1.13 – Example of an experimental set-up allowing the observation of individual sarcomeres. From (Shimamoto et al., 2009). (**A**) Schematic diagram of the mechanical measurements in myofibrils under an inverted phase-contrast microscope. (**B**) The phase-contrast image of a myofibril. (**C**) The intensity profile of phase-contrast image allows the following of individual sarcomere length. (Scale bar, 10 μm.)

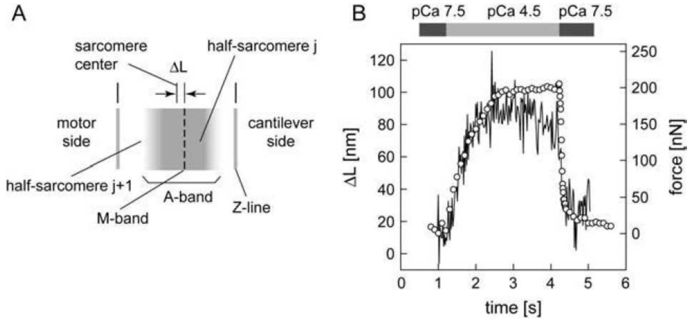

Fig. 1.14 – Displacement of the M-line upon activation by an increase in Ca^{2+} concentration. From Telley et al. (2006a). A myofibril segment containing ~10 half-sarcomeres with fluorescent markers on M-lines and Z-lines is mounted between a cantilever and a force transducer and is observed under a phase contrast microscope during activation by increase in Ca^{2+} concentration. (**A**) Schematic representation of two half-sarcomeres forming a sarcomere, in which the A-band is displaced to the right. The displacement *Delta*L is defined as the distance between the sarcomere center (measured from Z-line to Z-line) and the position of the M-band. Positive displacement is in direction of the cantilever side. (B) example of a displacement trace (outlined) of the A-band of one sarcomere and the corresponding force transient (circles).

1.3 Sarcomere inhomogeneities

1.3.1 Following individual half-sarcomeres

Recent developments in microscopic techniques allow one to follow in detail the striation generated by the succession of sarcomeres in a single myofibril (see *e.g.* Telley et al., 2006a). The experimental precision has reached such a level that it is possible to detect, using phase contrast (Shimamoto et al., 2009), the relative positions of both M-line and Z-lines at the level of a single sarcomere (see Fig.1.13). The contrast can be enhanced by attaching different fluorescent markers to the M-line and Z-Line (Telley et al., 2006a).

1.3.2 Non-uniformity during isometric contraction

Experimentally, the displacement of the M-line of a selected sarcomere can be recorded upon activation under hard device conditions. I.A. Telley was probably the first who systematically observed the development of heterogeneities within neighboring half-sarcomeres (Telley et al., 2006a) but the initial insight were obtained in (Rassier et al., 2003a). These observations were made in physiological range outside the notorious descending limb.

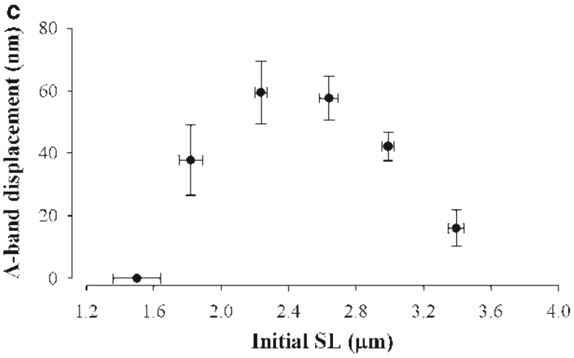

Fig. 1.15 – M-line displacement upon activation of a single sarcomere at different initial length. From Rassier and Pavlov (2010). In this paper a single sarcomere is clamped between two microneedle and activated. The displacement of the M-line indirectly recorded and show that a single isometrically contracting half-sarcomere is not symmetric. Values are means ± SEM

where inhomogeneity is expected and has been studied for a long time (Leonard et al., 2010). In Fig.1.14, we show one of the traces taken at the level of a single sarcomere in (Telley et al., 2006a). The displacement of the M-line (solid line on Fig.1.14B) closely follows the evolution the force development (see ○) and the asymmetric configuration remains stable during activation.

A stable shift of the M-line upon activation of a single sarcomere, held between two microneedles, has been recently reported in (Rassier and Pavlov, 2010). The amount of M-Line displacement depends on the total sarcomere length. The asymmetry disappears at both large and short elongations (see Fig.1.15).

1.3.3 Non-uniformity in response to an external force

At shorter time scales, S.Ishiwata *et al.*, studied in (Shimamoto et al., 2009) the evolution of the distribution of sarcomere length upon applying a fast positive force step (stretching) to an isometrically contracting single myofibril containing 13 sarcomeres (their apparatus is shown on Fig.1.13).

The main results of (Shimamoto et al., 2009) are summarized in Fig.1.16. On (Fig.1.16A, top panel) we show the tension *vs* time trace: the initially contracting myofibril first generates a tension P_0, then reaches a higher level P_1 at the end of the step, and upon sarcomere contraction quickly drops to the level P_2 before finally increasing again upon relaxation of the stretched sarcomeres. The maximal sarcomere length change ΔSL, measured 100 ms after the end of the step reveals 2 different populations of sarcomeres. The first population is ‘resisting’ the applied load and maintain a constant sarcomere length while the second population is ‘yielding’ in the sense that the sarcomere length increases considerably. Such separation into two distinct populations does not persist at large loadings (see Fig.1.16B), where all sarcomere end up in the ‘yielding’ category.

We have not discussed here in details different studies of sarcomere inhomogeneity on the descending limb (of the force *vs* sarcomere length relation) in particular those that have been recently performed by using a hard device protocol at the level of a single myofibrils (Rassier et al., 2003a). Here inhomogeneity may be related to ‘popping’ of certain sarcomeres which is a process outside the scope of our work. To our best knowledge, similar measurements during shortening have not been performed yet.

To summarize, numerous recent experiments reveal that the actively contracting muscle (or sarcomere) is not characterized by a homogeneous distribution of half-sarcomere

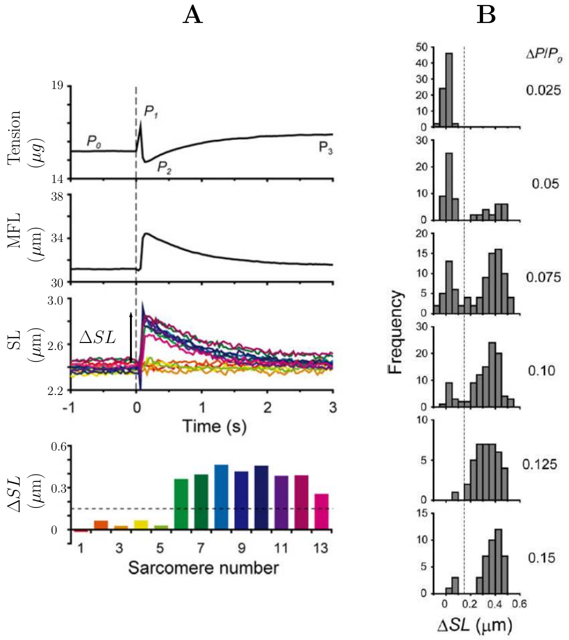

Fig. 1.16 – Evolution of the sarcomere following fast force stretch. From Shimamoto et al. (2009). The elongation of 13 sarcomeres is followed by a phase contract microscope after force steps of various amplitude are applied to the myofibril. (**A**), from top to bottom: tension *vs* time. The isometrically contracting myofibril generates a tension P_0. Then a fast force step is applied to a tension P_1 (rate $0.02P_0$/ms) followed by a relaxation of tension back to P_0 within a few seconds. Mean myofibril length (MFL) *vs* time. Sarcomere length *vs* time for the 13 sarcomeres in the segment under study (the colors correspond to the lower bar plot). ΔSL is the change in sarcomere length measured 100 ms after P_1 and reported *vs* the number of the sarcomere on the lower histogram. The dotted line indicates $\Delta SL = 150$ nm. (**B**): histograms of the observed ΔSL during the response to force steps of different amplitudes ($\Delta P/P_0 = 0.025,\ 0.05,\ 0.1,\ 0.125$, and 0.15). The vertical dotted line indicating $\Delta SL = 150$ nm separates two populations of sarcomeres, one 'yielding' (high elongation) and the other 'resisting' (lower elongations).

lengths. This question has not been addressed in full details from a theoretical perspective. In this manuscript we will propose an explanation of the onset of inhomogeneity outside the descending limb by using purely mechanical arguments.

Conclusions

The mechanical experiments reviewed in this Chapter reveal the complex machinery of muscle contraction in steady state regimes. Power-stroke is an important part of the mechanism whose place inside the bigger picture of muscle contraction has not been firmly established. It has been suggested in the literature (Huxley and Simmons, 1971; Huxley, 1969) that the power-stroke discharge is a purely mechanical process which does not require ATP consumption. In the next Sections, we carefully examine this hypothesis and question its final conclusion.

Very recent experiments revealed unambiguously the presence of length inhomogeneities not only in myofibrils but also inside individual sarcomeres. It remains to propose a mechanical explanation for the onset of these inhomogeneities.

In the next Chapter, we present experimental results focused particularly on the power-stroke and review some theoretical attempts to interpret these experiments.

Chapter 2

Power-stroke: experiments and theories

In this Chapter we describe in more detail the anatomic structure of myosin head and specify the nature of the conformational change that occurs during the power-stroke. Then, we review the main mechanical experiments that give insight into mechanism of the stroke. In particular, we describe the controversy around the power-stroke size interpretation based on either the whole fibers experiments or the single molecule experiments. Finally, we review different theoretical attempts to model the power-stroke and propose a new purely mechanical model of the power-stroke mechanism.

Contents

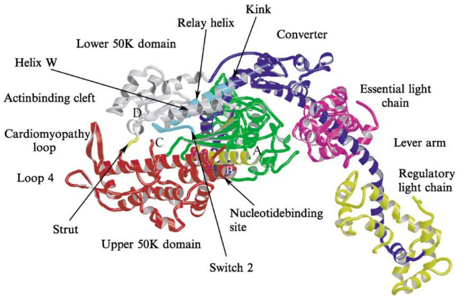

Fig. 2.1 – **Crystallographic structure of myosin sub-fragment S1.** From Geeves and Holmes (2005). Among the different substructures, we distinguish: the actin binding cleft that binds actin monomers, the nucleotide binding site, where the ATP is hydrolyzed and the regulatory light chain that links the head to the backbone. ATP hydrolysis induces a local conformational change in the converted sub-domain which is then amplified by the lever arm. The two structures of pre-power-stroke and post-power-stroke myosin heads are represented on Fig.2.2

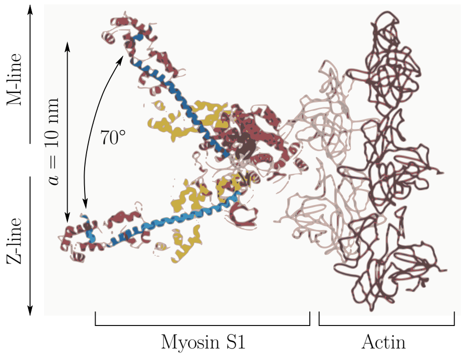

Fig. 2.2 – **Structure of the acto-myosin complex in pre and post-power-stroke**. Adapted from Irving et al. (2000), based on Rayment et al. (1993). The pre-power-stroke structure is oriented towards the M-line (upper structure) while post-power-stroke conformation (lower structure) turns towards the Z-line. Based on the work by Rayment *et al.* (Rayment et al., 1993) and Dominguez *et al.* (Dominguez et al., 1998). The swing of the lever arm by 70° correspond to an axial displacement of 10 nm towards the Z-line.

2.1 Anatomy of the myosin head

We have already briefly described the structure of myosin II in the Introduction (see Fig.1.6). It is then clear that the heavy meromyosin (HMM) has the ability to bind to actin filaments using the two globular parts called S1 whose atomic structure is known from X-ray crystallography (Rayment et al., 1993). In general, myosin head can be represented as a complex 3D arrangement of $\alpha -$ helices and $\beta -$ sheets (see Fig.2.1). The actin binding cleft enables the head to bind actin monomers, the nucleotide binding site is where ATP is hydrolyzed into ADP + Pi. Upon binding to actin, the converter domain undergoes a conformational change, amplified by the lever arm that swings over $\sim 70°$ towards the Z-line thereby generating a displacement of the tip of the lever arm of ∼10 nm (see Fig.2.2). Therefore, the cross-bridge can be viewed as a mechanical switch with one rotational degree of freedom corresponding to the orientation of the converter domain. It has been also shown that myosin heads and in particular, the lever arm has elastic properties (Ford et al., 1977; Huxley, 1957; Huxley and Simmons, 1971; Reconditi, 2006). In a recent work, M. Kaya and H. Higuchi questioned the linearity of the elasticity of the myosin. By pulling on a single molecule (Kaya and Higuchi, 2010) they showed that the elasticity of the head resides principally in the sub-fragment S1. The S2 sub-fragment is much stiffer but, being much longer than S1, can buckle under compressive loading.

2.2 Power-stroke experiments

2.2.1 Methods

As we explained in Sec.1.1.3, the power-stroke lasts only a few milliseconds. Therefore, to study its mechanism on has to design an experiment where the time scale of the ATP cycle does not interfere with the time-scale of the conformational change. The quick recovery experiment first designed by A.F Huxley (Huxley and Simmons, 1971) was aimed at resolving the mechanics and kinetics of the power-stroke by looking at the fast transient response of a muscle fiber following a shortening or stretching ramp. This type of experiment has been developed and performed principally by V. Lombardi, Y.Goldman, K.A.P Edman and K.W. Ranatunga groups in both length and force clamp settings (see *e.g.*, the review by Offer and Ranatunga, 2010). Bellow, we explain in some detail the experiment in length clamp. We have already described the experimental set-up for the force clamp experiment in Sec.1.2.1.

First a single fiber is mounted between the force transducer and the loudspeaker motor. The fiber is then activated at a sarcomere length of about 2.1 nm. It generates an isometric tension T_0 corresponding to the plateau of the tension *vs* sarcomere length relation (see Fig.1.11 and 2.4). After the isometric tension is reached, a fast length step δ is applied with a feedback from the striation follower. The step size is measured in nanometers per half-sarcomere (nm/hs) and it is completed in ∼100 μs (Huxley et al., 1981; Lombardi and Piazzesi, 1990; Piazzesi et al., 1992). The step amplitude is such that the final sarcomere length is still on the plateau region of the tension-sarcomere length relation.

In Fig.2.3(A) we show the evolution of the tension during a length clamp experiment and in Fig.2.4, we show the trajectory of the system in the tension *vs* sarcomere length diagram. The typical range of length changes is between +3 and -12 nm/hs, where the negative sign is for shortening. Experimentally, it is more difficult to separate the different transient steps in stretching than in shortening (Piazzesi et al., 1997). Also, for large stretching, cross-bridges start to detach (Brunello et al., 2007; Piazzesi et al., 1997) and the integrity of the sarcomere can be compromised like in the force-velocity experiments involving the yield (see Fig.1.12).

2.2.2 Interpretation of the fast transients

The response of a single muscle fiber submitted to a fast increment of length or tension can be decomposed into 4 phases:

- $0-150$ μs **(Phase 1)**($t=0$ corresponds to the beginning of the step). The tension (resp. length) changes simultaneously with the length step and reaches a level T_1 (resp. L_1) (see Fig.2.3B and C). Fig.2.5 shows that T_1(○) and L_1(●) are superimposed and show linear dependence on the step size. This suggests that phase 1 corresponds to purely elastic response of the fiber which is also being linear (Fusi et al., 2010; Huxley and Simmons, 1971; Linari et al., 2004).
- 150 μs $-$ 3 ms **(Phase 2)**. This phase starts at the end of the step. In hard device, the tension quickly recovers up to a plateau level called T_2 close to the initial level T_0 (see Fig.2.3B). In soft device, the half-sarcomeres shorten to a new length L_2 determined by a tangent method (see Fig.2.3D). When plotted against the step size, one can see that T_2 is almost equal to T_0 for step amplitude lower than $\sim$ 3nm/hs (see Fig.2.5, $\diamond$). At larger steps, T_2 decreases linearly with the step size. In force clamp, the L_2 curve superimposes with the T_2 curve except in a small interval near

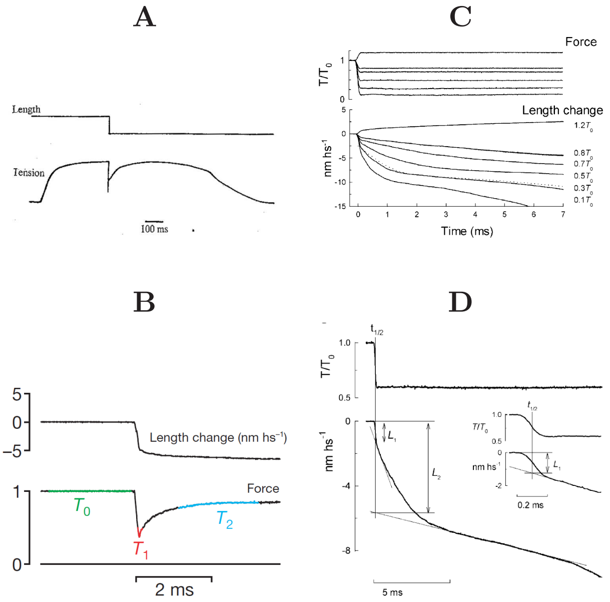

Fig. 2.3 – Quick recovery experiments: fast transient responses. (**A** and **B**): length clamp. (**C** and **D**): force clamp. Upper traces represent the response after a length step (**A**) or a force step (**C**) is applied to the fiber (large time window). The fast transients following the steps are shown with a more refined time scale on (**B**) and (**D**). In (**A**), the rising and decaying phases of the tension trace correspond to the onset (activation) and the end (relaxation) of electric stimulations, respectively. In length clamp experiments (see **A** and **B**), after the step is applied, the tension progressively recovers up to its initial value with a time scale of about 100 ms (**A**). On an expanded time scale (**B**), the tension first decays during the step up to T_1 (elastic response) and then partially recovers to a fraction of the initial tension, called T_2, within ~ 2 ms after the step (*quick recovery*). T_2, is characterized by a plateau on the tension *vs* time curve (barely visible on (**A**)). The fast transients phases 1 and 2 are shown in (**D**) for the force clamp setting. The half-sarcomere first shortens elastically up to L_1 and phase 2 sees an additional shortening up to L_2. Measurement of L_2 is done by a linear extrapolation of phase 3 to the middle of the step (see the construction lines on (**D**)). (**A**), from Huxley and Simmons (1971), (**B**) from Piazzesi et al. (2002b) (**C**) and (**D**) from Piazzesi et al. (2002a).

the initial tension T_0 where L_2 cannot be resolved (see Fig.2.5 (◆) and the discussion bellow). The transition $T_1 \to T_2$ lasts $\sim 1-2$ ms and is called the *quick force recovery*. In force clamp, phase 2 lasts $\sim 1-4$ ms. The time scale of the transition corresponds to the time scale of the power stroke in the cross-bridge cycle. Thus the $T_1 \to T_2$ and $L_1 \to L_2$ transitions are interpreted as the power-stroke event among the attached myosin heads (Chen and Brenner, 1993; Huxley and Simmons, 1971; Linari et al., 1997; Lombardi et al., 1992). At low step amplitudes, the power-stroke is sufficient to recover 100% of the initial tension because of the plateau on Fig.2.5. At larger step amplitudes, even after all the attached cross-bridges have stroked, the initial tension is recovered only partially.

- 3 ms – 0.5 s **(Phase 3 and 4)**. Phase 3 corresponds to the onset of the steady state process. It is signaled by the first detachments of myosin heads visible using X-ray diffraction techniques (Reconditi et al., 2004). During phase 4, in length clamp, the tension rises slowly (the characteristic time is about 100 ms) from the T_2 plateau and finally reaches a steady value that correspond to the initial T_0 (see Fig.2.3A). The final sarcomere length is still in the plateau region of the tension-sarcomere length relation (see Fig.1.11). In soft device, as we saw in Sec.1.2.2, phase 4 is characterized by a shortening at constant velocity. In both length and force clamp experiments, this last phase corresponds to cyclic attachment and detachment of the heads that

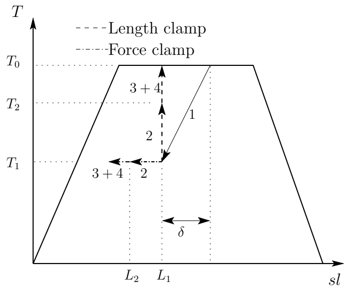

Fig. 2.4 – Schematic representation of the loading trajectory in length and force clamp experiments in the tension-sarcomere length plane (see Fig.1.11). The numbers indicates the different phases of the response in both length clamp and force clamp. Length clamp mode loading trajectory is represented by a dashed line. During phase 1 (continuous line), the same response is observed in length clamp and force clamp modes. During phase 2, in length clamp, the initial tension is partially recovered while the length is held at its final value. Subsequent force recovery is obtained during phase 3 and mostly in phase 4 when the attachment-detachment process gets involved. In force clamp, when a given fraction of the initial tension is attained at the end of the step, the fiber first shortens quickly to a new length L_2 (see also Fig.2.3). After a period of slower shortening (phase 3), the systems reaches a steady state shortening velocity (phase 4). The constant velocity of phase 4 is used to construct the force-velocity relation (see Fig.1.12).

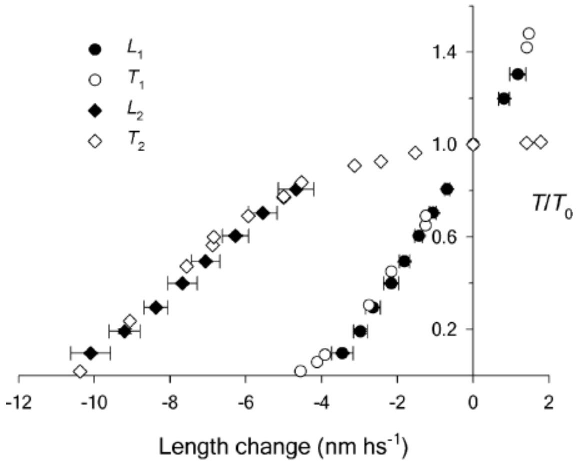

Fig. 2.5 – Quick recovery experiment: tension and half-sarcomere length change at the end of phase 2. T_1(○) and L_1(●) are the tension and half-sarcomere length attained at the end of the loading step. They correspond to the instant elastic response of the fiber. T_2(◇) and L_2(◆) are respectively the tension and half-sarcomere length change attained a the end of phase 2. The $T_1 \to T_2$ and $L_1 \to L_2$ transitions are interpreted as the power-stroke events among the attached myosin heads. In hard device, for low step amplitudes (< 3nm/hs), the full initial tension is restored after phase 2 (see the plateau). Subsequently, for larger steps, the power-stroke capacity is exhausted T_2 (resp. L_2) depends linearly on the applied length step (resp. force step). Remarkably, L_2 is not resolved for low force step amplitudes. Instead several papers report oscillatory response after small force steps (Edman and Curtin, 2001; Edman et al., 1988; Granzier et al., 1990; Sugi and Tsuchiya, 1981). From Piazzesi et al. (2002a).

act in concert like in a tug of war.

Fast transient experiments are used to determine the main characteristics of the power-stroke mechanism (Huxley and Simmons, 1971; Piazzesi et al., 2007). From phase 1, one can measure the elasticity of the muscle in the state of isometric contraction. By doing this experiment on skinned fibers, it is possible to modulate chemically the number of attached myosin heads (we explain in details this type of experiment in Sec.7.1.3, only the main results are presented here). This protocol allows to measure the stiffness of the myofilaments with results similar to those found more directly using the X-ray diffraction techniques (Huxley et al., 1994; Linari et al., 2004, 2009; Wakabayashi et al., 1994). One can also measure the fiber stiffness in *rigor mortis*, *i.e.* when ATP is depleted. In this condition, it is known that all $\sim$300 myosin heads of each half-sarcomere attach to the actin filament (Cooke and Franks, 1980). By knowing the filament compliance, we can then find the cross-bridges stiffness from the overall *rigor* stiffness. The value obtained with this method for frog muscles is about $2 - 3$ pN.nm^{-1} (Piazzesi et al., 2007).

The shortening observed in phase 2 in force clamp experiments is due to the power-stroke event which involves the attached heads. Therefore, after the filament compliance is taken into account, one can interpret the distance $L_1 - L_2$ as the power-stroke size. It ranges from $\sim$ 5 nm at high force ($T \approx T_0$) to $\sim$ 10 nm at low force (Linari et al., 2009; Reconditi et al., 2004). The value at low force is consistent with structural reconstruction for the acto-myosin complex (see Sec.7.1.1) (Dominguez et al., 1998; Rayment et al., 1993).

2.2.3 Length and force clamp experiments: similarities and differences

From Fig.2.5, one could conclude that the length and force clamp settings are equivalent and could simply replace one another in the study of the quick recovery. However, there are two main differences:

1. The results in length clamp experiments clearly show a plateau on the T_2 curve ($\diamond$ on Fig.2.5) while in force clamp experiments, similar plateau has never been resolved (dark diamonds). Experimentally, the measurement of L_2 for small force steps (near the initial tension T_0) appears to be difficult. In particular, oscillations have often been observed after a small force step was applied to an isometrically contracting muscle (Edman and Curtin, 2001; Edman et al., 1988; Granzier et al., 1990; Sugi and Tsuchiya, 1981).
2. In Fig.2.6, we show different rates of the quick force and velocity transients obtained for frog fibers in length and force clamp conditions. The rate is defined as the inverse of the time required to reach the value of force equal to $0.63(T_2 - T_1)$ from the value T_1 in length clamp experiment (or the value of length $0.63(L_2 - L_1)$ from the value of L_1 in force clamp). For length clamp, the rate is plotted against the step size δ (data from Ford et al. (1977)($\diamond$), Piazzesi et al. (1992)($\circ$), and Linari et al. (2009)($\square$)). As we did not find in the literature the measurements of the rate in force clamp, the data represented for force clamp (●) are estimates computed by the ratio L_2/v_2, where v_2 is the velocity of phase 2 reported in (Piazzesi et al., 2002a). Instead of representing the force clamp rate as a function of tension, we represented it as a function of L_2. Therefore, Fig.2.6 juxtaposes the rates of recovery in the same $T_2 - L_2$ conditions by using two different experimental settings. We clearly see that the time needed to complete phase 2 is about 5 times longer in force clamp experiments than in length clamp experiments. To our knowledge, this feature of fast force recovery has not been discussed previously in the literature and one of the objective of our

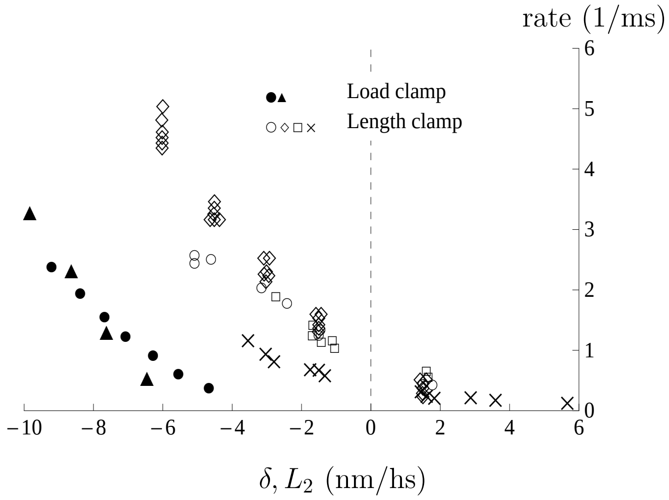

Fig. 2.6 – Quick recovery: rates of recovery. The rate is defined as the inverse of the time taken to reach $0.63(T_2 - T_1)$ from T_1 in length clamp (or $0.63(L_2 - L_1)$ from L_1 in force clamp). The length clamp data (open symbol) are from Ford et al. (1977) (◇), Piazzesi et al. (1992) (◎), and Linari et al. (2009) (□), Huxley and Simmons (1971) (×). Note that the data from Ford et al. (1977) and Linari et al. (2009) are obtain with frog type *rana temporaria* while all other results are from *rana esculenta*. In Ford et al. (1977), the rate is measured as the reciprocal of half time to reach T_2 from T_1. To be consistent, the results presented here are adjusted by a factor 0.5/0.63. The force clamp data (filled symbols) are represented as function of the elongation at the end of phase 2 (L_2). Load clamp data are from: Piazzesi et al. (2002a) (●), Decostre et al. (2005) (▲).

work is to propose the first explanation for this difference. To our best knowledge, no rate data for shortening steps larger than 6 nm are available, probably because, for larger shortening steps, the fiber starts to buckle (see for instance Piazzesi et al. (1992) Fig.2).

We also observe that only a few T_2 and T_1 points are reported on the stretching side in Fig.2.5, and, to our best knowledge, no data are available for do not include stretching increments above 6 nm. It was argued in (Piazzesi et al., 1997) that for stretches beyond 2 nm/hs, cross-bridges start to detach perturbing the measurement. Moreover, the detection of the end of phase 2 in those cases is not clearly marked by the presence of a characteristic plateau on the tension *vs* time curve. In fact, it has been suggested in (Brunello et al., 2007; Piazzesi et al., 1997) that additional mechanism are involved when muscle is stretched. First, in (Brunello et al., 2007), the authors have detected an increase in the instant stiffness of the system which they attributed to the attachment of the second head of the myosin molecule. Second, to explain the slow tension relaxation following a lengthening step G. Piazzesi *et al.* invoked a passive friction mechanism of the detached heads passively interacting with the actin filament (Piazzesi et al., 1997). We investigate these two possibilities within our model in Sec.7.5

2.3 Single molecule experiments

In the previous Section, we presented a family of experiments from which we could extract some information about the mechanism of the power-stroke. These reconstructions can be viewed as a 'top-down approach' as the corresponding experiments are realized on whole muscle fibers. Notice however that we are in fact interested in the force generation at the level of myosin molecules and complicate muscle architecture may actually be an

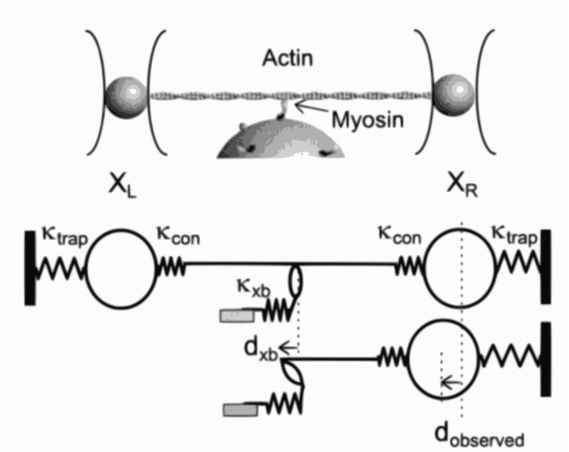

Fig. 2.7 – Experimental set-up using optical tweezers to detect single acto-myosin interactions. The upper panel is a cartoon of the '3 bead geometry' designed by Finer *et al.* in (Finer et al., 1994). A 10 μm actin filament is anchored on two latex beads (~ 1 μm) manipulated by independent optical traps. After the actin filament is put under a tension of $\sim 2pN$, it is presented to a 3^{rd} bead stick to a coverslip and covered with a low density of myosin sub-fragment S1 (or HMM) (see Fig.1.6). Acto-myosin interactions are observed by monitoring the positions X_L and X_R of the beads with a photodetector. Lower panel gives a mechanical representation of the system when a myosin molecule is attached. κ_{xb} is the stiffness of the cross-bridge, linked in series with the actin-bead connection stiffness, κ_{con} and the stiffness of the optical traps, κ_{trap}. Upon attachment, the myosin molecule produces a displacement d_{xb}. Due to the presence of other compliant elements, a displacement $d_{\text{observed}} \neq d_{\text{xb}}$ is measured by the photodetector. All the preparation is immersed in an appropriate solution containing ATP. From Veigel et al. (1998).

obstacle in the study of the microscopic mechanisms of force generation. Therefore, in the nineties, a whole new 'bottom-up' approach has been developed based on the revolutionary development of *optical tweezers*.

2.3.1 Optical tweezers

In 1970, A. Ashkin, showed the possibility to use forces gradients from a continuous laser to trap micron-sized particles (Ashkin, 1970). Later, he reported the first case of dielectric particle trapping by a single-beam gradient force trap (Ashkin et al., 1986). Since then, this technology called *optical tweezers* have found considerable applications in live sciences. Major examples are the studies by C. Bustamante *et al.* of DNA unfolding (Smith et al., 1996) or by J. Spuddish's and J.E. Molloy's groups on molecular motors (Finer et al., 1994; Mehta et al., 1997; Molloy et al., 1995; Veigel et al., 1998). We can also mention another single molecule technique used by T. Yanagida's group which is based on the use of microneedles instead of optical traps for nanomanipulation (Ishijima et al., 1996; Kitamura et al., 1999; Yanagida and Ishijima, 1995).

One of the most important experimental set-ups designed to study single acto-myosin interaction is known as the 'three beads geometry' (Finer et al., 1994). In Fig.2.7, we illustrate the main idea of the method: a 10 μm actin filament is attached to 2 latex beads (diameter $\sim$1 μm) trapped in two different laser beams. A third bead is coated with a low density of myosin molecules and glued to a coverslip. The low density coating is used to avoid multiple myosin attachments to the actin filament. The whole preparation is then immersed in an appropriate solution containing ATP (Veigel et al., 1998).

When the actin filament is brought in contact of the third bead, a single myosin molecule binds to actin and generates a force. This force is transmitted through the actin filament and displaces the two trapped beads whose positions (X_R and X_L on Fig.2.7) are

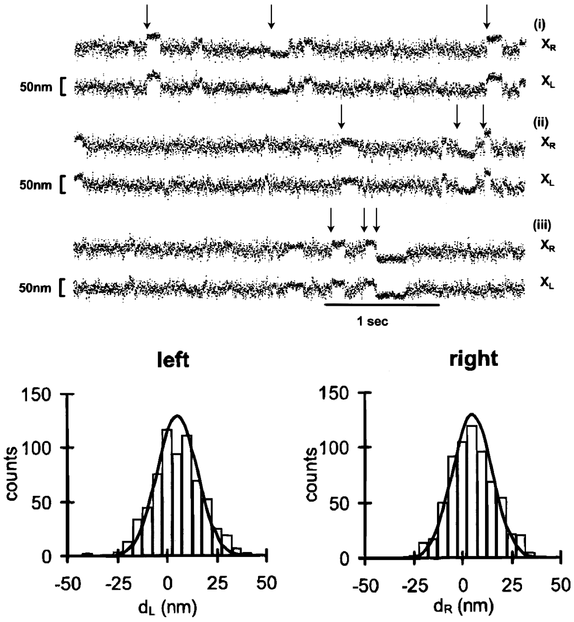

Fig. 2.8 – Displacement traces of trapped beads showing attachment events of myosin molecule. In each panel (i), (ii) and (iii), the upper and lower traces represent the displacements of the right and left bead respectively. The variance of the Brownian motion of the beads is considerably reduced upon attachment of myosin motor. Therefore one can measure the displacement generated by the power-stroke. In addition the change in variance gives information about the stiffness of the system. The lower traces show histograms of the beads displacements during the attachment events (left and right) with Gaussian fit. The mean displacement is 5 ± 10 nm. Adapted from (Veigel et al., 1998).

monitored using a photodetector. To compute the displacement of the myosin molecule from X_R and X_L, one has to take into account the stiffness of all elements of the mechanical pathway (see Fig.1.9, lower panel): κ_{xb}, the stiffness of the myosin itself which one would like to measure, κ_{con} the stiffness of the connections between the actin filament and the trapped beads and finally κ_{trap}, the stiffness of the two laser traps. Note that the actin stiffness is high compared to other stiffnesses involved, therefore its effects on the measurements can be neglected (Kojima et al., 1994). A review of the use of optical tweezers in the study of acto-myosin interactions can be found in (Knight, 2001).

In Fig.2.8, we show three displacement records of the left and right trapped beads (noted i,ii and iii). Some attachment ‘events’ are clearly distinguishable after the significant noise reduction (see the arrows on Fig.2.8). Upon attachment, the two beads undergo a correlated displacement in the same direction. If the stiffness of the trap is low compared to other stiffnesses in the system, then the bead-actin-bead part moves as a rigid body under the action of the myosin stroke. Three major pieces of information can be extracted from theses experiments:

1. If the trap stiffness is low compared to the cross-bridge stiffness, then it is expected that the displacements of the beads reflect directly the power-stroke size. In Fig.2.8, the lower panel shows the histograms of the left and right bead displacements measured after various attachment events. The mean displacement is ∼ 5nm. This value is twice as small as the previous value measured by using the same technique (Finer et al., 1994) principally because in the latter, only one bead displacement as been recorded. Similar values of ∼5 ± 10 nm are reported in (Molloy et al., 1995; Veigel et al., 1998) and also with other single molecule techniques (Kitamura et al., 1999; Yanagida et al., 2000).

2. The myosin stiffness κ_{xb} is determined from the displacement's variance change upon attachment. This is possible if we assume linear elasticity of the different components which leads to a Gaussian distribution of the displacements. In the absence of myosin motor, one can measure the stiffness of the optical trap κ_{trap} by analyzing the displacements of a single trapped bead. Then the displacements of two trapped beads, linked by an actin filament gives κ_{con} provided the actin filament stiffness is large compared to the connection stiffness (Kojima et al., 1994). Finally the stiffness of the cross-bridge is deduced from experiments involving the attachment events. In addition to this analysis of Brownian fluctuations, cyclic loading with and without attached motor provides additional information that leads to similar conclusions (Veigel et al., 1998). Several papers have then confirmed that the myosin stiffness must be around 0.5 pN.nm^{-1} (Knight, 2001; Mehta et al., 1997; Veigel et al., 1998). We recall that the typical stiffness deduced from fiber experiments is about 3 times higher (see Sec.7.1.3 and (Offer and Ranatunga, 2010; Piazzesi et al., 2007)).
3. A feedback loop can be used to constantly adjust the position of the optical trap in order to maintain a constant distance between the two beads. This would correspond to the length clamp set-up for muscle fibers. Using this technique, one expects to measure the maximum force a myosin can produce: the isometric force. J.E. Molloy reports an isometric force of 1.7 pN (Molloy et al., 1995). The isometric force per motor extracted from the whole muscle fiber experiments is in the range of 5 pN so about three times higher.

2.3.2 The power-stroke controversy

One can see that measurements in single molecule experiments and the results from fiber experiments are in contradiction which is a source of controversy in the field of muscle mechanics. First, as we have seen the maximum power-stroke size inferred from fiber experiments is about 10 nm, while single molecule experiments suggest a 5 nm stroke size. This is an average value; for a comprehensive review of stroke size data from single molecule techniques see (Tyska and Warshaw, 2002). An argument against the single molecule experiments is that the orientation of the myosin motor cannot be controlled so it may attach in some sub-optimal way to the actin filament. Therefore the 5 nm stroke may be just a low bound (Veigel et al., 1998). Some measurements with an artificially rebuilt myosin filament have been done by T. Yanagida's group and they report a 20 nm power-stroke size under low force conditions, with presumably less uncertainty on the relative orientation between the myosin heads and the actin filament (Ishijima et al., 1996). This can be taken as an upper bound, in view of the specially engineered geometry in these experiments.

Second, the instant cross-bridge stiffness measured from the whole fiber experiments is about $2-3$ pN.nm^{-1}. The corresponding value is about $0.5-0.7$ pN.nm^{-1} in single molecule experiment (note that A. Lewalle report a stiffness of 1.7 pN.nm^{-1} for *rigor* cross-bridges in (Lewalle, 2008)). The value from fiber level measurements is based on the hypothesis that all cross-bridges contribute to the stiffness in *rigor* condition (Linari et al., 1998; Piazzesi et al., 2007). Moreover, if some *rigor* cross-bridges remain 'slack', then one can expect the stiffness to be even higher than 3 pN.nm^{-1}. This was an argument proposed by J.Howard against the Huxley and Simmons theory (Huxley and Simmons, 1971) of the power-stroke (see (Howard, 1997; Huxley, 1998)).

To summarize, the issue remains unresolved and some independent pieces of evidence would need to appear for this controversy to be settled. Hozwever, recent papers suggest that the results from single molecule experiments have to be reevaluated (see **??**).

2.3.3 The energetics of muscle contraction

One source of additional information is provided by energetics. Several groups have been studying the maximum mechanical efficiency of muscle contraction from the measurement of the maximum power-output and heat release during isotonic shortening (phase 4, see Sec.1.2.2). These studies follows directly from the pioneering work of A.V Hill who first experimentally observed that an isometrically contracting muscle releases heat at a constant rate (Hill, 1938).

When the load is suddenly dropped, the muscle starts to shorten and this shortening is accompanied by an increase in heat liberation that is proportional to the allowed shortening range but does not depend of the load. This phenomenon is known as the Fenn effect. A.V. Hill concluded that the heat per unit length of shortening liberated by a fully activated muscle is a characteristic constant for a given muscle type which he denoted by a. Hence, for a given shortening distance x, the extra heat released is equal to ax. The macroscopic work performed by the muscle against a load T is Tx so that the total energy change during shortening x is $(T + a)\,x$ and the rate of energy liberation is $(T + a)\,\dot{x}$ where $\dot{x}$ is the shortening speed. Experimentally, Hill could directly show that the rate of extra energy liberation compared to isometric contraction varied linearly with the applied load and was zero for $T = T_0$, the isometric tension. Therefore, he derived the following relation directly from macroscopic energetics:

$$(T + a)\,\dot{\epsilon} = b\,(T - T_0) \tag{2.3.1}$$

This phenomenological formula providing the simplest hyperbolic force-velocity relation is often used as a constitutive relation for the whole muscle (see Sec.2.4.1).

If we now follow (Barclay et al., 2010), we can define the mechanical efficiency of a muscle as:

$$\xi_{\text{mec}} = \frac{\dot{\omega}}{\dot{\omega} + \dot{Q}}$$

where $\dot{\omega} = T\dot{x}$ is the mechanical power-output and $\dot{Q} = a\dot{x}$ is the rate of heat production during steady shortening. This value is different from what is sometimes called the thermodynamic efficiency ξ_{therm} which is the ratio of the rate of work and the rate of energy supply provided by ATP hydrolysis:

$$\xi_{\text{therm}} = \frac{\dot{\omega}}{\dot{F}_{\text{ATP}}}$$

where $\dot{F}_{\text{ATP}}$ is the rate of ATP consumption which is presumably higher that $\dot{\omega} + \dot{Q} = (T + a)\,\dot{x}$. This definition of efficiency takes into account the amount of ATP potentially consumed by the the contraction mechanism (for instance ion pumping, see Fig.1.9) and causing deviation from the hyperbolic force-velocity law.

Experiments on whole muscle and on isolated muscle fibers, reported in (Barclay et al., 2010), show that $\xi_{\text{mec}} \approx 50\%$ and $\xi_{\text{therm}} \approx 40\%$. For comparison, the typical efficiency of a car does not exceed 15 % if we consider all the losses in engine, transmission and accessories (U.S. Departement of Energy, 2011). Now the energy provided by the hydrolysis of one ATP molecule is ∼80 zJ or ∼20 $k_b\theta$ at room temperature (θ is the absolute temperature and k_b is the Boltzmann constant). If we assume that there is only one ATP molecule used per cycle (as shown on Fig.1.8), we expect the mechanical work of a single cross-bridge to be $\sim$ 30 zJ or $\sim 7.5 k_b \theta$.

Woledge *et al.* (Barclay et al., 2010), proposed a simple chemo-mechanical model (see the next chapter) which generate experimentally observed shape of the T_2 curve (see Fig.2.5). By computing $\int T_2(\delta)\, d\delta$ they estimate the work done during the power-stroke. Their chemo-mechanical model gives $\sim$ 45 zJ of work. Therefore, we may conclude that the cross-bridge stiffness derived from experimental measurement conducted on muscle fibers gives a realistic prediction of energetics.

On the other hand, from single molecule experiments, one can compute the mechanical work performed during the power-stroke as the product of the stiffness κ_{xb} and the square of the power-stroke size d_{xb}: $1/2\kappa_{xb} d_{xb}^2$ (Barclay et al., 2010). This gives a mechanical work of $\sim$15 zJ (by using $\kappa_{xb=0.7 \text{ pN.nm}^{-1}}$ and $d_{xb} = 5$ nm) which is about a third of the mechanical work inferred from the whole fiber measurements. Hence the value of single molecule stiffness appears to be inconsistent with muscle energetics. However, if one uses the cross-bridge stiffness obtained from fiber experiments in a conventional two states model of the power-stroke (not the special many state model of Barclay et al. (2010)), the resulting T_2 curve exhibits a region of negative slope (see Sec.2.4.3) which is not observed experimentally (see Fig.2.5).

One can see that the debate between the single proponents of single molecule measurements and the experts in fiber measurements is not over. The available techniques do not allow a direct measurement of the mechanical characteristics of the myosin head and of the power-stroke size. Therefore only indirect measurements are used with all the implied uncertainties. Great efforts have been made to match the macroscopic thermodynamics of muscle contraction with the mechanical measurements at the microscale.

The goal of the theoretical work is to contribute to these efforts and to try to reconstruct the macroscopic dynamics from the simplest model of the power-stroke. In this way we can link microscopic and macroscopic data and contribute to the resolution of the existing controversy. Therefore, we now turn to the discussion of the attempts of theoretical modeling of the power-stroke.

2.4 Theoretical modeling of muscle contraction

Before focusing specifically on the power-stroke, we review here several fundamental attempts to understand the mechanisms of muscle contraction. Characteristically, most of them avoid explicit reference to the power-stroke.

2.4.1 Phenomenological models

Historically, the first feature of muscle contraction studied in systematically set experiments was isotonic shortening (see Sec.1.2.2). In 1938, well before the sliding filament theory was put forward, A.V. Hill reported the dependence of shortening velocity on the applied force and measured the heat release during isotonic contraction (Hill, 1938). It was already known at that time that muscles exhibit a linear elastic response when submitted to fast length changes. Therefore to explain his experiments, Hill proposed a simple rheologic model including a linear elastic element with stiffness κ in series with a contractile element governed by a particular constitutive relation. This relation was derived by Hill from the measurements of heat release during isotonic contractions (see the previous

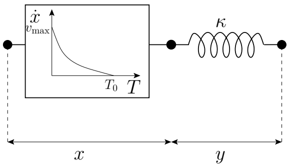

Fig. 2.9 – Phenomenological model proposed by A.V. Hill in (Hill, 1938). A linear elastic element of stiffness κ and strain ϵ_e is coupled in series to a 'contractile' element driven by the hyperbolic force-velocity relation Eq.(2.3.1). $v_{\max}$ is the maximum shortening velocity attained for $T = 0$ and T_0 is the *isometric force* or *stall force.*

Section and Fig.2.9):

$$(T + a)\,(\dot{x} + b) = c, \text{ with } a,\ b,\ c \text{ constant.}$$

The resulting model has been widely implemented into more complex models of muscle contraction. For instance D. Chapelle and co-workers used the relation (2.3.1) in their comprehensive model of heart contraction (Chapelle et al., 2001).

Notice that, in the above class of models, the microscopic molecular mechanism is lumped into a phenomenological relation. Thus Hill's Eq.(2.3.1) gives the hyperbolic the force-velocity which looked convincing because the coefficients turned out to be almost independent on temperature (Hill, 1938). However, the biological origin of these coefficients is unclear and the phenomenology provides no link between the macroscopic behavior and the mechanisms occurring at the microscale. After the sliding filament process has been discovered, A.F. Huxley proposed a model of the acto-myosin interaction that was supposed to link the macroscopic force-velocity relation with the details of the microscopic attachment-detachment process involving myosin motors (Huxley, 1957).

2.4.2 Huxley's 1957 model

In 1957, the details of the coupling between the cross-bridge mechanism and the ATP hydrolysis process were still not clear (the Lymn–Taylor cycle was published in 1971 Lymn and Taylor (1971)). A.F. Huxley proposed a model whose goal was to quantify the relative dynamics of actin and myosin filaments during contraction. The ideas contained in his 1957 paper form the baseline of almost all muscle contraction models published ever since (see the coming Sections). The model is illustrated on Fig.2.10.

In Huxley's model, the myosin head is represented by a linear spring connected to the backbone. The strain of the spring is denoted by x. Huxley assumed the existence of binding sites on the actin filament. The head undergoes thermal fluctuations that can stretch or compress the spring in a symmetric manner. Rectification of the noise is brought in by the binding and unbinding rate functions f and g. The latter describe the effect of chemical reactions which control the affinity of myosin for actin. Our Fig.2.10B shows how f and g may depend on x. Huxley supposed that attachment can only occur within an distance h from the resting position of the head therefore f is maximal at $x = h$ (to favor high force generating cross-bridges) and decreases with decreasing x. The rate of detachment g is assumed to be very high at $x < 0$ to prevent cross-bridges from being compressed. Otherwise, g is finite everywhere to ensure that when muscle activation stops, all heads can detach. The fact that the cross-bridges preferably attach in a stretched configurations is the 'ghost' of the power-stroke mechanism, the idea that in some way, energy must be stored and discharged upon attachment.

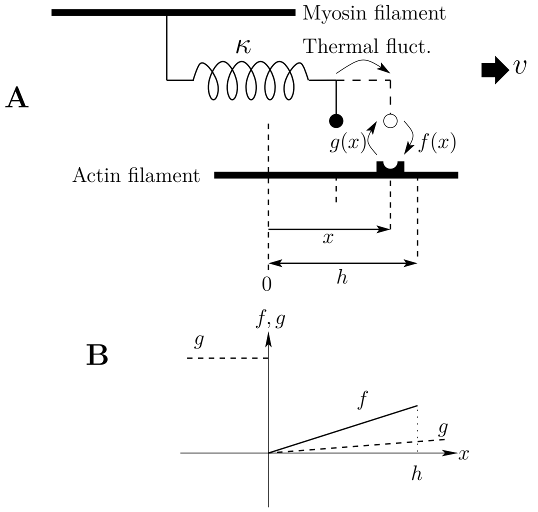

Fig. 2.10 – A.F. Huxley's model for acto-myosin interaction published in (Huxley, 1957). (**A**): sketch of the model. The myosin motor is connected to the backbone by a linear spring with stiffness κ. The resting strain of the spring is set to 0. The actual strain of the myosin head is x. The actin and myosin filaments are moving past each other at a velocity v. The myosin head undergoes thermal fluctuations that bring it with equal probability into stretched and compressed states. To bias this process, Huxley introduces the binding and unbinding functions f and g. To have a maximal mechanical efficiency, it is preferable to attach with a large strain, therefore f was chosen to depend linearly on x with a maximum at $x = h$, the maximum distance allowed for attachment and $f = 0$ for $x < 0$. The form of g is more subtle. Again to preserve mechanical efficiency, cross-bridges must detach if there are in compression, hence the high value of g for $x < 0$. The reason why g is finite everywhere is to ensure that when activation stops, the muscle completely relaxes *i.e.*, all heads detach.

Huxley's model also takes into account that each cross-bridge is convected at a velocity v towards the Z–line by the action of other motors. Denote $n(x,t)$ the normalized density of cross-bridges with strain x at time t. The kinetic equation for the population of cross-bridges can be written as follows:

$$\frac{Dn}{Dt} = \frac{\partial n}{\partial t} + v\frac{\partial n}{\partial x} = (n_0 - n) f - ng \tag{2.4.1}$$

$$T(t) = \kappa \int xn(t,x)\, dx \tag{2.4.2}$$

Hence, if the velocity v is high, the number of attached heads drops and therefore the tension T is reduced. In the case $v = const$ with f and g as shown on Fig.2.10, an analytic solution of the stationary version of Eq.(2.4.1) can be found and parameters can be adjusted to fit the force-velocity curve in shortening regimes. The parameter n_0 in Eq.(2.4.1) has been introduced in (Chapelle et al., 2011) to account for the fact that not all detached myosins can bind to actin at time t: first the power-stroke must be 'recharged' through ATP hydrolysis before the heads can bind again to actin (see Fig.1.8). In (Huxley, 1957), $n_0 = 1$.

As an example of the modern version of the Huxley approach we can mention the work of D. Chapelle *et al.* who explicitly relate the definition of f and g to the rate of ATP consumption and to the calcium concentration in order to simulate the contraction of cardiac muscle and its control by electrical stimuli from the pacemaker cells (Chapelle et al., 2011).

This recent model and the original 1957 Huxley's model can reproduce quite accurately the basic force-velocity relation, *i.e.* the steady state contraction mechanism. However, they cannot account for some particularities of the force velocity relation, for instance the fact that for loads larger than the isometric tension T_0, the muscle elongates a velocity much smaller than the direct extrapolation of the Hill's force velocity curve (Katz, 1939). Moreover it is known that for intermediate activation condition (intermediate Ca^{2+} concentration), muscles exhibit a regime of SPontaneous Oscillatory Contraction (SPOC, see (Ishiwata et al., 2011)) that might play a crucial role in the periodic contraction of heart muscles (Sasaki et al., 2005, 2006); these models cannot reproduce such phenomenon.

A particularity of those approaches is that the cross-bridge is formed in a stretched configuration. Therefore to be efficient, the motor has to accumulate elastic energy before binding. Huxley assumed that this energy accumulation originates from interactions with the thermal bath *before* binding. The experimental evidence of a quick force recovery after a sudden length change (see Sec.2.2) contradicted this hypothesis as it revealed that after the attached cross-bridges experience an elastic drop in force during the step, they are able to re-generate a force within a time scale that is incompatible with the ATP turnover which exclude the possibility of binding of fresh myosin heads. These experiments suggested the presence of a power-stroke mechanism inside the cross-bridge itself.

2.4.3 Power-stroke models

Huxley and Simmons' 1971 model

This work was inspired by an earlier paper published in 1969 by H.E. Huxley (Huxley, 1969). He proposed a model of muscle contraction where the cross bridge mechanical cycle includes a rotation of the S1 sub-fragment of myosin II (see Fig.2.2), with respect to the actin filament. This first picture of the power-stroke explains force generation by a local conformational change in the cross-bridge rather than by rectification of thermal noise prior to attachment. Indeed the storage of the required elastic energy can be time consuming (specially if the stiffness of the head is high) which is incompatible with the fast transient response observed after a sudden length change.

Following the work of H.E. Huxley, A.F. Huxley and R.M. Simmons proposed in (Huxley and Simmons, 1971) a model allowing one to explain the this quick force recovery quantitatively. The model is based on the association of 2 elements (see Fig.2.11):

1. A multistable element described by a discrete energy potential v. The associated internal degree of freedom ϵ_x is interpreted as the angular position of the myosin head with respect to actin. The discrete potential is shown on Fig.2.11A for the case of two energy wells. Each energy well is infinitely steep and the variable ϵ_x can be interpreted as a 'spin' degree of freedom. The 2 preferred states are separated by a distance a characterizing the power-stroke size. It must be noted that the energy barriers B_1 and B_0 are constant and therefore do not depend on the applied force.
2. A linear elastic element whose energy is of the type: $V_e\left(\epsilon_y, \epsilon_x\right) = 1/2\kappa\left(\epsilon_y - \epsilon_x\right)^2$ (see Fig.2.11B). ϵ_y is the overall strain in the cross-bridge. In the original 1971 model, the actin and myosin filaments are rigid therefore the applied length step corresponds to a direct change of ϵ_y.

While Huxley and Simmons used in their paper the language of chemical reactions, here we reformulate their theory in terms of general statistical mechanics. Consider a population of N cross-bridges connected in parallel. In thermal equilibrium, the tension is computed from the partition function (see Sec.4.1) of the system. We denote N_1 the

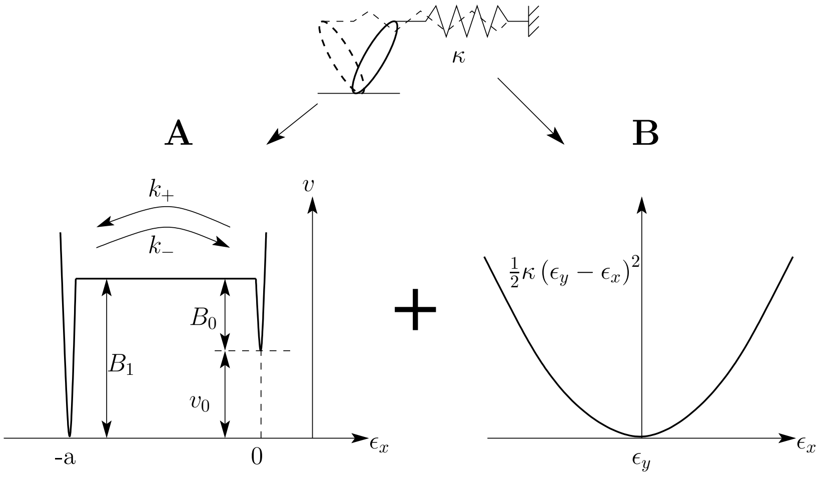

Fig. 2.11 – Power-stroke model proposed by A.F. Huxley and R.M. Simmons in 1971 in (Huxley and Simmons, 1971). (**A**): the conformational change of the myosin head is associated with the energy potential v. This potential allows only discrete positions (here to position $\epsilon_x = 0$ and $\epsilon_x = -a$). The energy offset of the right had energy well is v_0. Huxley introduced 2 arbitrary energy barriers B_1 and B_0 for the left to right and right to left transition respectively. (**B**): to take into account the elastic properties of the motor, he added an harmonic potential of stiffness κ to the double well potential. ϵ_y is the overall strain in the cross-bridge. As Huxley assumed rigid myofilaments, the length step applied on the fiber is equal to the change in ϵ_y. The transition rate between the 2 conformations are noted k_+ (pre-power-stroke to post-power-stroke) and k_- (post-power-stroke to pre-power-stroke).

number of cross-bridges with $\epsilon_x = -a$. The partition function for this model is[1]:

$$\begin{aligned}
\mathcal{Z}\left(e_y,\beta\right) &= \sum_{N_1=0}^{N}\binom{N}{N_1}\exp\left[-\beta\left(N_1\frac{1}{2}\kappa\left(\epsilon_y+a\right)^2+\left(N-N_1\right)\left(\frac{1}{2}\kappa\left(\epsilon_y^2\right)+v_0\right)\right)\right]\\
&= \left(\exp\left[-\beta\frac{1}{2}\kappa\left(\epsilon_y+a\right)^2\right]+\exp\left[-\beta\left(\frac{1}{2}\kappa\epsilon_y^2+v_0\right)\right]\right)^N
\end{aligned}$$

where $\beta = 1/k_b\theta$, k_b being the Boltzmann constant and θ the absolute temperature. Then, from the partition function the equilibrium tension after the quick recovery is given by:

$$T_2\left(\epsilon_y,\beta\right) = \frac{\partial F}{\partial \epsilon_y}, \text{where } F = -\frac{1}{\beta}\ln\left(\mathcal{Z}\left(\epsilon_y,\beta\right)\right)$$

$$T_2\left(\epsilon_y,\beta\right) = N\kappa\left(\epsilon_y+\frac{a}{2}-\frac{a}{2}\tanh\left(\frac{\beta}{2}\left(\kappa\epsilon_y a+\kappa\frac{a^2}{2}-v_0\right)\right)\right) \tag{2.4.3}$$

In isometric contraction ($\epsilon_y = \epsilon_y^0$) it was supposed that $N_1/N = 1/2$, which here would mean that the total energy of the 2 conformations are equal so $v_0 = \kappa\epsilon_y^0 a+\kappa a^2/2$. Therefore by eliminating v_0 we obtain:

$$T_2 = N\kappa\left(\epsilon_y+\frac{a}{2}-\frac{a}{2}\tanh\left(\frac{\beta}{2}\kappa a\left(\epsilon_y-\epsilon_y^0\right)\right)\right).$$

We can rewrite the preceding formula in a non dimensional form:

$$\overline{T}_2 = N\left(\overline{\epsilon}_y+\frac{1}{2}-\frac{1}{2}\tanh\left(\frac{\overline{\beta}}{2}\left(\overline{\epsilon}_y-\overline{\epsilon}_y^0\right)\right)\right),$$

---

[1] We use the following notation for the binomial coefficients: $\binom{N}{K} = \frac{N!}{K!(N-K)!}$

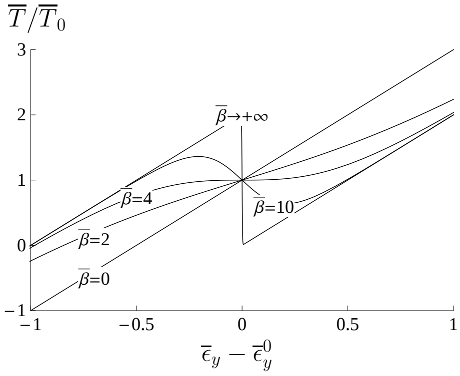

Fig. 2.12 – **T_2 curves obtained with Huxley and Simmons 1971 model** for different values of $\overline{\beta}$. We see that for $\overline{\beta}<4$, the curve is monotone, otherwise it develops a region of negative stiffness near $\epsilon_y=\epsilon_y^0$. The 2 linear regimes correspond to an homogeneous population of cross-bridges inside the left hand (post-power-stroke configuration) or in the right hand well (pre-power-stroke configuration).

with: $\overline{T}_2=T_2/(\kappa a)$, $\overline{\epsilon}_y=\epsilon_y/a$ and $\overline{\beta}=\kappa a^2/(k_b\theta)$. On Fig.2.12, we represent $\overline{T}_2/\overline{T_0}\left(\overline{\epsilon}_y\right)$, with $\overline{T}_0=\overline{T}_2\left(\overline{\epsilon}_y=\overline{\epsilon}_y^0\right)$, for different values of $\overline{\beta}$. The curves show two linear regimes corresponding to the cases where the cross-bridges are all in the left well (post-power-stroke conformation) and in the right well (pre-power-stroke conformation). For low values of $\overline{\beta}$, the $\overline{T}_2$ curve is monotone. At the critical value $\overline{\beta}=4$, the curve shows an incipient horizontal plateau as observed experimentally (see Fig.2.5). For $\overline{\beta}>4$, a region with negative stiffness starts to develop and, ultimately, when $\overline{\beta}\to\infty$, we observe a sharp transition between the 2 linear regimes. The Huxley and Simmons model is therefore potentially able to reproduce the plateau of the T_2 curve, by redistributing the cross-bridges between the 2 conformations.

The next step in the Huxley and Simmons theory is the treatment of the kinetics of the transition between the 2 conformations. Here by presenting a rigorous definition of the transition rates (see Fig.2.13), we reveal an inconsistency in the reasoning of Huxley and Simmons concerning the computation of the equilibration time between the two configuration even though it does not affect their results.

Huxley and Simmons denoted k_+ and k_- the transition rates from pre-power-stroke to post-power-stroke conformation and *vice-versa* (see Fig.2.11). According to Kramers theory for chemical reactions (see Sec.C.1.2 and Kramers (1940)),the rate constant k_+ and k_- are inversely proportional to the exponential function of the energy barriers. Then, in the Huxley and Simmons model, the size of the barriers depends on the elastic energy in the linear spring and on the shape of the potential v. We denote $\Delta\overline{V}_e\left(\overline{\epsilon}_y\right)=\frac{1}{2}\left(\overline{\epsilon}_y+1\right)^2-\frac{1}{2}\overline{\epsilon}_y^2=\overline{\epsilon}_y+\frac{1}{2}$, the difference in elastic energies between the 2 conformations at a given ϵ_y. The quantities B_1 and B_0 are constants as postulated by Huxley and Simmons.

We have to distinguish two cases:

1. If $\overline{\epsilon}_y<-\frac{1}{2}$ (see Fig.2.13A), then $\Delta V_e\left(\overline{\epsilon}_y\right)<0$ and the energy barrier from pre-power-stroke (right hand well) to post-power-stroke (left hand well) is equal to $\overline{B}_0$ while the barrier from post-power-stroke to pre-power-stroke is $B_1-\Delta V_e\left(\overline{\epsilon}_y\right)$
2. If $\overline{\epsilon}_y>\frac{1}{2}$ (see Fig.2.13B), then $\Delta V_e\left(\overline{\epsilon}_y\right)>0$ the energy barrier from pre-power-stroke (right hand well) to post-power-stroke (left hand well) is equal to $\overline{B}_0+\Delta V_e\left(\overline{\epsilon}_y\right)$ a the barrier from post-power-stroke to pre-power-stroke is B_1

Huxley and Simmons considered only the case $\overline{\epsilon}_y>\frac{1}{2}$. Following the preceding rules

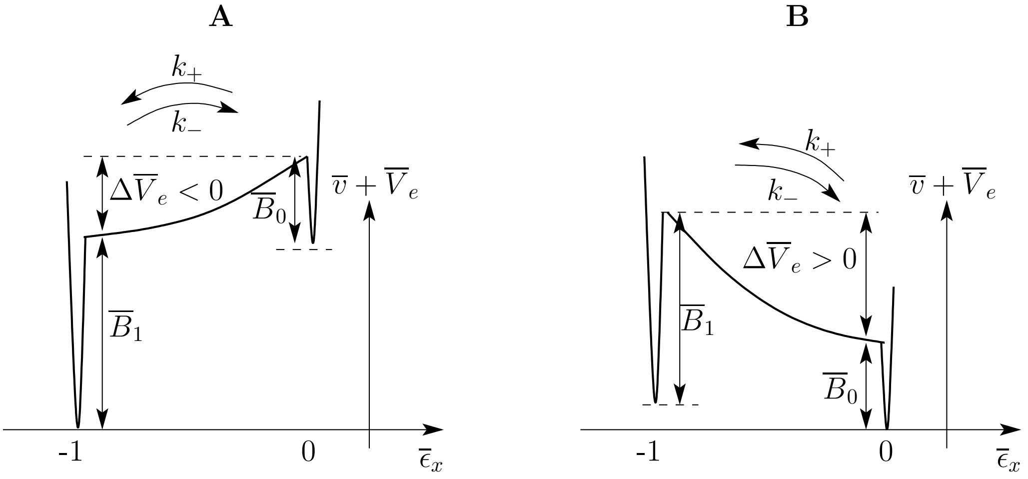

$\epsilon_y < -\dfrac{1}{2}$

$k_+ \left(\overline{\epsilon}_y\right) = \alpha \exp\left[-\overline{\beta B_0}\right] = const$

$k_- \left(\overline{\epsilon}_y\right) = \alpha \exp\left[-\overline{\beta}\left(\overline{B}_1 - \Delta\overline{V}_e\left(\overline{\epsilon}_y\right)\right)\right]$

$\epsilon_y > -\dfrac{1}{2}$

$k_+ \left(\overline{\epsilon}_y\right) = \alpha \exp\left[-\overline{\beta}\left(\overline{B}_0 + \Delta\overline{V}_e\left(\overline{\epsilon}_y\right)\right)\right]$

$k_- \left(\overline{\epsilon}_y\right) = \alpha \exp\left[-\overline{\beta B_1}\right] = const$

Fig. 2.13 – Consistent definition of the transition rates in the Huxley and Simmons model

the transition rates have to be defined as follows:

$$k_+\left(\overline{\epsilon}_y\right) = \begin{cases} \alpha \exp\left[-\overline{\beta B_0}\right] = k_+^0 = const & \text{if } \overline{\epsilon}_y < -\frac{1}{2} \\ \alpha \exp\left[-\overline{\beta}\left(\overline{B}_0 + \Delta\overline{V}_e\left(\overline{\epsilon}_y\right)\right)\right] & \text{if } \overline{\epsilon}_y > -\frac{1}{2} \end{cases} \tag{2.4.4}$$

$$k_-\left(\overline{\epsilon}_y\right) = \begin{cases} \alpha \exp\left[-\overline{\beta}\left(\overline{B}_1 - \Delta\overline{V}_e\left(\overline{\epsilon}_y\right)\right)\right] & \text{if } \overline{\epsilon}_y < -\frac{1}{2} \\ \alpha \exp\left[-\overline{\beta B_1}\right] = k_-^0 = const & \text{if } \overline{\epsilon}_y > -\frac{1}{2} \end{cases} \tag{2.4.5}$$

where α is a constant. In the model represented on Fig.2.13, $B_1 > B_0$ and thus $k_+^0 > k_-^0$.

Note that the 'chemical' rates k_+ and k_- depend continuously on the cross-bridge's overall strain ϵ_y. Usually, chemical reactions are viewed as jump processes between discrete 'sites' that have a fixed position in the conformational space. Here, instead the chemical states are represented not by points on the configurational space but by lines (see Fig.2.23).

Now for $\overline{\epsilon}_y < -1/2$ we can rewrite k_- as:

$$\begin{aligned} k_-\left(\overline{\epsilon}_y\right) &= k_+^0 \exp\left[-\beta\left(B_1 - B_0 - \Delta V_e\left(\overline{\epsilon}_y\right)\right)\right] \\ &= k_+^0 \exp\left[-\beta\left(v_0 - \Delta V_e\left(\overline{\epsilon}_y\right)\right)\right] \end{aligned}$$

and, because $\overline{v}_0 = \overline{\epsilon}_y^0 + \frac{1}{2}$, we obtain:

$$k_-\left(\overline{\epsilon}_y\right) = k_+^0 \exp\left[-\beta\left(\overline{\epsilon}_y^0 - \overline{\epsilon}_y\right)\right] \text{ for } \overline{\epsilon}_y < -\frac{1}{2} \tag{2.4.6}$$

and similarly

$$k_+\left(\overline{\epsilon}_y\right) = k_-^0 \exp\left[-\beta\left(\overline{\epsilon}_y - \overline{\epsilon}_y^0\right)\right] \text{ for } \overline{\epsilon}_y > -\frac{1}{2} \tag{2.4.7}$$

Hence, by assuming the evolution of the population N_1 in post-power-stroke conformation is governed by a jump process, we write:

$$\frac{dN_1}{dt} = k_+\left(N - N_1\right) - k_- N_1 = k_+ N - \left(k_+ + k_-\right) N_1.$$

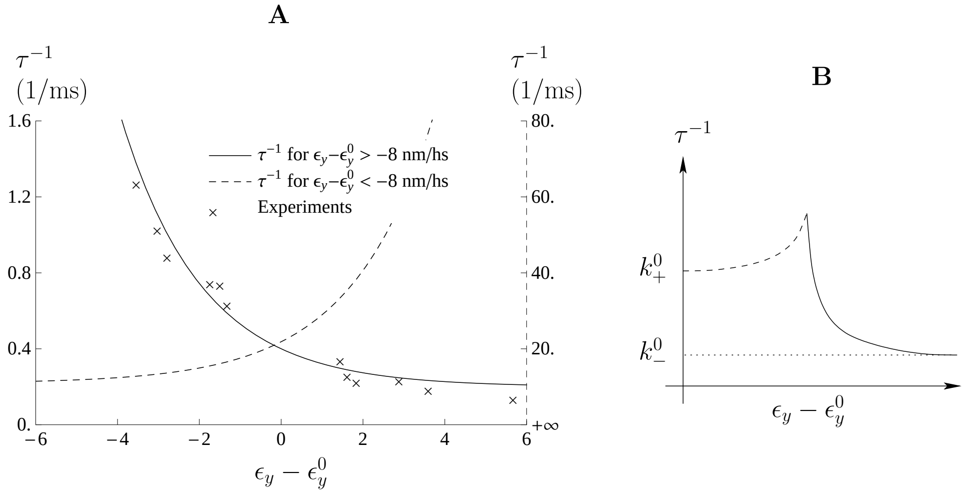

Fig. 2.14 – Consistent representation of the rate following Huxley and Simmons model. ×: experimental data from Huxley and Simmons (1971). Solid line: rate computed following Huxley and Simmons paper corresponding to the case $\overline{\epsilon}_y > -1/2$ (values to read on the left axis). The dashed line (values read on the right axis) corresponds to the case $\overline{\epsilon}_y < -1/2$. Note that in both cases the rates are finite for large $|\epsilon_y|$. Huxley and Simmons model suggests that for large shortening the rate will actually decrease with $\overline{\epsilon}_y$

The system will then reach equilibrium with a rate

$$\tau^{-1} = (k_+ + k_-) = \begin{cases} k_+^0 \left(1 + \exp\left[-\beta\left(\epsilon_y^0 - \epsilon_y\right)\right]\right) & \text{for } \epsilon_y < -\frac{1}{2} \\ k_-^0 \left(1 + \exp\left[-\beta\left(\epsilon_y - \epsilon_y^0\right)\right]\right) & \text{for } \epsilon_y > -\frac{1}{2} \end{cases} \tag{2.4.8}$$

With the parameters used by Huxley and Simmons, the condition $\epsilon_y > -1/2$ corresponds to $\epsilon_y - \epsilon_y^0 > -8$ nm/hs which covers the range of their measurements and match the experimental data (see Fig.2.14). However, one must keep in mind the consistency condition on ϵ_y when dealing with a different set of parameters and in particular a different value of ϵ_y^0.

Fig.2.14 shows the rate of equilibration obtained by Huxley and Simmons (solid line). (×) represent Huxley and Simmons experimental data. The parameters are adjusted to match the data with the solid line while maintaining the plateau of the T_2 curve ($k_-^0 = 0.2$, $\beta = 4$, $\overline{\epsilon}_y^0 = 1/2$ which corresponds to $\overline{v}_0 = 1$, same parameter as in Huxley and Simmons (1971)).

In the Huxley and Simmons model, because the energy barrier B_1 and B_0 do not depend on the applied load, the equilibration rate becomes constant for large values of $|\epsilon|_y$ (see Fig.2.14B). This property cannot remain if one considers a regularized version of the Huxley and Simmons potential (see Fig.2.15B). Even with the slightest smoothing, the barrier B_1 and B_0 becomes functions of ϵ_y and eventually disappear at large loadings; consequently, the equilibration rate cannot be kept constant in such regime an one should actually observe an increase (see Fig.2.15D).

Eisenberg and Hill's 1978 model

One of the main criticism about this otherwise extremely important model came from T.L. Hill and co-workers in (Eisenberg and Hill, 1978; Eisenberg et al., 1980). Huxley and Simmons model states that the transition between the 2 conformations implies stretching

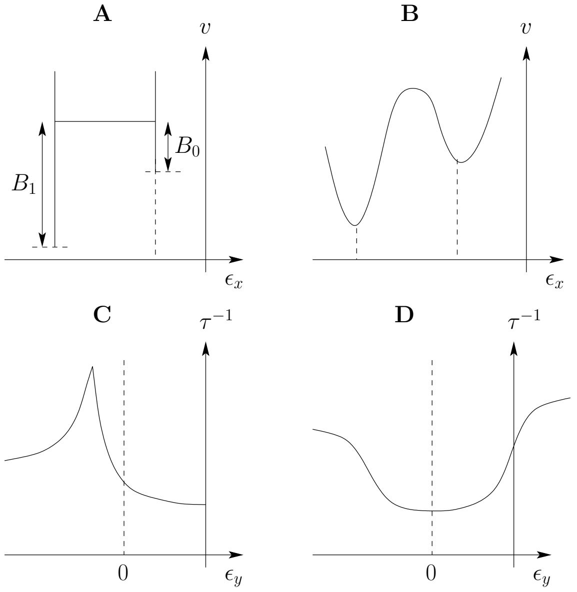

Fig. 2.15 – **Hard spin model *vs* soft spin model**. On (**A**), we schematically represent a bi-stable model of the type used by Huxley and Simmons characterized by infinitely steep wells and with fixed barriers B_1 and B_0 and on (**B**) we show a regularized version of this potential. (**A**) model in non-regularizable without removing this hypothesis of fixed barriers. When a force is applied on the Huxley and Simmons model B_1 and B_0 remains unchanged while with even the slightest smoothing of the potential, barriers are always removed at finite force. (**C**) and (**D**) shows the trends of the rate curves expected from models (**A**) and (**B**). With model (**A**), the rate decrease to a constant at large loading while with model, because of the removal of the fixed barriers, the rate always increases at large loadings.

of the spring by thermal fluctuations required to overcome the energy barrier. According to Hill *et al.*, this process is likely to be too slow to reproduce experiments, specially if the the parameter $\overline{\beta}$ is high since the rate of recovery is an exponential function of $\overline{\beta}$ (see Eq.(2.4.8)). As $\beta = \kappa a^2/(k_b\theta)$, an increase either in κ or a will considerably increase the equilibration time between the conformational states. Huxley and Simmons were of course aware of this drawback and therefore already in their original paper contemplated dividing the power-stroke into at least 2 sub-steps (see Huxley and Simmons (1971) and Fig.2.17). To overcome this difficulty, Hill and Eisenberg proposed a slightly different model.

In 1974, T.L. Hill in his attempt to formalize and unify the existing approaches to muscle contraction modeling, emphasized the necessity to compute free energy profiles and extract forces from the knowledge of the free energy (Hill and Chen, 1974). Following this idea, E. Eisenberg and T.L. Hill proposed in 1978, to associate some energy landscape with the conformational change then couple it with the energy of the spring. In the Huxley and Simmons model, the non dimensional energy of the spring is always equal to $1/2\left(\overline{\epsilon}_y - \overline{\epsilon}_x\right)^2$ with ϵ_x the internal degree of freedom equal to 0 or -1 depending on the conformation. In Eisenberg and Hill's model, the spring is now a bi-stable element whose energy depends on the internal degree of freedom $q \neq \epsilon_x$ (Eisenberg and Hill, 1978). In other word, the conformational change occur without net movement of the lever arm. They set:

$$\overline{V}_e\left(\overline{\epsilon}_y, \overline{\epsilon}_x, q\right) = \begin{cases} \frac{1}{2}\left(\epsilon_y\right)^2, & \text{if } q = 0 \\ \frac{1}{2}\left(\epsilon_y + 1\right)^2, & \text{if } q = -1 \end{cases}$$

Huxley and Simmons' and Eisenberg and Hill's models are compared on Fig.2.16. For the Huxley and Simmons model, the internal degree of freedom accounting for the con-

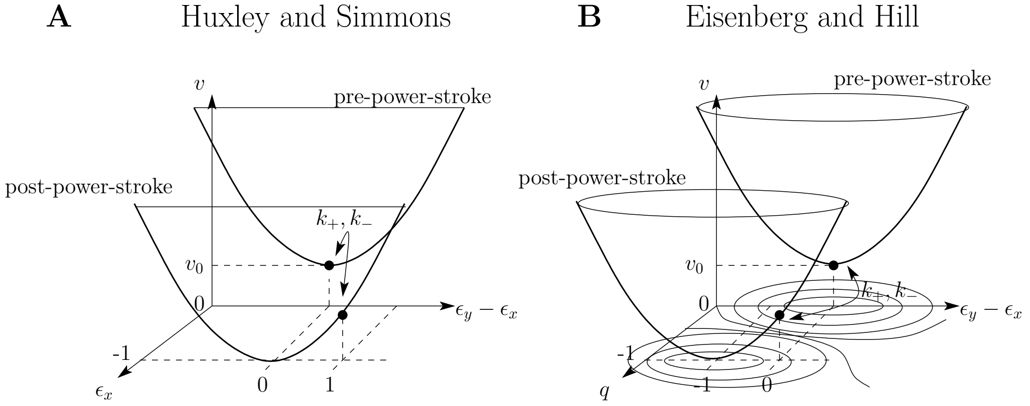

Fig. 2.16 – Huxley and Simmons' 1971 model *vs* Eisenberg and Hill's 1978 model. In both models, the conformational change is associated to a jump between two discrete values of an internal degree of freedom. In both conformations the energy of the cross-bridge is quadratic. In Huxley and Simmons' model (**A**), the internal degree of freedom is the rotation of the head ϵ_x so that the energy of the spring and the conformational change are tightly coupled, see the arrows showing the jump between the conformations on (**A**). In Eisenberg and Hill's model (**B**), the rotation ϵ_x is not associated to the conformational change which now depend on some other degree of freedom noted q. In both models, the tension attained at the end of the conformational change are the same. In both model we represent in the $\epsilon_x/q-(\epsilon_y-\epsilon_x)$ plane the level set of the energy landscape implicitly meant by Eisenberg and Hill although the continuous dynamics was still replaced by a jump process.

formational change is the rotation of the lever arm ϵ_x which takes discrete values (see Fig.2.16A). Note that in both models, the energy of the cross-bridge after the conformational change is the same and that relaxation of the tension occurs with a net change in $\epsilon_y - \epsilon_x$. Although Eisenberg and Hill, show an explicit energy landscape represented by level sets (see Fig.2.16B) in fact the continuous dynamics in their model was still replaced by the jump process.

The crucial feature in the approach of Eisenberg and Hill is that the transition between $q = 0$ and $q = -1$ states does not require stochastic stretching the elastic spring and so the transition rates between conformations have to be prescribed as phenomenological functions of the strain $\overline{\epsilon}_y - \overline{\epsilon}_x$. Hence there was still no formal link in this model between the rate functions and energy barriers.

Discussion

Nowadays the power-stroke is mostly modeled using Huxley and Simmons approach providing a direct link between the rate constants and the mechanical state of the spring. Also this approach is consistent with results of crystallographic studies which unambiguously shows the rotation of the lever arm following the conformational change (Dominguez et al., 1998; Rayment et al., 1993). However, as correctly stated by T.L. Hill, if the value of $\overline{\beta}$ is too large, the T_2 curve starts to develop a negative slope and the kinetics of the quick recovery might become too slow compared to experimental rate measurements (Piazzesi and Lombardi, 1995). This problem is illustrated on Fig.2.17. The energy of the system is represented against the overall strain in the cross-bridge ϵ_y. To reproduce the T_2 curve and in particular the interception of the T_2 curve with the abscissa (located at $\delta = -10$ on Fig.2.5), the size of the power-stroke (a) must be about $8 - 10$ nm (taking into account filament elasticity). If the stiffness of the spring is low (as sketched on Fig.2.17A), this $\sim$ 10 nm sliding can be achieved with only one conformational change without compressing the spring (a typical chemical "pathway" is indi-

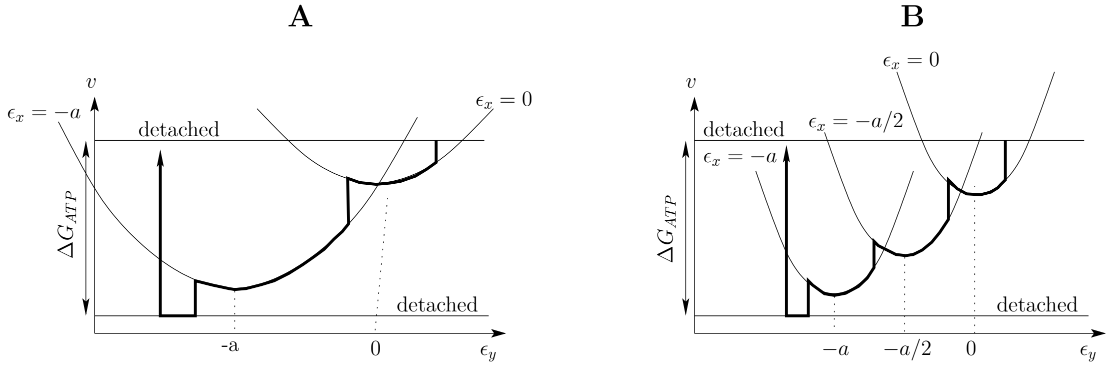

Fig. 2.17 – Free energy profiles for chemo-mechanical models. (**A**) case with low cross-bridge stiffness. In this case, only 2 attached states are needed to account for the maximum sliding required for the experimental T_2 curve. If the stiffness is higher (**B**), one or more intermediate conformations must be introduced to avoid compression of the cross-bridges. In both (**A**) and (**B**), there are 2 detached states whose energy is strain independent. The energy difference between these detached states is equal to energy supplied by ATP hydrolysis. The bold lines indicate an example of chemical pathway between the states.

cated with bold lines). On the other hand, a high stiffness (see Fig.2.17B) requires the definition of one or more sub-steps, otherwise the cross-bridge has to be considerably compressed before the conformational change can occur so the mechanical efficiency is reduced. This has lead to many discussions regarding the necessity of introducing intermediate states in the power-stroke (Huxley and Simmons, 1971; Linari and Lombardi, 2010; Offer and Ranatunga, 2010; Piazzesi and Lombardi, 1995; Smith et al., 2008) and the issue remains open.

2.4.4 Recent developments

The formalism introduced by Hill in the seventies for the modeling of muscle contraction (Eisenberg and Hill, 1978; Hill and Chen, 1974) has been widely used in the so-called chemo-mechanical models (As an example we can mention Piazzesi and Lombardi (1995) which is illustrated on Fig.2.18; see also Smith et al. (2008)). In this class of models, the different states of the cross-bridge cycle are associated with their own energy landscapes that depend on the strain in the cross-bridge. Usually, the energy of the detached states are constant and differ only by the energy level controlled by the ATP hydrolysis. An example of such model is sketched on Fig.2.17.

The 2 detached states are represented as strait lines. The attached states are usually described using Huxley and Simmons theory of the power-stroke with strain dependent rate functions satisfying locally detailed balance condition. Some rate functions (for attachment and detachment) are prescribed phenomenologically and are adjusted to fit experimental data. The choice of the rate constants creates the ‘preferred pathways’ among the states (see the bold lines on Fig.2.17). The rate functions used by V. Lombardi *et al.* in (Piazzesi and Lombardi, 1995) are shown on Fig.2.18B,C,D and E.

This type of modeling is wide spread in the community with different groups emphasizing different pathways and different number of attached states. For instance T.A.J Duke suggested a version with 3 attached states in (Duke, 1999). The rate constants for attachment and detachment do note depend on stretch so that, finally, this model has only a discrete set of parameters and is able to reproduce quantitatively many experimental observations for isotonic velocity transients. However, the quick force recovery is

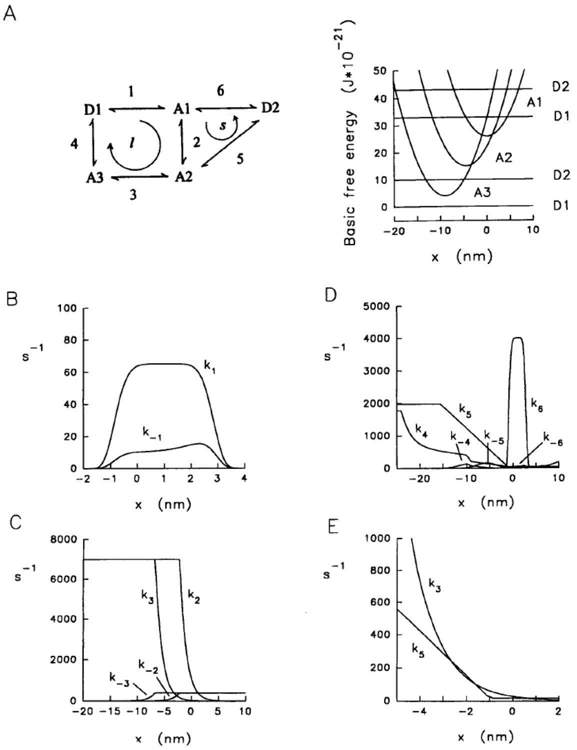

Fig. 2.18 – Chemo-mechanical model proposed by G.Piazzesi *et al.* in (Piazzesi and Lombardi, 1995). (**A** left): Ensemble of possible reactions between the different chemical states. A1–A2 are respectively the different attached states from pre– to post-power-stroke. D1 and D2 represent the M-ATP and M-ADP-Pi states respectively. (**A** right): Energy of the different states. Attached states are harmonic with the same stiffness κ and the detached states have a fixed energy. The difference between the energy of state D1 and D2 is the energy input from ATP hydrolysis. (**B**, **C** and **D**) shows the rate transition function between the states.

reproduced only qualitatively. Another simple chemo-mechanical model is proposed in (Cordova et al., 1992), with attachment and detachment rates depending on the strain in the myosin (like in (Huxley, 1957)). They also model the binding sites as energy wells whose depth depends on the cross-bridge strain. The model of V.Lombardi *et al.* shown on Fig.2.18 contains 3 attached states (A1, A2 and A3) and 2 detached states (D1 and D2) and they consider a chemical scheme with 6 forward rate functions and their reverse. Even more detailed schemes has been used by M. Linari and co-workers in order to account for specific effects of the chemical species present in muscle such as the inorganic phosphate. These models use up to 5 attached states and 4 detached states (Linari et al., 2010, 2009).

2.4.5 Brownian ratchet: purely mechanical model

Modeling molecular motors has been recently a very active field of bio-physics stimulated by the development of single molecule techniques (see Sec.2.3). The goal was to explain how a molecular motor (not necessarily muscle myosin II) can 'walk' on a track in a preferred direction provided that it is constantly hit by molecules from the surrounding solvent in a stochastic way.

In *Brownian ratchets* models, the idea is to trace one or several mesoscopic degrees of freedom (x) in full details. These degrees of freedom are explicitly associated with a particular energy landscape $V(x)$. Most of the other degrees of freedom are assumed to be equilibrated and are represented by a thermostat (white noise and dissipation) imposing finite temperature. In this framework, the inertial terms can often be neglected (overdamped regimes) and the motion of the particle is driven by the Langevin (Smoluchowsky) equation:

$$\eta \frac{dx}{dt} = -\partial_x V'(x) + \Gamma(t) \tag{2.4.9}$$

where η is the viscous drag coefficient and Γ is the random Langevin's force which is prescribed by the fluctuation dissipation theorem: $\langle \Gamma(t) \rangle = 0$ and $\langle \Gamma(t) \Gamma(t') \rangle = 2\eta k_b \theta \delta(t-t')$. $\langle . \rangle$ denote ensemble average and δ is the Dirac function.

The implicit non-equilibrium degrees of freedom representing non-equilibrium reservoir enter the model as an explicit *correlated* time dependent signal for instance a *colored* component of the noise and such model generate directional motion of the particle x if the potential $V(x)$ is asymmetric.

The colored component of the noise can take multiple forms (see the review by F. Jüllicher A. Ajdari and J. Prost (Jülicher et al., 1997)). For instance one can use a time-periodic force (*rocking*)

$$V(x,t) = V(x) + \psi(t) \text{ with } \langle \psi(t) \rangle = 0. \tag{2.4.10}$$

Another option is a time-periodic multiplier (*flashing*)

$$W(x,t) = \psi(t) V(x,t). \tag{2.4.11}$$

In Eq.(2.4.10) ψ has a clear mechanical meaning, it is an external force. For instance in (Magnasco, 1993) (and Fig.2.19A), the non-symmetric periodic potential $V(x)$ can be represented as a piecewise linear function of the position x while the time-periodic force $\psi(t)$ was assumed to be piecewise constant (with 0 time average). Of course, for sufficiently large $|\psi|$, the motor can work even at zero temperature, but when $|\psi|$ is small temperature is needed to overcome the energy barriers in V. When the potential shown in Fig.2.19A is rocked (see dashed lines), the distance traveled before the rocking is inverted is higher in the right direction than in the left direction. Hence a steady state flux to the right is generated. The same type of motion can be obtained with a symmetric potential and a non-symmetric time dependent force.

The function $\psi(t)$ is less obvious to interpret mechanically. It describes the affinity of the particle to certain 'states' in the energy landscape. A way to understand this is to assign different energy landscapes to different 'chemical states' (see Jülicher et al., 1997). This type of model is a generalization of the chemo-mechanical models presented in the previous sub-section. Each state i is characterized by an energy landscape W_i (see Fig.2.19B for a case with 2 states) where the motion of a particle is govern by a Langevin's equation of the type (2.4.9), with Γ prescribed by the fluctuation-dissipation theorem. Like in chemo-mechanical models, the transition rates between the sates are prescribed functions of the position x. The necessary condition to obtain a directed motion is to break detailed balance. For the case shown on Fig.2.19B, if detailed balance is satisfied, the transition functions k_1 and k_2 are related as follows:

$$k_1(x) = k_2(x) e^{-\beta(W_1(x) - W_2(x))}$$

Note that this relation is equivalent to the one used in the Huxley and Simmons model of the power-stroke to describe thermal equilibrium. Now, to break the detailed balance we can write (Chauwin et al., 1994):

$$k_1(x) = k_2(x) \left(\exp\left[\beta\left(W_1 - W2\right)\right] + \xi(x)\right)$$

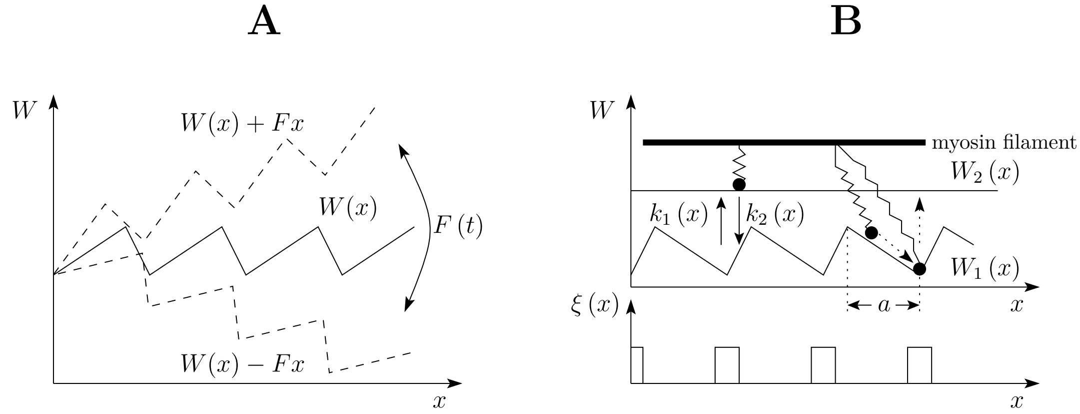

Fig. 2.19 – Thermal ratchets and multistate modeling. We show two examples of how to create a biased movement out of the classical overdamped Langevin's equation (2.4.9). (**A**): the motion of the particle x is driven by a non-symmetric potential W. In presence of a symmetric time periodic force $F(t)$ (here equal to $\pm F$), a finite steady state flux is generated in the direction of the lower gradient of W (here to the right). See Magnasco (1993). (**B**): the particle oscillate between 2 energy potential: W_1, representing an 'attached' state and W_2, representing a 'detached state'. The necessary condition to generate a directed motion is to break detailed balance between the transition function k_1 and k_2 (Chauwin et al., 1994; Prost et al., 1994), for instance by using $k_1(x) = k_2(x)\left(\exp\left[\beta\left(W_1 - W2\right)\right] + \xi(x)\right)$ where $\xi(x)$ controls the distance from thermal equilibrium. In both cases, the motor moves to the right.

where $\xi(x)$ is a prescribed function that controls the local deviation from thermal equilibrium (see Fig.2.19B, lower part). The presence of ξ ensures a directed motion (here to the right) (Jülicher and Prost, 1997): in the example shown on Fig.2.19, the particle has a higher probability to be 'pumped' to detached state W_2 when it has moved to the bottom of the sawtooth potential. This prevents the particles from moving backward where the slope of the potential is less steep.

A quadratic potential can be added to W_1 to take into account the elasticity of the motor (Guerin et al., 2010b; Placais et al., 2009). In those models the definition of the power-stroke is not associated with a conformational change occurring without net displacement along the track. From Fig.2.19B for instance it is not straightforward to identify a particular sequence of motion to be interpreted as the power-stroke and so it becomes ambiguous whether the motor is driven by the power-stroke or by the ratchet.

In another recent development H. Wang and G. Oster proposed their own definition of 'power-stroke models' and 'ratchet models' in (Wang and Oster, 2002). They consider a motor coupled to a 'load' or 'cargo' which it then attempts to move. Based on the fact that, in steady state regime the system is periodic in time, they write the energy balance as follows:

$$\dot{W}_M + \dot{W}_E - \dot{Q}_{out} + \dot{Q}_{in} = 0 \tag{2.4.12}$$

where W_M is the work done by the motor, W_E is the work done by external forces $-Q_{out}$ is the work done by the drag forces of the thermostat and Q_{in} is the work done by thermal forces from the thermostat. During one cycle, the motor consumes energy equal to ΔG_C at a rate r where ΔG_C is the free energy change in one reaction cycle (it correspond to the energy released by the ATP hydrolysis) and r is the rate of chemical reactions. They define the 'percent power stroke' of such model by:

$$f_P = \frac{\dot{W}_M}{r\left(-\Delta G_C\right)} \tag{2.4.13}$$

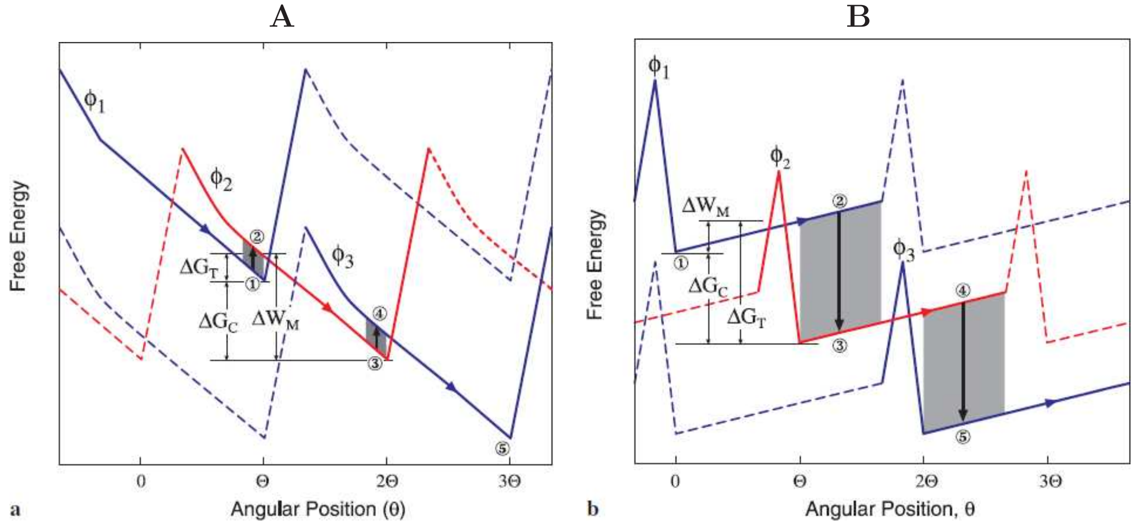

Fig. 2.20 – Examples of a power-stroke model (A) and of a ratchet model (B). From Wang and Oster (2002). The motor is driven by a series of periodic potentials ϕ_i shifted in the direction of increasing motor coordinate θ and with lower free energy at each step. **A** a power-stroke model. The amount of work done during one cycle (①→③) is negative and larger that the net free energy change ΔG_C, thus $f_P > 1$. **B**: a ratchet model. The forward motion occurs against energy gradients that moves the motor backward. Hence $\Delta W_M > 0$ and thus $f_R > 1$.

and similarly the 'percent ratchet' is defined as:

$$f_R = 1 - \frac{\dot{W}_M}{r\,(-\Delta G_C)} \tag{2.4.14}$$

Therefore a motor has two components added in such a way that $f_P + f_R = 1$. We can then qualify a given model a *power-stroke model* as soon as f_R exceeds a certain predefined proportion f_0.

Fig.2.20 shows two hypothetical motor systems modeled using the 'flashing' ratchet formalism. Each chemical state S_i is associated to an energy landscape ϕ_i (here all states have the same energy landscape for simplicity). Like in the model shown on Fig.2.19B, the transition between the states is forced at certain values of the coordinate (see the grey regions).

In (A), the free energy change due to the transition from ① to ② is positive while the energy change from ② to ③ corresponding to the power-stroke in this interpretation is negative and is larger than the net free energy change during the cycle ($\Delta W_M > -\Delta G_C$). As a result, the power-stroke component in Eq.(2.4.13) is larger that 1. This arises from the fact that the transition ①→② is not energetically preferable.

In Fig.2.20B, the forward motion (①→②) is achieved through diffusion against the energy gradient so the work done by the motor on the load is positive $\Delta W_M > 0$ and consequently $f_R > 1$.

In the above sense, the 'soft motor' model proposed by F.Jülicher and J.Prost illustrated in Fig.2.19B *et al.*, appears as a another power-stroke model.

To summarize, the ratchet models merge all degrees of freedom into one coordinate in such a way that the role played by the swing of the lever arm (usually associated with the power-stroke) remains unclear. On the other hand, in modern chemo-mechanical cycles, breaking detailed balance is hidden behind the fact that the energy of the detached stated attained at the end of the stroke and the energy of the detached state before attachment differ by the amount ΔG_{ATP} although they represent the same mechanical state (see Fig.2.17 and Piazzesi and Lombardi (1995); Smith et al. (2008)). In this sense these models do not provide clear guidance on how the underlying mechanical phenomena can be reproduced in the lab at larger scales.

It is also important to have in mind that most ratchet models and chemo-mechanical models reproduce the quick recovery only qualitatively, or if quantitatively then at the expense of introducing numerous intermediate power-stroke states (Linari et al., 2009). In fact, these models mostly focus on long time scales associated with the force-velocity relation. However, the well documented phenomenon of the swinging of the lever arm is probably essential for an efficient contraction and therefore, we believe it is necessary to capture also the fast transients revealing the inner working of the power-stroke mechanism inside theoretical models.

2.5 The proposed model of a half sarcomere

Here we list the main ingredients of what we call a mechanical model of the power-stroke. Such model should contain only few mesoscopic degrees of freedom, and be driven only through easily reproducible correlated compound of the noise. First of all, we distinguish the degrees of freedom associated with the attachment-detachment mechanism and with the power-stroke mechanism. In the original Huxley and Simmons model (see Fig.2.23A) the variable $y - x$ is associated with the stretching of the myosin-head elastic component and the conformational change was implicitly linked with a discrete variable x (spin model). As a generalization, we can consider x as a continuous variable as it was first implicitly suggested by E. Eisenberg and T.L. Hill (Eisenberg and Hill, 1978) and later implemented in (Marcucci and Truskinovsky, 2010). Here, we extend the latter model, where the cross-bridges were mechanically independent, by considering the simplest elastic interaction between the individual cross-bridges inside a half-sarcomere

2.5.1 Myosin head as a bi-stable spring

L. Marcucci and L. Truskinovsky (Marcucci and Truskinovsky, 2010) generalized the Huxley and Simmons model by replacing the discrete degree of freedom accounting for the conformation of the myosin head by a continuous variable (called here x). This degree of freedom can be interpreted as the projected angle between the sub-fragment S1 of the head (see Fig.2.2) and the actin filament. Since the structure of half-sarcomeres is essentially one dimensional, we choose to work with elongations instead of angles, reminding that in the case of x, there is a direct relation with the orientation of the myosin head. The introduction of a continuous variable eliminates the necessity to deal with multiple discrete configurations for the head domain (see the previous section). The model have to takes into account 2 mechanical characteristics of the myosin head:

1. The head has at least 2 distinct conformations, pre- and post-power-stroke which suggests that the potential has to be bi-stable.
2. The head must also have series elasticity that will enter the mechanical response T_1 after a length step (see Sec.2.2).

To account for the bi-stability of the myosin head, we associate with S1 a mechanical energy v modeled as a continuous piecewise quadratic function (see Fig.2.21). We

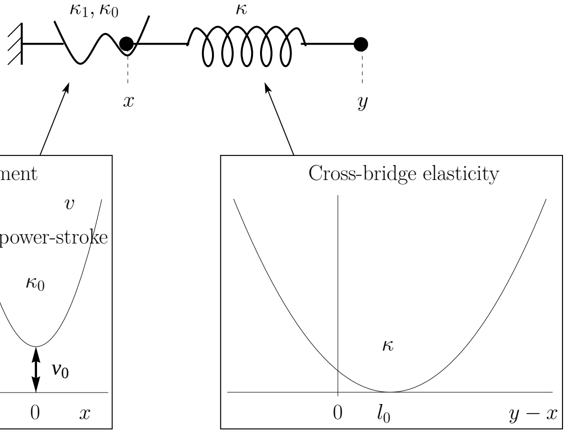

Fig. 2.21 – Mechanical model of a single cross-bridge . Each myosin S1 sub-fragment is associated with a bi-stable energy v modeled as a piecewise quadratic function of the rotational degree of freedom x. In addition to this non convex energy, we associate with S1 a series linear elastic element (with stiffness κ) that models the stretching of the lever arm.

intentionally use this rather simple form to make the computations analytically doable. In addition to this non convex energy, we associate with S1 a series linear elastic element (with stiffness κ) that models the stretching of the lever arm. Hence we can write the energy of a cross bridge as

$$V_{xb}\left(x,y\right) = v(x) + \frac{1}{2}\kappa(y-x-l_0)^2 \text{ where} \tag{2.5.1}$$

$$v\left(x\right) = \begin{cases} \frac{1}{2}\kappa_0(x)^2 + v_0 & \text{if } x > l, \\ \frac{1}{2}\kappa_1(x+a)^2 & \text{if } x \leq l. \end{cases} \tag{2.5.2}$$

l is the point of intersection of the 2 parabolas in the interval $[-a, 0]$ (see Fig.2.21). Later on, we will refer to the state $x = 0$ (resp. $x = -a$) as *well 0* (resp. *well 1*); those states are of course the pre-power-stroke and post-power-stroke conformation respectively. Parameters κ_1 and κ_0 are the respective stiffnesses of well 1 and well 0. In the limit $\kappa_0 \to \infty$ and $\kappa_1 \to \infty$, this model is similar to the model of Huxley and Simmons (Huxley and Simmons, 1971).

Notice that in Huxley and Simmons's model, a is a fixed distance between the pre- and post-power-stroke conformations. We explained in the previous section the problems with this approach. In our model, a is interpreted as the *characteristic length* of the conformational change rather than the unique size of the power-stroke. Note that experimentally, this distance cannot be measured directly, but crystallographic studies of the myosin II structure suggest that a is close to 10 nm (Dominguez et al., 1998; Holmes and Geeves, 2000; Rayment et al., 1993)

Another parameter v_0 is the energy difference between the pre-power-stroke and the post-power-stroke configurations. We would like $v\left(x\right)$ to be continuous in x, hence we impose the following relation between v_0 and l that defines v_0:

$$\frac{1}{2}\kappa_0(l)^2 + v_0 = \frac{1}{2}\kappa_1(l+a)^2, \tag{2.5.3}$$

the cross-bridge model is fully described by 4 parameters: κ_1,κ_0, l and a.

We assumed for simplicity that the spring in series with the bi-stable element was linear. However, in a recent paper, M.Kaya and H.Higuchi mention measured a non elastic

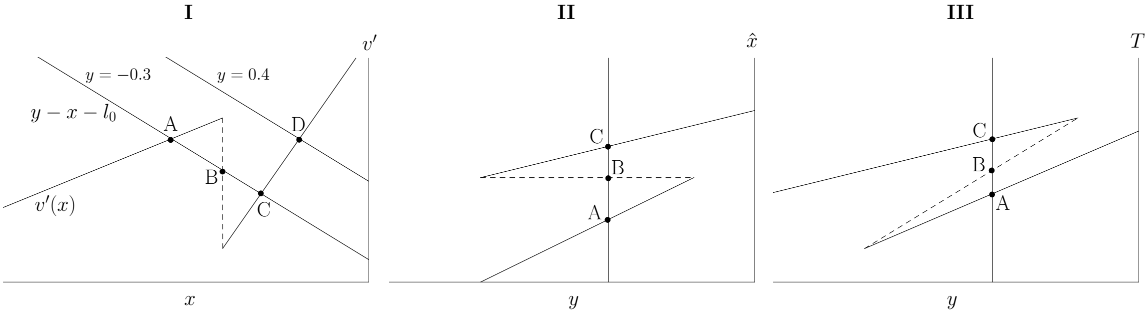

Fig. 2.22 – Metastability of a single cross-bridge . (**I**): equilibrium relation. The equilibrium positions in the double well potential are the solutions of $v'(x) = (y - x - l_0)$. We represented the solutions for $y = -0.3$ denoted A, B and C with B localized on the degenerate spinodal region and the unique solution D for $y = 0.4$. (**II**): Equilibrium position of x in double well potential *vs* y. The solid lines represent the metastable states and the dashed line the unstable state. (**III**) tension *vs* y in the different equilibrium configurations.

behaviour of the myosin head using optical tweezers (Kaya and Higuchi, 2010). They show basically two linear regime, and, in one of them, the elastic modulus is comparable to the one we use in our study, which comes from an indirect measurement via the full fiber elasticity (Piazzesi et al., 2007) (see Sec.7.1.3). The second linear regime correspond to the buckling of the S2 part and seems to be laying outside physiological regime of myosin.

2.5.2 Local minima of the energy landscape

In our description of the myosin head, we have separated the linear elasticity and the bi-stable potential. This is done to introduce local minima in the energy landscape of the cross-bridge. Indeed, at a given total length, one could have just considered the bi-stable potential which already shows elasticity characterized by κ_1 and κ_0. However, with this approach, which correspond to $\kappa \to \infty$ in our model, at fixed y, there is only one possible state x and thus no metastability. The introduction of an intermediate degree of freedom allows the transition of x between 2 locally stable equilibrium positions at fixed y, one in well 0 and the other in well 1. For a single cross-bridge, mechanical equilibrium at a fixed y is given the following relation:

$$v'(x) = y - x - l_0 \tag{2.5.4}$$

Due to the non convexity of v (2.5.4) has up to 3 solutions, labeled A, B and C on Fig.2.22A. Those 3 solutions exists only on a finite interval of y out of which only one equilibrium position remains available (see D). Fig.2.22II and III shows respectively the positions in the double well potential en the tension levels as functions of the controlled parameter y. Hence, our model which uses a regularized potential exhibits a finite interval of metastability while for instance, in the Huxley and Simmons model (see Fig.2.23A), the system at every y, can be either at $x = 0$ (pre-power-stroke) or $x = -1$ (post-power-stroke). A similar picture of multistable system has been investigated in (Guerin et al., 2010a) but for the kinetics in the framework of flashing ratchets model.

The level sets of the energy landscape for our cross-bridge model are represented on (see Fig.2.23B). The pre- and post-power-stroke states are identified as the local minima of this energy (represented by the dashed lines) and the transition takes place at $x = l$ (dotted line). When y is changed, the energy landscape is changes in such a way that one of the minima disappears and only one minimum remains while in Huxley and Simmons models the two states always exist. Another feature of our approach is that the distance

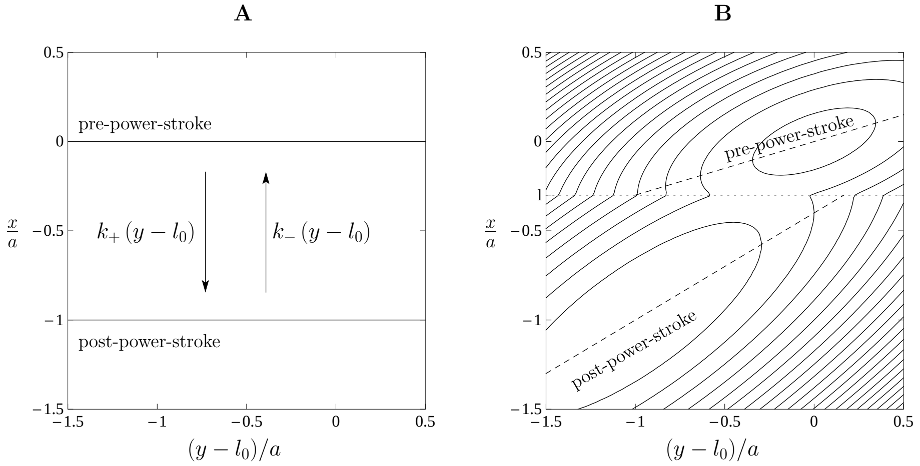

Fig. 2.23 – Chemo-mechanical cross-bridge model and our new cross-bridge model. (**A**): cross-bridge model from Huxley and Simmons model used in almost all chemo-mechanical models of muscle contraction. The orientation of the head $\bar{\epsilon}_x$ can take only a finite number of values (here 0 and -1). We propose to associate the orientation of the head to a continuous energy landscape v (see Eq(2.5.2)) so in a sense we are changing from an Ising spin model to a soft spin model. Like in the Huxley and Simmons model, the bi-stable element is coupled to a linear spring and ϵ_y denotes the overall strain of the cross-bridge. The dashed lines on **B** represent the minimum of the energy in each well. We see that for large enough $\bar{\epsilon}_y$, the bi-stability is lost, only one minimum remains available. Also the distance between the minima is not constant as soon as the stiffnesses in the wells are different. Parameters are: $\lambda_1 = 0.4$, $\lambda_0 = 0.7$, see Sec.2.5.3 for the definitions of non dimensional quantities

between the two minima varies with y while it is constant in Huxley and Simmons model. This property is needed to avoid the definition of multiple intermediate states in the power-stroke.

2.5.3 Mechanical model of a half-sarcomere

Model reduction

As we have seen in Chap.1, the half-sarcomere has a complex anatomical and molecular structure (see Fig.1.5) which we represented on Fig.2.24 as a network of connected springs. Both actin and myosin filaments are elastic (Huxley et al., 1994; Wakabayashi et al., 1994) so, in the overlapping region, each cross-bridge is mechanically coupled to its nearest neighbors by a portion of actin and myosin filaments with respective stiffnesses κ_a and κ_m. The segment of the filament stretching out of the overlapping region have stiffnesses κ_{FA} (for actin filament) and κ_{FM} for myosin filament. We can also take into account the presence of the giant protein *titin* which links the myosin filament to the M–line. Titin has a non-linear elastic behavior responsible for the passive response of muscle fiber (see Fig.1.11B). In physiological conditions, this passive elasticity is negligible.

In our complex but still very schematic picture, we do not represent the mechanical coupling between parallel half-sarcomere through the elasticity of the M– and Z–lines even though it may play an important in coherent oscillations involving different half-sarcomeres (Sato et al., 2011). As we have already mentioned, it is reasonable to neglect k_{TIT}, the elasticity of titin.

Let us first consider, the cross-bridges as elastic elements. The following computations was first presented in (Ford et al., 1981). The result was then used for the study of the influence of filament elasticity in isometric contraction in (Mijailovich et al., 1996). P–G.

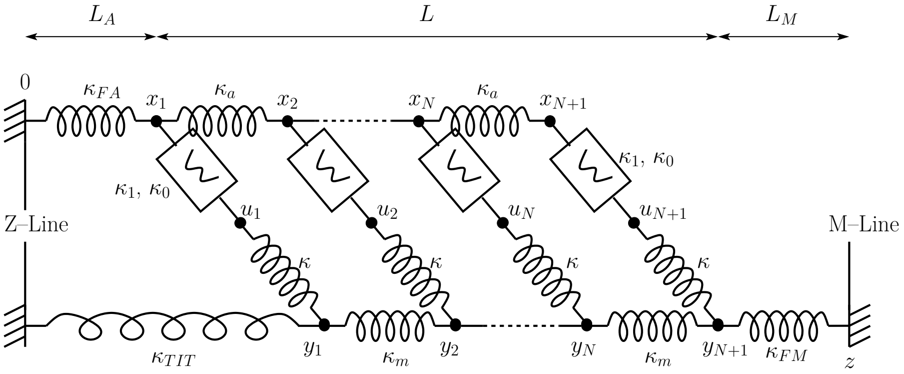

Fig. 2.24 – **Realistic model of a half-sarcomere**. The upper and lower chains of springs represents the actin and myosin filament respectively. The cross-bridges are represented by a bi-stable snap spring (κ_1, κ_0) connected in series to a linear spring κ. The part of the filament that are out of the overlapping region are characterized by the stiffnesses κ_{FA} (actin filament) and κ_{FM} (myosin filament). We can also take into account the effect of the giant protein *titin* through the elastic component κ_{TIT}

De Gennes introduced a similar computation in (De Gennes, 2001) to compute maximum pull out separating two strands of DNA.

Our mechanical system is presented on Fig.2.24. We define: L, the length of the overlapping region, L_A and L_M the length of actin and myosin filament that are out of the overlapping region. The total energy of the system is of the form:

$$V = \sum_{i=1}^{N} \frac{1}{2}\kappa_a \left(x_{i+1} - x_i\right)^2 + \sum_{i=1}^{N} \frac{1}{2}\kappa_m \left(y_{i+1} - y_i\right)^2 + \sum_{i_1}^{N+1} \frac{1}{2}\kappa \left(y_i - x_i\right)^2 + \frac{1}{2}\kappa_{FA} x_1^2 + \frac{1}{2}\kappa_{FM}\left(z - y_{N+1}\right)^2 \quad (2.5.5)$$

Then, the equilibrium conditions with respect to x_i and y_i are respectively:

$$-\frac{\partial V}{\partial x_i} = \kappa_a (x_{i+1} - 2x_i + x_{i-1}) + \kappa \left(y_i - x_i\right) = 0 \text{ for } i \geq 2 \quad (2.5.6)$$

$$-\frac{\partial V}{\partial y_i} = \kappa_m (y_{i+1} - 2y_i + y_{i-1}) - \kappa \left(y_i - x_i\right) = 0 \text{ for } i \leq N \quad (2.5.7)$$

$$-\frac{\partial V}{\partial x_1} = \kappa_a \left(x_2 - x_1\right) + \kappa \left(y_1 - x_1\right) - \kappa_{FA} x_1 = 0 \quad (2.5.8)$$

$$-\frac{\partial V}{\partial y_{N+1}} = \kappa_{FM}\left(z - y_{N+1}\right) - \kappa_m \left(y_{N+1} - y_N\right) - \kappa \left(y_{N+1} - x_{N+1}\right) = 0. \quad (2.5.9)$$

To simplify the analysis we consider the continuum limit. Then equilibrium equations can be written as:

$$\kappa_a \frac{\partial^2 x\left(\xi\right)}{\partial \xi^2} + \overline{\kappa}\left(y\left(\xi\right) - x\left(\xi\right)\right) = 0 \quad (2.5.10)$$

$$\kappa_m \frac{\partial^2 y\left(\xi\right)}{\partial \xi^2} - \overline{\kappa}\left(y\left(\xi\right) - x\left(\xi\right)\right) = 0 \quad (2.5.11)$$

where ξ is the coordinate counted from the center of the overlapping region while $\overline{\kappa} = \kappa / d\xi$, is the cross-bridge stiffness per unit length and $1/\kappa_a$ and $1/\kappa_m$ are the compliance per unit length of actin and myosin filaments respectively. The boundary conditions are $\partial y / \partial \xi = 0$

for $\xi = -L/2$ and $\partial x/\partial\xi = 0$ for $\xi = L/2$. The solution of Eqs.(2.5.10) and (2.5.11) is of the form:

$$\epsilon(\xi) = \epsilon_0 \cosh\left[\mu\left(\xi - \xi_0\right)\right] \tag{2.5.12}$$

$$\text{where } \mu^2 = \overline{\kappa}\left(\frac{1}{\kappa_m} + \frac{1}{\kappa_a}\right) \tag{2.5.13}$$

$$\text{and } \tanh\left[\mu\xi_0\right] = \frac{\kappa_a - \kappa_m}{\kappa_m + \kappa_a}\tanh\left[\mu L/2\right] \tag{2.5.14}$$

$$\epsilon_0 = \frac{\left(\frac{1}{\kappa_m} + \frac{1}{\kappa_a}\right)T}{2\mu\sinh\left[\mu L/2\right]\cosh\left[\mu\xi_0\right]} \tag{2.5.15}$$

To compute the overall stiffness of the system K we sum the elongation of the free filaments and the elongation of the overlapping region:

$$\frac{1}{K}T = \frac{1}{\kappa_{FM}}T + \frac{1}{\kappa_{FA}}T + \int_{-L/2}^{L/2}\frac{\partial y(\xi)}{\partial\xi}d\xi \tag{2.5.16}$$

After some computations we obtain:

$$\frac{1}{K} = \frac{1}{\kappa_{FA}} + \frac{1}{\kappa_{FM}} + L\frac{1}{\kappa_a + \kappa_m} + \frac{1}{2\kappa}\left(\coth\left[\mu L/2\right] + \frac{\kappa_a - \kappa_m}{\kappa_a + \kappa_m}\tanh\left[\mu L/2\right]\right) \tag{2.5.17}$$

We now consider the limit $\mu L \to 0$ (either short overlapping region or more interestingly $\mu \to 0$) and denoting $1/\kappa_{FA} = \frac{1}{\kappa_a}\left(L_{FA} - L\right)$ and $1/\kappa_{FM} = \frac{1}{\kappa_m}\left(L_{FM} - L\right)$ obtain:

$$\frac{1}{K} = \frac{1}{\kappa_a}\left(L_{FA} - \frac{2}{3}L\right) + \frac{1}{\kappa_m}\left(L_{FM} - \frac{2}{3}L\right) + \frac{1}{\kappa L} \tag{2.5.18}$$

which is the effective elasticity formula first obtained in (Ford et al., 1981). Hence, the overall compliance decomposes in a contribution related to the filaments and a part related to the cross-bridges:

$$K = \frac{K_{filaments}K_{cross-bridges}}{K_{filaments} + K_{cross-bridges}} \tag{2.5.19}$$

We now assume the half-sarcomere described on Fig.2.24 can be reduced, to a simpler system represented on Fig.2.25 with a bundle of N cross-bridges in parallel which in turn are connected in series to a spring κ_f lumping the contribution of actin and myosin filaments:

$$\frac{1}{\kappa_f} = \frac{1}{\kappa_a}\left(L_{FA} - \frac{2}{3}L\right) + \frac{1}{\kappa_m}\left(L_{FM} - \frac{2}{3}L\right). \tag{2.5.20}$$

Myofilament elasticity was largely ignored before the landmark works of H.E Huxley and K. Wakabayashi in 1994 (Huxley et al., 1994; Wakabayashi et al., 1994) who independently measured, using X-rays interference techniques, the elastic distortions of actin and myosin networks during muscle contraction. This discovery forced a complete reinterpretation of many experimental data where it was assumed that all the elasticity resided in the cross-bridges themselves.

In the rest of this Thesis, we assume that a series spring representing filaments elasticity is described by the energy:

$$V_f(z, y) = \frac{1}{2}\kappa_f\left(z - y - l_f\right)^2. \tag{2.5.21}$$

where z is the half-sarcomere length. In the limit $\kappa_f \to \infty$, this model becomes similar to the one studied in (Marcucci and Truskinovsky, 2010).

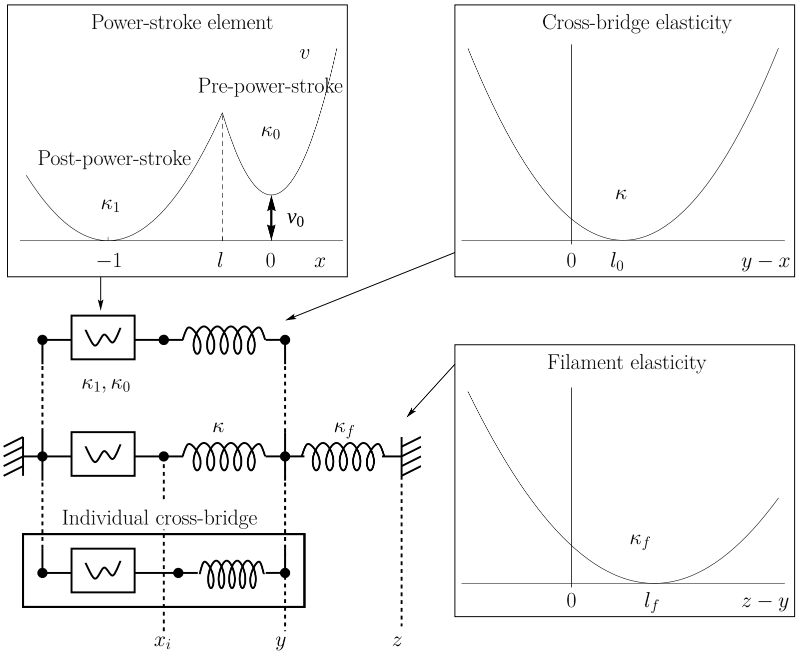

Fig. 2.25 – **Mechanical model of a half-sarcomere**. Left: schematic representation of the constitutive mechanical bricks of a half-sarcomere. The array of cross-bridges share the same total elongation ϵ_y. Together they are connected to a linear elastic element representing the elasticity of the myofilaments and possibly of other passive structures. The characteristic parameters are indicated besides the concerned elements. The characteristic energy profile of the different element are indicated by the surrounding plots.

The non dimensional form of the energy

In what follows it will be convenient to work with non dimensional quantities. A natural length scale is a, the power-stroke characteristic length, thus we define:

$$\overline{\epsilon_i} = \frac{x_i}{a};\ \overline{\epsilon_y} = \frac{y-l_0}{a};\ \overline{\epsilon} = \frac{z-(l_0+l_f)}{a} \text{ and } \overline{l} = \frac{l}{a}.$$

Next we define the characteristic force as κa and the characteristic energy as κa^2 and write the total energy in the form

$$\overline{V}\left(\epsilon_1, \dots, \epsilon_N, \overline{\epsilon_y}, \overline{\epsilon}\right) = \sum_{i=1}^{N} \left\{ \overline{v}\left(\overline{\epsilon_i}\right) + \frac{1}{2}\left(\overline{\epsilon_y} - \overline{\epsilon_i}\right)^2 \right\} + \frac{1}{2} N \lambda_f \left(\overline{\epsilon} - \overline{\epsilon_y}\right)^2 \tag{2.5.22}$$

where $\lambda_f = \kappa_f / (N\kappa)$ is the stiffness of the myofilament relative to the stiffness of the cross-bridges array and,

$$\overline{v}\left(\overline{\epsilon_i}\right) = \frac{1}{\kappa a^2} v\left(x\right) = \begin{cases} \frac{1}{2}\overline{\kappa}_0(\overline{\epsilon_i})^2 + v_0 & \text{if } \overline{\epsilon_i} > \overline{l}, \\ \frac{1}{2}\overline{\kappa}_1(\overline{\epsilon_i}+1)^2 & \text{if } \overline{\epsilon_i} \leq \overline{l}, \end{cases} \tag{2.5.23}$$

with $\overline{\kappa}_0 = \kappa_0/\kappa$ and $\overline{\kappa}_1 = \kappa_1/\kappa$. We also define:

$$\lambda_0 = \frac{\kappa_0}{k_0 + \kappa},\ \lambda_1 = \frac{\kappa_1}{k_1 + \kappa}, \tag{2.5.24}$$

The particular form chosen for λ_1 and λ_0, is convenient because then $\kappa\lambda_1$ and $\kappa\lambda_0$ represent the equivalent stiffnesses of the cross-bridge: $\frac{\kappa\kappa_1}{\kappa+\kappa_1}$ and $\frac{\kappa\kappa_0}{\kappa+\kappa_0}$. By definition, we have $0 < \lambda_1, \lambda_0 < 1$, where the upper bound is the limit of infinitely stiff wells. Here and later in the manuscript, for convenience, we drop the bars over normalized variables. Eq.(2.5.3), the relation between l and v_0 can then be rewritten as:

$$v_0 = \frac{1}{2}\frac{\lambda_1}{1-\lambda_1}(l+1)^2 - \frac{1}{2}\frac{\lambda_0}{1-\lambda_0}l^2 \tag{2.5.25}$$

It is instructive to list here the main non-dimensional parameters of the model. They include the two elasticities of the energy wells κ_1 and κ_0, the coupling parameter λ_f and the number of cross-bridges: N. Parameter l defines the location of the barrier between the pre– and the post-power-stroke state. We emphasize that N is finite (of the order of 100 (Piazzesi et al., 2007)) and therefore our system may exhibit the so called size effect (in classical statistical mechanics, $N \sim 10^{23}$). We also notice that since the temperature is finite there will be an additional parameter characterizing the amplitude of the thermal fluctuations with respect to the characteristic energy. In Chap.7, we match the model with observation and come up with an optimal set of values for our parameters.

Conclusions

In muscle mechanics, there have always been a distinction between the motors which are ATP driven and the power-strokes, which are mechanical processes driven by energy gradients. The conventional description of the power-stroke is based on the idea of infinitely narrow energy wells and it always implies the validity of Kramers approximation. In this way, the actual mechanics of the system is grossly misrepresented.

To deal with this question, we developed in this Chapter, a new model which captures the mot important mechanical ingredients of the power-stroke mechanism. In the next Chapters, we study the mechanics, the thermodynamics and the kinetics of our system preparing the way for the eventuel optimal parameter fit.

Chapter 3

Mechanical equilibrium at $\theta = 0$

Our goal is to study the response of our model of sarcomere to stepwise loading in length clamp and force clamp to see if it can reproduce the response observed in real muscle fiber (see section 2.2). Due to the presence of the non-convex bistable elements, the energy landscape of our system is rugous and is characterised by many local minima that can be identified in a purely mechanical framework. In this chapter we will restrict our analysis to these metastable states, postponing the study of dynamics till Chap.5. To adopt a mechanical vocabulary, we will speak as the system in *hard device* (resp. *soft device*) for the system under controlled total length (resp. force)

We assume that our parameters may vary in a broad range and specify their realistic values only in Chap.7 after we study the effect of finite temperature.

Contents

3.1 Energy landscape and metastable states

In hard device, the total elongation of the system is the controlled parameter. In that case, the normalized energy of our mechanical system is given by Eq.(2.5.22):

$$V\left(\epsilon_1, \ldots, \epsilon_N, \epsilon_y, \overline{\epsilon}\right) = \sum_{i=1}^{N} \left\{ v\left(\epsilon_i\right) + \frac{1}{2}\left(\epsilon_y - \epsilon_i\right)^2 \right\} + \frac{1}{2} N \lambda_f \left(\overline{\epsilon} - \epsilon_y\right)^2$$

where $\overline{\epsilon}$ is the loading parameter. In soft device, the energy of the system is the Gibbs energy:

$$W\left(\epsilon_i, \epsilon_y, \epsilon, \overline{\sigma}\right) = V\left(\epsilon_1, \ldots, \epsilon_N, \epsilon_y, \epsilon\right) - \overline{\sigma}\epsilon \tag{3.1.1}$$

where $\overline{\sigma}$ is the loading parameter.

3.1.1 Local minima of the energy

In hard device, the metastable states correspond to the zeros of the energy gradient so we have to solve [1]

$$\left\{ \begin{array}{rcl} \partial_i \left(V\left(\epsilon_1, \ldots, \epsilon_N, \epsilon_y, \overline{\epsilon}\right)\right) & = & 0, \text{ for all } 1 \leq i \leq N \\ \partial_y \left(V\left(\epsilon_1, \ldots, \epsilon_N, \epsilon_y, \overline{\epsilon}\right)\right) - & = & 0 \end{array} \right. . \tag{3.1.2}$$

In soft device, we have to minimize W by solving:

$$\left\{ \begin{array}{rcl} \partial_i \left(W\left(\epsilon_1, \ldots, \epsilon_N, \epsilon_y, \epsilon, \overline{\sigma}\right)\right) & = & 0, \text{ for all } 1 \leq i \leq N \\ \partial_y \left(W\left(\epsilon_1, \ldots, \epsilon_N, \epsilon_y, \epsilon, \overline{\sigma}\right)\right) & = & 0 \\ \partial_\epsilon \left(W\left(\epsilon_1, \ldots, \epsilon_N, \epsilon_y, \epsilon, \overline{\sigma}\right)\right) & = & 0 \end{array} \right. . \tag{3.1.3}$$

Due to the non-convexity of v, equations $\partial_i V = 0$ and $\partial_i W = 0$ have up to 3 solutions:

$$\begin{cases} \hat{\epsilon}_1\left(\epsilon_y\right) = \left(1 - \lambda_1\right)\left(\epsilon_y\right) - \lambda_1, & \text{if } \epsilon_i < l \\ \hat{\epsilon}_0\left(\epsilon_y\right) = \left(1 - \lambda_0\right)\left(\epsilon_y\right), & \text{if } \epsilon_i > l \\ \hat{\epsilon}_\star = l. \end{cases} \tag{3.1.4}$$

where ϵ_y still need to be determined from the Eqs.(3.1.2) or (3.1.3). Here $\hat{\epsilon}_\star$ is a degenerate 'spinodal' phase. Due to the permutational invariance of the energy, the equilibrium state depends only on the fraction of cross-bridges in each of the three phases. Denote $N_1, N_\star$ and N_0 the number of cross-bridges that occupy positions $\hat{\epsilon}_1, \hat{\epsilon}_\star$ and $\hat{\epsilon}_0$ respectively. We define the corresponding fractions:

- $n_1 = \frac{N_1}{N}$, the fraction of cross-bridge that occupy position $\hat{\epsilon}_1$,
- $n_0 = \frac{N_0}{N}$, the fraction of cross-bridge that occupy position $\hat{\epsilon}_0$,
- $n_\star = 1 - n_1 - n_0$, the fraction of cross-bridges at l.

The triplet $\xi = (n_1, n_\star, n_0)$ defines a *microscopic configuration* of the system. The number of possible configuration is of the order of 3^N so the energy landscape becomes extremely wiggly when N is large ($N \approx 100$ in a single half-sarcomere). This is the origin of complex behaviour in this mechanical systems. However, due to the permutational invariance of the cross-bridges, the total number of different configurations is reduced to: $\left(N+1\right)\left(N+2\right)/2 \ll 3^N$. This degeneracy is of course destroyed if full filament elasticity is taken into consideration.

---

[1] We use the following notation: $\partial_i = \frac{\partial}{\partial \epsilon_i}$ and $\partial_y = \frac{\partial}{\partial \epsilon_y}$

In the hard device, equation $\partial_y V = 0$ gives:

$$\hat{\epsilon}_y = \frac{1}{1+\lambda_f}\left(\lambda_f \overline{\epsilon} + \frac{1}{N}\sum_{i=1}^{N} \epsilon_i\right), \tag{3.1.5}$$

while in soft device, the equilibration conditions $\partial_y W = 0$ and $\partial_\epsilon W = 0$ gives:

$$\hat{\epsilon}_y = \frac{\overline{\sigma}}{N} + \frac{1}{N}\sum_{i=1}^{N} \epsilon_i, \tag{3.1.6}$$

$$\hat{\epsilon_z} = \hat{\epsilon}_y + \frac{\overline{\sigma}}{N\lambda_f}. \tag{3.1.7}$$

If we now eliminate ϵ_y from the energy (2.5.22) by using Eq.(3.1.5) we obtain, in hard device:

$$\tilde{V}\left(\epsilon_1, \dots, \epsilon_N, \overline{\epsilon}\right) = \sum_{i=1}^{N}\left\{ v\left(\epsilon_i\right) + \frac{1}{2}\left(\frac{1}{1+\lambda_f}\left(\lambda_f \overline{\epsilon} + \frac{1}{N}\sum_{i=j}^{N}\epsilon_j\right) - \epsilon_i\right)^2\right\} + \frac{1}{2}N\lambda_f\left(\frac{1}{1+\lambda_f}\overline{\epsilon} - \frac{1}{N\left(1+\lambda_f\right)}\sum_{i=1}^{N}\epsilon_i\right)^2 .$$

One can see that the individual cross-bridges ϵ_i interact now with the *mean field* generated by all other cross-bridges (see the second term of the first sum). The coupling parameter λ_f^{-1} controls the intensity of this interaction: the larger the coupling parameter, the stronger the mean-field interaction. In soft device, we obtain using Eqs.(3.1.6) and (3.1.7):

$$\tilde{W}\left(\epsilon_1, \dots, \epsilon_N, \overline{\sigma}\right) = \sum_{i=1}^{N}\left\{ v\left(\epsilon_i\right) + \frac{1}{2}\left(\frac{\overline{\sigma}}{N} + \frac{1}{N}\sum_{i=j}^{N}\epsilon_j - \epsilon_i\right)^2\right\} + \frac{1}{2}\frac{N}{\lambda_f}\left(\frac{\overline{\sigma}}{N}\right)^2 - \overline{\sigma}\left(\frac{\overline{\sigma}}{N}\frac{1+\lambda_f}{N\lambda_f} + \frac{1}{N}\sum_{i=1}^{N}\epsilon_i\right)$$

In this case, the level of coupling between cross-bridges is not affected by the value of λ_f, instead the coupling is inherent. In particular, the level of coupling is independent on the magnitude of the applied force $\overline{\sigma}$.

In hard device, the solution of the minimization problem for a given microscopic configuration $\xi = (n_1, n_\star, n_0)$ is:

$$\hat{\epsilon}_1\left(\overline{\epsilon}, \xi\right) = \frac{1-\lambda_1}{\lambda_f + \lambda_{xb}\left(\xi\right)}\left(\lambda_f \overline{\epsilon} - n_1\lambda_1 + n_\star l\right) - \lambda_1 \tag{3.1.8}$$

$$\hat{\epsilon}_0\left(\overline{\epsilon}, \xi\right) = \frac{1-\lambda_0}{\lambda_f + \lambda_{xb}\left(\xi\right)}\left(\lambda_f \overline{\epsilon} - n_1\lambda_1 + n_\star l\right) \tag{3.1.9}$$

$$\hat{\epsilon}_y\left(\overline{\epsilon}, \xi\right) = \frac{\lambda_f}{\lambda_f + \lambda_{xb}\left(\xi\right)}\left(\overline{\epsilon} - \frac{n_1\lambda_1 - n_\star l}{\lambda_f}\right) \tag{3.1.10}$$

where we have introduced the equivalent non-dimensional stiffness of the array of cross-bridges:

$$\lambda_{xb}\left(\xi\right) = n_1\lambda_1 + n_0\lambda_0 + n_\star. \tag{3.1.11}$$

Thus, the total tension in configuration ξ is given by:

$$\hat{T}\left(\overline{\epsilon},\xi\right) = N\frac{\lambda_f\lambda_{xb}\left(\xi\right)}{\lambda_f+\lambda_{xb}\left(\xi\right)}\left(\overline{\epsilon}+\frac{n_1\lambda_1-n_\star l}{\lambda_{xb}\left(n_1,n_\star,n_0\right)}\right), \tag{3.1.12}$$

where we recognize the equivalent stiffness of 2 springs in series $\frac{\lambda_{xb}\lambda_f}{\lambda_{xb}+\lambda_f}$. Finally, we can express the energy of configuration ξ as:

$$\hat{V}\left(\overline{\epsilon},\xi\right) = \frac{N}{2}\left(\frac{\lambda_f\left(n_1\lambda_1\left(\overline{\epsilon}+1\right)^2+n_0\lambda_0\overline{\epsilon}^2+n_\star\left(\overline{\epsilon}-l\right)^2\right)}{\lambda_f+\lambda_{xb}\left(\xi\right)}\right.$$
$$+\frac{n_1\lambda_1\left(n_0\lambda_0+n_\star(1+2l)\right)-n_\star l^2(n_\star+\lambda_f)}{\lambda_f+\lambda_{xb}\left(\xi\right)}$$
$$\left.+n_\star\frac{l^2}{1-\lambda_0}+2\left(n_0+n_\star\right)v_0\right). \tag{3.1.13}$$

In soft device, one finds:

$$\hat{\epsilon}_1\left(\overline{\sigma},\xi\right) = \frac{\left(1-\lambda_1\right)}{\lambda_{xb}\left(\xi\right)}\left(\frac{\overline{\sigma}}{N}-n_1\lambda_1+n_\star l\right)-\lambda_1, \tag{3.1.14}$$

$$\hat{\epsilon}_0\left(\overline{\sigma},\xi\right) = \frac{\left(1-\lambda_0\right)}{\lambda_{xb}\left(\xi\right)}\left(\frac{\overline{\sigma}}{N}-n_1\lambda_1+n_\star l\right), \tag{3.1.15}$$

$$\hat{\epsilon}_y\left(\overline{\sigma},\xi\right) = \frac{1}{\lambda_{xb}\left(\xi\right)}\frac{\overline{\sigma}}{N}-\frac{n_1\lambda_1-n_\star l}{\lambda_{xb}\left(\xi\right)}, \tag{3.1.16}$$

$$\hat{\epsilon}\left(\overline{\sigma},\xi\right) = \left(\frac{1}{\lambda_f}+\frac{1}{\lambda_{xb}\left(\xi\right)}\right)\frac{\overline{\sigma}}{N}-\frac{n_1\lambda_1-n_\star l}{\lambda_{xb}\left(\xi\right)}, \tag{3.1.17}$$

and the energy:

$$\hat{W}\left(\overline{\sigma},\xi\right) = -\frac{N}{2}\left(\frac{1}{\lambda_{xb}\left(\xi\right)}\left(\frac{\overline{\sigma}}{N}-n_1\lambda_1+n_\star l\right)^2\right.$$
$$\left.+\frac{\overline{\sigma}^2}{N^2\lambda_f}-2\left(n_0+n_\star\right)v_0-n_\star\frac{l^2}{1-\lambda_0}-n_1\lambda_1\right). \tag{3.1.18}$$

3.1.2 Existence domain of metastable states

Since $\hat{\epsilon_1}$ and $\hat{\epsilon}_0$ are increasing functions of $\overline{\epsilon}$ (see Eq.3.1.4),it is clear that for increasing ϵ_y (resp. decreasing ϵ_y), the condition $\hat{\epsilon_1} < l$ (resp. $\hat{\epsilon}_0 > l$) will ultimately be violated. This implies that a given configuration $(n_1, n_\star, n_0)$ exists only on a finite interval of $\overline{\epsilon}$ (or $\overline{\sigma}$). This is a fundamental difference between our model and existing chemo-mechanical models where the analogue chemical states are accessible at any level of loading ($\overline{\epsilon}, \overline{\sigma}$, see Sec.2.4.4).

More precisely, in hard device, a metastable state $(n_1, n_\star, n_0)$ exists in the interval $[\overline{\epsilon}_{\inf}, \overline{\epsilon}_{\sup}]$ defined by:

$$\overline{\epsilon}_{\inf}\left(\xi\right) = \frac{l\left(\lambda_f+\lambda_{xb}\left(\xi\right)\right)+\left(1-\lambda_0\right)\left(n_1\lambda_1-n_\star l\right)}{\lambda_f\left(1-\lambda_0\right)}, \tag{3.1.19}$$

$$\overline{\epsilon}_{\sup}\left(\xi\right) = \frac{\left(l+\lambda_1\right)\left(\lambda_f+\lambda_{xb}\left(\xi\right)\right)+\left(1-\lambda_1\right)\left(n_1\lambda_1-n_\star l\right)}{\lambda_f\left(1-\lambda_1\right)}. \tag{3.1.20}$$

The special cases are the homogeneous configurations $(1,0,0)$ and $(0,0,1)$ defined on $]-\infty, \overline{\epsilon}_{\text{sup}}(1,0,0)]$ and $[\overline{\epsilon}_{\text{inf}}(0,0,1), +\infty[$, respectively. In particular, for $\overline{\epsilon} < \overline{\epsilon}_{\text{inf}}(0,0,1)$ (resp. $\overline{\epsilon} > \overline{\epsilon}_{\text{sup}}(1,0,0)$) only configuration $(1,0,0)$ (resp. $(0,0,1)$) is available.

Similarly, in soft device, we define the lower and upper boundaries of the configuration $(n_1, n_\star, n_0)$:

$$\overline{\sigma}_{\text{sup}}(\xi) = N\left(\frac{l+\lambda_1}{1-\lambda_1}\lambda_{xb}(\xi) + n_1\lambda_1 - n_\star l\right), \tag{3.1.21}$$

$$\overline{\sigma}_{\text{inf}}(\xi) = N\left(\frac{l}{1-\lambda_0}\lambda_{xb}(\xi) + n_1\lambda_1 - n_\star l\right). \tag{3.1.22}$$

The homogeneous configurations are, of course, again special.

In Fig.3.1 and 3.2 we show a representation of all the metastable states in the case $N = 3$ in hard and soft device respectively. The parameters chosen for this computation are $\lambda_1 = 0.4, \lambda_0 = 0.7, l = -0.3, \lambda_f = 2$. The labels on the curve represent the configurations expressed in term of number of cross-bridges in different states rather than in terms of their fractions. Note that each configuration $(n_1, n_\star, n_0)$ exists on its own finite interval.

For the resulting picture to be non-trivial, we need to have the following inequality satisfied:

$$\begin{aligned}\Delta\overline{\epsilon}(\xi) &= \overline{\epsilon}_{\text{sup}}(\xi) - \overline{\epsilon}_{\text{inf}}(n_1, n_0)\\ &= \frac{(\lambda_1(\lambda_0 - 1 - l) + l\lambda_0)(n_1\lambda_1 + n_0\lambda_0 + n_\star + \lambda_f)}{\lambda_f(1-\lambda_0)(1-\lambda_0)}\end{aligned}$$

This implies the following relation between the parameters:

$$\lambda_1(\lambda_0 - 1 - l) + l\lambda_0 \geq 0$$

which correspond to $-1 < l < 0$.

3.1.3 Stability

The shape of the bistable potential $v(\epsilon)$ is very singular since the spinodal region is reduced to a single point. To study the stability, we remove temporarily this singularity by considering a smoother transition where the potential shows a negative second derivative in an extended spinodal interval $[l-t; l+t]$. Outside this interval the potential has a positive second derivative. Hence our singular case can be viewed as the limit of this smoothed potential when $t \to 0$. We also assume that the spinodal region makes the total energy twice continuously differentiable (class C^2). We present the discussion of the stability of metastable states in the hard device case, the result is the same in soft device even though it is not usually the case. Here, the similarity comes from the fact that the cross-bridges are arranged in parallel and not in series.

Within the present mode with landscape, for a given $\overline{\epsilon}$, the equation $\partial_i V = 0$ has up to 3 solutions, $\hat{e}_1(\overline{\epsilon}), \hat{e}_0(\overline{\epsilon})$ and $\hat{\epsilon}_\star(\overline{\epsilon})$, with $l - t \leq \hat{\epsilon}_\star(\overline{\epsilon}) \leq l + t$ for all $t > 0$. We define (no summation):

$$\begin{aligned}\partial_{ii}V(\overline{\epsilon}, \epsilon_1, \ldots, \epsilon_N, \epsilon_y)\big|_{\epsilon_i = \hat{\epsilon}_1(\overline{\epsilon}), \epsilon_y = \hat{\epsilon}_y(\overline{\epsilon}), \epsilon_{j\neq i} = \hat{\epsilon}_j(\overline{\epsilon})} &\equiv h_1(\overline{\epsilon}) > 0,\\ \partial_{ii}V(\overline{\epsilon}, \epsilon_1, \ldots, \epsilon_N, \epsilon_y)\big|_{\epsilon_i = \hat{\epsilon}_\star(\overline{\epsilon}), \epsilon_y = \hat{\epsilon}_y(\overline{\epsilon}), \epsilon_{j\neq i} = \hat{\epsilon}_j(\overline{\epsilon})} &\equiv h_\star(\overline{\epsilon}) < 0,\\ \partial_{ii}V(\overline{\epsilon}, \epsilon_1, \ldots, \epsilon_N, \epsilon_y)\big|_{\epsilon_i = \hat{\epsilon}_0(\overline{\epsilon}), \epsilon_y = \hat{\epsilon}_y(\overline{\epsilon}), \epsilon_{j\neq i} = \hat{\epsilon}_j(\overline{\epsilon})} &\equiv h_0(\overline{\epsilon}) > 0.\end{aligned}$$

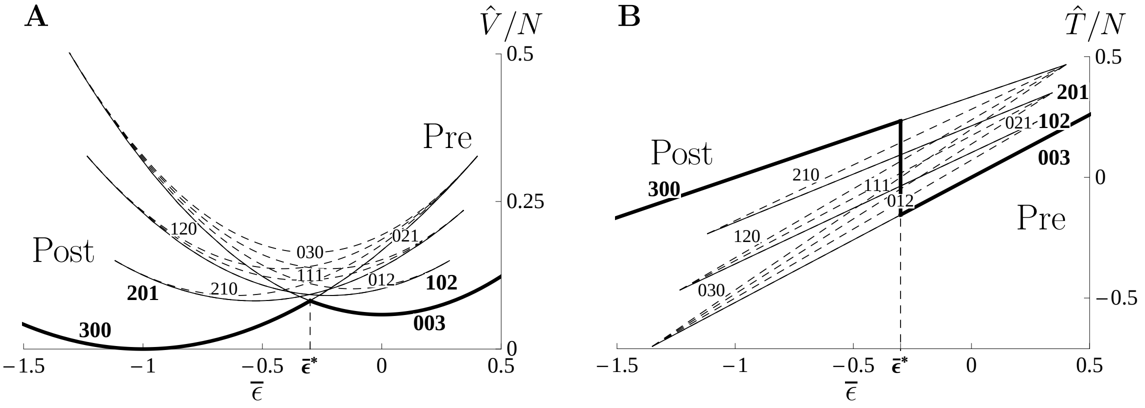

Fig. 3.1 – **Representation of the metastable states in hard device for a system with $N = 3$ cross-bridges** . For this picture we used the following parameters: $\lambda_1 = 0.4$, $\lambda_0 = 0.7$, $l = -0.3$, $\lambda_f = 2$. The bold triplet $N\{n_1, n_\star, n_0\}$, indicates the number of cross-bridges in each phase and identifies individual branches. Solid lines indicate the stable states, dashed lines the unstable ones and bold line, the global minimum. The position of the global minimum transition between the two affine configurations (300) and (003) is localised at $\overline{\epsilon} = \overline{\epsilon}^\star$.

For each case, the second derivative of V does not depend on ϵ_y. We further denote:

$$H_i\left(\overline{\epsilon}\right) = \partial_{ii} V\left(\overline{\epsilon}, \epsilon_1, \ldots, \epsilon_N, \epsilon_y\right)\big|_{\epsilon_i=\hat{\epsilon}_i(\overline{\epsilon}), \epsilon_y=\hat{\epsilon}_y(\overline{\epsilon}), \epsilon_{j\neq i}=\hat{\epsilon}_j(\overline{\epsilon})}\,, \; i = 1, \ldots, N \text{ (no summation)}$$

the N first diagonal terms of the Hessian. Each of them can be equal either to $h_1\left(\overline{\epsilon}\right)$, $h_0\left(\overline{\epsilon}\right)$ or $h^\star\left(\overline{\epsilon}\right)$. The other terms of the hessian $H\left(\overline{\epsilon}\right)$ are:

$$\partial_{ij}\, V\left(\overline{\epsilon}, \epsilon_1, \ldots, \epsilon_N, \epsilon_y\right)\big|_{\epsilon_i=\hat{\epsilon}_i(\overline{\epsilon}), \epsilon_j=\hat{\epsilon}_j(\overline{\epsilon}), e_{k\neq i,j}=\hat{\epsilon}_k(\overline{\epsilon}), \epsilon_y=\hat{\epsilon}_y(\overline{\epsilon})} = 0 \text{ for } i \neq j \tag{3.1.23}$$

$$\partial_{iy}\, V\left(\overline{\epsilon}, \epsilon_1, \ldots, \epsilon_N, \epsilon_y\right)\big|_{\epsilon_i=\hat{\epsilon}_i(\overline{\epsilon}), \epsilon_{j\neq i}=\hat{\epsilon}_j(\overline{\epsilon}), \epsilon_y=\hat{\epsilon}_y(\overline{\epsilon})} = -1 \text{ for } i = 1, \ldots, N \tag{3.1.24}$$

$$\partial_{yy}\, V\left(\overline{\epsilon}, \epsilon_1, \ldots, \epsilon_N, \epsilon_y\right)\big|_{\epsilon_i=\hat{\epsilon}_i(\overline{\epsilon}), \epsilon_y=\hat{\epsilon}_y(\overline{\epsilon})} = N\left(1 + \lambda_f\right). \tag{3.1.25}$$

Therefore,

$$H\left(\overline{\epsilon}\right) = \begin{pmatrix} H_1\left(\overline{\epsilon}\right) & 0 & \cdots & 0 & -1 \\ 0 & \ddots & \ddots & \vdots & \vdots \\ \vdots & \ddots & \ddots & 0 & \vdots \\ 0 & \cdots & 0 & H_N\left(\overline{\epsilon}\right) & -1 \\ -1 & \cdots & \cdots & -1 & N\left(1+\lambda_f\right) \end{pmatrix}.$$

From the form of $H\left(\overline{\epsilon}\right)$, it is clear that as soon as one term H_i is equal to $h^\star\left(\overline{\epsilon}\right)$, there are at least one principal minors of $H\left(\overline{\epsilon}\right)$that is negative. This means that the absence of cross-bridges in the spinodal region is mandatory for stability of the critical point for all $t > 0$. The equilibrium strain in the spinodal region remains between $-t$ and t and thus converges to l, when t goes to 0. Therefore, if $n_\star \neq 0$, the configuration $\left(n_1, n_\star, n_0\right)$ is necessary unstable. Hence among the $\left(N+1\right)\left(N+2\right)/2$ branches of equilibrium, $N\left(N+1\right)/2$ are unstable which leaves $N + 1$ stable branches. On Figs.3.1 and 3.2, showing the case $N = 3$, stable branches are identified by solid lines, unstable by dashed lines and the global minimum by bold lines.

3.1.4 The global minimum

Let us now consider, at a fix $\overline{\epsilon}$ and consider the energy of the stable configurations $\left(n_1, 0, 1 - n_1\right)$ as a a function of n_1. The goal is to determine the local minimum with

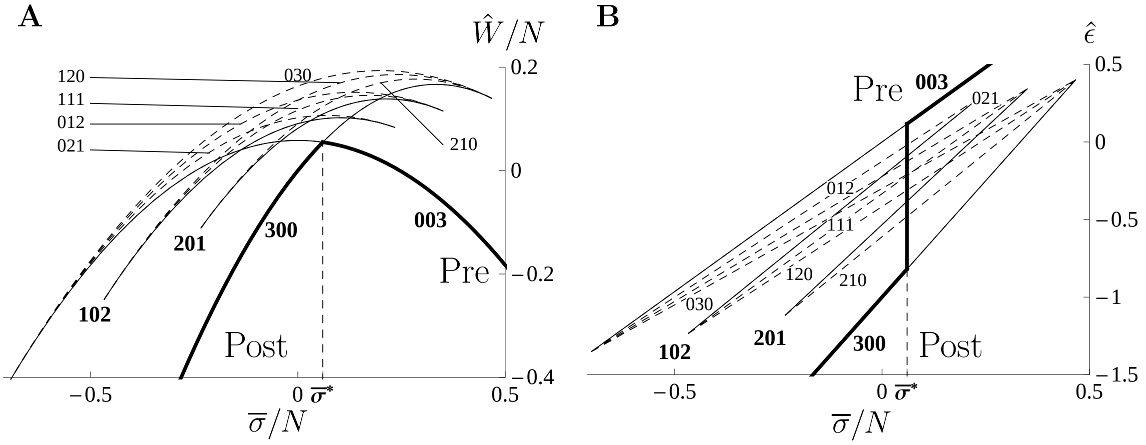

Fig. 3.2 – **Representation of the metastable states in soft device for a system with $N = 3$ cross-bridges** . For this picture we used the following parameters: $\lambda_1 = 0.4$, $\lambda_0 = 0.7$, $l = -0.3$, $\lambda_f = 2$. The bold triplet $N\,\{n_1, n_\star, n_0\}$, indicates the number of cross-bridges in each phase and identifies individual branches. Solid lines indicate the stable states, dashed lines the unstable ones and bold line, the global minimum. The position of the global minimum transition between the two affine configurations (300) and (003) is localised at $\overline{\sigma} = \overline{\sigma}^{\star}$.

the lowest energy level. The energy of the global minimum will be denoted $\hat{V}_{GM}$ in hard device and $\hat{W}_{GM}$ in soft device. As it was shown in section 3.1.2,

$$\hat{V}_{GM}(\overline{\epsilon}, n_1) = \begin{cases} \frac{N}{2}\frac{\lambda_1\lambda_f}{\lambda_1+\lambda_f}\left(\overline{\epsilon}+1\right)^2 & \text{if } \overline{\epsilon} < \overline{\epsilon}_{\inf}(0,0,1), \\ \frac{N}{2}\frac{\lambda_0\lambda_f}{\lambda_0+\lambda_f}\overline{\epsilon}^2 + Nv_0 & \text{if } \overline{\epsilon} > \overline{\epsilon}_{\sup}(1,0,0). \end{cases} \tag{3.1.26}$$

$$\hat{W}_{GM}(\overline{\sigma}, n_1) = \begin{cases} N\left(-\frac{1}{2}\left(\frac{1}{\lambda_1}+\frac{1}{\lambda_f}\right)\left(\frac{\overline{\sigma}}{N}\right)^2 + \frac{\overline{\sigma}}{N}\right) & \text{if } \overline{\sigma} < \overline{\sigma}_{\inf}\left(0,0,1\right), \\ N\left(-\frac{1}{2}\left(\frac{1}{\lambda_0}+\frac{1}{\lambda_f}\right)\left(\frac{\overline{\sigma}}{N}\right)^2 + v_0\right)) & \text{if } \overline{\sigma} > \overline{\sigma}_{\sup}\left(1,0,0\right). \end{cases} \tag{3.1.27}$$

Now between $\overline{\epsilon}_{\inf}(n_1, 0, 1-n_1)$ and $\overline{\epsilon}_{\sup}(n_1, 0, 1-n_1,)$ (resp. $\overline{\sigma}_{\inf}\left(n_1, 0, 1-n_1\right)$ and $\overline{\sigma}_{\sup}\left(n_1, 0n1-n_1\right)$), the energy in the stable local minima is parametrized by n_1:

$$\hat{V}\left(\overline{\epsilon}, n_1\right) = \frac{N}{2}\left(\frac{\lambda_f\left(n_1\lambda_1\left(\overline{\epsilon}+1\right)^2 + \left(1-n_1\right)\lambda_0\overline{\epsilon}^2\right)}{\lambda_f + n_1\lambda_1 + \left(1-n_1\right)\lambda_0} + \frac{n_1\lambda_1\left(1-n_1\right)\lambda_0}{\lambda_f + n_1\lambda_1 + \left(1-n_1\right)\lambda_0} + 2\left(1-n_1\right)v_0\right). \tag{3.1.28}$$

$$\hat{W}\left(\overline{\sigma}, n_1\right) = -\frac{N}{2}\left(\frac{1}{n_1\lambda_1 + \left(1-n_1\right)\lambda_0}\left(\frac{\overline{\sigma}}{N} - n_1\lambda_1\right)^2 + \frac{\overline{\sigma}^2}{N^2\lambda_f} - 2\left(1-n_1\right)v_0 - n_1\lambda_1\right). \tag{3.1.29}$$

If we assume for the time being that n_1 is a continuous variable, we can compute the second derivative of V and W with respect to n_1:

$$\partial_{n_1 n_1} V\left(\overline{\epsilon}, n_1\right) = -\frac{N}{2} \frac{\left(\lambda_f \lambda_1 \left(\overline{\epsilon}+1\right) + \lambda_0 \left(\lambda_1 - \overline{\epsilon}\lambda_f\right)\right)^2}{\left(n_1\lambda_1 + \left(1-n_1\right)\lambda_0 + \lambda_f\right)^3} \leq 0 \tag{3.1.30}$$

$$\partial_{n_1 n_1} W\left(\overline{\sigma}, n_1\right) = -\frac{N}{2} \left(\frac{2\left(\lambda_1-\lambda_0\right)^2 \left(\overline{\sigma}/N - n_1\lambda_1\right)^2}{\left(n_1\lambda_1 + \left(1-n_1\right)\lambda_0\right)^3} + \frac{2\lambda_1^2}{n_1\lambda_1 + \left(1-n_1\right)\lambda_0} \right) \leq 0 \tag{3.1.31}$$

which means that the minimum of the energy is attained either for $n_1 = 0$ or $n_1 = 1$. Therefore the stable configuration with the minimum energy is either $(1, 0, 0)$ or $(0, 0, 1)$. We came down to the same conclusion in soft device. We define $\overline{\epsilon}^\star$ (resp. $\overline{\sigma}^\star$), the point where $\hat{V}\left(\overline{\epsilon}, 1, 0, 0\right) = \hat{V}\left(\overline{\epsilon}, 0, 0, 1\right)$ (resp. $\hat{W}\left(\overline{\sigma}, 1, 0, 0\right) = \hat{W}\left(\overline{\sigma}, 0, 0, 1\right)$). Therefore:

$$\hat{V}_{GM}(\overline{\epsilon}) = \begin{cases} N\left(\frac{1}{2}\frac{\lambda_1\lambda_f}{\lambda_1+\lambda_f}\left(\overline{\epsilon}+1\right)^2\right) & \text{if } \overline{\epsilon} < \overline{\epsilon}^\star, \\ N\left(\frac{1}{2}\frac{\lambda_0\lambda_f}{\lambda_0+\lambda_f}\overline{\epsilon}^2 + v_0\right) & \text{if } \overline{\epsilon} > \overline{\epsilon}^\star, \end{cases} \tag{3.1.32}$$

and,

$$\hat{W}_{GM}(\overline{\sigma}) = \begin{cases} N\left(-\frac{1}{2}\left(\frac{1}{\lambda_1}+\frac{1}{\lambda_f}\right)\left(\frac{\overline{\sigma}}{N}\right)^2 + \frac{\overline{\sigma}}{N}\right) & \text{if } \overline{\sigma} < \overline{\sigma}^\star, \\ N\left(-\frac{1}{2}\left(\frac{1}{\lambda_0}+\frac{1}{\lambda_f}\right)\left(\frac{\overline{\sigma}}{N}\right)^2 + v_0\right)) & \text{if } \overline{\sigma} > \overline{\sigma}^\star. \end{cases} \tag{3.1.33}$$

Hence, when the absolute temperature θ goes to zero, if the system follows the global minimum, we observe a sharp transition either in force (in hard device) or in length (in soft device) (see Fig.3.1 for hard device and Fig.3.2 for soft device), as the system jumps from configuration $(1, 0, 0)$ to $(0, 0, 1)$. The details of the transition and the size of the barrier are still unclear, because, we do not know the path followed by the system to go between the configurations $(1, 0, 0)$ to $(0, 0, 1)$: we will discus this in details in section 3.3.

If we interpret our conclusions in the light of experimental results, and would identify the T_2 curve with the global minimum, we may notice that the mechanical approach predicts a sharp transition between the 2 linear regimes which, of course, is not observed in experiments (see Fig.2.5).

3.2 Influence of the parameters

Our non dimensional model depends on 5 parameters. Three of them, λ_1, λ_0 and l control the shape of the bistable potential, the fourth λ_f is the stiffness of the filaments and the fifth N is the number of cross-bridges. We will first study the influence of the shape of the double well potential. As a reference set we consider the following choice of parameters: $\lambda_1 = 0.5$, $\lambda_0 = 0.5$, $l = -0.5$ (a symmetric double well potential) and $\lambda_f = 1$. The energy and tension will be represented divided by N which gives 'per cross-bridge' values (Fig.3.3, 3.4, 3.5, 3.6, 3.7 and 3.8). To avoid the representation of all the local minima, we show only the contour of the region where metastable states are present (delimited by dotted lines), together with the stable configurations $(0.5, 0, 0.5)$, $(1, 0, 0)$ and $(0, 0, 1)$ (solid line),the unstable state $(0, 1, 0)$ (dashed line) and the global minimum (bold line).

3.2.1 Shape of the double well potential

Stiffness of pre and post-power-stroke configuration

Fig.3.3 and 3.4 show how the structure of the local minima depends on the stiffness of energy wells 1 and 0. Of course, a change in $\lambda_{1,0}$ changes the stiffness of the different

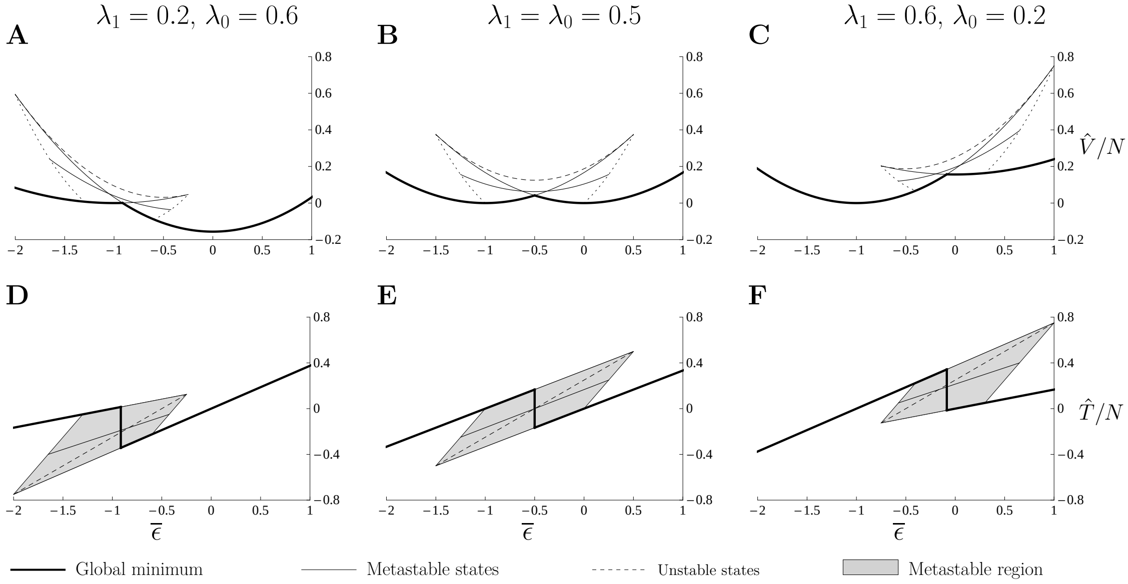

Fig. 3.3 – **Influence of the stiffness of pre-power-stroke and post-power-stroke states on the metastable states in hard device**. The values of λ_1 and λ_0 are indicated on the figure. The global minimum is represented with the thick line. We represented the 2 limit metastable states $(1, 0, 0)$ and $(1, 0, 0)$ together with the state $\left(\frac{1}{2}, 0, \frac{1}{2}\right)$ (continuous line). The unstable state $(0, 1, 0)$ is represented by the dashed line and dotted lines delimits the region of metastability.

configuration and also the transition point $\epsilon^\star$ is shifted to the right if $\lambda_1 > \lambda_0$ and to the left otherwise. Moreover the transition is no longer located in the center of the metastable region (compare with the bold figure representing the symmetric case $\lambda_1 = \lambda_0 = 1/2$). Also note that the energy minima (and therefore the zeros of tension) of the limit configurations $(1, 0, 0)$ and $(0, 0, 1)$ remain the same independently of the stiffnesses λ_1 and λ_0. This can be seen directly from the form of Eq.3.1.12, 3.1.17, where we also see that the zeros of intermediate configurations depend on the well stiffnesses.

Symmetric wells, influence of l

Parameter l Characterizes the limit point between the two wells of the potential v. It controls the value of the energy offset v_0 through Eq.(2.5.25). Fig.3.5 and 3.6 show that l shifts the metastable region but does not change its shape nor the relative position of the transition. We also see that the energy level of homogeneous configuration $(1, 0, 0)$ is not affected by l in accordance with the expression for $\hat{V}$ and $\hat{W}$ in Eq.(3.1.13) and Eq.(3.1.18): indeed l enters this expression through v_0 which disappears when $n_0 = n_\star = 0$.

3.2.2 Stiffness of the filaments and the energy gap

The elastic distortion measured in muscle fiber cannot be attributed only to the cross-bridges (Huxley et al., 1994; Wakabayashi et al., 1994). Our Fig.3.7 and 3.6 show, that when the filaments are compliant (finite λ_f), the existence interval of each configuration is different (see the tilted boundaries of the metastable region when λ_f is finite). Fig.3.7 and 3.6 are obtained with a non symmetric double well potential: $\lambda_1 = 0.4$, $\lambda_0 = 0.7$, $l = -0.3$. The points where the tension is equal to 0 remain the same independently of the value of λ_f. In addition, the position of the transition $\overline{\epsilon}^\star$ depends on λ_f in hard device (see Fig.3.7) while it is unchanged in soft device (see Fig.3.8). In the limit $\lambda_f \to 0$ (not

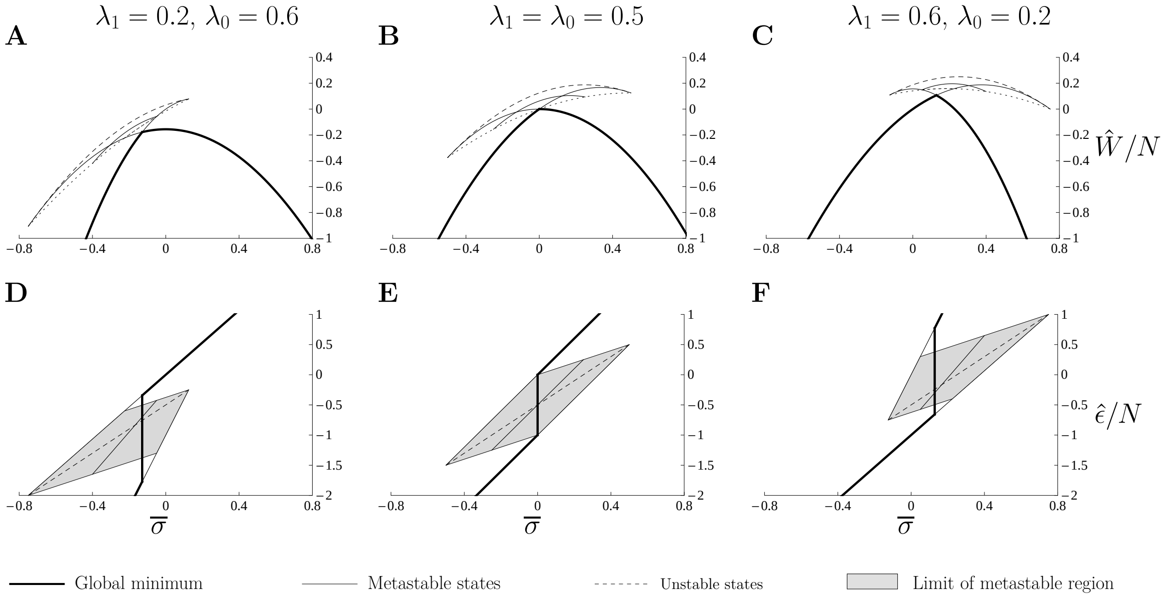

Fig. 3.4 – Influence of the stiffness of pre-power-stroke and post-power-stroke states on the metastable states in soft device. The values of λ_1 and λ_0 are indicated on the figure. The global minimum is represented with the thick line. We represented the 2 limit metastable states $(1,0,0)$ and $(1,0,0)$ together with the state $\left(\frac{1}{2},0,\frac{1}{2}\right)$ (continuous line). The unstable state $(0,1,0)$ is represented by the dashed line and dotted lines delimits the region of metastability.

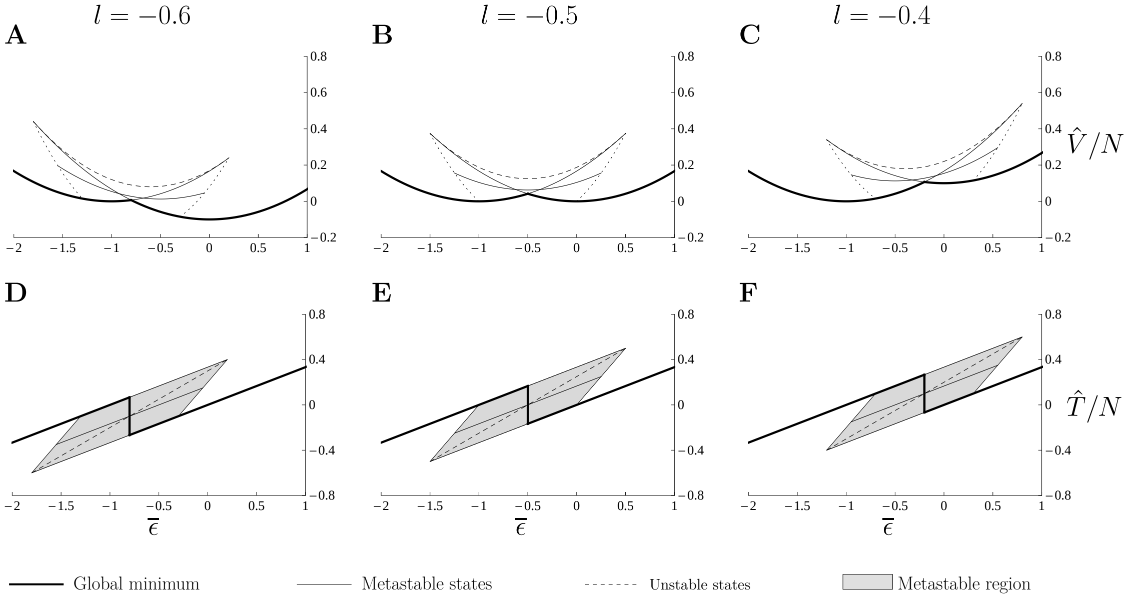

Fig. 3.5 – Influence of l on the structure of the energy landscape in hard device. The values used are indicated on the figures. The other parameters are: $\lambda_1 = \lambda_0 = 1/2; \lambda_f = 1$. The global minimum is represented with the thick line. We represented the 2 limit metastable states $(1,0,0)$ and $(1,0,0)$ together with the state $\left(\frac{1}{2},0,\frac{1}{2}\right)$ (continuous line). The unstable state $(0,1,0)$ is represented by the dashed line and dotted lines delimits the region of metastability.

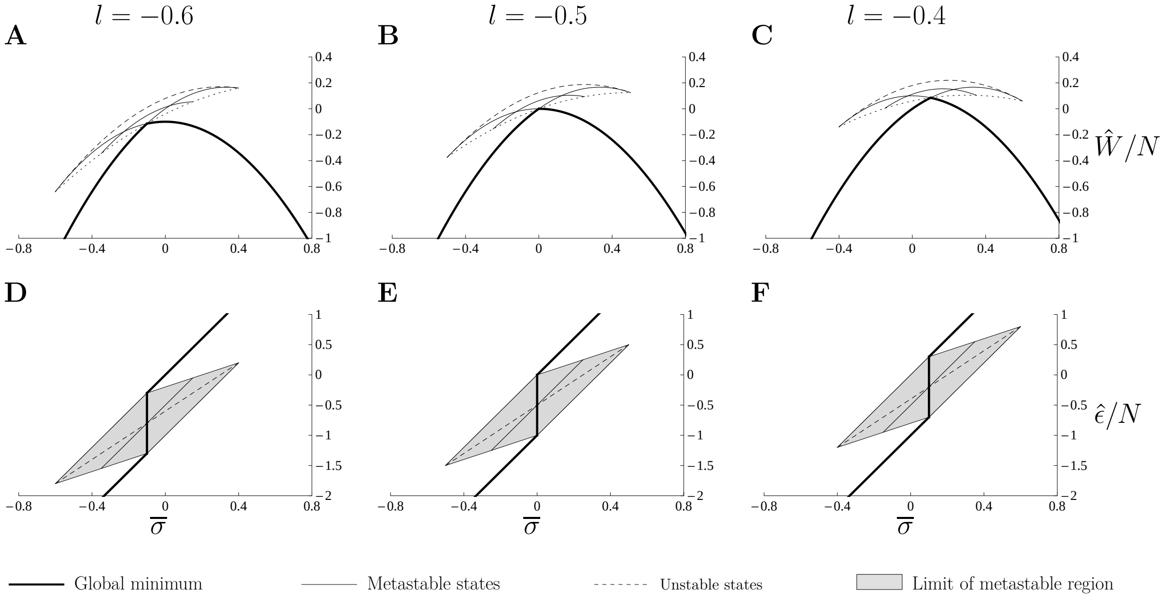

Fig. 3.6 – Influence of l on the structure of the energy landscape in soft device. The values used are indicated on the figures. The other parameters are: $\lambda_1 = \lambda_0 = 1/2; \lambda_f = 1$. The global minimum is represented with the thick line. We represented the 2 limit metastable states $(1,0,0)$ and $(1,0,0)$ together with the state $\left(\frac{1}{2},0,\frac{1}{2}\right)$ (continuous line). The unstable state $(0,1,0)$ is represented by the dashed line and dotted lines delimit the region of metastability.

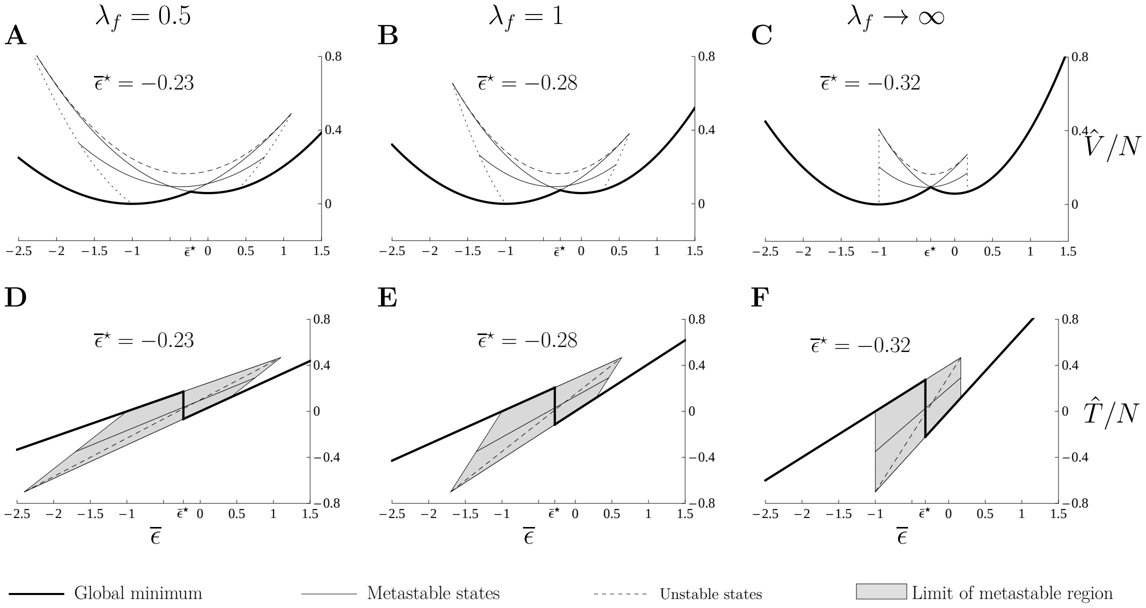

Fig. 3.7 – Influence of λ_f on the structure of the energy landscape in hard device. The values used are indicated on the figures. The other parameters are: $\lambda_1 = 0.4; \lambda_0 = 0.7; l = -0.3$.The global minimum is represented with the thick line. We represented the 2 limit metastable states $(1,0,0)$ and $(1,0,0)$ together with the state $\left(\frac{1}{2},0,\frac{1}{2}\right)$ (continuous line). The unstable state $(0,1,0)$ is represented by the dashed line and dotted lines delimit the region of metastability

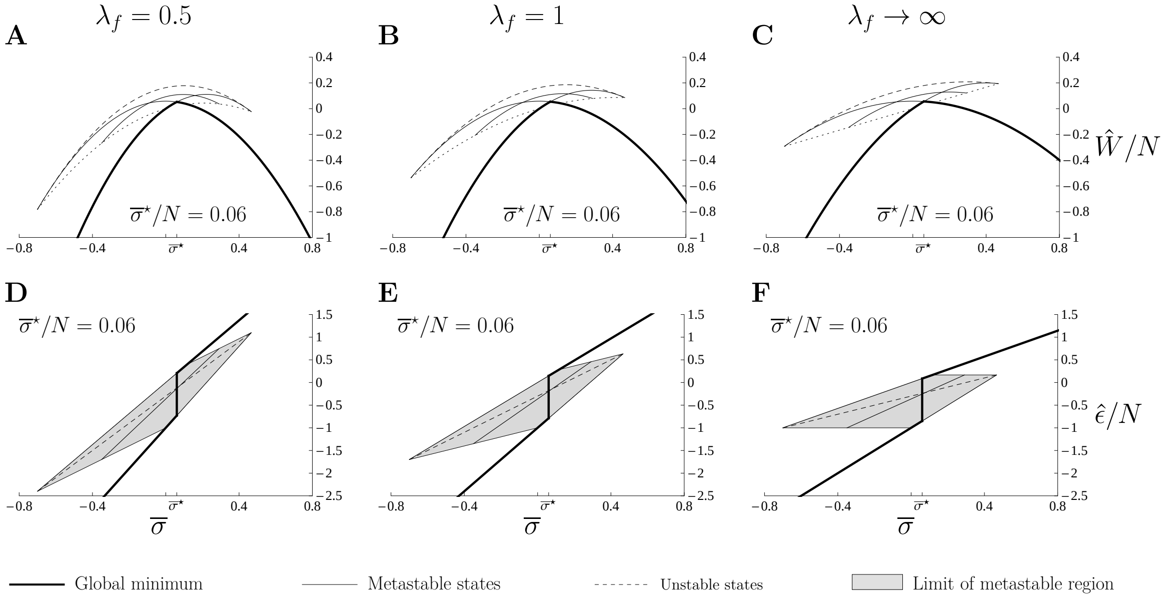

Fig. 3.8 – **Influence of λ_f on the structure of the energy landscape in soft device**. The values used are indicated on the figures. The other parameters are: $\lambda_1 = 0.4; \lambda_0 = 0.7; l = -0.3$.The global minimum is represented with the thick line. We represented the 2 limit metastable states $(1, 0, 0)$ and $(1, 0, 0)$ together with the state $\left(\frac{1}{2}, 0, \frac{1}{2}\right)$ (continuous line). The unstable state $(0, 1, 0)$ is represented by the dashed line and dotted lines delimit the region of metastability

shown here) the overall stiffness which has the form $\lambda_f \lambda_{xb} / \left(\lambda_f + \lambda_{xb}\right)$ tends to λ_f and the system looses exhibits an elastic behaviour.

In addition, the presence of smooth filament increases the asymmetry between shortening and stretching, when the system is asymmetric (here well 0 is stiffer than well 1). Thus, if we compare the tension *vs* elongation on Fig.3.7D and F, we see that the metastable domain is considerably extended in the shortening direction for $\lambda_f = 0.5$(see D) compared to $\lambda_f \to \infty$ (see F). Hence, augmenting the coupling between the cross-bridges, displace the wiggly domain of the energy landscape towards the working regime of the muscle *i.e.* towards shortening. This interesting effect of filament elasticity has not been discussed before and may be fundamental to explain the inherent asymmetry in the power-stroke mechanism.

Last but not least, the presence of a compliant filaments, introduces an energy gap between the global minimum and other metastable states in hard device (see Fig.3.9 and also observe on Fig.3.7 the gap between the global minimum and the metastable configuration $(0.5, 0, 0.5)$). In soft device this gap is always present and does not depend on the value of λ_f. In the hard device, when $\lambda_f \to \infty$, the energy levels of all configurations become the same at $\overline{\epsilon} = \overline{\epsilon}^\star$ (Fig.3.9A) indicating that, in order to shift from configuration $(1, 0, 0)$ to $(0, 0, 1)$ at $\theta = 0$, the system, following the ‘global minimum path’, can evolve through intermediate local minima. In contrast, when λ_f is finite, the metastable states are no longer accessible and the transition becomes a cooperative jump of the cross-bridges from pre to post-power-stroke. In other words, the presence of compliant myofilaments favours the homogeneous states, and thus enhances cooperativity in hard device. This effect is, of course, intrinsically present in soft device.

To conclude this section, we mention that the shape of the double well potential, controlled by λ_1, λ_0 and l, affects the size (λ_1 and λ_0) and the location (l) of the metastable

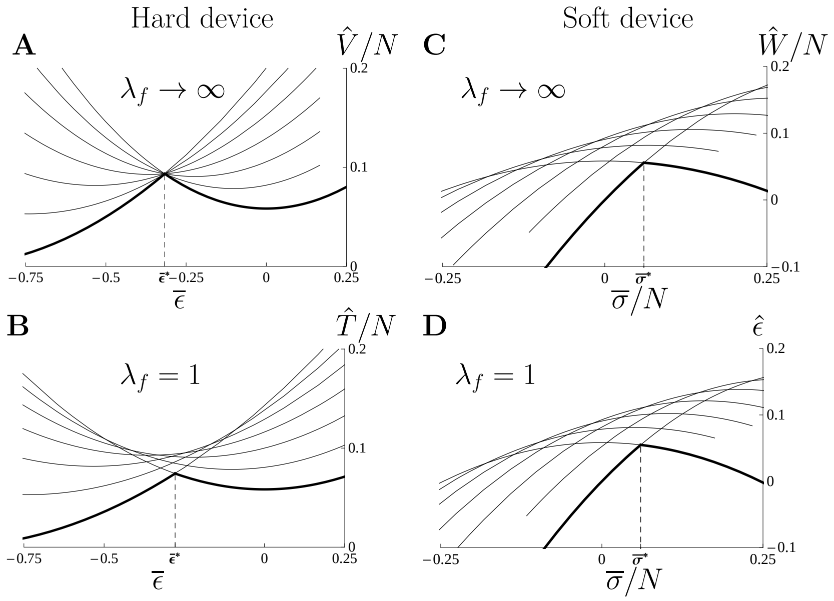

Fig. 3.9 – **Energy gap introduce by the filaments**. The thin lines represent the local minima in a system with 6 cross-bridges. The unstable states are not represented. The values of λ_f used are indicated on the figures. The other parameters are: $\lambda_1 = 0.4$; $\lambda_0 = 0.7$; $l = -0.3$.

region. When the stiffness of the filament λ_f changes, the stiffness of the configurations is changed accordingly but, λ_f as a larger impact on the energy landscape in hard device than in soft device. In particular, the stability interval for different configurations is different for $\lambda_f < \infty$ and the energy of the homogeneous configurations is lower in this case than in the rigid case $\lambda_f \to \infty$.

We observe that in principle, our system can exhibit non-affine (inhomogeneous) response but the presence of elastic coupling strongly favours coherent (affine) reaction to loading. The cooperative effect is needed to achieve the largest force recovery in both shortening and stretching.

3.3 Barrier structure in soft and hard device

We have seen that in both hard and soft devices our system possesses numerous metastable states which remains stable along a finite interval of the loading ($\overline{\epsilon}$ or $\overline{\sigma}$). In both devices, the global minimum is always in one of the homogeneous configurations $(1, 0, 0)$ and $(0, 0, 1)$ with a sharp transition at $\overline{\epsilon}^{\star}$ in hard device and $\overline{\sigma}^{\star}$ in soft device. However, we have also seen that, in hard device, the presence of compliant myofilaments introduces an energy gap between the global minimum and other metastable state while in soft device this gap is always present (Fig.3.9). The fact that the filament stiffness λ_f has less of an impact in the soft device is not surprising. Indeed, as one applies the force, the *information* transmitted to the array of cross-bridges is the same independently of the filament stiffness. Instead, in hard device, as the total length is fixed, the displacement of the array of cross-bridges ϵ_y is affected by the filament compliance. With this idea in mind, it is interesting to study in both hard and soft device how the system with different λ_f evolves from configuration $(0, 0, 1)$ to configuration $(1, 0, 0)$ when it is placed at the transition point ($\overline{\epsilon} = \overline{\epsilon}^{\star}, \overline{\sigma} = \overline{\sigma}^{\star}$).

To study the mechanism of the transition, we chose to represent the energy landscape,

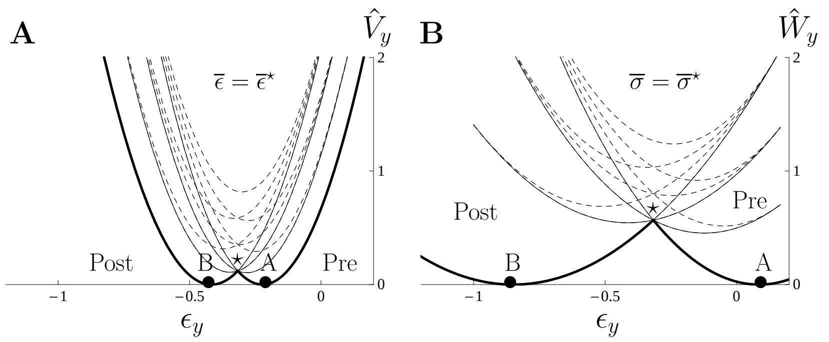

Fig. 3.10 – Energy dependence on the internal degree of freedom ϵ_y for $\overline{\epsilon} = \overline{\epsilon}_\star$ (A) and $\overline{\sigma} = \overline{\sigma}_\star$ (B). The parameters are the same as in Figs.3.1 and 3.1 and the units are the same in both A and B.Continuous lines indicate the stable states while dashed lines indicates the unstable ones. The thick line denote the global minimum. Global minimum is defined as 0

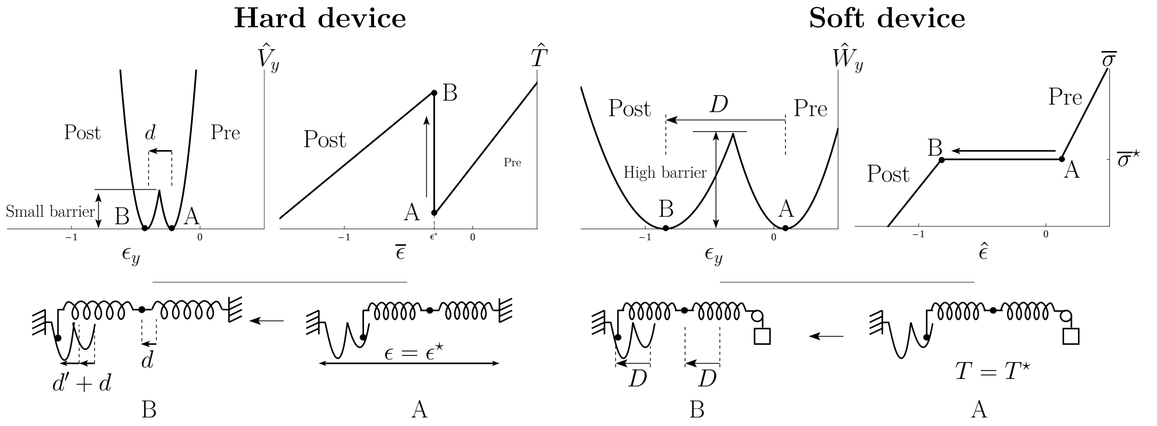

Fig. 3.11 – Schematic representation of the transition in a system composed of only 1cross-bridge and myofilaments in hard device. The system, initially at point A, as a single cross-bridge in the right hand well. In order to transit to the left well, ϵ_y is changed and due to the hard device constrain, the filament is stretched. To preserve mechanical equilibrium, the cross-bridge spring is also stretched and as a results a displacement d of ϵ_y results in a displacement $d + d'$ for the cross-bridge.

at $\overline{\epsilon} = \overline{\epsilon}^\star$, as a function of the common deformation of the cross-bridges: ϵ_y (see Fig.2.25). This reduced energy with parameters ϵ_i minimized out is denoted by $\hat{V}_y$ in hard device and $\hat{W}_y$ in soft device. It depends on $\overline{\epsilon}$ (resp.$\overline{\sigma}$), and on the configuration $(n_1, n^\star, n_0)$. The internal variable ϵ_y, may evolve in such a way that the system crosses many energy barriers while cross-bridges execute the power-stroke in a non cooperative manner. Instead a single barrier will be encountered if the power-stroke is done collectively.

Our Fig.3.10 represents the energy levels of $\hat{V}_y$ and $\hat{W}_y$ depending on the internal degree of freedom ϵ_y in a system with 3 cross-bridges and the same parameters as on Figs.3.1 and 3.2. The global minimum is indicated by the thick line. We marked by A and B the equilibrium positions corresponding to the initial and final states of the transition. In both hard and soft devices, we see that this transition is accomplished without visiting non-affine states. This means that in both cases, the transition can be viewed as a synchronized *switch* of all the cross-bridges from pre-power-stroke to post-power-stroke. However, as the two figures A and B are shown on the same scale, we notice that the distance *travelled* by ϵ_y from A to B is much shorter in hard device than in soft device and that the energy barrier is about 5 times higher in soft device than in hard device.

To explain this difference in the heigh of the energy barrier, let us consider a very simplified system made of only 1 cross-bridge connected to a filament (see Fig.3.3).

On the one hand, in hard device, the transition $A \to B$ at $\overline{\epsilon} = \overline{\epsilon}^{\star}$, corresponds to a change in ϵ_y of size d represented on the cartoon below the graph. Since the total length is fixed, a displacement in ϵ_y causes the filament to extend generating a force against the displacement. However, in order to keep mechanical equilibrium between the head and the filament, the head's spring is also extended by a distance d'. As a result, a displacement d of ϵ_y generates a displacement $d + d'$ on the head, and thereby allow the transition from pre-power-stroke to post-power-stroke.

On the other hand, in soft device, there is not such mechanical re-equilibrium between the myofilaments and the cross-bridge since the load is kept constant equal to $\overline{\sigma}^{\star}$. Hence, to go from pre-power-stroke to post-power stroke the variable ϵ_y has to cover the distance $D > d$. As a result, even though the system is stiffer in hard device ; which could have mislead us suggesting the naive conclusion that the transition barrier is higher in the stiffer system; the energy barrier in the soft device case is at least twice as big as in the case of hard device given that all other parameters are kept the same.

Conclusions

In this Chapter we have shown that our system evolves on a rugged energy landscape characterised by a large number of local minima. Each metastable state is fully characterised by the fraction of cross-bridges in post-power-stroke described by the parameter n_1.

We have also found, that the global minimum can be fully associated with the coherent response of affine states with $n_1 = 0$ or 1.

The presence of a mean field type elastic coupling between the cross-bridges enhances the synchronisation effect by creating an additional energy gap between the affine states and the non affine states.

Moreover, the global minima in hard and soft devices are similar, but the energy barriers in the two cases are very different. More specifically, to shift from one affine state to another, the system has to overcome a much larger energy barrier in soft device than in hard device. We observed a considerable influence of the coupling parameter λ_f on the asymmetry of the metastable domain. In particular, it contributes markedly to the asymmetry between shortening and stretching which is one of the main unresolved problems in muscle mechanics.

Chapter 4

Thermal equilibrium at $\theta \neq 0$

In the previous Chapter, we saw that the energy landscape of our system exhibits a large number of metastable states in which the system can be ‘trapped’ at zero temperature. As a result, the characteristic features of the experimental T_1 curve can be reproduced while those of the T_2 curve cannot. In this Chapter we will study the influence of temperature on the structure of the equilibrium response. The thermal forces will allow the system to travel between local minima thereby smoothing the transition. First of all, we assume thermal equilibrium and introduce the general framework of equilibrium statistical mechanics. We then compute the partition function of our system, the free energy, the tension/elongation curves isotherms or adiabats. In particular, we will study in detail the influence of the filament elasticity λ_f and the temperature on the structure of the free energy landscape.

Contents

4.1 Introduction

4.1.1 Why temperature matters ?

In the presentation of the anatomic structure of the muscle (see Sec.1.1), we saw that the length scale involved in the force generation was of the scale of a nanometer. At the same time, the measured stiffness of myosin head is of the order of 1 pN/nm (see Sec.2.3.2) which gives a characteristic energy of a less than 100 zJ [1]. The energy provided by the thermal fluctuations are of the order of $k_b\theta \approx 4$ zJ, where θ is the absolute temperature in K ($\theta \approx 300$°K) and k_b is the Boltzmann constant ($k_b \approx 1.38 \times 10^{-2}$zJ). For a single cross-bridge, this means that the thermal energy is sufficient to induce by itself a power-stroke, and therefore, we expect the system to be able to explore a large part of the energy landscape in addition to the two homogeneous configurations $(1, 0, 0)$ and $(0, 0, 1)$. In other words, we expect that in the presence of a finite temperature, the sharp transition we observed when the system was following the global minimum will be smoothed (see Sec.3.1.4). Taking into account equilibrium thermal fluctuations computation of the partition function from which, one can reconstruct all other thermodynamic quantities in equilibrium.

We will neglect the temperature dependent part of the free energy by assuming that the momentum part of the energy can be fully decoupled (Howard, 2001).

4.1.2 General formulas

We use the canonical description for our system of N cross-bridges, which assumes that:

– the temperature θ is fixed by a thermostat,

– the system does not exchange any particle with the environment (N is constant).

The fact that we consider N as a constant is a consequence of our assumption that no attachment-detachment process is involved during the fast transients following a rapid change in loading conditions (see Sec.2.2). Our configurational phase space is then:

$$\begin{aligned} \Omega_h &= (\epsilon_1, \ldots, \epsilon_N, \epsilon_y) \ \in \mathbb{R}^{N+1} \text{ in hard device,} \\ \Omega_s &= (\epsilon_1, \ldots, \epsilon_N, \epsilon_y, \epsilon) \ \in \mathbb{R}^{N+2} \text{ in soft device.} \end{aligned}$$

At equilibrium, canonical distribution can be written in the form:

$$p_h\left(\epsilon_1, \ldots, \epsilon_N, \epsilon_y, \overline{\epsilon}, \beta\right) = \frac{1}{\mathcal{Z}_h\left(\overline{\epsilon}, \beta\right)} \exp\left[-\beta V\left(\epsilon_1, \ldots, \epsilon_N, \epsilon_y, \overline{\epsilon}\right)\right] \text{ in hard device} \quad (4.1.1)$$

$$p_s\left(\epsilon_1, \ldots, \epsilon_N, \epsilon_y, \epsilon, \overline{\sigma}, \beta\right) = \frac{1}{\mathcal{Z}_s\left(\overline{\sigma}, \beta\right)} \exp\left[-\beta W\left(\epsilon_1, \ldots, \epsilon_N, \epsilon_y, \epsilon, \overline{\sigma}\right)\right] \text{ in soft device} \quad (4.1.2)$$

where $\beta = \kappa a^2/\left(k_b\theta\right)$ is the non dimensional ratio of the characteristic elastic energy of a single cross-bridge over the thermal energy. On the one hand, the limit $\beta \to 0$ corresponds to infinite temperature, which means that the behavior of the system becomes purely diffusive and does not 'feel' the energy landscape. In this regime, the notion of power-stroke becomes irrelevant. On the other hand, the limit $\beta \to \infty$ (or $\theta \to 0$) corresponds to the global minimum response we described in the previous Chapter. Note the difference between the athermal behavior at $\theta = 0$, where the system cannot escape from a

---

[1] 1 zJ = $10^{-21}J$. z stands for *zepta*.

metastable state and the behavior at $\beta \to \infty$ (corresponding to $\theta \to 0$), where the system exits metastable states with probability one and reaches the global minimum (see however the discussion of escape times in Sec.5.3.1).

The normalization constants (or partition functions) $\mathcal{Z}_h$ and $\mathcal{Z}_s$ are given by:

$$\mathcal{Z}_h(\overline{\epsilon}, \beta) = \int_{\mathbb{R}} \dots \int_{\mathbb{R}} \exp\left[-\beta V(\epsilon_1, \dots, \epsilon_N, \epsilon_y, \overline{\epsilon})\right] d\epsilon_1 \dots d\epsilon_N d\epsilon_y, \tag{4.1.3}$$

$$\mathcal{Z}_s(\overline{\sigma}, \beta) = \int_{\mathbb{R}} \dots \int_{\mathbb{R}} \exp\left[-\beta W(\epsilon_1, \dots, \epsilon_N, \epsilon_y, \epsilon, \overline{\sigma})\right] d\epsilon_1 \dots d\epsilon_N d\epsilon_y d\epsilon. \tag{4.1.4}$$

From partition functions one can compute the Helmholtz free energy F (the free energy at fixed volume in classical thermodynamics) and the Gibbs free energy G (the free energy at fixed pressure in classical thermodynamics):

$$F(\overline{\epsilon}, \beta) = -\frac{1}{\beta} \ln \mathcal{Z}_h(\overline{\epsilon}, \beta), \tag{4.1.5}$$

$$G(\overline{\sigma}, \beta) = -\frac{1}{\beta} \ln \mathcal{Z}_s(\overline{\sigma}, \beta), \tag{4.1.6}$$

The equilibrium tension and elongations are obtained from F and G by using the following relations:

$$T_2(\overline{\epsilon}, \beta) = \partial_{\overline{\epsilon}} F(\overline{\epsilon}, \beta) \text{ at fixed } \beta, \tag{4.1.7}$$

$$L_2(\overline{\sigma}, \beta) = -\partial_{\overline{\sigma}} G(\overline{\sigma}, \beta) \text{ at fixed } \beta. \tag{4.1.8}$$

In addition, we denote by S_h and S_s the entropies in hard and soft devices, respectively:

$$S_h(\overline{\epsilon}, \beta) = -\int p_h(\epsilon_1, \dots, \epsilon_N, \epsilon_y, \overline{\epsilon}) \ln\left(p_h(\epsilon_1, \dots, \epsilon_N, \epsilon_y, \overline{\epsilon})\right) d\epsilon_1 \dots d\epsilon_N d\epsilon_y \tag{4.1.9}$$

$$S_s(\overline{\sigma}, \beta) = -\int p_s(\epsilon_1, \dots, \epsilon_N, \epsilon_y, \epsilon, \overline{\sigma}) \ln\left(p_s(\epsilon_1, \dots, \epsilon_N, \epsilon_y, \overline{\sigma})\right) d\epsilon_1 \dots d\epsilon_N d\epsilon_y d\epsilon \tag{4.1.10}$$

which can be rewritten by using Eqs.(4.1.1) and (4.1.2):

$$S_h(\overline{\epsilon}, \beta) = \beta\left(\langle V\rangle_h(\overline{\epsilon}, \beta) - F(\overline{\epsilon}, \beta)\right), \tag{4.1.11}$$

$$S_s(\overline{\sigma}, \beta) = \beta\left(\langle W\rangle_s(\overline{\sigma}, \beta) - G(\overline{\sigma}, \beta)\right), \tag{4.1.12}$$

where $\langle\rangle_h$ and $\langle\rangle_s$ stands for the average over the phase space with probabilities (4.1.1) and (4.1.2) in hard and soft devices respectively. More precisely, the mean value of the energy is computed as follows:

$$\begin{aligned}
\langle V\rangle_h(\overline{\epsilon}, \beta) &= \frac{1}{\mathcal{Z}_h(\overline{\epsilon}, \beta)} \int \cdots \int V \exp\left[-\beta V\right] d\epsilon_1, \dots, d\epsilon_N, d\epsilon_y \\
&= -\frac{1}{\mathcal{Z}_h(\overline{\epsilon}, \beta)} \int \cdots \int \partial_\beta \exp\left[-\beta V\right] d\epsilon_1, \dots, d\epsilon_N, d_{\epsilon_y} \\
&= -\partial_\beta \ln\left(\mathcal{Z}_h(\overline{\epsilon}, \beta)\right)
\end{aligned}$$

and similarly the mean value of the Gibbs energy is given by:

$$\langle W\rangle(\overline{\sigma}, \beta) = -\partial_\beta \ln\left(\mathcal{Z}_s(\overline{\sigma}, \beta)\right).$$

The entropies in hard and soft devices are obtained by using Eq.(4.1.11) and Eq.(4.1.12) in the form:

$$S_h(\overline{\epsilon}, \beta) = -\beta\partial_\beta \ln\left(\mathcal{Z}_h(\overline{\epsilon}, \beta)\right) + \ln\left(\mathcal{Z}_h(\overline{\epsilon}, \beta)\right), \tag{4.1.13}$$

$$S_s(\overline{\sigma}, \beta) = -\beta\partial_\beta \ln\left(\mathcal{Z}_s(\overline{\sigma}, \beta)\right) + \ln\left(\mathcal{Z}_s(\overline{\sigma}, \beta)\right). \tag{4.1.14}$$

4.2 Thermal equilibrium

To compute the thermodynamical quantities in thermal equilibrium, we have to compute the partition functions $\mathcal{Z}_h$ and $\mathcal{Z}_s$. Here we present the direct computation that leads to non-explicit relations. In App.A.2, we construct a semi-analytic approximation using the fact that N is large and β is small.

4.2.1 Partition function

Due to the additive form of V and W, the integrations with respect to each variables ϵ_i, for $1 \leq i \leq N$, can be performed independently and we can write:

$$\mathcal{Z}_h\left(\overline{\epsilon},\beta\right) = \int \exp\left[-\beta\tfrac{1}{2}N\lambda_f\left(\overline{\epsilon}-\epsilon_y\right)^2\right]\left(\mathcal{Z}_1\left(\epsilon_y,\beta\right)+\mathcal{Z}_0\left(\epsilon_y,\beta\right)\right)^N d\epsilon_y, \tag{4.2.1}$$

$$\mathcal{Z}_s\left(\overline{\sigma},\beta\right) = \iint \exp\left[-\beta\left(N\lambda_f\tfrac{1}{2}\left(\epsilon-\epsilon_y\right)^2-\overline{\sigma}\epsilon\right)\right]\left(\mathcal{Z}_1\left(\epsilon_y,\beta\right)+\mathcal{Z}_0\left(\epsilon_y,\beta\right)\right)^N d\epsilon_y d\epsilon, \tag{4.2.2}$$

where

$$\mathcal{Z}_1\left(\epsilon_y,\beta\right) = \int_{-\infty}^{l} \exp\left[-\beta\left(\tfrac{1}{2}\kappa_1\left(x+1\right)^2+\tfrac{1}{2}\left(\epsilon_y-x\right)^2\right)\right]dx \tag{4.2.3}$$

$$\mathcal{Z}_0\left(\epsilon_y,\beta\right) = \int_{l}^{+\infty} \exp\left[-\beta\left(\tfrac{1}{2}\kappa_0 x^2+v_0+\tfrac{1}{2}\left(\epsilon_y-x\right)^2\right)\right]dx. \tag{4.2.4}$$

For convenience, we denote:

$$V_1\left(x,\epsilon_y\right) = \frac{1}{2}\kappa_1\left(x+1\right)^2+\frac{1}{2}\left(\epsilon_y-x\right)^2 \tag{4.2.5}$$

$$V_0\left(x,\epsilon_y\right) = \frac{1}{2}\kappa_0 x^2+v_0+\frac{1}{2}\left(\epsilon_y-x\right)^2, \tag{4.2.6}$$

which are the energies of a single cross-bridge in post-power-stroke state (well 1) and in pre-power-stroke state (well 0). One can compute the minimum of those 2 functions with respect to variable x:

$$\hat{V}_1\left(\epsilon_y\right) = \frac{1}{2}\lambda_1\left(\epsilon_y+1\right)^2,$$
$$\hat{V}_0\left(\epsilon_y\right) = \frac{1}{2}\lambda_0\epsilon_y^2+v_0$$

where $\lambda_{1,0} = \kappa_{1,0}/\left(1+\kappa_{1,0}\right)$. The computation of the integrals in $\mathcal{Z}_1$ and $\mathcal{Z}_0$ leads to the following exact expressions[2] (see details in appendix A.1.1):

$$\mathcal{Z}_1\left(\epsilon_y,\beta\right) = \sqrt{\tfrac{\left(1-\lambda_1\right)2\pi}{\beta}}\exp\left[-\beta\hat{V}_1\left(\epsilon_y\right)\right]\frac{1}{2}\mathrm{erfc}\left(-f_1\left(\epsilon_y,l,\beta\right)\right), \tag{4.2.7}$$

$$\mathcal{Z}_0\left(\epsilon_y,\beta\right) = \sqrt{\tfrac{\left(1-\lambda_0\right)2\pi}{\beta}}\exp\left[-\beta\hat{V}_0\left(\epsilon_y\right)\right]\frac{1}{2}\mathrm{erfc}\left(f_0\left(\epsilon_y,l,\beta\right)\right), \tag{4.2.8}$$

---

[2] with

$$\begin{aligned}\mathrm{erfc}:&\mathbb{R}\longrightarrow\,]0,2[\\ &x\longmapsto\frac{2}{\sqrt{\pi}}\int_{x}^{+\infty}\exp\left[-t^2\right]dt,\end{aligned}$$

where

$$f_1\left(\epsilon_y, x, \beta\right) = \sqrt{\frac{\beta}{2}}\left(\sqrt{\tfrac{1}{(1-\lambda_1)}}x + \sqrt{(1-\lambda_1)}\left(\tfrac{\lambda_1}{1-\lambda_1} - \epsilon_y\right)\right) \tag{4.2.9}$$

$$f_0\left(\epsilon_y, x, \beta\right) = \sqrt{\frac{\beta}{2}}\left(\sqrt{\tfrac{1}{(1-\lambda_0)}}x - \sqrt{(1-\lambda_0)}\epsilon_y\right). \tag{4.2.10}$$

In addition, in (4.2.2), we can also integrate analytically with respect to ϵ. However, in both hard and soft devices, the integration with respect to ϵ_y cannot be performed analytically without any simplifying assumptions (see Sec.A.3). Finally, the exact formulas for the partition functions can be presented in the form:

$$\mathcal{Z}_h\left(\overline{\epsilon}, \beta\right) = \int_{\mathbb{R}} \exp\left(-\beta F_y\left(\overline{\epsilon}, \epsilon_y, \beta\right)\right) d\epsilon_y, \tag{4.2.11}$$

$$\mathcal{Z}_s\left(\overline{\sigma}, \beta\right) = \sqrt{\tfrac{2\pi}{N\lambda_f\beta}} \int_{\mathbb{R}} \exp\left(-\beta G_y\left(\overline{\sigma}, \epsilon_y, \beta\right)\right) d\epsilon_y \tag{4.2.12}$$

where we introduced with the non-equilibrium (partially equilibrated) free Gibbs energies:

$$F_y\left(\overline{\epsilon}, \epsilon_y, \beta\right) = N\left(\frac{1}{2}\lambda_f\left(\overline{\epsilon} - \epsilon_y\right)^2 - \frac{1}{\beta}\ln\left(\mathcal{Z}_1\left(\beta, \epsilon_y\right) + \mathcal{Z}_0\left(\beta\epsilon_y\right)\right)\right) \tag{4.2.13}$$

$$G_y\left(\overline{\sigma}, \epsilon_y, \beta\right) = N\left(-\frac{\overline{\sigma}}{N}\epsilon_y - \frac{1}{2}\frac{\overline{\sigma}^2}{N^2\lambda_f} - \frac{1}{\beta}\ln\left(\mathcal{Z}_1\left(\beta, \epsilon_y\right) + \mathcal{Z}_0\left(\beta, \epsilon_y\right)\right)\right). \tag{4.2.14}$$

Let us discuss the different entries in F_y and G_y. The term $-1/\beta \log\left(\mathcal{Z}_1 + \mathcal{Z}_0\right)$ represents the free energy of the array of cross-bridges at a fixed ϵ_y. Considering the expression of Z_1 and Z_0 given by Eq.(4.2.7) and (4.2.8), we see that $-1/\beta \ln\left(\mathcal{Z}_1 + \mathcal{Z}_0\right)$ has a double well shape, which means that the array of cross-bridges behaves as a macroscopic bi-stable spring at a given ϵ_y. This is a direct consequence of the parallel arrangement used in our model. The other terms in (4.2.13) and (4.2.14) contain the control parameters, $\overline{\epsilon}$ and $\overline{\sigma}$, and also depend on the stiffness of the filaments λ_f. They do not depend on the temperature so the entropic elasticity in the system comes only from the non-linear part of the energy associated with the array of cross-bridges.

4.2.2 Free energy, tension and elongation in hard and soft devices

The free energies in hard and soft devices are obtained directly from the partition function using Eq.(4.1.5) and (4.1.6), respectively.

Equilibrium tension T_2 and elongation L_2 are obtained by differentiating F and G with respect to $\overline{\epsilon}$ and $\overline{\sigma}$ respectively. For T_2 we have:

$$\begin{aligned}
T_2\left(\overline{\epsilon}, \beta\right) &= -\frac{1}{\beta}\partial_{\overline{\epsilon}}\left(\ln\left(Z_h\left(\overline{\epsilon}, \beta\right)\right)\right) \\
&= -\frac{1}{\beta}\frac{\partial_{\overline{\epsilon}}\left(Z_h\left(\overline{\epsilon}, \beta\right)\right)}{Z_h\left(\overline{\epsilon}, \beta\right)} \quad \text{then from the expression (4.2.11)} \\
&= -\frac{1}{\beta Z_h\left(\overline{\epsilon}, \beta\right)}\int_{\mathbb{R}} -\beta N\lambda_f\left(\overline{\epsilon} - \epsilon_y\right)\exp\left[-\beta F_y\left(\overline{\epsilon}, \epsilon_y, \beta\right)\right] d\epsilon_y
\end{aligned}$$

The last formula can be also written in the short form:

$$T_2 = N\lambda_f\left(\overline{\epsilon} - \left\langle\epsilon_y\right\rangle_h\left(\overline{\epsilon}, \beta\right)\right) \tag{4.2.15}$$

where $\langle\epsilon_y\rangle_h$ is the mean value of ϵ_y in thermal equilibrium for the hard device given by:

$$\langle\epsilon_y\rangle_h(\overline{\epsilon},\beta) = \frac{1}{Z_h(\overline{\epsilon},\beta)}\int_{\mathbb{R}} \epsilon_y \exp\left[-\beta F_y(\overline{\epsilon},\epsilon_y,\beta)\right] d\epsilon_y. \tag{4.2.16}$$

This result is not surprising since, given the particular configuration of our system, with a linear spring attached to a non linear system of N cross-bridges. It is then quite clear that the tension will be equal to the mean elongation of the linear spring times the stiffness. This result is no longer valid if we consider non linear elastic myofilaments.

A similar computation gives in soft device:

$$L_2(\overline{\sigma},\beta) = \frac{\overline{\sigma}}{N\lambda_f} + \langle\epsilon_y\rangle_s(\overline{\sigma},\beta) \text{ with} \tag{4.2.17}$$

$$\langle\epsilon_y\rangle_s(\overline{\sigma},\beta) = \frac{1}{Z_s(\overline{\sigma},\beta)}\int_{\mathbb{R}} \epsilon_y \exp\left[-\beta G_y(\overline{\sigma},\epsilon_y,\beta)\right] d\epsilon_y, \tag{4.2.18}$$

Here, L_2 is then expressed as the sum of the elongation of the filament $\overline{\sigma}/(N\lambda_f)$ plus the mean elongation of the array of cross-bridges. The term $\overline{\sigma}/(N\lambda_f)$ does not depend on the temperature so the mean elongation of the series spring in thermal equilibrium can be obtained from purely mechanical formulas which is of course a consequence of linearity.

Let us next express the tension and elongation along isotherm as function of the mean position of the cross-bridges. The results are quite intuitive (for the details of calculation, see App.B.4.2). We recall that, in mechanical equilibrium at zero temperature:

$$\hat{\epsilon}_y = \frac{1}{1+\lambda_f}\left(\lambda_f\overline{\epsilon} + \frac{1}{N}\sum_{i=1}^{N}\epsilon_i\right) \text{ in hard device,}$$

$$\hat{\epsilon}_y = \frac{\overline{\sigma}}{N} + \frac{1}{N}\sum_{i=1}^{N}\epsilon_i \text{ in soft device.}$$

These equalities remain true at finite temperature, with $\frac{1}{N}\sum\epsilon_i$ being replaced by the mean values $\langle\epsilon_i\rangle$. Hence:

$$\langle\epsilon_y\rangle_h(\overline{\epsilon},\beta) = \frac{1}{1+\lambda_f}\left(\lambda_f\overline{\epsilon} + \langle\epsilon_i\rangle_h(\overline{\epsilon},\beta)\right) \text{ in hard device,} \tag{4.2.19}$$

$$\langle\epsilon_y\rangle_s(\overline{\sigma},\beta) = \frac{\overline{\sigma}}{N} + \langle\epsilon_i\rangle_s(\overline{\sigma},\beta) \text{ in soft device} \tag{4.2.20}$$

leading to

$$T_2(\overline{\epsilon},\beta) = N\frac{\lambda_f}{1+\lambda_f}\left(\overline{\epsilon} - \langle\epsilon_i\rangle(\overline{\epsilon},\beta)\right), \text{ in hard device,} \tag{4.2.21}$$

$$L_2(\overline{\sigma},\beta) = \frac{\overline{\sigma}}{N\lambda_f} + \frac{\overline{\sigma}}{N} + \langle\epsilon_i\rangle_s(\overline{\sigma},\beta), \text{ in soft device.} \tag{4.2.22}$$

To illustrate the above computations, we show on Fig.4.1 and Fig.4.2 the free energy and equilibrium tension *vs* elongation in hard and soft devices, respectively.

In hard device, at large temperature (low β), the free energy is convex (see Fig.4.1A) showing that the double well structure of the energy disappears; at low temperature, the free energy remains bi-stable and converges to the global minimum when $\beta \to \infty$. The non-convexity of the free energy is the result of parallel connection of the bistable elements and remains so in the thermodynamic limit ($N \to \infty$, see App.B.2). In this sense our system

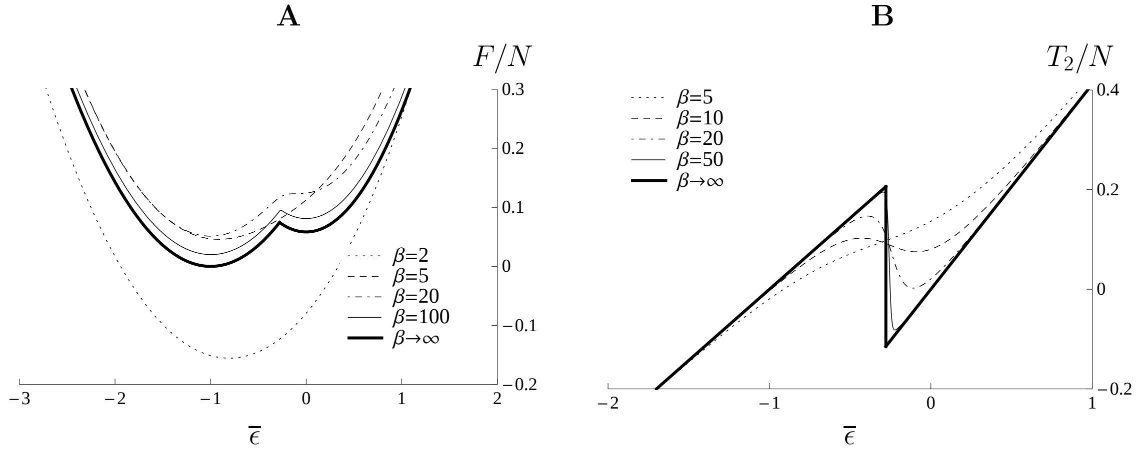

Fig. 4.1 – **Free energy and isotherm tension in hard device**. (**A**): free energy computed from Eq.(4.1.5), with different values of β (β =2, dotted line; $\beta = 5$, dashed line; $\beta = 20$, dot-dashed line and $\beta = 100$, solid line) and in the limit $\beta \to \infty$ (bold line). (**B**): isotherm tension computed from Eq.(4.2.15) for different values of β ($\beta = 5$, dotted line; $\beta = 10$, dashed line; $\beta = 20$, dot-dashed line and $\beta = 50$, solid line) and for $\beta \to \infty$ (bold line). Parameters other than β are: $\lambda_1 = 0.4$, $\lambda_0 = 0.7$, $l = -0.3$, $N = 10$ and $\lambda_f = 1$.

differs from classical distributed systems in which the free energy is always convex in the thermodynamic limit (Lebowitz and Lieb, 1969).

As a consequence of the non-convexity of the free energy in hard device, the equilibrium tension *vs* elongation curve shows a region of negative stiffness at low temperature (large β), while in soft device, the corresponding curve remains monotone (compare Fig.4.1B and 4.2B). Therefore, in hard device, the system operates in a inherently unstable state when it is brought into such spinodal state while it is always stable in soft device. This difference between hard and soft device survives in the thermodynamic limit $N \to \infty$ (see App.B.2).

In Fig.4.3, we compare the tension *vs* elongation relations in hard and soft devices for $\beta = 20$. The difference between the two responses suggests that, switching the control back and forth between hard and soft device will generate oscillations in the system (see Fig.4.3B). Indeed suppose first that the system is in thermal equilibrium at point P in hard device (dashed curve). If the control is suddenly changed to soft device, the system will equilibrate on the soft device equilibrium curve (solid line) at point Q. By switching the control back to hard device, one can move the system to point R and eventually to point S after a new switch to soft device. By periodically repeating this process, the system can be driven repeatedly through the states P,Q R and S.

4.2.3 Influence of the coupling parameter λ_f

Isotherms

We do not discuss here the effect of the change of the shape of the double well: it is similar what we observed at $\theta = 0$ (change in the stiffness of the phases and a shift in the position of the barrier (see Sec.3.2.1)).

The influence of filament elasticity is illustrated in Fig.4.4 for hard device and on Fig.4.5 for soft device. The value of β is taken to be equal to 10 and other parameters are: $\lambda_1 = 0.4,\ \lambda_0 = 0.7,\ l = -0.3,\ N = 100$ and $a = 1$.

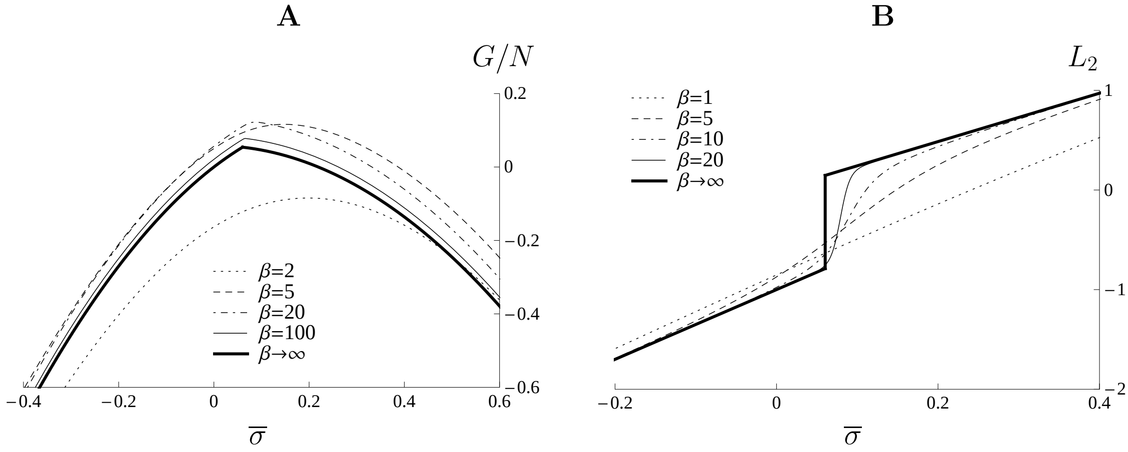

Fig. 4.2 – Gibbs free energy and isotherm elongation in soft device. (**A**): Gibbs free energy computed from Eq.(4.1.6), with different values of β (β =2, dotted line; $\beta = 5$, dashed line; $\beta = 20$, dot-dashed line and $\beta = 100$, solid line) and in the limit $\beta \to \infty$ (bold line). (**B**): isotherm elongation computed from Eq.(4.2.17) for different values of β ($\beta = 1$, dotted line; $\beta = 5$, dashed line; $\beta = 10$, dot-dashed line and $\beta = 20$, solid line) and for $\beta \to \infty$ (bold line). Parameters other than β are: $\lambda_1 = 0.4$, $\lambda_0 = 0.7$, $l = -0.3$, $N = 10$ and $\lambda_f = 1$.

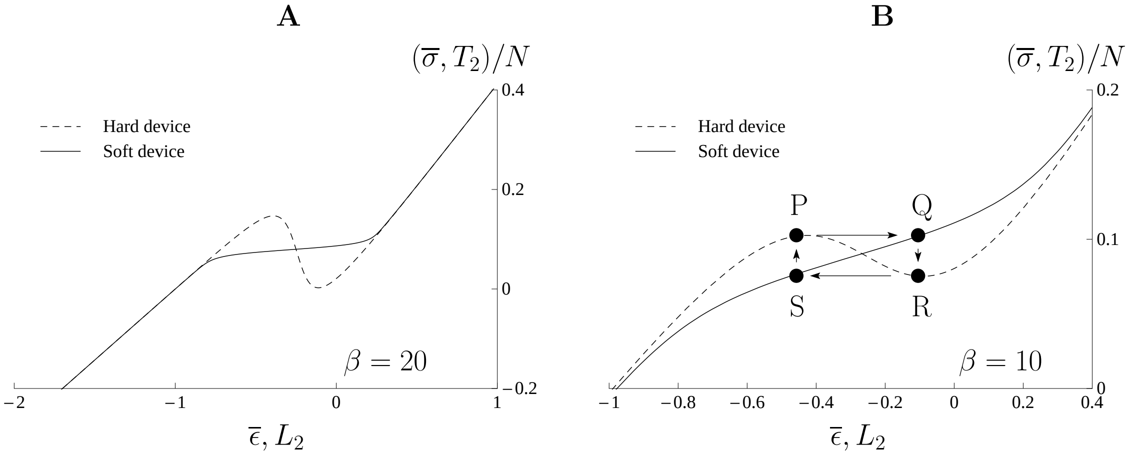

Fig. 4.3 – Tension *vs* elongation relation in hard (dashed line) and soft (solid lines) devices computed using Eq.(4.2.15) and (4.2.17). (**A**)is with $\beta = 20$ and (**B**) is zoomed on the transition region and with $\beta = 10$. To illustrate the meaning of the difference between hard and soft devices we propose the following experiment: the system is initially brought to point P in hard device. If the control is suddenly switched to soft device and the tension of point P($T_2\,(P)$) is clamped, the system will elongate spontaneously to point Q where it is in equilibrium at $L_2\,(Q)$ on the soft device diagram. Then if the controlled is switched back to hard device, the system will evolve to point R and then to point Q after switching again to soft device. Hence by switching back and forth hard and soft device, one can emphasize the different ensemble in of both modes. Parameters are: $\lambda_1 = 0.4,\ \lambda_0 = 0.7,\ l = -0.3,\ N = 10,\ \lambda_f = 1.$.

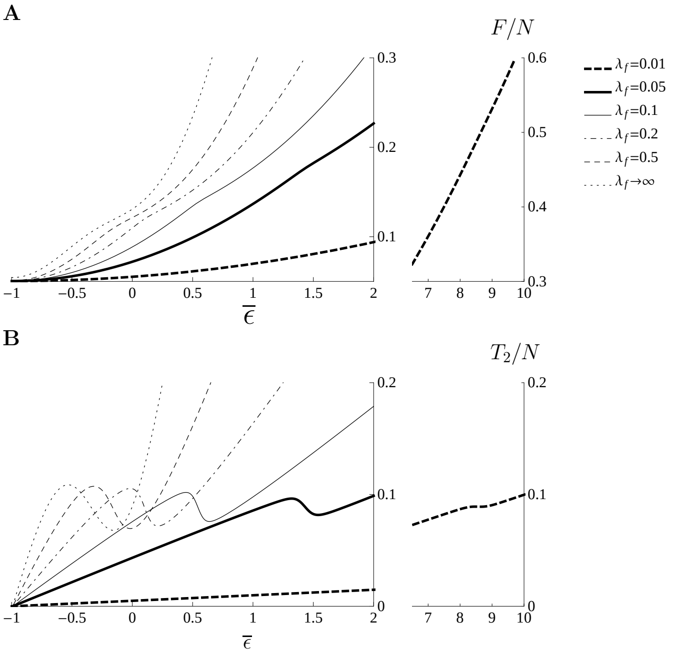

Fig. 4.4 – Influence of the coupling parameter in hard device. Free energy (**A**) and tension *vs* elongation (**B**) computed for different λ_f: $\lambda_f \to \infty$ (dotted line), $\lambda_f = 0.5$ (dashed line), $\lambda_f = 0.2$ (dot-dashed line), $\lambda_f = 0.1$ (solid line), $\lambda_f = 0.05$ (bold line) and $\lambda_f = 0.01$ (bold dashed line). The curves for $\lambda_f = 0.01$ (bold dashed lines) are continued with a different scale on the right plots to show the transition that occurs at larger imposed stretch. Other parameters are: $\lambda_1 = 0.4$, $\lambda_0 = 0.7$, $l = -0.3$ $\beta = 10$ and $N = 100$.

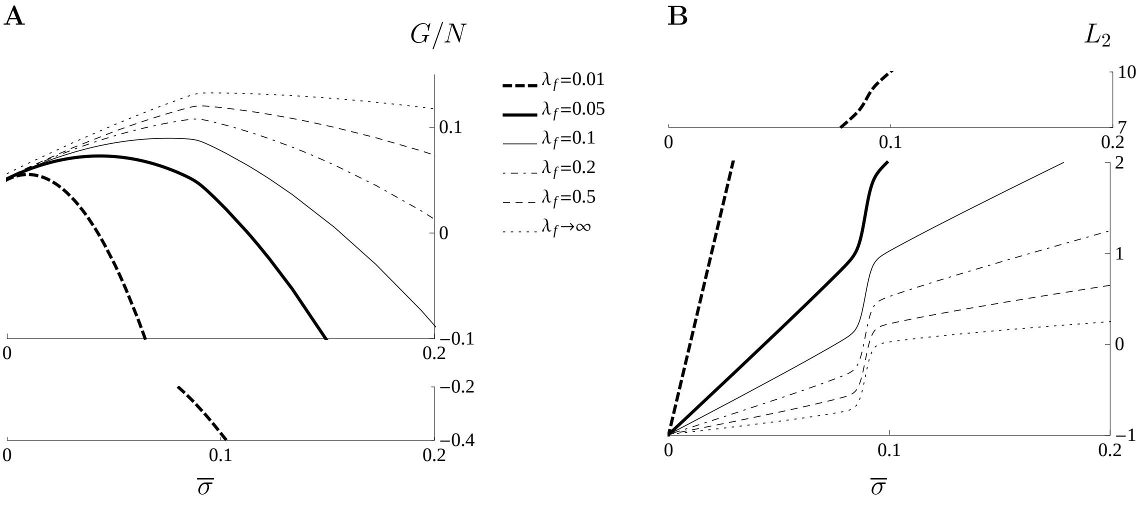

Fig. 4.5 – Influence of the coupling parameter in soft device. Gibbs Free energy (**A**) and elongation *vs* tension (**B**), computed for different values of $\lambda_f \to \infty$ (dotted line), $\lambda_f = 0.5$ (dashed line), $\lambda_f = 0.2$ (dot-dashed line), $\lambda_f = 0.1$ (solid line), $\lambda_f = 0.05$ (bold line) and $\lambda_f = 0.01$ (bold dashed line). The curves for $\lambda_f = 0.01$ are continued using a different scale to show the transition that occurs at larger tension. Other parameters are: $\lambda_1 = 0.4$, $\lambda_0 = 0.7$, $l = -0.3$ $\beta = 10$ and $N = 100$.

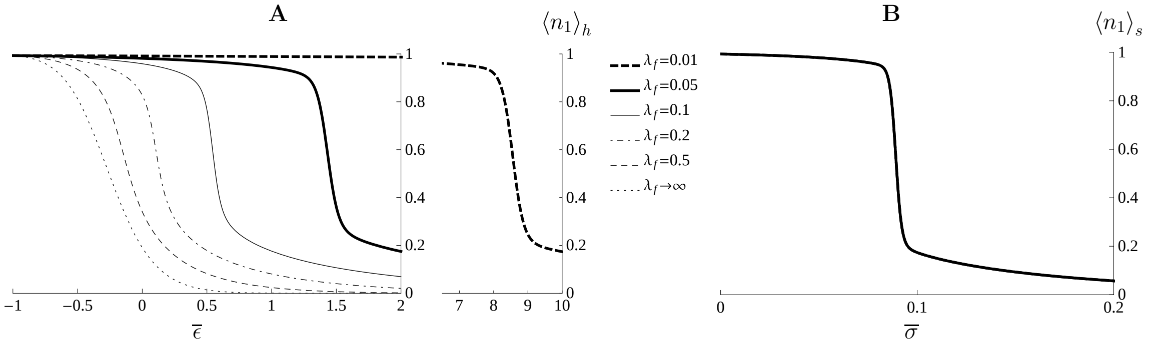

Fig. 4.6 – Fraction of cross-bridges in post-power-stroke in hard (**A**) and soft (**B**) devices for different value of the coupling parameter λ_f: $\lambda_f = 0.01$ (bold dashed line), $\lambda_f = 0.05$ (bold lines), $\lambda_f = 0.1$ (solid lines), $\lambda_f = 0.2$ (dot-dashed line), $\lambda_f = 0.5$ (dashed line) and $\lambda_f \to \infty$ (dotted line). In soft device, all curves superimpose. Other parameters are: $\lambda_1 = 0.4$, $\lambda_0 = 0.7$, $l = -0.3$ $\beta = 10$ and $N = 100$.

In hard device, when λ_f decreases, the transition is shifted towards larger $\overline{\epsilon}$, the tension *vs* elongation elongation curve becomes monotone and the free energy becomes convex (see Fig.4.4 bold dashed lines). This behavior can be explained by the fact that when the filaments are softer than the array of cross-bridges ($\lambda_f \ll 1$), one sees mostly the passive response of the series spring which has a convex (parabolic) energy. As a consequence, the two linear branches of the tension *vs* elongation curve approach the same slope: λ_f.

In soft device, the position of the transition in not affected by the coupling parameter (see Fig.4.5). For all λ_f, the Gibbs free energy remains concave (see Fig.4.5A) and the elongation *vs* tension relation is monotone (see Fig.4.5B).

Weaker series spring favors collective behavior

We denote by $\langle n_1 \rangle_{h,s}$ the fraction of cross-bridges in post-power-stroke in thermal equilibrium. We obtain (see the details of this computation in App.B.4.1):

$$\langle n_1 \rangle_h (\overline{\epsilon}) = \frac{1}{\mathcal{Z}_h (\overline{\epsilon})} \int \frac{\mathcal{Z}_1 (\epsilon_y)}{\mathcal{Z}_1 (\epsilon_y) + \mathcal{Z}_0 (\epsilon_y)} \exp\left[-\beta F_y (\overline{\epsilon}, \epsilon_y)\right] d\epsilon_y \tag{4.2.23}$$

$$\langle n_1 \rangle_s (\overline{\sigma}) = \frac{1}{\mathcal{Z}_s (\overline{\sigma})} \int \frac{\mathcal{Z}_1 (\epsilon_y)}{\mathcal{Z}_1 (\epsilon_y) + \mathcal{Z}_0 (\epsilon_y)} \exp\left[-\beta G_y (\overline{\sigma}, \epsilon_y)\right] d\epsilon_y \tag{4.2.24}$$

with $\mathcal{Z}_1$ and $\mathcal{Z}_0$ given by Eqs.(4.2.7) and (4.2.8). We denote by $\overline{\epsilon}_{1/2}$ (resp. $\overline{\sigma}_{1/2}$) the value of $\overline{\epsilon}$ (resp.$\overline{\sigma}$) for which $\langle n_1 \rangle_h (\overline{\epsilon}) = 1/2$ (resp. $\langle n_1 \rangle_s (\overline{\sigma}) = 1/2$). At fixed ϵ_y, the fraction of cross-bridges in post-power-stroke is given by $\frac{\mathcal{Z}_1(\epsilon_y)}{\mathcal{Z}_1(\epsilon_y)+\mathcal{Z}_0(\epsilon_y)}$. We denote:

$$\langle n_1 \rangle_y (\epsilon_y) = \frac{\mathcal{Z}_1 (\epsilon_y)}{\mathcal{Z}_1 (\epsilon_y) + \mathcal{Z}_0 (\epsilon_y)}. \tag{4.2.25}$$

This function of ϵ_y is the same in hard and soft devices and does not depend on λ_f.

Our next Fig.4.6 shows that, in hard device, lowering the value of λ_f favors a sharp transition between high and low fraction of post-power-stroke cross-bridges. This means that the presence of an interaction due to the elasticity of the backbone enhances collective behavior of the cross-bridges: the power-stroke takes place almost simultaneously in all elements. In soft device (see Fig.4.6), the curve $\langle n_1 \rangle_s$ *vs* $\overline{\sigma}$ is identical for all values λ_f because in G_y (see Eq.(4.2.14)), the terms containing λ_f do not depend on ϵ_y. As a result, those terms come out of the integral in Eq.(4.2.24) and simply cancel with similar terms in the denominator.

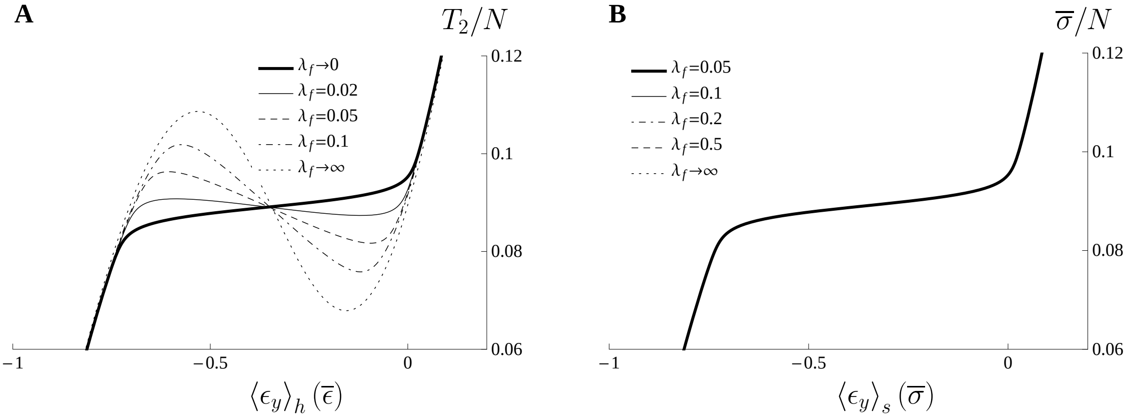

Fig. 4.7 – Comparison of the influence of λ_f in hard (A) and soft (B) devices. We show the parametric plots $\left(\langle \epsilon_y \rangle_h (\overline{\epsilon}), T_2(\overline{\epsilon})\right)$ (see A) and $\left(\langle \epsilon_y \rangle_s (\overline{\sigma}), \overline{\sigma}\right)$ obtained with Eq.(4.2.16) and (4.2.18) respectively for different values of λ_f: $\lambda_f \to 0$ (bold line), $\lambda_f = 0.02$ (solid line), $\lambda_f = 0.05$ (dashed line), $\lambda_f = 0.1$ (dot-dashed line) and $\lambda_f = \infty$ (dotted line). In soft device (see B), all curves superimpose. The curve in hard device converges to the curve in soft device as λ_f decreases. Other parameters $\lambda_1 = 0.4$, $\lambda_0 = 0.7$, $l = -0.3$, $N = 100$ and $\beta = 10$.

Hard device behavior converges to soft device behavior for weak coupling

To remove the effect of the strain in the series spring that shifts the transition towards larger elongations (see Figs.4.4 and 4.5), we show the parametric plots $\left(\langle \epsilon_y \rangle_h (\overline{\epsilon}), T_2(\overline{\epsilon})\right)$ and $\left(\langle \epsilon_y \rangle_s (\overline{\sigma}), \overline{\sigma}\right)$ on Fig.4.7 A and B respectively. The mean values of ϵ_y are obtained from (see Eqs.(4.2.16) and (4.2.18)).

In soft device (see Fig.4.5B) the curves for different λ_f superimpose showing that the behavior of the cross-bridge array is not affected by the stiffness of the filaments (the reason is similar to the one implied in the discussion of $\langle n_1 \rangle_s$). In hard device (see Fig.4.5A), the coupling parameter reduces the negative stiffness of the T_2 *vs* $\langle \epsilon_y \rangle_h$ curve and in the limit of weak coupling, we see that the hard device device curve converges to the soft device curve.

4.3 Negative slope

By using Eq.(4.2.15) and (4.2.17), and differentiating with respect to the loading we obtain:

$$\frac{\partial T_2}{\partial \overline{\epsilon}}(\overline{\epsilon}, \beta) = N\lambda_f \left(1 - \frac{\partial}{\partial \overline{\epsilon}} \langle \epsilon_y \rangle_h (\overline{\epsilon}, \beta)\right)$$

$$\frac{\partial L_2}{\partial \overline{\sigma}}(\overline{\sigma}, \beta) = \frac{1}{N\lambda_f} + \frac{\partial}{\partial \overline{\sigma}} \langle \epsilon_y \rangle_s (\overline{\sigma}, \beta)$$

The computation of the derivative of $\langle \epsilon_y \rangle_h$ and $\langle \epsilon_y \rangle_s$ is straightforward. We obtain:

$$\frac{\partial T_2}{\partial \overline{\epsilon}}(\overline{\epsilon}, \beta) = N\lambda_f \left(1 - \beta N \lambda_f \mathrm{Var}\,(\epsilon_y)_h (\overline{\epsilon}, \beta)\right) \tag{4.3.1}$$

$$\frac{\partial L_2}{\partial \overline{\sigma}}(\overline{\sigma}, \beta) = \frac{1}{N\lambda_f} + \beta \mathrm{Var}\,(\epsilon_y)_s (\overline{\sigma}, \beta) \tag{4.3.2}$$

where $\mathrm{Var}\,(\epsilon_y)_{h,s} = \left\langle \epsilon_y^2 \right\rangle_{h,s} - \langle \epsilon_y \rangle_{h,s}^2$ is the variance of ϵ_y in equilibrium. On the one hand, as the variance is positive, the slope of the L_2 curve is always positive. Moreover, since

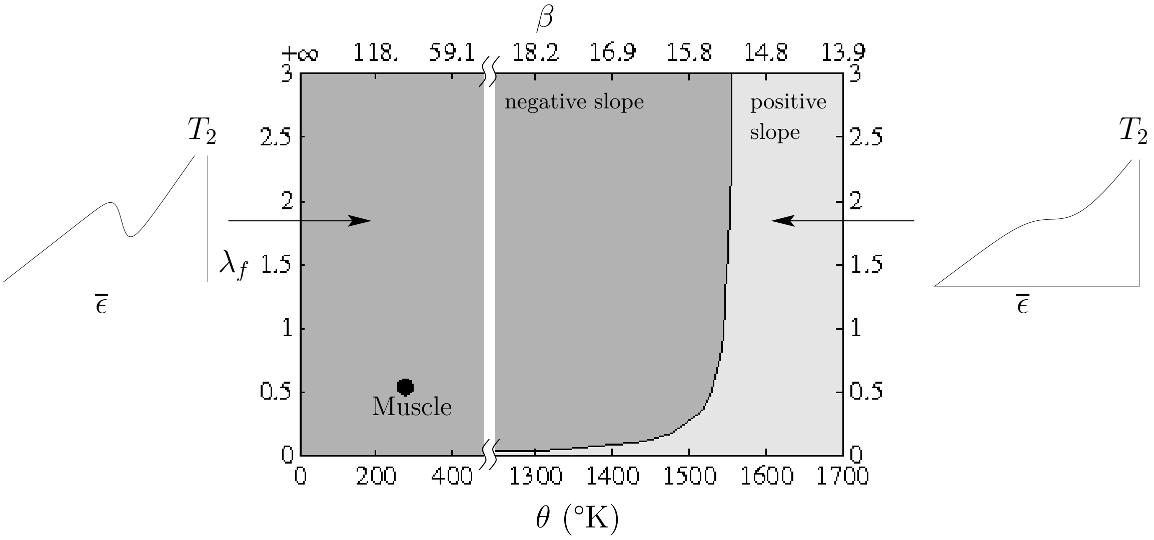

Fig. 4.8 – **Phase diagram for the slope of the T_2 curve**. The graph is obtained by computing the slope of the T_2 curve for 50 points in the interval $\left[\overline{\epsilon}_{1/2} - 0.5, \overline{\epsilon}_{1/2} + 0.5\right]$, using Eq.(4.3.1). This is because the slope at $\overline{\epsilon}_{1/2}$ is not always negative (*e.g.* $\overline{\epsilon}_{1/2}$ can be located at near the end of the transition where the slope is positive). We indicate as examples, on the left, the free energy and the T_2 curve for $\lambda_f = 2$ and $\theta = 59.1$ (corresponding to $\theta = 400$K), in the region of negative slope and, on the right, the free energy and T_2 curve for $\lambda_f = 1.5$ and $\beta = 14.5$ (corresponding to $\theta = 1631$K), in the region of positive slope. (●) indicates the set (λ_f, β) adjusted to fit muscle experiments. The other parameters used for this figure are obtained from the fitting procedure explained in Sec.7.1 (see Tab.7.1 on p.139)

in G_y, the term containing λ_f does not contains ϵ_y (see Eq.(4.2.14)), the variance of ϵ_y in soft device does not depend on λ_f. Hence the slope of $L_2\left(\overline{\sigma}\right)$ curve depends on λ_f only through the additive $1/\left(N\lambda_f\right)$ which, given that N is large, can be viewed as a small contribution.

On the other hand, the slope of $T_2\left(\overline{\epsilon}\right)$ curve depends in a non trivial way on both λ_f and β (see Eq.(4.3.1)). Fig.4.8 shows a phase diagram in the space of parameters λ_f and β identifying the domains where the slope of the T_2 curve is everywhere positive (no spinodal region). The boundary is obtained by computing the slope with Eq.(4.3.1) for 50 points within $\left[\overline{\epsilon}_{1/2} - 0.5, \overline{\epsilon}_{1/2} + 0.5\right]$ and testing positiveness. The parameters used in this figure are those obtained from the fitting procedure explained in Sec.7.1 (see Tab.7.1 on p.139); the set (β, λ_f) corresponding to muscle experiments is indicated by the (○).

Fig.4.8 shows that the presence of the negative slope depends strongly on β, with a sharp transition located around $\beta = 15.5$, which corresponds to a temperature of ~ 1550°K (with the chosen set of parameters). The dependence on λ_f is weaker: the slope becomes positive only when $\lambda_f \to 0$ but in this range, we saw that the transition region become infinitely narrow (see Fig.4.4A). We illustrate the phase diagram by showing in the inserts T_2 associated with particular points: on the left, with $\lambda_f = 2$ and $\theta = 59.1$ (corresponding to $\theta = 400$K) and on the right with $\lambda_f = 1.5$ and $\beta = 14.5$ (corresponding to $\theta = 1631$K).

4.4 Adiabats

The observed negative stiffness associated with the thermal equilibrium response is disturbing. One can think however that the power-stroke operates at such short time scale that the temperature does not have time to equilibrate during the quick recovery and the response is closer to adiabatic one than to isothermal one. Therefore, bellow we compute

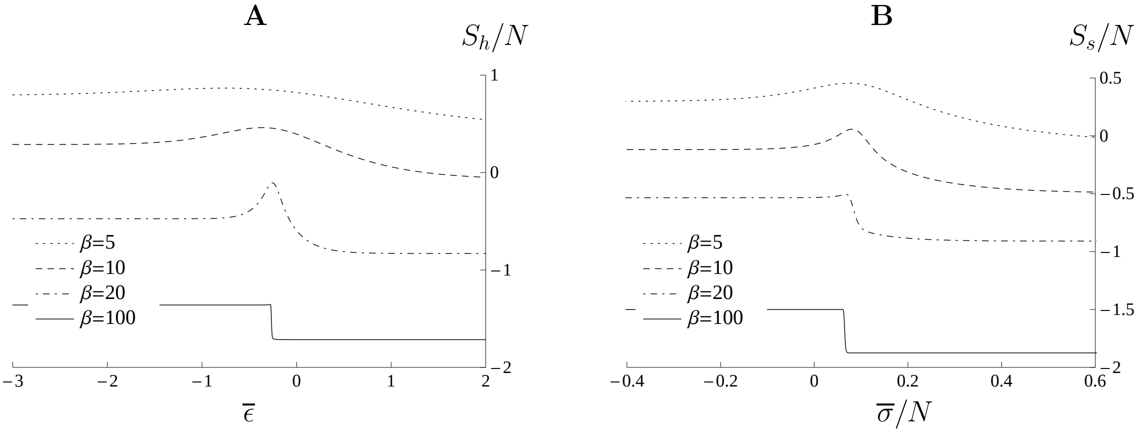

Fig. 4.9 – **Influence of temperature on entropy** in hard (**A**) and soft devices (**B**), for different values of β (dotted line: $\beta = 5$; dashed line: $\beta = 10$; dot-dashed line: $\beta = 20$; Continuous line: $\beta = 100$). The curves are obtained from direct computation of Eq.(4.1.11) and (4.1.12). Other parameters are: $\lambda_1 = 0.4$, $\lambda_0 = 0.7$, $l = -0.3$, $N = 10$, $\lambda_f = 1.$ and $a = 1$.

the adiabatic response (iso-entropic) of our system by assuming that the initial entropy is conserved during the loading. When the load step is applied from the central region of the T_2 *vs* elongation curve, the system is eventually brought into a region where the number of available state is lower than in the initial configuration. If the response is iso-entropic, one expects the temperature to rise which tends to smooth the equilibrium curve.

4.4.1 Entropy

We begin with the computation of the entropy along the isotherms. The entropy has been computed from the partition function using Eq.4.1.13 and Eq.(4.1.14) in hard and soft devices respectively.

Fig.4.9 shows the entropy *vs* loading curves ($\overline{\epsilon}$ or $\overline{\sigma}$) at different temperatures (dotted line: $\beta = 5$; dashed line: $\beta = 10$; dot-dashed line: $\beta = 20$; solid line: $\beta = 100$). The other parameters are the same as in Fig.4.1 ($\lambda_1 = 0.4$, $\lambda_0 = 0.7$, $l = -0.3$, $N = 10$, $\lambda_f = 1.$ and $a = 1.$).

The entropy in soft device (B) is always larger than in hard device (A) because there is an additional degree of freedom in soft device (ϵ_z). Moreover, since the double well is asymmetric (in this case $\lambda_0 > \lambda_1$), the entropy is higher at large shortening than at large stretching (the asymptotic values of the entropy are computed in App.B.3.3).

In the central region, the entropy presents a maximum as, near the transition, the system can both states; this maximizes ‘disorder’ and increases the entropy. When the temperature is large ($\beta \to 0$), this peak is smoothed as the diffusion starts to dominate while for low temperatures ($\beta \to \infty$), the system follows the global minimum and we observe a sharp transition between two intervals of constant entropy.

4.4.2 Temperature change along the adiabats

Along the adiabats, the temperature β varies in such a way that:

$$S_h\left(\overline{\epsilon}, \beta\right) = S_h\left(\overline{\epsilon}^0, \beta^0\right) \text{ in hard device,} \tag{4.4.1}$$

$$S_s\left(\overline{\epsilon}, \beta\right) = S_s\left(\overline{\sigma}^0, \beta^0\right) \text{ in soft device,} \tag{4.4.2}$$

where $\overline{\epsilon}^0$, $\overline{\sigma}^0$ and β^0 are initial conditions. We choose $\overline{\epsilon}^0 = \overline{\epsilon}_{1/2}$ and $\overline{\sigma}^0 = \overline{\sigma}_{1/2}$. We compute the value of the non-dimensional temperature β that ensures that the entropy S is equal

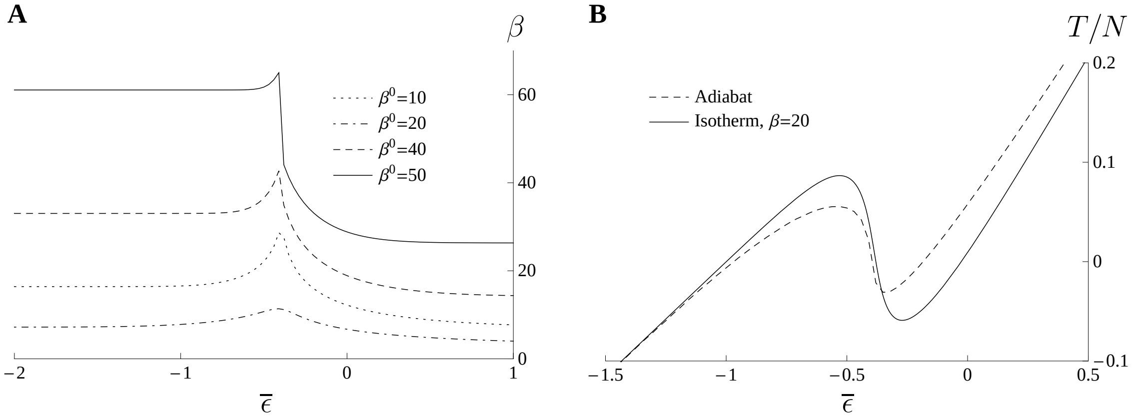

Fig. 4.10 – **Adiabatic response in hard device**. (**A**): Temperature change for various initial temperature: $\beta^0 = 5$ (dotted line), $\beta^0 = 10$ (dashed line), $\beta^0 = 20$ (dot-dashed line) and $\beta^0 = 30$ (solid line). (**B**): $T_2(\overline{\epsilon})$, computed along isotherm (solid line) and along adiabat (dashed line) with $\beta^0 = 10$. Parameters are: $\lambda_1 = 0.4$, $\lambda_0 = 0.7$, $l = -0.3$ and $N = 100$.

to the initial value using a dichotomy algorithm (at all levels of loading). We know that the initial state of the system is located in the transition region where the microstructure is not homogeneous ($\langle n_1 \rangle \neq 1, 0$), and the entropy is high (see Fig.4.9). After the step, the system evolves towards more homogeneous configurations so its entropy decreases along the corresponding isotherm. Hence in adiabatic response, the temperature of the system increases (and thus β decreases).

Fig.4.10 shows the adiabtic response of the system in the hard device. On (Fig.4.10A), we represent the change in β under the assumption of constant entropy. Due to the asymmetry of the double well potential ($\lambda_1 = 0.4$, $\lambda_0 = 0.7$), the entropy is not at its maximal value when $\langle n_1 \rangle_h = 1/2$. Hence, in shortening β first increases before finally decreasing to a constant value. The constant temperature, reached in stretching, is lower than in shortening because the stiffness of the system is lower in stretching than in shortening ($\lambda_1 < \lambda_0$). The asymptotic values of the temperature can be computed analytically (see App.B.3.3) As β^0 decreases the variations of β decrease as well since the system becomes more diffusive.

On Fig.4.10B, we compare the T_2 curve along the isotherm for $\beta = 20$ (solid line) with the T_2 curve along the adiabat (dashed line). We see that the stiffness persists along the adiabat even though the transition becomes smoother.

The adiabatic response in soft device is shown on Fig.4.11. The variation of β is similar to the case of hard device but the sharp transition in β occurs at smaller values of β^0 compared with the hard device case. The adiabatic L_2 curve is similar to the isotherm (see Fig.4.11).

We conclude that the adiabatic response is basically similar to the isothermal response and in particular it also shows a region of negative stiffness in hard device for the same values of parameters. So far, the systematic study of the presence of a negative slope in adiabats has not been made for the whole range of λ_f and β but we checked that, for realistic sets of parameters, the responses are similar in adiabatic and isothermal regimes (see Sec.7.2.3).

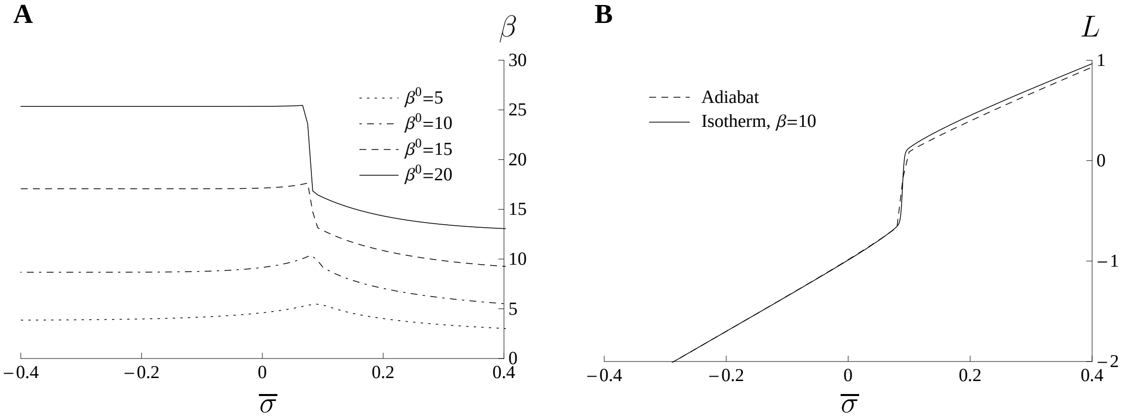

Fig. 4.11 – **Adiabatic response in soft device**. (**A**): Temperature change for various initial temperature: $\beta^0 = 5$ (dotted line), $\beta^0 = 10$ (dashed line), $\beta^0 = 15$ (dot-dashed line) and $\beta^0 = 320$ (solid line). (**B**): $L_2(\overline{\sigma})$ computed along isotherm (solid line) and along adiabat (dashed line) with $\beta^0 = 10$. Parameters are: $\lambda_1 = 0.4$, $\lambda_0 = 0.7$, $l = -0.3$ and $N = 10$.

4.5 Partially equilibrated system

4.5.1 The double well nature of the non-equilibrium energy landscapes

To better understand the difference between hard and soft devices and to illuminate the influence of the coupling parameter λ_f, we consider the partially equilibrated system with two degrees of freedom: ϵ_y and $\overline{\epsilon}$ in hard device and ϵ_y and $\overline{\sigma}$ in soft device. Here, $\overline{\epsilon}$ and $\overline{\sigma}$ are the control parameters and ϵ_y is the internal degree of freedom we would like to track. The probability densities of ϵ_y are:

$$p_y^h(\overline{\epsilon}, \epsilon_y, \beta) = \frac{1}{\mathcal{Z}_h(\overline{\epsilon}, \beta)} \exp\left[-\beta F_y(\overline{\epsilon}, \epsilon_y, \beta)\right] \text{ in hard device,} \tag{4.5.1}$$

$$p_y^s(\overline{\epsilon}, \epsilon_y, \beta) = \frac{\sqrt{\frac{2\pi}{\beta N \lambda_f}}}{\mathcal{Z}_s(\overline{\epsilon}, \beta)} \exp\left[-\beta G_y(\overline{\sigma}, \epsilon_y, \beta)\right] \text{ in soft device,} \tag{4.5.2}$$

with F_y and G_y given by (see Eq.(4.2.13) and (4.2.14)):

$$F_y(\overline{\epsilon}, \epsilon_y, \beta) = N\left(\frac{1}{2}\lambda_f(\overline{\epsilon} - \epsilon_y)^2 - \frac{1}{\beta}\ln\left(\mathcal{Z}_1(\beta, \epsilon_y) + \mathcal{Z}_0(\beta\epsilon_y)\right)\right),$$
$$G_y(\overline{\sigma}, \epsilon_y, \beta) = N\left(-\frac{\overline{\sigma}}{N}\epsilon_y - \frac{1}{2}\frac{\overline{\sigma}^2}{N^2\lambda_f} - \frac{1}{\beta}\ln\left(\mathcal{Z}_1(\beta, \epsilon_y) + \mathcal{Z}_0(\beta, \epsilon_y)\right)\right),$$

where the functions $\mathcal{Z}_1$ and $\mathcal{Z}_0$ (see Eq.(4.2.7) and (4.2.8)) do not depend on the coupling parameter λ_f. The first term in G_y, which depends on λ_f, is quadratic and 'produces' a gaussian probability distribution centered on $\overline{\epsilon}$. $-1/\beta\ln(\mathcal{Z}_1 + \mathcal{Z}_0)$ generates a sum of two gaussian distributions centered at 0 and -1 (see Eq.(4.2.7) and (4.2.8)). Hence, changing the value of the coupling parameter can lead to switching from a convex energy landscape to a non-convex energy landscape in terms of ϵ_y.

We illustrate the probability density of ϵ_y and the non-equilibrium free energy F_y on Fig.4.12A and B respectively for two different values of the coupling parameter λ_f: 0.05 (solid line) and 0.2 (dashed line). For $\lambda_f = 0.05$, the partially equilibrated energy landscape is non-convex and the probability density shows two peaks at $\epsilon_y \approx -0.7$ and $\epsilon_y \approx -0.1$. Instead for $\lambda_f = 0.2$, F_y is convex and the probability density has a single

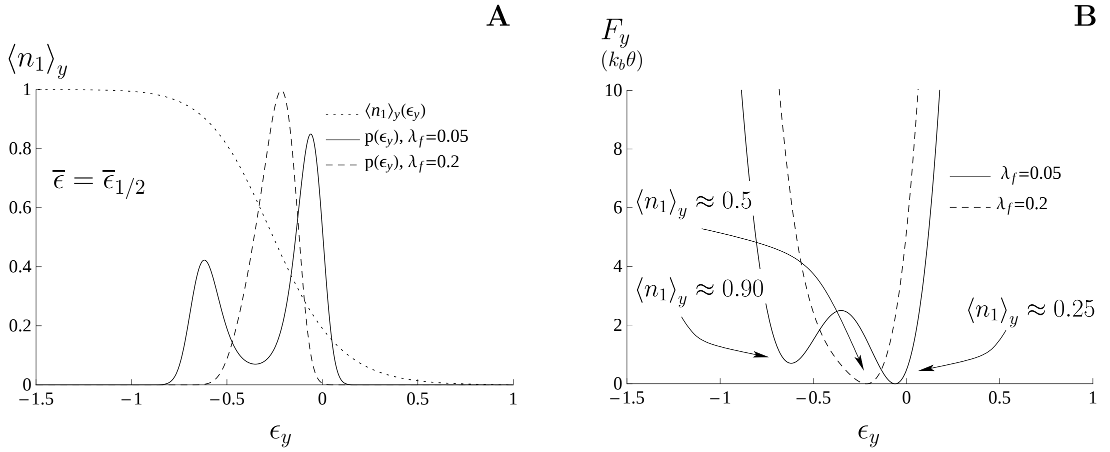

Fig. 4.12 – Non-equilibrium energy landscape in hard device at $\overline{\epsilon} = \overline{\epsilon}_{1/2}$. (**A**): marginal probability density of ϵ_y computed using Eq.(4.5.1) for $\lambda_f = 0.05$ (solid line) and $\lambda_f = 0.2$ (dashed line). The dotted line shows the mean fraction of post-power-stroke cross-bridges *vs* ϵ_y computed using Eq.(4.2.25). This curve is not affected by the value of λ_f. (**B**): Partially equilibrated energy landscape F_y given by Eq.(4.2.13) at $\overline{\epsilon} = \overline{\epsilon}_{1/2}$ for $\lambda_f = 0.05$ (solid line) and $\lambda_f = 0.2$ (dashed line). The arrows indicates the fraction of post-power-stroke cross-bridges corresponding to ϵ_y in the bottom of the non-equilibrium energy wells. Other parameters are: $\lambda_1 = 0.4$, $\lambda_0 = 0.7$, $l = -0.3$, $N = 100$ and $\beta = 10$.

peak at $\epsilon_y \approx -0.25$. We also show the mean fraction of post-power-stroke cross-bridges at fixed ϵ_y by the dotted line ($\langle n_1 \rangle_y$ given by Eq.(4.2.25)). We recall that $\langle n_1 \rangle_y$ does not depend on the value of λ_f.

In must be noted that in both cases ($\lambda_f = 0.2$ and $\lambda_f = 0.05$), as the curves are obtained for $\overline{\epsilon} = \overline{\epsilon}_{1/2}$, the equilibrium fraction of post-power-stroke cross-bridges is 1/2. 1/2 is obtained through $\int \langle n_1 \rangle_y \exp\left[-\beta F_y\right] d\epsilon_y$ (see Eq.(4.2.25) and App.B.4.1). Hence this equilibrium value is achieved either with a single value of ϵ_y (≈ -0.25, see Fig.4.12 dashed lines), for $\lambda_f = 1$, corresponding to a mixed microstructure ($\langle n_1 \rangle_y \approx 0.5$ indicated by the arrow on Fig.4.12B) or by mixing two more homogeneous configurations, for $\lambda_f = 0.05$ with $\langle n_1 \rangle_y \approx 0.9$ and $\langle n_1 \rangle_y \approx 0.25$ corresponding to the two minima of the non-equilibrium (*macroscopic wells*). In other words, at low λ_f, there are two populations of half-sarcomeres (two different ϵ_y): one is pre-power-stroke and the other in post-power-stroke. At large λ_f, there is only one population of half-sarcomere (one ϵ_y) with a mixed microstructure.

In soft device, if we replace $\mathcal{Z}_s$ by its expression (4.2.2), we see that the terms depending on λ_f in (4.5.2) vanish, and unexpectedly the distribution $p_y^s(\epsilon_y)$ does not depend on λ_f (see Fig.4.5). Hence, the presence of macroscopic wells in soft device does not depend on λ_f (see the reduced Gibbs free energy G_y - Eq.(4.2.14)): the terms containing λ_f are not related to the internal parameters ($\epsilon_1, \ldots, \epsilon_N$, and, ϵ_y) and the double well $\frac{1}{\beta}\ln\left(\mathcal{Z}_1 + \mathcal{Z}_0\right)$ is 'tilted' by the term $\frac{\overline{\sigma}}{N}\epsilon_y$, so, at moderate $\overline{\sigma}$ (*i.e.* $\overline{\sigma} \approx \overline{\sigma}_{1/2}$), the probability distribution of ϵ_y is always bi-modal. On Fig.4.13, we show the probability density (see A) and the non-equilibrium energy landscape G_y (see B) for $\lambda_f = 0.05$ and $\lambda_f = 0.2$. We conclude that in soft device, the average fraction $\langle n_1 \rangle_s$ is always obtained by mixing two homogeneous configurations with two different values of ϵ_y (see Fig.4.13B).

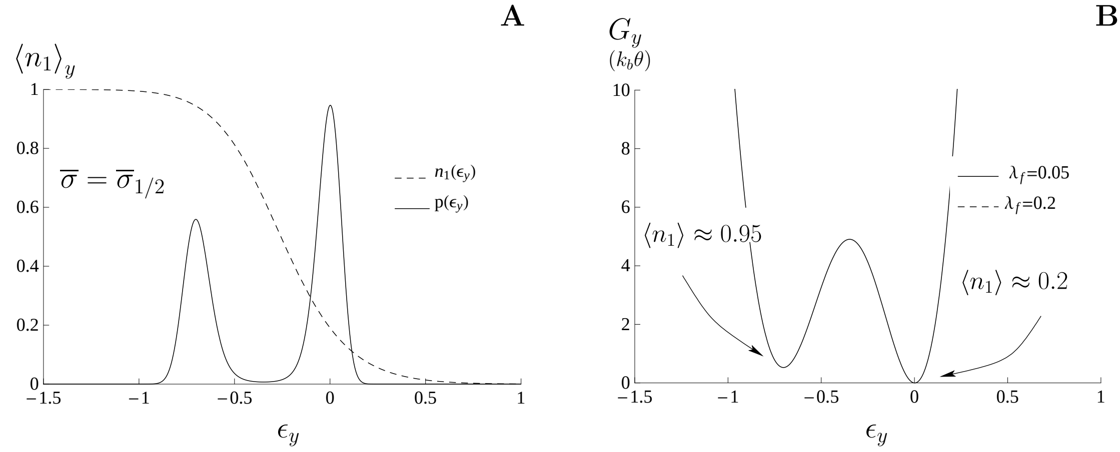

Fig. 4.13 – Non-equilibrium energy landscape in soft device at $\overline{\sigma} = \overline{\epsilon}_{1/2}$. (**A**): marginal probability density of ϵ_y computed using Eq.(4.5.2) for $\lambda_f = 0.05$ and $\lambda_f = 0.2$ (the two curves superimpose). The dotted line shows the mean fraction of post-power-stroke cross-bridges *vs* ϵ_y computed using Eq.(4.2.25). This curve is not affected by the value of λ_f. (**B**): Partially equilibrated energy landscape G_y given by Eq.(4.2.14) at $\overline{\sigma} = \overline{\sigma}_{1/2}$ for $\lambda_f = 0.05$ and $\lambda_f = 0.2$ (the curves also superimposes). The arrows indicates the fraction of post-power-stroke cross-bridges corresponding to ϵ_y in the bottom of the non-equilibrium energy wells. Other parameters are: $\lambda_1 = 0.4$, $\lambda_0 = 0.7$, $l = -0.3$, $N = 100$ and $\beta = 10$.

4.5.2 Energy barriers

When we compare Fig.4.12 and 4.13, we observe that for the same set of parameter, one can get a convex energy landscape in hard device and a non-convex energy landscape in soft device (see the dashed lines corresponding to $\lambda_f = 0.2$ on Fig.4.12 and 4.13B). Moreover, when both hard and soft devices exhibit macroscopic wells (see solid lines), the two minima in ϵ_y are separated by a larger distance in soft device than in hard device. Simultaneously, the energy barrier is higher in soft device than in hard device (*e.g.* the barrier is $\sim 4k_b\theta$ on Fig.4.13B and $\sim 1k_b\theta$ on Fig.4.12B). This result echoes our computations at zero temperature (see Fig.3.10) and suggests that the transition between the wells will be considerably slower in soft device than in hard device.

To support this conclusion, on Fig.4.14(left, A and D), we plot the isolines of the non-equilibrium free energy F_y *vs* ϵ_y and $\overline{\epsilon} - \overline{\epsilon}_{1/2}$ with and without a double well structure (upper part for $\lambda_f = 0.05$ and lower part for $\lambda_f = 0.5$ respectively). The energy landscapes are modified to remove the global tilt in the $\overline{\epsilon}$ direction and all parameters other than λ_f are taken to be the same in both figures ($\lambda_1 = 0.4$, $\lambda_0 = 0.7$, $l = -0.3$, $N = 100$ and $\beta = 10$). The bold lines represent the mean value of ϵ_y (see Eq.4.2.16). On the right ((B) and (E)) we show the T_2 curves corresponding to (A) and (D) respectively. The curves are normalized by the tension T_0 at $\overline{\epsilon}_{1/2}$. On (C) and (F) we show two typical trajectories of ϵ_y in the energy landscapes (A) and (D) for $\overline{\epsilon} = \overline{\epsilon}_{1/2}$. These trajectories are obtained from Langevin simulation of a single half-sarcomere with 100 cross-bridges at $\overline{\epsilon} = \overline{\epsilon}_{1/2}$ (see the next Chapter).

The upper part of Fig.4.14 shows that for a double well non-equilibrium energy landscape, the system oscillates between the 2 long-living states indicated by the black dots (see also Fig.4.14C). In each state, the corresponding tension is either higher or lower than the equilibrium tension and it corresponds to the the tensions generated by homogeneous half-sarcomeres (see the correspondence with the dashed lines on Fig4.14B). The resulting equilibrium tension, shown by the circle in the middle, can then be obtained

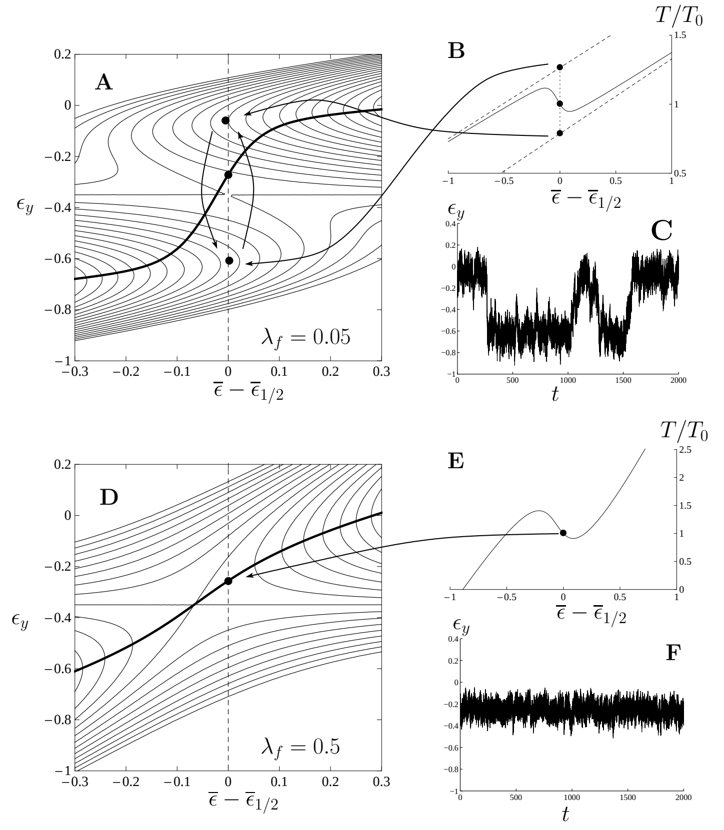

Fig. 4.14 – Trajectories in the non equilibrium energy landscape in hard device and influence of the coupling parameter. We show the non-equilibrium energy landscape (**A** and **D**), the T_2 curve (**B** and **E**) and a typical trajectory of ϵ_y at $\overline{\epsilon} = \overline{\epsilon}_{1/2}$ (**C** and **F**) for two values of the coupling parameter: $\lambda_f = 0.05$ (**A**, **B** and **C**) and $\lambda_f = 0.5$ (**D**, **E** and **F**). The T_2 curves are normalized by the equilibrium tension T_0 at $\overline{\epsilon} = \overline{\epsilon}_{1/2}$. On (**B**), the dashed lines represent the tension in the homogeneous configurations with all cross-bridges in post-power-stroke or in pre-power-stroke. In the presence of a double well F_y (upper part), the equilibrium tension is achieved by mixing the 2 homogeneous configurations between which ϵ_y oscillates (see C). Such system is therefore very unlikely to be found in the equilibrium value whereas, with a single well F_y, the system can equilibrates with a mixed microstructure and does not oscillate (see lower part).

only by averaging the trajectories of an inhomogeneous assembly of many homogeneous half-sarcomeres.

On the lower part of Fig.4.14, $\lambda_f = 0.5$ and the function F_y has a single-well structure. Consequently, a single state with a heterogeneous microstructure is reached and no oscillations are observed (see Fig.4.14D).

The persistence of a a double well structure has a serious impact on the kinetics of the system. As shown by Fig.4.14(A) and (D), when $\overline{\epsilon}$ is changed slightly with respect to $\overline{\epsilon}_{1/2}$ the equilibrium immediately shifts to the affine states where the microstructure is homogeneous, but the double well structure is still present. We saw that when the double well structure is present, the system spends most of the time either at low ϵ_y or high ϵ_y and occasionally switches position while crossing the energy barrier. Hence, for small load changes, the system will reach equilibrium on a much slower time scale if the double well structure is maintained, since cross-bridges may have to collectively cross an energy barrier.

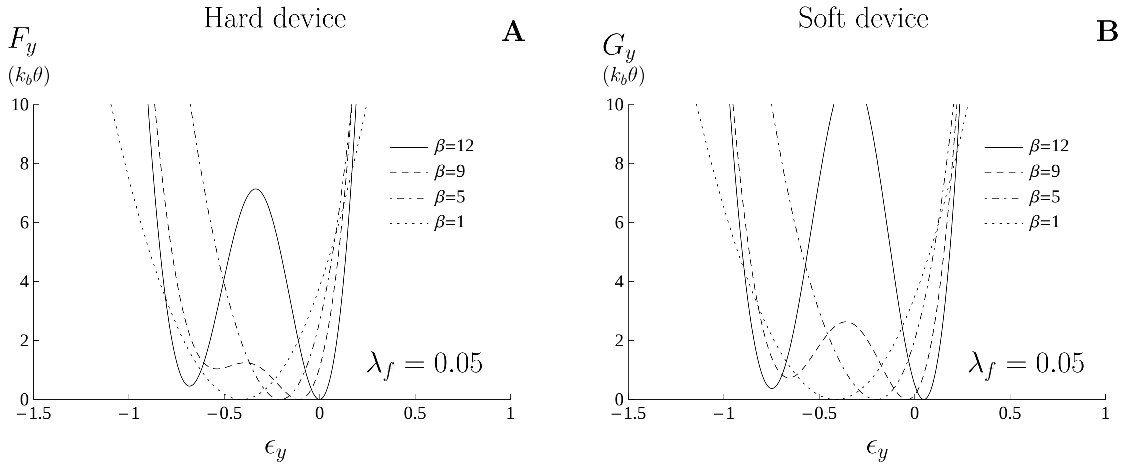

Fig. 4.15 – Influence of temperature on the non-equilibrium free energy. (**A**): hard device. (**B**): soft device. Dotted lines: $\beta = 1$. Dot-dashed lines: $\beta = 5$. Dashed lines: $\beta = 9$. Continuous line: $\beta = 12$. When the temperature increases (β decreases), the free energy becomes convex, the double well structure disappears and the microstructure is less ordered. Parameters are: $\lambda_1 = 0.4$, $\lambda_0 = 0.7$, $l = -0.3$, $N = 100$, $a = 1$, $\beta = 10$, with $\lambda_f = 0.05$

Kinetic phase diagram

The double well nature of the free energy $F_y(\epsilon_y, \overline{\epsilon})$, at $\overline{\epsilon} = \overline{\epsilon}_{1/2}$, exists in a subdomain of the parametric space (β, λ_f). As shown on Fig.4.15(A) (where $\lambda_f = 0.05$), a decrease in β (increase of temperature θ) convexifies the non-equilibrium free energy F_y. The effect of temperature is the same in soft device (see Fig.4.15B).

In Fig.4.16, we show a phase diagram indicating the domain of existence for the double well structure of $F_y\left(\epsilon_y, \overline{\epsilon}_{1/2}\right)$ in the space of λ_f and β. The solid line is obtained numerically in Mathematica® using the set of parameters obtained after fitting the model to experimental data (see Sec.7.1 and Tab.7.1 on p.139). The chosen set $(\beta, \lambda_f) = (85, 0.53)$ is indicated by the $(\times)$. As expected, at a given temperature θ, there is a critical value of λ_f at which the energy landscape becomes convex. We illustrate the two domain by showing the non-equilibrium energy landscapes at $\overline{\epsilon} = \overline{\epsilon}_{1/2}$ and $\overline{\sigma} = \overline{\sigma}_{1/2}$ for two selected points (on the left, $\beta = 119$ and $\lambda_f = 1$ and on the right, $\beta = 25$ and $\lambda_f = 1.5$). We see that in both domains, $G_y\left(\epsilon_y, \overline{\sigma}_{1/2}\right)$ is non convex.

The convexity of F_y and G_y can be verified analytically at a given value of ϵ_y by computing the second derivative. In hard device we have:

$$\partial_{yy}F_y(y) = \lambda_f - \beta\frac{Z_1(\epsilon_y,\beta)\,\mathcal{Z}_0(\epsilon_y,\beta)}{\left(Z_1(\epsilon_y,\beta)+\mathcal{Z}_0(\epsilon_y,\beta)\right)^2}\left((\lambda_1-\lambda_0)\,\epsilon_y+\lambda_1\right)^2 + \lambda_1\frac{\mathcal{Z}_1(\epsilon_y,\beta)}{Z_1(\epsilon_y,\beta)+\mathcal{Z}_0(\epsilon_y,\beta)} + \lambda_0\frac{\mathcal{Z}_0\left(\epsilon_{\epsilon_y,\beta}\right)}{Z_1(\epsilon_y,\beta)+\mathcal{Z}_0(\epsilon_y,\beta)}. \tag{4.5.3}$$

Since $\partial_{yy}G_y(y) = \partial_{yy}F_y(y) - \lambda_f$ we see that λ_f has no impact on the convexity of G_y. We would like to derive an asymptotic criterion for the non convexity of F_y considering the case $\beta \gg 1$. We know that, in the limit $\beta \to \infty$, the system converges to the global minimum where $\overline{\epsilon}_{1/2} = \overline{\epsilon}^\star$ (see Sec.3.1.4). Then, the non-equilibrium free energy F_y converges to the reduced energy $\hat{V}_y$ (represented on Fig.3.10, thick line; see Sec.3.3), and the eventual interval of non convexity shrinks to $\epsilon_y^\star$ (represented with a $\star$ on Fig.3.10). We recall that $\epsilon_y^\star$ must satisfy: $\frac{1}{2}\lambda_1\left(\epsilon_y^\star+1\right)^2 = \frac{1}{2}\lambda_0\epsilon_y^{\star 2} + v_0$ which means that the exponential parts in $\mathcal{Z}_1$

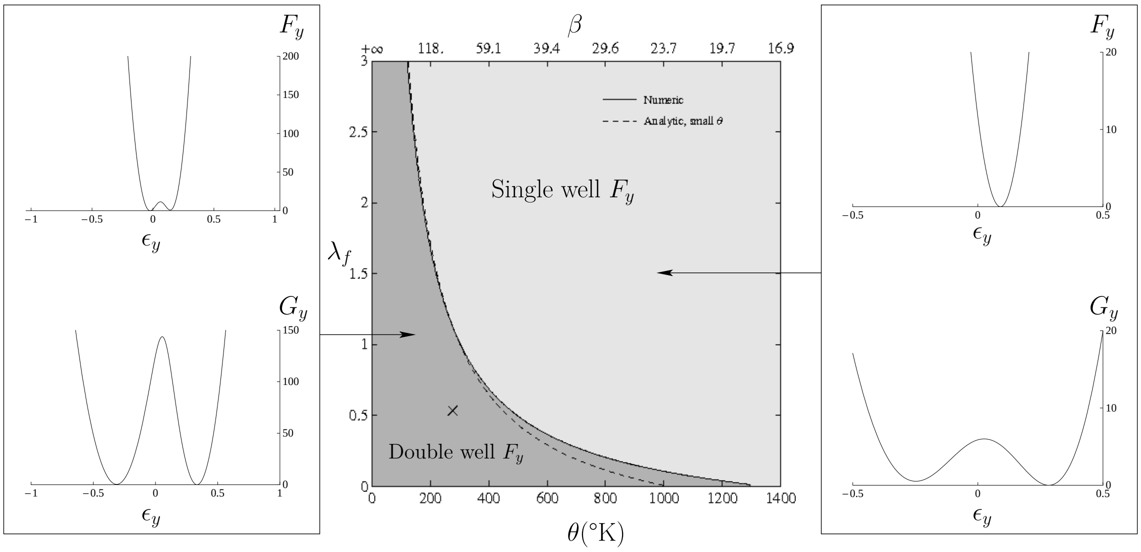

Fig. 4.16 – **Kinetic phase diagram**. The region in the lower-left corner is the domain where the probability density of ϵ_y shows two peaks when the mean fraction of post-power-stroke bridges is equal to 1/2 (*i.e.* when $\overline{\epsilon} = \overline{\epsilon}_{1/2}$). On the left, we represent the two non-equilibrium energy landscapes in hard (F_y) and soft (G_y) devices corresponding to the point $\beta = 118$, $\lambda_f = 1$. On the right, we show F_y and G_y corresponding to the point $\beta = 25$, $\lambda_f = 1.5$. The cross denotes the values (θ, λ_f) used for muscle simulation ($\beta = 85.3$ and $\lambda_f = 0.53$). The boundary between the 2 domains is obtained by numerically testing the presence of 2 minima in the non-equilibrium free energy at $\overline{\epsilon} = \overline{\epsilon}_{1/2}$ and at $\overline{\sigma} = \overline{\sigma}_{1/2}$. The dashed line is an approximation of the boundary for low temperatures (see Eq.(4.5.4)). This plot is obtained with the parameters adjusted to muscle fiber experiments (see Sec.7.1 and Tab.7.1 on p.139).

and $\mathcal{Z}_0$ are equal (see Eq.4.2.7 and 4.2.8). Thus (4.5.3) reduces to the asymptotic relation:

$$\partial_{yy}F_y\left(\epsilon_y\right) \approx \lambda_f - \beta\frac{\sqrt{\left(1-\lambda_1\right)\left(1-\lambda_0\right)}}{\left(\sqrt{1-\lambda_1}+\sqrt{1-\lambda_0}\right)^2}\left(\left(\lambda_1-\lambda_0\right)\epsilon_y+\lambda_1\right)^2 + \frac{\lambda_1\sqrt{1-\lambda_1}+\lambda_0\sqrt{1-\lambda_0}}{\sqrt{1-\lambda_1}+\sqrt{1-\lambda_0}} \tag{4.5.4}$$

The corresponding isoline, $\partial_{yy}F_y\left(\epsilon_{y^\star}\right) = 0$, is represented with a dashed line on Fig.4.16. It matches asymptotically the numerical computation as θ decreases but also provides a good approximation in the whole domain.

As we have already mentioned, in soft device, the convexity of G_y does not depend on λ_f. Using the same method as in hard device we find that G_y becomes convex for:

$$\beta < \frac{\lambda_1\sqrt{1-\lambda_1}+\lambda_0\sqrt{1-\lambda_0}}{\sqrt{1-\lambda_1}+\sqrt{1-\lambda_0}}\left(\frac{\sqrt{\left(1-\lambda_1\right)\left(1-\lambda_0\right)}}{\left(\sqrt{1-\lambda_1}+\sqrt{1-\lambda_0}\right)^2}\left(\left(\lambda_1-\lambda_0\right)\epsilon_y+\lambda_1\right)^2\right)^{-1} \tag{4.5.5}$$

which correspond to $\beta < 16$ and $\theta > 1480$°C at realistic values of other parameters.

Conclusions

By introducing finite temperature in our system, we observed that our the mechanical energy landscape with exponentially many wells has been smoothed. However, due to the parallel arrangement of the cross-bridges, our model markedly differs from classical distributed systems and preserves a non-convex energy landscape even in the thermodynamic limit for sufficiently low temperatures.

Near the metastable region, where the isometric contraction is supposed to take place, the systems operates in an inherently unstable regime in hard device, characterized by an effective negative stiffness that ultimately disappear at large temperature.

The diminishing of the parameter λ_f, acts similar but not equivalent to a decrease in temperature. It enhances the cooperative transition between pre- and post-power-stroke states but has only little effect on the presence of negative stiffness.

At the same time, the coupling parameter has a dramatic effect on the shape non-equilibrium energy landscape in hard device. A reduction of λ_f creates a barrier between a population of pre-power-stroke half-sarcomeres and a population of post-power-stroke half-sarcomere. This separation is always present in soft device however the energy barrier is at least twice as high as in hard device. Due to bi-stability of the effective free energy, the system oscillates at the macroscopic level and spends only a small fraction of time near its microscopically equilibrium state.

Chapter 5

Kinetics

We saw in Chapter 4, that the reduced energy landscape exhibits 2 macroscopic wells in the region of the transition ($\overline{\epsilon} = \overline{\epsilon}_{1/2}$ and $\overline{\sigma} = \overline{\sigma}_{1/2}$) even at finite temperature. In this chapter, we study the kinetics of the system when the controlled parameter evolves in time. First, we treat the simple case of zero temperature. Then, we present the analytical study of first passage times and discuss the Kramers approximation. Finally we introduce the Langevin's equation for our system and study numerically its stochastic response to length steps and load steps.

Contents

5.1 Kinetics at $\theta = 0$

5.1.1 System of ODEs

In this sub-section we investigate the response of our system submitted in standard physiological length and load clamp experiments by using first the classical mechanical framework. We neglect the fluctuations produced by the thermal bath ($\theta \to 0$ or $\beta \to \infty$) but keep the dissipative friction within the cross-bridges described by a viscous force $-\eta\dot{\epsilon}_i$. Also, we assume that all other (linear) elastic elements are considered conservative.Later we show that this assumption is consistent with experimental results on muscle fiber (see Sec.7.1).

To nondimensize times are we use the time scale $\tau = \eta/\kappa$.

We choose as initial condition the metastable state $n_1 = 0.5$ at $\overline{\epsilon}^0 = \overline{\epsilon}^\star$ in hard device and $\overline{\sigma}^0 = \overline{\sigma}^\star$ in soft device. This implies that the system is initially stable. Then, we apply ramps of different amplitudes. In real experiments, the step is applied as fast as possible so that T_1 and L_1 can be associated with a purely elastic response (see Sec.7.1 and (Huxley and Simmons, 1971; Smith et al., 2008)). To stay close to experiments, we have chosen $t_{ramp} \ll \tau$. It what follows we use $t_{ramp} = 0.1$ in arbitrary units and we compute the tension and elongation as a function of time.

Without thermal noise, the system of governing equations is completely determinist and all the cross-bridges in the same well are exactly at the same position at the same time. Thus the system reduces to a set of two (dimensionless) ordinary differential equations (ODE). In hard device we obtain:

$$\begin{cases} \dot{\epsilon}_1 & = -\partial_{\epsilon_1} v\left(\epsilon_1\right) + \frac{1}{1+\lambda_f}\left(\lambda_f \overline{\epsilon}\left(t\right) + n_1^0\epsilon_1 + n_0^0\epsilon_0\right) - \epsilon_1 \\ \dot{\epsilon}_0 & = -\partial_{\epsilon_0} v\left(\epsilon_0\right) + \frac{1}{1+\lambda_f}\left(\lambda_f \overline{\epsilon}\left(t\right) + n_1^0\epsilon_1 + n_0^0\epsilon_0\right) - \epsilon_0 \end{cases}$$

where $\epsilon_1\left(t\right)$ is the position of the cross-bridges in well 1 and $\epsilon_0\left(t\right)$ is the position of the cross-bridges in well 0. In soft device, the system takes the form:

$$\begin{cases} \dot{\epsilon}_1 & = -\partial_{\epsilon_1} v\left(\epsilon_1\right) + \frac{\overline{\sigma}(t)}{N} + n_1^0\epsilon_1 + n_0^0\epsilon_0 - \epsilon_1 \\ \dot{\epsilon}_0 & = -\partial_{\epsilon_0} v\left(\epsilon_0\right) + \frac{\overline{\sigma}(t)}{N} + n_1^0\epsilon_1 + n_0^0\epsilon_0 - \epsilon_0 \end{cases}$$

In hard device the tension $T\left(t\right)$ is given by:

$$T\left(t\right) = \frac{N\lambda_f}{1+\lambda_f}\left(\overline{\epsilon}\left(t\right) - n_1^0\epsilon_1\left(t\right) - n_0^0\epsilon_0\left(t\right)\right),$$

and, in soft device, the total elongation is:

$$L(t) = \frac{\overline{\sigma}\left(t\right)}{N}\left(1 + \frac{1}{\lambda_f}\right) + n_1^0\epsilon_1 + n_0^0\epsilon_0.$$

Notice that if $t_{ramp} \gg \tau$, viscous relaxation will start taking place during the ramp itself while if $t_{ramp} \ll \tau$, only the elastic response will be activated, with the cross-bridges remaining almost at the same position in their wells.

5.1.2 Length clamp and load clamp experiments

On Fig.5.1(A), we plot the tension versus time for different length change experiments, starting all from the same configuration $n_1 = 0.5$ (denoted as S). In (B) we represent the evolution in time of the total elongation for different changes in load starting from point S.

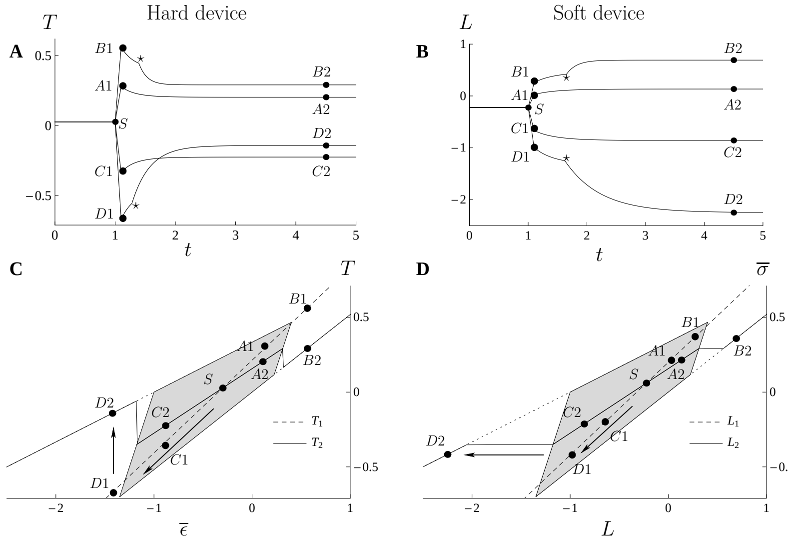

Fig. 5.1 – Visco-elastic response of a half sarcomere in hard and soft devices. (**A**) (resp. (**B**)): tension (resp. elongation) evolution in time for 4 different step sizes. The system is initially in configuration $(1/2, 0, 1/2)$ represented by point S. Then a ramp of duration $t_{ramp} = 0.1$ is applied (in **A** a length ramp and in **B** a force ramp) from S to A_1, B_1, C_1 and D_1. When the ramp is finished, the system relaxes to a new tension (**A**) or elongation (**B**). The final steady state are noted A_2, B_2, C_2 and D_2. (**C**) and (**D**), the state of the system after the ramp (dashed line) and after viscous relaxation (continuous line) are represented for different step sizes. The point A_1, B_1, *etc...* and A_2, B_2, *etc...* correspond to the trajectories shown in (**A**) and (**B**). The gray region is the existence domain of metastable states. Parameters are: $\lambda_1 = 0.4$, $\lambda_0 = 0.7$, $l = -0.3$, $\lambda_f = 2$ and $N = 300$.

In both hard and soft devices, we distinguish two phases in the transient response. First, the tension or elongation changes during the ramp (from S to A1, B1, etc...). This is an elastic behavior ($t_{ramp} \ll \tau$), leading to a straight line in the graph tension *vs* total elongation (dashed line on the right figure of Fig.5.1C and D). This straight line corresponds to the T_1 curve. When the ramp is finished, the tension (resp. elongation) readjusts to its a new equilibrium value (from A1, B1 etc... to A2, B2 etc...). Here two cases can be distinguished. First, the amplitude of the ramp is small enough so that the configuration $n_1 = 0.5$ still exists for the final total elongation or tension (cases A and C, in the gray region). In that case, we have an exponential decay as the system equilibrates back to its initial configuration $n_1 = 0.5$ at a new length (tension) (paths $A_1 \to A_2$, and $C_1 \to C_2$), the heads remaining in the same well. Second, the amplitude of the ramp is large and the configuration no longer exists for the final total elongation (tension) (cases B and D leads outside the gray region); then we observe a response with 2 times scales. The first one is due to the motion of the heads in their initial well, up to the point where the cross-bridges in the well reach the spinodal point. Then, the cross-bridges have to transit to the new well. There is then an acceleration of the tension or elongation evolution (indicated by the $\star$ on Fig.5.1A and B).

By comparing the time response of the system in both hard and soft devices, we observe that the rates of recovery are higher in hard device than in soft device as it was suggested by the analysis of the energy landscape (see Sec.3.1.4).

To conclude, we observe that if we wanted to reproduce the quick recovery experiments using a mechanical model that does not take into account temperature, it would have been natural to interpret the experimental T_1 curve as the instant response of our visco-elastic system (points A1, B1, etc...). Then T_2 (resp. L_2) would be identified with the final tension (resp. elongation) (points A2, B2, etc...). However, we have shown that within this framework, it is not possible to reproduce the experimental T_2 curve (see Fig.2.5). Instead we obtained a discontinuous T_2 curve with the jumps located at the boundary of the metastability domain for the initial configuration.

5.2 Kinetics at finite temperature

5.2.1 Elements of theory

We recall that our relatively low parametric mechanical system is immersed in a medium with a large ($\sim 10^{23}$) number of degrees of freedom. These degrees of freedom are assumed to be equilibrated and are represented in our model by a thermostat imposing finite temperature θ. In our framework, the inertial terms can be neglected (*overdamped* regime) and the motion of a point-like particle X in a potential $V(X)$ is governed by the Langevin equation:

$$\eta \frac{dX}{dt} = -V'(X) + \sqrt{2\eta k_b \theta}\,\Gamma(t) \tag{5.2.1}$$

where η is the viscous drag coefficient and $\Gamma(t)$ is the white noise whose strength is prescribed by the fluctuation dissipation theorem: $\langle \Gamma(t) \rangle = 0$ and $\langle \Gamma(t)\Gamma(t') \rangle = \delta(t-t')$. Here, $\langle . \rangle$ denote ensemble average and δ is the Dirac function. With these notations, $\Gamma(t)$ can be interpreted as the derivative of a Wiener process whose property is to be non-differentiable (Gardiner, 2004). Therefore, it is more natural to rewrite Eq.(5.2.1) as the Stochastic Differential Equation (SDE)

$$dX^t = \frac{1}{\eta}\left(-V'\left(X^t\right)dt + \sqrt{2k_b\theta}\,dB^t\right)$$

where dB^t is the increment of a Wiener process with variance dt. As in the previous Section, we define $\tau = \eta/\kappa$ as our characteristic time and, using the notation introduced in Sec.2.5.3 rewrite the preceding equation in the following non-dimensional form:

$$d\overline{X}^t = -\overline{V}'\left(\overline{X}\right)\overline{dt} + \sqrt{2\beta^{-1}}\,\overline{dB^t} \tag{5.2.2}$$

where $\beta = \kappa a^2/(k_b\theta)$ and $\overline{dB^t} \sim \mathcal{N}(0,1)$[1]. From now on, the bars will be dropped for convenience. For a given initial condition $X^0 = x_0$ The solution of (5.2.2) is:

$$X^t = X^0 + \int_0^t -V'\left(X^t\right)dt + \sqrt{2\beta^{-1}}\int_0^t dB^t$$

where, the second integral is an Itô stochastic integral which is defined, for a given division $t_1, \ldots, t_n$ of the time interval $[0,t]$ and for an arbitrary function f as follows[2]:

$$\int_0^t f(t)\,dB^t = \underset{n\to\infty}{\text{m.s.}\lim}\left[\sum_{i=1}^{n} f(t_{i-1})\left(B^{t_i} - B^{t_{i-1}}\right)\right]$$

The essential properties of the brownian increment dB^t are:

$$\int_{t_i}^{t_{i+1}} \left(dB^t\right)^2 = t_{i+1} - t_i; \quad \int_{t_i}^{t_{i+1}} \left(dB^t\right)^{n+2} = 0 \text{ for all } n > 0 \tag{5.2.3}$$

---

[1] Notation: $X \sim \mathcal{N}(0,1)$ means that the probability density of X is a normal distribution with zeros mean and variance 1. $p(x) = \frac{1}{\sqrt{2\pi}}\exp\left[-\frac{t^2}{2}\right]$

[2] A random variable X^n converges in mean square to the random variable X with the notation $\underset{n\to\to\infty}{\text{m.s.}\lim}\,[X^n] = X$ if and only if $\lim_{n\to\infty}\left\langle (X^n - X)^2 \right\rangle = 0$.

Now consider an arbitrary function f of our stochastic variable X^t interpreted as a solution of Eq.(5.2.2). By expanding $df\left(X^t\right)$, and using (5.2.3), we obtain the so-called Itô formula which describes the change of variable in the context of stochastic differential equations:

$$df\left(X^t\right) = \left[-V'\left(X^t\right)f'\left(X^t\right) + \beta^{-1}f''\left(X^t\right)\right]dt + \sqrt{2\beta^{-1}}f'\left(X^t\right)dB^t$$

This formula will be extensively used in Chap.6.

Now, at each time t, the random variable X^t has a probability density $p(x,t) > 0$ such that $\int p(x,t)\,dx = 1$. Next, for an arbitrary function f we write:

$$\begin{aligned}\frac{d}{dt}\left\langle f\left(X^t\right)\right\rangle = \int f(x)\frac{\partial p(x,t)}{\partial t}dx &= \left\langle -V'\left(X^t\right)f'\left(X^t\right) + \beta^{-1}f''\left(X^t\right)\right\rangle \\ &= \int\left[-V'(x)f'(x) + \beta^{-1}f''(x)\right]p(x,t)\,dx.\end{aligned}$$

which after integration by parts and discarding the surface terms gives:

$$\int f(x)\frac{\partial p(x,t)}{\partial t}dx = \int f(x)\left[\frac{\partial}{\partial x}\left[V'(x)p(x,t)\right] + \beta^{-1}\frac{\partial^2}{\partial x^2}p(x,t)\right]dx. \tag{5.2.4}$$

Since this equality is true for arbitrary f, we obtain the the (forward) Fokker–Planck equation:

$$\frac{\partial p(x,t)}{\partial t} = \frac{\partial}{\partial x}\left[V'(x)p(x,t)\right] + \beta^{-1}\frac{\partial^2}{\partial x^2}p(x,t)\ \text{for}\ t > t_0 \tag{5.2.5}$$

with the initial condition $p(x,t_0) = p_0(x)$.

The two problems (5.2.2) and (5.2.5) are equivalent under the condition that V' is lipschitzian and that there exist $C \in \mathbb{R}$ such that $V'(x) \leq C(1+|x|)$. There exists a number of numerical methods to solve the problem of finding $p(x,t)$ in both approaches (Allaire, 2007; Kloeden and Platen, 1999). Numerical solutions of the Fokker–Planck equation will be performed using finite volume or finite elements methods (see App.D.1). In these methods, the 'numerical cost' increases exponentially with the dimension d of the phase space (the dimension of the discretization grid), thus they are not adapted to solve problems with $d > 3$. Here we have $d \sim 100$ so we would need to dramatically reduce the dimension of the system in order to use its Fokker–Planck description and implement finite volume or finite element methods. We present an attempt of such model reduction in Chap.6. In the following, we will use numerical simulation of the stochastic trajectories by dealing directly with stochastic dynamics of the variable X^t.

5.2.2 Numerical simulation of stochastic trajectories

The exact relation between the solution of Fokker–Planck equation and the trajectory of the stochastic process X^t is that (Graham and Talay, 2010):

$$p(x,t) = \left\langle p_0\left(X^t_{x,t_0}\right)\right\rangle \tag{5.2.6}$$

where X^t_{x,t_0} represents the stochastic realizations of X^T that start at the point x at time t_0. By using the strong law of large numbers we approximate the mean value by the empirical sum over N_r independent realizations of the stochastic process:

$$\left\langle p_0\left(X^t_{x,t_0}\right)\right\rangle = \lim_{N_r\to\infty}\frac{1}{N_r}\sum_{i=1}^{N_r}p_0\left(X^{t,i}_{x,t_0}\right). \tag{5.2.7}$$

Where $X_{x,t_0}^{t,i}$ with $1 \leq i \leq N_r$ is a family of trajectories of the stochastic process X_{x,t_0}^{t} solution of Eq.(5.2.2) with the initial condition $X_{x,t_0}^{t_0} = x$.

In order to simulate a trajectory of $X_{t,x}^{T}$, we use the Euler algorithm. This method was chosen because the drift and diffusion terms in our problem are relatively simple ($V'(x)$ is piecewise linear and the diffusion coefficient is constant). We have also found that the numerical convergence was fast enough to avoid the use of more sophisticated algorithms.

To explain the numerical method, we introduce Δt the time step of the simulation and denote by n the number of time steps in the time interval $[t, T]$. The discretization scheme is the following:

$$X^{i+1} = X^i + \left(-V'\left(X^i\right)\right)\Delta t + \sqrt{2\beta^{-1}}\left(B^{i+1} - B^i\right) \tag{5.2.8}$$

where $\left(B^{i+1} - B^i\right) \sim \mathcal{N}(0, \sqrt{\Delta t})$. This scheme is consistent by construction and is numerically stable (Kloeden and Platen, 1999). By solving finite difference equations, we obtain a family of simulated trajectories $X_{x,t_0}^{t,i,n}$ with $1 \leq i \leq N_r$. Then we obtain the approximation of the solution of the Fokker–Planck equation:

$$p^{n,N_r}(x,t) = \frac{1}{N_r}\sum_{i=1}^{N_r} p_0\left(X_{t_0,x}^{t,i,n}\right). \tag{5.2.9}$$

Now the error can be decomposed as follows (Graham and Talay, 2010):

$$\left|p(x,t) - p^{n,N_r}(x,t)\right| \leq \left|p(x,t) - \left\langle p_0\left(X_{x,t_0}^{T,n}\right)\right\rangle\right| + \left|\left\langle p_0\left(X_{x,t_0}^{t,n}\right)\right\rangle - p^{n,N_r}(x,t)\right|. \tag{5.2.10}$$

The first term denoted $\alpha(n)$ is the *discretization error* and the second term denoted $\beta(n, N_r)$ is the statistical error. It is known from the central limit theorem that $\beta(n, N_r) \sim \mathcal{N}(0,1)$ when $N_r \to \infty$ as $1/\sqrt{N_r}$. For the Euler scheme it can be shown that the discretization error α is bounded as follows (Graham and Talay, 2010; Kloeden and Platen, 1999):

$$|\alpha| \leq \frac{C}{\sqrt{n}}. \tag{5.2.11}$$

In most of the cases, where the drift and diffusion functions are sufficiently smooth, the convergence of the scheme with order 1 is guaranteed (Graham and Talay, 2010). In actual computations, the unit of non dimensional time must be constructed from the smallest 'physical time' if one would like to capture the effect of the fastest processes. In our case, we achieved a good numerical convergence with $\Delta t = 10^{-3} \ll 1$ and with $N_r \sim 500$.

5.3 First passage times and equilibration of populations

Before studying the kinetic response at finite temperature numerically, it is instructive to first obtain an estimate of the operative timescales in our system. we observe that, during a typical experiment, the system will go from one well of the free energy landscape to another well corresponding to its final equilibrium state. On its way, the system have to cross different energy barriers, and the barrier crossing process will dictate the time scale of recovery. Here, we will investigate two one-dimensional barrier crossing processes that are relevant for our system. First, at the level of a single cross-bridge would study the barrier crossing in the energy landscape $V_{xb}(\epsilon_1, \epsilon_y) = v(\epsilon_1) + 1/2(\epsilon_y - \epsilon_1)^2$ at fixed ϵ_y. Second, we'll study the barrier crossing in the reduced free energy landscape $F_y(\epsilon_y)$ obtained in Sec.4.5.

5.3.1 First passage times

Consider a particle X undergoing a drift-diffusion motion in an energy landscape $V(X)$ which possesses two wells located at $\hat{x}_1$ and $\hat{x}_0$, with $\hat{x}_1 < \hat{x}_0$. Assume also that the two wells are separated by an energy barrier located at point $x = l$. Suppose the particle is initially at $\hat{x}_0$ at time t_0. We would like to know: what is the average time before the particle that starts at $\hat{x}_0$ reaches a given position x ? The standard solution of this *escape time problem* in 1-D can be found in most textbooks on stochastic processes. In App.C we recall the main steps of the derivation of the solution. Here we just present the final formulas Let $\mathcal{T}(t_0, x_0 \to x)$ be the first passage time at x starting from the position $\hat{x}_0$ at time t_0. The function $\mathcal{T}(t_0, x_0 \to b)$ is the solution of the following elliptic equation (see App.C):

$$\left[-V'(x)\frac{d}{dx_0} + \beta^{-1}\frac{d^2}{dx_0^2}\right]\langle\mathcal{T}(x_0 \to b)\rangle = -1 \tag{5.3.1}$$

with the boundary conditions

$$\left.\frac{d}{dx_0}\langle\mathcal{T}(x_0 \to x)\rangle\right|_{x_0=-\infty} = 0; \quad \langle\mathcal{T}(x_0 \to x)\rangle|_{x_0=x} = 0. \tag{5.3.2}$$

This problem has an analytical solution. In the case of a passage from x_0 to x one can show that:

$$\langle\mathcal{T}(\hat{x}_0 \to x)\rangle = \beta\int_x^{\hat{x}_0}\exp[\beta V(s)]\left(\int_s^{+\infty}\exp[-\beta V(y)]\,dy\right)ds. \tag{5.3.3}$$

Similarly, for the passage time from $\hat{x}_1$ to x one finds:

$$\langle\mathcal{T}(\hat{x}_1 \to x)\rangle = \beta\int_{\hat{x}_1}^{x}\exp[\beta V(s)]\left(\int_{-\infty}^{s}\exp[-\beta V(y)]\,dy\right)ds \tag{5.3.4}$$

5.3.2 Kramers approximation

In 1940, H.A. Kramers derived an approximate formula for the mean first passage time inside a double well potential when the energy barrier is large compared to $k_b\theta$ (see (Kramers, 1940)). The result is extensively used in reaction rate theory constituting the basics of the chemo-mechanical models of muscle contraction (see the review by P. Hanggi (Hanggi et al., 1990) and our discussion on chemo-mechanical models in Sec.2.4.4).

Consider for instance a single cross-bridge, and associate with it the energy potential $V_{xb}(\epsilon, \epsilon_y) = v(\epsilon) + 1/2\,(\epsilon_y - \epsilon)^2$ where ϵ_y is fixed. We recall that for a given ϵ_y, V_{xb} has two minima at $\hat{\epsilon}_0 > l$ and at $\hat{\epsilon}_1 < l$. We would like to compute $\langle\mathcal{T}(\hat{\epsilon}_1 \to \epsilon)\rangle$ (see Eq.(C.1.6)) for $l < \epsilon < \hat{\epsilon}_0$. A numerical integration is doable in Eqs.(5.3.3) and (C.1.6) with the use of special function. However, Kramers allows one to derive a simple asymptotic formula in the limit $\beta \to \infty$. The result will be slightly different from the most well known Kramers formula as we consider a piecewise parabolic potential rather than a twice differentiable potential; note that Kramers himself treated this special case in his 1940 paper (Kramers, 1940). The computations are detailed in App.C. In the limit $\beta \to \infty$, Eqs.(C.1.6) and (5.3.3) can be written as

$$\langle\mathcal{T}(\hat{\epsilon}_1 \to \epsilon)\rangle \sim \sqrt{\frac{2\pi(1-\lambda_1)}{\beta}}\exp[\beta(V_1(l) - V_1(\hat{\epsilon}_1))]\left(\frac{1}{a_1(l)} - \frac{1}{a_0(l)}\right) \tag{5.3.5}$$

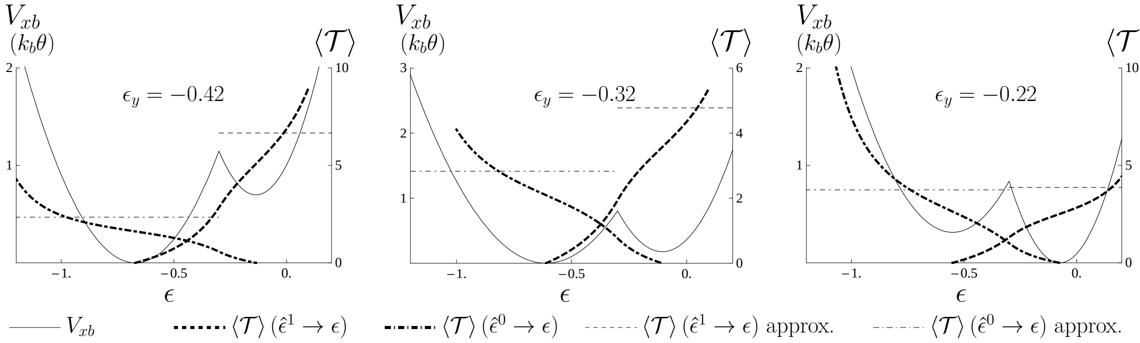

Fig. 5.2 – Mean first passage time in the double well potential represented for 3 different values of ϵ_y indicated on the graphs. $\epsilon_y = -0.32$ (middle) represents the position of the energy barrier in the potential F_y at $\overline{\epsilon} = \overline{\epsilon}_{1/2}$ (see Eq.(4.2.13)). Continuous line represents the energy landscape in unit of $k_b\theta$. Thick dotted line and dot-dashed line represent $\langle\mathcal{T}(\hat{\epsilon}_1 \to \epsilon)\rangle$ and $\langle\mathcal{T}(\hat{\epsilon}_0 \to \epsilon)\rangle$ computed with Eq.(C.1.6) in arbitrary units. The corresponding Kramers approximation obtained using Eqs.(C.1.7) and (C.1.8) are represented by thin dashed and dot-dashed lines respectively. Parameters are: $\lambda_1 = 0.4$, $\lambda_0 = 0.7$, $l = -0.3$, $\lambda_f = 0.05$, $\beta = 10$ and $N = 100$.

and

$$\langle\mathcal{T}(\hat{\epsilon}_0 \to \epsilon)\rangle \sim \sqrt{\frac{2\pi(1-\lambda_0)}{\beta}} \exp\left[\beta\left(V_0(l) - V_0(\hat{\epsilon}_0)\right)\right]\left(\frac{1}{a_1(l)} - \frac{1}{a_0(l)}\right). \tag{5.3.6}$$

One can see that, in the limit of large temperatures, the escape time increases exponentially with the energy barrier $V_1(l) - V_1(\hat{\epsilon}_1)$ (resp. $V_0(l) - V_0(\hat{\epsilon}_0)$) which is of course the classical Arrhenius formula. Note that the pre-factor also depends on β which is not the case if the energy landscape is smooth. These results revealing an exponentially distributed mean exit time have been obtained rigorously in a more general context by M.V Day in (Day, 1983).

In Fig.5.2, we show the escape times for a single cross-bridge at different values of ϵ_y ($-0.42, -0.32$ and -0.22 indicated on the figure). Here, $\epsilon_y = -0.32$ corresponds to the position of the energy barrier in the potentials F_y and G_y at $\overline{\epsilon} = \overline{\epsilon}_{1/2}$ (resp.$\overline{\sigma} = \overline{\sigma}_{1/2}$) (see Fig.4.15 and Eqs.4.2.13 and 4.2.14). The continuous line represents the energy landscape V_{xb} and the thick dashed line (resp. thick dot-dashed line) represents the mean first passage time from the left well (resp. right well) computed with the use of special functions. The energy is represented in unit of $k_b\theta$ and the time is in non dimensional units. Kramers approximation of the escape times is indicated by the thin dashed lines.

One can see for the chosen value of β ($\beta = 10$), the Kramers approximation gives a correct order of magnitude estimate for the time to jump energy barriers whose size is of the order of $\sim 1 k_b\theta$. However, the details of the behavior near the barrier are lost in this approximations. Also one case see that, as ϵ_y increases (or decreases), the energy barrier disappears and the Kramers approximation cannot be used anymore to describe the kinetics of the transition.

5.3.3 Transition rates and equilibrium of population

Next consider an ensemble of N particle $x_i(t)$ undergoing stochastic motion in the potential V. We are now interested in the characteristic time before the fraction of particles in each well reaches steady states. We then have to consider the flux of particles starting at $\hat{x}_0$ that the cross the barrier l towards $\hat{x}_1$ which we denote by k_1. This quantity corresponds to the famous transition rate functions used to describe chemical reactions. It can be shown that the escape rate r correspond to the first eigenvalue of the Fokker–Planck equation of the system (Schuss, 2010) and that it simply corresponds to the inverse of the mean escape time

$$k_1 = \frac{1}{2} \langle \mathcal{T} (\hat{x}_0 \to l) \rangle^{-1} \tag{5.3.7}$$

and similarly we have:

$$k_0 = \frac{1}{2} \langle \mathcal{T} (\hat{x}_1 \to l) \rangle^{-1} \tag{5.3.8}$$

The net flux of probability from one well to the other will be a combination of k_1 and k_0 which depend only on the initial position and the height of the barrier if $\beta \to \infty$. Also, when $\beta \to \infty$ the probability density is for all time t localized near the bottom of the wells so that the whole system can be described by the fraction of particle occupying each well. Hence, the real dynamics described by the Fokker–Planck equation can be replaced by jump dynamics ruled by a master equation. Now consider the ensemble of N particles. With the particle $x_i(t)$, we associate the following random variable

$$Y_t^i = \begin{cases} 1 & \text{if } x_i(t) < b \\ 0 & \text{if } x_i(t) \geq b \end{cases} \text{ such that } N_1(t) = \sum_{i=1}^{N} Y_t^i$$

which represents the number of particle in well 1 at time t. In steady state, the evolution of the stochastic variable Y_t^i is defined by a jump process:

$$\begin{aligned} \mathbb{P}\left(Y_{t+dt}^i = 1 - Y_t^i\right) &= k_{Y_t^i} dt, \text{ so we have} \\ \mathbb{P}\left(N_1(t+dt) = N_1(t) - 1\right) &= \binom{N_1(t)}{1} k_1 dt = N \frac{N_1(t)}{N} k_1 dt \\ \mathbb{P}\left(N_1(t+dt) = N_1(t) + 1\right) &= \binom{N - N_1(t)}{1} k_0 dt = N \frac{N - N_1(t)}{N} k_0 dt. \end{aligned}$$

Therefore, $N_1(t)$ satisfy the following master equation:

$$\frac{dN_1(t)/N}{dt} = -k_1 \frac{N_1(t)}{N} + k_0 \frac{N - N_1(t)}{N} \text{ with } N_1(t = t_0) = N_1^0 \tag{5.3.9}$$

where N_1^0 is the initial number of particles in well 1 at time t_0. Now denote by $n_1 = N_1/N$ the fraction of particles in well 1. For finite N, n_1 is a discrete variable which follows (5.3.9). It can be shown that in the limit $N \to \infty$, the discrete solution of the preceding master equation on $N_1(t)$ converges to the continuous solution of the following initial value problem on n_1 (see Kurtz, 1971, 1972, 1970):

$$\frac{dn_1(t)}{dt} = k_0 - (k_1 + k_0) n_1(t), \text{ with } n_1(t) = n_1^0$$

Finally, we see that the characteristic time of the evolution of the population in the wells, called *equilibration time* is:

$$\tau = (k_1 + k_0)^{-1} = \left(\frac{1}{2} \langle \mathcal{T} (\hat{x}_1 \to b) \rangle^{-1} + \frac{1}{2} \langle \mathcal{T} (\hat{x}_0 \to b) \rangle^{-1} \right)^{-1} \tag{5.3.10}$$

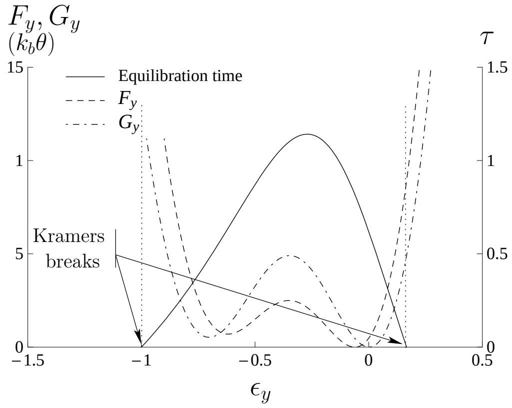

Fig. 5.3 – Equilibration time in the double well potential V_xb depending on ϵ_y. Continuous line: equilibration time in non dimensional units computed using Eq.(5.3.10). Dashed line (resp. dot dashed line): reduced free energy landscape F_y (resp. G_y) in unit of $\kappa_b\theta$. The dotted line delimits the domain where V_{xb} has 2 minima. Beyond those limits, there is no energy barrier and therefore Kramers approximation is no more valid. The equilibration time in V_{xb} is maximum for values of ϵ_y corresponding to the higher energy level in F_y and G_y. Then the equilibration time decreases exponentially to 0 where the double well structure of V_{xb} is lost. Parameters are the same as on Fig.5.2

5.3.4 Microscopic and macroscopic time scales

We show on Fig.5.3, the equilibration time τ (in arbitrary units), inside the double well potential V_{xb} depending on the value of ϵ_y. This computation tells us how fast, cross-bridge elongation of the bundle, a single cross-bridge will equilibrate between its two conformations. Note that the results we present here are valid only in the limit $\beta \to \infty$.

The dashed and dot-dashed lines represents the energy profiles F_y and G_y respectively for $\bar{\epsilon} = \bar{\epsilon}_{1/2}$ and $\bar{\sigma} = \bar{\sigma}_{1/2}$. Thus we can see the probability of a particular ϵ_y together with the equilibration time in the corresponding double-well potential. The dotted lines delimit the interval of ϵ_y where V_{xb} has 2 minima. Beyond those limits, there is no energy barrier and therefore Kramers approximation is no more valid. The equilibration time is maximum (~ 1.5) when $\epsilon_y \approx -0.32$. This value corresponds to the point where, in equilibrium, half of the population is in well 1 (see Fig.5.2, middle). Then, the equilibration time decays to 0 at the point points where the double well structure of V_{xb} is lost (indicated by the vertical dotted lines and the arrows). We see that the lower equilibration times are found near the most probable values of ϵ_y located in the bottom of the macro-wells. Beyond those values of ϵ_y the double well structure is lost and therefore Kramers approximation of the escape times cannot be used. This result shows that a description of the kinetics of the system in terms of chemical reactions implicitly assuming the validity of Kramers approximation, is valid only on a finite interval of the internal parameters.

The other time scale of interest is the equilibration time for the macroscopic wells at different values of the loading. We compute this time scale using Eq.(5.3.10), in the limit $\beta \to \infty$ as long as the 2 wells are present in F_y and G_y. Fig.5.4 shows the equilibration time between the macroscopic wells in hard (continuous line) and soft devices (dashed line) for $\beta = 10$ (A) and $\beta = 20$ (B). We have represented the equilibration time in soft device as a function of $\delta L_2 = L_2\left(\bar{\sigma}\right) - L_2\left(\bar{\sigma}_{1/2}\right)$, instead of $\bar{\sigma}$. This allows us to compare the characteristic times in hard and soft devices at the same level of elongation.

In both hard and soft devices, the equilibration time for the macroscopic wells is larger than the equilibration time for the case of a single cross-bridge at fixed ϵ_y. This effect is strongly amplified by increasing β (compare Fig.5.4 A and B). This is simply due to the

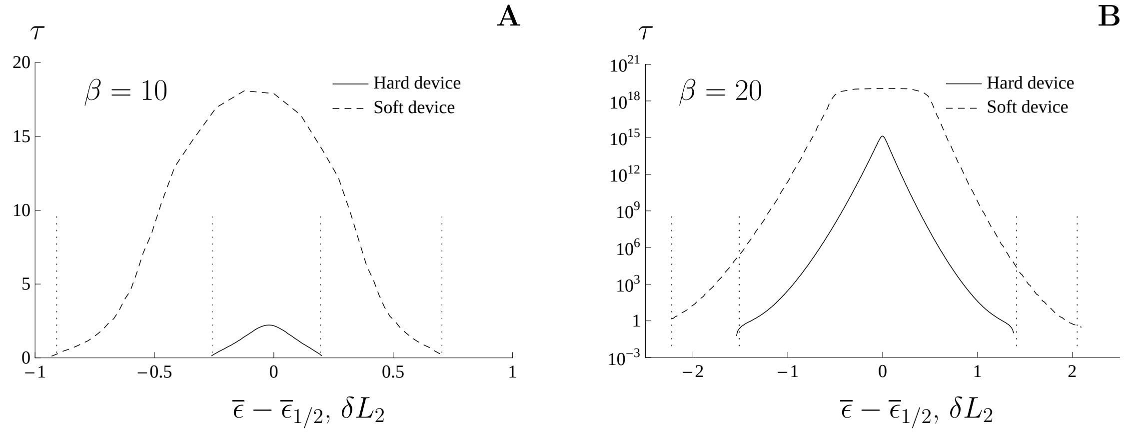

Fig. 5.4 – Equilibration time in F_y and G_y energy landscapes. (**A**): $\beta = 10$. (**B**): $\beta = 20$. For the hard device case (continuous line), the equilibration time in F_y is represented against the step size from the middle of the transition ($\overline{\epsilon} - \overline{\epsilon}_{1/2}$). In soft device (dashed line), the equilibration time is plotted against $\delta L_2 = L_2(\overline{\sigma}) - L_2(\overline{\sigma}_{1/2})$, instead of $\overline{\sigma}$. This allows to compare the characteristic times taken to reach the same final elongation. The vertical dotted lines indicate the interval where F_y and G_y present two macroscopic wells, which indicate slower kinetics. We observe a plateau on the soft device equilibration time curve at $\beta = 20$ (**B**, dashed line). The concerned range of elongations corresponds to the plateau of the $L_2 vs\ \overline{\sigma}$ curve, and thus to the same tension $\overline{\sigma} = \overline{\sigma}_{1/2}$; hence the equilibration rates are the same. The equilibration time between macroscopic wells is much higher than the equilibration time in V_{xb} (compare with Fig.5.3). In addition the equilibration time is higher in soft device than in hard device and so is the interval of slower kinetics. Parameters are the same as on Fig.5.2

fact that the transition between the macroscopic wells requires a collective configuration switch of the cross-bridges. Indeed, as we already discussed in Sec.4.5, the left macroscopic well correspond to a preferred post-power-stroke conformation and the right macroscopic well corresponds to a preferred pre-power-stroke. The fact that the transition between macroscopic wells requires simultaneous transitions in of all the cross-bridges increases the free energy barriers and thus the equilibration time.

We observe an interesting plateau in the case of the soft device at $\beta = 20$ (see Fig.5.4B, dashed line). The concerned range of elongation values corresponds to the plateau of the L_2 curve, and thus the tension along this plateau remains constant: $\overline{\sigma} = \overline{\sigma}_{1/2}$. The equilibration time is considerably higher in soft device (dashed line) than in hard device (continuous line) as a consequence of the higher energy barrier in G_y.

In addition, the domain with two macroscopic wells (materialized by vertical dotted lines on Fig.5.4) is larger in soft device than in hard device. Again beyond these limits, the energy barrier disappears and Kramers approximation can no longer be used.

To summarize, in both hard and soft devices, the response of the system will be slow if the loading is such that the double well structures of F_y and G_y are preserved, compared to larger load changes where potentials have single-well structure. Moreover, this interval of *slow kinetics* is larger in soft device than in hard device.

In the next section, we use stochastic dynamics to investigate in details the kinetics of the quick recovery without approximations.

5.4 Stochastic response to length and load steps

5.4.1 Langevin's equations

To model the actual time dependent behavior of the system we need to study its stochastic dynamics in the full configurational space of the variables $\epsilon_i, \epsilon_y, \epsilon_z$. We recall that the cross-bridges are under the influence of several forces:

- dissipative drag force due to internal kinetics of the conformational change and the interaction with the surrounding media. We model it as a viscous force proportional to the velocity of a cross-bridge:

$$f_i^v = -\eta \dot{x}_i = -\eta \dot{\epsilon}_i \tag{5.4.1}$$

- constant thermal agitation modeled as non correlated random forces which verifies the following fluctuation dissipation relations

$$f_i^\theta = \sqrt{2\eta\kappa_b\theta}\,\Gamma_i\left(t\right) \text{ with } \left\langle \Gamma\left(t\right)\right\rangle = 0 \text{ and } \left\langle \Gamma_i\left(t\right)\Gamma_i\left(t'\right)\right\rangle = \delta\left(t-t'\right), \tag{5.4.2}$$

δ denotes here the Dirac's distribution.

For simplicity, we assume that the dynamics of the variables ϵ_y and ϵ_z can be associated with the same viscosity η and the same noise intensity $\sqrt{2\eta\kappa_b\theta}$. We will reconsider this hypothesis in the next in Sec.7.4.2. We denote by $\tau = \frac{\eta}{\kappa}$. τ the characteristic time and write the non dimensional time as $\overline{t} = t/\tau$. In hard device, we consider the following system of overdamped Langevin's equations:

$$\begin{cases} \dot{\epsilon}_i\left(t\right) & = \partial_{\epsilon_i} V\left(\epsilon_i^t\right) + \epsilon_y^t - \epsilon_i^t + \sqrt{2\beta^{-1}}\Gamma\left(t\right) \quad \text{for } 1 \le i \le N \\ \dot{\epsilon}_y\left(t\right) & = N\left(-\left(1+\lambda_f\right)\epsilon_y^t + \lambda_f \overline{\epsilon}\left(t\right) + \frac{1}{N}\sum\limits_{i=1}^{N}\epsilon_i^t\right) + \sqrt{2\beta^{-1}}\Gamma_y\left(t\right) \end{cases}$$

which we rewrite as a set of stochastic differential equations (SDE):

$$\begin{cases} d\epsilon_i^t = \left(\partial_{\epsilon_i} V\left(\epsilon_i^t\right) + \epsilon_y^t - \epsilon_i^t\right)dt + \sqrt{2\beta^{-1}}dB_i^t \quad \text{for } 1 \le i \le N & \text{(5.4.3a)} \\ d\epsilon_y^t = N\left(-\left(1+\lambda_f\right)\epsilon_y^t + \lambda_f\overline{\epsilon}\left(t\right) + \dfrac{1}{N}\displaystyle\sum_{i=1}^{N}\epsilon_i^t\right)dt + \sqrt{2\beta^{-1}}dB_y^t. & \text{(5.4.3b)} \end{cases}$$

Similarly in soft device we obtain:

$$\begin{cases} d\epsilon_i^t = \left(\partial_{\epsilon_i} V\left(\epsilon_i^t\right) + \epsilon_y^t - \epsilon_i^t\right)dt + \sqrt{2\beta^{-1}}dB_i^t \quad \text{for } 1 \le i \le N & \text{(5.4.4a)} \\ d\epsilon_y^t = N\left(-\epsilon_y^t + \dfrac{\overline{\sigma}\left(t\right)}{N} + \dfrac{1}{N}\displaystyle\sum_{i=1}^{N}\epsilon_i^t\right)dt + \sqrt{2\beta^{-1}}dB_y^t & \text{(5.4.4b)} \\ d\epsilon_z^t = N\left(\dfrac{\overline{\sigma}\left(t\right)}{N} - \lambda_f\left(\epsilon - \epsilon_y\right)\right)dt + \sqrt{2\beta^{-1}}dB^t. & \text{(5.4.4c)} \end{cases}$$

Here dB_i^t is the increment of a Wiener process, with zero mean and variance dt. We compute the time response of the system to a ramp loading by solving equations (5.4.3) and (5.4.4) numerically.

5.4.2 Simulation of the quick recovery

In the following, the parameters are: $\lambda_1 = 0.4$, $\lambda_0 = 0.7$, $l = -0.3$, $\beta = 10$ and $N = 100$ and we study 2 cases: $\lambda_f = 0.05$ where F_y presents macroscopic wells (see Figs.4.12 and 4.13) and $\lambda_f = 1$ where F_y in convex. The numerical parameters used for these simulations are: $N_r = 1000$ and $\Delta t = 10^{-3}$. The duration of the step is 0.1. In the the following plots, we will represent the 95% confidence interval computed with a non-biased estimate of the variance.

Initial conditions

The initial state of our system is defined as the state of thermal equilibrium at $\overline{\epsilon} = \overline{\epsilon}_{1/2}$ in hard device and $\overline{\sigma} = \overline{\sigma}_{1/2}$ in soft device. For the chosen set of parameters, in the initial state, the reduced free energies F_y and G_y present 2 macroscopic wells with a large equilibration time between the wells (see Fig.5.4). To avoid time consuming simulations, it is natural to chose initial distribution close to the thermal equilibrium one. We denote l_y^h (resp. l_y^s) the value of ϵ_y for which F_y (resp. G_y) reaches its maximal value between the macroscopic wells. We define:

$$n_y^h(\overline{\epsilon}, \beta) = \frac{1}{\mathcal{Z}_h(\overline{\epsilon}, \beta)} \int_{-\infty}^{l_y^h} \exp\left[-\beta F_y(\epsilon_y, \beta, \overline{\epsilon})\right] d\epsilon_y \tag{5.4.5}$$

$$n_y^s(\overline{\sigma}, \beta) = \frac{1}{\mathcal{Z}_s(\overline{\sigma}, \beta)} \int_{-\infty}^{l_y^s} \exp\left[-\beta G_y(\epsilon_y, \beta, \overline{\sigma})\right] d\epsilon_y \tag{5.4.6}$$

the cross-bridges populations in the left macroscopic well in hard and soft device respectively. We denote by $n_y^{h,0} = n_y^h\left(\overline{\epsilon}_{1/2}, \beta\right)$ and $n_y^{s,0} = n_y^s\left(\overline{\sigma}_{1/2}, \beta\right)$, the initial populations. In each macroscopic wells, the probability density is localized near the minimum (see Figs.4.12 and 4.13), and the time to reach the steady state density locally is much smaller than the time to equilibrate between the wells. Therefore we have to ensure only that our initial condition have the correct partition of populations between the 2 macroscopic wells. This is achieved by simply choosing a fraction $n_y^{h,0}$ (resp. $n_y^{s,0}$) of our N_r realizations at the bottom of the left macroscopic well. For this set of realizations, we have in hard device: $\epsilon_y(t = 0) = \underset{\epsilon_y < l_y^h}{\operatorname{argmin}}\left(F_y(\epsilon_y)\right)$, and similarly in soft device . The remaining realizations are chosen at the bottom of the right macroscopic well.

Now, for a given realization, the initial value of ϵ_y is known and so the initial fraction $\langle n_1 \rangle^0 (\epsilon_y)$ of post-power-stroke cross-bridges is known (see Figs.4.12 and 4.13). Hence for each realization a fraction $\langle n_1 \rangle^0 (\epsilon_y)$ of the N cross-bridges are chosen to be at the bottom of well 1 and the rest at the bottom of well 0. Finally, in soft device, the value of ϵ_z is initialized so that $\overline{\sigma}_{1/2} = N\lambda_f (\epsilon_z - \epsilon_y)$ in each realization.

To further illustrate the initial configuration of the system, it is instructive to follow the motion of only two internal degrees of freedom (ϵ_1, ϵ_y) where ϵ_1 represents the configuration of an arbitrary cross-bridge. When the system is at equilibrium, these variables evolve in a free energy landscape obtained by equilibrating the system with respect to the other

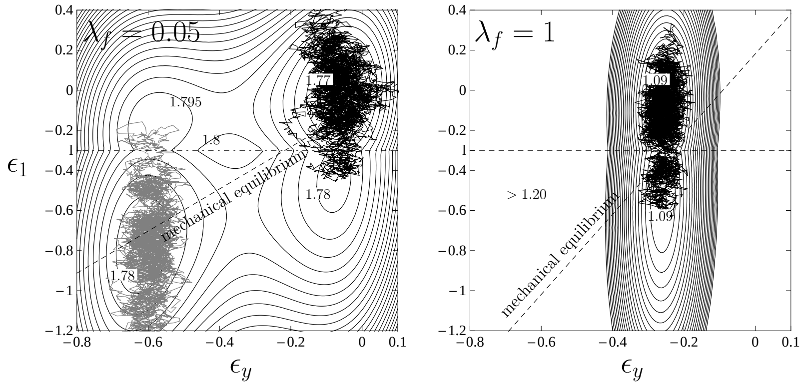

Fig. 5.5 – Representation of 2 independent trajectories (duration 5) of randomly chosen cross-bridges initiated in each macro-well of the equilibrium energy landscape F_{1y} (see Eq.5.4.8) with $\overline{\epsilon} = \overline{\epsilon}_{1/2}$. The parameters are the same as in Figs.4.12 and 4.13 with $\lambda_f = 0.05$ (left) and $\lambda_f = 1$ (right). The dashed line represent the mechanical equilibrium relation: $\epsilon_1 = (1 + \lambda_f)\,\epsilon_y + \lambda_f \overline{\epsilon}_{1/2}$. The dot-dashed line represents the limit between the 2 wells in v.Energy at the bottom of the wells and at the energy barrier is indicated in units of $k_b\theta$on each plots and the energy increment between two consecutive lines is equal to $0.5\kappa_b\theta$. Parameters are: $\lambda_1 = 0.4$, $\lambda_0 = 0.7$, $l = -0.3$, $N = 100$, $\beta = 10$

internal variables $\epsilon_2, \ldots, \epsilon_N$. More precisely, in the case of hard device we obtain

$$\begin{aligned} p\left(\epsilon_1, \epsilon_y | \overline{\epsilon}, \beta\right) &= \frac{1}{\mathcal{Z}_h\left(\overline{\epsilon}, \beta\right)} \int_{\mathbb{R}} \cdots \int_{\mathbb{R}} e^{-\beta V\left(\epsilon_1, \ldots, \epsilon_N, \epsilon_y, \overline{\epsilon}\right)} d\epsilon_2 \ldots d\epsilon_N \\ &= \frac{1}{\mathcal{Z}_h\left(\overline{\epsilon}, \beta\right)} \exp\left(-\beta F_{1y}\left(\epsilon_1, \epsilon_y, \overline{\epsilon}, \beta\right)\right) \end{aligned} \tag{5.4.7}$$

$$\begin{aligned} \text{where} \quad F_{1y}\left(\epsilon_1, \epsilon_y, \overline{\epsilon}, \beta\right) &= v\left(\epsilon_1\right) + \frac{1}{2}\left(\epsilon_y - \epsilon_1\right)^2 + \frac{1}{2} N \lambda_f \left(\overline{\epsilon} - \epsilon_y\right)^2 \\ &\quad - \frac{1}{\beta}(N-1) \ln\left(\mathcal{Z}_1\left(\epsilon_y, \beta\right) + \mathcal{Z}_0\left(\epsilon_y, \beta\right)\right) \end{aligned} \tag{5.4.8}$$

Similarly in the case of soft device, we obtain the expression for the Gibbs partially equilibrated free energy in the form

$$\begin{aligned} G_{1y}\left(\epsilon_1, \epsilon_y, \overline{\sigma}, \beta\right) &= v\left(\epsilon_1\right) + \frac{1}{2}\left(\epsilon_y - \epsilon_1\right)^2 - \frac{1}{2} \frac{\overline{\sigma}^2}{N \lambda_f} - \overline{\sigma} \epsilon_y \\ &\quad - \frac{1}{\beta}(N-1) \ln\left(\mathcal{Z}_1\left(\epsilon_y, \beta\right) + \mathcal{Z}_0\left(\epsilon_y, \beta\right)\right) \end{aligned} \tag{5.4.9}$$

Note that our previously introduced free energies F_y and G_y are obtained by integration of F_{1y} and G_{1y} over ϵ_1.

In Fig.5.5 and 5.6 (with $\overline{\epsilon} = \overline{\epsilon}_{1/2}$ in hard device and $\overline{\sigma} = \overline{\sigma}_{1/2}$ in soft device), we show the trajectories of 2 selected independent realizations in the plane (ϵ_1, ϵ_y) at $\overline{\epsilon} = \overline{\epsilon}_{1/2}$ and $\overline{\sigma} = \overline{\sigma}_{1/2}$, each one initiated in a different macro-well. The time goes from 0 to 5 (5000 steps). The contours represent the free energy levels expressed in unit of $k_b\theta$; the energy difference between 2 consecutive isolines is $5.10^{-3} k_b\theta$.

We observe once again that the response of the system in soft device does not depend on the value of λ_f (see Fig. 5.6). We also notice that no jumps occurs between the macro-wells (we tested it on a period of 300 arbitrary units with $\beta = 10$). For low values of λ_f (see Fig. 5.5A), the cross-bridges spend most of the time in one conformational state. The configuration is close to the equilibrium line (dashed, marked 'mechanical equilibrium'),

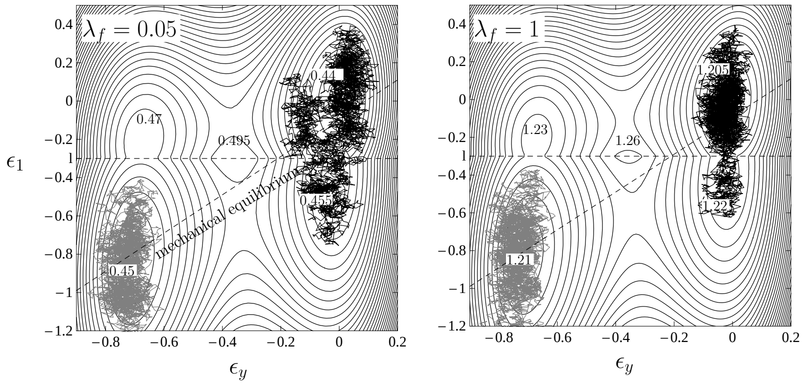

Fig. 5.6 – Representation of 2 independent trajectories (duration 5) of randomly chosen cross-bridges initiated in each macro-well of the equilibrium energy landscape G_{1y} (Eq.5.4.9) with $\overline{\epsilon} = \overline{\epsilon}_{1/2}$. The parameters are the same as in Figs.4.12 and 4.13 with $\lambda_f = 0.05$ (left) and $\lambda_f = 1$ (right). The dashed line represent the mechanical equilibrium relation: $\epsilon_1 = (1 + \lambda_f)\,\epsilon_y + \lambda_f \overline{\epsilon}_{1/2}$. The dot-dashed line represents the limit between the 2 wells in v.Energy at the bottom of the wells and at the energy barrier is indicated in units of $k_b\theta$on each plots and the energy increment between two consecutive lines is equal to $0.5\kappa_b\theta$. Parameters are: $\lambda_1 = 0.4$, $\lambda_0 = 0.7$, $l = -0.3$, $N = 100$, $\beta = 10$

representing the mechanical equilibrium of the filament with (see Eq. 3.1.5):

$$\epsilon_y = \frac{1}{1+\lambda_f}\left(\lambda_f \overline{\epsilon} + \langle \epsilon_1 \rangle\right) \text{ in hard device} \tag{5.4.10}$$

$$\epsilon_y = \langle \epsilon_1 \rangle + \frac{\overline{\sigma}}{N} \text{ in soft device} \tag{5.4.11}$$

These observations emphasize the effect of the mean field interaction between the cross-bridges. It creates macroscopic wells in which the system can be ‘kinetically trapped’. Indeed, when macroscopic wells are present, the equilibration time in the reduced free energy landscape F_y and G_y is large and depends exponentially on temperature (see Fig.5.4) even if the energy barrier in F_y and G_y is only a few $k_b\theta$ high (see Figs.4.12 and 4.13). In a 2D energy landscape, a realization initialized in one macroscopic well does not jump to the other one (in physically observable times). The presence of elastic filaments implies that on the full energy landscape (which depends on all degrees of freedom), the the cross-bridges are strongly confined in a domain where they mostly adopt the post-power-stroke or pre-power-stroke conformation, and going from one domain to the other requires a ‘massive’ collective stroke (or reverse stroke) which is an event with very low probability.

Quick recovery in hard device

Fig.5.7 shows the time evolution of the relative tension T/T_0 in response to a ramp loading where, T_0 is the isothermal tension at $\overline{\epsilon} = \overline{\epsilon}_{1/2}$. The time origin is set at the end of the step (this is for graph clarity as only few points are computed before the step). We presented the tension response to 4 different step sizes, 2 in stretching and 2 in shortening (+0.6, +0.1, −0.1, and −0.6 nm) with 2 different values of λ_f: $\lambda_f = 0.05$ (Fig.5.7A) and $\lambda_f = 1$ (Fig.5.7B). In the former case, the reduced free energy landscape exhibits 2 macroscopic wells while it is always convex in the latter case. We represented with thin lines the 95% confidence interval (computed using a non biased estimate of the variance).

On the one hand, for the lower step sizes ($\delta = 0.1$ and $\delta = -0.1$) on Fig.5.7(A), the (final) free energy landscape F_y still has a double well structure (see Fig.5.4A, $\overline{\epsilon} - \overline{\epsilon}_{1/2} = \pm 0.1$ is between the dotted vertical lines). As a consequence, the recovery is much slower

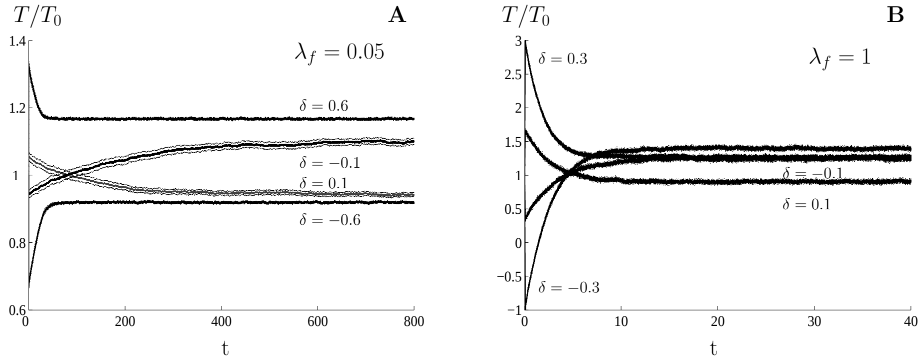

Fig. 5.7 – **Evolution of the mean tension in time** (1000 independent realizations) after length step of various amplitudes ($\delta = 0.6, 0.1, -0.1$ and -0.6; indicated on the figure) form the middle of the transition ($\overline{\epsilon} = \overline{\epsilon}_{1/2}$) where $T = T_0$. The 0 time corresponds to the end of the step. The thin lines denotes the 95% confidence interval. The parameters are the same as in figure 5.2($\lambda_1 = 0.4$, $\lambda_0 = 0.7$, $l = -0.3$, $\beta = 10$ and $N = 100$) with $\lambda_f = 0.05$ (**A**) and $\lambda_f = 1$ (**B**). In (**A**, the double well structure of F_y is preserved for the steps $\delta = \pm 0.1$. As a results the kinetic of the response is slow and the system barely reaches equilibrium after 800 units of time. When $\lambda_f = 1$ (**B**), the kinetics are independent from the step size and the system has reached steady state after ~ 15 units of time. Parameters are: $\lambda_1 = 0.4$, $\lambda_0 = 0.7$, $l = -0.3$, $N = 100$, $\beta = 10$.

than for larger step sizes ($\delta = \pm 0.6$ on Fig.5.7A) and barely attains the steady state at the end of the 800 units of time long experiment.

On the other hand, Fig.5.7B shows that in the case $\lambda_f = 1$ (no macroscopic wells), the recovery rate is the same are the same independently of the step size. The responses to both large ($\delta = \pm 0.3$) and small ($\delta = \pm 0.1$) step amplitudes, are faster than in the case $\lambda_f = 0.05$ (note the different time scaling), which of course results from the absence of macroscopic wells in F_y.

Notice also that the confidence interval is larger for low step amplitudes than for large step amplitude (see Fig.5.7). The mean values of the tension represented on Fig.5.7 are obtained from $\langle \epsilon_y \rangle$ (see Eq.4.2.15) and is computed by summing the contributions of both macroscopic wells each having their own dispersion. This leads to the increase in the global variance.

The tension levels reached at the end of the simulation (after 800 units of time for the case $\lambda_f = 0.05$, and 40 units of time for the case $\lambda_f = 1$), are reported on Fig.5.8 (□, with bars indicating the 95% confidence interval) together with the equilibrium isotherm (line). In both cases, $\lambda_f = 0.05$ (Fig.5.8A) and $\lambda_f = 1$ (Fig.5.8B) the tensions attained at the end of the simulation match the isothermal values computed with Eq.(4.2.15). The higher confidence interval of the case $\lambda_f = 1$ (see Fig.5.8B), is a direct consequence of the higher stiffness which multiplies the variance on ϵ_y.

Quick recovery in soft device

In the case of soft device, we consider a system initially at $\overline{\sigma}_{1/2}$. It undergoes a load step of duration 0.1 units of time, to a tension $\alpha\overline{\sigma}_{1/2}$ with $0 < \alpha < 1.6$. The change in elongation $\delta L_2 = L_2(\overline{\sigma}) - L_2(\overline{\sigma}_{1/2})$ is represented on Fig.5.9 for 2 different filament stiffnesses: $\lambda_f = 0.05$ (Fig.5.9A) and $\lambda_f = 1$ (Fig.5.9B). As in hard device, we represented the elongation traces for 4 different step sizes ($\overline{\sigma}/\overline{\sigma}_{1/2} = \pm 1.2$ and $\overline{\sigma}/\overline{\sigma}_{1/2} = \pm 1.05$); the lower step sizes correspond to the cases where G_y has a double well structure. Note that, in order to compare the kinetics in hard and soft devices, the step sizes are chosen in such a way that the final elongations δL_2 correspond to the length step sizes applied in hard

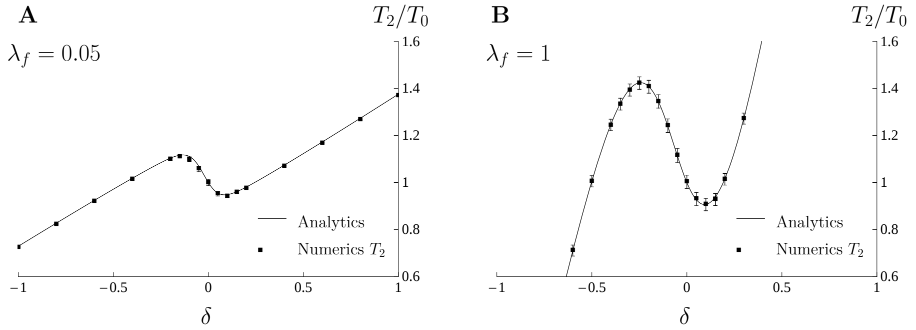

Fig. 5.8 – **Thermal equilibrium tension**. Comparison between the tension obtained after 800 units of time (**A** with $\lambda_f = 0.05$) or 40 units of time (**B** with $\lambda_f = 1$) of stochastic simulations (□) with analytic computation of the isotherm (continuous line, from Eq.4.2.15). The error bars indicate the 95%confidence interval (1000 independent realizations). The isotherm obtained using stochastic simulation matches the analytic computations. The higher confidence interval of the case $\lambda_f = 1$ (**B**), is a direct consequence of the higher stiffness that multiplies the variance on ϵ_y Other Parameters are the same as on Fig.5.2($\lambda_1 = 0.4$, $\lambda_0 = 0.7$, $l = -0.3$, $\beta = 10$ and $N = 100$. Parameters are: $\lambda_1 = 0.4$, $\lambda_0 = 0.7$, $l = -0.3$, $N = 100$, $\beta = 10$)

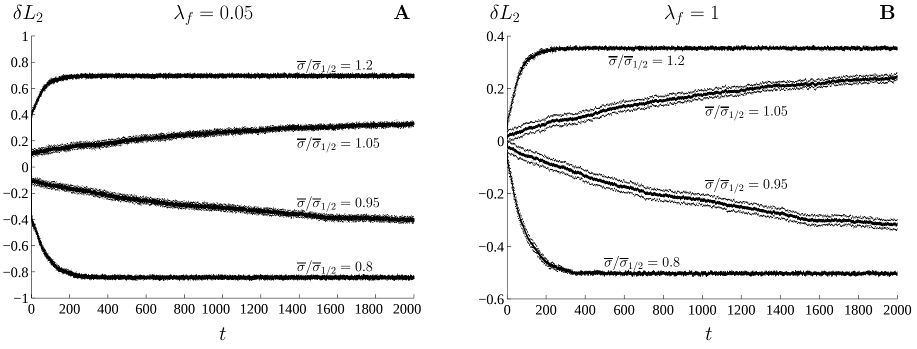

Fig. 5.9 – **Evolution of $\delta L_2 = L_2 - L_2\left(\overline{\sigma}_{1/2}\right)$ with time** obtained with stochastic simulations (1000 independent realizations). Thick lines: mean trajectories. Thin lines: 95% confidence interval. The origin of time is set to the end of the load step. We see that some trajectories has not reached their equilibrium state even after 2000 units of time. This confirms that soft device transients are slower than hard device transients. The parameters are the same as in figure 5.2($\lambda_1 = 0.4$, $\lambda_0 = 0.7$, $l = -0.3$, $\beta = 10$ and $N = 100$), with $\lambda_f = 0.05$ (**A**) and $\lambda_f = 1$ (**B**).

device.

In the case $\overline{\sigma}/\overline{\sigma}_{1/2} = \pm 1.05$, it is only after 2000 units of time, that the elongation reaches a steady state value and this remains true for both filament stiffnesses (Fig.5.9 A and B). This is in agreement with the much higher equilibration time, than in the case of hard device, computed in the previous section (see Fig.5.4).The values attained after 2000 units of time are close to the isotherm computed using Eq.(4.2.17) (see Fig.5.10).

The results of our stochastic simulations are therefore confirming our previous observations:

- the kinetic response of the system in soft device is not affected by the filament elasticity λ_f (see Fig.5.9), while in hard device, for high values of λ_f, the double well structure of F_y is lost and the quick recovery is accelerated with respect to lower values of λ_f (see Fig.5.7)
- For a comparable final point on the isothermal tension *vs.* elongation curve, the soft device response to a load step is slower than the hard device response (compare Fig.5.9 with 5.7). This strengthens the conclusions obtained on the study of the

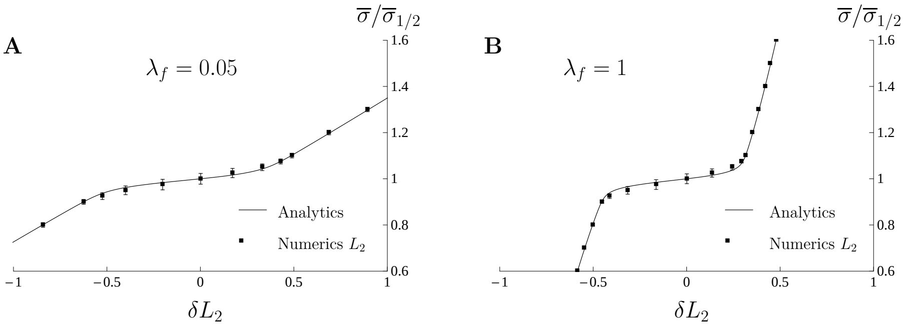

Fig. 5.10 – Thermal equilibrium change in elongation ($\delta L_2 = L_2 - L_2(\overline{\sigma}_{1/2})$) obtained using analytic computations (line) compared to tension obtained after 2000 units of time using stochastic computation (squares, 1000 independent realizations). (**A**): $\lambda_f = 0.05$. (**B**): $\lambda_f = 1$. Error bars indicate the 95% confidence interval.The parameters are the same as in figure 5.2($\lambda_1 = 0.4$, $\lambda_0 = 0.7$, $l = -0.3$, $\beta = 10$ and $N = 100$).

energy barriers and the equilibration time scales in the reduced energy landscapes F_y and G_y.

Conclusions

Our main conclusion is that the presence of macroscopic energy wells in the reduced energy landscape leads to kinetics dominated response when the system undergoes a load change.

Furthermore, we showed that the range where the chemical description of the system can be used (Kramers approximation), is limited to the domain of parameters where macroscopic wells exist. Beyond the limits of this interval, ‘chemical states’ cannot be defined and Kramers approximation breaks.

Unlike the case of the soft device, the kinetics in hard device is directly linked to the amplitude of the coupling parameter. Thus, at low λ_f the quick force recovery is slow which is coherent with the presence of a double well non-equilibrium energy landscape. Instead at high λ_f, a single well energy landscape favors much faster recovery. It must be noted that the double well structure of the non-equilibrium energy landscape always disappear at large loadings hence faster kinetics in comparison to small loadings. In addition, the speed of the recovery is always slower in the soft device than in the hard device.

Chapter 6

Equivalent model of a half-sarcomere

The computations in the last section are quite costly in terms of computer time as they require the simulation of the trajectories of $N+1$ stochastic variables. To deal with many half-sarcomeres in series, one can't afford to have such a detailed description of each half-sarcomere. Here, we attempt to develop a reduced model capturing only the most important aspects of the dynamics of our system.

Contents

6.1 Homogenization of stochastic systems

6.1.1 Preliminary examples

The goal of *model reduction*, is to describe the behavior of many (microscopic) degrees of freedom by following only few (macroscopic) degrees of freedom. It may happen that the number of the required microscopic degrees of freedom is still 'large'. The reduction works when there exist a separation of time scales which allows one to eliminate the fast variable by considering only their equilibrium values.

As an example, where such reduction is has been used successfully, we can mention chemical kinetics. There, the goal is to describe the evolution of different species in a solution where several (many) reactions occurs transforming some species into others. This system can have a large number of degrees of freedom if one considers all the species in solution.

One typical approach (see *e.g.* Gorban and Karlin, 2004) is to assume that several species are in *quasi-equilibrium*, so that we can divide the phase space of concentration, into orthogonal sub-manifolds characterizing slow and fast species. The definition of a projector for the full system is necessary to transform the vector field in the space of concentration into the vector field on the quasi equilibrium manifold. As a consequence of this decomposition, the knowledge of reaction rate constants of 'fast' reactions is not required and the dynamics on the quasi-equilibrium manifold is defined as the quasi equilibrium projection of the 'slow sub-system' of the full system of kinetic equations.

In Chap.5, we already encounter a case of model reduction when we dealt with first passage dynamics and assumed partial equilibration of population in a double well potential (see Sec.C.2). There, following Kramers (1940), we assumed that the time required to equilibrate in each of the wells was negligible compared to the escape time. In this way, we could reduce the stochastic motion of the system in the energy landscape to a jump.

Another type of reduction is based on the assuming that the number of particle is large. Then the stochastic dimension of the dynamics disappears through averaging and at the macro-scale, the process is described by a deterministic system.

6.1.2 Adiabatic elimination of ϵ_y

In Chap.5, we saw that the dynamics of a half sarcomere can be modeled by the following set of SDE (non-dimensional time):

$$\begin{cases} d\epsilon_i^t = \dfrac{1}{\eta} b\left(\epsilon_i, \epsilon_y\right) dt + \sqrt{2\beta^{-1}} dB_i^t \quad \text{for } 1 \leq i \leq N & \text{(5.4.3a)} \\ d\epsilon_y^t = \dfrac{1}{\eta_y} b_y^h\left(\epsilon_1, \ldots, \epsilon_N, \overline{\epsilon}, t\right) dt + \sqrt{2\beta_y^{-1}} dB_y^t, & \text{(5.4.3b)} \end{cases}$$

where $\beta = \frac{\eta}{k_b \theta}$ and $\beta_y = \frac{\eta_y}{k_b \theta}$. These expressions result from the fluctuation-dissipation theorem. The drift forces are given by:

$$b\left(\epsilon_i, \epsilon_y\right) = -\partial_{\epsilon_i} v\left(\epsilon_i^t\right) + \epsilon_y^t - \epsilon_i^t \tag{6.1.2}$$

$$b_y^h\left(\epsilon_1, \ldots, \epsilon_N, \overline{\epsilon}\right) = N\left(-\left(1 + \lambda_f\right)\epsilon_y^t + \lambda_f \overline{\epsilon}\left(t\right) + \frac{1}{N}\sum_{i=1}^{N} \epsilon_i^t\right) \tag{6.1.3}$$

Similarly in the soft device:

$$\begin{cases} d\epsilon_i^t = \dfrac{1}{\eta} b\left(\epsilon_i, \epsilon_y\right) dt + \sqrt{2\beta_i^{-1}} dB_i^t \quad \text{for } 1 \leq i \leq N & \text{(5.4.4a)} \\ d\epsilon_y^t = \dfrac{1}{\eta_y} b_y^s\left(\epsilon_1, \ldots, \epsilon_N, \overline{\sigma}\right) dt + \sqrt{2\beta_y^{-1}} dB_y^t & \text{(5.4.4b)} \\ d\epsilon_z^t = \dfrac{1}{\eta_z} b_z^s\left(\epsilon_z, \epsilon_y, \overline{\sigma}\right) dt + \sqrt{2\beta_z^{-1}} dB^t & \text{(5.4.4c)} \end{cases}$$

where $\beta_z = \frac{\eta_z}{k_b \theta}$ and

$$b_y^s\left(\epsilon_1, \ldots, \epsilon_N, \overline{\sigma}\right) = N\left(-\epsilon_y^t + \frac{\overline{\sigma}(t)}{N} + \frac{1}{N}\sum_{i=1}^{N} \epsilon_i^t\right) \tag{6.1.5}$$

$$b_z^s\left(\epsilon_z, \epsilon_y, \overline{\sigma}\right) = N\left(\frac{\overline{\sigma}(t)}{N} - \lambda_f\left(\epsilon_z - \epsilon_y\right)\right) \tag{6.1.6}$$

These equations were written assuming that the drag coefficients associated with different variable are of the same scale. Hence the intensity of the thermal fluctuations is the same in all SDEs. Noticed also that in Eqs.(5.4.4b) and (5.4.4c), the drift coefficients are proportional to N. Thus, when N is large, the thermal fluctuations becomes negligible compared to the drift in these equations. This means that the motion of the variables ϵ_y and ϵ_z is nearly determinist. Furthermore, we have shown in Sec.7.1 that the drag coefficients η_y and η_z associated with variables ϵ_y and ϵ_z respectively are negligible compared to the drag coefficient η which we associate with variables ϵ_i.

We begin with rewriting the systems (6.1.1) and (6.1.4) in the following non-dimensional form:

$$\begin{cases} d\epsilon_i^t = b\left(\epsilon_i, \epsilon_y\right) dt + \sqrt{2\beta^{-1}} dB_i^t \quad \text{for } 1 \leq i \leq N & \text{(6.1.7a)} \\ d\epsilon_y^t = \dfrac{1}{\gamma_y} b_y^h\left(\epsilon_1, \ldots, \epsilon_N, \overline{\epsilon}\right) dt + \sqrt{2\beta^{-1}\dfrac{1}{\gamma_y}} dB_y^t & \text{(6.1.7b)} \end{cases}$$

and

$$\begin{cases} d\epsilon_i^t = b\left(\epsilon_i, \epsilon_y\right) dt + \sqrt{2\beta^{-1}} dB_i^t \quad \text{for } 1 \leq i \leq N & \text{(6.1.8a)} \\ d\epsilon_y^t = \dfrac{1}{\gamma_y} b_y^s\left(\epsilon_1, \ldots, \epsilon_N, \overline{\sigma}\right) dt + \sqrt{2\beta^{-1}\dfrac{1}{\gamma_y}} dB_y^t & \text{(6.1.8b)} \\ d\epsilon_z^t = \dfrac{1}{\gamma_z} b_z^s\left(\epsilon_z, \epsilon_y, \overline{\sigma}\right) dt + \sqrt{2\beta^{-1}\dfrac{1}{\gamma_z}} dB^t & \text{(6.1.8c)} \end{cases}$$

where $\gamma = \eta_y/\eta$ and $\gamma = \eta_z/\eta$. In our case, $\gamma_y \rightarrow 0$ and $\gamma_z \rightarrow 0$. From the point of view of numerical simulations, the time step Δt have to be small compared to γ_y and γ_z in order to correctly capture the fast fluctuations of ϵ_y, ϵ_z. Choosing to keep this small parameters γ_y and γ_z in the simulations is not an option as it will be prohibitively time consuming.

In the limit $\gamma_{y,z} \rightarrow 0$, we can ‘adiabatically eliminate’ the fast variables ϵ_y and ϵ_z. The detailed proof of the following reduction procedure can be found in (Gardiner, 2004; Lelièvre et al., 2010; Risken, 1988).

Consider two stochastic variables X_1^t and X_2^t driven by the following set of SDEs:

$$\begin{cases} dX_1^t = b_1\left(X_1^t, X_2^t\right) dt + \sqrt{2\beta^{-1}} dB_1^t & \text{(6.1.9a)} \\ dX_2^t = \dfrac{1}{\gamma} b_2\left(X_1^t, X_2^t\right) dt + \sqrt{2\beta^{-1}\dfrac{1}{\gamma}} dB_1^t. & \text{(6.1.9b)} \end{cases}$$

Suppose $\gamma \to 0$. Then the dynamics of X_2^t is infinitely fast compared to the dynamics of X_1^t which means that for a given value of X_1^t, the probability distribution of X_2^t can be considered as equilibrium at a given X_1^t:

$$p\left(x_2, t\right) \approx p_{X_1^t}\left(x_2\right), \tag{6.1.10}$$

where $p_{X_1^t(x)}$ is the solution

$$b_2\left(x_1, x_2\right) p_{X_1^t}\left(x_2\right) + \beta^{-1} \partial_{x_2} p_{X_1^t}\left(x_2\right) = 0 \quad \text{at fixed } X_1^t. \tag{6.1.11}$$

Going back to SDEs, we can write[1]:

$$\begin{cases} dX_1^t = \overline{b}_1\left(X_1^t\right) dt + \sqrt{2\beta^{-1}} dB_1^t & (6.1.12\text{a}) \\ X_2^t \sim p_{X_1^t} & (6.1.12\text{b}) \end{cases}$$

where $\overline{b}_1$ is obtained by averaging b_1 over X_2:

$$\overline{b}_1\left(x_1\right) = \int b\left(x_1, x_2\right) p_{X_1^t}\left(x_2\right) dx_2. \tag{6.1.13}$$

In our system, in hard and soft device, the stationary probability distributions of ϵ_y^t and ϵ_z^t for a given set $\epsilon_1^t, \ldots, \epsilon_N^t$ are canonical. Then, in hard device, we can write:

$$\begin{cases} d\epsilon_i^t = \overline{b}\left(\epsilon_i\right) dt + \sqrt{2\beta^{-1}} dB_i^t \quad \text{for } 1 \leq i \leq N & (6.1.14\text{a}) \\ \epsilon_y^t \sim p^h_{\epsilon_1^t, \ldots, \epsilon_N^t} & (6.1.14\text{b}) \end{cases}$$

where $\overline{b}\left(\epsilon_i\right)$ is computed with:

$$p^h_{\epsilon_1^t, \ldots, \epsilon_N^t}\left(e_y\right) = \frac{1}{\mathcal{Z}_y^h\left(\epsilon_1^t, \ldots, \epsilon_N^t, \overline{\epsilon}\right)} \exp\left[-\beta V\left(\epsilon_1^t, \ldots, \epsilon_N^t, e_y, \overline{\epsilon}\right)\right] \tag{6.1.15}$$

$$\mathcal{Z}_y^h\left(\epsilon_1^t, \ldots, \epsilon_N, \overline{\epsilon}\right) = \int e^{-\beta V\left(\epsilon_1^t, \ldots, \epsilon_N^t, e_y, \overline{\epsilon}\right)} de_y \tag{6.1.16}$$

Observe that we obtained an effective dynamic on the N–dimensional slow-manifold $(\epsilon_1, \ldots, \epsilon_N)$. The computation of $\overline{b}$ is straightforward since b depends linearly on ϵ_y (see Eq.(6.1.2)). We obtain (for $1 \leq i \leq N$):

$$\overline{b}\left(\epsilon_i^t\right) = -v'\left(\epsilon_i^t\right) + \left\langle \epsilon_y^t \right\rangle^h_{\epsilon_1^t, \ldots, \epsilon_N^t} - \epsilon_i^t, \text{ with} \tag{6.1.17}$$

$$\left\langle \epsilon_y^t \right\rangle_{\epsilon_1^t, \ldots, \epsilon_N^t} = \int e_y p^h_{\epsilon_1, \ldots, \epsilon_N}\left(e_y\right) de_y = \hat{\epsilon}_y = \frac{1}{1+\lambda_f}\left(\lambda_f \overline{\epsilon} + \frac{1}{N}\sum_{i=1}^{N} \epsilon_i^t\right). \tag{6.1.18}$$

Similar computations for soft device, give:

$$\left\langle \epsilon_y^t \right\rangle^s_{\epsilon_1^t, \ldots, \epsilon_N^t} = \frac{\overline{\sigma}}{N} + \frac{1}{N}\sum_{i=1}^{N} \epsilon_i^t \tag{6.1.19}$$

$$\left\langle \epsilon_z^t \right\rangle^s_{\epsilon_1^t, \ldots, \epsilon_N^t} = \frac{\overline{\sigma}}{N\lambda_f} + \frac{\overline{\sigma}}{N} + \frac{1}{N}\sum_{i=1}^{N} \epsilon_i^t. \tag{6.1.20}$$

---

[1] Notation: $X \sim p$ means that the random variable X has a probability density p

To summarize we obtained that, in the limit of a purely elastic behavior of the myofilaments (in the limit $\gamma_y \to 0$ and $\gamma_z \to 0$), the reduced sets of Langevin's equations (6.1.7) and (6.1.8) can be written as:

$$\begin{cases} d\epsilon_i^t = b\left(\epsilon_i^t, \left\langle \epsilon_y^t \right\rangle^h_{\epsilon_1^t,\dots,\epsilon_N^t}\right) dt + \sqrt{2\beta^{-1}}\, dB_i^t \quad \text{for } 1 \le i \le N & (6.1.21a) \\ \text{where} & \\ \left\langle \epsilon_y^t \right\rangle^h_{\epsilon_1^t,\dots,\epsilon_N^t} = \dfrac{1}{1+\lambda_f} \left(\lambda_f \overline{\epsilon} + \dfrac{1}{N} \displaystyle\sum_{i=1}^{N} \epsilon_i^t \right), & (6.1.21b) \end{cases}$$

in the hard device and as

$$\begin{cases} d\epsilon_i^t = b\left(\epsilon_i^t, \left\langle \epsilon_y^t \right\rangle^h_{\epsilon_1^t,\dots,\epsilon_N^t}\right) dt + \sqrt{2\beta^{-1}}\, dB_i^t \quad \text{for } 1 \le i \le N & (6.1.22a) \\ \text{where} & \\ \left\langle \epsilon_y^t \right\rangle^s_{\epsilon_1^t,\dots,\epsilon_N^t} = \dfrac{\overline{\sigma}}{N} + \dfrac{1}{N} \displaystyle\sum_{i=1}^{N} \epsilon_i^t & (6.1.22b) \\ \text{and} & \\ \left\langle \epsilon_z^t \right\rangle^s_{\epsilon_1^t,\dots,\epsilon_N^t} = \dfrac{\overline{\sigma}}{N\lambda_f} + \dfrac{\overline{\sigma}}{N} + \dfrac{1}{N} \displaystyle\sum_{i=1}^{N} \epsilon_i^t & (6.1.22c) \end{cases}$$

in the soft device.

Notice that in Eq.(6.1.21) and (6.1.22) we still have N degrees of freedom. We cannot reduce further the size of the system as there is no obvious *small parameter*.

However, we are still dealing with a rather simple system as the cross-bridges are all equivalent and all driven by the same drift term b.

In the following sections we describe our attempts to simplify the dynamics further by using the remaining permutational symmetry.

Most of these attempts implies solving Fokker–Planck equations. The numerical methods implemented to simulate numerically the solutions are described in App.D.1.

6.2 General framework

6.2.1 Initial set of equations

For a fixed trajectory of ϵ_y, as the cross-bridges are arranged in parallel, they are mechanically independent. We then write that the conditional probability densities for individual cross-bridges are equal and that the conditional probability for bundle of cross-bridges is equal to the product of individual conditional probabilities:

$$p\left(\epsilon_1, \dots, \epsilon_N | \epsilon_y, t\right) = \prod_{i=1}^{N} \overline{p}\left(e_i | \epsilon_y, t\right). \tag{6.2.1}$$

In this case the overall probability can be written:

$$p\left(\epsilon_1, \dots, \epsilon_N, \epsilon_y, t\right) = \prod_{i=1}^{N} \overline{p}\left(\epsilon_i | \epsilon_y, t\right) \overline{p}_y\left(\epsilon_y, t\right). \tag{6.2.2}$$

Consider now the system of SDE (6.1.21) where ϵ_y has been adiabatically eliminated. Then replacing $\langle\epsilon_y\rangle$ by ϵ_y we can write:

$$\begin{cases} d\epsilon_i^t = b\left(\epsilon_i^t, \epsilon_y^t\right) dt + \sqrt{2\beta^{-1}} dB_i^t, \text{ for } 1 \le i \le N & (6.2.3a) \\ \epsilon_y^t = f\left(\epsilon_1^t, \dots, \epsilon_N^t, t\right) & (6.2.3b) \end{cases}$$

where f, represents the force balance between the myofilament and the array of cross-bridges. As we know, f has a different expressions in hard and soft device:

$$f\left(\epsilon_1^t, \dots, \epsilon_N^t, t\right) = \frac{1}{1+\lambda_f}\left(\lambda_f \overline{\epsilon}(t) + \frac{1}{N}\sum_{i=1}^{N} \epsilon_i^t\right) \text{ in the hard device}$$

$$f\left(\epsilon_1^t, \dots, \epsilon_N^t, t\right) = \frac{\overline{\sigma}}{N} + \frac{1}{N}\sum_{i=1}^{N} \epsilon_i^t \text{ in the soft device.}$$

Therefore, we are interested in the case where f is linear with respect to $\epsilon_1, \dots, \epsilon_N$, however the analysis can be done in the general case.

In fact, the macroscopic parameter we are interested in is ϵ_y because it is directly linked to the tension (through Eq.(4.2.15)) and the total elongation (through Eq.(4.2.17)). Therefore, our first task will be to derive a reduced description at the macroscale by using ϵ_y as the only variable.

To this end we derive a stochastic differential equation (SDE) on ϵ_y by using Itô formula (see Sec.5.2). Then, by integrating the Fokker–Planck equation for the whole system including ϵ_i and ϵ_y over $\epsilon_1, \dots, \epsilon_N$, we obtain the desired 1-D partial differential (PDE) equation on the probability density of ϵ_y. The computation of the coefficient of this equation will require the corresponding closure conditions.

6.2.2 Itô calculus

First, we apply Itô formula (Gardiner, 2004; Mahnke et al., 2009) to equation (6.2.3b):

$$\begin{aligned} d\epsilon_y^t = d\left(f\left(\epsilon_1^t, \dots, \epsilon_N^t, t\right)\right) = \Bigg(& \partial_t f\left(\epsilon_1^t, \dots, \epsilon_N^t, t\right) \\ & + \sum_{i=1}^{N} b\left(\epsilon_i^t, \epsilon_y^t\right) \partial_i f\left(\epsilon_1^t, \dots, \epsilon_N^t, t\right) \\ & + \sum_{i,j=1}^{N} \left(\left(H.H^T\right)_{ij} \partial_{i,j} f\left(\epsilon_1^t, \dots, \epsilon_N^t, t\right)\right)\Bigg) dt \\ & + \sum_{i,j=1}^{N} \left(H_{ij} \partial_i f\left(\epsilon_1^t, \dots, \epsilon_N^t, t\right) dB_j^t\right) \end{aligned} \qquad (6.2.4)$$

where $H = \sqrt{2\beta^{-1}}\mathbb{I}_N$, with $\mathbb{I}_N$, the $N \times N$ identity matrix.

We denote:

$$h_i = \partial_i f\left(e_1, \dots, \epsilon_N, t\right), \text{ for all } 1 \le i \le N. \qquad (6.2.5)$$

In view of the linearity of the function f, parameters h_i are constants. Since $h_i \to 0$ as $N \to \infty$, the variable ϵ_y is only weakly affected by microscopic parameters ϵ_i and can therefore be considered a macroscopic degree of freedom.

The system (6.2.3) becomes:

$$\begin{cases} d\epsilon_i^t = b\left(\epsilon_i^t, \epsilon_y^t\right) dt + \sqrt{2\beta^{-1}} dB_i^t, \text{ for } 1 \le i \le N & \text{(6.2.6a)} \\ d\epsilon_y^t = \left(\partial_t f\left(\epsilon_1^t, \dots, \epsilon_N^t, t\right) + \sum_{i=1}^{N} h_i b\left(\epsilon_i^t, \epsilon_y^t\right)\right) dt + \sqrt{2\beta^{-1}} \sum_{i=1}^{N} \left(h_i dB_i^t\right). & \text{(6.2.6b)} \end{cases}$$

where the permutational invariance is visible through the fact that b is the same for all $1 \le i \le N$. We denote:

$$b_y\left(\epsilon_1^t, \dots, \epsilon_N^t, \epsilon_y^t, t\right) = \partial_t f\left(\epsilon_1^t, \dots, \epsilon_N^t, t\right) + \sum_{i=1}^{N} h_i b\left(\epsilon_i^t, \epsilon_y^t\right) \tag{6.2.7}$$

and thus Eq.(6.2.6) becomes:

$$\begin{cases} d\epsilon_i^t = b\left(\epsilon_i^t, \epsilon_y^t\right) dt + \sqrt{2\beta^{-1}} dB_i^t, \text{ for } 1 \le i \le N & \text{(6.2.8a)} \\ d\epsilon_y^t = b_y\left(\epsilon_1^t, \dots, \epsilon_N^t, \epsilon_y^t, t\right) dt + \sqrt{2\beta^{-1}} \sum_{i=1}^{N} \left(h_i dB_i^t\right). & \text{(6.2.8b)} \end{cases}$$

6.2.3 Averaged Fokker–Planck Equation

We define the following vectors of $N+1$ elements

$$\underline{\epsilon}^t = \left(\epsilon_1^t, \dots, \epsilon_y\right) \in \mathbb{R}^{N+1} \tag{6.2.9}$$

$$\underline{b}\left(\underline{\epsilon}, t\right) = \left(b\left(\underline{\epsilon}, t\right), \dots, b\left(\underline{\epsilon}, t\right), b_y\left(\underline{\epsilon}, t\right)\right) \in \mathbb{R}^{N+1} \tag{6.2.10}$$

and introduce the $N \times N+1$ matrix:

$$\underline{\underline{\omega}} = \sqrt{2\beta^{-1}} \begin{pmatrix} 1 & & 0 \\ & \ddots & \\ 0 & & 1 \\ h_1 & \cdots & h_N \end{pmatrix} \tag{6.2.11}$$

Our system of $N+1$ Langevin's equations is equivalent to the following Fokker–Planck equation (see Sec.5.2 and Gardiner (2004)):

$$\partial_t p\left(\underline{\epsilon}, t\right) = \sum_{i=1}^{y} \partial_i \left(-b_i\left(\underline{\epsilon}, t\right) p\left(\underline{\epsilon}, t\right) + \frac{1}{2} \sum_{j=1}^{y} \left(\underline{\underline{\omega}}.\underline{\underline{\omega}}^T\right)_{ij} \partial_j p\left(\underline{\epsilon}, t\right)\right) \tag{6.2.12}$$

where p is the probability density of the whole system (introduced in Eq.(6.2.2)) and where

$$\underline{\underline{\omega}}.\underline{\underline{\omega}}^T = 2\beta^{-1} \begin{pmatrix} 1 & & & h_1 \\ & \ddots & & \vdots \\ & & 1 & h_N \\ h_1 & \cdots & h_N & \overline{h} \end{pmatrix} \text{ with } \overline{h} = \sum_{i=1}^{N} h_i^2. \tag{6.2.13}$$

We also prescribe the initial condition $p\left(\underline{\epsilon}, t=0\right) = p_0\left(\underline{\epsilon}\right)$. Next, we integrate the Fokker–Planck equation (6.2.12) with respect to $\epsilon_1, \dots, \epsilon_N$. We denote:

$$\overline{p}_y\left(\epsilon_y, t\right) = \int \cdots \int p\left(\underline{\epsilon}, t\right) d\epsilon_1 \dots d\epsilon_N \text{ , and write} \tag{6.2.14}$$

$$\partial_t \overline{p}_y(\epsilon_y,t) = \sum_{i=1}^{N} \int \cdots \int \partial_i \left(- b_i(\underline{\epsilon},t)\, p(\underline{\epsilon},t) + \sum_{j=1}^{y} \frac{1}{2} \left(\underline{\underline{\omega}}.\underline{\underline{\omega}}^T \right)_{ij} \partial_j p(\underline{\epsilon},t) \right) d\epsilon_1 \ldots d\epsilon_N$$
$$+ \partial_y \left(\int \cdots \int \left(-b_y(\underline{\epsilon},t)\, p(\underline{\epsilon},t) \right) + \sum_{j=1}^{y} \frac{1}{2} \left(\underline{\underline{\omega}}.\underline{\underline{\omega}}^T \right)_{yj} \partial_j p(\underline{\epsilon},t)\, d\epsilon_1 \ldots d\epsilon_N \right).$$

Since p and all its derivatives vanish at the boundaries of the integration domain, we are left with:

$$\partial_t \overline{p}_y(\epsilon_y,t) = \partial_y \int \cdots \int \left(-b_y(\underline{\epsilon},t)\, p(\underline{\epsilon},t) \right) d\epsilon_1 \ldots d\epsilon_N + \beta^{-1} \overline{h} \partial_{yy} \overline{p}_y(\epsilon_y,t) \tag{6.2.15}$$

Now we use the independence relation (6.2.1) in the multiple integral to extract an equation for $p_y(\epsilon_y,t)$:

$$\partial_t \overline{p}_y(\epsilon_y,t) = \partial_y \left(-\overline{b}_y(\epsilon_y,t)\, \overline{p}_y(\epsilon_y,t) \right) + \beta^{-1} \overline{h} \partial_{yy} \overline{p}_y(\epsilon_y,t), \tag{6.2.16}$$

Here, we implicitly defined:

$$\overline{b}_y(\epsilon_y,t) = \int \cdots \int b_y(\underline{\epsilon},t) \prod_{i=1}^{N} \overline{p}(\epsilon_i|\epsilon_y,t)\, d\epsilon_1 \ldots d\epsilon_N.. \tag{6.2.17}$$

Recall that in Eq.(6.2.16), $\overline{h}$ is a function of N. As $N \to \infty$, since $\overline{h} \to 0$, the diffusion term in (6.2.16) vanishes and in the limit, the dynamics of ϵ_y becomes deterministic. This shows that ϵ_y is indeed a macroscopic degree of freedom.

We see from Eq.(6.2.17), that closing the system describing the reduced dynamics requires the knowledge of the microscopic conditional probability $p(\epsilon_i|\epsilon_y,t)$ so we need an additional *closure* relation to solve the problem. In the next section, we discuss a simple system where the power-stroke element v is quadratic and where the closure relation can be derived from the micro-model.

6.3 Exact solution: single well potential

The Ornstein Uhlenbeck process describes the motion of a particle in a parabolic energy in the presence of thermal fluctuations. The solution of this process can be found analytically (Gardiner, 2004; Risken, 1988) and we use it to illustrate our reduction procedure.

In this section, we suppose here that our double well potential v is replaced by a single parabola: $v(\epsilon) = 1/2\epsilon^2$.

The set of equation, corresponding to (6.2.3) can be written as:

$$\begin{cases} d\epsilon_i^t = \left(\epsilon_y^t - 2\epsilon_i^t \right) dt + \sqrt{2\beta^{-1}} dB_i^t, \text{ for } 1 \le i \le N & \text{(6.3.1a)} \\ \epsilon_y = \dfrac{1}{1+\lambda_f} \left(\lambda_f \overline{\epsilon}(t) + \dfrac{1}{N} \displaystyle\sum_{i=1}^{N} \epsilon_i^t \right) & \text{(6.3.1b)} \end{cases}$$

From (6.2.5) and (6.2.13), we can obtain the following explicit relations:

$$h_i = 1/\left(N(1+\lambda_f) \right) \text{ for } 1 \le i \le N$$
$$\overline{h} = 1/\left(N(1+\lambda_f)^2 \right)$$

Now by using Itô formula we obtain:

$$\begin{cases} d\epsilon_i^t = \left(\epsilon_y^t - 2\epsilon_i^t\right) dt + \sqrt{2\beta^{-1}} dB_i^t, \text{ for } 1 \le i \le N & (6.3.2a) \\ d\epsilon_y^t = \dfrac{1}{1+\lambda_f} \left(\lambda_f \overline{\epsilon}'(t) + \epsilon_y^t - 2\dfrac{1}{N}\displaystyle\sum_{i=1}^N \epsilon_i^t\right) dt + \sqrt{2\beta^{-1}} \dfrac{1}{N(1+\lambda_f)} \displaystyle\sum_{i=1}^N dB_i^t. & (6.3.2b) \end{cases}$$

Next, we use the equilibrium relation to express $1/N \sum \epsilon_i^t$ in (6.3.2b) as:

$$\frac{1}{N}\sum_{i=1}^N \epsilon_i^t = (1+\lambda_f)\,\epsilon_y^t - \lambda_f \overline{\epsilon}(t)$$

Then we obtain

$$\begin{cases} d\epsilon_i^t = \left(\epsilon_y^t - 2\epsilon_i^t\right) dt + \sqrt{2\beta^{-1}} dB_i^t, \text{ for } 1 \le i \le N \\ d\epsilon_y^t = \dfrac{1}{1+\lambda_f} \left(\lambda_f \overline{\epsilon}'(t) + 2\lambda_f \overline{\epsilon}(t) - (1+2\lambda_f)\,\epsilon_y^t\right) dt + \sqrt{2\beta^{-1}} \dfrac{1}{N(1+\lambda_f)} \displaystyle\sum_{i=1}^N dB_i^t. \end{cases}$$

Notice that the effective drift term b_y does not depend on ϵ_is. This is the reason why for this simple case, we don't need a closure relation to solve the problem (see below). Instead, we can explicitly compute the homogenized drift coefficient using (6.2.17):

$$\overline{b}_y(\epsilon_y, t) = \int_{\mathbb{R}^N} \frac{1}{1+\lambda_f}\left(\lambda_f \overline{\epsilon}'(t) + 2\lambda_f \overline{\epsilon}(t) - (1+2\lambda_f)\,\epsilon_y\right) \prod_{i=1}^N \overline{p}(\epsilon_i|\epsilon_y, t)\, d\epsilon_1 \dots d\epsilon_N. \tag{6.3.4}$$

The term $\lambda_f \overline{\epsilon}'(t) + 2\lambda_f \overline{\epsilon}(t) - (1+2\lambda_f)\,\epsilon_y$ does not depend on ϵ_i and can be removed from the integral. Due to the normalization condition $\int \prod p = 1$ can write:

$$\overline{b}_y(\epsilon_y, t) = \frac{1}{1+\lambda_f}\left(\lambda_f \overline{\epsilon}'(t) + 2\lambda_f \overline{\epsilon}(t) - (1+2\lambda_f)\,\epsilon_y^t\right). \tag{6.3.5}$$

We observe that this expression depends only on ϵ_y. The homogenized Fokker–Planck equation can be written explicitly:

$$\partial_t \overline{p}_y(\epsilon_y, t) = \partial_y\left(-\overline{b}_y(\epsilon_y, t)\,\overline{p}_y(\epsilon_y, t)\right) + \frac{\beta^{-1}}{N(1+\lambda_f)^2}\partial_{yy}\overline{p}_y(\epsilon_y, t). \tag{6.3.6}$$

In this particular case, we don't need to know the form of $\overline{p}(\epsilon_i|\epsilon_y, t)$ to completely characterize the dynamics of ϵ_y.

Notice that the diffusion term in Eq.(6.3.6) vanishes when $N \to \infty$ thereby reducing the PDE to a one-dimensional ODE. This shows that for a system with infinitely many linear cross-bridges the macroscopic behavior is deterministic.

The stationary solution of Eq.(6.3.6) can be written as:

$$\overline{p}_y^s(\overline{\epsilon}, \epsilon_y) = \frac{1}{\overline{\mathcal{Z}}_y(\overline{\epsilon})} \exp\left[-\beta N 2(1+\lambda_f)\left(\frac{1}{2}\left(\frac{1}{2}+\lambda_f\right)\epsilon_y^2 - \lambda_f \overline{\epsilon}\epsilon_y\right)\right] \tag{6.3.7}$$

$$\text{where } \overline{\mathcal{Z}}_y(\overline{\epsilon}) = \left(\frac{\pi}{\beta N\left(\frac{1}{2}+\lambda_f\right)}\right)^{\frac{1}{2}} \exp\left[\beta N(1+\lambda_f)\frac{(\lambda_f \overline{\epsilon})^2}{\left(\frac{1}{2}+\lambda_f\right)}\right]. \tag{6.3.8}$$

It is instructive to compare this expression with equilibrium distribution for the whole system without an assumption that ϵ_y is linked to other variables through purely mechanical equilibrium conditions:

$$p_y^s\left(\overline{\epsilon},\epsilon_y\right)=\frac{1}{\mathcal{Z}_y\left(\overline{\epsilon}\right)}\exp\left[-\beta N\left(\frac{1}{2}\left(\frac{1}{2}+\lambda_f\right)\epsilon_y^2-\lambda_f\overline{\epsilon}\epsilon_y\right)\right] \tag{6.3.9}$$

$$\text{with } \mathcal{Z}_y\left(\overline{\epsilon}\right)=\left(\frac{2\pi}{\beta N\left(\frac{1}{2}+\lambda_f\right)}\right)^{\frac{1}{2}}\exp\left[\beta N\frac{\left(\lambda_f\overline{\epsilon}\right)^2}{2\left(\frac{1}{2}+\lambda_f\right)}\right]. \tag{6.3.10}$$

The effective energy landscape for the reduced system from the potential for the full system by a constant $2\left(1+\lambda_f\right)$ which depends on the coupling coefficient λ_f. This is a consequence of the adiabatic elimination procedure leading to Eq.(6.3.1): by eliminating the fluctuation at the scale of ϵ_y we increased the effective stiffness of the system. However, as ϵ_y only appears in quadratic terms in the energy, the adiabatic elimination leaves the mean value of ϵ_y unchanged.

6.3.1 Recovery relations

So far, we have derived an equation only for $\overline{p}_y\left(\epsilon_y,t\right)$, which, if we are only interested in the macroscopic quantities, is sufficient. However, $p\left(\epsilon_i|\epsilon_y,t\right)$ is still unknown to finish the solution, it is necessary to express it through $\overline{p}_y$. To this end, we integrate the full Fokker–Planck equation Eq.(6.2.12) with respect to $\epsilon_2,\ldots,\epsilon_N$. We are then left with the following 2-D Fokker–Planck on the joint probability density $p\left(\epsilon_1,\epsilon_y,t\right)$:

$$\begin{aligned}\partial_t p\left(\epsilon_1,\epsilon_y,t\right)&=\partial_1\left(-b_1\left(\epsilon_1,\epsilon_y\right)p\left(\epsilon_1,\epsilon_y,t\right)+\beta^{-1}\partial_i p\left(\epsilon_1,\epsilon_y,t\right)\right)\\&\quad+\partial_y\left(-b_y\left(\epsilon_y,t\right)p\left(\epsilon_1,\epsilon_y,t\right)+\frac{\beta^{-1}}{N\left(1+\lambda_f\right)^2}\partial_y p\left(\epsilon_1,\epsilon_y,t\right)\right)\\&\quad+2\frac{\beta^{-1}}{N\left(1+\lambda_f\right)}\partial_{1y}p\left(\epsilon_1,\epsilon_y,t\right)\end{aligned} \tag{6.3.11}$$

where again the most important feature is that the drift term for ϵ_y depends only on ϵ_y. This allows one to integrating it with respect to $\epsilon_2,\ldots,\epsilon_N$. Due to the permutational invariance, a similar equation can be written for each ϵ_i. After solving Eqs.(6.3.11) and (6.2.16) we obtain $p\left(\epsilon_i|\epsilon_y,t\right)$ using its definition:

$$p\left(\epsilon_i|\epsilon_y,t\right)=\frac{p\left(\epsilon_i,\epsilon_y,t\right)}{\overline{p}\left(\epsilon_y,t\right)}. \tag{6.3.12}$$

6.3.2 Results

When v is quadratic, the integration of 6.2.17 can be done explicitly. Hence, in this particular case, the 1D averaged model for ϵ_y is indeed 'equivalent' to the original N Langevin equations (6.3.1). On Fig. 6.1(A), we show the mean trajectories of ϵ_y obtained after a step of -1 nm obtained from the full Langevin system and from the equivalent model. Fig.6.1(B) shows the probability distribution and the corresponding histograms from 10^4 independent realizations of the Langevin's system. Dashed lines represent the Boltzmann probability density for the complete system without adiabatic elimination so we can appreciate the effect of the $2\left(1+\lambda_f\right)$ factor presented in Eqs.(6.3.7) and (6.3.9). The parameters are: $\lambda_f=1$, $N=100$ and $\beta=5$.

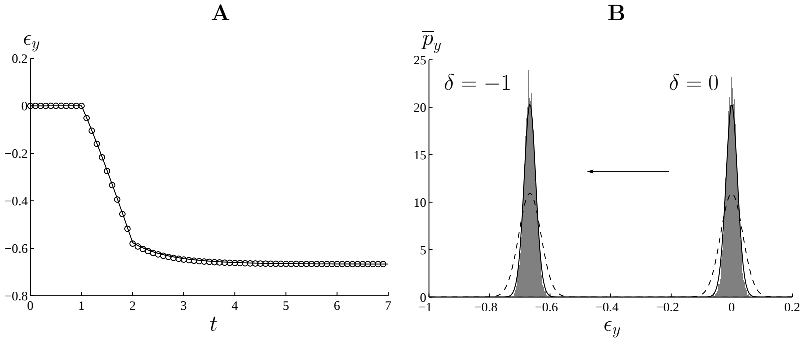

Fig. 6.1 – Equivalent model with an Ornstein Uhlenbeck process. Comparison between full Langevin simulation and equivalent model in the case where v is a simple quadratic potential. (**A**): open squares and circles represent the mean value over 10^4 Langevin simulations for 1 nm release respectively; dashed line and solid line represent the mean value from the equivalent model for the same step size. (**B**): histogram from the langevin simulations (filled) and probability density (lines) from the equivalent model before (right) and after (left) a 1 nm shortening step. The dashed lines show the Boltzmann probability density for the full system without adiabatic elimination (see Eq.(6.3.9)). Parameters are: $\lambda_f = 1$, $N = 100$ and $\beta = 5$.

6.4 Double well potential

6.4.1 Initial set of equations

We now turn to back to the double well potential v is given by (2.5.2). The total energy of the system is:

$$V(\epsilon_1, \ldots, \epsilon_N, \epsilon_y, \overline{\epsilon}, t) = \sum_{i=1}^{N} \left\{ v(\epsilon_i) + \frac{1}{2}(\epsilon_y - \epsilon_i)^2 \right\} + \frac{1}{2} N \lambda_f \left(\overline{\epsilon}(t) - \epsilon_y\right)^2 .$$

By assuming a purely elastic behavior of the filaments, we obtain the following system of governing equations:

$$\begin{cases} d\epsilon_i^t = b\left(\epsilon_i^t, \epsilon_y^t\right) dt + \sqrt{2\beta^{-1}} dB_t^i, \text{ for } 1 \le i \le N & (6.4.1a) \\ \epsilon_y^t = \dfrac{1}{1+\lambda_f} \left(\lambda_f \overline{\epsilon}(t) + \dfrac{1}{N} \displaystyle\sum_{i=1}^{N} \epsilon_i \right) & (6.4.1b) \end{cases}$$

where

$$b(\epsilon_i, \epsilon_y) = -v'(\epsilon_i) + (\epsilon_y - \epsilon_i), \text{ for } 1 \le i \le N, \tag{6.4.2}$$

Again the particularity of this mechanical system is that all the cross-bridges are characterized by the same drift term b.

6.4.2 Itô calculus

Using the definition presented in Sec.5.2, we obtain:

$$h_i = \frac{1}{N(1+\lambda_f)}. \tag{6.4.3}$$

Therefore we have $h_i \to 0$ when $N \to \infty$ and ϵ_y is a macroscopic variable, which is only weakly affected by fluctuations at the microscopic level. Next we write the analog of

(6.2.6):

$$\begin{cases} d\epsilon_i^t = b\left(\epsilon_i^t, \epsilon_y^t\right) dt + \sqrt{2\beta^{-1}} dB_t^i, \text{ for } 1 \le i \le N & (6.4.4a) \\ d\epsilon_y^t = \dfrac{1}{1+\lambda_f}\left(\lambda_f \overline{\epsilon}'(t) + \epsilon_y^t - \dfrac{1}{N}\displaystyle\sum_{i=1}^{N}\left(\epsilon_i^t + v'\left(\epsilon_i^t\right)\right)\right) dt & \\ \qquad + \sqrt{2\beta^{-1}} \dfrac{1}{N(1+\lambda_f)} \displaystyle\sum_{i=1}^{N} dB_i^t & (6.4.4b) \end{cases}$$

and replace the term $1/N \sum \epsilon_i^t$ in (6.4.4b) by using the equilibrium relation (6.4.1b) to obtain:

$$\begin{cases} d\epsilon_i^t = b\left(\epsilon_i^t, \epsilon_y^t\right) dt + \sqrt{2\beta^{-1}} dB_t^i, \text{ for } 1 \le i \le N & (6.4.5a) \\ d\epsilon_y^t = \dfrac{1}{1+\lambda_f}\left(\lambda_f \left(\overline{\epsilon}'(t) + \overline{\epsilon}(t) - \epsilon_y^t\right) - \dfrac{1}{N}\displaystyle\sum_{i=1}^{N} v'\left(\epsilon_i^t\right)\right) dt & \\ \qquad + \sqrt{2\beta^{-1}} \dfrac{1}{N(1+\lambda_f)} \displaystyle\sum_{i=1}^{N} dB_i^t & (6.4.5b) \end{cases}$$

We observe that, in equation (6.4.5b), only the term $\sum v'\left(\epsilon_i^t\right)$ depends on $\epsilon_1, \ldots, \epsilon_N$.

6.4.3 Equivalent of Fokker–Planck equation

We can perform the integration (6.2.17) to compute the drift term in the averaged Fokker–Planck equation:

$$\overline{b}_y(\epsilon_y, t) = \frac{1}{1+\lambda_f}\left(\lambda_f\left(\overline{\epsilon}'(t) + \overline{\epsilon}(t) - \epsilon_y\right) - \frac{1}{N}\sum_{i=1}^{N}\int\cdots\int v'(\epsilon_i)\prod_{i=1}^{N}\overline{p}(\epsilon_i|\epsilon_y, t)\, d\epsilon_1 \ldots d\epsilon_N\right). \tag{6.4.6}$$

Since $v'(\epsilon_i)$ depends only on ϵ_i, all term of the sum are equal to:

$$\langle v'(x)\rangle_y = \int_{\mathbb{R}} v'(x)\, \overline{p}(x|\epsilon_y, t)\, dx. \tag{6.4.7}$$

In the expression of $\langle v'(x)\rangle_y$, the term $\overline{p}(x|\epsilon_y, t)$ is unknown and therefore this integral cannot be computed. We are left at this stage with the following implicit relation:

$$\overline{b}_y(\epsilon_y, t) = \frac{1}{1+\lambda_f}\left(\lambda_f\left(\overline{\epsilon}'(t) + \overline{\epsilon}(t) - \epsilon_y\right) - \langle v'(x)\rangle_y\right). \tag{6.4.8}$$

The corresponding one dimensional Fokker–Planck equation on ϵ_y takes the form:

$$\partial_t \overline{p}_y(\epsilon_y, t) = \partial_y\left(-\overline{b}_y(\epsilon_y, t)\, \overline{p}_y(\epsilon_y, t)\right) + \beta^{-1}\frac{1}{N(1+\lambda_f)^2}\partial_{yy}\overline{p}_y(\epsilon_y, t). \tag{6.4.9}$$

Before discussing different approximations of $\langle v'(x)\rangle_y$, we can use the same methodology to derive a similar Fokker–Planck equation in the soft device (details are presented in appendix D.4):

$$\partial_t \overline{p}_y(\epsilon_y, t) = \partial_y\left(-\overline{b}_y(\epsilon_y, t)\, \overline{p}_y(\epsilon_y, t)\right) + \beta^{-1}\frac{1}{N}\partial_{yy}\overline{p}_y(\epsilon_y, t) \tag{6.4.10}$$

$$\text{where now } \overline{b}_y(\epsilon_y, t) = \frac{1}{N}\left(\overline{\sigma}'(t) + \overline{\sigma}(t)\right) - \langle v'(x)\rangle_y. \tag{6.4.11}$$

Once again, the expression for $\overline{b}_y(\epsilon_y, t)$ remains implicit.

6.4.4 Comments

Observe that the impact of the thermal fluctuations is different in hard and soft device. Indeed by looking at equations (6.4.9) and (6.4.10), we see that the diffusion coefficients are equal $\beta^{-1}/(N(1+\lambda_f)^2)$ in hard device and β^{-1}/N in soft device. As $\lambda_f > 0$, we see that the diffusion will be stronger in soft device than in hard device. Physically it comes from the fact that the system in soft device has one additional degree of freedom ϵ_z. The trace of this additional source of entropy is still visible in the averaged 1D-Fokker–Planck equation. Moreover, when $\lambda_f \to \infty$, both the drift term and the diffusion coefficient in Eq.(6.4.9) vanish, however the diffusion coefficient decays as $1/\lambda_f^2$ while the drift decays only as $1/\lambda_f$. Hence for weakly interacting cross-bridges, the behavior of ϵ_y becomes progressively more deterministic. Indeed, as $\lambda_f \to \infty$, the total length is imposed in a deterministic way, and the elongation of the myofilaments becomes negligible. In this limit $\epsilon_y = \overline{\epsilon}$ and diffusion is absent. This, does not happen in the soft device because, even with stiff filaments, the variables ϵ_y and ϵ_z are free to diffuse.

When N is large, the noise term is vanishing (in practice, in our model, N and β are in of the order 100 meaning that the noise term is of the order of 10^{-4}) reducing the problem to a simple ODE:

$$\partial_t \overline{p}_y(\epsilon_y, t) = \partial_y\left(-\overline{b}_y(\epsilon_y, t)\,\overline{p}_y(\epsilon_y, t)\right). \tag{6.4.12}$$

However, this does not mean that temperature plays no role at the macroscopic level, since in the computation of $\overline{b}_y$, the integration of v' does take into account the noise at the level of the cross-bridges through $\overline{p}(\epsilon_i|\epsilon_y)$.

Notice also that in the previous section, where potential was quadratic, the Fokker–Planck equation on ϵ_y (see Eq.6.3.6) was self-consistent as the drift term depended only on ϵ_y. In Eqs.(6.4.11) and (6.4.8), the drift still depends on $p(\epsilon_i|\epsilon_y, t)$ which now cannot be obtained without knowing the dynamics of ϵ_y. Hence, one needs to find a realistic closure relation that would either express $p(\epsilon_i|\epsilon_y, t)$ as a function of $\overline{p}_y(\epsilon_y, t)$ or directly postulate the resulting expression for $\overline{b}_y(\epsilon_y, t)$. In the next section we investigate two possibilities:

- One can naively assume that $\langle v'(x)\rangle_y = v'(\langle x\rangle_y)$ and use the equilibrium relation (6.4.1b) to compute $\overline{b}_y(\epsilon_y, t)$. We call this *mean field approximation*
- One can assume that $\overline{p}(x|\epsilon_y, t) = \overline{p}_s(x|\epsilon_y)$, which is the stationary conditional probability density. In our case, $\overline{p}_s(x|\epsilon_y)$ is a Boltzmann distribution parametrized by ϵ_y. We call it the *equilibrium approximation.*

Below, We will show that the mean field approximation gives poor results regarding both the stationary mean value of ϵ_y (we will not recover the T_2 curve), and the kinetics of the recovery. The equilibrium approximation will be able to reproduce the steady state mean value of ϵ_y but will fail to capture kinetics. In a subsequent section, we present another reduction technique which gives satisfactory results but only when the applied ramp loading increments are sufficiently large (closure relation).

6.5 Different approximations

6.5.1 The mean field approximation

To close our reduced model problem, we need a way to compute $\langle v'(x)\rangle_y$. One possibility is to consider the mean field approximation:

$$\langle v'(x)\rangle_y = v'(\langle x\rangle_y), \tag{6.5.1}$$

which is exact when v is linear (see Sec.6.3). In the hard device, the average position $\langle x\rangle_y$ is given by:

$$\begin{aligned}\langle x\rangle_y &= \int_{-\infty}^{+\infty} x\overline{p}\left(x|\epsilon_y\right)dx \\ &= \frac{1}{N}\int_{-\infty}^{+\infty}\sum_{i=1}^{N} x_i\overline{p}^N\left(x_i|\epsilon_y\right)dx_1\ldots dx_N \\ &= \left(1+\lambda_f\right)\epsilon_y-\lambda_f\overline{\epsilon}\left(t\right)\end{aligned} \tag{6.5.2}$$

where we used Eq.(6.4.1b). Similarly in the soft device, we have:

$$\langle x\rangle_y = \epsilon_y - \frac{\overline{\sigma}}{N}. \tag{6.5.3}$$

By using this approximation the drift terms $\overline{b}_y$ in the Fokker–Planck equations (6.4.9) and (6.4.10) can be computed as follows:

$$\begin{aligned}\overline{b}_y\left(\epsilon_y,t\right) = \frac{1}{1+\lambda_f}&\left(\lambda_f\left(\overline{\epsilon}'\left(t\right)+\overline{\epsilon}\left(t\right)-\epsilon_y\right)\right. \\ &\left.-v'\left(\left(1+\lambda_f\right)\epsilon_y-\lambda_f\overline{\epsilon}\left(t\right)\right)\right) \text{ in hard device,}\end{aligned} \tag{6.5.4}$$

$$\overline{b}_y\left(\epsilon_y,t\right) = \frac{1}{N}\left(\overline{\sigma}'\left(t\right)+\overline{\sigma}\left(t\right)\right)-v'\left(\epsilon_y-\frac{\overline{\sigma}}{N}\right) \text{ in soft device.} \tag{6.5.5}$$

where $\overline{b}_y$ now depends only on ϵ_y. It can be replaced into Eq.(6.4.9) and (6.4.10) which allows one to obtain $\overline{p}_y$. Unlike the case of the single well (see Sec.6.3), the rigorous derivation of a 2D Fokker–Planck equation of the type of Eq.(6.3.11) is not possible in this setting since the b_y term will in general depend on $\epsilon_2,\ldots,\epsilon_N$. Hence, this first method does not allow to recover the dynamics of individual cross-bridges ($p\left(\epsilon_i|\epsilon_y,t\right)$) from the knowledge of $\overline{p}_y$ without an additional closure relation.

The computational results obtained from this approximation are shown on Figs.6.2 and 6.3. These figures are obtained with the set of parameter fitted to muscle data (see Tab.7.1 on p.139). We see that the model based on mean field approximation fails to reproduce neither the stationary state (measured after 5ms, compare □ with ■) nor the transients. In the hard device, this is particularly visible for the mean trajectories (see Fig.6.2(A)): the equivalent model (solid lines) never fits the Langevin simulations (dashed lines) except during the application of the step because it does not allow the change in the distribution of the cross-bridges (purely elastic response, see the T_1 curve on Fig.6.2(B)).

Also, one can see that the shape of the T_2 curve corresponds to the local minimum of the energy defined by the initial fraction of cross-bridges in post-power-stroke n_1^0 (thick dot-dashed line). However, the upper and lower boundaries of this local minimum branch correspond to the upper and lower limits for configurations $(1,0,0)$ and $(0,0,1)$ respectively, rather that the upper and lower limits for the configurations $\left(n_1^0,0,0\right)$ and $\left(0,0,n_1^0\right)$. This is a direct consequence of the mean field approximation which considers only the mean position of the cross-bridges as a representation of the whole set. The mean position, at a given ϵ_y can either be in well 1 or in well 0 hence the whole assembly of cross-bridges is considered as effectively homogeneous. Hence, the boundaries correspond to those of the homogeneous configurations. The fact that the T_2 curves tracks the configuration $\left(n_1^0,0,0\right)$

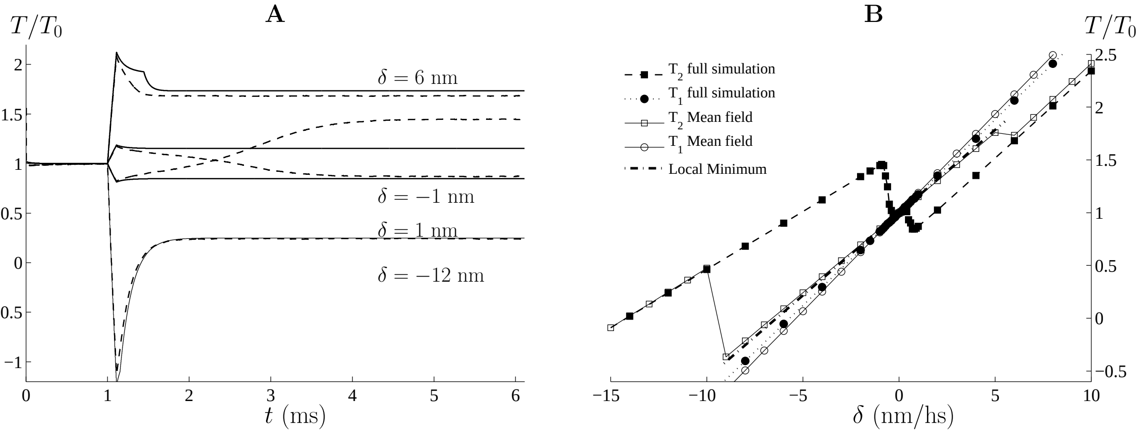

Fig. 6.2 – **Results obtained with the mean field approximation in hard device**. (**A**): trajectories obtained for different step size (indicated on the plot) using the full Langevin simulation (dashed lines) and the equivalent model with the mean field approximation (solid lines); (**B**):T_1 and T_2 curves obtained using the mean-field approximation in a hard device (open ○ and □) compared to the corresponding curves obtained using the full simulations (● and ■). The dot dashed line represent the metastable state corresponding to the initial state of the system. The parameter used for this results are adjusted to muscle experimental data (see Sec.7.1 and Tab.7.1 on p.139).

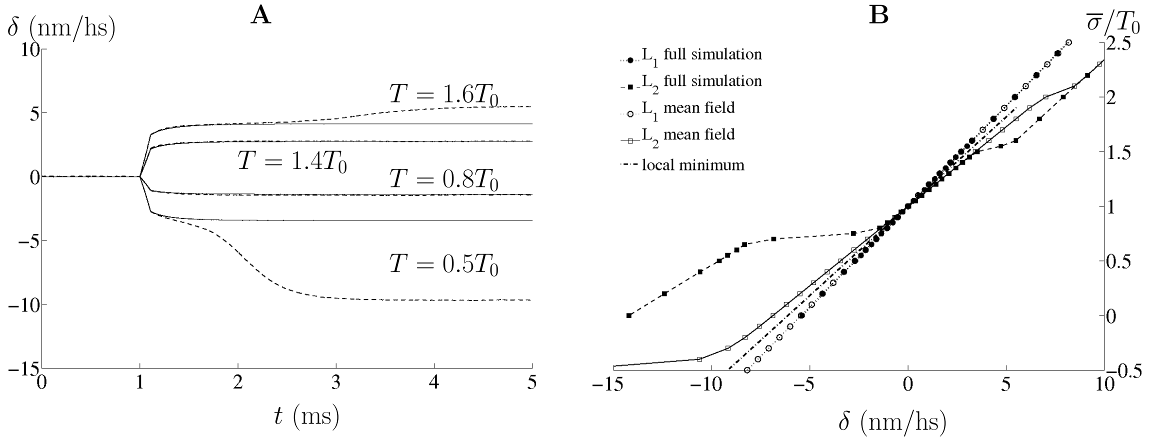

Fig. 6.3 – **Results obtained with the mean field approximation in soft device**. (**A**): trajectories obtained for different step size (indicated on the plot) using the full Langevin simulation (dashed lines) and the equivalent model with the mean field approximation (solid lines); (**B**):L_1 and L_2 curves obtained using the mean-field approximation in a hard device (○ and □) compared to the corresponding curves obtained using the full simulations (● and ■). The dot dashed line represent the metastable state corresponding to the initial state of the system. The parameter used for this results are adjusted to muscle experimental data (see Sec.7.1 and Tab.7.1 on p.139).

is due to the fact that the initial distribution of ϵ_y is chosen to ensure the correct fraction of cross-bridges in post-power-stroke.

To summarize, one can see that the mean field approximation is not adequate to describe an effective behavior of the half sarcomere. The main problem with this method is that we completely neglect the effect of thermal fluctuations at the scale of a cross-bridge, by considering only an average value of the characteristic quantities. The only random entry is the diffusion of ϵ_y (see Eqs.6.4.9 and 6.4.10), which comes with the multiplier $(N\beta)^{-1} \approx 10^{-4}$. It turns out that this weak diffusion is not sufficient to escape from the initial macroscopic well.

6.5.2 Equilibrium approximation

Another approximation is based on the assumption that the distribution of ϵ_i with respect to ϵ_y is an equilibrium one, namely:

$$p\left(\epsilon_i|\epsilon_y,t\right) = \overline{p}_s\left(\epsilon_i|\epsilon_y\right) = \frac{1}{\mathcal{Z}_1\left(\epsilon_y\right)+\mathcal{Z}_0\left(\epsilon_y\right)}\exp\left[-\beta\left(v\left(\epsilon_i\right)+\frac{1}{2}\left(\epsilon_y-\epsilon_i\right)^2\right)\right] \tag{6.5.6}$$

$$\text{where } \mathcal{Z}_1\left(\epsilon_y,\beta\right) = \int_{-\infty}^{l}\exp\left[-\beta\left(\frac{1}{2}\frac{\lambda_1}{1-\lambda_1}\left(x+1\right)^2+\frac{1}{2}\left(\epsilon_y-x\right)^2\right)\right]dx$$

$$\text{and } \mathcal{Z}_0\left(\epsilon_y,\beta\right) = \int_{-\infty}^{l}\exp\left[-\beta\left(\frac{1}{2}\frac{\lambda_0}{1-\lambda_0}x^2+v_0+\frac{1}{2}\left(\epsilon_y-x\right)^2\right)\right]dx.$$

We can now compute $\langle v'(x)\rangle_y$ by using this probability density to obtain:

$$\begin{aligned}\langle v'(x)\rangle_y &= \int_{-\infty}^{+\infty} v'(x)\,\overline{p}_s\left(x|\epsilon_y\right)dx\\ &= \int_{-\infty}^{l}\frac{\lambda_1}{1-\lambda_1}\left(x+1\right)\frac{\exp\left[-\beta\left(\frac{1}{2}\frac{\lambda_1}{1-\lambda_1}\left(x+1\right)^2+\frac{1}{2}\left(\epsilon_y-x\right)^2\right)\right]}{\mathcal{Z}_1\left(\epsilon_y\right)+\mathcal{Z}_0\left(\epsilon_y\right)}dx\\ &\quad+\int_{l}^{+\infty}\frac{\lambda_0}{1-\lambda_0}x\frac{\exp\left[-\beta\left(\frac{1}{2}\frac{\lambda_0}{1-\lambda_0}x^2+v_0+\frac{1}{2}\left(\epsilon_y-x\right)^2\right)\right]}{\mathcal{Z}_1\left(\epsilon_y\right)+\mathcal{Z}_0\left(\epsilon_y\right)}dx.\end{aligned} \tag{6.5.7}$$

To compute this integral we have to calculate the following quantities:

$$\langle x\rangle_1\left(\epsilon_y\right) = \int_{-\infty}^{l} x\frac{\exp\left[-\beta\left(\frac{1}{2}\frac{\lambda_1}{1-\lambda_1}\left(x+1\right)^2+\frac{1}{2}\left(\epsilon_y-x\right)^2\right)\right]}{\mathcal{Z}_1\left(\epsilon_y\right)+\mathcal{Z}_0\left(\epsilon_y\right)}dx, \text{ and} \tag{6.5.8}$$

$$\langle x\rangle_0\left(\epsilon_y\right) = \int_{l}^{+\infty} x\frac{\exp\left[-\beta\left(\frac{1}{2}\frac{\lambda_0}{1-\lambda_0}x^2+v_0+\frac{1}{2}\left(\epsilon_y-x\right)^2\right)\right]}{\mathcal{Z}_1\left(\epsilon_y\right)+\mathcal{Z}_0\left(\epsilon_y\right)}dx \tag{6.5.9}$$

They can be expressed in terms of special functions and can be rewritten then in the form:

$$\langle x\rangle_1\left(\epsilon_y\right) = \frac{\mathcal{Z}_1\left(\epsilon_y\right)}{\mathcal{Z}_1\left(\epsilon_y\right)+\mathcal{Z}_0\left(\epsilon_y\right)}\left(\left(1-\lambda_1\right)\epsilon_y-\lambda_1-\Delta_1\left(\epsilon_y\right)\right) \tag{6.5.10}$$

$$\langle x\rangle_0\left(\epsilon_y\right) = \frac{\mathcal{Z}_0\left(\epsilon_y\right)}{\mathcal{Z}_1\left(\epsilon_y\right)+\mathcal{Z}_0\left(\epsilon_y\right)}\left(\left(1-\lambda_0\right)\epsilon_y+\Delta_0\left(\epsilon_y\right)\right) \tag{6.5.11}$$

where $(1-\lambda_1)\,\epsilon_y-\lambda_1$ and $(1-\lambda_0)\,\epsilon_y$ are the position of the minima for the energy well 1 and 0, respectively, and Δ_1 and Δ_0 are positive numbers which are negligible when temperature is low ($\beta \to +\infty$) or when we consider infinitely steep wells (see Sec.A.2):

$$\Delta_1\left(\epsilon_y\right)=\sqrt{\frac{2\left(1-\lambda_1\right)}{\beta\pi}\frac{\exp\left[-f_1\left(\epsilon_y\right)^2\right]}{\operatorname{erfc}\left(-f_1\right)\left(\epsilon_y\right)}} \tag{6.5.12}$$

$$\Delta_0\left(\epsilon_y\right)=\sqrt{\frac{2\left(1-\lambda_0\right)}{\beta\pi}\frac{\exp\left[-f_0\left(\epsilon_y\right)^2\right]}{\operatorname{erfc}\left(f_0\right)\left(\epsilon_y\right)}}. \tag{6.5.13}$$

Here the functions f_1 and f_0 are defined by Eqs.(4.2.9) and (4.2.10). Now we can substitute (6.5.10) and (6.5.11) into (6.5.7) and obtain:

$$\langle v'\rangle_y\left(\epsilon_y\right)=\frac{\lambda_1}{1-\lambda_1}\left(\langle x\rangle_1\left(\epsilon_y\right)+\frac{\mathcal{Z}_1\left(\epsilon_y\right)}{\mathcal{Z}_1\left(\epsilon_y\right)+\mathcal{Z}_0\left(\epsilon_y\right)}\right)+\frac{\lambda_0}{1-\lambda_0}\langle x\rangle_0\left(\epsilon_y\right) \tag{6.5.14}$$

which is true in both hard and soft devices. If we substitute this expression into (6.4.8) and (6.4.11) for hard and soft devices, respectively we obtain:

$$\begin{aligned}\overline{b}_y\left(\epsilon_y\right)=\frac{1}{1+\lambda_f}&\Bigg(\lambda_f\overline{\epsilon}'\left(t\right)+\lambda_f\left(\overline{\epsilon}-\epsilon_y\right)\\&-\frac{\mathcal{Z}_1\left(\epsilon_y\right)}{\mathcal{Z}_1\left(\epsilon_y\right)+\mathcal{Z}_0\left(\epsilon_y\right)}\left(\lambda_1\left(\epsilon_y+1\right)-\frac{\lambda_1}{1-\lambda_1}\Delta_1\left(\epsilon_y\right)\right)\\&-\frac{\mathcal{Z}_0\left(\epsilon_y\right)}{\mathcal{Z}_1\left(\epsilon_y\right)+\mathcal{Z}_0\left(\epsilon_y\right)}\left(\lambda_0\epsilon_y+\frac{\lambda_0}{1-\lambda_0}\Delta_0\left(\epsilon_y\right)\right)\Bigg)\end{aligned} \tag{6.5.15}$$

in the hard device and

$$\begin{aligned}\overline{b}_y\left(\epsilon_y\right)=\frac{1}{N}&\Bigg(\overline{\sigma}'\left(t\right)+\overline{\sigma}\\&-\frac{\mathcal{Z}_1\left(\epsilon_y\right)}{\mathcal{Z}_1\left(\epsilon_y\right)+\mathcal{Z}_0\left(\epsilon_y\right)}\left(\lambda_1\left(\epsilon_y+1\right)-\frac{\lambda_1}{1-\lambda_1}\Delta_1\left(\epsilon_y\right)\right)\\&-\frac{\mathcal{Z}_0\left(\epsilon_y\right)}{\mathcal{Z}_1\left(\epsilon_y\right)+\mathcal{Z}_0\left(\epsilon_y\right)}\left(\lambda_0\epsilon_y+\frac{\lambda_0}{1-\lambda_0}\Delta_0\left(\epsilon_y\right)\right)\Bigg),\end{aligned} \tag{6.5.16}$$

in the soft device. We recall that the quantity $\mathcal{Z}_1/(\mathcal{Z}_1+\mathcal{Z}_0)$ represent the equilibrium fraction of cross-bridges in post-power-stroke at a given ϵ_y.

The drift force given by equation (6.5.15) and equation (6.5.16) reflects the nature of an effective potential for a 1 dimensional sarcomere. One can show that, in thermal equilibrium, this effective potential is nothing else but the non equilibrium energy landscape F_y (G_y in soft device), derived previously in Eqs.(4.2.14) and (4.2.13). Indeed, in the hard device, we recall the expression of F_y:

$$F_y\left(\epsilon_y,\beta\right)=N\left(\frac{1}{2}\lambda_f\left(\overline{\epsilon}-\epsilon_y\right)^2-\frac{1}{\beta}\log\left(\mathcal{Z}_1\left(\epsilon_y,\beta\right)+\mathcal{Z}_0\left(\epsilon_y,\beta\right)\right)\right).$$

Its derivative with respect to ϵ_y can be written in the form:

$$\begin{aligned}\partial_y F_y\left(\epsilon_y,\beta\right)=N&\Bigg(-\lambda_f\left(\overline{\epsilon}-\epsilon_y\right)\\&-\frac{1}{\beta}\frac{\partial_y\mathcal{Z}_1\left(\epsilon_y,\beta\right)+\partial_y\mathcal{Z}_0\left(\epsilon_y,\beta\right)}{\mathcal{Z}_1\left(\epsilon_y,\beta\right)+\mathcal{Z}_0\left(\epsilon_y,\beta\right)}\Bigg).\end{aligned} \tag{6.5.17}$$

A straightforward computation gives:

$$\partial_y \mathcal{Z}_1(\epsilon_y,\beta) = \mathcal{Z}_1(\epsilon_y,\beta)\left(-\beta\lambda_1(\epsilon_y+1) - \Delta_1(\epsilon_y,\beta)\right) \tag{6.5.18}$$
$$\partial_y \mathcal{Z}_0(\epsilon_y,\beta) = \mathcal{Z}_0(\epsilon_y,\beta)\left(-\beta\lambda_0\epsilon_y + \Delta_0(\epsilon_y,\beta)\right), \tag{6.5.19}$$

where Δ_1 and Δ_0 are given by Eq.(6.5.12) and Eq.(6.5.13). This allows us to write the final expression for the force derived from F_y:

$$\begin{aligned}-\partial_y F_y(\epsilon_y,\beta) = N\Bigg(&\lambda_f(\overline{\epsilon}-\epsilon_y)\\ &-\frac{\mathcal{Z}_1(\epsilon_y,\beta)}{\mathcal{Z}_1(\epsilon_y,\beta)+\mathcal{Z}_0(\epsilon_y,\beta)}\left(\lambda_1(\epsilon_y+1)+\Delta_1(\epsilon_y,\beta)\right)\\ &-\frac{\mathcal{Z}_0(\epsilon_y,\beta)}{\mathcal{Z}_1(\epsilon_y,\beta)+\mathcal{Z}_0(\epsilon_y,\beta)}\left(\lambda_0(\epsilon_y)-\Delta_0(\epsilon_y,\beta)\right)\Bigg).\end{aligned} \tag{6.5.20}$$

Similarly, in the soft device, we obtain:

$$\begin{aligned}-\partial_y G_y(\epsilon_y,\beta) = N\Bigg(&\frac{\overline{\sigma}}{N}\\ &-\frac{\mathcal{Z}_1(\epsilon_y,\beta)}{\mathcal{Z}_1(\epsilon_y,\beta)+\mathcal{Z}_0(\epsilon_y,\beta)}\left(\lambda_1(\epsilon_y+1)+\Delta_1(\epsilon_y,\beta)\right)\\ &-\frac{\mathcal{Z}_0(\epsilon_y,\beta)}{\mathcal{Z}_1(\epsilon_y,\beta)+\mathcal{Z}_0(\epsilon_y,\beta)}\left(\lambda_0(\epsilon_y)-\Delta_0(\epsilon_y,\beta)\right)\Bigg).\end{aligned} \tag{6.5.21}$$

These expressions look rather similar to Eq.(6.5.15) and Eq.(6.5.16); the difference coming from the terms with Δ_1 and Δ_0. In fact, the two expressions are equivalent. To prove this we write (omitting the variables for clarity):

$$\begin{aligned}\frac{\mathcal{Z}_1}{\mathcal{Z}_1+\mathcal{Z}_0}\frac{\lambda_1}{1-\lambda_1}\Delta_1 &= -\frac{\mathcal{Z}_1}{\mathcal{Z}_1+\mathcal{Z}_0}\Delta_1 + \frac{\mathcal{Z}_1}{\mathcal{Z}_1+\mathcal{Z}_0}\frac{1}{1-\lambda_1}\Delta_1\\ -\frac{\mathcal{Z}_0}{\mathcal{Z}_1+\mathcal{Z}_0}\frac{\lambda_0}{1-\lambda_0}\Delta_0 &= \frac{\mathcal{Z}_0}{\mathcal{Z}_1+\mathcal{Z}_0}\Delta_0 - \frac{\mathcal{Z}_0}{\mathcal{Z}_1+\mathcal{Z}_0}\frac{1}{1-\lambda_0}\Delta_0.\end{aligned}$$

Here, the first terms are the same as in Eq.(6.5.20) and Eq.(6.5.21). Now, using the expression of f_1 and f_0 given by Eqs.(4.2.9) and (4.2.10), the second terms are explicitly:

$$\begin{aligned}\frac{\mathcal{Z}_1}{\mathcal{Z}_1+\mathcal{Z}_0}\frac{1}{1-\lambda_1}\Delta_1 = \frac{1}{\beta}\frac{1}{\mathcal{Z}_1+\mathcal{Z}_0}\exp\Bigg[&-\frac{\beta}{2}\lambda_1(\epsilon_y+1)^2\\ &-\frac{\beta}{2}\left(\sqrt{\frac{1}{1-\lambda_1}}l+\sqrt{1-\lambda_1}\left(\frac{\lambda_1}{1-\lambda_1}-\epsilon_y\right)\right)^2\Bigg]\end{aligned}$$

and

$$\begin{aligned}-\frac{\mathcal{Z}_0}{\mathcal{Z}_1+\mathcal{Z}_0}\frac{1}{1-\lambda_0}\Delta_0 = \frac{1}{\beta}\frac{1}{\mathcal{Z}_1+\mathcal{Z}_0}\exp\Bigg[&-\frac{\beta}{2}\left(\lambda_0\epsilon_y^2+2v_0\right)\\ &-\frac{\beta}{2}\left(\sqrt{\frac{1}{1-\lambda_0}}l-\sqrt{1-\lambda_0}\epsilon_y\right)^2\Bigg].\end{aligned}$$

The exponent being expanded, we get:

$$\begin{aligned}\frac{\mathcal{Z}_1}{\mathcal{Z}_1+\mathcal{Z}_0}\frac{1}{1-\lambda_1}\Delta_1 &= \frac{1}{\beta}\frac{1}{\mathcal{Z}_1+\mathcal{Z}_0}\exp\left[-\frac{\beta}{2}\left(\frac{\lambda_1}{1-\lambda_1}\left(l+1\right)^2+\left(\epsilon_y-l\right)^2\right)\right]\\ -\frac{\mathcal{Z}_0}{\mathcal{Z}_1+\mathcal{Z}_0}\frac{1}{1-\lambda_0}\Delta_0 &= -\frac{1}{\beta}\frac{1}{\mathcal{Z}_1+\mathcal{Z}_0}\exp\left[-\frac{\beta}{2}\left(\frac{\lambda_0}{1-\lambda_0}l^2+2v_0+\left(\epsilon_y-l\right)^2\right)\right].\end{aligned}$$

Here, in the exponential terms we recognize the energies of well 1 and well 0, $v\left(x\right)+1/2\left(\epsilon_y-x\right)^2$, which are equal for $x=l$. Hence $\frac{\mathcal{Z}_1}{\mathcal{Z}_1+\mathcal{Z}_0}\frac{1}{1-\lambda_1}\Delta_1-\frac{\mathcal{Z}_0}{\mathcal{Z}_1+\mathcal{Z}_0}\frac{1}{1-\lambda_0}\Delta_0=0$, and we have proven that, in for the stationary process:

$$-\partial_y F_y\left(\epsilon_y,\beta,\overline{\epsilon}\right)=\left(1+\lambda_f\right)N\overline{b}_y\left(\epsilon_y,\overline{\epsilon}\right)\ \text{in hard device} \tag{6.5.22}$$

$$-\partial_y G_y\left(\epsilon_y,\beta,\overline{\sigma}\right)=N\overline{b}_y\left(\epsilon_y,\overline{\sigma}\right)\ \text{in soft device.} \tag{6.5.23}$$

Now, the stationary solution of the one dimensional Fokker–Planck equations (6.4.9) and (6.4.10) can be written explicitly:

$$\overline{p}_{y,s}\left(y,\beta,\overline{\epsilon}\right)=\frac{1}{\overline{Z}_h\left(\overline{\epsilon},\beta\right)}\exp\left(-\beta N\left(1+\lambda_f\right)^2\int_0^y-\overline{b}_y\left(x,\beta,\overline{\epsilon}\right)dx\right)\ \text{in the hard device} \tag{6.5.24}$$

$$\overline{p}_{y,s}\left(y,\beta,\sigma\right)=\frac{1}{\overline{\mathcal{Z}}_s\left(\overline{\sigma},\beta\right)}\exp\left(-\beta N\int_0^y-\overline{b}_y\left(x,\beta,\overline{\epsilon}\right)dx,\right)\ \text{in the soft device} \tag{6.5.25}$$

Notice that, we have identified the effective potentials as $\left(1+\lambda_f\right)F_y$ in the hard device and G_y in the soft device.

The fact that we again obtain an additional stiffness in the hard device is the consequence of the adiabatic elimination of ϵ_y (see Sec.6.1.2), not the approximation we used for $p\left(\epsilon_i|\epsilon_y\right)$ (see Eq.6.5.6). We have already found similar result in the case of a single well potential (see Eqs.6.3.7 and 6.3.9 and the following comments).

From the stationary distributions (6.5.24) and (6.5.24), the equilibrium mean value of ϵ_y denoted by $\overline{\langle\epsilon_y\rangle_h}$ in hard device and by $\overline{\langle\epsilon_y\rangle_s}$ in soft device, can be computed explicitly. This allows us to obtain the tension *vs* elongation relations in steady state:

$$\overline{T}_2\left(\overline{\epsilon}\right)=N\lambda_f\left(\overline{\epsilon}-\overline{\langle\epsilon_y\rangle_h}\right)\ \text{in the hard device,} \tag{6.5.26}$$

$$\overline{L}_2\left(\overline{\sigma}\right)=\frac{\overline{\sigma}}{N\lambda_f}+\overline{\langle\epsilon_y\rangle_s}\ \text{in the soft device.} \tag{6.5.27}$$

In contrast to the mean field theory, in the equilibrium approximation we do take into account thermal fluctuation at the scale of a cross-bridge distribution in equilibrium. Therefore, we recover exactly the results of the full simulation regarding the T_1-T_2 and L_1-L_2 curves, including the kinetic trapping (see Fig.6.4). Moreover, the equilibrium T_2 and L_2 curves computed using the stationary equilibrium distribution of the equivalent model matches exactly the thermal equilibrium curves computed within the full model (see solid lines obtained with Eqs.6.5.26 and 6.5.27).

However, the kinetics of the full system cannot be reproduced faithfully. From, the comparison of selected trajectories shown on Fig.6.5, we observe that the equivalent model (dashed lines) reaches steady state faster than the full Langevin system (solid lines) for low step amplitudes (see Fig.6.6). The faster kinetics of the equivalent model can be explained by the fact that we neglected the equilibration time of the cross-bridges by assuming equilibrium upfront.

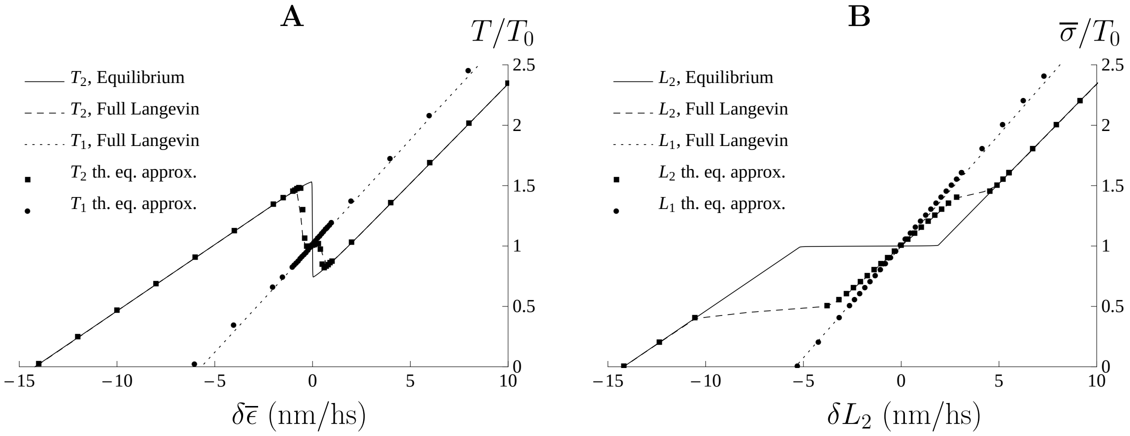

Fig. 6.4 – Equilibrium T_2 and L_2 curves obtained with full Langevin simulations and equivalent model with equilibrium approximation. (**A**): hard device. (**B**): soft device. Solid line: Equilibrium T_2 and L_2 curves obtained with the stationary distribution of the equivalent model. Dashed lines: T_2 and L_2 curves obtained with the full Langevin simulations (after 5 ms). Dotted lines: T_1 and L_1 curves obtained with the full Langevin simulations. (●): T_1, L_1 curves obtained with the equivalent model. (■): T_2 and L_2 curves obtained with the equivalent model (after 5 ms).Parameters are listed in Tab.7.1 on p.139.

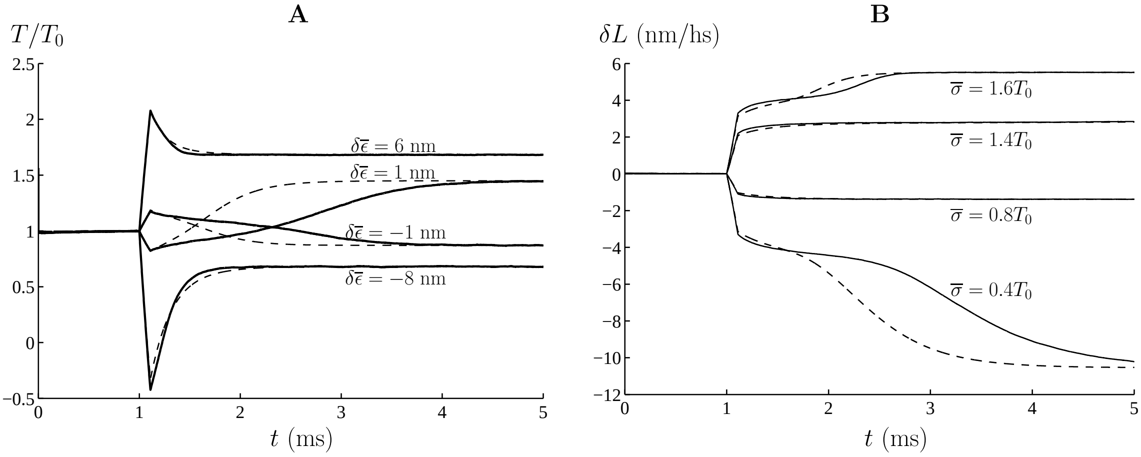

Fig. 6.5 – Selected trajectories with full Langevin simulation and equivalent model with equilibrium approximation. Solid lines: Full Langevin simulations; dashed lines: equivalent model with equilibrium approximation. (**A**): Tension *vs* time for $\delta\bar{\epsilon} = 6, 1, -1$ and -8 nm/hs. (**B**): elongation *vs* time for $\overline{\sigma} = 1.6, 1.4, 0.8$ and $0.4T_0$. Parameters are listed in Tab.7.1 on p.139.

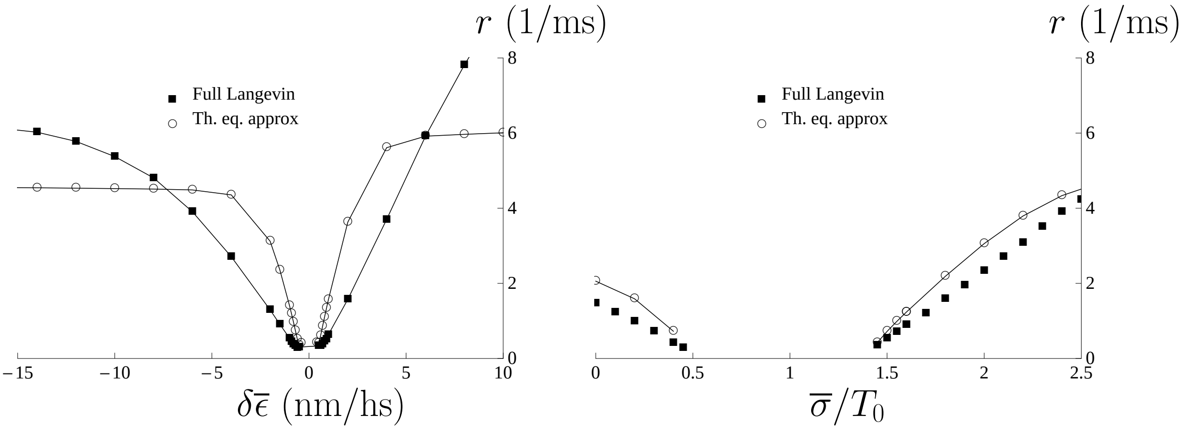

Fig. 6.6 – **Rate of recovery obtained with full Langevin simulation and the equivalent model with equilibrium approximation.** (**A**): hard device. (**B**): soft device. The rate is measured as the inverse of the time to reach $0.63\,(T_2 - T_1)$ from T_1 (resp. $0.63\,(L_2 - L_1)$ from L_1). (○): rate measured obtained with the equivalent model. (■): rate measured with the full Langevin simulations. Parameters are listed in Tab.7.1 on p.139.

6.6 The weak coupling model

In this Section we present a different approach to the derivation of a reduced model. Previously, we tried to derive a 1-D equation on ϵ_y and the conclusion was that the subtleties of the dynamical behavior of the system are lost when one tries to simplify the kinetics of a single cross-bridge to get an approximate picture at the macroscale. In fact, the kinetics of the system is mainly defined by the microscopic kinetics of the conformational change at the cross-bridge scale. Hence, instead of deriving an equation on the macroscopic degree of freedom ϵ_y, we shall take an opposite way and try to derive a PDE for a single cross-bridge. The challenge here is to take into account the cooperative effects while remaining at the scale of an individual cross-bridge.

6.6.1 The method

In our initial system, (6.2.3), we can replace ϵ_y given by (6.2.3b) to obtain:

$$d\epsilon_i^t = b\left(\epsilon_1^t, \ldots, \epsilon_N^t\right) dt + \sqrt{2\beta^{-1}} dB_i^t \text{ for } \imath = 1, \ldots, N \tag{6.6.1}$$

where the drift term b now depends on all ϵ_i-s and is the same for all $1 \leq i \leq N$. As we have done previously for the system (6.2.6), we can write the corresponding Fokker–Planck equation for the probability density $p\left(\epsilon_1, \ldots, \epsilon_N, t\right)$:

$$\partial_t p\left(\epsilon_1, \ldots, \epsilon_N, t\right) = \sum_{i=1}^{N} \left\{\partial_i \left[-b\left(\epsilon_1, \ldots, \epsilon_N, t\right) p\left(\epsilon_1, \ldots, \epsilon_N, t\right)\right] + \beta^{-1} \partial_{ii} p\left(\epsilon_1, \ldots, \epsilon_N, t\right)\right\}. \tag{6.6.2}$$

Next, we consider the following anzats:

$$p\left(\epsilon_1, \ldots, \epsilon_N, t\right) = \prod_{i=1}^{N} \overline{p}\left(\epsilon_i, t\right) \tag{6.6.3}$$

which is equivalent to assuming the complete independence of different cross-bridges. This assumption is different from Eq.(6.2.1) which does not contain any approximation: the cross-bridges, in that expression, were independent on the condition that ϵ_y is fixed. Here, we essentially assume that the probability density of a single cross-bridge depends on the mean field only weakly and this dependence can be treated independently for each sarcomere. Moreover, it is implied that all half-sarcomeres are statistically independent and that all marginal probability densities are the same ($\overline{p}$ does not depend on i).

To obtain a reduced model, we can now integrate Eq.(6.6.2), over $\epsilon_2, \ldots, \epsilon_N$. We obtain the following non-linear kinetic equation:

$$\partial_t \overline{p}\left(\epsilon_1, t\right) = \partial_1 \left[- \int \left\{ b\left(\epsilon_1, \ldots, \epsilon_N, t\right) \prod_{i=2}^{N} \overline{p}\left(\epsilon_i, t\right) d\epsilon_2, \ldots, d\epsilon_N \right\} \overline{p}\left(\epsilon_1, t\right) \right] + \beta^{-1} \partial_{11} \overline{p}\left(\epsilon_1, t\right) \tag{6.6.4}$$

where the non-linearity comes from the drift which is function of the solution $\overline{p}\left(\epsilon_i, t\right)$. The model can now be specified in the cases of hard and soft devices.

6.6.2 Special cases: hard and soft devices

In both hard and soft devices, the drift term associated with the variable ϵ_1 was initially:

$$b\left(\epsilon_1^t, \epsilon_y^t\right) = -v'\left(\epsilon_1\right) + \frac{1}{2}\left(\epsilon_y^t - \epsilon_1^t\right).$$

If we replace ϵ_y using Eq.(3.1.5) and (3.1.6) we obtain:

$$b\left(\epsilon_1, \ldots, \epsilon_N, t\right) = -v'\left(\epsilon_1\right) + \tfrac{\lambda_f}{1+\lambda_f} \overline{\epsilon}\left(t\right) + \tfrac{1}{N\left(1+\lambda_f\right)} \sum_{i=2}^{N} \epsilon_i + \left(\tfrac{1}{N\left(1+\lambda_f\right)} - 1 \right) \epsilon_1. \tag{6.6.5}$$

in the hard device and

$$b\left(\epsilon_1, \ldots, \epsilon_N, t\right) = -v'\left(\epsilon_1\right) + \tfrac{\overline{\sigma}(t)}{N} + \tfrac{1}{N} \sum_{i=2}^{N} \epsilon_i + \left(\tfrac{1}{N} - 1 \right) \epsilon_1. \tag{6.6.6}$$

in the soft device. After replacing the drifts terms (6.6.5) and (6.6.6) in (6.6.2), only the terms containing $\sum \epsilon_i$ remain to be integrated. The other terms integrate to one because of normalization. Since all $\overline{p}$s are equivalent the multi-variable integral reduces to a sum of single variable $\int x \overline{p}\left(x, t\right) dx$. Finally, for both hard and soft devices, we obtain:

$$\partial_t \overline{p}\left(\epsilon_1, t\right) = \partial_1 \left[- \left(-v'\left(\epsilon_1\right) + g\left(t\right) + \overline{m}\left(t\right) - q\epsilon_1 \right) \overline{p}\left(\epsilon_1, t\right) \right] + \beta^{-1} \partial_{11} \overline{p}\left(\epsilon_1, t\right) \tag{6.6.7}$$

where $g\left(t\right) = \tfrac{\lambda_f}{1+\lambda_f} \overline{\epsilon}\left(t\right)$; $\overline{m} = \tfrac{N-1}{N\left(1+\lambda_f\right)} \displaystyle\int x \overline{p}\left(x, t\right) dx$; $q = 1 - \tfrac{1}{N\left(1+\lambda_f\right)}$ in the hard device and $g\left(t\right) = \tfrac{\overline{\sigma}(t)}{N}$; $\overline{m} = \tfrac{N-1}{N} \displaystyle\int x \overline{p}\left(x, t\right) dx$; $q = 1 - \tfrac{1}{N}$ in the soft device.

Notice that in both models the drift is a function of the mean value $\overline{m}$ of the variable ϵ_1 which encompasses the collective effect of the bundle of cross-bridges. In the hard device, we see that $\overline{m}$ vanishes when $\lambda_f \to \infty$, which is coherent with the fact that coupling diminishes with increasing λ_f. In the soft device, the coupling is always present and the drift does not depend on λ_f.

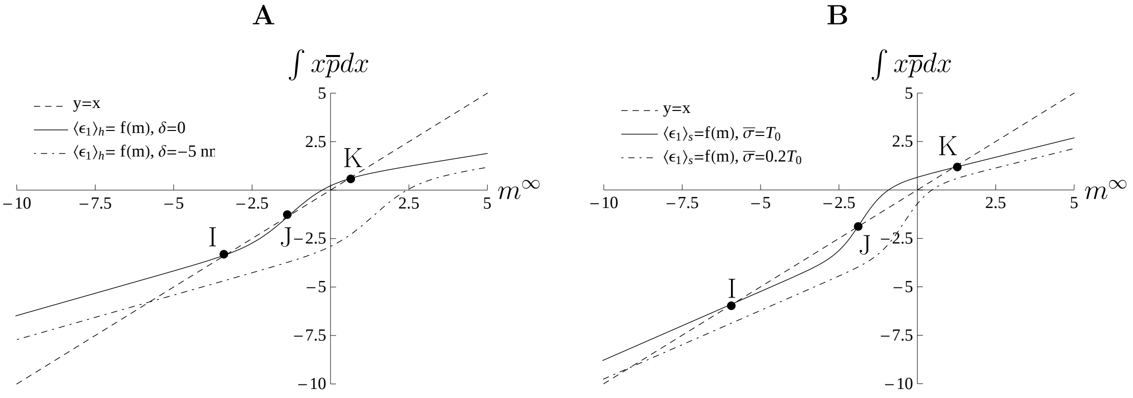

Fig. 6.7 – Existence of 2 solutions for the non linear 1 dimensional Fokker–Planck equation in hard device (**A**) and soft device (**B**). The solid lines represent the mean value of ϵ_1 *vs* m^{∞} for different loadings. (**A**): from $\delta = -10$ to $\delta = 10$. (**B**): from 0 to $2T_0$. The dashed line is the identity ($y = x$). The thick lines mark the isometric conditions. The problem (6.6.12) can have up to 3 solutions marked I,J and K. I and K are stable and J is unstable. As the loading changes, only one solution remains. The parameters are listed in Tab.7.1 on p.139. In particular $\lambda_f = 0.53$.

To recover the equilibrium tension–elongation curve, we have to compute the mean value of ϵ_1 by using the solution of Eq.(6.6.7). We obtain:

$$\left\langle \epsilon_y \right\rangle_h (t) = \frac{1}{1+\lambda_f} \left(\lambda_f \overline{\epsilon}(t) + \left\langle \epsilon_1 \right\rangle_h (t) \right), \text{ in hard device} \tag{6.6.8}$$

$$\left\langle \epsilon_y \right\rangle_s (t) = \left\langle \epsilon_1 \right\rangle_s (t) + \frac{\overline{\sigma}(t)}{N}, \text{ in soft device,} \tag{6.6.9}$$

$$\text{where } \left\langle \epsilon_1 \right\rangle_{h,s} (t) = \int x \overline{p}(x,t)\, dx, \tag{6.6.10}$$

which allows us to compute the macroscopic quantities.

6.6.3 Multiple stationary solutions

As we have already mentioned, the kinetic Eq.(6.6.7) is non linear since $\overline{m}$ depends on $\overline{p}$. It can have more than one stationary solution. To investigate this possibility, we first express the stationary solution of equation (6.6.7) in terms of ϵ_1 and m^{∞}, the still unknown asymptotic value of m (the details of the computation are in App.D.5):

$$\overline{p}^{\infty}\left(\epsilon_1, g, \overline{m}^{\infty}, \beta\right) = \frac{1}{\overline{\mathcal{Z}}\left(g, \overline{m}^{\infty}, \beta\right)} \exp\left[-\beta\left(v\left(\epsilon_1\right) - g\epsilon_1 - \overline{m}^{\infty}\epsilon_1 + \tfrac{1}{2}q\epsilon_1^2\right)\right] \tag{6.6.11}$$

where $\overline{m}^{\infty} = \frac{N-1}{N\left(1+\lambda_f\right)} m^{\infty}$ in the hard device and $\overline{m}^{\infty} = \frac{N-1}{N} m^{\infty}$ in the soft device. Next we write the following consistency relation which takes the form of an algebraic relation:

$$m^{\infty} = \int x \overline{p}^{\infty}\left(x, g, \overline{m}^{\infty}\right) dx, \tag{6.6.12}$$

In hard device, when $\lambda_f \to \infty$, then $\overline{m}^{\infty} \to 0$ and in this limit Eq.(6.6.12) has only one solution which is in agreement with the fact that all cross-bridges are independent.

Fig.6.7 shows the solutions of (6.6.12) in hard (see A) and soft (see B) devices. In both (A) and (B), we show two $\int x\overline{p}^{\infty}dx$ *vs* m^{∞} curves (see solid line and dot-dashed line) that corresponds to two values of the loading parameter g. In hard device (A), the solid line

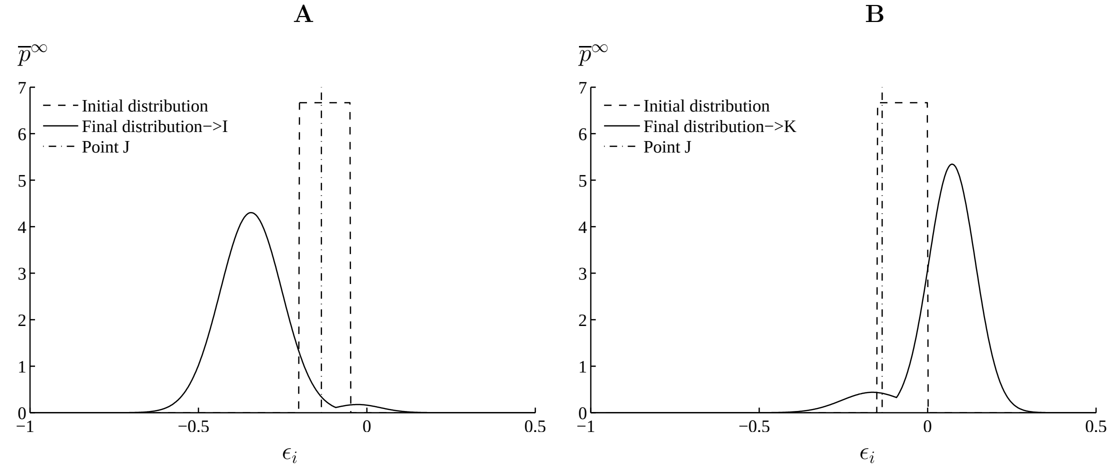

Fig. 6.8 – **Probability density associated to points I and K and instability of point J**. Solid lines: probability density associated to point I (**A**) and K (**B**), the solutions of the consistency equation (6.6.12) in hard device. Dashed lines show two different initial conditions associated to mean values around point J (indicated by the vertical dot-dashed line) that converged to the to stable distribution.

corresponds to $\overline{\epsilon} = \overline{\epsilon}^0$ (isometric condition) and the dot-dashed to $\overline{\epsilon} = \overline{\epsilon}^0 - 5$ nm/hs. In soft device, the solid lines corresponds to $\overline{\sigma} = T_0$ and the dot-dashed line to $\overline{\sigma} = 0.2T_0$.

One can see that for small loads, Eq.(6.6.12) has up to 3 solutions (marked I, J and K on Fig.6.7). Solutions I and J are stable. They are represented by the solid line on Fig.6.8 for the hard device case. Stability of point J was checked numerically by running simulations with various initial distributions compatible with mean values close and equal to J (the vertical dot-dashed line represents point J on Fig.6.8). Dashed lines on Fig.6.8 show examples of such initial conditions that converged to distributions corresponding to points I and K. Based on this we conclude that stationary solutions I and K are stable while distribution J is unstable.

When the load g is changed (see Fig.6.7 dot-dashed line), the curves $\int x\overline{p}^{\infty}dx$ *vs* m^{∞} remain parallel, while shifting in the horizontal direction. For sufficiently large loadings, there is only one intersection with the identity line and so Eq.(6.6.11) has only one stable solution. We show on Fig.6.9, that the interval of loading where 2 solutions exist coincides with the interval where the non-equilibrium energy landscapes F_y and G_y have two minima. We conclude that the two stable solutions correspond to the homogeneous configurations localized in the macroscopic wells.

6.6.4 Weak coupling model *vs* full Langevin dynamics

On Fig.6.10, we show three snapshots of the probability density for a single cross-bridge obtained from the full Langevin simulations (histograms) and compared with the weak coupling model (lines). The left column shows the response to a shortening step of 1 nm/hs in hard device and the right column, the response to a force step of $-0.7T_0$.

Light gray and dark gray histograms show the cross-bridges probability density for two types of realizations. Light gray histograms represent realizations initialized in the left macroscopic well (post-power-stroke). Dark gray histograms result from realizations initialized in the right macroscopic well (pre-power-stroke). The dot-dashed line (resp. dashed line) is the first (resp. second) solution Eq.(6.6.7) corresponding in steady state to point I (resp. K) on Fig.6.7.

We see that the first solution of Eq.(6.6.7) corresponds to the distribution of cross-

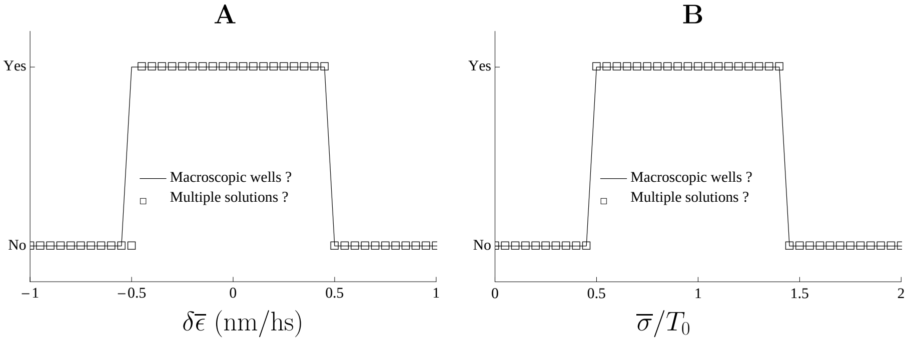

Fig. 6.9 – Existence of multiple solution and macroscopic wells for different loadings. (**A**): hard device. (**B**): soft device. (□): Presence of multiple stationary solutions of Eq.(6.6.12) at different loadings. Solid line: presence of macroscopic wells in the non equilibrium energy landscapes F_y and G_y (see Eqs.(4.2.13) and (4.2.14)) for different loadings.

bridges within the left macroscopic well (dot-dashed lines superimposes on light gray histograms) and the second solution of Eq.(6.6.7) corresponds to the distribution of cross-bridges within the left macroscopic well (dot-dashed lines superimposes on dark gray histograms).

We recall that the overall cross-bridge density is obtained by summing the contributions of both macroscopic wells according to the initial equilibrium probability to be in the left macroscopic well n_y (see Sec.5.4.2). The (○) represent the sum of the histograms which is matched by the solid line representing sum of the two solutions of Eq.(6.6.7). In steady states before and after the step (first and last row of Fig.6.10), the exact equilibrium density of cross-bridges is represented by the (□). It is satisfactorily reproduced by both the full Langevin dynamics and the equivalent weak coupling model.

To summarize, the effect of coupling is correctly taken into account by the non linearity of Eq.(6.6.7). Each of the two solutions of the non-linear problem corresponds to a particular type of half-sarcomere, remaining in a particular macroscopic well (pre-power-stroke or post-power-stroke) characterized by a particular value average value of ϵ_y. In a sense, by using our approximation, we replaced the energy landscape with two macroscopic wells by two single well landscapes separated by an infinite barrier.

The main question regarding this approximation concerns is the precise role played by n_y. Here the kinetics of the system is well reproduced by taking n_y constant (equal to its initial value), meaning that as long as two solutions exist, their respective weights remain equal to n_y and $1 - n_y$. As soon as one of these two solutions disappears and only at that moment, the two densities merge and afterwards coincide with the remaining solution (see the last row of Fig.6.10).

We observe that in the full system, the two distributions can merge *before* the double well structure is lost, by crossing the barrier of the non-equilibrium energy landscape. However, this process is not allowed in the weak coupling approximation as the ϵ_y dimension is not present. Therefore, we expect to see a difference between the two approaches only in the range where the barrier is sufficiently small and the full system allows reequilibration between the macroscopic wells. This occurs only at the boundaries of the existence domain for the macroscopic wells (see Fig.6.9).

To take into account the missing phenomenon in the weak coupling model, one needs to prescribe a dynamics for n_y that would mimic the barrier crossing. One possibility is to model the time dependence of n_y by a jump process between two states, the transition

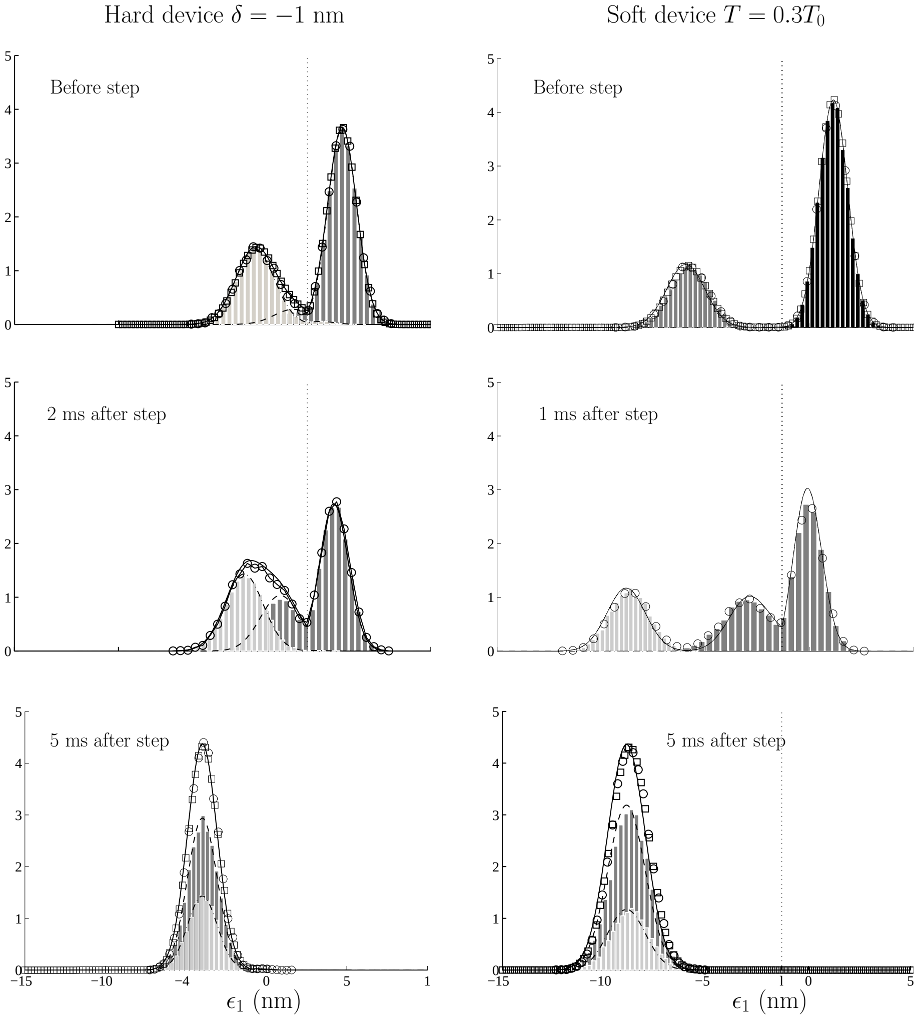

Fig. 6.10 – Comparison between the weak-coupling model and the full Langevin dynamics. We compare the results of Langevin's simulation (histograms) with the solution of (6.6.7) (lines). Left column: snapshots of the cross-bridges probability density after a shortening step of 1 nm in hard device. Right column: snapshots of the cross-bridge probability density following a shortening step of $0.7T0$ in soft device. First line: before the step; second line: 2 ms and 1 ms after the step and third line 5 ms after the step. Distinct histograms represent the trajectories initialized in the left macroscopic well (light gray) and and in the right macroscopic well (dark gray), multiplied respectively by n_y and $1 - n_y$, the stationary probabilities to be in the left hand macro-well and right hand macro-well in isometric contraction. These histogram corresponds to the first (dashed line) and second (dot-dashed line) solution of (6.6.7), with the same normalization by n_y and $1 - n_y$ respectively (see I and K on on Fig.6.7). The solid line corresponds to dashed lines + dot-dashed line and (○) correspond to dark gray + light gray. (□): analytic probability density in thermal equilibrium, represented only before the step (1st) and 5ms after the step (3rd row). The overall probability density of the cross-bridges is the sum of the two solutions of (6.6.7).

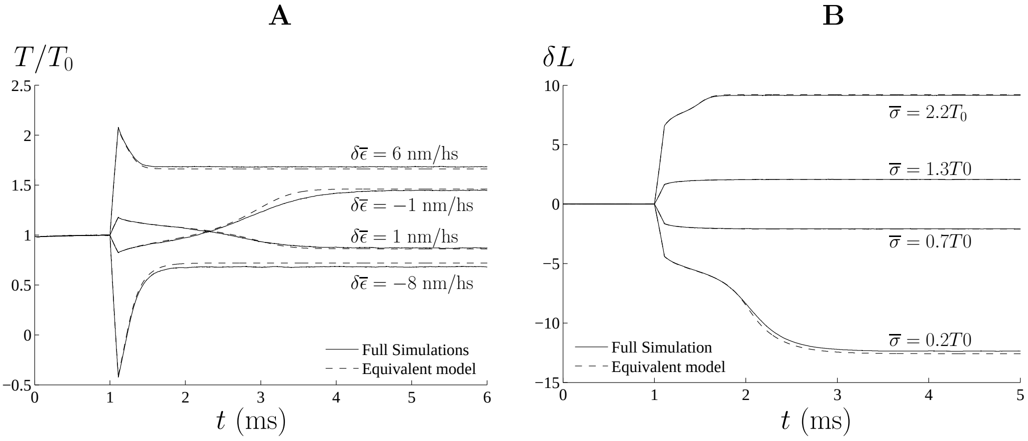

Fig. 6.11 – Mean trajectories of from the weak coupling model compared to the full simulation. (**A**): tension *vs* time in hard device for $\delta\overline{\epsilon} = 6, 1, -1$ and -9 nm/hs. (**B**): elongation *vs* time in soft device for $\overline{\sigma} = 2.2, 1.30.7$ and $0.2T_0$. Solid lines: mean trajectories from the full Langevin simulations (500 realizations). Dashed lines: mean trajectories from the weak coupling model.

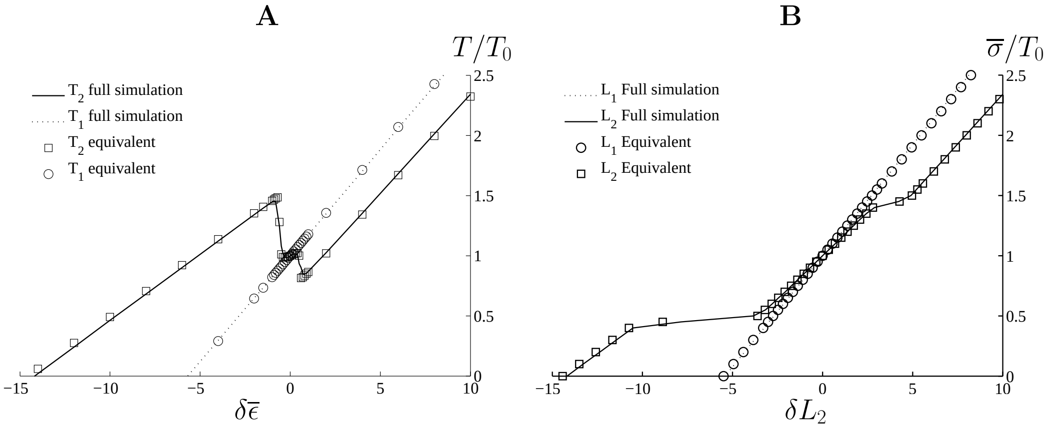

Fig. 6.12 – Equilibrium tension and elongation from the weak coupling model and from the full simulations. (**A**): hard device. (**B**): soft device. Dotted lines: T_1 and L_1 from full Langevin simulations. Solid lines: T_2 and L_2 from full Langevin simulations. (□): T_2 and L_2 from weak coupling equivalent model. (○): T_1 and L_1 from weak coupling equivalent model.

probability being defined by the transition rate corresponding to the macroscopic wells (see Sec.C.2). With our set of parameters, such refinement is not really necessary as the interval where the barrier between the macroscopic wells is comparable to $k_b\theta$ is very narrow.

6.6.5 Results

The results obtained by using the weak coupling approximation for various loading steps are compared with the full Langevin simulations in Figs.6.11, 6.12 and 6.13. The overall kinetics of the full system is very well reproduced but we notice a slight difference in the steady state values (see Fig.6.11). This difference remains small as shown in Fig.6.12 where we present the T_1, T_2, L_1 and L_2 curves obtained from the weak coupling model and from the full model. On the histograms shown in Fig.6.10, one can see this difference particularly in soft device, where we observe a shift of the probability density, the diffusion being correctly reproduced. This difference comes from the fact that the

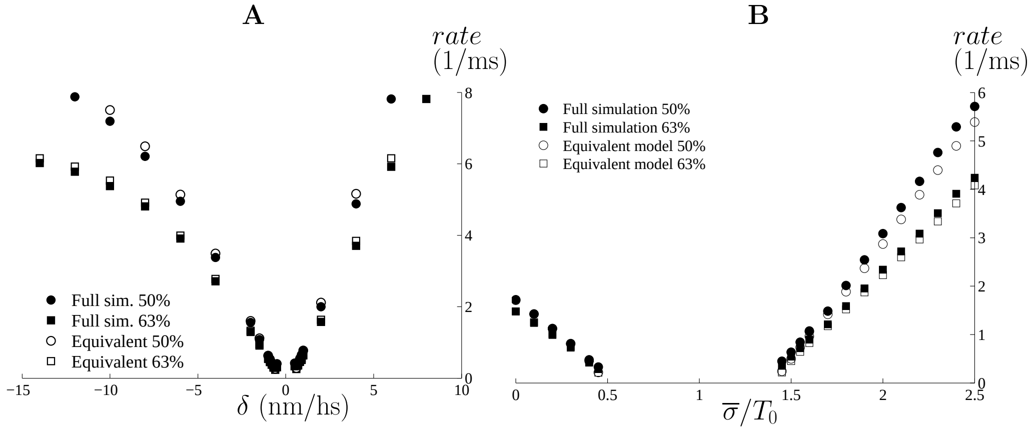

Fig. 6.13 – Rate obtained from the weak coupling model and from the full simulations. (**A**): hard device. (**B**): soft device. (◎ and ○): inverse of the time to reach $0.63\,(T_2 - T_1)$ from T_1 with the full simulations and with the equivalent model respectively. (■ and □): inverse of the time to reach $0.5\,(T_2 - T_1)$ from T_1 with the full simulations and from the equivalent model respectively.

zeros of the drift term in the full system is not exactly the same as the ones in the weak coupling approximation model. We also notice a small difference in the rate curves shown on Fig.6.13. However, in general, compared to both our previous attempts (see Fig.6.6), the weak coupling approximation gives much better results.

6.7 Further developments

Before concluding this Chapter, we can discuss briefly another (ongoing) attempt to obtain an efficient reduced model. Instead of restricting ourselves to a one dimensional reduced model for ϵ_y (like in Sec.6.2) or for ϵ_i (like in Sec.6.6) we can try now to derive a two-dimensional model which would targets the time evolution of the joint probability density for ϵ_y and ϵ_1. Following the method proposed in Sec.6.2, we start with the following set of SDE:

$$\begin{cases} d\epsilon_i^t = b\left(\epsilon_i^t, \epsilon_y^t\right) dt + \sqrt{2\beta^{-1}} dB_i^t, \ \text{for } 1 \le i \le N \\ d\epsilon_y^t = b_y\left(\epsilon_1^t, \dots, \epsilon_N^t, \epsilon_y^t, t\right) dt + \sqrt{2\beta^{-1}} \sum_{i=1}^{N} \left(h_i dB_i^t\right). \end{cases}$$

which corresponds to the following Fokker–Planck equation:

$$\partial_t p\left(\underline{\epsilon}, t\right) = \sum_{i=1}^{y} \partial_i \left(-b_i\left(\underline{\epsilon}, t\right) p\left(\underline{\epsilon}, t\right) + \frac{1}{2} \sum_{j=1}^{y} \left(\underline{\underline{\omega}} . \underline{\underline{\omega}}^T \right)_{ij} \partial_j p\left(\underline{\epsilon}, t\right) \right)$$

We then integrate with respect to $\epsilon_2, \dots, \epsilon_N$ and find:

$$\begin{aligned} \partial_t p\left(\epsilon_1, \epsilon_y, t\right) &= \partial_1 \left(-b_1\left(\epsilon_1, \epsilon_y\right) p\left(\epsilon_1, \epsilon_y, t\right) + \beta^{-1} \partial_i p\left(\epsilon_1, \epsilon_y, t\right)\right) \\ &+ \partial_y \left(- \int \cdots \int b_y\left(\epsilon_1, \epsilon_y, t\right) p\left(\epsilon_1, \dots, \epsilon_N, \epsilon_y, t\right) d\epsilon_2, \dots, d\epsilon_N + \beta^{-1} \overline{h} \partial_y p\left(\epsilon_1, \epsilon_y, t\right) \right) \\ &+ 2\beta^{-1} h_1 \partial_{1y} p\left(\epsilon_1, \epsilon_y, t\right). \end{aligned}$$

where h_1 and $\overline{h}$ are given by Eqs.(6.2.5) and (6.2.13). To simplify the integral term, we write:

$$p\left(\epsilon_1,\ldots,\epsilon_N,t\right)=p\left(\epsilon_2,\ldots,\epsilon_N|\epsilon_1,\epsilon_y,t\right)p\left(\epsilon_1,\epsilon_y,t\right) \tag{6.7.1}$$

which is a direct generalization of Eq.(6.2.2), and substitute into the integral. We obtain:

$$\begin{aligned}\partial_t p\left(\epsilon_1,\epsilon_y,t\right)=\partial_1&\left(-b_1\left(\epsilon_1,\epsilon_y\right)p\left(\epsilon_1,\epsilon_y,t\right)+\beta^{-1}\partial_1 p\left(\epsilon_1,\epsilon_y,t\right)\right)\\&+\partial_y\left(-\overline{b}_y\left(\epsilon_1,\epsilon_y,t\right)p\left(\epsilon_1,\epsilon_y,t\right)+\beta^{-1}\overline{h}\partial_y p\left(\epsilon_1,\epsilon_y,t\right)\right)\\&\qquad+2\beta^{-1}h_1\partial_{1y}p\left(\epsilon_1,\epsilon_y,t\right).\end{aligned}$$

where

$$\overline{b}_y\left(\epsilon_1,\epsilon_y,t\right)=\int\cdots\int b_y\left(\epsilon_1,\ldots,\epsilon_y\right)p\left(\epsilon_2,\ldots,\epsilon_N|\epsilon_1,\epsilon_y,t\right)d\epsilon_2,\ldots,d\epsilon_N. \tag{6.7.2}$$

Needless to say that as in Sec.6.2, a closure relation is needed to determine $p\left(\epsilon_2,\ldots,\epsilon_N|\epsilon_1,\epsilon_y,t\right)$. We are presently trying different plausible options.

Conclusions

The dynamics of our systems can be viewed as a combination two phenomena: the individual behavior of a cross-bridge at fixed ϵ_y and collective interaction of many parallel cross-bridges exposed to the mean field.

In an attempt to compute an effective drift affecting the mesoscopic degree of freedom ϵ_y, we simplified the dynamics of the single cross-bridge by assuming thermal equilibrium at the microscale. This lump model produces an effective drift at the mesoscale and allows one to compute the effective diffusion coefficient as a function of the coupling parameter. Although the resulting reduced model gives satisfactory results, the kinetics of the full Langevin's system cannot be reproduced with sufficient accuracy because we oversimplify the dynamics of individual cross-bridges.

Therefore we designed another model based on a non-linear equation describing the evolution of the probability density for a single cross-bridge ϵ_i with an effective drift that incorporates the non-local interactions with the mean field. This effective model effectively reduces ∼100 Langevin's equation into a PDE and remarkably accurately reproduces the mechanical response of our system.

Chapter 7

Realistic model of a half-sarcomere

In this Chapter we match quantitatively the experimental results with the predictions of our model. To do so we need to identify the essential experimental data on muscle fibers and propose a mechanical interpretation of phase 1 and 2 of the quick recovery. After the parameters are matched to available experimental data, we present two possible interpretations of the T_2 curve and discuss the power-stroke controversy. An interesting conclusion of our parameter fit is that the single half-sarcomere behaves as 'cold system'. In the last section, we present the results of stochastic simulations of the kinetics of the quick recovery end expose the quantitative difference of the response in hard and soft devices.

Contents

Non dimensional parameters				Dimensional parameters					
λ_1	0.29	β	85	k_1	1.33	pN.nm^{-1}	κ_f	150	pN.nm^{-1}
λ_0	0.6	N	86	k_0	0.6	pN.nm^{-1}	$k_b\theta$	3.82	zJ
λ_f	0.53	$\overline{T_0}$	14.7	κ	3.29	pN.nm^{-1}	T_0	480	pN
$\overline{l}_s$	-0.131	$\overline{l}_h$	-0.093	a	10	nm	l_h	-0.93	nm
$\overline{\epsilon}^0$	0.42			$\overline{\epsilon}^0$	4.2	nm	l_s	-1.31	nm
				η	0.38	ms.pN.nm^{-1}			

Tab. 7.1 – **Parameters of the model**. The experimental data used to find this set of parameters can be found in (Holmes and Geeves, 2000; Linari et al., 1998, 2009; Piazzesi et al., 2007). They correspond to frog muscle (*rana temporaria*).

7.1 Identification of parameters

In this section, as we try to adjust the parameters of the model to the experimental data, we will start writing the non-dimensional quantities again with over-lines to avoid confusion with dimensioned quantities. The parameters of the non-dimensional model are listed in table 7.1.

The difficulty of the parameter identification lies in the fact that the experimental results vary depending on the animal species. Thu, most of quick recovery experiments are done on frog or rabbits, for instance, the experimental results presented in Chap.2 (see Fig.2.5) are obtained with frog *rana esculenta*. However, the most documented frog type in literature is *rana temporaria*. We therefore chose to adjust our parameters to this type of muscle and mostly rely on the experimental results from (Holmes and Geeves, 2000; Linari et al., 1998, 2009; Piazzesi et al., 2007).

7.1.1 Parameter found directly in the literature

The first parameter a will be obtained from structural analysis of myosin II protein. We have shown in Chap.2 (see Figs.2.1 and 2.2) that the tertiary structure can be found in two conformations forming an angle of ∼70°.This corresponds to an axial displacement of the lever arm end of ∼10nm (Dominguez et al., 1998; Holmes and Geeves, 2000; Piazzesi et al., 1992; Rayment et al., 1993) (see Fig.2.2). We therefore choose to set the characteristic length in our model to $a = 10$ nm.

The absolute temperature θ is set to 277.15 °K which correspond to 4 °C. This is the temperature at which most experiments on frog muscles have been done (Piazzesi et al., 1992).

7.1.2 Linear regimes of the $T_2(\delta)$ curve

We have shown in the previous Chapters that for large shortening (resp. stretching), the equilibrium tension $\overline{T}_2$ coincides with the tension generated by configuration $(1,0,0)$ (for large shortening) and $(0,0,1)$ (for large stretching). We denote the tension in these regimes as $\overline{T}_2^-$ and $\overline{T}_2^+$. Using equation (3.1.12) with $n_1 = 1$ we obtain:

$$\overline{T}_2^-(\overline{\epsilon}) = \frac{\lambda_1\lambda_f}{\lambda_1+\lambda_f}\left(\overline{\overline{\epsilon}}+1\right) \tag{7.1.1}$$

$$\overline{T}_2^+(\delta) = \frac{\lambda_0\lambda_f}{\lambda_0+\lambda_f}\overline{\epsilon} \tag{7.1.2}$$

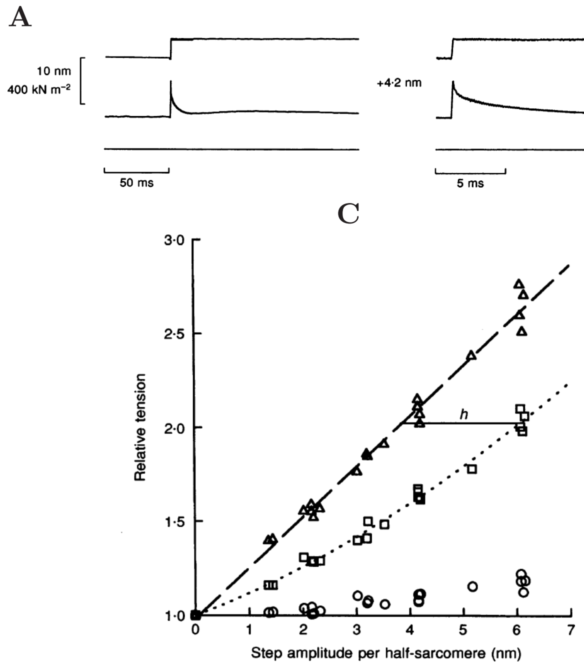

Fig. 7.1 – **Quick recovery in stretching experiments** adapted from Piazzesi et al. (1997). (**A**) and (**B**) show the evolution of length (upper trace) and tension (lower trace) with time. On (**B**), the time scale is expanded to resolve the quickest part of the transient. Note that unlike in shortening (see Fig.2.3), the end of the quick recovery is not marked by a clear plateau on the tension time curve. (**C**) shows an extrapolation of the T_2 curve in stretching, obtained after a multi-exponential analysis of the tension transients for different step sizes. △: T_1 curve. ◎: T_2 measured by a linear extrapolation of the tension-time curve and □ indicates the points corresponding to the "reverse power-stroke" obtained after the multi-exponential analysis. We used the slope of this extrapolated T_2 to fit the parameters of the model.

Experimentally, the tension $\overline{T_2^-}$ drops to 0 when a step δ_2 is applied to the initial elongation $\overline{\epsilon}^0$. Therefore we can write:

$$\overline{\epsilon}^0 = -1 - \overline{\delta}_2. \tag{7.1.3}$$

Denote the slope of the $\overline{T_2^-}$ curve as $s_{\overline{T_2^-}}$. Experimentally, the T_2 curves are normalized to the tension in the isometric contraction T_0 (see Fig.2.5). Hence:

$$\overline{s}_{T_2^-} = s_{T_2^-}\frac{T_0}{\kappa} = N\frac{\lambda_1\lambda_f}{\lambda_1+\lambda_f}. \tag{7.1.4}$$

In stretching, the identification of T_2 points is more difficult than in shortening as no characteristic T_2^- related plateau can be clearly observed on the tension-time curves a few ms after the step (Ford et al., 1977; Martyn et al., 2002; Piazzesi et al., 1992; Ranatunga et al., 2002). Nevertheless, G. Piazzesi *et al.* in (Piazzesi et al., 1997) have extracted from a multi-exponential analysis of the recovery process, the curve which they attributed to the end of the reversal of the power-stroke process (see Fig.7.1). We identify the slope of this theoretical curve ($s_{T_2^+}T_0/\kappa$) with the stiffness of the configuration $(0, 0, 1)$. Therefore, we can write:

$$\overline{s}_{T_2^+} = N\frac{\lambda_0\lambda_f}{\lambda_0+\lambda_f}. \tag{7.1.5}$$

7.1.3 Stiffness measurements

In our model, the overall elasticity is provided by both filaments (κ_f) and the cross-bridges. The latter include the linear spring κ and the elasticity brought by the double well potential (κ_1, κ_0). So far, we have not mentioned the viscosities of these components. The question of viscoelasticity is crucial for the interpretation of the experimental results: if the viscosity of one element is very high compared to others, this element will not deform during the fast loading (visco-elasticity). The first question is then: which of our mechanical elements will participate in the elastic response to sudden length changes ?

It is clear from Fig.2.5 that the stiffness associated with the T_1 curve and the stiffness of the linear part of the T_2 curve are different. So far this feature is not reproduced by any of the existing models before (Marcucci and Truskinovsky, 2010). Also, from the length clamp experiment in stretching, we see that the stiffness of T_2^+ response is different from the stiffness of T_2^- response (Piazzesi et al., 1997). This suggests an asymmetry in the double well potential ($\kappa_1 \neq \kappa_0$), which was first explored in (Marcucci and Truskinovsky, 2010).

Let us suppose, for the time being, that every component of our half-sarcomere participates in the elastic response. In this case, one expects the instant stiffness measured in isometric contraction (corresponding to the slope of T_1 curve) to be different from the instant stiffness measured during or after the quick recovery as the relative populations in wells 1 and 0 have changed. Notice however that in double step experiments done in (Lombardi et al., 1992), the stiffness measured after a second step is applied following the the quick recovery indicates less than 2% difference with the original isometric stiffness obtained in the first step. This experimental results suggests that the motion of the heads in the double well potential ($\overline{\epsilon}_i$) is not involved in the building of the instant stiffness. Hence, the viscous force of kinetic origin associated with the conformational change (degree of freedom $\overline{\epsilon}_i$) is high compared to other viscous forces. Therefore we need to take into account only the contributions due to the linear spring (κ) inside the cross-bridges and due to the series spring (κ_f).

Experimentally, it is possible to control the chemical environment inside the fiber by removing the cell membrane (‘skinning’). In particular, this procedure allows one to perform length step experiments at various calcium concentrations pCa [1]. We recall that calcium ions bind to tropomyosin complex to allow the attachment of myosin heads to actin (see Fig.1.9). Therefore, by changing the calcium environment, one can change the number of attached motors (N). Our Fig.7.2(A) shows that the active force decreases when calcium concentration is reduced (pCa increases), which is coherent with a reduction of the number of cross-bridges. Now, if we apply fast length steps of various amplitudes under different calcium concentrations, we can see that the instant elasticity changes with calcium concentration and so with the number of cross-bridges (see Fig.7.2(B)).

Based on these arguments, we assume that the purely elastic response in our model, is given by Eq.(4.2.21) where the mean position of the cross-bridges, $\langle \epsilon_i \rangle_h$ is maintained at its initial value:

$$\overline{T}\left(\overline{\delta}\right) = N\frac{\lambda_f}{1+\lambda_f}\left(\overline{\epsilon}^0 + \overline{\delta} - \langle \overline{\epsilon}_i \rangle_h^0\right) \tag{7.1.6}$$

where $\langle \overline{\epsilon}_i \rangle_h^0$, is the mean position of a cross-bridge in the double well potential during isometric contraction (before the step). The relation (7.1.6) holds also in soft device

---

[1] pCa$= -\log\left(\left[Ca^{2+}\right]\right)$

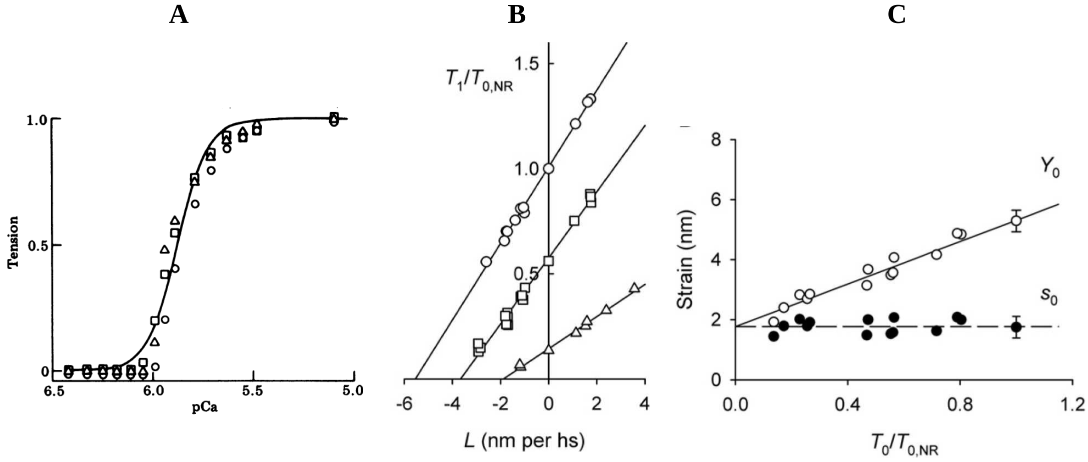

Fig. 7.2 – Influence of calcium concentration of the elasticity of the fiber. (**A**): from Brandt et al. (1980). Force-pCa relation: The isometric tension is measured for different calcium concentration. Changing the calcium modifies the number of attached motors. Experiments done on skinned rabbit psoas fibers and the different symbol represent different fibers. The tension is normalized to the tension at saturating pCa. (**B** and **C**): from (Linari et al., 2009) where the number of attached motors is modified using BTS (N-benzyl-p-toluene sulfonamide) rather than calcium but the effect is the same. (**B**): Measurement of T_1 at different BTS concentration, open circles represent the control case. Experiments made on frog (*rana temporaria*). The slopes are different showing that the elastic spring of the cross-bridges participates in the instant elastic response. The intercept of different T_1 curves with the abscissa, noted $-Y_0$, is reported on (**C**) against the isometric tension (open circles). The filled circles are obtained by subtracting the filament elongation according to Eq.(7.1.8). This shows that the strain in the elastic spring of the cross-bridges (noted s_0) does not depend on the number of attached motors

where the tension $\overline{\sigma}$ is imposed and we where measure the evolution of $\overline{\delta}$ so the T_1 and L_1 curves are the same with this hypothesis.

Now, Fig.7.2B, shows the T_1 curves obtained at different calcium concentrations. We call $-Y_0$, the intersection of the linear extrapolation of T_1 experimental curve with abscissa. Based on Fig.7.2B, one can anticipate a relation $T_0 = K(T_0)Y_0$, between Y_0 and T_0. Here K has the dimension of a stiffness and depends on T_0. Our Fig.7.2C (○) shows that this relation is in fact linear but surprisingly the value of Y_0 at $T_0 = 0$ is not equal to zero. Hence the relation is of the type: $Y_0 = \alpha + \gamma T_0$ where α and γ are constants. We can rewrite Eq.(7.1.6) with dimensioned quantities in the following way:

$$Y_0 = \frac{T_0}{\kappa_x N} + \frac{T_0}{\kappa_f}. \tag{7.1.7}$$

Next, we notice that in equilibrium, the tension T_0 is equal to the sum of the cross-bridges spring forces. Hence, T_0 is proportional to N: $T_0 = NF_0$ and Eq.(7.1.7) becomes:

$$Y_0 = \frac{F_0}{\kappa_x} + \frac{T_0}{\kappa_f}. \tag{7.1.8}$$

From (7.1.8) we can identify the slope of the $Y_0 - T_0$ relation with the compliance of the myofilaments ($1/\kappa_f$). The value from Fig.7.2C, is $\kappa_f = 166$ pN.nm^{-1} which is in agreement with the independent estimates obtained using X-ray diffraction technique (Dobbie et al., 1998; Huxley et al., 1994; Piazzesi et al., 2002b; Reconditi et al., 2004; Wakabayashi et al., 1994). For our simulations, we choose a slightly smaller value $\kappa_f = 150$ pN.nm^{-1}, proposed in (Piazzesi et al., 2007).

Another interesting piece of information recoverable from the $Y_0 - T_0$ relation is that the force of isometrically contracting myosin heads is a constant F_0. Similarly, the interception of the $Y_0 - T_0$ curve with the Y-axis (F_0/κ) is the strain in the linear spring of the cross-bridges (denoted by s_0 and represented with solid circles on Fig.7.2). Therefore, we can conclude that, in the steady state, the force produced by each head is an intrinsic characteristic which does not depends on the number of attached motors.

Going back to non-dimensional quantities, we can use Eq.(7.1.6) to identify the slope of the T_1 curve in control condition (saturated pCa) with the parameters of our model as follows:

$$\overline{s}_{T_1} = s_{T_1} T_0 = N \frac{\lambda_f}{1+\lambda_f} \text{ which leads to the final estimate:}$$

$$\lambda_f = \frac{s_{T_1}}{N - s_{T_1}} \tag{7.1.9}$$

Stiffness in *rigor mortis*

It is known that when ATP is depleted from the medium all 300 myosin heads are bound to actin (*rigor mortis*). Stiffness measurements in *rigor* have also been performed in (Linari et al., 2007, 1998) giving the value which we denote by $s^R_{T_1}$. Then Eq.(7.1.9) can be rewritten as:

$$\lambda_f = \frac{s^R_{T_1}}{N\left(1 - \frac{s^R_{T_1}}{N_R}\right)} \text{ with } N_R = 300. \tag{7.1.10}$$

Now, if we write the definition of the non-dimensional isometric tension:

$$\overline{T_0} = \frac{T_0}{\kappa_x a}, \tag{7.1.11}$$

We can solve the system of Eq. (7.1.4) to Eq.(7.1.11), knowing the filament stiffness κ_f and find the values all the non-dimensional parameters except l (see Tab.7.1).

7.1.4 Hard device experiments in *rigor mortis*

We have seen in Sec.7.1.3 that one can assume that the only viscous component in our system model is the bi-stable snap-spring. We denote by η the drag coefficient associated with the variables ϵ_i. Once again, the parameter η can be viewed as an internal friction in the rotating part of the converter domain. Its value can be estimated from the length step experiments performed in rigor, where it is known that the cross bridges are all in their post-power-stroke configuration (Holmes and Geeves, 2000; Rayment et al., 1993; Reconditi et al., 2003).

Indeed, let us assume that all the ~ 300 cross-bridges are attached and that the cross bridge mechanisms are initially all in the post-power-stroke state. If we apply a fast length step to this system, we expect a single exponential relaxation with a characteristic time of η/κ.

Fig.7.3 shows the experimental results indicating the visco-elastic response to different step sizes (the data were provided by M.Linari from University of Florence). One can show that the value $\eta \approx 0.38$ ms.pN/nm fits very well the experimental relaxation curves (see Fig.7.3). This value of the drag coefficient corresponds to a characteristic time of ~ 0.1 ms. Note that this value will not affect the conclusions of our numerical experiments since it will be hidden in the scale of the time axis. A better estimate of the drag coefficient is certainly

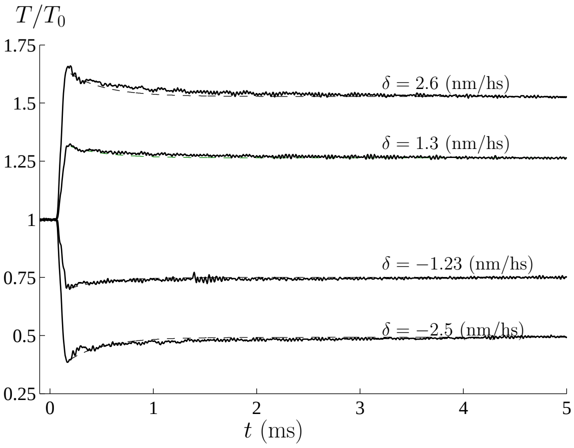

Fig. 7.3 – **Rigor transient** (continuous lines provided by M.Linari from the University of Florence) fitted with single exponential corresponding to the visco-elastic response of our system with all 300 cross-bridges attached in their post-power-stroke configuration (dashed lines). The value of the drag coefficient found is $\eta = 0.38$

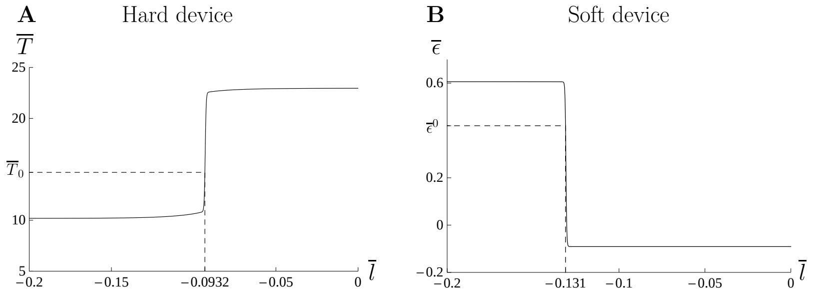

Fig. 7.4 – **Fit of $\overline{l}$ in hard and soft device**. (**A**): The total elongation is fixed to the isometric elongation $\overline{\epsilon}^0$ and the isotherm tension is computed at different values of $\overline{l}$. From experiment, the isometric tension is $\overline{T}_0 = 14.7$. We used a simple dichotomy algorithm to find $\overline{l} = 0.0932$. (**B**): The total tension is set to $\overline{T}_0 = 14.7$ and the total elongation ϵ in isotherm is represented for different values of $\overline{l}$. The value of $\overline{l}$ corresponding to $\epsilon = 0.42$ is -0.131.

possible, but we will see that even this coarse fitting gives already good predictions for the rate of the quick recovery (see Sec.7.4).

7.1.5 Isometric contraction: determination of l

In isometric contraction, our model must be able to reproduce the steady state tension $\overline{T_0} = 14.7$. As we do not take into account the attachment-detachment process, we cannot model the isometric contraction in full detail by taking into account that the system is maintained out of equilibrium by the constant ATP supply. Nevertheless, we know that in steady state isometric contraction the tension is constant, which suggest that even if the individual cross-bridges are constantly attached and detached, the number of attached ones remains constant. Also X-ray diffraction measurements suggests that the average orientation of the heads does not change during isometric contraction (Dobbie et al., 1998; Irving et al., 2000). Therefore, we can reasonably assume that the tension T_0 corresponds to the isotherm T_2 at $\overline{\epsilon} = \overline{\epsilon}^0$. This hypothesis may be reconsidered in a broader model that also takes into account the attachment-detachment process.

In Fig.7.4(A) we show the dependence of $\overline{T_0}$ on the value of $\overline{l}$. We use a simple dichotomy algorithm to specify the value of $\overline{l}$ which ensure that $\overline{T}_0 = 14.7$. The result is

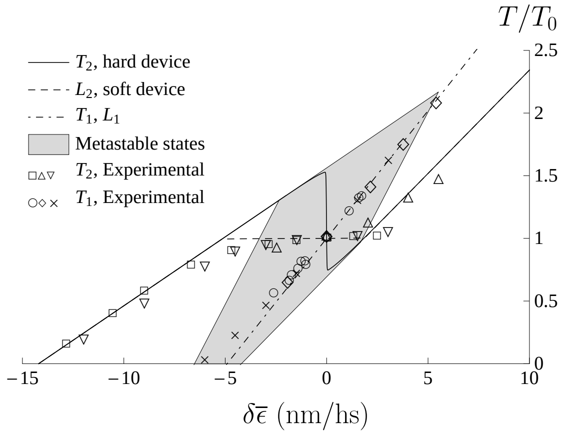

Fig. 7.5 – Isotherms fitted to experimental data. Representation of the isotherm quantities T_2 (continuous line) and L_2 (dashed line) computed using Eq.(4.2.15) and (4.2.17) and the elastic response T_1, L_1 (dot-dashed line) computed using Eq.(7.1.6), compared to experimental data. Experimental points are taken from Ford et al. (1977)(T_1: ×, T_2: ▽), Brunello et al. (2007)(T_1: ◇, T_2: △) and Linari et al. (2009)(T_1: ◎, T_2: □). The tension isotherm (continuous line) presents a sharp transition between 2 linear regimes corresponding the the global minimum. This is due to the high value of β ($\beta = 85$). The half-sarcomere behaves like a 'cold system'. For the same reason the response in soft device shows a plateau at $T = T_0$.

$l_h = -0.093$.

We apply the same procedure in soft device to find the value of $\overline{l}$ which is equivalent to $\overline{\epsilon}^0 = 0.42$. In this case we find $\overline{l_s} = -0.131$ (see Fig.7.4B). This discrepancy means that, at the level of a single half sarcomere, the isometric contraction does not represent the same tension-elongation state in hard and soft devices. At this stage of the work, we cannot conclude definitively on the value of l. However, this question will be resolved in Sec.8.4.1, where we study a more general system representing a chain of half-sarcomeres.

We observe that in both hard and soft devices, the fit data is very sensitive to the value of $\overline{l}$ because a small change in $\overline{l}$ may lead to a very large change in $\overline{T}_0$ (resp. $\overline{\epsilon}^0$) (see Fig.7.4). This sensitivity has its origin in the large value of β ($\beta = 85$) obtained after fitting other parameters. Indeed such a low temperature makes the transition between the linear regimes of T_2 (resp. L_2) very sharp indicating that the half-sarcomere is a 'cold' system with very coherent behavior (see next section).

7.2 Equilibrium response

7.2.1 Isotherms

The linear regimes of the T_2 curve correspond to the tension in almost homogeneous configurations $(1, 0, 0)$ and $(0, 0, 1)$. In between these linear regimes, the system evolves through in homogeneous or non-affine configurations. The nature of the configurations may be different depending on our interpretation of the T_2 curve.

In experiments, the tension T_2 is associated with a plateau on the tension-time curve occurring a few millisecond after the step. This short-time steady state, is compatible with the idea that T_2 corresponds to an equilibrium isotherm.

On Fig.7.5, we compare the isotherms computed in hard and soft device (continuous line and dashed line) with experiments from Ford et al. (1977)(T_1: ×, T_2: ▽), Brunello et al. (2007)(T_1: ◇, T_2: △) and Linari et al. (2009)(T_1: ◎, T_2: □). The experimental points are different from those presented in the introduction (see Fig.2.5) because

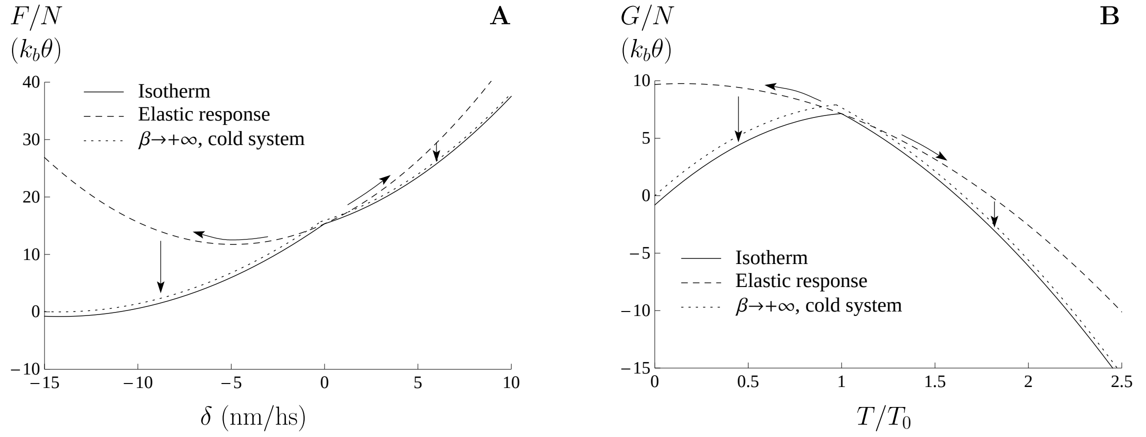

Fig. 7.6 – Free energy in isotherms. (**A**): hard device. (**B**): soft device. The isotherms (continuous lines) are computed using Eq.(4.1.5) and (4.1.6). The dashed lines represent the energy in the elastic response corresponding to T_1 (resp. L_1) computed from Eq.(7.1.6). The dotted lines represent the global minima given by Eq.(3.1.32) and (3.1.33) corresponding to the limit $\beta \to \infty$ in our system. The arrows indicate example of loading path in both stretching and shortening.

they do not correspond to the same frog species (*rana esculenta* in introduction and *rana temporaria* here). We have therefore adjusted our model to *rana temporaria*, which is better documented than other types of frog muscles. However, we were not able to find experimental L_2 points. The gray region represents the existence domain for the metastables states at $\theta = 0$ (see Sec.3.1.2) and the dot dashed line is obtained using Eq.(7.1.6) which represents the elastic response of the filament and the linear spring of the myosin head in both hard and soft devices.

As it is expected from the fitting procedure, both hard and soft device isotherms fit the linear segments of the T_2 curve. Since our value of β is large compared to 1, the isotherm is very close to the behavior of the system following the global minimum of the energy at $\theta = 0$ (see Sec.3.1.4). On the one hand, we observe, in hard device, a sharp transition between the two linear regimes on the T_2 curve. This is incompatible with experimental data showing a plateau (see solid line on Fig.7.5 compared to △, ▽ and □). On the other hand, our L_2 curve does contain a plateau (dashed line). We recall that the soft device value of l is different from the hard device value. If one had taken $l = -0.093$ (the hard device value) for both case, the plateau of the L_2 curve would have been at $T/T_0 \approx 1.25$ rather than 1.

In general, after all parameters have been adjusted to experimental data, the behavior of our half-sarcomere is very close to the purely mechanical system at zero temperature, with a sharp transition between the two homogeneous configurations $(1, 0, 0)$ and $(0, 0, 1)$ (see Fig.7.5 and 7.6). However, this does not mean that the role of temperature can be neglected. Indeed, when $\beta \to \infty$ we still observe in thermally equilibrated system a transition between the wells separated by a barrier (which may take a long time), while the purely mechanical system at $\theta = 0$ cannot escape a metastable state as long as it exists (see the gray region on Fig.7.5). We already encountered the same difference ($\theta \to 0$*vs.* $\theta = 0$) in the model problem of escaping from a well (see Chap.5): when temperature is finite the probability of exiting an attractor is equal to 1 while if $\theta = 0$ the trajectory always end up at the attractor if the initial position is in the domain of attraction (see *e.g.* Schuss, 2010, Chap.6).

7.2.2 Variation of parameters

The parameters listed in Tab.7.1 enabled us to reproduce the linear parts of the T_2 and L_2 curves and to capture the isometric tension in thermal equilibrium. However, the values found in literature and the data from experiments, carry some uncertainty. In particular, we are interested in the key values of a and κ, which are a subject heated debate in the community (see Sec.2.3.2). The combination of those two parameters gives the value of β, that (as we shown in Chap.4) controls the main conclusion that the power-stroke mechanism operates at negative stiffness. The values in Tab.7.1 correspond to measurements presented in (Piazzesi et al., 2007). However, stiffness values and power-stroke amplitudes can also be taken from other sources.

Notice that in our model, the isometric tension T_0 is necessarily located between the tension generated by a full post-power-stroke half-sarcomere and the tension generated by a full pre-power-stroke half-sarcomere:

$$N\frac{\lambda_0\lambda_f}{\lambda_0+\lambda_f}\bar{\epsilon}^0 \leq T_0 \leq N\frac{\lambda_1\lambda_f}{\lambda_1+\lambda_f}\left(\bar{\epsilon}^0+1\right) \tag{7.2.1}$$

Using Eq.(7.1.5) and (7.1.3), we obtain the lower bound for a:

$$a \geq -\left(\delta_2+\frac{1}{s_{T_2^+}}\right) \tag{7.2.2}$$

Now from (Piazzesi et al., 1997), the slope of the T_2 curve in stretching is 1.5 times higher than in shortening, leading to $a > 8.14$ nm. If we take the same slope in both stretching and shortening we obtain $a > 5.5$ nm which is closer to the values obtained from the single molecule experiments (see Sec.2.3.2). We can also obtain a lower boundary for κ by requiring that λ_0 and λ_1 are strictly between 0 and 1. This leads to the estimate:

$$\kappa > \frac{s^R_{T_1}}{N_R}\left(1-\left(\frac{s^R_{T_1}}{\kappa_f}\left(1-\frac{\kappa_f}{\max\left[s_{T_2^+},s_{T_2^-}\right]T_0}\right)\right)+\frac{-\delta_1 s^R_{T_1}}{T_0}\right)^{-1}. \tag{7.2.3}$$

In addition, with a given set (κ, a), and with all other parameters listed in Tab.7.1, there must be a value of l for which $T_2\left(\bar{\epsilon}^0\right) = T_0$. This condition has been tested numerically.

On Fig.7.7A and B, we show, in gray regions, the domains of admissible values for a and κ with all other parameters listed in Tab.7.1 and with $s_{T_2^+}/s_{T_2^-} = 1$ (see A) or 1.5 (see B). The isolines indicate the values of β. For each cases, we represent on (C) and (D) the T_2 curves corresponding to the selected points indicated on the parametric diagrams (A) and (B).

When $s_{T_2^+}/s_{T_2^-} = 1$ (see A and C), for low values of β (point I), the T_2 curve exhibits a plateau which is not localized a T_0 as expected from experiments. For higher β (see points J and K) a region with negative slope is always present at T_0. Meanwhile, for $s_{T_2^+}/s_{T_2^-} = 1.5$, the negative slope persists over the whole domain of admissible κ and a and for the set of parameters obtained from (Piazzesi et al., 2007) (point R). Moreover, the T_2 curve in almost all admissible region shows a sharp transition between the two linear and remains very close to the global minimum.

Next we mention that the value of the cross-bridge stiffness κ obtained by G.Piazzesi *et al.* in (Piazzesi et al., 2007) is $\sim$ 3.3 pN.nm^{-1}; it is higher than the highest value measured using single molecule techniques, (A. Lewalle report a value of 1.7 pN.nm^{-1} form rabbit muscle (Lewalle, 2008); see also our discussion in Sec.2.3.2). More recently G.

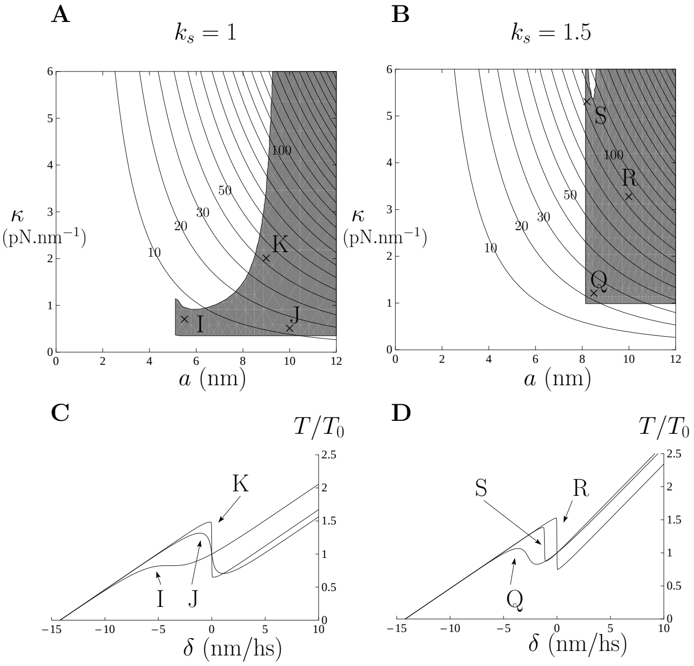

Fig. 7.7 – **Influence of a and κ on the T_2 curve**. On (**A**) and (**B**), we show the domain of admissible values of a and κ (gray region) for $k_s = 1$ (**A**) and $k_s = 1.5$ (**B**), where $k_s = s_{T_2^+}/s_{T_2^-}$. The isolines show the values of β. The T_2 curves (**C**) and (**D**) correspond to the point indicated on (**A**) and (**B**). I: $\kappa = 0.7$, $a = 5.5$; J: $\kappa = 0.5$, $a = 10$; K: $\kappa = 2$, $a = 9$. Q: $\kappa = 1.2$, $a = 8.5$; R: $\kappa = 3.27$, $a = 10$; K: $\kappa = 5.3$, $a = 8.2$. R corresponds to the experimental data from (Piazzesi et al., 2007). Other parameters are listed in Tab.7.1.

Offer and K.W. Ranatunga mention that, the experimental uncertainties in the stiffness measurements may lead to an overestimate of κ and suggest to use the intermediate value 2pN.nm^{-1} (Offer and Ranatunga, 2010). This value, would also lead to negative stiffness with our model.

To summarize, we have shown here that the presence of negative stiffness on the equilibrium T_2 curve is certain over a wide range of realistic sets of parameters in the present model. Given this instability, however, the force recovery for both small shortening and small stretching is the strongest. For instance, upon stretching, the equilibrium force quickly drops which can greatly help to avoid damaging the fiber by a sudden elongation. Such strongly non-linear response appears to be essential for muscle activity. Mechanical mechanisms may be designed to operate exactly in the domain of negative stiffness. We shall discuss this issue more thoroughly in the conclusions section of this work (see Chap.8.4.4)

7.2.3 Adiabats

We have seen in the previous section that, if the L_2 and T_2 curves are interpreted as isotherms, the state of the system after the quick recovery corresponds to the state of the cold system at and, in particular, we do not obtain the plateau on the T_2 curve. We would like now to explore the possibility of T_2 and L_2 being adiabats instead of isotherms, since it is known that adiabats in bi-stable chains provides ‘smoother’ response than isotherms (see *e.g.* Efendiev and Truskinovsky, 2010).

Along adiabats, the entropy S is constant so we have to compute for a given loading the

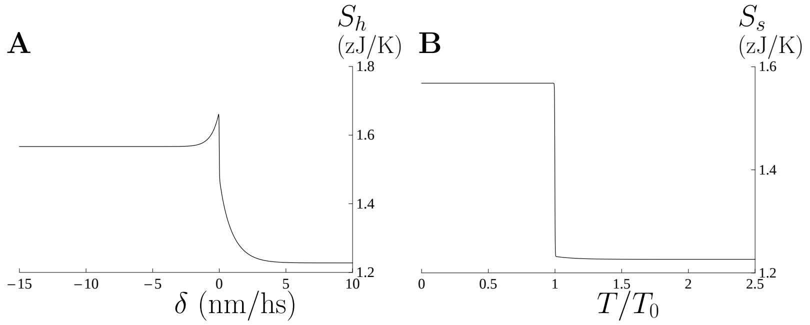

Fig. 7.8 – **Evolution of entropy along isotherms**.(**A**): hard device. (**B**): soft device. Entropy are computed using Eq.(4.1.11) and (4.1.12).

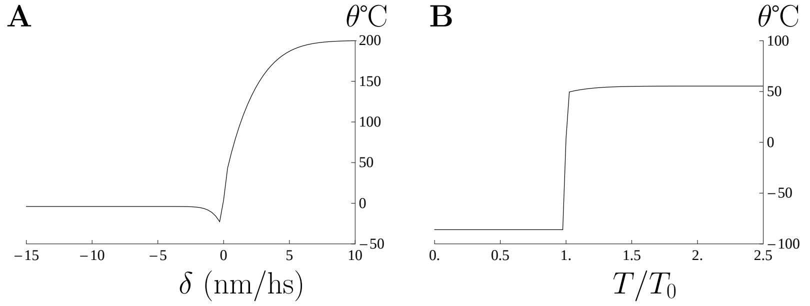

Fig. 7.9 – **Evolution of temperature along adiabats**. (**A**): hard device. (**B**): soft device. The results are computed using equation Eq.(4.1.11) and (4.1.12).

value of the non-dimensional temperature β that keeps the entropy S equal to the initial value. Yet we know that the initial state of the system is located in the transition region where the microstructure is not homogeneous ($\langle n_1 \rangle \neq 1, 0$). In this region, the entropy is high (see Fig.4.9) while after the step, the system evolves towards more homogeneous configurations with lower entropy. Hence in adiabatic response, the temperature of the system will increase leading to the desired smoothing of the T_2 curve.

The temperature change in adiabatic loading is computed by numerically solving the following equations on β:

$$S_h\left(\overline{\epsilon}, \beta\right) = S_h\left(\overline{\epsilon}^0, \beta\right) \text{ in hard device,} \tag{7.2.4}$$

$$S_s\left(\overline{\epsilon}, \beta\right) = S_s\left(\overline{\sigma}^0, \beta\right) \text{ in soft device,} \tag{7.2.5}$$

Here the expression of S_h and S_s should be taken from Eq.(4.1.11) and (4.1.12), respectively.

In Fig.7.9, we show the evolution of temperature along the adiabats in hard (A) and soft (B) devices. In hard device, the entropy achieves its maximum value at the state of isometric contraction so the temperature increases in both stretching in shortening. The lower stiffness of well 1 induce a smaller increase in temperature on the shortening side, whereas in stretching, the temperature increment reaches 200°C as stiffness of well 0 is higher. In soft device, the behavior is closer to the zero temperature limit with a sharp transition between two intervals of constant entropy (again controlled by the stiffness of the double well). Hence, in this case, the temperature is essentially constant in both stretching and shortening.

Finally we see on Fig.7.10 that the mechanical response of the system along the adiabats (dashed lines) is very close to the isothermal response (continuous line) although the transitions in both hard and soft device are slightly less steep (as expected). We can

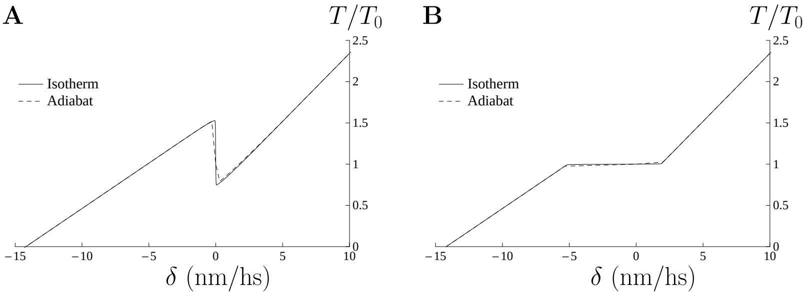

Fig. 7.10 – **Evolution of mechanical response along adiabats**. (**A**): hard device. (**B**): soft device. The results are computed using equation Eq.(4.1.11) and (4.1.12).

therefore conclude that the sharp transition around the state of isometric contraction obtained in isotherm cannot be avoided assuming that the response is adiabatic.

7.3 Variable size of the power-stroke

7.3.1 Definition of the power-stroke

The question of the power-stroke size is a source of continuous controversy. As we discussed in the introduction (see Sec.2.3.2), single molecule measurements show a power-stroke size of $\sim$ 5 nm (Kitamura et al., 1999; Knight et al., 2001; Mehta et al., 1997; Molloy et al., 1995; Veigel et al., 1998), while structural reconstruction are more consistent with a distance of $\sim$ 10 nm between the pre-power-stroke and the post-power-stroke conformations (Dobbie et al., 1998; Dominguez et al., 1998; Holmes and Geeves, 2000; Irving et al., 2000; Rayment et al., 1993). Recent chemomechanical models devide the full power-stroke into multiple sub-steps of reduced amplitude (2 sub-steps of 5 nm each or more) (Linari and Lombardi, 2010; Smith et al., 2008). It is important to notice that single molecule experiments are performed on isometrically contracting molecules, *i.e.* in presence of ATP, while structural analysis are made on crystallized proteins, 'frozen' in a given conformation. Our model can conciliate both approach as the power-stroke is not viewed anymore as a fixed distance between rigid conformations but as a continuous deformation.

In order to proceed, we first we need to give a clear definition of what we call 'power-stroke', and relate this definition to experimental measurements. We see two possibilities.

1. We can define the power-stroke as the relative mean position in the double well potential ($\langle\epsilon_i\rangle$) measured against the mean position in isometric contraction. Such power-stroke can be interpreted as the motion of the tip of the lever arm (the end of the blue chains on Fig.2.2) if we assume that the lever arm is rigid.
2. If the lever arm is elastic, which seems more realistic (see results published in (Dobbie et al., 1998; Irving et al., 2000; Kaya and Higuchi, 2010), which suggests that the instant elasticity of the myosin head resides in the S1 part of the molecule, *i.e.* in the lever arm, rather than in the S2 subfragment), then it is more likely that the experimentally measured power-stroke corresponds to the movement of the tip of the lever arm *i.e.* to ϵ_y in our model. This is particularly visible in X-ray experiments where the signal attributed to the tilt of the lever arm changes during the step. This proves that the lever arm participates in the elastic response (Irving et al., 2000).

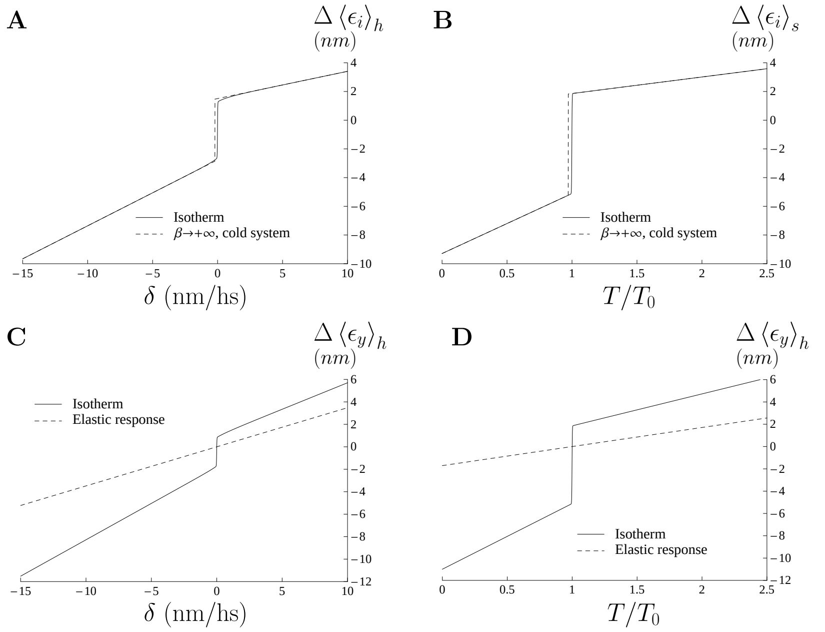

Fig. 7.11 – Amplitude of the power-stroke.(**A** and **C**): hard device. (**B** and **D**): soft device. On (**A**) and (**B**), the mean displacement in the double well with respect to the initial position ($\Delta \langle \epsilon_i \rangle_h = \langle \epsilon_i \rangle_h (\overline{\epsilon}) - \langle \epsilon_i \rangle_h (\overline{\epsilon}^0)$ in hard device, $\Delta \langle \epsilon_i \rangle_s = \langle \epsilon_i \rangle_s (\overline{\sigma}) - \langle \epsilon_i \rangle_s (T_0)$ in soft device) is represented against the loading, in isotherm (continuous line) and in the limit $\theta \to 0$ (dashed line). The isotherms are computed using direct numerical integration.

7.3.2 Single molecule and whole fiber experiments

To illustrate this difference in Fig.7.11A and B we show the mean displacement in the double well while C and D show the evolution of $\langle \epsilon_y \rangle$. In A and B the continuous lines represent the isotherms and the dashed line the mean position in the limit $\theta \to 0$. In C and D, the continuous line represents the isotherm and the dashed line shows the elastic response computed using Eq.(4.2.19) and (4.2.20) where the mean position in the double well remains equal to its initial value. In all cases, the responses show the typical sharp transition between two linear regimes. No matter what interpretation is adopted for the power-stroke, we see that its amplitude is reduced at low force (resp. length) steps.

On Fig.7.12, we represented the tension as a function of the mean displacements $\Delta \langle \epsilon_y \rangle$ (A) and $\Delta \langle \epsilon_i \rangle$ (B) , in hard and soft devices (continuous and dashed lines respectively). The squares represent results from X-ray experiments (Reconditi et al. (2004), similar results are also presented in Piazzesi et al. (2007)). We can see the results of removing successively the filament elastic distortion (A) and the elastic distortion of the head (B). Note that we did not use the instabilities of different components used in (Reconditi et al., 2004). This can explain some differences with our curves. We see however that our model reproduces quite accurately the movement observed in X-rays experiments. The differences may come from the estimates of filament elasticity or simply from experimental dispersion.

Last but not least, we observe in Fig.7.12, that the size of the stroke near the isometric condition is close to 5 nm in both (A) and (B), so it is the same no matter whether we define the power-stroke as the displacement in the double well or as the movement of the tip of the lever arm. Interestingly, this distance matches precisely the value obtained from single molecule experiments (Kitamura et al., 1999; Knight et al., 2001; Mehta et al., 1997; Molloy et al., 1995; Veigel et al., 1998). Therefore our results show that the two

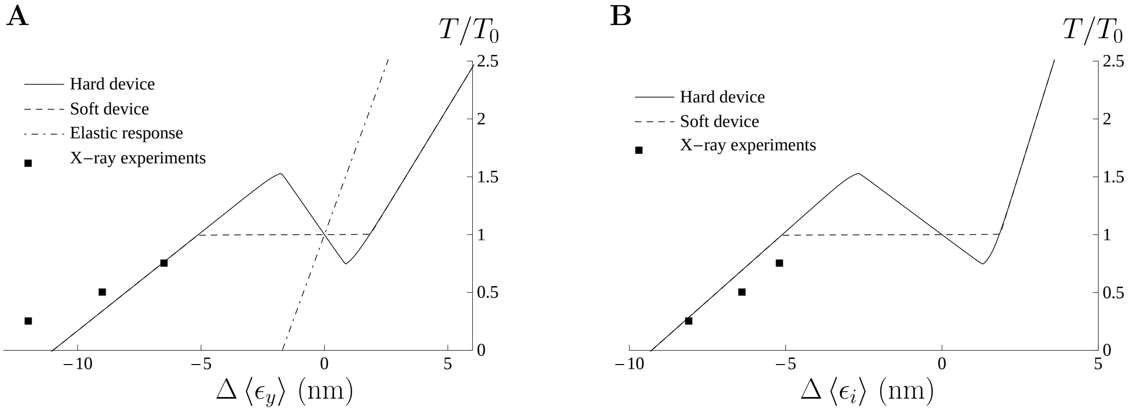

Fig. 7.12 – Amplitude of the power-stroke compared with X-ray measurements from (Reconditi et al., 2004).(**A**): Displacement of the tip of the lever arm in hard (continuous line) and soft device (dashed line). The dot-dashed line shows the elastic response. (**B**): Displacement in the double well potential in hard (continuous line) and soft device (dashed line). □ represent the displacement measured using X-ray diffraction techniques. The difference between theoretical and experimental curves may be due to the variability in the siffnesses estimates and also the experimental dispersion. Nevertheless we see that our model predicts the correct order of magnitudes. In addition, the power-stroke size is about 5 nm near isometric condition, in both (**A**) and (**B**). This is fully coherent with results from single molecule experiments from (Kitamura et al., 1999; Knight et al., 2001; Mehta et al., 1997; Molloy et al., 1995; Veigel et al., 1998). Hence our model can conciliate both approach for measuring the size of the power-stroke.

approaches (single molecule experiments *vs* fiber experiments) can be reconciled in our framework and be viewed as providing independent and consistent measurements of the power-stroke size.

7.4 Kinetics of the quick force recovery

7.4.1 Equilibration times

Following the analysis made in Sec.C.1.2, we can represent on Fig.7.13, the equilibration time in the reduced energy landscapes F_y and G_y by using the fitted parameters (from Tab.7.1). As we previously observed, the equilibration time is much longer in the

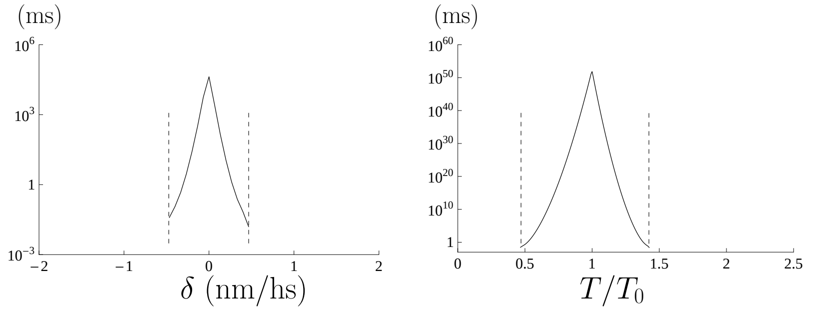

Fig. 7.13 – Equilibration time in the macroscopic wells computed according to Kramers approximation (see Sec.5.3.4). (**A**): Hard device. (**B**): soft device. The equilibration time can be computed as long as the double well structure of F_y (resp. G_y) is present (between the vertical dashed lines). The equilibration time is much larger in soft device (**B**) than in hard device (**A**) and so does the domain of slow kinetics

soft device (B) than in the hard device (A) which has been a major unresolved puzzle. In both cases, the time to equilibrate achieves its maximum in the condition $\delta\overline{\epsilon} = 0$ and $\overline{\sigma} = T_0$ and remains high as long as the double well structure of the reduced free energy landscapes is preserved (between the vertical dotted lines on Fig.7.13). The domain of slow kinetics in hard does not exceed 0.5 nm/hs in both shortening and stretching; our model suggests that it is much larger in the soft device (between $0.5T_0$ and $1.4T_0$). Hence we expect that the dynamic response in the soft device will be slow on a much larger loading interval than in the hard device.

7.4.2 Solving stochastic differential equations

For the direct numerical simulation of quick force recovery, we assume that ϵ_y is always in mechanical equilibrium. By making this assumption, we follow the experimental evidence that the viscosity associated with myofilaments is negligible compared to the viscosity associated with the power-stroke element. Then after the adiabatic elimination of the fast variable ϵ_y in (see Sec.6.1.2), we obtain the following dynamics for the system see Eqs.(6.1.21) and (6.1.22):

$$\begin{cases} d\epsilon_i^t = b\left(\epsilon_i^t, \epsilon_y\right) dt + \sqrt{2\beta^{-1}} dB_i^t \quad \text{for } 1 \leq i \leq N & (7.4.1a) \\ \epsilon_y = \dfrac{1}{1+\lambda_f}\left(\lambda_f \overline{\epsilon} + \dfrac{1}{N}\displaystyle\sum_{i=1}^{N} \epsilon_i^t\right) & (7.4.1b) \end{cases}$$

in the hard device and

$$\begin{cases} d\epsilon_i^t = b\left(\epsilon_i, \epsilon_y\right) dt + \sqrt{2\beta^{-1}} dB_i^t \quad \text{for } 1 \leq i \leq N & (7.4.2a) \\ \epsilon_y = \dfrac{\overline{\sigma}}{N} + \dfrac{1}{N}\displaystyle\sum_{i=1}^{N} \epsilon_i^t & (7.4.2b) \\ \epsilon_z = \dfrac{\overline{\sigma}}{N\lambda_f} + \dfrac{\overline{\sigma}}{N} + \dfrac{1}{N}\displaystyle\sum_{i=1}^{N} \epsilon_i^t & (7.4.2c) \end{cases}$$

in the soft device.

In practice, we uses a simple explicit Euler algorithm to solve these systems. The time step has to be small compared to 1. We chose $\Delta t = 10^{-3}$. The number of independent realizations is $N_r = 500$ (see Sec.5.2).

7.4.3 Numerical experiments

Initial conditions

In hard device, we suppose that our system is initially placed in thermal equilibrium such that the initial isothermal tension is equal to T_0 (in hard device) and the initial itothermal elongation is equal to $\overline{\epsilon}^0$. Since the equilibration time is very slow around the initial conditions, we initiate a fraction n_y of the N_r realizations in the left macroscopic well (As we did in Sec. 5.4.2). With our set of parameters, we have $n_y^h \approx 0.33$ and $n_y^s \approx 0.27$. If we compute the fraction $\langle n_1 \rangle$ of cross-bridges in post-power-stroke state at $\overline{\epsilon} = \overline{\epsilon}^0$ and $\overline{\sigma} = T_0$, we obtain: $\langle n_1 \rangle^h \approx 0.37$ in the hard device and $\langle n_1 \rangle^s \approx 0.27$ in the soft device.

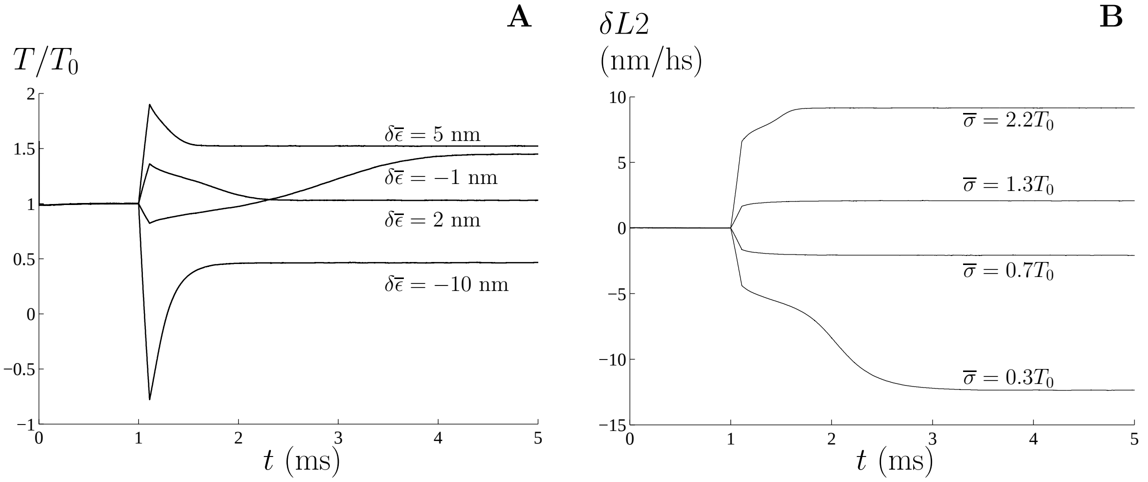

Fig. 7.14 – Dynamical response computed numerically (**A**): Hard device, mean relative tension. (**B**): soft device, mean relative elongation. The time is in millisecond. In soft device, for step size larger that the slow kinetic domain (see Fig.7.13), *i.e.* $T = 1.3T_0$ and $T = 0.7T_0$, the systems reaches a steady state that does not correspond to the isotherm (see Fig.7.15). For small load steps, the system is kinetically trapped in macroscopic wells.

Evolution of tension and elongation with time

Our Fig.7.14 shows the time evolution of the normalized tension T/T_0 (A) and the relative elongation $\delta L_2 = L_2(\overline{\sigma}) - L_2(\overline{\sigma}^0)$ measured in nm/hs (nanometer per half-sarcomere)(B) following various length and load steps (indicated on the figure). In the hard device, we see that for $\delta = -1$ and $\delta = 2$ nm/hs, the system evolves to its stationary state following a dynamic process with 2 time scales, the first one is slower than the second one. This is particularly visible on the curve $\delta = -1 nm/hs$ where the velocity of the recovery clearly changes about 2.3 ms after the beginning of the step. This observation is qualitatively similar to what we have seen at $\theta = 0$ in Chap.5 (see Fig.5.1): first the microscopic configuration of the system is mixed and the cross-bridges evolves in both wells of the bistable potential. After some time, (denoted by a $\star$ on 5.1), all the cross-bridges end up in the same post-power-stroke state. In the meantime, the barrier of the double well potential disappears thereby increasing the velocity. As in Fig.5.1, for larger length step, such change in velocity is less visible.

In soft device (see Fig.7.14B), at low force steps ($T = 1.3T_0$ and $T = .7T_0$), the system is brought to a state where the double well structure of G_y is still present (see Fig.7.13). Consequently, the system equilibrates quickly in the macroscopic wells and reaches a quasi steady state. This steady state does not correspond to thermal equilibrium because the system is kinetically trapped. For larger load steps ($T = 2.2T_0$ and $T = 0.3T_0$), like in hard device, we observe an evolution of the elongation with two characteristic times, which is again in accordance with our computations at zero temperature (see Fig.5.1). Such response with 2 time scales does not seem to be observed in physical experiments (see Fig.2.3). This is a limitation of our model and it is most probably due to the fact that we simulate only a single half sarcomere while the fibers contains many sarcomeres in series and in parallel (see Sec.1.1) which gives rise to collective effects (see Chap.8).

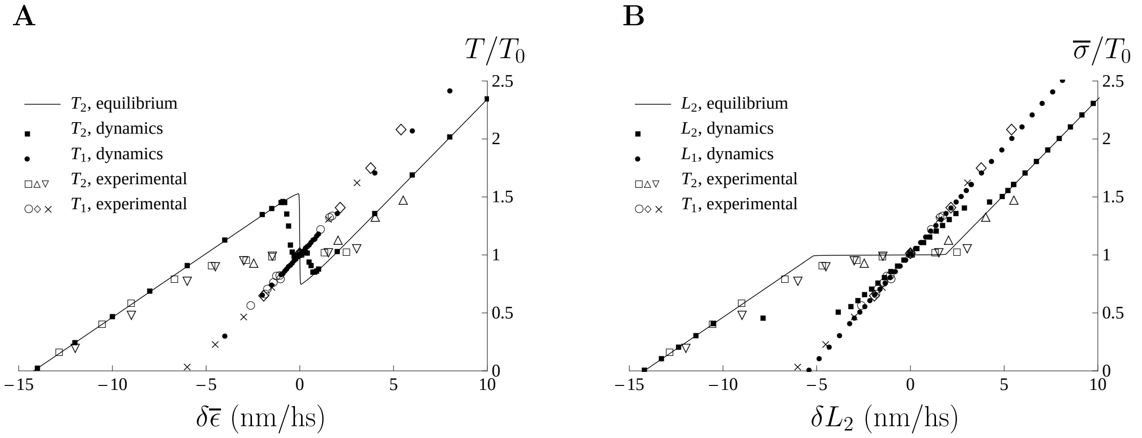

Fig. 7.15 – Equilibrium computed with stochastic simulations. (**A**): Hard device. (**B**): soft device. Continuous line: thermal equilibrium computed using Eq.(4.2.15) (**A**) and (4.2.17)(**B**). (■): Tension and elongation attained 5 ms after the step (numerics). (●): Tension and elongation attained at the end of the step. Experimental points are taken from Ford et al. (1977)(T_1: ×, T_2: ▽), Brunello et al. (2007)(T_1: ◇, T_2: △) and Linari et al. (2009)(T_1: ◎, T_2: □). The experimental data shown here are all from hard device experiments, but we remind that the linear part of L_2 and T_2 are the same (see Fig.2.5). We did not find L_2 curve for the frog type used here (*rana temporaria*). We observe the consequence of the slow equilibration time in soft device: on (**B**), the system cannot reach equilibrium around $T/T_0 = 1$. This qualitatively explains why the L_2 curve cannot be resolved experimentally around T_0 (Edman and Curtin, 2001; Edman et al., 1988; Granzier et al., 1990; Sugi and Tsuchiya, 1981). Note that the domain of slow kinetics is more localized around T_0 in these experiments (typically between $0.9T_0$ and $1.1T_0$). We see that one could also observe such very slow kinetics in hard device, but on a very short interval of δ.

Numerical T_2 and L_2 curves

In Fig.7.15(A and B, ■), we report the tension and elongation attained after 5 ms of recovery (where the system reaches a quasi steady state) on Fig.7.15(A and B, ■). Open symbols refer to experimental data from Ford et al. (1977)(T_1: ×, T_2: ▽), Brunello et al. (2007)(T_1: ◇, T_2: △) and Linari et al. (2009)(T_1: ◎, T_2: □). Although we did not find experimental data for the load clamp quick recovery, we expect L_1 and L_2 curve to superimpose over T_1 and T_2 curve exepts around $T = T_0$ (see Fig.2.5). The tension and elongation attained at the end of the step (T_1, L_1) are represented by (●) and we see that they match the experimental points reasonably well. The continuous lines are the isotherms.

Observe that in both hard (A) and soft (B) devices, there is an interval of kinetic trapping, where the system does not reach thermal equilibrium after 5 ms. In both cases, this interval corresponds to the persistence of the macroscopic wells as shown in Fig.7.13. Once again, such 'kinetic trapping' interval is much smaller in the hard than in the soft device.

Rate of recovery

The rate of recovery is usually defined as the inverse of the time required to reach $0.5\,(T_2 - T_1)$ starting from T_1. Simulated rate curves (■, device and ●, soft device) are compared with experimental data on Fig.7.16. The length clamp data are from Ford et al. (1977) (◇), Piazzesi et al. (1992) (×), and Linari et al. (2009) (□). The load clamp data (◎) are estimated from the velocity during phase 2 of the quick recovery published in (Piazzesi et al., 2002a). These points are obtained from *rana esculenta*. For this type of frog, the interception of the T_2 curve is at about −10 nm while it is at about −15 nm for

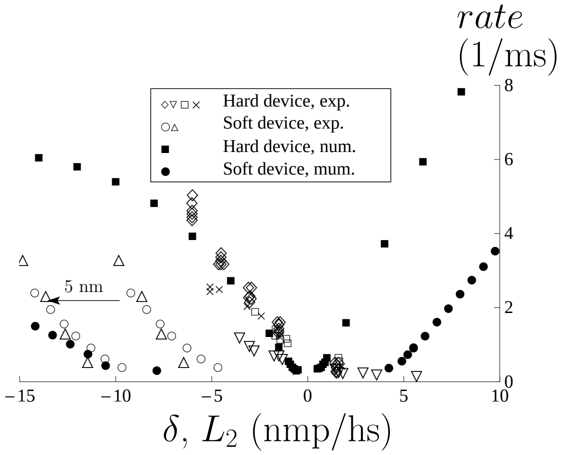

Fig. 7.16 – **Rate curves in hard and soft device** compared with experimental results. The length clamp data (open symbol) are from Huxley and Simmons (1971)(▽) Ford et al. (1977) (◇), Piazzesi et al. (1992) (×) and Linari et al. (2009) (□). The load clamp data (◎) are estimated from the velocity during phase 2 of the quick recovery Piazzesi et al. (2002a). (△) are from Decostre et al. (2005). These points (◎, △) are obtained from *rana esculenta* for which the intercept of the T_2 curve is about -10 nm while it is about -15 nm for *rana temporaria.* We arbitrarily displaced the experimental points of *rana esculenta* by 5 nm to the left (see the arrow) to compare with the results of our simulations (●). (■) represent the rate curve obtained in hard device. Our simulations match the available measurements. We observe that the rate is not exponential as in chemo-mechanical models (Huxley and Simmons, 1971) but saturates at large loadings. Experimental observations of this saturation of the rate in shortening has been reported in (Piazzesi and Lombardi, 1995; Ranatunga et al., 2002).

rana temporaria. We arbitrarily displaced the experimental points of *rana esculenta*(◎) by 5 nm to the left (see the arrow) to compare with the shape of experimental and theoretical curves (●).

The results of our simulations can't be fit with a simple exponential curve, as one may expect for a single chemical transition. In particular, we observe a plateau for large shortening steps. Similar results indicating non exponential rate curves have been obtained in some models (Smith and Sleep, 2004; Smith and S.M., 2008). In experimental rate curves, non-exponential behavior has been reported in (Martyn et al., 2002; Ranatunga et al., 2002)(rabbit psoas fibers). Our results are also coherent with the fact that for large steps, the two macro-well structure of the landscape disappears and thus the evolution becomes of non-Kramers type.

Note that we do not show the results for steps near the initial state (between our 'vertical lines'). In this region the system does not reach the thermal equilibrium within the time of observation (here 5ms). As we have seen, it is trapped in macro-wells. This region of extremely slow force recovery is larger in the soft device than in the hard device, which of course follows from our discussion on the peculiarities of the energy landscape. This also explains at least qualitatively why the quick recovery cannot be observed for small load steps in the soft device (Edman and Curtin, 2001; Piazzesi et al., 2002a): On Fig.2.5, no points are reported for soft device above $0.8T_0$ and in (Edman and Curtin, 2001), the authors observe an damped oscillatory response of the fiber length at such applied force steps. Our simulations also predict a slower recovery in soft than in hard device. We are not aware any systematic comparison in the literature of the rate of phase 2 between in hard and soft device, but our examination of various experimental curves (Piazzesi et al., 2002a, 2007; Ranatunga et al., 2002) seems to agree with the model.

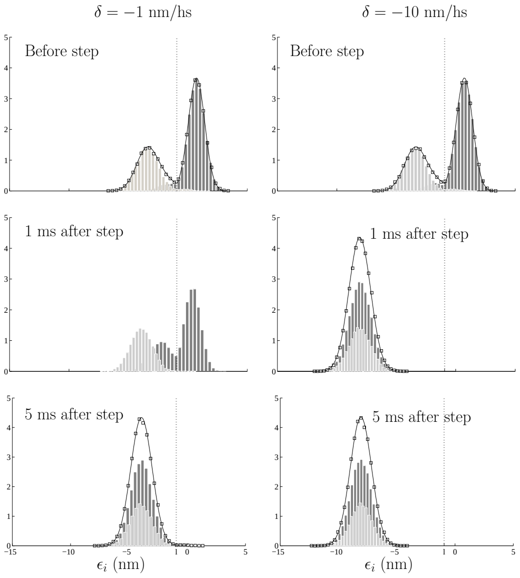

Fig. 7.17 – Evolution of the population in the double well potential in hard device. Left column: $\delta = -1$. Right column: $\delta = -10$. Dark gray (resp. light gray) histogram represents the cross-bridges positions for the realizations initialized in the left macroscopic well (resp. right macroscopic well). Continuous line represents the equilibrium probability density in the double well for the given step size. The □ are obtained by summing the 2 histograms weighted by the initial fraction of population in the left macroscopic well ($\langle n_y \rangle$): $\square = n_y \times$ light-gray $+ (1 - n_y) \times$ dark-gray. The dotted line indicates the limit between pre-power-stroke and post-power-stroke configurations. In steady state, the results of Langevin simulations matches the analytic computation of the probability distribution. The transition is slower after low steps than after large step.

Evolution of the probability distributions

In Figs.7.17 and 7.18, we show the statistics of the cross-bridge positions ϵ_i in the double well potential v which also illustrate the power-stroke dynamics and reveals the cooperative effects. The light gray histograms show the distribution of cross-bridges for $n_y N_r$ realizations starting in the left macroscopic well and the dark gray histograms, for the $(1 - n_y) N_r$ realizations starting in the right macroscopic well. As we already discussed in Sec.4.5, the two populations contain essentially pre-power-stroke (dark gray) and post-power-stroke (light gray) cross-bridges (the vertical dotted line shows the separation between the two wells). The overall distribution of the cross-bridges is obtained by adding the contributions due to two populations with the corresponding weights n_y and $(1 - n_y)$: $\square = n_y \times$ light-gray $+ (1 - n_y) \times$ dark-gray. The continuous lines represent the distribution in thermal equilibrium.

The kinetic trapping is clearly visible in Fig.7.18(left column): the distribution remains bi-modal after 5ms while it should have reached a single mode equilibrium (continuous line).

In addition, we observe that for steps allowing to escape from the macroscopic wells (see Fig.7.17 and 7.18 right column) 1 ms after the step (see middle rows), the pre-power-stroke population (dark gray) exectute the conformational change in a collective manner, avoiding the energy barrier at l.

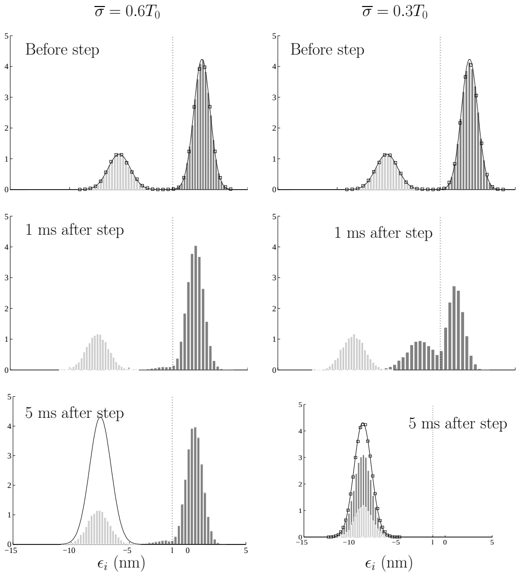

Fig. 7.18 – Evolution of the population in the double well potential in soft device. Left column: $T/T_0 = 0.6$. Right column: $T/T_0 = 0.3$. Dark gray (resp. light gray) histogram represents the cross-bridges positions for the realizations initialized in the left macroscopic well (resp. right macroscopic well). Continuous line represents the equilibrium probability density in the double well for the given step size. The $\square$ are obtained by summing the 2 histograms weighted by the initial fraction of population in the left macroscopic well (n_y): $\square = n_y \times$ light-gray $+ (1 - n_y) \times$ dark-gray. The dotted line indicates the limit between pre-power-stroke and post-power-stroke configurations. In steady state, the results of Langevin simulations matches the analytic computation of the probability distribution only for large step, this shows the kinetic trapping of the cross-bridges for low load step (left column).

7.5 Muscle response to stretching

7.5.1 Experimental evidence

We have already seen in the introductory Chaps.1 and 2 that skeletal muscles exhibit different behaviors in shortening and stretching. For instance it is known (Katz, 1939) that the force-velocity relation is strongly non-symmetric with a very slow increase of velocity with force as the force exceeds the isometric tension T_0 and all the way till the yield state is reached (see Fig.1.12). We recall onece againt that muscle mechanism is designed first of all to generate a force during contraction, and its main physiological regime is shortening. However, in order to preserve its integrity, muscle must be able to 'resist' stretching. Since this regime is physiologically so different, some additional mechanisms to the ones considered above may be activated upon elongation. Those mechanisms are most probably passive, given the damping role the muscle plays during stretching.

We also recall that the passive elasticity of muscle fibers is known to be negligible under physiological conditions but becomes critical when the sarcomeres enters the descending limb of the tension *vs* sarcomere length relation (see Fig1.11). In single myofibrils, titin is the main source source of passive alasticity (Cazorla et al., 2000; Linke et al., 1997) and it has been shown recently (Leonard et al., 2010) that titin can regulate the force on the descending limb even without the contribution of the cross-bridges.

However, even before reaching the descending limb, we can already observe some difference between shortening and stretching. In particular this concerns the response of muscle fiber to fast length changes in hard device. In Fig.7.19, we show the response of

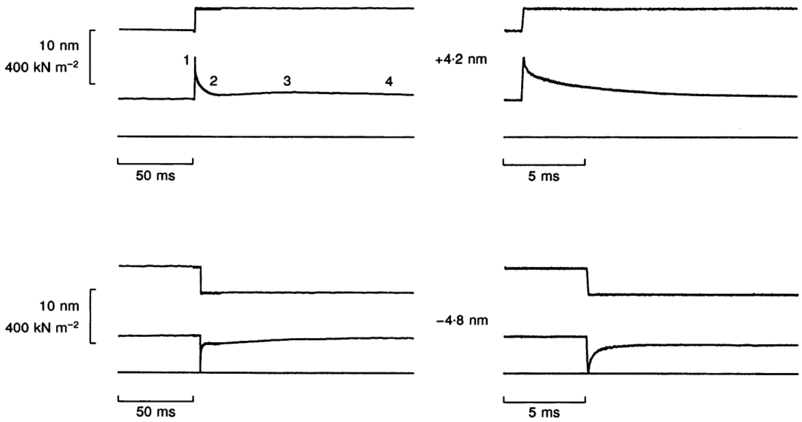

Fig. 7.19 – Asymmetry in the response of a fiber to comparable step stretch and release. From (Piazzesi et al., 1997). Left column: tension responses to a lengthening step of 4.2 nm/hs(upper panel) and a shortening step of 4.8 nm/hs (lower panel). In each panel, from top to bottom, traces are: length change per half-sarcomere, tension response, resting tension. The figures close to the tension record in the left upper panel indicate the various phases of the transient as introduced in Sec.2.2.2. Right column shows the fast transient of the response on an expanded time scale.

a muscle fiber to equal step size applied in the hard device setting in stretching (upper panel) and shortening (lower panel). On each plot, from top to bottom we see the sarcomere length, the tension and the resting tension. The numbers on the upper left plot show the various phases of the transients as introduced in Sec.2.2.2. The right panel shows the fast transients on an expanded time scale.

First we observe that the force recovery is faster in shortening than in stretching and particularly during phase 2. Second, in shortening, the end of phase 2 is clearly identified by the presence of a plateau on the tension *vs* time curve in the lower-right panel while in stretching, such plateau does not really exists which raises the question of the definition of T_2. Usually, in shortening, T_2 is determined by the extrapolation of the tangent to the tension *vs* time curve on the plateau. Instead, in stretching, T_2 is usually interpreted as the tension measured after about 2 ms delay following the step (Brunello et al., 2007). The difficulty of clearly identifying the end of phase 2 poses the question of the existence of a *reverse power-stroke* or *power-stroke repriming* in stretching. In fact, it has been shown by X-ray diffraction analysis that the early phase of the recovery in stretching is accompanied by a change in the orientation of the myosin heads which strongly suggested that repriming does occur after a sudden elongation(Lombardi et al., 1995).

In (Piazzesi et al., 1997), a multi-exponential fit has been performed for the tension *vs* time curve in response to stretching. It suggests that the reverse power-stroke should be completed within ~1 ms after the step and from this analysis a T_2 curve can be extracted from experiments (see Fig.7.1).

Interestingly, there is an experimental evidence that even the elastic response, T_1 is non symmetric in stretching and shortening. Thus, in (Brunello et al., 2007), a slight increase in stiffness has been reported and it has been shown that the associated change in the X-ray diffraction pattern is compatible with the idea of the attachment of the *second head* of the myosin whose role was so far obscure. Hence, attachment of the second head could be one of the additional mechanisms that helps to prevent the fiber from dramatic elongation by increasing its stiffness. In addition, the slow delay of the force recovery on the ms timescale has been attributed in (Piazzesi et al., 1997) to *passive friction* of the myosin heads on the actin filament. These new mechanisms can be incorporated into our model.

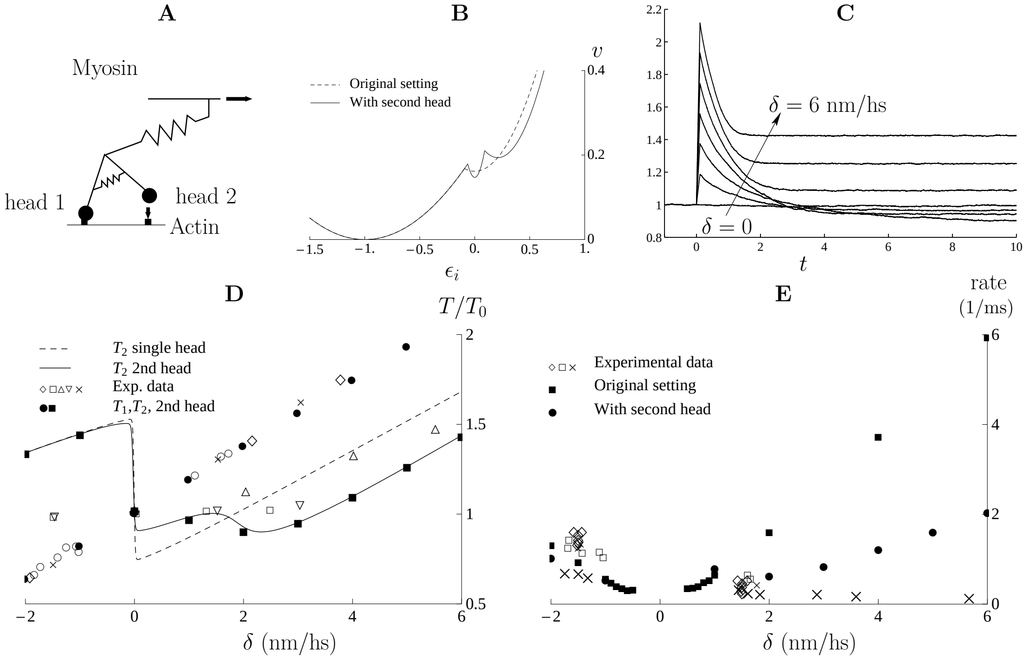

Fig. 7.20 – **Response of a model with second head**. (**A**): cartoon representing the dimeric structure of myosin II and the mechanism of attachment of the second head. (**B**): example of a 3 well potential (solid line) compared to the original double well potential (dashed line). (**C**): tension *vs* time for step sizes from 0 to 6 nm/hs. (**D**): equilibrium response of the double head system. Dashed line: Analytic T_2 curve with the single head model; solid line: analytic T_2 curve with second head; (● and ■): T_1 and T_2 curve obtained numerically with the second head model. (**E**): rate curve with experimental data (open symbols), rate obtained with the single head model (■) and with the second head model (●).

7.5.2 Additional mechanical mechanisms

Here, present an attempt to match the experimental data in stretching by implementing two additional physical mechanisms: the second head and the passive friction due to partial detachment of cross-bridges from actin filaments.

Second head

Our working hypothesis will be that the binding of the second head occurs when the lever arm angle for the attached head becomes larger that a critical value ϵ_c. Beyond this threshold, the energy of the cross-bridge should start favoring energetically the state where both heads are attached. Hence we model the presence of this additional state with two heads attached as a third well in our potential $v(x)$.

In Fig.7.20A and B, we show a sketch of a double headed cross-bridge system together with an example of energy landscape with three wells (see B solid line; dashed line represents the intial double well energy landscape). Our (C) shows tension *vs* time trajectories for six stretching steps, from $\delta = 0$ to $\delta = 6$ nm/hs. The presence of an additional well introduces a second transition in the T_2 curve as shown on Fig.7.20D by the solid line representing the analytical computation. The T_1 curve remains basically unchanged (●). The presence of an additional energy barrier also reduces the relaxation rate (see Fig.7.20D). Unfortunately, this model cannot reproduce the increase in stiffness observed along the T_1 in (Brunello et al., 2007). To account for this phenomenon, one can make the linear spring of the myosin head non-linear by say, doubling its stiffness at $\epsilon_i > \epsilon_c$. To summarize, the introduction of an additional well can flatten the T_2 curve near the origin which

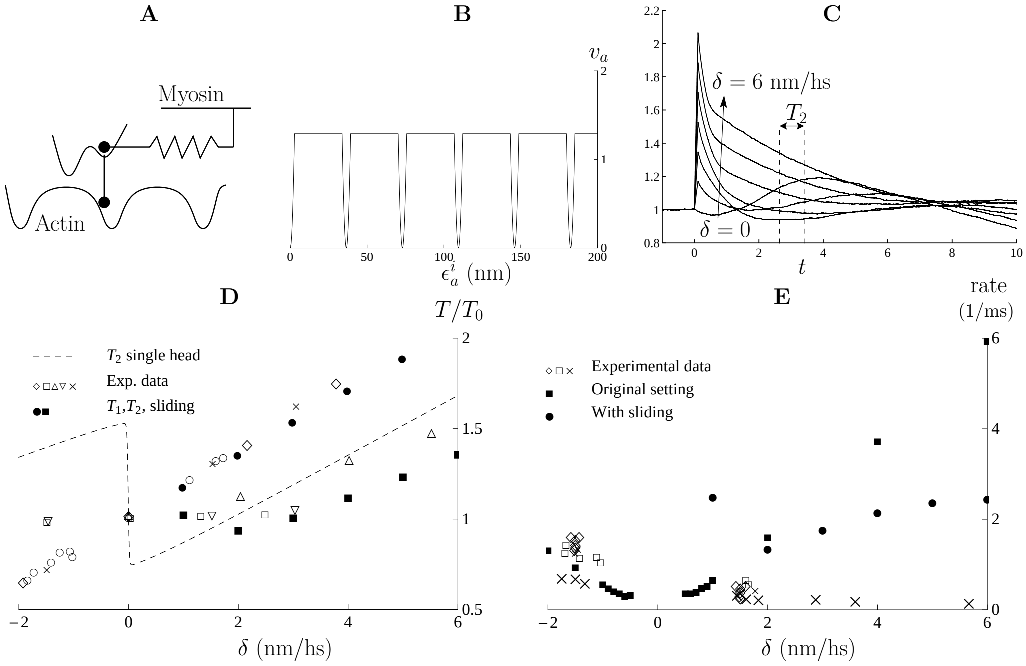

Fig. 7.21 – Response of a model with passive friction. (**A**): cartoon a single myosin interacting with a periodic potential representing the actin filament. (**B**): example of a periodic potential representing actin with a parabolic binding site every 36.5 nm. (**C**): tension *vs* time for step sizes from 0 to 6 nm/hs. The interval between the vertical dashed line indicates where the tension T_2 is measured. (**D**): Equilibrium response of the system. Dashed line: Analytic T_2 curve with the single head model; (● and ■): T_1 and T_2 curve obtained numerically with the second head model. Open symbols are experimental data. (**E**): rate curve with experimental data (open symbols), rate obtained with the single head model (■) and with the passive friction model (●).

is a desirable effect. However, it remains unclear whether the second head can be indeed adequately represented by the third well and whether it is indeed involved in the fast force recovery.

Passive friction

To model passive friction, we unfreeze a degree of freedom which represents the position of the myosin head on the actin filament. We denote the strain associated with this new degree of freedom by ϵ_a^i. The interaction with the actin filament is modeled by a periodic potential $v_a\left(\epsilon_a^i\right)$. The choice for v_a is very broad. We can mention for instance the sawtooth potential often used in Brownian ratchet models (see Sec.2.4.5. However, with this type of potential, it is difficult to determine when the cross-bridge is attached or when it is detached unless we explicitly introduce another potential for the detached state and the corresponding rate functions as illustrated on Fig.2.19. Therefore, we consider a periodic potential where the biding sites are clearly identified by parabolic wells with stiffness κ_a and between biding sites, the energy landscape is flat. We show such potential on Fig.7.21B, with a periodicity of 36.5 nm as it is expected for actin filaments (see Sec.1.1.2). One can also use a potential with a finer succession of wells located every 5.5 nm and representing individual monomers.

The particularity of this model is that, at finite temperature, the system in hard device has no stationary state and the isothermal tension is always equal to zero. Indeed, the time to escape from an 'actin well' is finite so in long time limit the tension always relaxes to zero within a finite time. To circumvent this problem, we assumed that T_0, $\kappa_a \to \infty$.

Therefore, we start with the same initial conditions as in the case of fully attached cross-bridges and we introduced the periodic potential with finite κ_a only at the beginning of the step. The periodic potential is then maintained throughout the simulation.

The computed tension *vs* time curves are shown on Fig.7.21C. Due to sliding, the response curves do not exhibit a plateau like in our original model so the definition of T_2 is no longer obvious, like in experiments. Note that the shortening response is almost not affected by the presence of the actin potential since the drag coefficient associated with ϵ_a is chosen to be about 10 times larger than the drag coefficient associated with the double well potential. Thus, upon shortening, we do observe a plateau before the tension starts to decrease due to the incipient movement along the filament.

To define T_2 in stretching, we used the method proposed in (Brunello et al., 2007). It is then the average tension between 2.5 and 3.5 ms after the step (between the vertical dashed lines on Fig.7.21C). Interestingly, for small stretches (see $\delta = 0,1$ nm/hs on C), we observed a non monotone response with an increase in tension before the system starts to relax. This is simply due to the fact that when ϵ_a starts to increase after the step, the tension in the cross-bridges automatically decreases. This triggers a power-stroke which temporarily increases the tension. When the stretch is loo large the such power-stroke event is does not take place.

The T_2 curve we obtained within this model (see Fig.7.21D(■)) is very similar to the curve obtained by using the model with the second head (see Fig.7.20D). The result, of course, depends strongly on the way we 'measure' T_2. The rate curve is also similar but it 'saturates' faster. In fact, as soon as the cross-bridges detaches, the sliding velocity starts to be controlled by the drag coefficient η_a which we associate with ϵ_a. At that point, the rate becomes constant as it is expected from experiments.

To conclude, within both the second head model and the passive friction mpdel, we obtained a slower growth of the T_2 curve which goes in the direction of lowering the force on a fast time scale to prevent the damage of the fiber. Furthermore, the absence of a plateau on the tension *vs* time relation in stretching (and only in stretching) is correctly reproduced by the passive friction. So far the experimental rates have not been matched quantitatively but at least we can now reproduce a constant asymptotic rate in stretching. In fact, the experimental rate data in stretching are rare. The data shown on 7.20E and 7.21E (×) are those published in (Huxley and Simmons, 1971) and to the best of our knowledge there have been no other paper reporting the rates above 2 nm/hs in stretching.

7.6 System with distributed elasticity

In the Introduction, we have shown how our system with an array of cross-bridges connected in series with a linear spring can be used as a simplified representation of a much more complex model accounting for the elasticity of the myofilaments. In a more adequate model, each cross-bridge would have to be elastically connected to its nearest neighbors (see Fig.2.24). Here we present several preliminary numerical results obtained within this more complex framework.

7.6.1 The model

Our model of a half-sarcomere with distributed elasticity is shown in Fig.2.24. The potential energy of this system must take into account the following entries:

1. The elastic energies of the terminal springs which include actin and myosin filaments and a single titin protein. All these elements will be assumed linear for simplicity:

$$E_{fil} = \frac{\kappa_{FA}}{2}(x_1)^2 + \frac{\kappa_{FM}}{2}(y_{tot} - y_{N+1})^2 + \frac{\kappa_{TIT}}{2}(y_1 - l_{TIT})^2 \tag{7.6.1}$$

2. The linear elastic energies of the series of springs for the actin and myosin filament, connecting the cross-bridges:

$$E_{el} = \sum_{i=1}^{N} \frac{\kappa_a}{2}(x_{i+1} - x_i)^2 + \sum_{i=1}^{N} \frac{\kappa_m}{2}(y_{i+1} - y_i)^2 \tag{7.6.2}$$

3. The non-linear double well elastic energies of the cross-bridges which are the same as in the simplified lump model:

$$E_{xbs} = \sum_{i=1}^{N+1} \left[v(u_i - x_i) + \frac{\kappa}{2}(y_i - u_i)^2 \right] \tag{7.6.3}$$

The potential v discribing the double well will be again assumed to be bi-quadratic:

$$\begin{aligned} v(u_i - x_i) &= \tfrac{\kappa_1}{2}(u_i - x_i + a)^2 \qquad && u_i - x_i \leq -l \\ v(u_i - x_i) &= \tfrac{\kappa_0}{2}(u_i - x_i)^2 + v_0 \qquad && u_i - x_i \geq -l \end{aligned} \tag{7.6.4}$$

The non-dimensional quantities are constructed in the same way as in the case of the lump model. In the non-dimensional variables, the total energy of the distributed system can be written as follows:

$$\begin{aligned} V = \frac{\kappa_{FA}}{2}(x_1)^2 + \frac{\kappa_{TIT}}{2}(y_1 - l_{TIT})^2 + \frac{\kappa_{FM}}{2}(z - y_{N+1})^2 \\ + \sum_{i=1}^{N} \left[\frac{\kappa_a}{2}(x_{i+1} - x_i)^2 + \frac{\kappa_m}{2}(y_{i+1} - y_i)^2 \right] \\ + \sum_{i=1}^{N+1} \left[\frac{1}{2}(y_i - u_i)^2 + v(u_i - x_i) \right] \end{aligned}$$

where the dimensionless potential v is

$$v(u_i - x_i) = \begin{cases} \frac{\kappa_1}{2}(u_i - x_i + 1)^2 & \text{if } u_i - x_i \leq -l \\ v(u_i - x_i) = \frac{\kappa_0}{2}(u_i - x_i)^2 + v_0 & \text{if } u_i - x_i \geq -l \end{cases} \tag{7.6.5}$$

In muscle the myosin filament is three times stiffer that the actin filament (Huxley et al., 1994; Wakabayashi et al., 1994).

Therefore, to simplify the computations, we consider the myosin filament as a rigid bar which correspond to $\kappa_m \to \infty$ and $\kappa_M \to \infty$. Then titin will also be neglected at this stage.

Under these assumptions, the total energy simplifies considerably:

$$V = \frac{\kappa_{FA}}{2}(x_1)^2 + \sum_{i=1}^{N} \frac{\kappa_a}{2}(x_{i+1} - x_i)^2 + \sum_{i=1}^{N+1} \left[\frac{1}{2}(z - u_i)^2 + v(u_i - x_i) \right] \tag{7.6.6}$$

7.6.2 Mechanical system at $\theta = 0$

We consider our system under the hard device setting. Therefore, z is the controlled parameter. The set of equations for the system at $\theta = 0$ is obtained by differentiating the energy (7.6.6) with respect to the variables x_i, u_i at a given z. For the u_i (the cross-bridges), we can write:

$$-\left(y_i - u_i\right) + v'(u_i - x_i) = 0 \tag{7.6.7}$$

while for the springs, we obtain:

$$\begin{aligned} &k_a\left(2x_i - x_{i+1} - x_{i-1}\right) - v'(u_i - x_i) = 0 \, \text{for } i = 2, \ldots, N \\ &k_a\left(x_{N+1} - x_N\right) - v'(u_{N+1} - x_{N+1}) = 0 \\ &k_a\left(x_1 - x_2\right) + \kappa_{FA} x_1 - v'(u_1 - x_1) = 0 \end{aligned} \tag{7.6.8}$$

Notice that both sets of equations involve non-linear terms. To specify the expression for $v'(\epsilon)$, we introduce the 'spin' vector (δ_i) which represents the current configuration of the cross-bridges: $\delta_i = 0$ if cross-bridge with index i is in well 0 and $\delta_i = 1$ if cross-bridge with index i is in well 1. We also introduce a vector of (κ_i), which represents the different rigidities felt by the cross-bridges in their particular configurations: $k_i = k_0 + (k_1 - k_0)\delta_i$.

Assuming that the vector (δ_i) is known, we can solve for the variables u_i explicitly:

$$\kappa_i\left(u_i - x_i + \delta_i\right) = -\frac{\kappa_i}{1+\kappa_i}\left(x_i - \delta_i\right) + \frac{\kappa_i}{1+\kappa_i} z \tag{7.6.9}$$

The corresponding strains along the actin fiber satisfy the following system of linear finite difference equations:

$$\begin{aligned} \kappa_a\left(x_i - x_{i+1}\right) + \kappa_{FA} x_i + \frac{k_i}{1+k_i} x_i &= \frac{\kappa_i}{1+\kappa_i}\left(\delta_i + z\right) \ \text{ for } i = 1 \\ \kappa_a\left(2x_i - x_{i+1} - x_{i-1}\right) + \frac{\kappa_i}{1+\kappa_i} x_i &= \frac{\kappa_i}{1+\kappa_i}\left(\delta_i + z\right) \ \text{ for } i \in [2, N] \\ \kappa_a\left(x_i - x_{i-1}\right) + \frac{\kappa_i}{1+\kappa_i} x_i &= \frac{\kappa_i}{1+\kappa_i}\left(\delta_i + z\right) \text{for } i = N+1 \end{aligned} \tag{7.6.10}$$

This system can also be solved analytically by inverting a tridiagonal matrix but we will not provide the solution here. The parameters of the model have been adjusted to the experimental data following a similar procedure as the one detailed in Sec.7.1.

We observe that, in the distributed system there is no permutational invariance for the cross-bridges. Therefore, the equilibrium positions in the double well potential are different for all the cross-bridges and there is no configuration scalar like n_1 replacing the configuration vector (δ_i).

In our Fig.7.22A, we show the tension-elongation curve along the local minima of the energy which are characterized by the presence of a single front separating a population in pre-power-stroke from a population in post-power-stroke. Dashed lines represent configurations were post-power-stroke cross-bridges are located to the right of the front. On the lowest curve, the front is at the very right position and at the upper curve, the front is located to the very left. Solid lines represent configurations were post-power-stroke cross-bridges are located to the left of the front. On the upper line, the front is at the very left and at the bottom line, the front is at the right.

We observe that the limits of the metastable region are no longer linear like in the case of the lump modef. Another fundamental difference is that the global minimum path (see bold line in Fig.7.22 and the blow up) goes through a succession of non affine states where now ther is a front separating pre-power-stroke cross-bridges from post-power-stroke

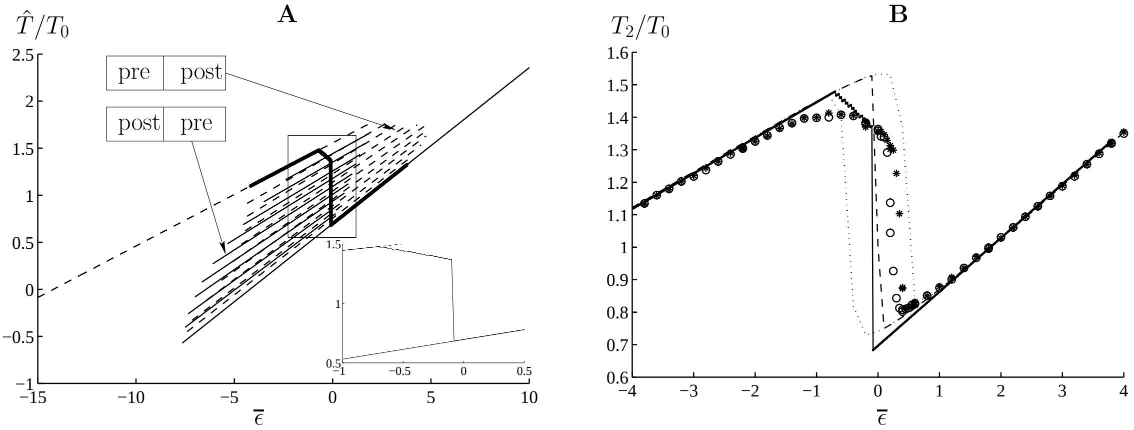

Fig. 7.22 – **Realistic model of a half-sarcomere: equilibrium in hard device**. (**A**) equilibrium at $\theta = 0$. Dashed lines and solid lines: local minima of the energy characterized by a front separating a population of cross-bridges in pre-power-stroke and a population of cross-bridges in post-power-stroke as indicated by the rectangles. For clarity we represent only ten states for each configurations. Solid line: Global minimum. The insert shows a blow up of the transition region. (**B**): thermal equilibrium. (◎): simulations initialized at $\delta = 4$ nm/hs in a full pre-power-stroke configuration. ($*$): simulations initialized at $\delta = -4$ nm/hs in a full post-power-stroke configuration ($*$) and (◎) form an hysteresis in the center. Dotted line shows the hysteresis obtained with the same protocol using the parallel model. Dashed line: thermal equilibrium obtained with the parallel model.

cross-bridges. Remarkably this front is not moving continuously but undergoes a jump at a critical value of the total strain. Although we do not discuss other configurations here, one can show that, since the myosin filament is rigid, there is always only one front characterizing the global minimum. In the case of compliant myosin filament we expect the presence of two fronts which does not of course exclude the possibility of a jump along the global minimum path.

7.6.3 Equilibrium system at $\theta \neq 0$

As in the case of the lump model, we can now consider the thermal equilibrium for the variables describing the power-stroke. For simplicity, the variables associated with the filament (x_i) will be viewed as mechanically equilibrated. Behind this is the implicit assumption that they equilibrate much faster. We denote the fluctuating variables as $\epsilon_i^t = u_i^t - x_i^t$ and write the associated stochastic differential equations:

$$d\epsilon_i^t = \left[\epsilon_i(t) - v'(\epsilon_i^t) + (z - \epsilon_i^t - x_i^t)\right] dt + \sqrt{2/\beta^{-1}} dB_i^t. \tag{7.6.11}$$

Once again, the linear elastic spring are assumed to be in equilibrium:

$$\begin{aligned} \kappa_a \left(x_1^t - x_2^t\right) + \kappa_{FA} x_1^t + x_1^t &= (z - \epsilon_1^t) \text{ for } i = 1 \\ \kappa_a \left(2x_i^t - x_{i+1}^t - x_{i-1}^t\right) + x_i^t &= (z - \epsilon_i^t) \text{ for } i \in [2, N] \\ \kappa_a \left(x_{N+1}^t - x_N^t\right) + x_{N+1}^t &= (y - \epsilon_{N+1}) \text{ for } i = N+1 \end{aligned} \tag{7.6.12}$$

We consider two types of initial configurations: either all cross-bridges are in well 1 ($\forall i$, $\epsilon_i = -1$) or all the cross-bridges are in well 0 ($\forall i$, $\epsilon_i = 0$). In both cases, the actin springs are equilibrated within this initial configuration.

In our Fig.7.22B, we show the results of numerical simulations. Instead of starting with an inhomogeneous structure in the transition region like we did for the lump system, here we initiate the simulation either in the post-power-stroke homogeneous phase (see $*$) or in

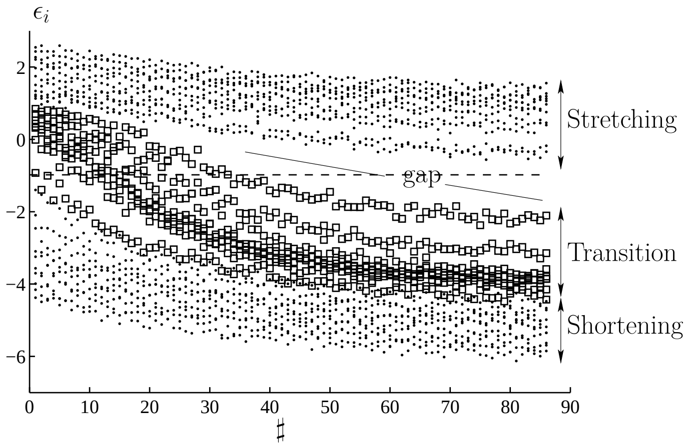

Fig. 7.23 – Distribution of average strain of each cross-bridge in thermal equilibrium at different lengths. The dashed line indicate the separation between the two wells: well 0 is at the top and well 1 at the bottom. (●) represent the equilibrium obtained in stretching and shortening outside the transition region. (□) shows the equilibrium distribution for different steps in the transition region. Note the gap between the transition curve and the stretching curves.

the pre-power-stroke homogeneous phase (see ◎). We then apply quick strain increments of different amplitude. For the ($*$) branch the initial position is at $\delta = -4.2$ nm/h and for the (◎) branch, the initial position if at $\delta = 4.2$ nm/hs. For comparison, the equilibrium T_2 curve of the lump model is represented by the dashed line and the mechanical global minimum by the solid line.

We observe that the transitions obtained with simulations starting in pre-power-stroke (◎) and simulations starting in post-power-stroke do not superimpose which reveals the presence of a macroscopic kinetic trapping. However, this hysteresis is much smaller than the hysteresis obtained within the lump model (see dotted lines). This result suggest that the kinetics of the quick recovery in hard and soft device will be faster with the distributed model than with the lump model even though the general shape of the thermal equilibrium curve and, in particular, the presence of a negative slope would survive. Notice also that the T_2 curve is smoothened in the model with distributed elasticity comparing to the lump model which also makes the results more realistic.

We show on Fig.7.23 the distribution of the snap-springs in the double well potential along the chain of 86 cross-bridges for different values of the applied elongations. The horizontal dashed line indicates the limit between well 0 which is above it and well 1 which is below it. The dotted curves represent the cases when the chain is fully in pre-power-stroke (above the dashed line) or fully in post-power-stroke (below the dashed line). They correspond, respectively to stretching and shortening outside the transition region. In the middle (see ‘transition’), we represent with squares (□) the configurations with inhomogeneous distribution of cross-bridges in the two wells. These configurations are contain a front propagating from righ to left when the loading changes from stretching to shortening. Remarkably, as predicted by the global minimum curve (see Fig.7.22 A, dashed line) the front does not propagate continuously from left to right but rather exhibits a jump between a homogeneous and an inhomogeneous configurations (see ‘gap’ on Fig.7.22).

The above preliminary results for this much more complicated mechanical system are showing that the main features of the mechanical response of the half-sarcomere have been already captured by the lump model. However, the presence of additional degrees of freedom allows for a smoother transition and accelerates the recovery as the λ_f related constraint leading in the lump model to an extremely coordinated behaviour of the cross-bridges is (partially) removed. These results also suggest the development of new experiments, where the propagation of the 'power-stroke front' could be detected during the quick recovery. Recent measurements performed at the scale of the single half-sarcomere are are showing that such experiments are now technically achievable (Rassier and Pavlov, 2010; Telley et al., 2006a).

7.7 Negative stiffness and stability

The presence of a negative slope in the T_2 curve has always been a puzzle for both the physiologists and biophysicists. Already within the model of Huxley and Simmons (see Sec.2.4.3), it was realized that a large β ($\beta > 4$) is responsible for a negative slope on the T_2 curve (see $\beta > 4$ on Fig.2.12). There are two possible mechanisms potentially leading to this phenomenon. As $\beta = \kappa a^2 / (k_B \theta)$, the negative slope would appear either as a result of large κ, the cross-bridge stiffness, or, as a result of an increase in a, the characteristic amplitude of the power-stroke. In the original Huxley and Simmons model, $a \approx 8$ nm and $\kappa \approx 0.2$ pN.nm^{-1} and the corresponding T_2 curve is flat or slightly monotone (see $\beta = 4$ on Fig.2.12). Both single molecule experiments (see Sec.2.3) and direct stiffness measurements on muscle fibers (see Sec.7.1.3) have shown that κ is at least 3 times larger (0.7 pN.nm^{-1} in (Veigel et al., 1998) and 3 pN.nm^{-1} in (Piazzesi et al., 2007)). Therefore, both types of experiments lead to the negative slope.

Most of the existing power-stroke models consider the behavior of an entire muscle fiber as a direct extrapolation of the single half-sarcomere if not a single cross-bridge. The power-stroke is modeled as a quick equilibration process between two to three configurations of attached cross-bridge (Huxley and Simmons, 1971; Piazzesi and Lombardi, 1995; Smith et al., 2008; Smith and Sleep, 2004). It has been repeatedly mentioned that that when parameters are fit to experimental data, the myosin head stiffness and the power-stroke size are such that the effective T_2 curve contains a region of negative stiffness. Most strikingly, this is precisely the region where the system is operating during isometric contractions (Cordova et al., 1992; Duke, 1999; Huxley and Tideswell, 1996; Vilfan and Duke, 2003).

Since negative stiffness is infinitely associated with instability, efforts have been made to eliminate the negative slope on the T_2 curve. One proposed solution is to increase the number of 'sub-steps' in the power-stroke mechanism which is equivalent to reducing the characteristic distance a (see Sec.2.4.4 and Fig.2.17, (Linari and Lombardi, 2010; Smith et al., 2008)). For instance A.F Huxley and S. Tideswell proposed a model introducing two sub-strokes in (Huxley and Tideswell, 1996). Another idea is to consider distributed pre-strain in the cross-bridges to account for the possibility to bind at different actin site (Huxley and Tideswell, 1996). This additional quenched inhomogeneity introduces more 'randomness' in the system and, as in the case of temperature, helps to reduce the negative slope. This idea was also used in (Marcucci and Truskinovsky, 2010).

It may be however, that a single half-sarcomere is indeed operating in the regime of negative stiffness but that rearrangement occurs within an ensemble of many half sarcomeres and in our Chap.8 finally the negative stiffness disappears at the macroscales (Efendiev and Truskinovsky, 2010; Puglisi and Truskinovsky, 2000) (see (Duke, 1999)).

Here we discuss the possibility that the negative stiffness of the power-stroke mechanism

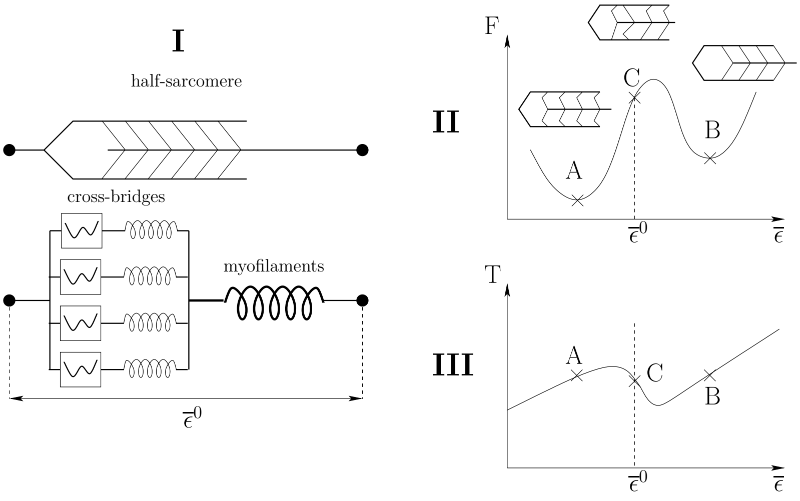

Fig. 7.24 – Effective behavior of a single half-sarcomere. (**I**): sketch of a half-sarcomere in hard device. The array of parallel cross-bridges is coupled to a linear spring in series lumping the effect of myofilaments elasticities. Our study showed that this system is characterized by a double well free energy potential as represented on (**II**). In each of the well, the cross-bridges are in affine state: either all in post-power-stroke (point A) or all in pre-power-stroke (point B) and the mixed microstructure (point C) is highly unstable. Such energy landscape is associated to a tension *vs* elongation relation displaying a region of negative stiffness (see **III**). We showed that, in order to reproduce the tension generated by muscle fibers in isometric contraction the half sarcomere must be in the unstable state C. This position is sustainable is we directly control the elongation at the level of a single half-sarcomere, but within a chain were individual units are free to elongate and shorten, half-sarcomeres will be found mostly in state A and B.

is stabilized by an active control system requiring ATP consumption.

Observe that the presence of 'negative stiffness' is actually an essential property of many biological systems that involve collective action of molecular motors (Guerin et al., 2010b; Placais et al., 2009). In this sense it is not surprising to encounter it also in muscles. When a system is operating in a region with negative stiffness in hard device, a slight change in elongation generates a large change in force. Analogously, in soft device, if the system is placed on the plateau of the L_2 curve, a slight change in force generate large shortening. This high sensitivity is used by biological systems (and also by electronic devices) to amplify an input signal. As an example we can mention hair cells which use negative stiffness to efficiently transduce the mechanical signal generated by the movement of the cilia into electric signal (Martin et al., 2000).

7.7.1 Unstable half-sarcomere

The presence of negative stiffness signals the non convexity of the and indicates that the system operates in the spinodal region (point C on Fig.7.24II). In the stables states A and B in FIg.7.24, all cross-bridges are either in post-power-stroke or in pre-power-stroke (*affine states*) while the state C corresponds to more complex microstructure (*non-affine state*). A simple way to illustrate the instability of state C is to consider the half-sarcomere initially positioned in state C and connected in series to a 'dashpot' with drag coefficient η (see Fig.7.25). When the system is released, the elongation of the half-sarcomere ϵ_z relaxes to -1 which correspond to the energy minimum with all cross-bridges in post-power-stroke (state A) (see Fig.7.25B).

By holding a single half-sarcomere in the hard device, one can of course stabilize state C. If the unstable half-sarcomere is connected with other elements there must be an active mechanism that, either triggers oscillations between state A and state B in such a way

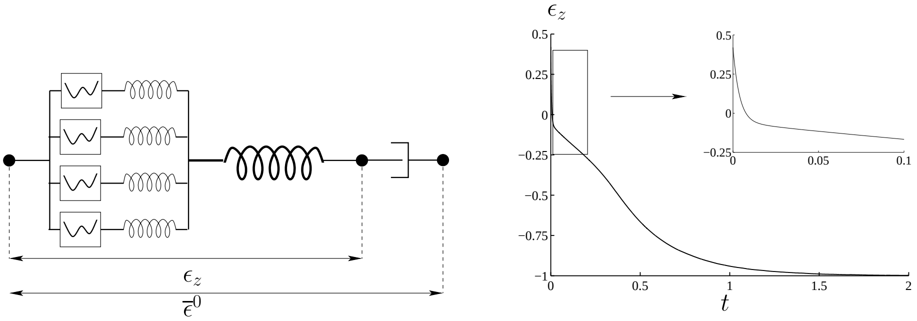

Fig. 7.25 – Instability of a single half-sarcomere released from isometric condition (point C). left: half-sarcomere in series with a dashpot, the total length is controlled. Right: elongation of the half-sarcomere ϵ_z *vs* time after the system is released from point C ($e_z = \overline{\epsilon}^0$). The system relaxes in its full post-power-stroke configuration at $\epsilon_z = -1$ (state A).

that the time averaged state is C, or directly stabilizes the state C.

7.7.2 Active stabilization mechanisms

The role of negative stiffness in muscle contraction and its stabilization was first emphasized by T.A.J Duke and further explored by A. Vilfan and T.A.J. Duke (Duke, 1999; Vilfan and Duke, 2003). The value of β used in their model is $\sim$40 corresponding to a characteristic length of 8 nm and a cross-bridge stiffness of 2.5 pN.nm^{-1} which corresponds to the domain of negative slope in our phase diagram (see Fig.4.8). The model of Vilfan and Duke belongs to the chemo-mechanical family as they phenomenologically prescribe transition rate functions for different discrete states. We should mention however that their rate functions are parametrized by several constants so the number of free parameters remains reasonable.

In the presence of attachment-detachment process, Vilfan and Duke observed the onset of oscillations that stabilize the system around the region of negative stiffness(see Fig.7.26). Their explanation is based on the fact that the cross-bridges may preferably detach from actin in the post-power-stroke state and preferably attach in pre-power-stroke.

More specifically, when the majority of bound motors are in post-power-stroke state (A2, see Fig.7.26B), the model prescribes a higher detachment rate and consequently, the number of attached motor decreases thereby increasing the force per attached motor ((1)→(2)). When the upper limit of stability in the post-power-stroke state is reached, the system abruptly jumps to the other branch of the T_2 curve in which most bound motors are in pre-power-stroke state (A1) ((2)→(3)). As the detachment rate is low in state A1, the number of bound cross-bridges increases and the force per motor decreases ((3)→(4)). Finally the system reaches the lower limit of the hysteresis loop and the cross-bridges jumps back into the post-power-stroke configuration. Then the cycle repeats itself ((4)→(1)).

This simple scheme explains how an isometrically contracting muscle may be consuming ATP without net change in elongation at the macroscopic scale. The consumed energy is fully dissipated as the system is constantly oscillating to remain in average in the region of instability. P. Martin *et al.* used the same argument to explain how the active hair bundle in the ear constantly adapts to maintain the system in the unstable regime (Martin et al., 2000).

Following (Vilfan and Frey, 2005), we can propose a simple mechanical set-up generating oscillations at the level of a single half-sarcomere (see Fig.7.27A). Let us arrange

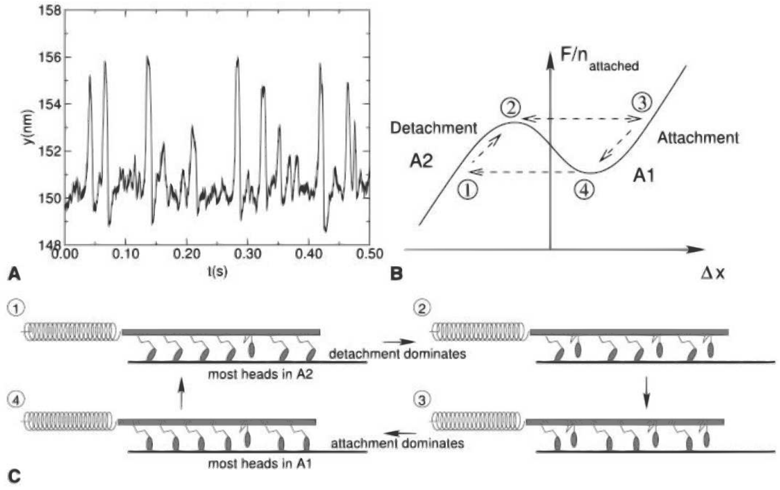

Fig. 7.26 – **Instabilities of an assembly of cross-bridges in near isometric conditions**. Taken from (Vilfan and Duke, 2003). (**A**): oscillations of an array of cross-bridges in isometric conditions. The presence of a negative slope leads to oscillations in a system where attachment and detachment occurs: (1) when the majority of bound motors are in state A2 (post-power-stroke), the average detachment rate is higher than attachment rate (this is prescribed by the model), thus the number of attached motor decreases thereby increasing the force per motor ((1)→(2)). When the upper limit of the hysteresis is reached, the system abruptly jumps to the other fixed point in which most bound motors are in state A1 (pre-power-stroke) ((2)→(3)). As the detachment rate is low in state A1, the number of bound cross-bridges increases and the force per motor decreases ((3)→(4)). Finally the system reaches the lower limit of the hysteresis loop and the cross-bridges jumps back in post-power-stroke conformation and the cycle repeats((4)→(1)).

in parallel a so-called *delayed force activator* and a *power-stroke element* which is characterized by a tension *vs* length relation with a region of negative stiffness $T_2\left(\epsilon\left(t\right)\right)$. For simplicity, we use a piecewise linear force elontation relation represented on Fig.7.27D(solid line). The force delayed activation element is characterized by the following constitutive relation:

$$\frac{d\sigma}{dt}=\frac{1}{\tau}\left(\kappa_a\epsilon\left(t\right)-\sigma\left(t\right)\right). \tag{7.7.1}$$

When $\epsilon\left(t\right)=\epsilon^0=const$, and $\sigma\left(t_0\right)=0$, the stress $\sigma\left(t\right)$ increases exponentially with the characteristic time τ till it stabilizes at the level equal to $\kappa_a\epsilon^0$. We put this mechanical system in a soft device, where the total tension $T=\sigma\left(t\right)+T_2\left(\epsilon\left(t\right)\right)$ is held constant and we fix $T=0.2$. Suppose that the initial condition is chosen. This means that the system to be $\epsilon\left(t=0\right)=0$, which is located in the center of the unstable region, where $T_2=0$ (see Fig.7.27D).

First, as the load increases, ϵ decreases due to the negative slope effect. Then, as ϵ decreases, the force activation mechanism starts to reduce the tension σ which induces a further increase in T_2 and further decrease in ϵ. This process continues until the system reaches the point α on the T_2 *vs* ϵ curve where the elongation ϵ jump to the stable branch at point β. Such sudden elongation activates an increase in σ and therefore a decrease in T_2 accompanied by a decrease in ϵ up to point γ where a new jump occurs. The system is now in δ so the tension σ starts to decrease which again generates an increase in both T_2 and σ bringing the system back to point α where the whole cycle restarts. It is clear that with this mechanism, the time average value of ϵ is 0 (see Fig.7.27B and D).

One can see that this rather simple mechanical feedback device is able to generate self oscillation under isotonic conditions. As we have already mentioned, such oscillatory behavior is present in many dynamic cellular processes involving for instance auditory

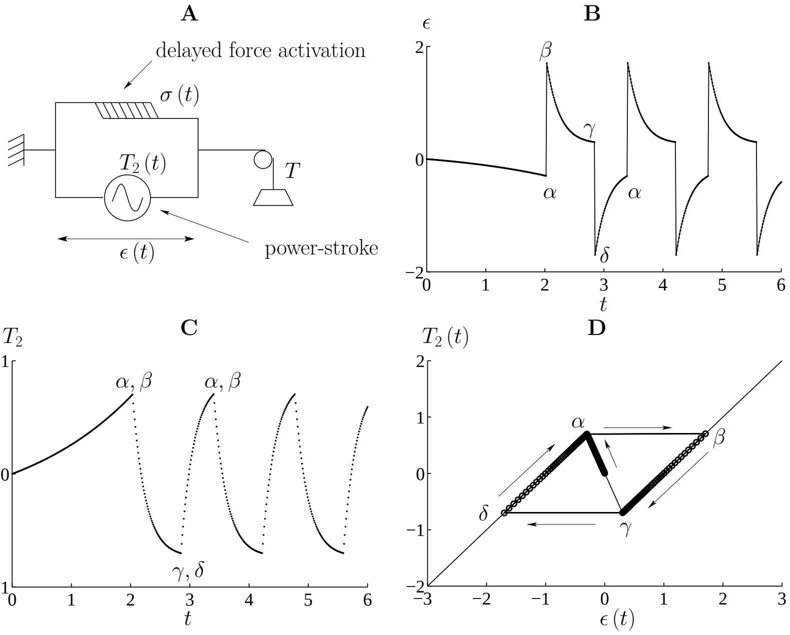

Fig. 7.27 – Response of a force delayed activation coupled to a power-stroke element. (**A**): mechanical set-up. A force delayed activation mechanism is connected in parallel to a power-stroke element showing a region of negative stiffness which we characterize by a piece-wise linear relation $T_2(\epsilon)$ represented by a solid line on (**D**). This system is load in soft device and the applied tension T is constant; here, $T = 0.2$. (**B**) and (**C**) show the evolution of ϵ and T_2 *vs* time. The system is initialized at $\epsilon = 0$ in the center of the unstable region ($T_2 = 0$). The parametric trajectory $(\epsilon(t), T_2(t))$ is represented by circles on (**D**).

hair bundles, or rod-like bacterium *Esherichia coli* (Grill et al., 2005; Günther and Kruse, 2007; Kruse and Jülicher, 2005). In the context of muscle we can mention the SPontaneous Oscillatory Contraction (SPOC), which has been observed at intermediate muscle activation (see the recent review on the subject by Ishiwata et al., 2011). This oscillatory regime is also observed under physiological conditions for cardiac muscles. In fact, P.-Y. Plaçais *et al.* demonstrated that the auto-oscillatory movement can take place in in *in vitro* motility assays composed of randomly distributed myosin molecules and actin filaments suggesting that this property is inherent to the contractile proteins (Placais et al., 2009).

Of course, in the muscle context, the inner working of the force delayed activation element is still not clear and can be viewed only as a prototypical phenomenological representation of the attachment-detachment process. However, our simple numerical experiment suggests a way to build an actual experimental soft device set-up at the level of a single sarcomere. This seems accessible in view of the recent results published in (Rassier and Pavlov, 2010). For a single sarcomere, the T_2 *vs* ϵ relation shows actually two regions with negative slope (see Fig.8.3), so, depending on the initial elongation, one should be able to observe different hysteresis loops within the same general range of applied loads.

7.7.3 Direct mechanical stabilization

In the previous models our system responded only passively to external loadings hence, the isometric unstable state was maintained only on average. There exist however a possibility to stabilize the state C shown on Fig.7.24 directly by applying periodic (or correlated) mechanical excitation immitating ATP activity. This idea of parametric resonnance is used

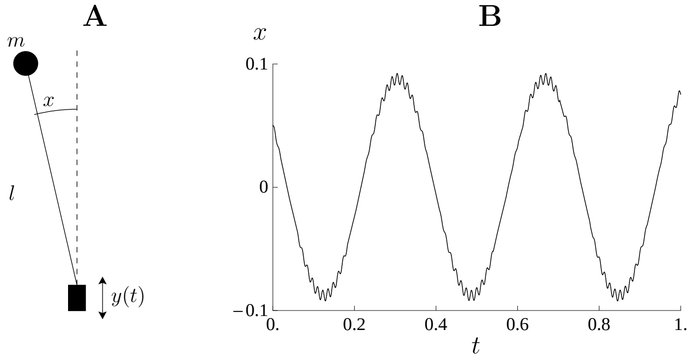

Fig. 7.28 – **Stabilization of an inverted pendulum**. (**A**): the inverted pendulum with a mobile base $y(t)$. (**B**): example of stabilization by rapid oscillation of the base from Eq.(7.7.3). Parameters are: $g = 10$ m.s^{-2}, $l = 1$ m, $A = 0.05$ m, $\omega = 500$ s^{-1}

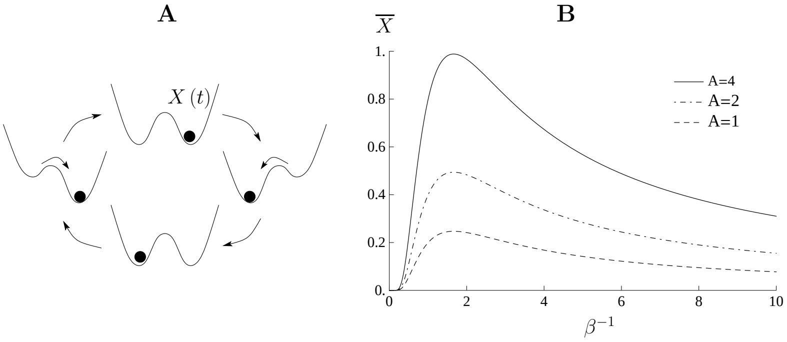

Fig. 7.29 – **Stochastic resonance**. When a periodic force is added to a double well potential, the particle $X(t)$ oscillate between the wells (**A**). The amplitude of the displacement in X are shown in (**B**) as a function of the diffusion coefficient β^{-1} for 3 different amplitudes of the periodic force: $A = 1$ (dashed line), $A = 2$ (dot-dashed line) and $A = 4$ (solid line).

for instance to stabilize an inverted pendulum or a launching rocket (see Fig.7.28A). The equation of motion for an inverted pendulum with a mobile support can be written:

$$l\ddot{x} - \ddot{y}\sin(x) = g\sin(x) \tag{7.7.2}$$

where x is the angle of the pendulum with the vertical axis, y is the vertical position of the support base, l is the length of the massless bar and g is acceleration of gravity. Suppose that $y(t)$ is an harmonic function $y = A\sin(\omega t)$. Then the equation of motion becomes (Mathieu equation):

$$\ddot{x} + \left(-\frac{g}{l} + \frac{A}{l}\omega^2 \sin(\omega t)\right)\sin(x) = 0$$

The numerical simulation reported on Fig.7.28 shows that, for sufficiently fast oscillations of the support, the pendulum indeed oscillates around the unstable upward position. More sophisticated stabilization strategies outside the linear regime are developed for instance in (Carbo et al., 2010).

7.7.4 Stochastic resonance

Yet another stabilizing mechanism which takes randomness into account is based on the idea of stochastic resonnance (Gammaitoni et al., 1998; Grossmann et al., 1993; Jung, 1993). Suppose that the double well potential $v(x)$ is periodically tilted so that the system constantly oscillates between states A and B and the time averaged position is in state C (see Fig.7.29). Suppose also that the system is subjected to Gaussian white noise. Then, we write the following SDE describing the system dynamics in the form:

$$dX^t = \left(-\partial_X V + F\left(t\right)\right) dt + \sqrt{2\beta^{-1}} dB^t \tag{7.7.3}$$

where $F\left(t\right)$ is a time periodic force with frequency ω, *e.g.*:

$$F\left(t\right) = A \cos\left(\omega t + \phi\right). \tag{7.7.4}$$

Consider a symmetric double well potential V with two minima located at $+\hat{x}$ and $-\hat{x}$. denote r_0 and r_1 the transition rates over the energy barrier ΔV from both wells. In the limit $\beta \to \infty$, and since here we are dealing with a symmetric V, the transition rates r_0 and r_1 and can be expressed as an exponential function of the energy barrier :

$$r_0 = r_1 = K \exp\left[-\beta \Delta V\right] \text{ with } K \in \mathbb{R} \tag{7.7.5}$$

Under the periodic forcing (7.7.4), those transition rate become periodic:

$$r_+\left(t\right) = r_0 \exp\left[\beta A \hat{x} \cos\left(\omega t\right)\right] \tag{7.7.6}$$

$$r_-\left(t\right) = r_1 \exp\left[-\beta A \hat{x} \cos\left(\omega t\right)\right] \tag{7.7.7}$$

Then it can be shown that also the average position $\langle X \rangle$ becomes a periodic function ot time. In the limit of small temperature ($\beta \to \infty$), the mean amplitude of the particle's position $\langle \overline{X} \rangle$ has the following limit:

$$\left\langle \overline{X}\left(\beta\right) \right\rangle = \beta A \hat{X}^2 2 r_0 \left(4 r_0^2 + \omega^2\right)^{-\frac{1}{2}} \tag{7.7.8}$$

Our Fig.7.29 shows the dependence of $\langle \overline{X} \rangle$ on β^{-1} for different amplitudes of the periodic force (dashed line $A = 1$, dot-dashed line $A = 2$, solid line $A = 4$). One can see that the amplitude reaches its maximum at a particular temperature (*stochastic resonnance*).

In this Chapter (but also in Chap.8), we saw that the response of our system to a load step was dominated by kinetics. This result questions our initial hypothesis of the power-stroke as a purely mechanical process and suggests that ATP may be playing an important role even at the short time scale involved in the power-stroke. The activity of ATP in the power-stroke would justify the use of a periodic (correlated) function that can stabilize the unstable state and accelerate the kinetics through stochastic resonnance. It is likely that again the presence of coupling enhances the effect of a local stochastic resonance and synchronizes the response maximize force recovery.

Conclusions

In the previous sections we proposed a model with only 6 parameters (λ_1, λ_0, l, N, λ_f, β) plus two additional conditions describing the isometric contraction ($\overline{\epsilon}^0$ and T_0). In this section we were able to fit the available experimental data and construct an adequate model of a half-sarcomere.

We have shown that the isometric contraction is robustly characteristic by a strong effective negative stiffness. This allows the system to operate with maximum number of wells in the energy landscape.

By simulating the response to fast load steps in hard and soft devices, we observed that kinetics dominates at experimental time scales. The kinetic response reveals the double well nature of the non-equilibrium energy landscape which is the origin of the trapping phenomenon. The scale of slowing down is dramatically larger in soft device than in hard device.

In addition we proposed an extension of our model to explain the puzzling asymmetry between the response in shortening and the response in stretching. In the later case, a decrease in both the tension T_2 and the rate is obtain by either modeling the presence of the second myosin head or the passive friction of the detaching heads on the myofilaments.

We also presented preliminary results on our ongoing work on a system with distributed elasticity. The main conclusion regarding the presence of negative stiffness remains the same but we have access to a richer panel of available microstructures.

We investigated several mechanisms that would allow the system to stabilize in the spinodal region of the energy. These mechanisms involve continuous energy supply and are therfore implicitely linked to ATP activity. The need of such active stabilization would mean that the power-stroke mechanism requires ATP for its functionning.

After our attempts to reproduce experimental data in the setting of a single half sarcomere, we see that he mystery of the plateau in the T_2 curve remains unresolved. In the next Chapter, where we consider a series arrangement of half-sarcomeres, this problem will disappear and the responses in hard and soft devices will become more similar but the difference in kinetics will remain.

Chapter 8

Chain of half-sarcomeres

In a muscle fiber, thousands of sarcomeres are tightly interconnected and it is this bundle of active elements that ultimately generates the macroscopic force. In this Chapter, we consider a series arrangement of half-sarcomere and address the question of how the different behaviors observed experimentally in hard and soft device for the single unit translate into the behavior of the whole fiber. Following the same approach as in the case of a single half-sarcomere, we start with a description of the local minima in the purely mechanical setting. In particular, we study in detail the case of 2 half-sarcomeres in series forming a sarcomere. We show that the presence of the coupling parameter, augments the wiggliness of the non-equilibrium energy landscape as it was the case for a single half-sarcomere. Finally, we derive an asymptotic formula for the free energy of a chain in the thermodynamic limit and show that the behaviors in hard and soft devices becomes more similar from the points of view of equilibrium but a difference remains in kinetics.

Contents

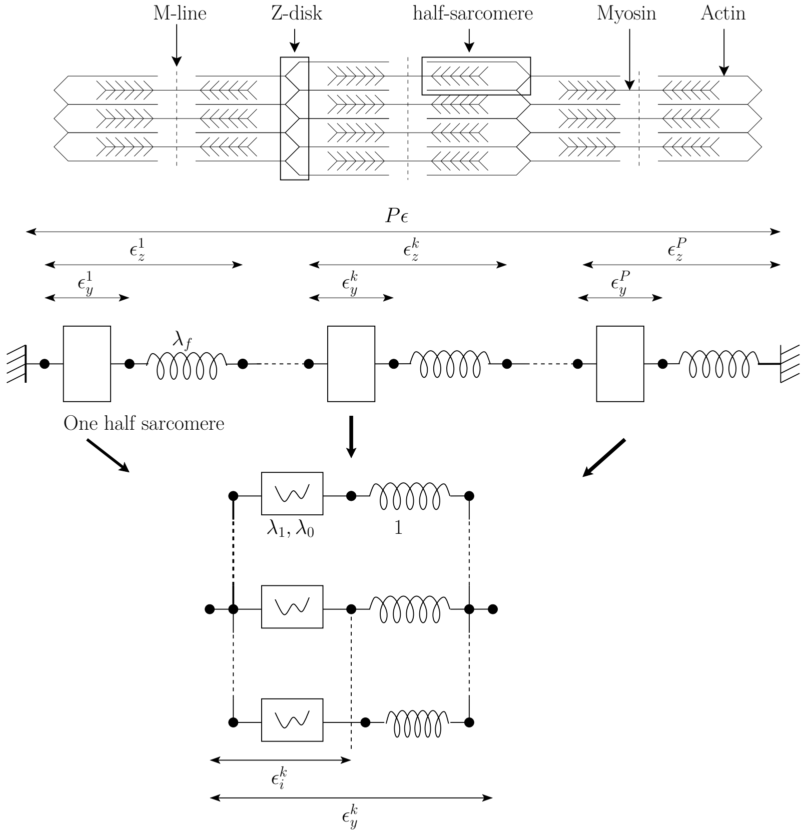

Fig. 8.1 – Mechanical model of a chain of sarcomeres. Upper panel: sketch of an assembly of sarcomere in the longitudinal axis of the fiber. Lower panel: our mechanical model with an assembly of series half-sarcomeres. P denotes the number of half-sarcomeres connected in series. The elongation of half-sarcomere k is noted ϵ_z^k. The elongation of the array of cross-bridges of half-sarcomere k is ϵ_y^k and inside the array of cross-bridges, the elongation of cross-bridge i is noted ϵ_i^k. The total elongation of the chain is $\overline{\epsilon} = \frac{1}{P} \sum\limits_{k=1}^{P} \epsilon_z^k$.

8.1 Mechanical model

We consider an assembly of P half-sarcomeres in series. Each half-sarcomere contains N cross-bridges connected in parallel and a linear spring representing the myofilaments (see Fig.8.1). The total elongation of the chain is $P\epsilon$ where ϵ denotes the mean elongation per half-sarcomere. In the half-sarcomere with index k, ϵ_z^k is the total elongation, ϵ_y^k is the elongation of the cross-bridge array and ϵ_i^k is the elongation of the cross-bridge with index i. For simplicity, we assume that each units contains the same number of cross-bridges: N. We denote $\underline{\epsilon} = \left(\epsilon_1^1, \dots, \epsilon_N^1, \dots, \epsilon_1^P, \dots, \epsilon_N^P, \epsilon_y^1, \dots, \epsilon_y^P, \epsilon_z^1, \dots, \epsilon_z^P\right)$ the vector containing all $P\left(N+2\right)$ degrees of freedom. The total energy of the system is given by:

$$V\left(\underline{\epsilon}\right) = \sum_{k=1}^{P} \left\{ \sum_{i=1}^{N} \left(v\left(\epsilon_i^k\right) + \frac{1}{2}\left(\epsilon_y^k - \epsilon_i^k\right)^2 \right) + N\lambda_f \frac{1}{2}\left(\epsilon_z^k - \epsilon_y^k\right)^2 \right\} \tag{8.1.1}$$

where v is the double well potential introduced in Chap.2 (see Eq.2.5.23).

In the hard device, the total elongation of the chain is fixed: $P\epsilon = P\overline{\epsilon} = \sum\limits_{k=1}^{P} \epsilon_z^k$. $\overline{\epsilon}$ is then the applied elongation per half-sarcomere. In the soft device case, the tension $\overline{\sigma}$ is imposed.

8.1.1 Mechanical equilibria

Metastable states

In order to understand the inner working of this system, we first start with describing the equilibrium response at zero temperature as we did in Chap.3. In hard device, we prescribe the total: $\epsilon = \overline{\epsilon}$ and we compute $\hat{V}\left(\overline{\epsilon}\right)$, the energy with all internal variables are minimized. In soft device, we minimize $W = V - \overline{\sigma}\epsilon$ where $\overline{\sigma}$ is the applied tension. The analysis follows (Puglisi and Truskinovsky, 2000) where the authors deal with a chain of bistable spring. Here instead, we have a chain of elements where each element is a parallel bundle of bi-stable springs and linear elastic spring.

The metastable states of the system are obtain by minimizing:

$$V\left(\underline{\epsilon}, \overline{\epsilon}\right) - T\left(\overline{\epsilon} - \frac{1}{P}\sum_{k=1}^{P} \epsilon_z^k\right) = \psi\left(\epsilon, \overline{\epsilon}, T\right) \text{ in hard device}$$

$$W\left(\underline{\epsilon}, \overline{\sigma}\right) = V\left(\underline{\epsilon}\right) - \overline{\sigma}\sum_{k=1}^{P} \epsilon_z^k \text{ in soft device.} \tag{8.1.2}$$

with T, the Lagrange multiplier associated with the hard device constrain. In hard device the minimisation problem is:

$$\operatorname{grad}\psi\left(\left(\underline{\epsilon}, \overline{\epsilon}, T\right)\right) = \underline{0} \tag{8.1.3}$$

and similarly in soft device it is:

$$\operatorname{grad} W\left(\underline{\epsilon}, \overline{\sigma}\right) = \underline{0} \tag{8.1.4}$$

Along the coordinate ϵ_i^k we have:

$$\partial_{\epsilon_i^k}\psi\left(\underline{\epsilon}, \overline{\epsilon}, T\right) = v'(\epsilon_i^k) - \epsilon_y^k + \epsilon_i^k = 0 \text{ in the hard device} \tag{8.1.5}$$

$$\partial_{\epsilon_i^k} W\left(\underline{\epsilon}, \overline{\sigma}\right) = v'(\epsilon_i^k) - \epsilon_y^k + \epsilon_i^k = 0 \text{ in the soft device.} \tag{8.1.6}$$

As in the case of a single sarcomere, equations $\partial_{\epsilon_i^k}\psi = 0$ and $\partial_{\epsilon_i^k}\phi = 0$ can have up to 3 solutions:

$$\begin{cases} \hat{\epsilon}_1^k\left(\epsilon_y^k\right) = \left(1-\lambda_1\right)\left(\epsilon_y^k\right) - \lambda_1, & \text{if } \epsilon_i^k < l \\ \hat{\epsilon}_0^k\left(\epsilon_y^k\right) = \left(1-\lambda_0\right)\left(\epsilon_y^k\right), & \text{if } \epsilon_i^k \geq l \\ \hat{\epsilon}_\star^k = l. & \end{cases} \tag{8.1.7}$$

Then we define the triplet $\xi^k = \left(n_1^k, n_\star^k, n_0^k\right)$, denoting the fraction of cross-bridges in half-sarcomere k that occupy position $\hat{\epsilon}_1^k$, $\hat{\epsilon}_\star^k$ and $\hat{\epsilon}_0^k$ respectively. The vector ξ^k defines the microstructure of half-sarcomere k. We will next denote $\underline{\xi} = \left(\xi^1, \ldots, \xi^k\right)$, the configuration of the whole chain. Obviously we have: $n_1^k + n_\star^k + n_0^k = 1$ for all $1 \leq k \leq P$. For a given configuration ξ^k, the equilibrium value of ϵ_y^k in the half-sarcomere k is given by:

$$\hat{\epsilon}_y^k\left(\xi^k, \overline{\epsilon}\right) = \frac{1}{\lambda_{xb}^k\left(\xi^k\right)}\left(\frac{T\left(\overline{\epsilon}\right)}{N} - n_1^k\lambda_1 + n_\star^k l\right) \text{ in hard device} \tag{8.1.8}$$

$$\hat{\epsilon}_y^k\left(\xi^k, \overline{\sigma}\right) = \frac{1}{\lambda_{xb}^k\left(\xi^k\right)}\left(\frac{\overline{\sigma}}{N} - n_1^k\lambda_1 + n_\star^k l\right) \text{ in soft device,} \tag{8.1.9}$$

$$\text{where } \lambda_{xb}(\xi^k) = n_1^k\lambda_1 + n_0^k\lambda_0 + n_\star^k. \tag{8.1.10}$$

The elongation of half-sarcomere k is obtained from the equation $\epsilon_z^k = \epsilon_y^k + T\left(\overline{\epsilon}, \underline{\xi}\right)/\left(N\lambda_f\right)$ in hard device and soft devices (with $\overline{\sigma}$ instead of $T\left(\overline{\epsilon}\right)$ in soft device). Finally we close the system by writing the relation between the tension T (resp. $\overline{\sigma}$ in soft device) and the total elongation $\overline{\epsilon}$ (resp.ϵ in soft device) which can be written in the form:

$$\overline{\epsilon} = \frac{1}{P}\sum_{k=1}^{P}\left\{\epsilon_y^k + \frac{T\left(\overline{\epsilon},\xi\right)}{N\lambda_f}\right\} \text{ in the hard device} \tag{8.1.11}$$

$$\epsilon = \frac{1}{P}\sum_{k=1}^{P}\left\{\epsilon_y^k + \frac{\overline{\sigma}}{N\lambda_f}\right\} \text{ in the soft device} \tag{8.1.12}$$

After computations, an equilibrium state can be written as follows:

$$\hat{T}\left(\overline{\epsilon},\underline{\xi}\right) = N\left(\frac{1}{\lambda_f} + \frac{1}{P}\sum_{k=1}^{P}\frac{1}{\lambda_{xb}\left(\xi^k\right)}\right)^{-1}\left(\overline{\epsilon} + \frac{1}{P}\sum_{k=1}^{P}\frac{n_1^k\lambda_1 - n_\star^k l}{\lambda_{xb}\left(\xi^k\right)}\right) \qquad \text{(hard device)} \tag{8.1.13}$$

$$\hat{\epsilon}\left(\overline{\sigma},\underline{\xi}\right) = \left(\frac{1}{\lambda_f} + \frac{1}{P}\sum_{k=1}^{P}\frac{1}{\lambda_{xb}\left(\xi^k\right)}\right)\frac{\overline{\sigma}}{N} - \frac{1}{P}\sum_{k=1}^{P}\frac{n_1^k\lambda_1 - n_\star^k l}{\lambda_{xb}\left(\xi^k\right)} \qquad \text{(soft device).} \tag{8.1.14}$$

As in the case of a single half-sarcomere, the formulas are identical. The influence of the microstructure of the chain ξ, appears only through the sums over k. Therefore there is an additional permutational invariance among different half-sarcomeres for a given configuration $\left(\xi^1,\ldots,\xi^P\right)$. We define the stiffness of the chain for a given configuration $\underline{\xi}$ by:

$$\lambda\left(\underline{\xi}\right) = \left(\frac{1}{\lambda_f} + \frac{1}{P}\sum_{k=1}^{P}\frac{1}{\lambda_{xb}\left(\xi^k\right)}\right)^{-1} \tag{8.1.15}$$

Then, the energy of a given configuration can be written as follows:

$$\begin{aligned}\hat{V}\left(\overline{\epsilon},\underline{\xi}\right) = NP\Bigg[&\lambda\left(\underline{\xi}\right)\left(\overline{\epsilon} + \frac{1}{P}\sum_{k=1}^{P}\frac{n_1^k\lambda_1 - n_\star^k l}{\lambda_{xb}\left(\xi^k\right)}\right)^2 \\ &-\frac{1}{2}\frac{1}{P}\sum_{k=1}^{P}\left(\frac{\left(n_1^k\lambda_1 - n_\star^k l\right)^2}{\lambda_{xb}\left(\xi^k\right)} - C\left(\xi^k\right)\right)\Bigg] \text{ in hard device,}\end{aligned} \tag{8.1.16}$$

$$\begin{aligned}\hat{W}\left(\overline{\sigma},\underline{\xi}\right) = NP\Bigg[&-\frac{1}{2}\frac{1}{\lambda_f}\left(\frac{\overline{\sigma}}{N}\right)^2 - \frac{1}{P}\sum_{k=1}^{P}\left\{\frac{1}{2}\frac{1}{\lambda_{xb}\left(\xi^k\right)}\left(\frac{\overline{\sigma}}{N} - n_1^k\lambda_1 + n_\star^k l\right)^2\right\} \\ &+\frac{1}{P}\sum_{k=1}^{P}C\left(\xi^k\right)\Bigg] \text{ in soft device,}\end{aligned} \tag{8.1.17}$$

where $C(\xi^k) = (n_0^k + n_\star^k)v_0 + \frac{1}{2}n_1^k\lambda_1 + \frac{1}{2}n_\star^k\frac{1}{1-\lambda_0}l^2$

It is easy to check that one can also write

$$\hat{T}\left(\overline{\epsilon},\xi\right) = \frac{\partial\hat{V}\left(\overline{\epsilon},\xi\right)}{\partial\left(P\overline{\epsilon}\right)} \text{ in hard device,} \tag{8.1.18}$$

$$\hat{\epsilon}\left(\overline{\sigma},\xi\right) = -\frac{\partial\hat{W}\left(\overline{\sigma},\xi\right)}{\partial\overline{\sigma}} \text{ in soft device.} \tag{8.1.19}$$

In order to have a better understanding of the internal configuration of the chain, we also compute the elongation of each given half-sarcomere k:

$$\hat{\epsilon}_z^k \left(\overline{\epsilon}, \xi^k\right) = \frac{1}{\lambda_{xb}\left(\xi^k\right)} \left(\frac{\hat{T}\left(\overline{\epsilon}, \xi\right)}{N} - n_1^k \lambda_f + n_\star^k l \right) + \frac{\hat{T}\left(\overline{\epsilon}, \xi\right)}{N \lambda_f}, \text{ in hard device} \tag{8.1.20}$$

$$\hat{\epsilon}_z^k \left(\overline{\sigma}, \xi^k\right) = \left(\frac{1}{\lambda_f} + \frac{1}{\lambda_{xb}\left(\xi^k\right)} \right) \frac{\overline{\sigma}}{N} - \frac{n_1^k \lambda_f - n_\star^l l}{\lambda_{xb}\left(\xi^k\right)}, \text{ in soft device.} \tag{8.1.21}$$

In hard device (see Eq.8.1.20), the elongation of a given half-sarcomere depends on the configuration of the whole chain (ξ) through the tension $\hat{T}$ given by Eq.(8.1.13) while in soft device (see Eq.8.1.21), the local elongation depends only on the local configuration (ξ^k). Moreover, in hard and soft devices all half-sarcomeres with the same microstructure ξ^k have the same elongation.

Stability

The stability of a given equilibrium configuration can be checked using the Hessian matrix. Let us consider first the generic case where the spinodal region of the double well is not reduced to a single point. Here we present the hard device case only; the stability related conclusions are the same in soft device.

After eliminating the hard device constrain $\overline{\epsilon} = \frac{1}{P} \sum \epsilon_z^k$, we rewrite the energy as a function of $(P-1)(N+2) + P + 1$ variables:

$$\tilde{V}\left(\epsilon_1^1, \dots, \epsilon_y^P\right) = V\left(\epsilon_1^1, \dots, \epsilon_y^P, P\overline{\epsilon} - \sum_{k=1}^{P} \epsilon_{z^k}\right)$$

Consider first the entries of the Hessian associated with $k = 1, \dots, P$. We have seen that the equation $\partial_{\epsilon_i^k} \tilde{V} = 0$ have up to 3 solutions, $\hat{e}_1(\overline{\epsilon}), \hat{e}_0(\overline{\epsilon})$ and $\hat{\epsilon}_\star(\overline{\epsilon})$, with $l - t \leq \hat{\epsilon}_\star(\overline{\epsilon}) \leq l + t$ for all $t > 0$.

We denote:

$$H_i^k(\overline{\epsilon}) = \partial_{ii}^k V\left(\overline{\epsilon}, \underline{\epsilon}\right), \; i = 1, \dots, N, y, z$$

the N first diagonal terms of the Hessian. Each of them can be equal either to $h_1^k(\overline{\epsilon})$, $h_0^k(\overline{\epsilon})$ or $h_\star^k(\overline{\epsilon})$ where:

$$\partial_{ii}^k V\left(\overline{\epsilon}, \underline{\epsilon}\right)\Big|_{\epsilon_i^k = \hat{\epsilon}_1^k(\overline{\epsilon}), \epsilon_{j\neq i}^{m\neq k} = \hat{\epsilon}_j^m(\overline{\epsilon}), \epsilon_{y^k} = \hat{\epsilon}_y^k(\overline{\epsilon}), \epsilon_{y^{m\neq k}} = \hat{\epsilon}_y^m(\overline{\epsilon}) \epsilon_{z^k} = \hat{\epsilon}_y^k(\overline{\epsilon}), \epsilon_{z^{m\neq k}} = \hat{\epsilon}_y^m(\overline{\epsilon})} \equiv h_1^k(\overline{\epsilon}) > 0,$$

$$\partial_{ii}^k V\left(\overline{\epsilon}, \underline{\epsilon}\right)\Big|_{\epsilon_i^k = \hat{\epsilon}_\star^k(\overline{\epsilon}), \epsilon_{j\neq i}^{m\neq k} = \hat{\epsilon}_j^m(\overline{\epsilon}), \epsilon_{y^k} = \hat{\epsilon}_y^k(\overline{\epsilon}), \epsilon_{y^{m\neq k}} = \hat{\epsilon}_y^m(\overline{\epsilon}) \epsilon_{z^k} = \hat{\epsilon}_y^k(\overline{\epsilon}), \epsilon_{z^{m\neq k}} = \hat{\epsilon}_y^m(\overline{\epsilon})} \equiv h_\star^k(\overline{\epsilon}) < 0,$$

$$\partial_{ii}^k V\left(\overline{\epsilon}, \underline{\epsilon}\right)\Big|_{\epsilon_i^k = \hat{\epsilon}_\star^k(\overline{\epsilon}), \epsilon_{j\neq i}^{m\neq k} = \hat{\epsilon}_j^m(\overline{\epsilon}), \epsilon_{y^k} = \hat{\epsilon}_y^k(\overline{\epsilon}), \epsilon_{y^{m\neq k}} = \hat{\epsilon}_y^m(\overline{\epsilon}) \epsilon_{z^k} = \hat{\epsilon}_y^k(\overline{\epsilon}), \epsilon_{z^{m\neq k}} = \hat{\epsilon}_y^m(\overline{\epsilon})} \equiv h_0^k(\overline{\epsilon}) > 0.$$

The other entries of the Hessian $H^k(\overline{\epsilon})$ are, for a single half-sarcomere:

$$\begin{aligned}
&\partial_{ij}^k V\left(\overline{\epsilon}, \underline{\epsilon}\right) = 0 \text{ for } i \neq j \\
&\partial_{iy}^k V\left(\overline{\epsilon}, \underline{\epsilon}\right) = -1 \text{ for } i = 1, \dots, N \\
&\partial_{yy}^k V\left(\overline{\epsilon}, \underline{\epsilon}\right) = N\left(1 + \lambda_f\right) \\
&\partial_{iz}^k V\left(\overline{\epsilon}, \underline{\epsilon}\right) = 0 \\
&\partial_{yz}^k V\left(\overline{\epsilon}, \underline{\epsilon}\right) = -N\lambda_f, \text{ for } 1 \leq k \leq P-1 \\
&\partial_{zz}^k V\left(\overline{\epsilon}, \underline{\epsilon}\right) = N\lambda_f, \text{ for } 1 \leq k \leq P-1
\end{aligned}$$

Therefore we can write:

$$H^k(\overline{\epsilon}) = \begin{pmatrix} H_1^k(\overline{\epsilon}) & 0 & \cdots & 0 & -1 & 0 \\ 0 & \ddots & \ddots & \vdots & \vdots & \vdots \\ \vdots & \ddots & \ddots & 0 & \vdots & \vdots \\ 0 & \cdots & 0 & H_N^k(\overline{\epsilon}) & -1 & 0 \\ -1 & \cdots & \cdots & -1 & N(1+\lambda_f) & -N\lambda_f \\ 0 & \cdots & \cdots & -1 & -N\lambda_f & N\lambda_f \end{pmatrix}, \text{ for } 1 \leq k \leq P-1$$

and for the last half-sarcomere:

$$H^P(\overline{\epsilon}) = \begin{pmatrix} H_1^P(\overline{\epsilon}) & 0 & \cdots & 0 & -1 \\ 0 & \ddots & \ddots & \vdots & \vdots \\ \vdots & \ddots & \ddots & 0 & \vdots \\ 0 & \cdots & 0 & H_N^P(\overline{\epsilon}) & -1 \\ -1 & \cdots & \cdots & -1 & N(1+\lambda_f) \end{pmatrix}$$

These matrices contains the blocks with the following dimensions: $H^k \in \mathbb{R}^{(N+2)\times(N+2)}$ and $H^P \in \mathbb{R}^{(N+1)\times(N+1)}$. Now, we consider the terms coupling sarcomere k with half-sarcomere $m \neq k$ in the Hessian corresponding to the whole chain:

$$\partial_{zz}^{km\neq k} V(\overline{\epsilon}, \underline{\epsilon}) = N\lambda_f \qquad (8.1.22)$$

$$\partial_{zy}^{kP} V(\overline{\epsilon}, \underline{\epsilon}) = N\lambda_f. \qquad (8.1.23)$$

Hence the complete Hessian can be written in the form:

$$H^P(\overline{\epsilon}) = \begin{pmatrix} H^1(\overline{\epsilon}) + C & C & \cdots & C & C^P \\ C & \ddots & \ddots & \vdots & \vdots \\ \vdots & \ddots & \ddots & C & \vdots \\ C & \cdots & C & H^{P-1}(\overline{\epsilon}) + C & C^P \\ {}^T(C^P) & \cdots & \cdots & {}^T(C^P) & H^P \end{pmatrix}$$

$$\text{where} \quad C = \begin{pmatrix} 0 & & & \\ & \ddots & & \\ & & 0 & \\ & & & N\lambda_f \end{pmatrix} \in \mathbb{R}^{(N+2)\times(N+2)}$$

$$\text{and} \quad C^P = \begin{pmatrix} 0 & & \\ & \ddots & \\ & & 0 \\ & & N\lambda_f \end{pmatrix} \in \mathbb{R}^{(N+2)\times(N+1)}.$$

The computation of the principal minors is too technical to be written in full details here. But one can show, using this technique that if all cross-bridges are in a stable position, the chain of half-sarcomere is stable. However, we see that as soon as a single cross-bridge stays in the spinodal region, H^k cannot be positive definite (see Eq.8.1.1) and so the whole chain becomes unstable. In must be noted that for the case of a chain of bistable element, each, being characterized by a double well potential of the type of our v, the whole chain can be stable even in the presence of one unstable element (Puglisi and Truskinovsky, 2000).

Existence domain of metastable configurations

As in the case of one half-sarcomere, different metastable states exist on different finite intervals of the variation of the loading parameters. The solution of the minimization problem gives the equilibrium position of each cross-bridge in the double well potential. We use and (8.1.8) and (8.1.9) in Eq.(8.1.7) to obtain:

$$\begin{cases} \hat{\epsilon}_1^k\left(T,\xi^k\right) = \frac{1-\lambda_1}{\lambda_{xb}\left(\xi^k\right)}\left(\frac{T}{N} - n_1^k\lambda_1 + n_\star^k l\right) - \lambda_1 & \text{if } \epsilon_1^k\left(T,\xi^k\right) < l, \\ \hat{\epsilon}_0^k\left(T,\xi^k\right) = \frac{1-\lambda_0}{\lambda_{xb}\left(\xi^k\right)}\left(\frac{T}{N} - n_1^k\lambda_1 + n_\star^k l\right) 1 & \text{if } \epsilon_0^k\left(T,\xi^k\right) > l, \\ \hat{\epsilon}_\star^k\left(T,\xi^k\right) = l \end{cases} \tag{8.1.24}$$

For a given half-sarcomere must k we must therefore have:

$$\frac{T\left(\overline{\epsilon},\underline{\xi}\right)}{N} \leq \frac{\left(l+\lambda_1\right)\lambda_{xb}\left(\xi^k\right)}{1-\lambda_1} + n_1^k\lambda_1 - n_\star^k l \qquad \text{if } \epsilon_i^k = \hat{\epsilon}_1^k, \tag{8.1.25}$$

$$\frac{T\left(\overline{\epsilon},\underline{\xi}\right)}{N} > \frac{l+\lambda_{xb}\left(\xi^k\right)}{1-\lambda_0} + n_1^k\lambda_1 - n_\star^k l \qquad \text{if } \epsilon_i^k = \hat{\epsilon}_0^k \tag{8.1.26}$$

In soft device, the criteria are the same modulo replacing T by $\overline{\sigma}$. Hence, in soft device, a given configuration ξ exists in the interval:

$$\max_{\xi^k}\left(\frac{l+\lambda_{xb}\left(\xi^k\right)}{1-\lambda_0} + n_1^k\lambda_1 - n_\star^k l\right) \leq \frac{\overline{\sigma}}{N} \leq \min_{\xi^k}\left(\frac{\left(l+\lambda_1\right)\lambda_{xb}\left(\xi^k\right)}{1-\lambda_1} + n_1^k\lambda_1 - n_\star^k l\right) \tag{8.1.27}$$

Of course the limit configuration $\{(1,0,0),\ldots,(1,0,0)\}$ (all cross-bridges in post-power-stroke, *affine states*) does not have a lower bound and respectively configuration $\{(0,0,1),\ldots,(0,0,1)\}$ (all cross-bridges in pre-power-stroke) does not have an upper bound. In hard device, the metastability domain can be defined in terms of $\overline{\epsilon}$ as follows:

$$\begin{aligned} &\max_{\xi^k}\left(\lambda\left(\underline{\xi}\right)\left(\frac{l+\lambda_{xb}\left(\xi^k\right)}{1-\lambda_0} + n_1^k\lambda_1 - n_\star^k l\right) - \frac{1}{P}\sum_{k=1}^{P}\frac{n_1^k\lambda_1 - n_\star^k l}{\lambda_{xb}\left(\xi^k\right)}\right) \\ &\leq \overline{\epsilon} \leq \\ &\min_{\xi^k}\left(\lambda\left(\underline{\xi}\right)\left(\frac{\left(l+\lambda_1\right)\lambda_{xb}\left(\xi^k\right)}{1-\lambda_1} + n_1^k\lambda_1 - n_\star^k l\right) - \frac{1}{P}\sum_{k=1}^{P}\frac{n_1^k\lambda_1 - n_\star^k l}{\lambda_{xb}\left(\xi^k\right)}\right) \end{aligned} \tag{8.1.28}$$

In Fig.8.2 we illustrate those computations by showing the energy, tension and elongation levels for a chain with six half-sarcomeres. Suppose first that each half-sarcomere is in its global minimum configuration $(1,0,0)$ or $(0,0,1)$, having all its cross-bridges either in pre- or post-power-stroke. On Fig.8.2B (resp. D), the branches at the very left and right correspond to affine states with all half-sarcomeres in post-power-stroke and pre-power-stroke, respectively. To shift from one limiting branch to another, half-sarcomeres progressively switch to pre-power-stroke and the chain goes through a sequence of *non-affine states* characterized by inhomogeneous distribution of strain. The global minimum path is indicated by the bold line on Fig.8.2 it also contains inhomogeneous configurations.

If we take into account all local minima, the lines showed on Fig.8.2 will split into many sub-branches where individual cross-bridges of the same half-sarcomere are allowed now to be both in pre- and post-power-stroke states.

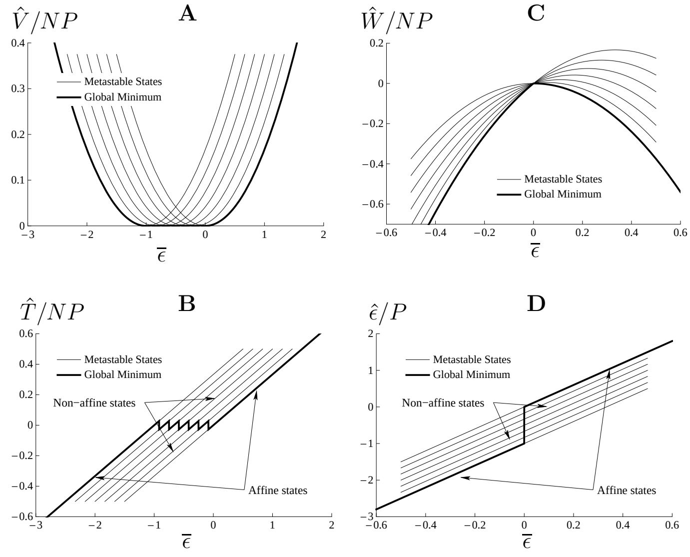

Fig. 8.2 – Configuration involving homogeneous half-sarcomeres in hard and soft device device for a chain of 6 half-sarcomeres. (**A**) and (**B**): hard device energy (**A**) and (**B**) tension. (**C** and (**D**): soft device energy (**C**) and elongation (**D**) Here we show only the configurations containing half-sarcomeres either in full pre-power-stroke or post-power-stroke configuration. On the branch at the very left (resp. right), all half-sarcomeres are in post-power-stroke (resp. pre-power-stroke) (*affine state*). In between the system goes through a sequence of *non-affine states*. The global minimum path is shown by the bold line. It goes through non-affine states in the hard device but not in the soft device. Parameters are: $\lambda_1 = \lambda_0 = 0.5,\ l = -0.5,\ \lambda_f = 1,\ N = 10$.

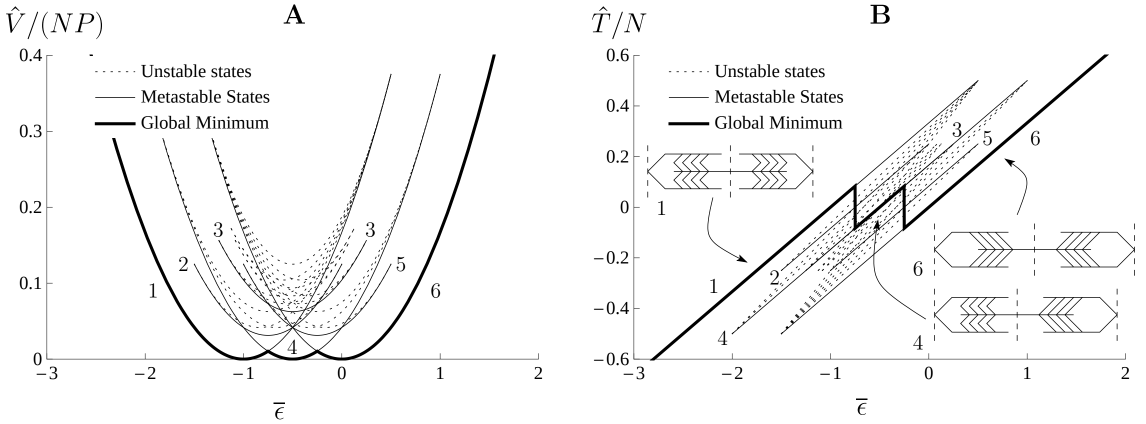

Configurations		
1:$\{(1,0),(1,0)\}$	**2**:$\{(1,0),(\frac{1}{2},\frac{1}{2})\}$ & $\{(\frac{1}{2},\frac{1}{2}),(1,0)\}$	**3**:$\{(\frac{1}{2},\frac{1}{2}),(\frac{1}{2},\frac{1}{2})\}$
4:$\{(1,0),(0,1)\}$&$\{(0,1),(1,0)\}$	**5**:$\{(\frac{1}{2},\frac{1}{2}),(0,1)\}$ & $\{(0,1),(\frac{1}{2},\frac{1}{2})\}$	**6**:$\{(0,1),(0,1)\}$

Fig. 8.3 – Local minima for 2 half-sarcomeres with 2 cross-bridges per half-sarcomere in hard device. (**A**) shows the energy in the local minima computed using Eq.(8.1.16) and (8.1.28). (**B**) represents the tension in the local minima computed with Eq.(8.1.13). The stable states are represented by solid lines and unstable states by dotted lines. The configurations of the stable states are indicated in the table bellow. The global minimum is shown with the thick line. In addition to the affine states $\{(1,0),(1,0)\}$ and $\{(0,1),(0,1)\}$, the system following the global minimum path (thick line) visits the new degenerate non-affine state $\{(1,0),(0,1)\}/\{(0,1),(1,0)\}$. The cartoons on (**B**) shows the configuration of the sarcomere in the 3 configuration of the global minimum (**1**, **4** and **6**). In the non-affine state **4**, and the M-line is not in the center of the structure anymore. Parameters are: $\lambda_1 = \lambda_0 = 0.5$, $l = -0.5$ (symmetric double well), $\lambda_f = 1$, $N = 2$, $P = 2$.

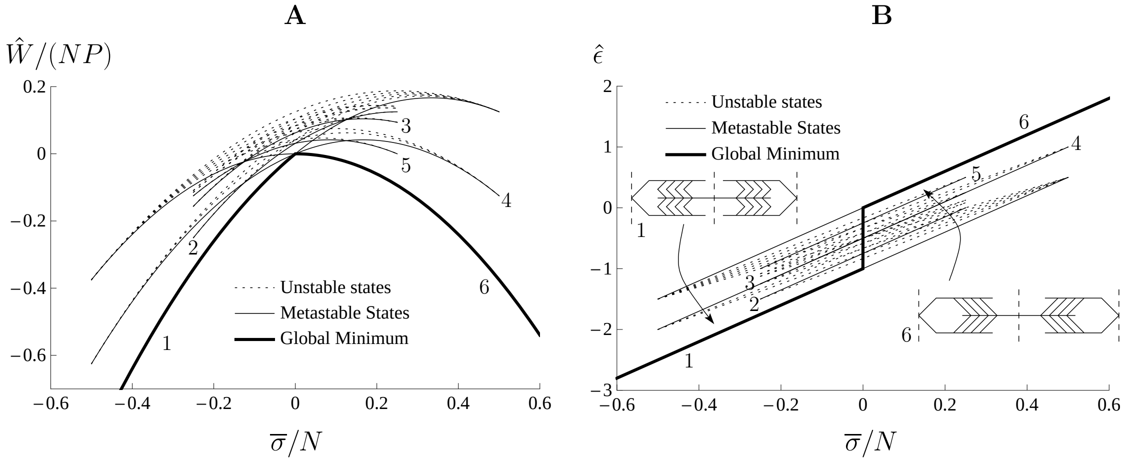

Configurations		
1:$\{(1,0),(1,0)\}$	**2**:$\{(1,0),(\frac{1}{2},\frac{1}{2})\}$ & $\{(\frac{1}{2},\frac{1}{2}),(1,0)\}$	**3**:$\{(\frac{1}{2},\frac{1}{2}),(\frac{1}{2},\frac{1}{2})\}$
4:$\{(1,0),(0,1)\}$&$\{(0,1),(1,0)\}$	**5**:$\{(\frac{1}{2},\frac{1}{2}),(0,1)\}$ & $\{(0,1),(\frac{1}{2},\frac{1}{2})\}$	**6**:$\{(0,1),(0,1)\}$

Fig. 8.4 – Local minima for 2 half-sarcomeres with 2 cross-bridges per half-sarcomere in soft device. (**A**) shows the energy in the local minima computed using Eq.(8.1.17) and (8.1.27). (**B**) represents the elongation in the local minima computed with Eq.(8.1.14). The stable states are represented by solid lines and unstable states by dotted lines. The configurations of the stable states are indicated in the table bellow. The global minimum is shown with the thick line. Unlike in hard device (see Fig.8.3), the systems switches between the two affine states $\{(1,0),(1,0)\}$ and $\{(0,1),(0,1)\}$ without visiting the non affine states $\{(1,0),(0,1)\}/\{(0,1),(1,0)\}$. The cartoons on (**B**) shows the configuration of the sarcomere in the 2 affine configurations of the global minimum (**1**, and **6**). Parameters are: $\lambda_1 = \lambda_0 = 0.5$, $l = -0.5$ (symmetric double well), $\lambda_f = 1$, $N = 2$, $P = 2$.

The ensuing picture is rather complicated and therefore we first study the simplest case of a single sarcomere containing two half-sarcomeres ($P = 2$). The local minima of the energy, for this problem are shown on Fig.8.3(hard device) and 8.4(soft device). For this figure, we used a symmetric double well potential ($\lambda_1 = \lambda_0 = 0.5$, $l = -0.5$) and represent metastable states by solid lines, unstable states by dotted lines and the global minimum by the bold line. Each stable configuration is labeled by a number whose correspondence with the particular configuration specified in the table. Within parenthesis, the first pair indicates the fraction of cross-bridges in pre- and post-power-stroke for the first half-sarcomere and the second pair gives the same information for the second half-sarcomere. For instance the labeling **2**:$\{(\frac{1}{2},\frac{1}{2}),(1,0)\}$ correspond to a configuration where in the first half-sarcomere, 1/2 of the cross-bridges in post-power-stroke and 1/2 in pre-power-stroke; in the second half-sarcomere, all the cross-bridges in post-power-stroke.

In the hard device (see Fig.8.3), the system following the global minimum path (bold line) goes through the following sequence of non affine states $\{(1,0),(0,1)\}/\{(0,1),(1,0)\}$ (state 4 on Fig.8.3) where one half-sarcomere is always in pre-power-stroke and another is always in post-power-stroke. The cartoon on Fig.8.3(B) shows a single sarcomere in the 3 configurations comprising the global minimum. Notice that, in the two affine branches where the chain is homogeneous (1 and 6), the M-line (see the middle vertical dashed line) is in the middle of the structure while in the non-affine state (branch 4), the two half-sarcomeres are not equally stretched and the M-line is not in the center of the sarcomere anymore (it can be shifted in both directions).

In the soft device (see Fig.8.4), the situation is different: the system in global minimum directly switches between the homogeneous configurations $\{(1,0),(1,0)\}$ and $\{(0,1),(0,1)\}$

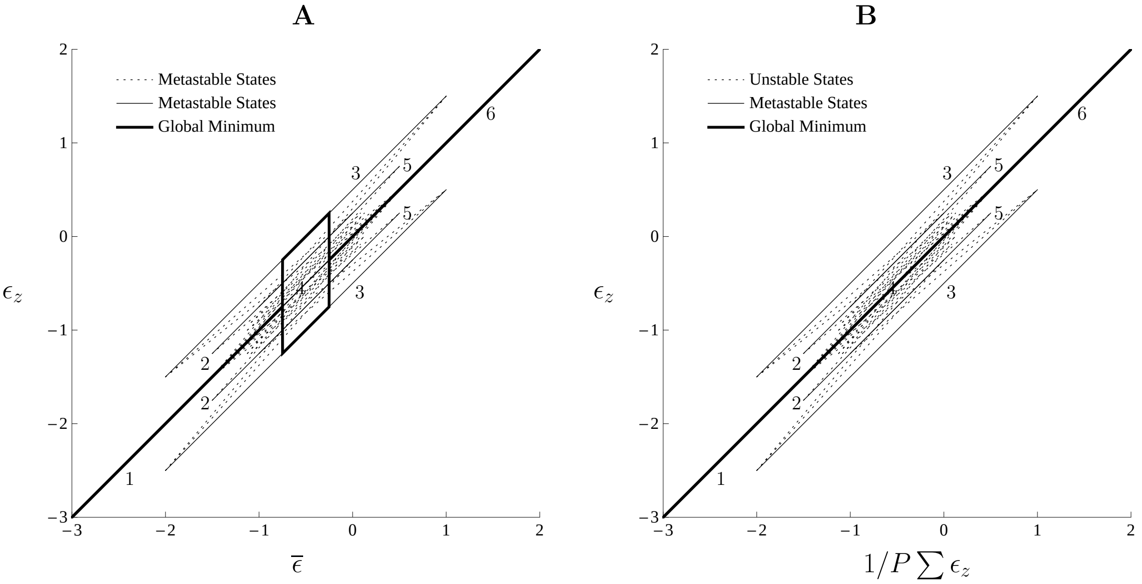

Configurations		
1:$\{(1,0),(1,0)\}$	**2**:$\{(1,0),(\frac{1}{2},\frac{1}{2})\}$ & $\{(\frac{1}{2},\frac{1}{2}),(1,0)\}$	**3**:$\{(\frac{1}{2},\frac{1}{2}),(\frac{1}{2},\frac{1}{2})\}$
4:$\{(1,0),(0,1)\}$&$\{(0,1),(1,0)\}$	**5**:$\{(\frac{1}{2},\frac{1}{2}),(0,1)\}$ & $\{(0,1),(\frac{1}{2},\frac{1}{2})\}$	**6**:$\{(0,1),(0,1)\}$

Fig. 8.5 – Elongation of the two half-sarcomeres in the local minima with a symmetric double well potential. (**A**): hard device. (**B**): soft device. The configurations of the stable states (solid lines) are indicated by the tables bellow the curves. Unstable states are indicated by dotted-lines and the global minimum by the bold lines. In hard device (see **A**), the system following the global minimum transits through non-affine states where the distribution of half-sarcomeres is inhomogeneous (see configuration 3). In soft device (see **B**), the system remains homogeneous. Parameters are: $\lambda_1 = \lambda_0 = 0.5$, $l = -0.5$, $\lambda_f = 1$, $N = 2$ and $P = 2$.

without visiting the non-affine states so the distribution of strain within the half-sarcomeres remains uniform.

We can also compare the strain inside individual half-sarcomeres to the mean elongation (total length divided by the number of half-sarcomeres) on Fig.8.5. For each non-affine state, the two traces show the elongation of individual half-sarcomeres. For affine states (see configurations 1,4 and 6), the elongation is homogeneously distributed and the curve coincides with the diagonal. In soft device, the global minimum (see bold line on Fig.8.5), is always on the diagonal, hence the half-sarcomeres are always equally stretched unlike the in hard device.

Those above analytic results confirm the numerical results in (Vilfan and Duke, 2003) (see Fig.8.15A) where the authors used a chemo-mechanical model of the cross-bridge cycle and discovered the existence of non affine-states characterized by inhomogeneous distribution of sarcomere elongations. Here we are making a link between their findings based on a kinetic Monte–Carlo model and our explicit energy landscape describing individual sarcomeres.

We further illustrate the stretching induced transitions on Fig.8.6 (hard device) and Fig.8.7 (soft device), showing a system with $P = 2$ and $N = 3$. There we use a non-symmetric double well potential ($\lambda_1 = 0.4$, $\lambda_0 = 0.7$, $l = -0.3$).

By taking into account the permutational invariance one can see that this system has 10 metastable states, listed in the table below the graphs. Since the double well potential

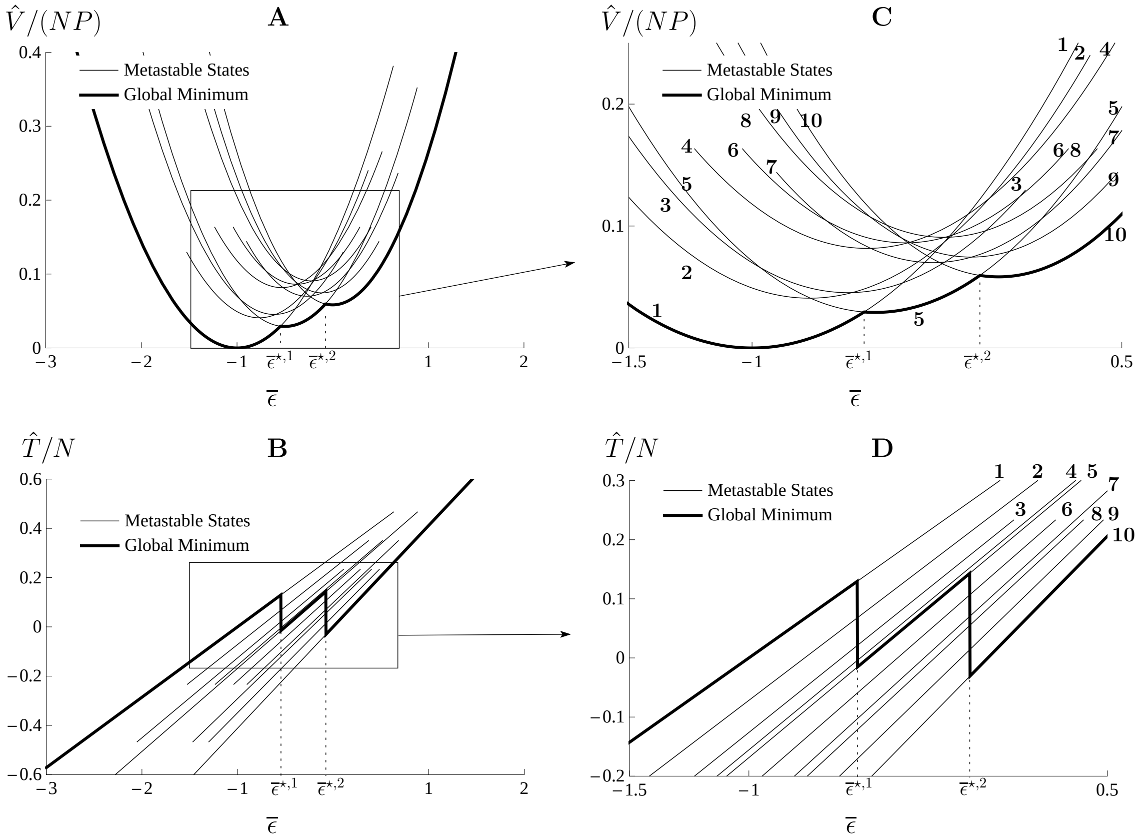

Configurations				
1:$\{(1,0),(1,0)\}$	**2**:$\{(\frac{2}{3},\frac{1}{3}),(1,0)\}$	**3**:$\{(\frac{1}{3},\frac{2}{3}),(1,0)\}$	**4**:$\{(\frac{2}{3},\frac{1}{3}),(\frac{2}{3},\frac{1}{3})\}$	**5**:$\{(0,1),(1,0)\}$
6:$\{(\frac{1}{3},\frac{2}{3}),(\frac{2}{3},\frac{1}{3})\}$	**7**:$\{(0,1),(\frac{2}{3},\frac{1}{3})\}$	**8**:$\{(\frac{1}{3},\frac{2}{3}),(\frac{1}{3},\frac{2}{3})\}$	**9**:$\{(0,1),(\frac{1}{3},\frac{2}{3})\}$	**10**:$\{(0,1),(0,1)\}$

Fig. 8.6 – **Detail of the transition in hard device** for a chain of 2 half-sarcomeres with 3 cross-bridges per half-sarcomere and a non symmetric double well potential. (**A**) and (**B**): energy of the metastable states; (**C**) and (**D**) corresponding tensions. On each curve, the solid lines indicate the metastable states and the bold line, the global minimum. (**C**) and (**D**) are zooms of (**A**) and (**B**) on the transition. The numbers besides the lines indicates the configurations listed in the table bellow. In the table, we list the different independent configurations of the metastable states only. All permutations of a given configuration are equivalent. The system following global minimum path goes through configurations where each sarcomere have all the cross-bridges either in pre-power-stroke or in post-power-stroke (here configurations **1**→**5**→**10**). The configurations with more 'mixed' microstructure have higher energy (see **D**). Parameters are: $\lambda_1 = 0.4$, $\lambda_0 = 0.7$, $l = -0.3$, $\lambda_f = 1$, $N = 2$, $P = 2$.

is non-symmetric, the energy landscape is tilted and the different energy correspond to different stiffnesses. In both hard and soft devices, the branches with the higher energy are those with the most 'mixed' microstructures. These heterogeneous microstructures also have the shortest existence intervals. One can see that, the system following the global minimum in hard device goes successively through a sequence of non-affine states (see **1**→**5**→**10** on Fig.8.6C and D). In the soft device, there in only one transition located at $\overline{\sigma} = \overline{\sigma}^{\star}$ where all non-affine configurations have the same energy (see Fig.8.7).

The corresponding distribution of elongations inside the chain is shown in Fig.8.8. Unlike the symmetric case when potential was symmetric (see Fig.8.5), the lines characterizing each configurations are not longer parallel to the diagonal. However, despite all these differences, the general result regarding the ubiquitous presence of inhomogeneously distributed elongations remains the same.

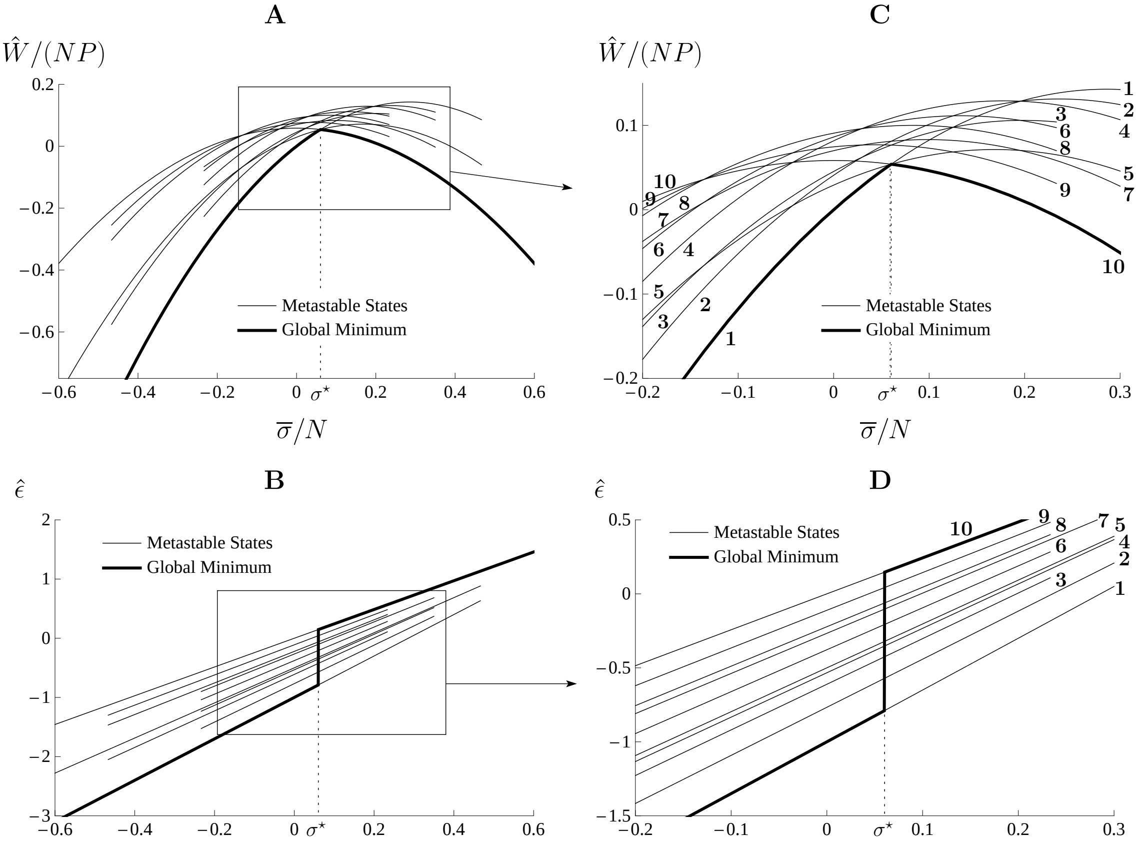

Configurations				
1:$\{(1,0),(1,0)\}$	**2**:$\{(\frac{2}{3},\frac{1}{3}),(1,0)\}$	**3**:$\{(\frac{1}{3},\frac{2}{3}),(1,0)\}$	**4**:$\{(\frac{2}{3},\frac{1}{3}),(\frac{2}{3},\frac{1}{3})\}$	**5**:$\{(0,1),(1,0)\}$
6:$\{(\frac{1}{3},\frac{2}{3}),(\frac{2}{3},\frac{1}{3})\}$	**7**:$\{(0,1),(\frac{2}{3},\frac{1}{3})\}$	**8**:$\{(\frac{1}{3},\frac{2}{3}),(\frac{1}{3},\frac{2}{3})\}$	**9**:$\{(0,1),(\frac{1}{3},\frac{2}{3})\}$	**10**:$\{(0,1),(0,1)\}$

Fig. 8.7 – Detail of the transition in soft device for a chain of 2 half-sarcomeres with 3 cross-bridges per half-sarcomere. Here the double well is non-symmetric. (**A**) and (**B**) show the energy of the metastable states; (**C**) and (**D**) the corresponding elongation. On each curve, the solid lines indicate the metastable states and the thick line, the global minimum. (**C**) and (**D**) are zooms of (**A**) and (**B**) on the transition. The numbers besides the lines indicates the configurations listed in the table bellow. In the table, we list the different configurations of the metastable states only. The system following global minimum transit experience only a single transition at $\overline{\sigma} = \overline{\sigma}^\star$ from $\{(1,0),(1,0)\}$ to $\{(0,1),(0,1)\}$ where all states with homogeneous sarcomeres (**1**, **5** and **10**) have the same energy. Unlike in hard device (see Fig.8.6), the system does not transit through non-affine configurations (here **5**). Parameters are: $\lambda_1 = 0.4$, $\lambda_0 = 0.7$, $l = -0.3$, $\lambda_f = 1$, $N = 2$, $P = 2$.

8.1.2 Non-equilibrium energy landscape in the case $P = 2$

Transition between global minimum configurations

In the case of a single sarcomere ($P = 2$), we can investigate further the mechanism of transition between different metastable states by showing how the partially relaxed energy depends on the internal degree of freedom ϵ_z^1, the elongation of the first sarcomere.

Consider a system with two half-sarcomeres under hard device conditions initially in state $\{(1,0),(1,0)\}$ (we omit the unstable states for simplicity, see Fig.8.9, A). If one pushes the M–line (related to variable ϵ_z^1) to the left then the first half-sarcomere is compressed and the second one is stretched. We already know that a compressed half-sarcomere will favor homogeneous post-power-stroke microstructure while a stretched

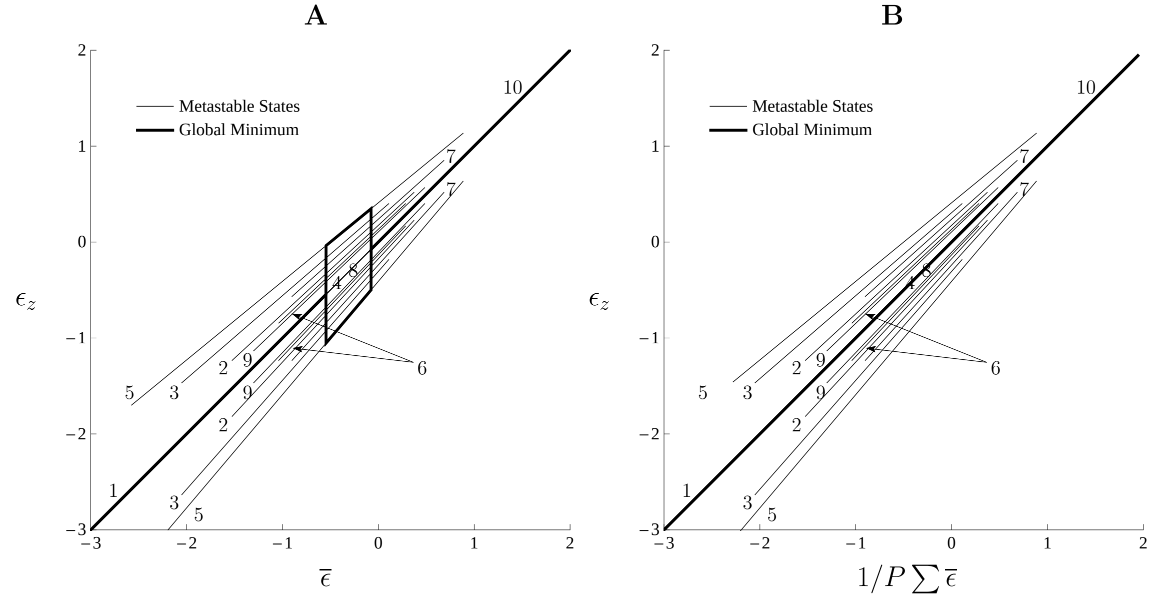

Configurations

1:$\{(1,0),(1,0)\}$	**2**:$\{(\frac{2}{3},\frac{1}{3}),(1,0)\}$	**3**:$\{(\frac{1}{3},\frac{2}{3}),(1,0)\}$	**4**:$\{(\frac{2}{3},\frac{1}{3}),(\frac{2}{3},\frac{1}{3})\}$	**5**:$\{(0,1),(1,0)\}$
6:$\{(\frac{1}{3},\frac{2}{3}),(\frac{2}{3},\frac{1}{3})\}$	**7**:$\{(0,1),(\frac{2}{3},\frac{1}{3})\}$	**8**:$\{(\frac{1}{3},\frac{2}{3}),(\frac{1}{3},\frac{2}{3})\}$	**9**:$\{(0,1),(\frac{1}{3},\frac{2}{3})\}$	**10**:$\{(0,1),(0,1)\}$

Fig. 8.8 – Elongation of the two half-sarcomeres in the local minima with a non-symmetric double well potential. (**A**): hard device. (**B**): soft device. The configurations of the stable states (solid lines) are indicated by the tables bellow the curves and global minimum by the bold lines. In hard device (see **A**), the system following the global minimum transits through non-affine states where the distribution of half-sarcomeres is inhomogeneous (see configuration 3). In soft device (see **B**), the system remains homogeneous. Parameters are: $\lambda_1 = 0.4$, $\lambda_0 = 0.7$, $l = -0.3$, $\lambda_f = 1$, $N = 2$ and $P = 2$.

half-sarcomere will go in a homogeneous pre-power-stroke microstructure. Hence, if we follow the global minimum path, we end up with the configuration $\{(1,0),(0,1)\}$ (see Fig.8.9, B). Now if we pull the M–line ϵ_z^1 to the right, the first half-sarcomere elongates and the second one is compressed; as a result, the system ends up in the configuration $\{(0,1),(1,0)\}$ which is the mirror image of the previous one (see Fig.8.9, C).

The situation is different if we are in the soft device. Consider again two half-sarcomeres initially in the configuration $\{(1,0),(1,0)\}$ at $\overline{\sigma} = \overline{\sigma}^\star$ (see Fig.8.9, D), where the energies of configurations $\{(1,0),(0,1)\}$ and $\{(1,0),(1,0)\}$ are equal (see Fig.8.7). The state of the second half-sarcomere can be either (1,0) or (0,1). When the M–line (related to variable ϵ_z^1) is displaced, the first half-sarcomere changes configuration but it does not modify the state of the second half-sarcomere, which remains either in the state (1,0) or (0,1) (see 8.9, E and F).

To illustrate this transition further, we plot on Fig.8.10, the energy of different configurations *vs* ϵ_z^1, when the system is at the transition $\overline{\epsilon} = \overline{\epsilon}^{\star,1}$ in hard device (see Fig.8.10, A and B) and at the transition point $\overline{\sigma} = \overline{\sigma}^\star$ in soft device (see Fig.8.10, C and D). The solid lines represent the metastable states, the dotted lines, the unstable states and the bold lines, the global minimum. The parameters are $P = 2$, $N = 2$, $\lambda_1 = 0.4$, $\lambda_0 = 0.7$, $l = -0.3$ (non symmetric double well potential) and we use $\lambda_f = 1$ in (A) and (C) and $\lambda_f \to \infty$ in (B) and (D). The labeling of the metastable configurations is detailed in the table bellow the curves. The energy of the global minimum is set to 0 arbitrarily.

In the hard device, the system placed initially in configuration $\{(1,0),(1,0)\}$ (see Fig.8.10, right column **1**) can switch to $\{(1,0),(0,1)\}$ (see **2**) when ϵ_z^1 is reduced and to

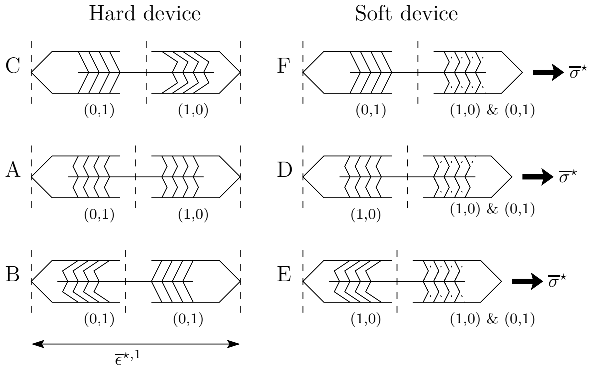

Fig. 8.9 – **Illustration of the transition in hard and soft device**. In hard device (left column), we start with a sarcomere in configuration $\{(1,0),(1,0)\}$ at the first transition ($\overline{\epsilon} = \overline{\epsilon}^{\star,1}$, see A). If the M-line (corresponding to ϵ_z^1 in the model is displaced to the left (see B), the first half-sarcomere shortens and the second lengthens and the systems ends up in configuration $\{(1,0),(0,1)\}$. If the M-line is displaced to the right (see C), the first half-sarcomere is lengthen so the second shortens and the system reaches configuration $\{(0,1),(1,0)\}$. In soft device at $\overline{\sigma} = \overline{\sigma}^{\star}$ (right column), we start with the first half-sarcomere in post-power-stroke (see D). The second half-sarcomere can be in equilibrium either in pre-power-stroke (0,1) or in post-power-stroke (1,0), without affecting the energy of the system (at $\overline{\sigma} = \overline{\sigma}^{\star}$ all homogeneous configurations have the same energy, see Fig.8.7C). Therefore, moving the M-line only affects the state of the first half-sarcomere (see E and F).

$\{(0,1),(1,0)\}$ (see **2'**) if ϵ_z^1 is increased.

In the soft device (see Fig.8.10, right column) the configurations $\{(1,0),(1,0)\}$ (see **1**) and $\{(1,0),(0,1)\}$ (see **2**) superimpose and the system transforms to one of these configurations $\{(0,1),(1,0)\}$ or $\{(0,1),(0,1)\}$ by increasing ϵ_z^1 (see **2**' and **6**). Note that configuration $\{(0,1),(0,1)\}$ (see **6**) is directly accessible in the soft device (at $\overline{\sigma} = \overline{\sigma}^{\star}$) while it requires further stretching in the hard device up to $\overline{\epsilon} = \overline{\epsilon}^{\star,2}$ (the position of the second transition, see Fig.8.6).

Finally, we observe that, as in the case of a single half-sarcomere, the energy barrier to overcome at the transition is higher in the soft device than in the hard device (compare Fig.8.10A and C). However, in the hard device, the system initially in configuration $\{(1,0),(1,0)\}$ (see **1**) cannot reach directly the final configuration $\{(0,1),(0,1)\}$ (**6** is not available in Fig.8.10A). Instead it has to undergo the second transition at $\overline{\epsilon} = \overline{\epsilon}^{\star,2}$. In the soft device, the final configuration $\{(0,1),(0,1)\}$ (see **6**) is directly reachable from $\{(1,0),(1,0)\}$ at $\overline{\sigma} = \overline{\sigma}^{\star}$. In a nutshell, to go from one limiting configuration to the other, the system in the hard device have to go through several transitions with small barriers while the soft device system can reach the final state through only one transition but with a much bigger barrier.

The above discussion raises the fundamental question of what is the 'chemical state' in the chemo-mechanical models. For instance, if we interpret different non-affine configurations of a sarcomere as distinct chemical states with their own kinetic constants, we recover in our framework the idea of multiple intermediate configurations proposed by Huxley and Simmons and still broadly used in chemo-mechanical modeling.

Influence of coupling

In Fig.8.10 we compare the energy landscape as a function of the inner degree of freedom ϵ_z^1 at $\lambda_f = 1$ (see A and C) and $\lambda_f \to +\infty$ (see B and D). In both hard and soft devices, at finite λ_f, as the system undergoes a transition along the global minimum path (say $\overline{\epsilon} = \overline{\epsilon}^{\star,1}$ in hard device and $\overline{\sigma} = \overline{\sigma}^{\star}$ in soft device), the kinetic trajectories describing

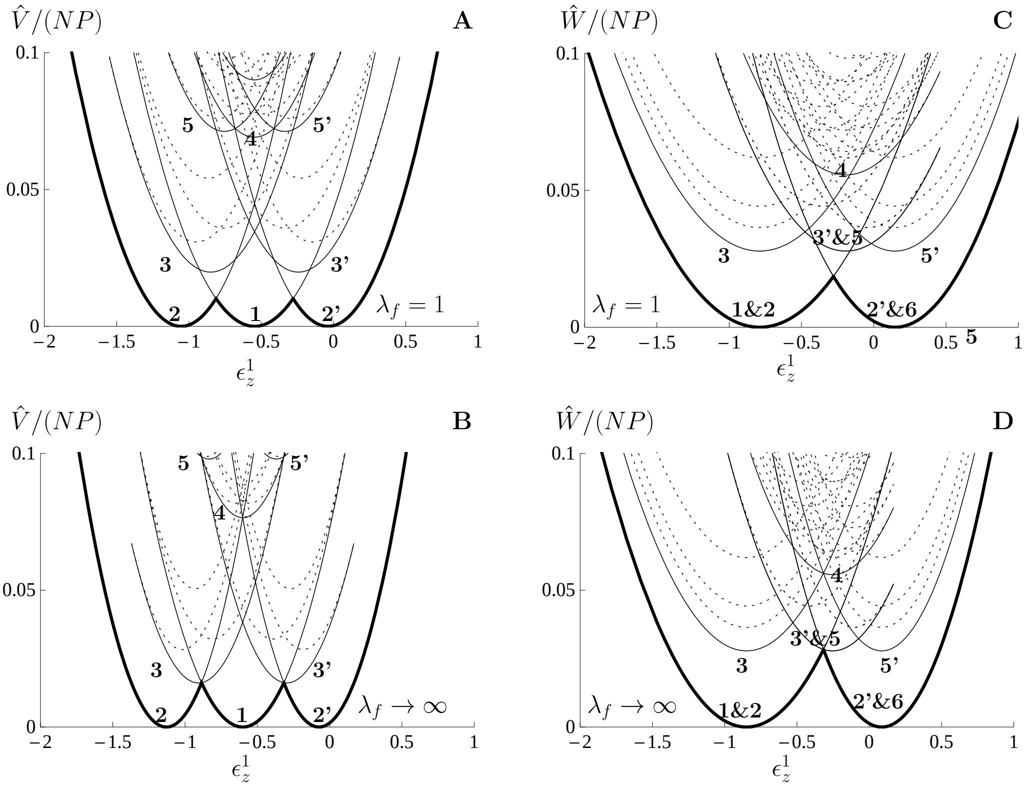

Configurations				
1:$\{(1,0),(1,0)\}$	**2**:$\{(1,0),(0,1)\}$	**2'**:$\{(0,1),(1,0)\}$	**3**:$\{(1,0),(\frac{1}{2},\frac{1}{2})\}$	**3'**:$\{(\frac{1}{2},\frac{1}{2}),(1,0)\}$
4:$\{(\frac{1}{2},\frac{1}{2}),(\frac{1}{2},\frac{1}{2})\}$	**5**:$\{(\frac{1}{2},\frac{1}{2}),(0,1)\}$	**5'**:$\{(0,1),(\frac{1}{2},\frac{1}{2})\}$	**6**:$\{(0,1),(0,1)\}$	

Fig. 8.10 – Transition between configuration in the global minimum for 2 half-sarcomeres ($P = 2$).Energy of the different configurations *vs* the inner degree of freedom ϵ_z^1 at the transition $\overline{\epsilon} = \overline{\epsilon}^{\star,1}$ in hard device (**A** and **B**, see Fig.8.6) and at the transition $\overline{\sigma} = \overline{\sigma}^{\star}$ in soft device (**C** and **D**, see Fig.8.7). In all figures, solid lines represent the metastable states ($N = 2$) and dotted lines represent unstable states. The parameters are $P = 2$, $N = 2$, $\lambda_1 = 0.4$, $\lambda_0 = 0.7$, $l = -0.3$ (non symmetric double well) and we use $\lambda_f = 1$ in (A) and (C) and $\lambda_f \to \infty$ in (B) and (D). The labels of metastable configurations are detailed in the table bellow the curves. The energy of the minimum is set to 0 arbitrarily and the scale is the same in all plots. In hard device (see **A** and **B**), the system starting from $\{(1,0),(1,0)\}$ (see **1**) can visit 2 symmetric configurations $\{(1,0),(0,1)\}$ (see **2**) and $\{(0,1),(1,0)\}$ (see **2'**). In soft device (see **C** and **D**) $\{(1,0),(1,0)\}$ $\{(1,0),(0,1)\}$ and are equivalent (see **1&2** on) and the system can directly reach the final configuration $\{(0,1),(0,1)\}$ (see **6**, is absent in hard device). At finite λ_f (upper line), the energy of intermediate configurations (*e.g.* $\left\{(1,0),\left(\frac{1}{2},\frac{1}{2}\right)\right\}$, see **3**) are high compared to when $\lambda_f \to \infty$ (see lower line).

the switch between the ground state configurations does not imply visiting any other states (stable or unstable). For instance in Fig.8.10 (A) and (B), we study the transition from $\{(1,0),(1,0)\}$ (see **1**) to $\{(1,0),(0,1)\}$ (see **2**) and we see that the intermediate configurations $\left\{(1,0),\left(\frac{1}{2},\frac{1}{2}\right)\right\}$ or $\left\{\left(\frac{1}{2},\frac{1}{2}\right),(1,0)\right\}$ (see **3** and **3'**) cannot be reached.

However, as λ_f increases, the gap between the ground states and those intermediate configurations tends to 0 allowing a transition through mixed microstructures. This shows that, as in the single half-sarcomere, the presence of soft myofilament introduces cooperativity among the cross-bridges and thus favors homogeneous (affine) configuration (see Sec.3.2.2). We also see that the presence of stiff myofilament tends to lower the barriers (compare Fig.8.10 upper line to lower line) suggesting that the kinetics of the system will be faster as λ_f increases (weaker coupling).

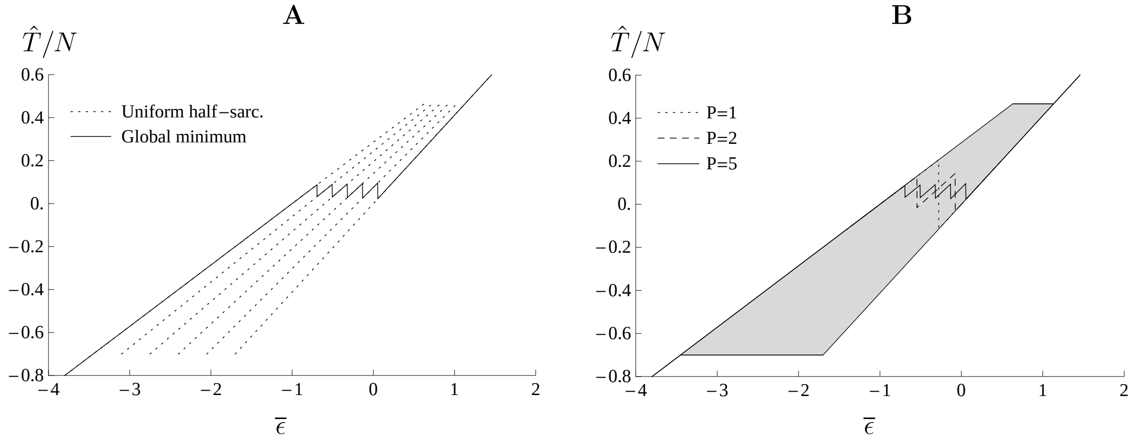

Fig. 8.11 – **Evolution of the metastable domain for** $P > 2$**.** (**A**): Representation of the non-affine states with only homogeneous half-sarcomere (dotted lines) and the global minimum (solid line) for $P = 5$. The non-affine states are in the metastable domain whose contours are represented in (**B**) by the solid lines. The metastable domain is the same for all P. On (**B**), we represent the global minimum for $P = 1$ (dotted line), $P = 2$ (dashed line) and $P = 5$ (solid line). Parameters are: Parameters are: $\lambda_1 = 0.3$, $\lambda_0 = 0.7$, $l = -0.3$ (non-symmetric double well potential)

8.1.3 Continuum limit

In the previous section, we discussed (for a simple case of 2 half-sarcomeres) how the system rearranges internally under external driving as it follows the global minimum of the energy. Here we study the tension *vs* elongation curves for larger values of P all the way to infinity. We recall that the value of P does not affect the global minimum response in the soft device: there is always a single transition at $\overline{\sigma} = \overline{\sigma}^{\star}$. So the corresponding energy *vs* tension relation along the global minimum path is shown in Fig.8.7 for any P.

In Fig.8.11A, we show the non-affine states with homogeneous half-sarcomeres (see dotted lines) for the case $P = 5$. The boundaries of these metastable states delimit a 'metastable domain' where all non-affine states are located. On Fig.8.11B, we show that the boundaries of this metastable domain do not change with P. On (B), we also represent the global minimum for $P = 1$ (dotted line), $P = 2$ (dashed line) and $P = 5$ (solid line). When P increases, the transition become more wiggly as the systems goes through more non-affine states.

We further illustrate the global minimum path in Fig.8.12 (A and B) where the energy of the global minimum in hard device for $P = 1$ (dotted line), $P = 2$ (dot-dashed line), $P = 5$ (dashed line) and $P = 20$ (continuous line). The other parameters are: $\lambda_1 = 0.3$, $\lambda_0 = 0.7$, $l = -0.3$ (note that here, the value of N doesn't matter). The energy becomes more and more convex as P increases which also corresponds to smoothing the energy landscape (already at $P = 5$ the wiggles are barely visible on Fig.8.12B). In the limit $P \to \infty$, relaxed energy is convex but not strictly convex: see for the case $P = 20$ on Fig.8.12, the interval where the energy depends linearly on the elongation (see also (Puglisi and Truskinovsky, 2000; Rogers and Truskinovsky, 1997)). The convexification of the energy in the thermodynamic limit is expected (Lebowitz and Lieb, 1969).

In Fig.8.12(C and D), we represent the corresponding tension *vs* elongation curves on Fig.8.12(C and D). As P increases, the number of transition increases while the size of the wiggles decreases. In the limit $P \to \infty$, the hard device behavior along the global minimum converges to the soft device behavior (see bold line). Hence, although for the

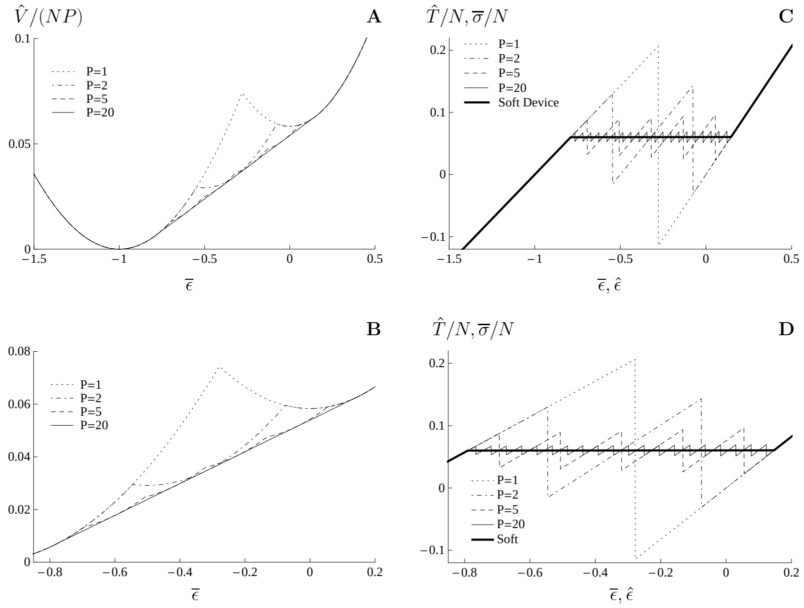

Fig. 8.12 – **Continuum limit as** $P \to \infty$. Energy *vs* elongation (**A** and **B**) and tension *vs* elongation (**C** and (**D**)) in the global minimum for different half-sarcomere chain: $P = 1$ (dotted line), $P = 2$ (dot-dashed line), $P = 5$ (dashed line), $P = 20$ (continuous line). (**B**) and (**D**) are zooms of (**A**) and (**C**). On (**C**) and (**D**), we also represent the elongation *vs* applied tension relation in soft device (bold line). As P increases, the energy landscape is smoothed and becomes convex (see **A**). The tension *vs* elongation relation converges to the soft device elongation *vs* applied tension relation and exhibits a plateau (**B**). Parameters are: $\lambda_1 = 0.4$, $\lambda_0 = 0.7$, $l = -0.3$ (note that here, the value of Nxb does't matter).

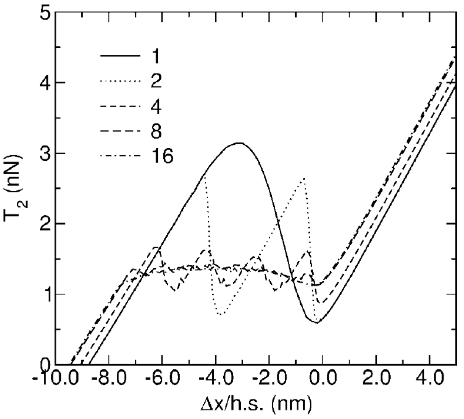

Fig. 8.13 – T_2 **curves obtained by A.Vilfan and T.A.J Duke** for $P = 1$ (solid line), $P = 2$ (dotted line), $P = 4$ (short-dashed line), $P = 8$ (long-dashed line) and $P = 16$ (dot-dashed line). From Vilfan and Duke (2003) Fig.8. The curves are obtained from numerical simulations based on a chemo-mechanical model by measuring the tension attained 2 ms after a stretch/release in hard device. The value of β used for their simulations is about 40.

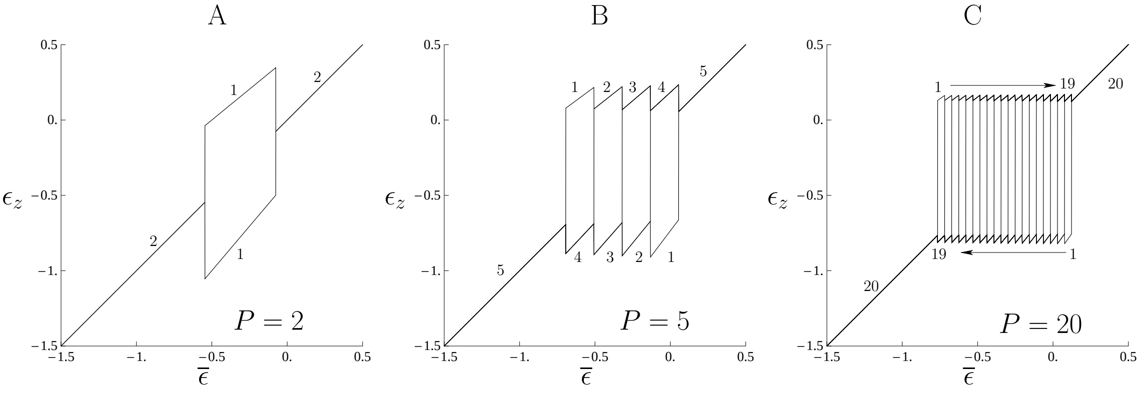

Fig. 8.14 – Elongation of half-sarcomeres in global minimum for different chain length in hard device. (**A**): $P = 2$; (**B**): $P = 5$; (**C**): $P = 20$. In the region of the transition, the global minimum is characterized by inhomogeneous half-sarcomere elongations: the upper branch contains pre-power-stroke half-sarcomeres and the lower branch post-power-stroke half-sarcomeres. The numbers indicates how many half-sarcomere are in each branch at a given $\overline{\epsilon}$. In soft device, the elongation is always the same in all half-sarcomeres so the systems remains on the diagonal. Parameters are: $\lambda_1 = 0.4$, $\lambda_0 = 0.7$, $l = -0.3$.

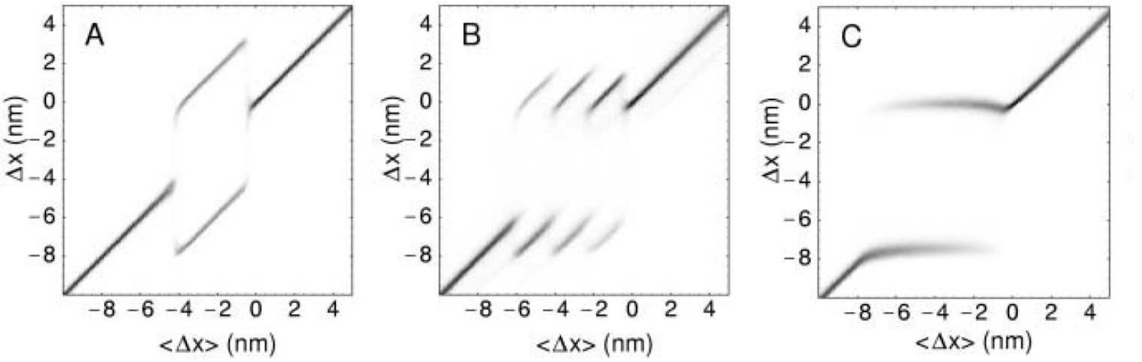

Fig. 8.15 – Probability density of transient stretches of individual half-sarcomeres (y-axis) compared to the mean elongation of the half-sarcomere (total length divided by the number of units). From Vilfan and Duke (2003) Fig.9. (**A**): $P = 2$; (**B**): $P = 4$, (**C**): $P = 32$. The curves where obtained using a chemo-mechanical model including attachment-detachment and simulating quick force recovery experiments. The value used for the parameters are similar to the one we presently use (unless there is no double well potential). In particular their value of β is about 40.

single half-sarcomere, we saw that the T_2 curve and L_2 curve describing ground states cannot coincide (see Figs.3.1 and 3.2), when many half-sarcomeres are connected in series, the 2 curves superimpose. If one takes also into account the less favorable non-affine states, our system can exhibit a much more complex path with possibly much more additional wiggles.

Fig.8.14 we shows the distribution of half-sarcomere elongations in hard device for different applied elongations and for different fiber lengths (A: $P = 2$, B: $P = 5$ and C: $P = 20$). For this figure , we used a non-symmetric double well potential: $\lambda_1 = 0.4$, $\lambda_0 = 0.7$, $l = -0.3$. Within the transition, the population of half-sarcomere splits into 2 categories: the first one being stretched above average (top trace above diagonal) and the other under average (bottom trace bellow diagonal). The number beside the curves indicates on each portion the number of half-sarcomere in each category. Theses analytical results are in full agreement with the numerical computations based on a kinetic Monte–Carlo model where sarcomeres are viewed as bi-stable elements (Vilfan and Duke, 2003) (see Fig.8.15). Their model assumes a single stiffness for the cross-bridges so the slopes of the different branches showing the different sarcomere elongations are all equal to 1. With our model, the presence of an asymmetric double well allows one to generate a more complex picture where the different branches can have different slopes (see Fig.8.14).

Moreover these simulations are done at finite temperature. In our language, the value they used for β is about 40 so their system can already be considered as ‘cold’. So the the results in this paper are nothing else but the global minimum of the energy. This suggest that the statistical baggage of their model is of secondary importance.

We remark that it is an actual challenge in experiment to measure the distribution of half-sarcomere elongation under different loading conditions. Such experiments could give a way to measure indirectly the stiffness of the pre-power-stroke and post-power-stroke configurations, directly linked to the mechanical characteristics of our double well potential. We discuss the potential evidence of the half sarcomere in inhomogeneity in Sec.1.3.

8.2 Single sarcomere at $\theta \neq 0$ $(P = 2)$

Before studying the whole chain at finite temperature we analyze the simplest case of two half-sarcomeres in series forming a sarcomere. In this case the number of degrees of freedom is still low and we can perform semi-analytical computations without simplifying assumptions.

8.2.1 Partition functions

In the general case, the partition function are given by:

$$\mathcal{Z}_h^P\left(\overline{\epsilon},\beta\right) = \int \exp\left[-\beta\left(V\left(\overline{\epsilon},\underline{\epsilon}\right)\right)\right] \mathbb{1}_{\frac{1}{P}\sum \epsilon_z^k = \overline{\epsilon}} d\underline{\epsilon} \qquad \text{in hard device,} \tag{8.2.1}$$

$$\mathcal{Z}_s^P\left(\overline{\sigma},\beta\right) = \int \exp\left[-\beta\left(W\left(\overline{\sigma},\underline{\epsilon}\right)\right)\right] d\underline{\epsilon} \qquad \text{in soft device.} \tag{8.2.2}$$

where V and W are given by Eq.(8.1.1) and (8.1.2) respectively and $\mathbb{1}$ is the indicator function.

For all values of P, we can integrate independently with respect to all ϵ_i^k for $1 \leq i \leq N$ and $1 \leq k \leq P$ independently like we did for the single half-sarcomere case (see Sec.4.2.1). Furthermore, in soft device, the full integration can be performed without any simplifying assumptions for arbitrary P due to the absence of coupling between different half-sarcomeres. More precisely, the partition function in the soft device can be written as the product of single half-sarcomeres partition functions (see Sec.4.2.1):

$$\mathcal{Z}_s^P\left(\overline{\sigma},\beta\right) = \left(\mathcal{Z}_s\left(\overline{\sigma},\beta\right)\right)^P = \left(\sqrt{\frac{2\pi}{N\beta\lambda_f}} \int \exp\left[-\beta G_y\left(\overline{\sigma},x,\beta\right)\right] dx\right)^P. \tag{8.2.3}$$

The difficulty in the hard device, comes essentially from the constraint $\mathbb{1}_{\frac{1}{P}\sum \epsilon_z^k = \overline{\epsilon}}$ in Eq.(8.2.1) which couples degrees of freedom associated with different half-sarcomeres. We will show in the next section how to deal with this problem in the limit $P \to \infty$. In the case $P = 2$, we obtain:

$$\mathcal{Z}_h^2\left(\overline{\epsilon},\beta\right) = \iiint \exp\left[-\beta\left(F_y\left(\epsilon_z^1,\epsilon_y^1,\beta\right) + F_y\left(2\overline{\epsilon}-\epsilon_z^1,\epsilon_y^2,\beta\right)\right)\right] d\epsilon_y^1 d\epsilon_y^2 d\epsilon_z^1 \tag{8.2.4}$$

where F_y and G_y have been introduced in Chap.4:

$$F_y\left(\overline{\epsilon},\epsilon_y,\beta\right)=N\left(\frac{1}{2}\lambda_f\left(\overline{\epsilon}-\epsilon_y\right)^2-\frac{1}{\beta}\ln\left(\mathcal{Z}_1\left(\beta,\epsilon_y\right)+\mathcal{Z}_0\left(\beta\epsilon_y\right)\right)\right) \tag{4.2.13}$$

$$G_y\left(\overline{\sigma},\epsilon_y,\beta\right)=N\left(-\frac{\overline{\sigma}}{N}\epsilon_y-\frac{1}{2}\frac{\overline{\sigma}^2}{N^2\lambda_f}-\frac{1}{\beta}\ln\left(\mathcal{Z}_1\left(\beta,\epsilon_y\right)+\mathcal{Z}_0\left(\beta,\epsilon_y\right)\right)\right). \tag{4.2.14}$$

The integration with respect to ϵ_z^1 can be done independently from ϵ_y^1 and ϵ_y^2; we obtain:

$$\mathcal{Z}_h^2\left(\overline{\epsilon},\beta\right)=\sqrt{\frac{2\pi}{\beta NP\lambda_f}}\iint\exp\left[-\beta F_y^2\left(\overline{\epsilon},\epsilon_y^1,\epsilon_y^2,\beta\right)\right]d\epsilon_y^1 d\epsilon_y^2 \tag{8.2.5}$$

$$\text{where } F_y^2\left(\overline{\epsilon},\epsilon_y^1,\epsilon_y^2,\beta\right)=NP\left\{\frac{1}{2}\lambda_f\left(\overline{\epsilon}-\frac{1}{P}\left(\epsilon_y^1+\epsilon_y^2\right)\right)^2\right.$$
$$\left.-\frac{1}{\beta}\frac{1}{P}\ln\left[\left(\mathcal{Z}_1\left(\epsilon_y^1,\beta\right)+\mathcal{Z}_0\left(\epsilon_y^1,\beta\right)\right)\left(\mathcal{Z}_1\left(\epsilon_y^2,\beta\right)+\mathcal{Z}_0\left(\epsilon_y^2,\beta\right)\right)\right]\right\}. \tag{8.2.6}$$

In the soft device we can also define a partially equilibrated Gibbs free energy which is simply the sum of two G_y functions for each half-sarcomere:

$$G_y^2\left(\overline{\sigma},\epsilon_y^1,\epsilon_y^2,\beta\right)=G_y\left(\overline{\sigma},\epsilon_y^1,\beta\right)+G_y\left(\overline{\sigma},\epsilon_y^2,\beta\right) \tag{8.2.7}$$

8.2.2 Isotherms

From the partition functions $\mathcal{Z}_h^2$ and $\mathcal{Z}_s^2$, we can compute the free energy of a single sarcomere:

$$F^2\left(\overline{\epsilon},\beta\right)=-\frac{1}{\beta}\ln\left(\mathcal{Z}_h^2\left(\overline{\epsilon},\beta\right)\right) \qquad \text{in hard device} \tag{8.2.8}$$

$$G^2\left(\overline{\sigma},\beta\right)=-\frac{1}{\beta}\ln\left(\mathcal{Z}_s^2\left(\overline{\sigma},\beta\right)\right) \qquad \text{in soft device.} \tag{8.2.9}$$

The isotherms tension–elongation space can be obtained by differentiating of F^2 and G^2 with respect to $P\overline{\epsilon}$ and $\overline{\sigma}$ respectively. We obtain:

$$T_2^2\left(\overline{\epsilon},\beta\right)=N\lambda_f\left(\overline{\epsilon}-\frac{1}{P}\left\langle\epsilon_y^1+\epsilon_y^2\right\rangle_h^2\left(\overline{\epsilon},\beta\right)\right) \tag{8.2.10}$$

$$L_2^2\left(\overline{\epsilon},\beta\right)=P\left(\frac{\overline{\sigma}}{N}+\left\langle\epsilon_y\right\rangle_s\left(\overline{\sigma},\beta\right)\right) \tag{4.2.17}$$

$$\text{where } \left\langle\epsilon_y^1+\epsilon_y^2\right\rangle_h^2\left(\overline{\epsilon},\beta\right)=\frac{1}{Z_h^2\left(\overline{\epsilon},\beta\right)}\iint\left(\epsilon_y^1+\epsilon_y^2\right)\exp\left[-\beta F_y^2\left(\overline{\epsilon},\epsilon_y^1,\epsilon_y^2,\beta\right)\right]d\epsilon_y^1 d\epsilon_y^2, \tag{8.2.11}$$

$$\text{and } \left\langle\epsilon_y\right\rangle_s\left(\overline{\sigma},\beta\right)=\frac{1}{Z_s\left(\overline{\sigma},\beta\right)}\int\epsilon_y\exp\left[-\beta G_y\left(\overline{\sigma},\epsilon_y\beta\right)\right]d\epsilon_y. \tag{8.2.12}$$

Since all half-sarcomeres are independent the formula for L_2 in the soft device is the same as in the case of a single half-sarcomere. The free energies F^2 and G^2 and the isotherms T_2^2 and L_2^2 are represented on Fig.8.16 for the following set of parameters: $\lambda_1=0.4$, $\lambda_0=0.7$, $l=-0.3$, $\lambda_f=1$ and $N=10$.

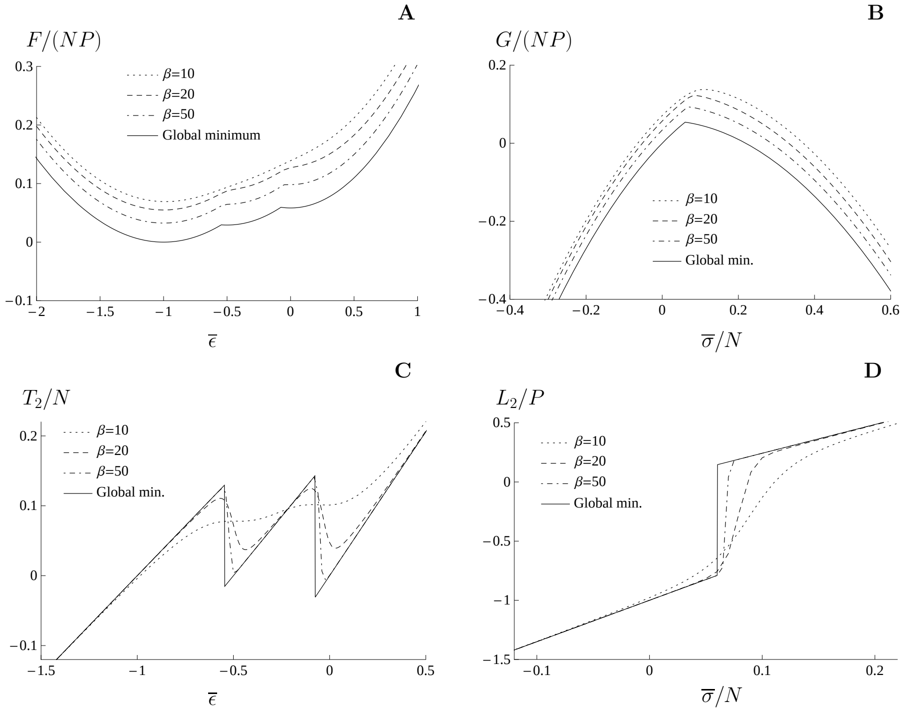

Fig. 8.16 – **Isotherms for one sarcomere.** (**A**): Free energy in hard device obtained from Eq.(8.2.8). (**B**): Gibbs free energy in soft device obtained from Eq.(8.2.9). (**C**): T_2 curve obtained from Eq.(8.2.10). (**D**): L_2 curve obtained from Eq.(4.2.17). On each curve, we represent plots for: $\beta = 10$ (dotted line), $\beta = 20$ (dashed line), $beta = 50$ (continuous line) and in the global minimum (solid line). Like in the single half-sarcomere case, when β increases, the system gets closer to the global minimum. In soft device (**B** and **D**), since the different half-sarcomeres behave independently, the curves are the same as in the case of one half-sarcomere (see Fig.4.2). Parameters are: $\lambda_1 = 0.4$, $\lambda_0 = 0.7$, $l = -0.3$, $\lambda_f = 1$, $N = 10$.

On the one hand, as previously observed at the level of a single half-sarcomere, as β decreases, the free energy in hard device becomes convexified (see Fig.8.16). We will show in the next section that the free energy becomes convex at any temperature in the thermodynamics limit $P \to \infty$.

On the other hand, the T_2 curve develops two regions of negative slope as β increases (see Fig.8.16C). The presence of regions with negative slope was already noticed in (Vilfan and Duke, 2003) (see Fig.8.13), they also linked them to the presence of non-affine states ($\{(1,0),(0,1)\}$ and $\{(0,1),(1,0)\}$) characterized by different elongations of different half-sarcomeres in isometric contraction. The explanation of this phenomenon was only qualitative in that paper. Here we reconstruct explicitly these curves from statistical mechanics at finite temperature and show that the negative slope can be viewed as a finite size effect. The isotherms in soft device (see Fig.8.16B and D) are the same as in the case of a single half-sarcomere (see Fig.4.2).

8.2.3 Reduced energy landscape

In the previous Section, we introduced the non-equilibrium energy landscapes F_y^2 and G_y^2, in the space of the internal degrees of freedom ϵ_y^1 and ϵ_y^2 and on the loading. As in the case of a single half-sarcomere in the hard device, F_y^2 contains the first term that depends on λ_f and generates a Gaussian distribution around $\frac{1}{2}\left(\epsilon_y^1 + \epsilon_y^2\right) = \overline{\epsilon}$. The second term in $-1/\beta \ln\left((\mathcal{Z}_1(\epsilon_y^1) + \mathcal{Z}_0(\epsilon_y^1))(\mathcal{Z}_1(\epsilon_y^2) + \mathcal{Z}_0(\epsilon_y^2))\right)$ is a sum of four Gaussian distributions.

On Fig.8.17, we represent the isolines of F_y^2 *vs* ϵ_y^1 and ϵ_y^2 for low λ_f (A, B and C,

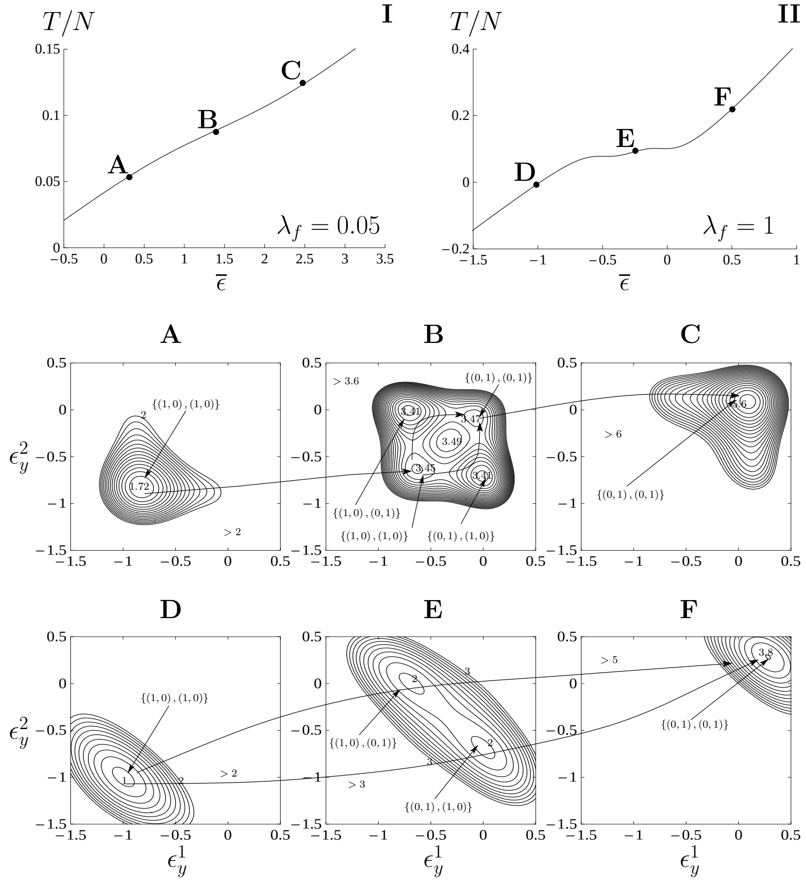

Fig. 8.17 – Reduced energy landscape in hard device for two half-sarcomeres. In the first row we represent the tension in thermal equilibrium *vs* the applied elongation per half-sarcomere for 2 different values of λ_f: $\lambda_f = 0.05$ (**I**) and $\lambda_f = 1$ (**II**). On each plot, we marked 3 points: **A**, **B** and **C** for $\lambda_f = 0.05$ and **D**, **E** and **F** for $\lambda_f = 1$. To each of those point corresponds a reduced free energy landscape F_y^2 (see Eq.(8.2.6)) function of the cross-bridges elongations ϵ_y^1 and ϵ_y^2 represented on the lower panel. For $\lambda_f = 0.05$ (see **A**, **B** and **C**), the reduced energy landscape present 4 local minima when $\overline{\epsilon}$ is in the middle of the transition (see **B**). For $\lambda_f = 1$, the system presents only 2 local minima. Other parameters are: $\lambda_1 = 0.4$, $\lambda_0 = 0.7$, $l = -0.3$, $N = 10$ and $\beta = 10$.

$\lambda_f = 0.05$) and large λ_f (D, E and F, $\lambda_f = 1$) in unit of $k_b\theta$. In the first row, we show the isotherms T_2 for two values of λ_f (I: $\lambda_f = 0.05$ and II: $\lambda_f = 1$). The corresponding energy landscapes are represented on the second and third row. For low λ_f (see Fig.8.17I and A, B, C), the energy landscape exhibits four *macroscopic wells* at intermediate loadings (see B). Each macroscopic well corresponds to a particular microstructure ($\{(1,0),(1,0)\}$, $\{(1,0),(0,1)\}$, $\{(0,1),(1,0)\}$ and $\{(0,1),(0,1)\}$). At larger loading (A, on the shortening side and C, on the stretching side), the multi-well structure disappears and the remaining well correspond the homogeneous microstructure: $\{(1,0),(1,0)\}$ (see A) and $\{(0,1),(0,1)\}$ (see C). As the load changes from A to C, the systems can stay in the affine state $\{(1,0),(1,0)\}$ until the other affine state $\{(0,1),(0,1)\}$ becomes available. Then, it jumps to this new configuration spending only a small fraction of 'time' in the non affine states $\{(1,0),(0,1)\}$ or $\{(0,1),(1,0)\}$ (see the arrows indicating trajectories).

At large λ_f (see Fig.8.17II and D, E, F, where $\lambda_f = 1$), the energy landscape for intermediate value of the loading (see E) shows only two wells corresponding to the 2 non-affine states $\{(1,0),(0,1)\}$ and $\{(0,1),(1,0)\}$. Hence when going from D to F, the system spends significant amount of 'time' in the non affine state.

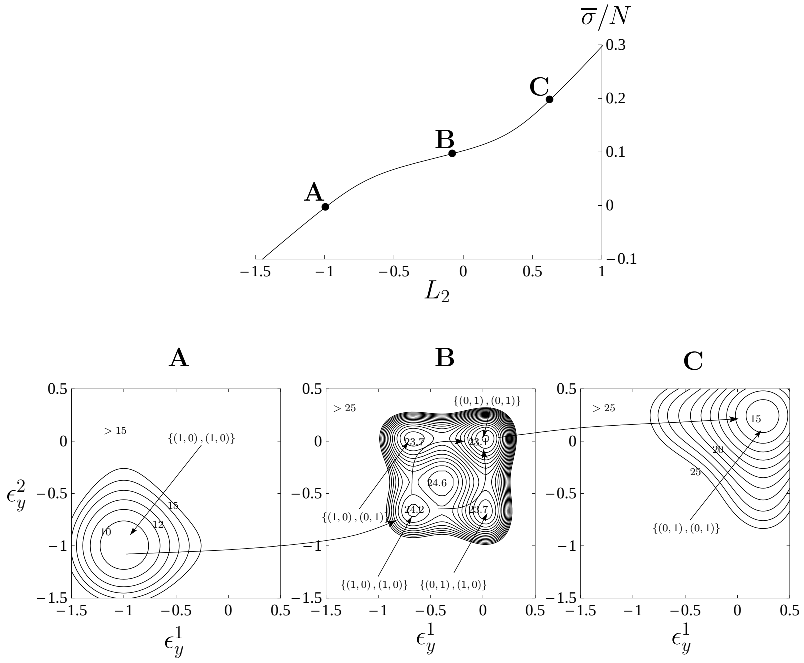

Fig. 8.18 – **Reduced energy landscape in soft device for two half-sarcomeres**. On the first row, we represent the L_2 curve and indicate 3 points, A at $\overline{\sigma}/N = \overline{\sigma}_{1/2}/N - 0.1$, B at $\overline{\sigma}/N = \overline{\sigma}_{1/2}/N$ and C at $\overline{\sigma}/N = \overline{\sigma}_{1/2}/N + 0.1$. On the second row, we represent G_y^2 *vs* ϵ_y^1 and ϵ_y^2 corresponding to the points A, B and C see Eq.(8.2.7). The parameters are: $\lambda_1 = 0.4$, $\lambda_0 = 0.7$, $l = -0.3$, $N = 10$ and $\beta = 10$ and $\lambda_f = 0.5$.

We conclude that, like in the single half-sarcomere case where low values of λ_f favors homogeneous distribution of the cross-bridges (see Sec.4.2.3), the presence of strong coupling (low λ_f) favors homogeneous strain distribution also along the chain of half-sarcomeres, the non affine states being only transitory populated.

In soft device, the dependence of G_y^2 on λ_f is only due to the term $\sigma^2/(N^2\lambda_f)$ and therefore has no effect on the dependence on ϵ_y^1 and ϵ_y^2. Isolines of G_y are shown on Fig.8.18 for 3 different loadings: $\overline{\sigma}/N = \overline{\sigma}_{1/2}/N - 0.1$ (A), $\overline{\sigma}/N = \overline{\sigma}_{1/2}/N$ (B) and $\overline{\sigma}/N = \overline{\sigma}_{1/2}/N + 0.1$ (C) and for $\lambda_f = 0.5$. The corresponding points on the L_2 curve are represented on the upper part of the figure. Like F_y^2 in hard device at low λ_f (see Fig.8.17), G_y^2 present four macroscopic wells when $\overline{\sigma}$ is close to $\overline{\sigma}_{1/2}$ the system spends most of the 'time' in the affine states. Note that Fig.8.17 and 8.18 corresponds $N = 10$ and the energy barriers between the macroscopic wells are of the order of $k_b\theta$. The barrier will of course be proportionally higher with more realistic values of N ($N \sim 100$).

8.3 Chain of half-sarcomeres with $P > 2$

8.3.1 Partition functions

After the detailed illustrations in the previous section, here we turn to the general case of $P > 2$. The partition function in the soft device can be again obtained as the product of individual partition functions like in the case $P = 2$ (see Eq.8.2.3):

$$\mathcal{Z}_s^P(\overline{\sigma}, \beta) = \left(\mathcal{Z}_s(\overline{\sigma}, \beta)\right)^P = \left(\sqrt{\frac{2\pi}{N\beta\lambda_f}} \int \exp\left[-\beta G_y(\overline{\sigma}, x, \beta)\right] dx\right)^P .$$

In the hard device, the computation is more difficult because of the constrain $\sum \epsilon_z^k = P\bar{\epsilon}$. However a semi-explicit answer can still be obtained in the limit $\beta \to \infty$, $P \to \infty$.

Starting with Eq.(8.2.1), we first perform the integration with respect to all ϵ_i^k for for $1 \leq i \leq N$ and $1 \leq k \leq P$. We obtain:

$$\mathcal{Z}_h^P\left(\bar{\epsilon}, \beta\right) = \int \exp\left[-\beta\left(\sum_{k=1}^{P} F_y\left(\epsilon_z^k, \epsilon_y^k, \beta\right)\right)\right] \mathbb{1}_{\left\{\frac{1}{P}\sum \epsilon_z^k = \bar{\epsilon}\right\}} d\epsilon_y^1 \dots d\epsilon_y^P d\epsilon_z^1 \dots d\epsilon_z^P \tag{8.3.1}$$

where $\mathcal{Z}_1$ and $\mathcal{Z}_0$ are given by Eqs.(4.2.7) and (4.2.7).

To simplify the computation of the partition function, we assume that individual half-sarcomeres can be only either in full pre-power-stroke or post-power-stroke configuration ($(1,0,0)$ or $(0,0,1)$). This means that we neglect all the local minima with $n_1^k \neq 0, 1$ for all $1 \leq k \leq P$ and retain only the states where each half-sarcomere is in global minimum which is in agreement with our conclusion that a single half-sarcomere is a 'cold' system (these state were represented by solid lines on Fig.8.2). More specifically we make the following hypothesis for all $1 \leq k \leq P$:

$$\mathcal{Z}_1\left(\epsilon_y^k, \beta\right) + \mathcal{Z}_0\left(\epsilon_y^k, \beta\right) = \begin{cases} \sqrt{\frac{2\pi(1-\lambda_1)}{\beta}} \exp\left[-\beta\lambda_1 \frac{1}{2}\left(\epsilon_y^k + 1\right)^2\right] & \text{if } \alpha_k = 1 \\ \sqrt{\frac{2\pi(1-\lambda_0)}{\beta}} \exp\left[-\beta\left(v_0 + \lambda_0 \frac{1}{2}\left(\epsilon_y^k\right)^2\right)\right] & \text{if } \alpha_k = 0. \end{cases} \tag{8.3.2}$$

so that $\mathcal{Z}_1 / \left(\mathcal{Z}_1 + \mathcal{Z}_0\right) = 0$ or 1. Then we can rewrite the partition function as:

$$\begin{aligned} \mathcal{Z}_h^P\left(\bar{\epsilon}, \beta\right) = \sum_{\alpha} \int \exp\Bigg[-\beta N \sum_{k=1}^{P} \frac{1}{2}\left(\epsilon_z^k - \epsilon_y^k\right)^2 - \frac{1}{\beta}\frac{1}{2} \ln\left(\frac{2\pi(1-\lambda_{\alpha_k})}{\beta}\right) \\ + \frac{1}{2}\lambda_{\alpha_k}\left(\epsilon_y^k + \alpha_k\right)^2 + \left(1-\alpha_k\right) v_0\Bigg] \mathbb{1}_{\left\{\sum \epsilon_z^k = P\bar{\epsilon}\right\}} d\epsilon_y^1 \dots d\epsilon_y^P d\epsilon_z^1 \dots d\epsilon_z^P \end{aligned} \tag{8.3.3}$$

where α represents a vector $(\alpha_1, \dots, \alpha_P)$ with $\alpha_k = 0$ or 1. Next, we can integrate with respect to all ϵ_y^k to obtain:

$$\begin{aligned} Z_h^P\left(\bar{\epsilon}, \beta\right) = \sum_{\alpha} A_\alpha \int \exp\left[-\beta N \sum_{k=1}^{P} \frac{1}{2}\mu_k\left(\epsilon_z^k + \alpha_k\right)^2 + \left(1-\alpha_k\right) v_0\right] \mathbb{1}_{\left\{\sum \epsilon_z^k = P\bar{\epsilon}\right\}} d\epsilon_z^1 \dots d\epsilon_z^P \\ \text{where } \mu_k = \frac{\lambda_{\alpha_k}\lambda_f}{\lambda_{\alpha_k} + \lambda_f} \quad \text{and } A_\alpha = \prod_{k=1}^{P}\left(\frac{2\pi\left(1-\lambda_{\alpha_k}\right)}{\beta}\right)^{\frac{N}{2}}\left(\frac{2\pi}{\beta N\left(\lambda_f + \lambda_{\alpha_k}\right)}\right)^{\frac{1}{2}}. \end{aligned} \tag{8.3.4}$$

From here, we follow (Efendiev and Truskinovsky, 2010). To perform the integration with respect to $\epsilon_z^1, \dots, \epsilon_z^P$, we introduce:

$$\begin{cases} \epsilon_z^k + \alpha_k & = z_k - z_{k-1} \\ z_0 & = 0 \\ z_P & = P\bar{\epsilon} + \sum\limits_{k=1}^{P} \alpha_k. \end{cases} \tag{8.3.5}$$

and change variable in the integral accordingly. We rewrite $\mathcal{Z}_h^P$ as:

$$\begin{aligned} \mathcal{Z}_h^P\left(\bar{\epsilon}, \beta\right) = \sum_{\alpha} \Bigg\{ A_\alpha \exp\left[-\beta N\left(\frac{1}{2}\mu_P z_P^2 + \sum_{k=1}^{P}\left(1-\alpha_k\right) v_0\right)\right] \\ \int \exp\left[-\beta N\left(\frac{1}{2}\underline{z}^T.\underline{\underline{T}}^P.\underline{z} - 2\mu_P z_P \underline{e}^T.\underline{z}\right)\right] d\underline{z} \Bigg\} \end{aligned} \tag{8.3.6}$$

where $\underline{z} = \begin{pmatrix} z_1 \\ \vdots \\ z_{P-1} \end{pmatrix}$; $\underline{e} = \begin{pmatrix} 0 \\ \vdots \\ 0 \\ 1 \end{pmatrix}$; $\underline{\underline{T}}^M = \begin{pmatrix} \mu_1+\mu_2 & -\mu_2 & 0 & \cdots & 0 \\ -\mu_2 & \mu_2+\mu_3 & -\mu_3 & \ddots & \vdots \\ 0 & -\mu_3 & \ddots & \ddots & 0 \\ \vdots & \ddots & \ddots & \ddots & -\mu_{M-1} \\ 0 & \cdots & 0 & -\mu_{M-1} & \mu_{M-1}+\mu_M \end{pmatrix}$

Here x^T denotes the transpose of x. We now compute the Gaussian integral by using the following classical result:

$$\int \exp\left[-\beta N\left(\frac{1}{2}\underline{z}^T.\underline{\underline{T}}.\underline{z} - 2\mu_M z_M \underline{e}^T.\underline{z}\right)\right] d\underline{z} =$$

$$\left(\frac{2\pi}{\beta N}\right)^{\frac{P-1}{2}} \left(\det\left(\underline{\underline{T}}^P\right)\right)^{-\frac{1}{2}} \exp\left[\beta N \frac{1}{2}\left(\mu_P z_P\right)^2 \left(\underline{\underline{T}}^P\right)^{-1}_{P-1P-1}\right]. \quad (8.3.7)$$

The determinant of P as well as $\left(\underline{\underline{T}}^P\right)^{-1}_{P-1P-1}$, the last entries in the inverse of $\underline{\underline{T}}^P$ can be obtained explicitly:

$$\det\left(\underline{\underline{T}}^P\right) = \prod_{k=1}^{P} \mu_k \sum_{k=1}^{P} \frac{1}{\mu_k}, \quad (8.3.8)$$

$$\begin{aligned} \left(\underline{\underline{T}}^P\right)^{-1}_{P-1P-1} &= \frac{1}{\det\left(\underline{\underline{T}}^P\right)} (-1)^{2(N-1)} \det\left(\underline{\underline{T}}^{P-1}\right) \\ &= \frac{\prod_{k=1}^{P-1} \mu_k \sum_{k=1}^{P-1} \frac{1}{\mu_k}}{\prod_{k=1}^{P} \mu_k \sum_{k=1}^{P} \frac{1}{\mu_k}}. \end{aligned} \quad (8.3.9)$$

After the substitution of these relations to Eq.(8.3.6), we obtain the following Ising problem:

$$\mathcal{Z}_h^v\left(\bar{\epsilon}, \beta\right) = \sum_\alpha A_\alpha B_\alpha \exp\left[-\beta N P\left(\frac{1}{2}\left(\frac{1}{P}\sum_{k=1}^{v}\frac{1}{\mu_k}\right)^{-1}\left(\bar{\epsilon} + \sum_{k=1}^{P}\alpha_k\right)^2 + \sum_{k=1}^{P}\left(1-\alpha_k\right) v_0\right)\right] \quad (8.3.10)$$

$$\text{where } B_\alpha = \left(\frac{2\pi}{\beta N}\right)^{\frac{P-1}{2}} \left(\prod_{k=1}^{P}\mu_k \sum_{k=1}^{P}\frac{1}{\mu_k}\right)^{-\frac{1}{2}}. \quad (8.3.11)$$

Since the energy depends only on $\sum \alpha$ (‘average magnetization’) and summation is over all spin configurations $\{\alpha\}$ it is now convenient to introduce

$$p = \frac{1}{P}\sum_{k=1}^{P}\alpha_k,\ 0 \le p \le 1, \quad (8.3.12)$$

which represents the fraction of half-sarcomeres in full post-power-stroke conformation. We see that Z_h^P depends only on the sum and the product over k, hence the particular order of half-sarcomere in the chain does not matter. Therefore, $\sum\limits_{\alpha}$ reduces to a discrete sum over p, from 0 to 1 taking into account the multiplicity of each configuration with a given p. After some manipulations, $\mathcal{Z}_h^P$ can be put into the form:

$$\begin{aligned}
\mathcal{Z}_h^P\left(\overline{\epsilon},\beta\right) &= \sum_{p=0}^{1}\binom{P}{Pp}K\left(p\right)\exp\left[-\beta NP\left(\frac{1}{2}\left(\frac{p}{\mu_1}+\frac{1-p}{\mu_0}\right)^{-1}\left(\overline{\epsilon}+p\right)^2+\left(1-p\right)v_0\right)\right] \\
\text{where } K\left(p\right) &= \left(\frac{2\pi}{\beta}\right)^{\frac{(N+2)P-1}{2}}\sqrt{\frac{N}{P}}N^{-P} \\
&\quad\times\frac{\left(1-\lambda_1\right)^{p\frac{NP}{2}}\left(1-\lambda_0\right)^{(1-p)\frac{NP}{2}}\left(\lambda_f+\lambda_1\right)^{-p\frac{P}{2}}\left(\lambda_f+\lambda_0\right)^{-(1-p)\frac{P}{2}}}{\mu_1^{p\frac{P}{2}}\mu_0^{(1-p)\frac{P}{2}}\left(\frac{p}{\mu_1}+\frac{1-p}{\mu_0}\right)^{\frac{1}{2}}}
\end{aligned} \tag{8.3.13}$$

If P is large, we can expand the binomial coefficients by using Stirling formula and transform the sum into an integral over $[0,1]$. We then obtain the more compact expression:

$$\mathcal{Z}_h^P\left(\overline{\epsilon},\beta\right)\approx\left(\frac{2\pi}{\beta}\right)^{\frac{(N+2)P-1}{2}}\frac{N^{\frac{1}{2}-P}}{\sqrt{2\pi}}\int_0^1\phi\left(p\right)\exp\left[-P\left(\psi\left(\overline{\epsilon},\beta,p\right)\right)\right]dp \tag{8.3.14}$$

$$\begin{aligned}
\text{with } \psi\left(\overline{\epsilon},\beta,p\right) &= N\beta\left(\frac{1}{2}\left(\frac{p}{\mu_1}+\frac{1-p}{\mu_0}\right)^{-1}\left(\overline{\epsilon}+p\right)^2+\left(1-p\right)v_0\right) \\
&\quad-\frac{N}{2}\left(p\ln\left(1-\lambda_1\right)+\left(1-p\right)\ln\left(1-\lambda_0\right)\right) \qquad , \\
&\quad+p\ln\left(p\right)+\left(1-p\right)\ln\left(1-p\right)+\frac{p}{2}\ln\left(\lambda_1\lambda_f\right)+\frac{1-p}{2}\ln\left(\lambda_0\lambda_f\right)
\end{aligned} \tag{8.3.15}$$

$$\text{and } \phi\left(p\right)=\left[\left(\frac{p}{\mu_1}+\frac{1-p}{\mu_0}\right)\left(p\left(1-p\right)\right)\right]^{-\frac{1}{2}} \tag{8.3.16}$$

When $\beta\to\infty$, ψ reduces to the mechanical energy of a chain with a fraction p of half-sarcomeres in post-power-stroke:

$$\psi\left(\overline{\epsilon},\beta,p\right)\underset{\beta\to\infty}{\longrightarrow}N\beta\left(\frac{1}{2}\left(\frac{p}{\mu_1}+\frac{1-p}{\mu_0}\right)^{-1}\left(\overline{\epsilon}+p\right)^2+\left(1-p\right)v_0\right) \tag{8.3.17}$$

and therefore, all entropic elasticity terms disappear. For finite β, we can still obtain analytical results in the thermodynamic limit $P\to\infty$.Indeed, by using Laplace method in Eq.(8.3.18) we can write:

$$\mathcal{Z}_h^P\left(\overline{\epsilon},\beta\right)\approx\left(\frac{2\pi}{\beta}\right)^{\frac{(N+2)P-1}{2}}N^{\frac{1}{2}-P}\frac{\phi\left(p^{\star,h}\right)\exp\left[-P\psi\left(\overline{\epsilon},\beta,p^{\star,h}\right)\right]}{\left(P\,\partial_p^2\psi\left(\overline{\epsilon},\beta,p\right)\big|_{p=p^{\star,h}}\right)^{\frac{1}{2}}} \tag{8.3.18}$$

where $p^{\star,h}$ is the minimum of ψ in the interval $]0,1[$. For large shortening (resp. stretching), as the single half-sarcomere case, we have $p=1$ (resp. 0) and therefore the asymptotics changes to:

$$\mathcal{Z}_h^P\left(\overline{\epsilon},\beta\right) \approx \left(\frac{2\pi}{\beta}\right)^{\frac{(N+2)P-1}{2}} \frac{N^{\frac{1}{2}-P}}{\sqrt{2\pi}} \frac{\phi\left(1\right)\exp\left[-P\psi\left(\overline{\epsilon},\beta,1\right)\right]}{\left(P\;\partial_p\psi\left(\overline{\epsilon},\beta,p\right)\big|_{p=1}\right)^{\frac{1}{2}}} \qquad \text{if } p^{\star,h}=1 \tag{8.3.19}$$

$$\text{and } \mathcal{Z}_h^P\left(\overline{\epsilon},\beta\right) \approx \left(\frac{2\pi}{\beta}\right)^{\frac{(N+2)P-1}{2}} \frac{N^{\frac{1}{2}-P}}{\sqrt{2\pi}} \frac{\phi\left(0\right)\exp\left[-P\psi\left(\overline{\epsilon},\beta,0\right)\right]}{\left(P\;\partial_p\psi\left(\overline{\epsilon},\beta,p\right)\big|_{p=0}\right)^{\frac{1}{2}}} \qquad \text{if } p^{\star,h}=0 \tag{8.3.20}$$

In the limit $\beta\to\infty$, $p^{\star,h}$ converges to the the fraction of post-power-stroke half-sarcomeres that minimizes the mechanical energy, and we recover results from Sec.8.1.1.

8.3.2 Isotherms

Based on Eq.(8.3.18) the equilibrium free energy for a chain of half-sarcomeres in hard device can be written in the form:

$$F^P\left(\overline{\epsilon},\beta\right) \approx -\frac{1}{\beta}\left(\frac{(N+2)\,P-1}{2}\ln\left(\frac{2\pi}{\beta}\right) - P\psi\left(\overline{\epsilon},\beta,p^{\star,h}\right).\right), \tag{8.3.21}$$

Then the equilibriul tension is:

$$T_2^P\left(\overline{\epsilon},\beta\right) \approx N\left(\frac{p^{\star,h}}{\mu_1}+\frac{1-p^{\star,h}}{\mu_0}\right)\left(\overline{\epsilon}+p^{\star,h}\right). \tag{8.3.22}$$

In soft device, since the partition function is the product of individual and independent partition functions for each half-sarcomere, the Gibbs free energy and the total elongation of a chain are simply P times the results for a single half-sarcomere:

$$G^P\left(\overline{\sigma},\beta\right) = -\frac{1}{\beta}P\ln\left(\mathcal{Z}_s\left(\overline{\epsilon},\beta\right)\right), \tag{8.3.23}$$

$$L_2^P\left(\overline{\sigma},\beta\right) = P\left(\frac{\overline{\sigma}}{N\lambda_f}+\left\langle\epsilon_y\right\rangle_s\left(\overline{\sigma},\beta\right)\right). \tag{8.3.24}$$

There $\mathcal{Z}_s$ is given by Eq.(4.2.12) and $\left\langle\epsilon_y\right\rangle_s$ by Eq.(4.2.18).

The equilibrium mean fraction of half-sarcomere in post-power-stroke, $\left\langle p\right\rangle_h$ simply corresponds in hard device to the minimum $p^{\star,h}$ of ψ (given by Eq.8.3.15):

$$\left\langle p\right\rangle_h\left(\overline{\epsilon},\beta\right) = p^{\star,h} \text{ in hard device.} \tag{8.3.25}$$

The argumentation here is the same as in the case of a single half-sarcomere (see App.B.4.1. In soft device, to find $\left\langle p\right\rangle_s$ we first write the probability for sarcomere one to be in post-power-stroke configuration:

$$q_1\left(\overline{\sigma},\beta\right) = \frac{1}{\mathcal{Z}_s\left(\overline{\sigma},\beta\right)} \underset{-\infty<\left\{\epsilon_i^1\right\}<l}{\int\cdots\int} \quad \underset{\underline{\epsilon}\backslash\left\{\epsilon_i^1\right\}}{\int\cdots\int} \exp\left[-\beta W\left(\overline{\sigma},\underline{\epsilon}\right)\right]d\underline{\epsilon}$$

where the energy W is given by Eq.(8.1.2). Due to independence of individual half-sarcomeres, all integrals for half-sarcomeres $2,\ldots P$ simplifies and only the integrals related to the first half-sarcomere remain. We integrate further with respect to $\epsilon_1^1\ldots\epsilon_1^N$ to obtain:

$$q_1\left(\overline{\sigma},\beta\right) = \frac{\iint\left(\mathcal{Z}_1\left(\epsilon_y^1,\beta\right)\right)^N\exp\left[-\beta\left(\frac{1}{2}N\lambda_f\left(\epsilon_z^1-\epsilon_y^1\right)^2-\overline{\sigma}\epsilon_z^1\right)\right]d\epsilon_y^1 d\epsilon_z^1}{\iint\left(\mathcal{Z}_1\left(\epsilon_y^1,\beta\right)+\mathcal{Z}_0\left(\epsilon_y^1,\beta\right)\right)^N\exp\left[-\beta\left(\frac{1}{2}N\lambda_f\left(\epsilon_z^1-\epsilon_y^1\right)^2-\overline{\sigma}\epsilon_z^1\right)\right]d\epsilon_y^1 d\epsilon_z^1}$$

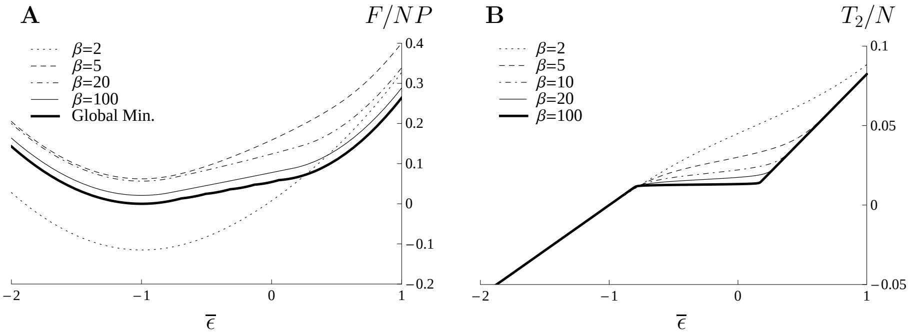

Fig. 8.19 – Influence of temperature on the thermal equilibrium of a chain of half-sarcomeres in hard device. (**A**): free energy for $\beta = 2$ (dotted line), 5 (dashed line), 20 (dot-dashed line), 100 (solid line) and in the global minimum (bold line). (**B**): T_2 curve for $\beta = 2$ (dotted line), 5 (dashed line), 10 (dot-dashed line), 20 (solid line) and 100 (bold line). The free energy is convex and the tension is monotone for all β. As β increases, the T_2 curves develops a plateau. Other parameters are: $\lambda_1 = 0.4$, $\lambda_0 = 0.7$, $l = -0.3$, $\lambda_f = 1$ and $N = 10$.

After yet another integration with respect to ϵ_z^1 we obtain:

$$q_1(\overline{\sigma}, \beta) = \frac{\int \left(\frac{\mathcal{Z}_1\left(\epsilon_y^1, \beta\right)}{\mathcal{Z}_1\left(\epsilon_y^1, \beta\right) + \mathcal{Z}_0\left(\epsilon_y^1, \beta\right)} \right)^N \exp\left[-\beta G_y\left(\overline{\sigma}, \epsilon_y, \beta\right)\right] d\epsilon_y^1}{\int \left(\mathcal{Z}_1\left(\epsilon_y^1, \beta\right) + \mathcal{Z}_0\left(\epsilon_y^1, \beta\right)\right)^N \exp\left[-\beta G_y\left(\overline{\sigma}, \epsilon_y, \beta\right)\right] d\epsilon_y^1}. \qquad (8.3.26)$$

Again, due to independence, the probability for any half-sarcomere in the chain to be in post-power-stroke is given by q_1. The same computation can be performed to find q_0, the probability for one half-sarcomere to be in pre-power-stroke and we find that $q_0 = 1 - q_1$. Hence the probability to have P_1 half-sarcomeres in the chain in post-power-stroke can be expressed as a Bernoulli law with parameters P and q_1:

$$\mathbb{P}\left(P_1 = X\right) = \binom{P}{N} q_1^X \left(1 - q_1\right)^{P-X} \qquad (8.3.27)$$

We can then conclude that the average fraction of post-power-stroke half-sarcomere in soft device is:

$$\langle p \rangle_s = q_1\left(\overline{\sigma}, \beta\right) \text{ where the } \textit{rhs} \text{ can be computed numerically from Eq.(8.3.26).} \qquad (8.3.28)$$

We illustrates the above computations in Figs.8.19, 8.20, 8.21 and 8.22. The appearence of the free energy and tension *vs* elongation relation for soft device is similar to what was already presented in Chap.4.

In the hard device, the increases of the temperature enhances the convexity of the energy landscape exactly as in the case of a single half-sarcomeres. However, as temperature is reduced (β increases), the T_2 curve does not exhibit anymore a region of negative stiffness but rather develops a plateau like it is observed in experiments. This result is consistent with the general result that in the thermodynamic limit ($P \to \infty$), the free energy of a distributed system is always convex.

In Fig.8.20, we show how the number of cross-bridges N affects the state of thermal equilibrium. A reduction of N smooths the transition on the T_2 curve (see B) and convexifies the energy landscape (see A) and in this sense decreasing N has a similar effect as reducing β. This is a so-called finite size effect studied extensively by T.L. Hill in (Hill, 1964). In experiment, the transition between the plateau and the linear part of the T_2

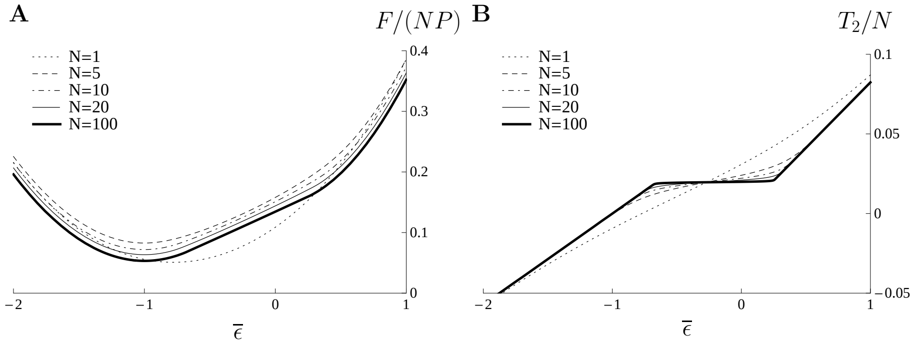

Fig. 8.20 – Influence of the number of cross-bridges on the thermal equilibrium of a chain of half-sarcomeres in hard device. Free energy (**A**) and tension (**B**) for $N = 1$ (dotted line), 5 (dashed line), 10 (dot-dashed line), 20 (solid line) and 100 (bold line). The free energy is convex and the tension ois monotone for all β. As β increases, the T_2 curves develops a plateau. Other parameters are: $\lambda_1 = 0.4$, $\lambda_0 = 0.7$, $l = -0.3$, $\lambda_f = 1$ and $\beta = 10$.

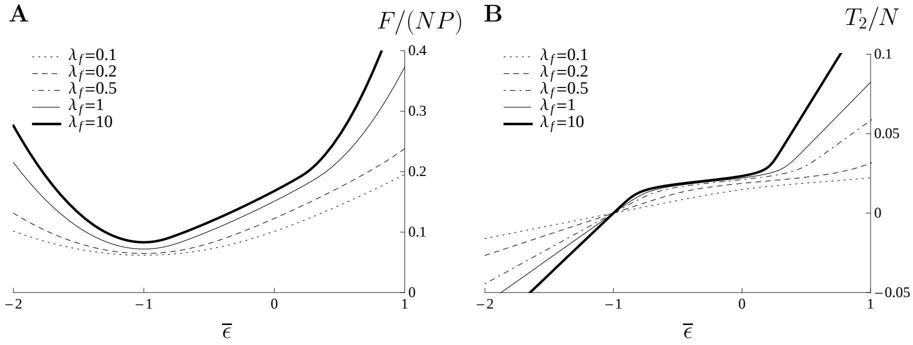

Fig. 8.21 – Influence of the coupling parameter on the thermal equilibrium of a chain of half-sarcomeres in hard device. Free energy (**A**) and tension (**B**) for $\lambda_f = 01$ (dotted line), 0.2 (dashed line), 0.5 (dot-dashed line), 1 (solid line) and 10 (bold line) The position of the transition is shifted to larger $\overline{\epsilon}$ when λ_f decreases. Other parameters are: $\lambda_1 = 0.4$, $\lambda_0 = 0.7$, $l = -0.3$, $N = 10$ and $\beta = 10$.

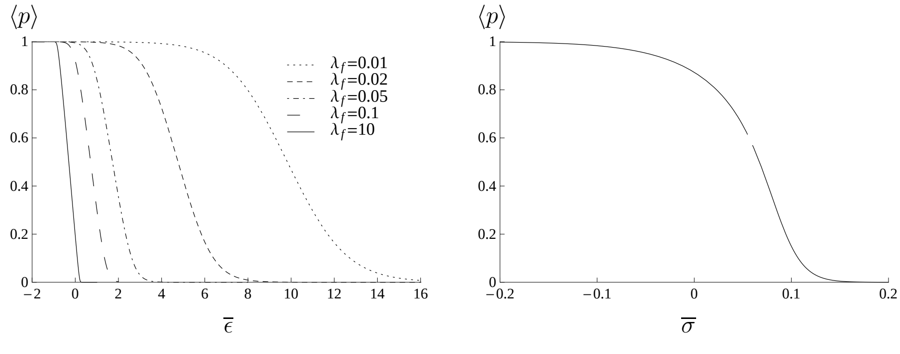

Fig. 8.22 – **Evolution of the fraction of post-power-stroke half-sarcomere in hard and soft devices**. (**A**): evolution of p for different values of the coupling parameter: $\lambda_f = 0.01$ (dotted line), 0.02 (dashed line), 0.05 (dot-dashed line), 0.1 (long dashed line), and 10 (solid line). In soft device, the curve (**B**) does not depend on λ_f. Parameters are: $\lambda_1 = 0.4$, $\lambda_0 = 0.7$, $l = -0.3$, β

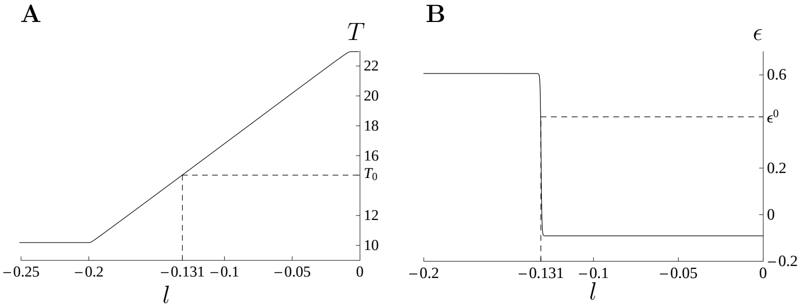

Fig. 8.23 – **Fit of the parameter l in hard (A) and soft (B) devices** for a chain of half-sarcomere. The curve in soft device is the same as for the single half-sarcomere (see Fig.7.4). The value of l found in hard and soft devices to reproduce the isometric conditions is now the same unlike with the single half-sarcomere.

curve in shortening is not sharp as predicted by our model (see Figs.8.24 and 8.25) which may be a manifestation of the finite size effect mentioned above ($N \sim 100$).

The effect of the coupling parameter λ_f is illustrated in Figs.8.21 and 8.22. As in the case of a single half-sarcomere in a system with soft filament (low λ_f), the transition is shifted towards larger values of the total strain (see Fig.8.21). However, the transition occurs at the same equilibrium tension. Overall making the coupling stronger (reducing λ_f) leads to smoothing of the transition thereby increasing the size of the region with inhomogeneous non-affine response at the microscale (see Fig.8.22A). This effect is absent in soft device where $\langle p \rangle_s$ does not depend on λ_f.

8.4 Adjusting parameters

In this section we study the kinetics of a chain of half-sarcomeres submitted to fast load steps. First, we re-adjust the parameters of the model following the procedure described in Sec.7.1 and see Tab.7.1 on p.139.

8.4.1 The stata of isometric contractions

In this section, we readjust our parameter selection from a half-sarcomere level to the level o the whole sarcomere chain. The values of λ_1, λ_0, N, β, ϵ^0 and T_0 should obviously be the same as in the case of a single half-sarcomere. We recall that in Sec.7.1.5, the value of l was chosen to fit the initial conditions ($L_2 = \epsilon^0$ and $T_2 = T_0$) and that the optimal choice was different in hard and soft devices (see Fig.7.4). In Fig.8.23, we show the equilibrium tension (A) and the elongation (B) corresponding to the initial conditions $\overline{\epsilon} = \epsilon^0$ and $\overline{\sigma} = T_0$ in hard and soft devices. In soft device (see Fig.8.23B), the curve is the same as for the single half-sarcomere and the optimal value of l is -0.131 in non-dimensional units. However, in hard device, the curve is radically different, and we no longer see a sharp transition at $l \approx -0.09$. Instead the optimal fit is achieved at the same value of l as in the soft device corresponding to the equilibrium tension T_0. Therefore, in the case of a half-sarcomere chain, the isometric conditions can be matched with the same set of parameters in hard and soft device.

8.4.2 Thermal Equilibrium

We can now apply the general formula describing thermal equilibrium in a sarcomere chain (obtained in the previous section) to our particular model with parameters adjusted

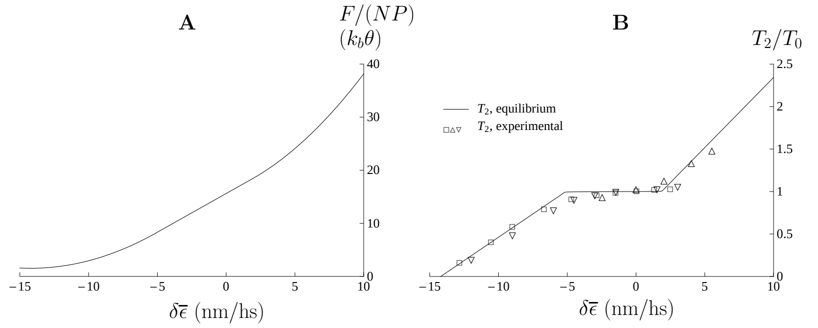

Fig. 8.24 – Thermal Equilibrium with the fitted model in hard device. (**A**): Free energy F in unit of $k_b\theta$ obtained from Eq.(8.3.21). (**B**): T_2 curve obtained from Eq.(8.3.22). Experimental data for the T_2 curve are from: Ford et al. (1977) (▽), Brunello et al. (2007) (△) and Linari et al. (2009) (□).

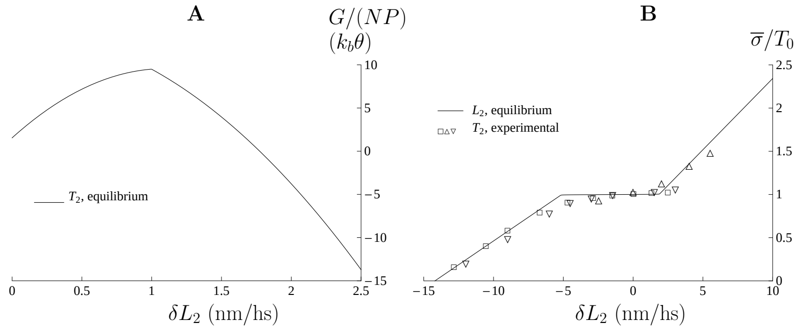

Fig. 8.25 – Thermal Equilibrium with the fitted model in soft device. (**A**): Free energy G in unit of $k_b\theta$ computed from Eq.(8.3.23). (**B**): L_2 curve computed using Eq.(8.3.24). Experimental data are for the hard device response from: Ford et al. (1977) (▽), Brunello et al. (2007) (△) and Linari et al. (2009) (□).

to experimental data. The equilibrium free energy (in units of $k_b\theta$) and the tension *vs* elongation relations in hard and soft devices are shown respectively on Figs.8.24 and 8.25.

First, we observe that in hard device, the free energy is convex. The free energy gap between the isometric state and the ground state is about $12k_b\theta$ (see Fig.8.24). This value is of the order of mechanical work produced by a single motor ($\sim 8k_b\theta$) if we consider that 40% of the energy from ATP is converted into mechanical work (see Sec.2.3.3). It is understood that this estimate based on the free energy is only valid for quasi-static evolution (Jarzynski, 1997). Therefore it is likely that the mechanical work performed during the quick recovery is lower than $12k_b\theta$ and thus closer to experimental estimates (Barclay et al., 2010). The same free energy gap is seen on Fig.8.25A, which represents the equilibrium Gibbs free energy in soft device. In order to reproduce accurately the energetics of the power stroke one has to keep track of the heat (Sekimoto, 2010).

Second, we observe that the isothermal tension *vs* elongation relations are the same in hard and soft devices (compare Figs.8.24B and 8.25B). We see that the negative slope observed in the case of a single half-sarcomere is no longer present. This agrees with experimental data if the T_2 curve is interpreted as equilibrium response. We notice, however, that the plateau is more marked in our computation than in experiments, which is either due to experimental uncertainties or due to early detachment of cross-bridges at the end of the quick recovery (see the effect of the reduction of the number of cross-bridges on Fig.8.20).

On Fig.8.26, we show the equilibrium fraction of post-power-stroke half-sarcomeres in

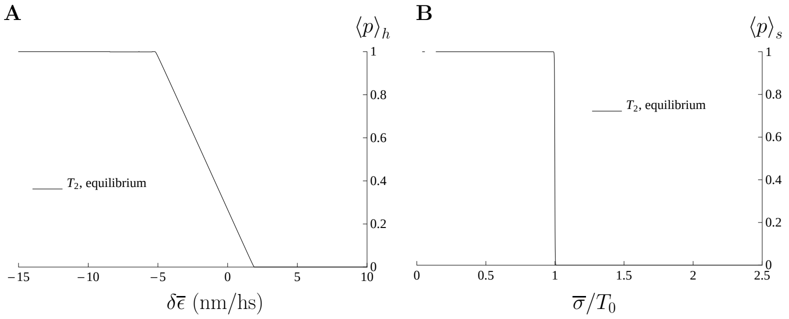

Fig. 8.26 – Fraction of post-power-stroke half-sarcomeres in hard (A) and soft device(B). The curves are obtained from Eqs.(8.3.25) (**A**) and (8.3.28) (**B**). In hard device, for steps sizes, between −5 and +2 nm/hs, the system equilibrates in a non affine configuration. In particular, the isometric state 27% of the half-sarcomeres are in post-power-stroke and 67% are in pre-power-stroke. In soft device, we also have $\langle p \rangle_s = 0.27$, for $\overline{\sigma} = T0$, but the whole chain immediately shift to full post-power-stroke (resp. full pre-power-stroke) with a change in force in the shortening direction (resp. stretching direction).

hard (A) and soft devices (B). The two curves are radically different. In hard device, we observe a linear transition going from $\delta\overline{\epsilon} = +2$ to $\delta\overline{\epsilon} = -5$ nm/hs corresponding to the plateau on the T_2 curves. This reminds us that in thermal equilibrium, the plateau corresponds a succession of non affine states with heterogeneous arrangement of pre- and post-power-stroke half-sarcomeres. In particular, in the isometric state, 27% of the half-sarcomeres are in post-power-stroke. this proportion is the same in the soft device at $\overline{\sigma} = T_0$ but in this cases, the slightest change in the applied tension automatically brings the system either in full post-power-stroke (lower force) or full pre-power-stroke (higher force) (see Fig.8.26B).

8.4.3 Kinetics

Method

In this section, We simulate the response of a fiber with 20 half-sarcomeres in series, by tracking its stochastic dynamics in the full configuration space. The isometric conditions is obtained by setting 27% of the half-sarcomeres in post-power-stroke. As we consider the myofilaments to be instantly equilibrated the form of the system of Langevin's equation describing the system in the hard device takes the form:

$$\left\{\begin{aligned} d\epsilon_i^{k,t} &= b\left(\epsilon_i^{k,t}, \epsilon_y^{k,t}\right) dt + \sqrt{2\beta^{-1}} dB_i^{k,t}, \text{ for } 1 \le i \le N \text{ and } 1 \le k \le P && (8.4.1a)\\ \epsilon_y^{k,t} &= \frac{T^t}{N} + \frac{1}{N}\sum_{i=1}^{N} \epsilon_i^{k,t} \text{ for } 1 \le k \le P && (8.4.1b)\\ T^t &= \frac{N\lambda_f}{1+\lambda_f}\left(\overline{\epsilon} - \frac{1}{NP}\sum_{k=1}^{P}\sum_{i=1}^{N}\epsilon_i^{k,t}\right) && (8.4.1c)\end{aligned}\right.$$

In soft device the system can be written as:

$$\left\{\begin{aligned} d\epsilon_i^{k,t} &= b\left(\epsilon_i^{k,t}, \epsilon_y^{k,t}\right) dt + \sqrt{2\beta^{-1}} dB_i^{k,t}, \text{ for } 1 \le i \le N \text{ and } 1 \le i \le P && (8.4.2a)\\ \epsilon_y^{k,t} &= \frac{\overline{\sigma} t}{N} + \frac{1}{N}\sum_{i=1}^{N} \epsilon_i^{k,t} && (8.4.2b)\end{aligned}\right.$$

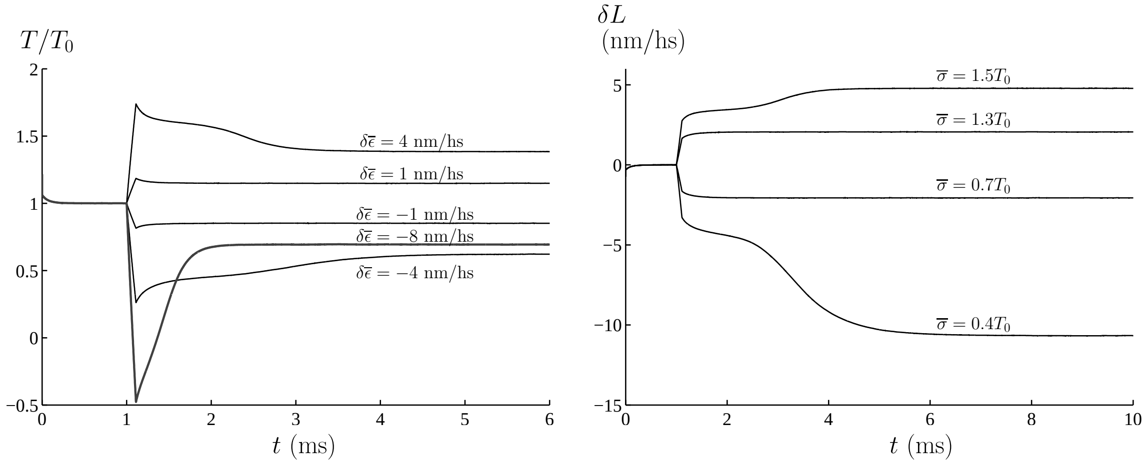

Fig. 8.27 – Response of fitted model to length steps (A) and load steps (B). The system initially in isometric condition undergoes a step completed in 110 μs. In hard device (**A**), we represent the response to steps with $\delta\overline{\epsilon} = 4, 1, -1, -4$ and -8 nm/hs. In soft device (**B**), we represents the response the load steps: $\overline{\sigma}/T_0 = 1.5, 1.3, 0.7$ and 0.4.

Notice that in our simple NN chain there is no direct interaction between adjacent half-sarcomeres but instead each sarcomere interacts with a mean field imposed by the tension. We also see that the values of ϵ_z^k are not needed to compute the solution. This implies that, within our model, the kinetics of the chain does not depend on the particular succession of configurations which is probably an oversimplification. Notice also that physically, it is more likely that the real fiber produces a regular pattern of half-sarcomeres in the chain, however, within the model, we observe the same response for a chain in which *e.g.*, the first K half-sarcomeres are in post-power-stroke and for a chain in which these K half-sarcomeres are regularly spread in the chain.

The system of equations (8.4.1) and (8.4.2) are simulated using a first order Euler algorithm with a time step $\Delta t = 10^{-3}$ and with 100 independent realizations ($N_r = 100$) (see Sec.5.2 and references therein).

Results for a chain of 20 half-sarcomeres

On Fig.8.27 we show the collective response in the system with $P = 20$ half-sarcomere at different step sizes in hard (see A) and soft (see B) devices. In hard device: $\delta\overline{\epsilon} = 4, 1, -1, -4, -8$ nm/hs and in soft device $\overline{\sigma}/T_0 = 1.5, 1.3, 0.7, 0.4$. For the lowest represented step sizes, the system equilibrates in less than 1/2 ms to an apparent steady state. For larger steps, the system reaches a steady state in two steps, the the first shorter than the second (see $\delta\overline{\epsilon} = -4$ nm/hs on Fig.8.27A and $\overline{\sigma} = 0.4T0$ on B). For the largest steps applied, (see $\delta\overline{\epsilon} = -8$ nm/hs on Fig.8.27A), the slow steps become barely visible. Such recovery with two time scale was already visible in the single half-sarcomere at finite temperature (see Figs.7.14, 5.7 and 5.9) but it has not been observed in experiments. This discrepancy can be explained by the fact that we use a very organized assembly of half-sarcomeres all having the same number of cross-bridges. It is likely that with a more heterogeneous sample of half-sarcomeres, this problem will disappear. This argument has been already put forward in (Duke, 1999) as an explanation for the absence of a absence of a region with negative stiffness on the T_2 curve.

In Fig.8.28, we report the tension and elongation attained at the end of our simulations

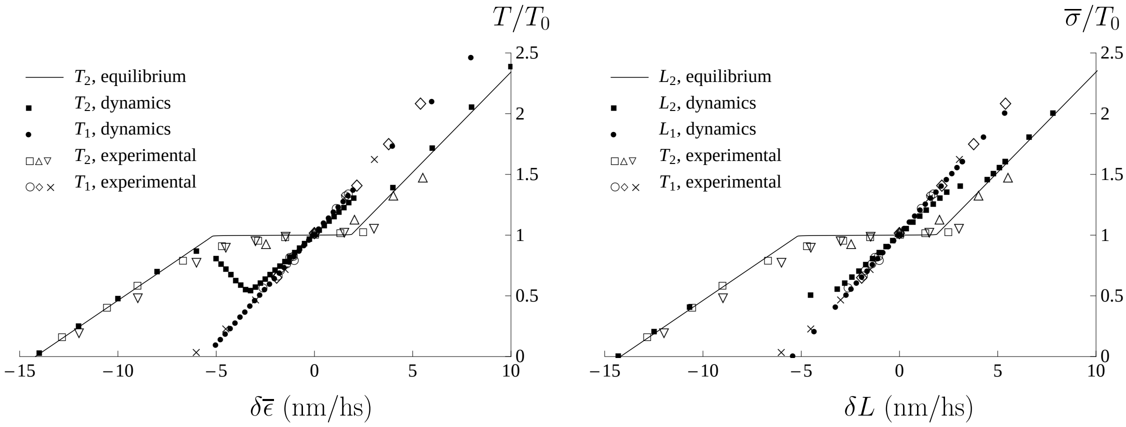

Fig. 8.28 – Comparison between thermal equilibrium and kinetic equilibrium in hard (A) and soft (B) devices. (**A**): Hard device. (**B**): soft device. Continuous line: thermal equilibrium computed using Eq.(8.3.22) (**A**) and (8.3.24)(**B**). (■): Tension and elongation attained at the end of the simulation (in hard device after 5 ms and in soft device after 10 ms). (●): Tension and elongation attained at the end of the step (T_1 and L_1). Experimental points (open symbols) are taken from (Ford et al., 1977)(T_1: ×, T_2: ▽), (Brunello et al., 2007)(T_1: ◇, T_2: △) and (Linari et al., 2009)(T_1: ⊚, T_2: □).

(in hard device, after 6 ms and in soft device, after 10 ms) . In hard device (see A), there is a large interval of shortening steps ($5 \leq \delta\bar{\epsilon} \leq 2$ nm./hs) where the system is not able to reach equilibrium after the time of simulation which is chosen to be compatible with the time of observations in real physical experiments. The thermal equilibrium is indicated by the solid line. Similarly, in the soft device (see Fig.8.28B), the system does not reach equilibrium after 10 ms for $0.4 \leq \overline{\sigma}/T_0 \leq 1.5$. We observe that the two intervals of interest, in hard and soft devices, span the same region on the tension/elongation plane, where slow kinetics dominate. We also observe that the kinetic trapping that was more pronounced in soft device, than in hard device for the single half-sarcomere (see Fig.7.15), is now similar for both types of experiments. As we have shown for the case of 2 half-sarcomeres, (see Sec.8.2.3), such kinetic trapping is the consequence of the mean field interaction introduced by the soft myofilaments.

This results shows that, our model is not able to reproduce the kinetics of the quick recovery fully adequately with in apurely mechanical framework with only Brownian motion helping the system to escape from a local minimum.

Even though the power-stroke is taking place at shorter time scales than the full Lymn-Taylor cycle, we can speculate that one needs to integrate the active effect of ATP in our model to accelerate the power-stroke transition.

Also, recall that our model neglects the interactions between adjacent half-sarcomeres. Such interactions may provoke power-stroke wave propagation in the fiber and accelerate the transition making propagation of a switch wave easier than successive nucleation. We found no evidence of such waves in the literature of quick recovery experiments but the waves might displace at high speed and be barely visible given the size of the experimental samples (few mm).

In Fig.8.29, we compare the rates obtained from our simulations to available experimental data. As a consequence of the kinetic trapping, we observe slower recovery within the chain than within the single half-sarcomere in hard device while in the soft device the rate remains similar (compare Fig.8.29 with Fig.7.16, ■ for hard device and ● for soft device). However, the general shapes of the kinetic curves obtained in simulations (filled

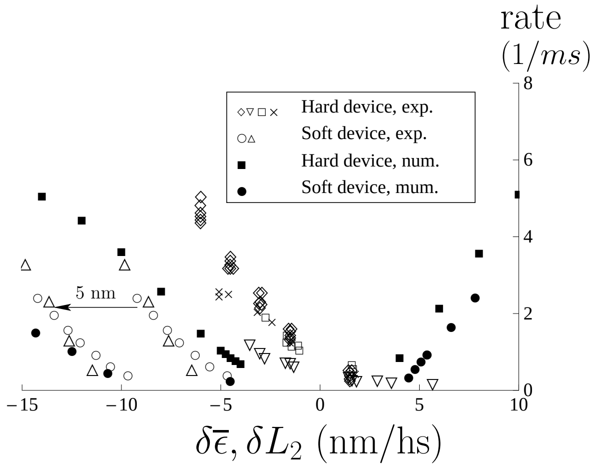

Fig. 8.29 – **Comparison of the rates of recovery in hard and soft devices**. The length clamp experimental data (open symbol) are from Huxley and Simmons (1971) (▽), Ford et al. (1977) (◇), Piazzesi et al. (1992) (×), and Linari et al. (2009) (□). The load clamp data (◎) are estimated from the velocity during phase 2 of the quick recovery (Piazzesi et al., 2002a). (△) are from Decostre et al. (2005). These points (◎, △) are obtained from *rana esculenta* for which the intercept of the T_2 curve is about −10 nm while it is about −15 nm for *rana temporaria*. We arbitrarily displaced the experimental points of *rana esculenta* by 5 nm to the left (see the arrow) to compare with the results of our simulations (●). (■) represent the rate curve obtained in hard device.

symbols) remain similar to the shapes of the experimental curve (open symbols). Most importantly, we still observe a slower recovery in soft device (●) than in hard device (■).

To illustrate the inner mechanism of the transition inside the chain, we show on Figs.8.30 and 8.31, how the fractions of post-power-stroke cross-bridges in each half-sarcomere evolve in time as the system responds to different load steps. On the figures, the sarcomeres are labeled $1, \dots, 20$ (see ♯) and the time is in ms. To match the initial isometric conditions, the last 5 half-sarcomeres are assumed to be in equilibrium in the post-power-stroke configuration ($\langle n_1 \rangle = 1$). When the step size is so small that the systems is kinetically trapped, the configuration of the chain remains the same throughout the simulation (see Figs.8.30 and 8.31, first rows). At larger steps (see second row), the fraction of post-power-stroke cross-bridges increase/decrease in all half-sarcomeres simultaneously. Again we do not observe any sign of wave propagation phenomena. This is a direct consequence of our assumption regarding the the mean field interaction among both the cross-bridges and the half-sarcomeres. Notice however, that the anatomic structure and the various connections between different contractile units, (such as the M-lines and the Z-disks and titin (see Figs.8.1 and 1.5)), may contribute additional non-locality of ferromagnetic type forcing all half sarcomeres to move coherently.

8.4.4 Sarcomere length inhomogeneities

We have presented in Chap.1, recent experiments showing half-sarcomere length inhomogeneities in a single myofibril. The time scales involved in these experiment are still too large to be interpreted fully with our power-stroke model. However, here we present the results of numerical tests performed in the adequate condition of the quick force recovery.

In our Fig.8.32, we show the displacement of the M-line expected if a single sarcomere is submitted to length increment $\delta\bar{\epsilon}$ in the hard device. The figure was the same obtained using the results from our analysis at zero temperature and the curve superimposes of

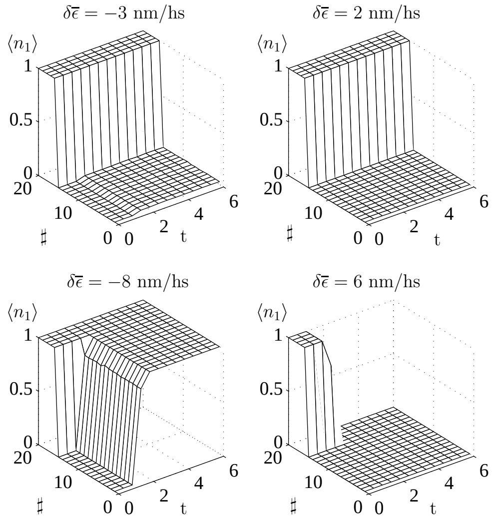
$\delta\overline{\epsilon} = -3$ nm/hs
$\delta\overline{\epsilon} = 2$ nm/hs
$\delta\overline{\epsilon} = -8$ nm/hs
$\delta\overline{\epsilon} = 6$ nm/hs

Fig. 8.30 – Evolution of the fraction of post-power-stroke, cross-bridges during the quick recovery in hard device for a chain of 20 half-sarcomeres. Each plot shows the evolution of the mean fraction of post-power-stroke cross-bridges $\langle n_1 \rangle$ for each of the 20 half-sarcomeres (sarcomeres are identified by the numbers $1, \ldots, 20$, see ♯). Initially, 5 half-sarcomeres are in full post-power-stroke ($\langle n_1 \rangle = 1$) to satisfy the conditions of the isometric contraction (see Sec.8.4.1). Left column: the response to 2 shortening steps ($\delta\overline{\epsilon} = -3$ and -8 nm/hs). Right column: the response to 2 stretching steps ($\delta\overline{\epsilon} = 2$ and 6 nm/hs).

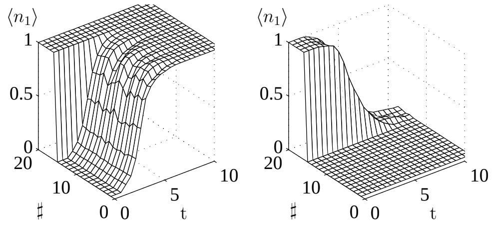
$\overline{\sigma} = 0.8T_0$
$\overline{\sigma} = 1.2T_0$
$\overline{\sigma} = 0.4T_0$
$\overline{\sigma} = 1.45T_0$

Fig. 8.31 – Evolution of the fraction of post-power-stroke, cross-bridges during the quick recovery in soft device for a chain of 20 half-sarcomeres. Each plot shows the evolution of the mean fraction of post-power-stroke cross-bridges $\langle n_1 \rangle$ for each of the 20 half-sarcomeres (sarcomeres are identified by the numbers $1, \ldots, 20$, see ♯). Initially, 5 half-sarcomeres are in full post-power-stroke ($\langle n_1 \rangle = 1$) to satisfy the conditions of the isometric contraction (see Sec.8.4.1). Left column: the response to 2 shortening steps ($\overline{\sigma} = -0.8$ and $0.4T_0$). Right column: the response to 2 stretching steps ($\overline{\sigma} = 1.2$ and $1.45T_0$).

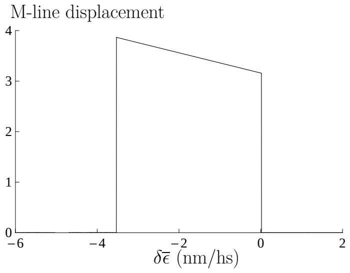

Fig. 8.32 – Displacement of the M-line in a single sarcomere. Computed at zero temperature. The computation with the fitted β superimpose on this curve (*cold system*). This result should be observed after the quick recovery following a length increment $\delta\overline{\epsilon}$. Note that the symmetric of this picture can also be observed because of permutational invariance.

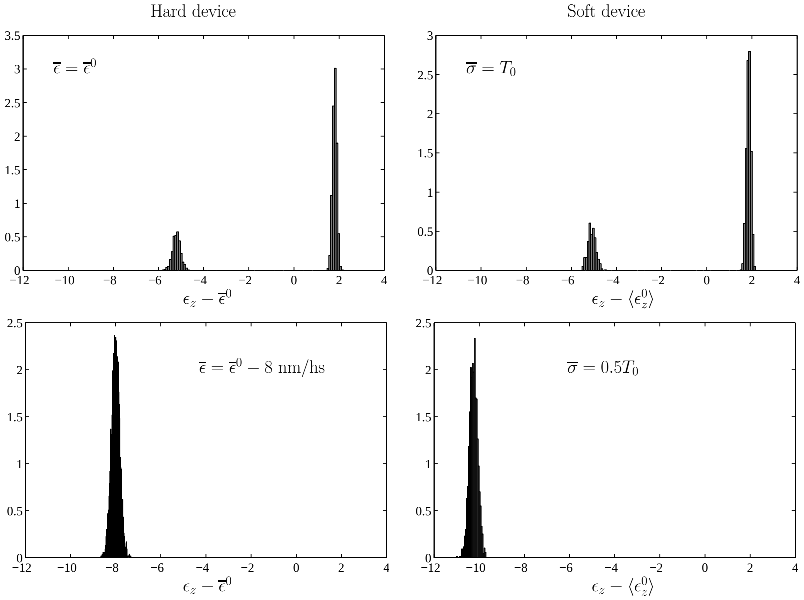

Fig. 8.33 – Distribution of half-sarcomeres elongations. Left column: hard device. Right column: soft device. Upper row: isometric conditions ($\overline{\epsilon} = \overline{\epsilon}^0$ and $\overline{\sigma} = T_0$), we observe a bi-modal distribution of the half-sarcomere elongation. Lower-row: response in shortening ($\delta\overline{\epsilon} = -8$ nm/hs and $\overline{\sigma} = 0.5T_0$) showing a uni-modal distribution.

the thermal equilibrium (the value of β is large). Note that the displacement shown on Fig.8.32 is an absolute displacement. Due to the permutational invariance, the symmetric of this picture can also be observed (negative displacements). Our model predicts a linear dependence of the M-line displacement on the step size in hard device. For large elongation increments, the M-line displacement drops to zero. In soft device, one should observe no displacement of the M-line.

In Fig.8.33, we show the distribution of the shift of the half-sarcomere elongation with respect to the mean initial elongation in hard device (left column) and soft device (right column). Before the step is applied (isometric conditions), the distribution of half-sarcomere length is bi-modal whereas, after the the quick recovery (lower-row), the system ends up in the affine state characterized by a uni-modal elongation distribution. These results confirm the experimental observations reported in (Shimamoto et al., 2009) (see Fig.1.16) even though these results were obtained following ‘slow’ force steps.

Conclusions

In this Chapter, we have shown that a chain of half-sarcomeres in series, responds to loads in a highly non-affine way due to instability of individual half-sarcomeres. The mechanical energy landscape is even more wiggly for the chain than for the unit, and the global minimum path passes through sequence of inhomogenous microstructures before reaching the affine states where all half-sarcomeres are either in pre-power-stroke or post-power-stroke conformation.

When temperature is taken intoa account, the equilibrium free energy becomes convex in the thermodynamic limit and the tension *vs* elongation relations become similar in hard and soft devices. For finite system however, considerable size effect can be expected

The effects of the coupling parameter is still felt in the chain and we have shown that the non-equilibrium energy landscape contains multiple additional energy wells corresponding to different arrangements of haf-sarcomeres.

The presence of these macroscopic wells considerably slow down the kinetics of the response to fast load change in the hard device, which exhibits the same kinetic trapping as in the soft device. The absence of next-to nearest interactions may be one of the main reasons preventing more coherent and more rapid response to fat loadings.

Our model is able to predicts the M-line displacement of a single half-sarcomere submitted to various elongation increments in the hard device and qualitatively reproduce the transition from bi-modal elongation distribution to uni-modal elongation distribution in response to load increments observed in recent experiments.

General Conclusions

In this manuscript, we proposed a series of mathematical models aimed at reproducing the mechanical behavior of a muscle fiber in response to quick length (hard device) and force (soft device) increments.

The time scale of this response ($\sim$1 ms) is shorter than the time scale associated with with ATP turnover (30 ms) which suggests that the power-stroke mechanism is a 'purely' mechanical phenomenon. Following this idea, we attempted a far reaching generalization of the classical Huxley and Simmons model (Huxley and Simmons, 1971) by assuming that the bi-stable nature of the myosin head is represented by a *continuous* piecewise parabolic potential. We used a simplified representation of the half-sarcomere by neglecting the spatial heterogeneity and assuming that the cross-bridges are arranged in parallel. The bundle of cross-bridges was connected in series to a linear spring lumping the myofilament elasticity. This series elasticity introduces a *mean field interaction* between the cross-bridges which is responsible for the *cooperative effects*. The study of these effects constitutes the mean focus of our work.

First, we analyzed the fine structure of the energy landscape associated with a single half-sarcomere. We showed that the global minimum path for the system driven quasistatically in both devices goes through affine states only. The transition between two affine states is localized at a particular value of the loading. At this stage we could already see the crucial difference between the loadings in the hard and soft devices. Thus, we have shown that, the energy barrier between the two affine states is much lower in the hard device than in the soft device. In addition, we have shown that the mean field interaction increases the coherency of the response by creating an *energy gap* between the affine states and the non-affine states.

Next, we studied thermal equilibrium and showed that, due to parallel arrangement of the cross-bridges, the free energy of a half-sarcomere remains *non-convex* even in the thermodynamic limit ($N \to \infty$). We have also shown that at low temperatures, the T_2 curve exhibits a region of *negative stiffness*. Most importantly, we have shown that the negative stiffness survives when the parameters of our model are adjusted to fit the available experimental data. This result confirms that during isometric contraction the half-sarcomeres are working in an *inherently unstable* regime. The presence of an elastic mean field interaction between the cross-bridges strongly affects the energy landscape. When the interaction is weak, the distribution of cross-bridges in pre-power-stroke and post-power-stroke states, is uni-modal. Instead, when the interaction is strong, we observed a *bi-modal distribution* revealing the continuous switching back and forth between the two affine configurations. This result confirms that the mean field interaction preserves the coherent response at the temperature of experimental observations.

The kinetics of our system is compatible with the available experimental data and the parameters can be chosen in such a way that the relaxation rates fit the observed values. More specifically, we observed that the response to fast load increments is dominated by kinetics at the observational time scales and that, at least at small loading increments, reaching equilibrium cannot be expected in standard experiments. In particular, we have shown that our model reproduces well the anomalously slower kinetics observed experimentally in soft device. We have identified a *kinetic trapping* phenomenon which we explicitly linked to the mean field interaction neglected in previous modeling attempts. The kinetic trapping is more pronounced in soft device and could be the main reason why the plateau of the T_2 curve had never been resolved experimentally.

To make our modeling more realistic we applied the model to distributed system representing an arrangement of many half-sarcomeres in series. The main result here is that the 'macroscopic' equilibrium curves in hard and soft devices become similar. In particular, the T_2 curve of an infinite chain exhibits the desired plateau despite the negative slope at the microscale. However, the behaviors in hard and soft device are not identical. Thus, in soft device, the system following the global minimum path switches directly from one affine state, with all half-sarcomeres in pre-power-stroke, to another affine state where all half-sarcomere are in post-power-stroke, without ever visiting the non-affine states. Instead, in hard device, the global minimum path goes through a range of *non-affine states* where each half-sarcomere is either in pre-power-stroke or post-power-stroke. The non-affine states are characterized by a highly heterogeneous distribution of strain among the half-sarcomeres. There is a growing experimental evidence that this type of heterogeneities is indeed present in isometrically contracting sarcomeres.

We observed that for the sarcomere chain the domains of kinetic trapping become similar in hard and soft devices. This feature is not confirmed by experiments which suggests that our model should be modified by adding some *active elements*. Those elements will be able to stabilize homogeneous states with negative stiffness and will accelerate the kinetics. The ensuing active oscillations at the scale of a sarcomere will then combine with the predicted passive oscillations at the scale of a cross-bridge creating a peculiar *oscillations inside oscillations* functioning regime for the power stroke machinery.

Finally, we have shown that despite the high number of degrees of freedom in a half-sarcomere, it is possible to capture the essential features of its overall kinetic response within a *reduced model* containing only one degree of freedom. Although in our system there is no obvious small parameter, allowing one to perform the standard adiabatic elimination, the fact that the cross-bridges are identical justifies the reduction. We have shown that, within the set of parameters compatible with experiments, the 'equivalent' model can reproduce successfully both the transients and the equilibrium states of the full model. Such model reduction allows one to construct effective algorithms dealing with stochastic evolution of a large number of interacting sarcomeres at the scale of a myofibril and to perform the MD type direct numerical simulations addressing the dynamic response of the whole muscle.

In response to the two main questions raised in the Introduction we can say the following:

1. *The observed difference of kinetic responses in soft and hard devices emphasizes the importance of mechanics in the interpretation of the physiological performance of skeletal muscles. The abandoning of the restricted chemo-mechanical framework has allowed us to reveal the mechanical subtleties of the power stroke response and made our extension of the Huxley–Simmons model compatible with observations. As we have shown, mechanics appear to be the only framework, where the puzzling kinetic data could be properly rationalized.*

2. *Our model establishes a solid link between the observed inhomogeneity of half-sarcomere lengths and the negative stiffness of the individual half-sarcomeres. In this way we have found a transparent explanation for both the experiments and the results of the previous large scale Monte Carlo simulations which had so far remained equally opaque. Our findings reinforce the idea that from the point of view of mechanics the power stroke element operates in an inherently unstable state.*

Regarding the issue of the ATP involvement in the short time scale performance of the power stroke, our work has generated more questions than answers. We have shown that the ATP related activity may be relevant not only for the *recharging* of the power stroke mechanism as in the usual Lymn–Taylor scheme, but also for *active stabilization* of the conformational change precisely in the ‘unstable’ spinodal region. This peculiar feature of the force generating machinery at the microscale, which has interesting analogs in modern design of high performance mechanical equipment (*e.g.* fly by wire systems), promises to become the signature of the mechanical engineering design of the future.

APPENDIX A

Computation of the partition function

This appendix gives the details of the computation of the partition function and its differents approximations. The definitions of the partition functions in hard and soft device are:

$$\mathcal{Z}_h\left(\overline{\epsilon},\beta\right)=\int_{\mathbb{R}}\dots\int_{\mathbb{R}}\exp\left[-\beta V\left(\epsilon_1,\dots,\epsilon_N,\epsilon_y,\overline{\epsilon}\right)\right]d\epsilon_1\dots d\epsilon_N d\epsilon_y, \tag{4.1.3}$$

$$\mathcal{Z}_s\left(\overline{\sigma},\beta\right)=\int_{\mathbb{R}}\dots\int_{\mathbb{R}}\exp\left[-\beta W\left(\epsilon_1,\dots,\epsilon_N,\epsilon_y,\epsilon,\overline{\sigma}\right)\right]d\epsilon_1\dots d\epsilon_N d\epsilon_y d\epsilon. \tag{4.1.4}$$

where V and W are respectively the energy and the Gibbs energy of the system given by Eqs. (2.5.22) and (3.1.1).

A.1 Exact computations

A.1.1 Z_1 and Z_0

In Eqs.(4.1.3) and (4.1.4), we integrate with respect to ϵ_i and obtain:

$$\mathcal{Z}_h\left(\overline{\epsilon},\beta\right)=\int_{\mathbb{R}}e^{-\beta\frac{1}{2}N\lambda_f\left(\overline{\epsilon}-\epsilon_y\right)^2}\left(\mathcal{Z}_1\left(\epsilon_y,\beta\right)+\mathcal{Z}_0\left(\epsilon_y,\beta\right)\right)^N d\epsilon_y, \tag{4.2.1}$$

$$\mathcal{Z}_s\left(\overline{\sigma},\beta\right)=\iint\exp\left[-\beta\left(N\lambda_f\left(\epsilon-\epsilon_y\right)^2-\overline{\sigma}\epsilon\right)\right]\left(\mathcal{Z}_1\left(\epsilon_y,\beta\right)+\mathcal{Z}_0\left(\epsilon_y,\beta\right)\right)^N d\epsilon_y d\epsilon \tag{4.2.1}$$

with $\mathcal{Z}_1$ and $\mathcal{Z}_0$ defined by:

$$\mathcal{Z}_1\left(\epsilon_y,\beta\right)=\int\limits_{-\infty}^{+\infty}e^{-\beta V_1\left(x,\epsilon_y\right)}dx-\int\limits_{l}^{+\infty}\exp\left[-\beta V_1\left(x,\epsilon_y\right)\right]dx \tag{A.1.1}$$

$$\mathcal{Z}_0\left(\epsilon_y,\beta\right)=\int\limits_{-\infty}^{+\infty}e^{-\beta V_0\left(x,\epsilon_y\right)}dx-\int\limits_{-\infty}^{l}\exp\left[-\beta V_0\left(x,\epsilon_y\right)\right]dx. \tag{A.1.2}$$

with:

$$V_1\left(x,\epsilon_y\right)=\frac{1}{2}\kappa_1\left(x+1\right)^2+\frac{1}{2}\left(\epsilon_y-x\right)^2 \tag{4.2.5}$$

$$V_0\left(x,\epsilon_y\right)=\frac{1}{2}\kappa_0x^2+v_0+\frac{1}{2}\left(\epsilon_y-x\right)^2. \tag{4.2.6}$$

The minima of V_1 and V_0 with respect to x are:

$$\hat{V}_1(\epsilon_y) = \frac{1}{2}\lambda_1(\epsilon_y+1)^2,$$
$$\hat{V}_0(\epsilon_y) = \frac{1}{2}\lambda_0\epsilon_y^2 + v_0.$$

The integral over $\mathbb{R}$ can be computed without difficulty and we obtain:

$$\mathcal{Z}_1(\epsilon_y,\beta) = \sqrt{\tfrac{(1-\lambda_1)2\pi}{\beta}}\exp\left[-\beta\hat{V}_1(\epsilon_y)\right]\left(1-\sqrt{\tfrac{\beta}{2\pi(1-\lambda_1)}}\int_l^{+\infty}\exp\left[-\beta\Delta V_1(x,\epsilon_y)\right]dx\right), \tag{A.1.3}$$

$$\mathcal{Z}_1(\epsilon_y,\beta) = \sqrt{\tfrac{(1-\lambda_0)2\pi}{\beta}}\exp\left[-\beta\hat{V}_0(\epsilon_y)\right]\left(1-\sqrt{\tfrac{\beta}{2\pi(1-\lambda_0)}}\int_{-\infty}^{l}\exp\left[-\beta\Delta V_0(x,\epsilon_y)\right]dx\right), \tag{A.1.4}$$

with

$$\Delta V_1(x,\epsilon_y) = V_1(x,\epsilon_y) - \hat{V}_1(\epsilon_y) \tag{A.1.5}$$
$$\Delta V_0(x,\epsilon_y) = V_0(x,\epsilon_y) - \hat{V}_0(\epsilon_y) \tag{A.1.6}$$

The remaining integrals can easily be computed numerically using special functions. Therefore the exact expressions of $\mathcal{Z}_1$ and $\mathcal{Z}_0$ are:

$$\mathcal{Z}_1(\epsilon_y,\beta) = \sqrt{\tfrac{(1-\lambda_1)2\pi}{\beta}}\exp\left[-\beta\hat{V}_1(\epsilon_y)\right]\frac{1}{2}\mathrm{erfc}\left(-f_1(\epsilon_y,\beta)\right), \tag{4.2.7}$$
$$\mathcal{Z}_1(\epsilon_y,\beta) = \sqrt{\tfrac{(1-\lambda_0)2\pi}{\beta}}\exp\left[-\beta\hat{V}_0(\epsilon_y)\right]\frac{1}{2}\mathrm{erfc}\left(f_0(\epsilon_y,\beta)\right), \tag{4.2.8}$$

with

$$\mathrm{erfc}:\mathbb{R} \longrightarrow\ ]0,2[\tag{A.1.7}$$
$$x \longmapsto \frac{2}{\sqrt{\pi}}\int_x^{+\infty}\exp\left[-t^2\right]dt \tag{A.1.8}$$

and

$$f_1(\epsilon_y,\beta) = \sqrt{\frac{\beta}{2}}\left(\sqrt{\tfrac{1}{(1-\lambda_1)}}l + \sqrt{(1-\lambda_1)}\left(\tfrac{\lambda_1}{1-\lambda_1}-\epsilon_y\right)\right), \tag{A.1.9}$$
$$f_0(\epsilon_y,\beta) = \sqrt{\frac{\beta}{2}}\left(\sqrt{\tfrac{1}{(1-\lambda_0)}}l - \sqrt{(1-\lambda_0)}\epsilon_y\right). \tag{A.1.10}$$

A.1.2 Exact expression of $\mathcal{Z}_h$ and $\mathcal{Z}_s$

The expression of Z_1 and Z_0 are replaced into Eqs.(4.1.3) and (4.1.4). In (4.1.4), the integration with respect to ϵ is straightforward and we obtain:

$$\mathcal{Z}_h(\overline{\epsilon},\beta) = \int_{\mathbb{R}}\exp\left[-\beta\frac{1}{2}N\lambda_f(\overline{\epsilon}-\epsilon_y)^2\right]\left(\mathcal{Z}_1(\epsilon_y,\beta)+\mathcal{Z}_0(\epsilon_y,\beta)\right)^N d\epsilon_y, \tag{A.1.11}$$

$$\mathcal{Z}_s(\overline{\sigma},\beta) = \left(\frac{2\pi}{\beta N\lambda_f}\right)^{\frac{1}{2}}\exp\left[\frac{\beta}{2}\frac{\overline{\sigma}^2}{N\lambda_f}\right]\int_{\mathbb{R}}\exp\left[\beta\overline{\sigma}\epsilon_y\right]\left(\mathcal{Z}_1(\epsilon_y,\beta)+\mathcal{Z}_0(\epsilon_y,\beta)\right)^N d\epsilon_y \tag{A.1.12}$$

which can be rewritten as

$$\mathcal{Z}_h\left(\bar{\epsilon},\beta\right) = \int_{\mathbb{R}} \exp\left(-\beta F_y\left(\bar{\epsilon},\epsilon_y,\beta\right)\right)\epsilon_y, \tag{4.2.11}$$

$$\mathcal{Z}_s\left(\overline{\sigma},\beta\right) = \sqrt{\tfrac{2\pi}{N\lambda_f\beta}}\int_{\mathbb{R}} \exp\left(-\beta G_y\left(\overline{\sigma},\epsilon_y,\beta\right)\right)d\epsilon_y \tag{4.2.12}$$

with the reduced free energy and Gibbs free energy

$$F_y\left(\bar{\epsilon},\epsilon_y,\beta\right) = \frac{1}{2}\lambda_f\left(\bar{\epsilon}-\epsilon_y\right)^2 - \frac{1}{\beta}\ln\left(\mathcal{Z}_1\left(\beta,\epsilon_y\right)+\mathcal{Z}_0\left(\beta\epsilon_y\right)\right) \tag{4.2.13}$$

$$G_y\left(\overline{\sigma},\epsilon_y,\beta\right) = -\frac{\overline{\sigma}}{N}\epsilon_y - \frac{1}{2}\frac{\overline{\sigma}^2}{N^2\lambda_f} - \frac{1}{\beta}\ln\left(\mathcal{Z}_1\left(\beta,\epsilon_y\right)+\mathcal{Z}_0\left(\beta,\epsilon_y\right)\right), \tag{4.2.14}$$

A.2 Extended wells approximation

The exact expressions give by Eqs.(4.2.11) and (4.2.12) are not explicit due to the presence of the erfc functions in $\mathcal{Z}_1$ and $\mathcal{Z}_0$ (see Eqs.4.2.7 and 4.2.8). Here we derive semi-analytic expressions by considering that the energy barrier in the double well potential v is high compared to $\kappa_b\theta$. This condition, corresponding to the limit $\beta \to \infty$, implies that the cross-bridges remain confined near the bottoms of the wells and thus one can extend the integration in Eqs.(4.2.3) and (4.2.4) from $-\infty$ to $+\infty$. We call this approximation the *extended wells approximation* (noted EWA).

A.2.1 Approximation of $\mathcal{Z}_1$ and $\mathcal{Z}_0$

In (A.1.3) and (A.1.4), the terms in the integrals are exponentially decaying with x, as soon as the minimum of V_1 and V_0 are respectively inferior and superior to l. These condidtions are satisfied if :

$$\epsilon_y < \frac{l+\lambda_1}{1-\lambda_1} \text{ for } V_1 \tag{A.2.1}$$

$$\epsilon_y > \frac{l}{1-\lambda_0} \text{ for } V_0 \tag{A.2.2}$$

One can also interpret this condition as the actual existence of 2 distinct wells in $v\left(x\right) + \frac{1}{2}\left(\epsilon_y - x\right)^2$. Then, if l is not 'too close' from the bottom of the well, or in other words, if the energy barrier is large compared to β, we can neglect the integrals in (A.1.3) and (A.1.4) leaving Z_1 and Z_0 as the result of the integration over all $\mathbb{R}$:

$$\mathcal{Z}_1\left(\epsilon_y,\beta\right) \approx \sqrt{\frac{\left(1-\lambda_1\right)2\pi}{\beta}}\exp\left(-\frac{\beta}{2}\lambda_1\left(\epsilon_y+1\right)^2\right), \tag{A.2.3}$$

$$\mathcal{Z}_0\left(\epsilon_y,\beta\right) \approx \sqrt{\frac{\left(1-\lambda_0\right)2\pi}{\beta}}\exp\left(-\frac{\beta}{2}\left(\lambda_0\epsilon_y^2+2v_0\right)\right). \tag{A.2.4}$$

A.2.2 Validity

To derive a criterion for both approximation we first rewrite, after trivial manipulations, ΔV_1 and ΔV_0 as:

$$\begin{aligned}
\beta\Delta V_1\left(x,\epsilon_y\right) &= \frac{\beta}{2}\left(\sqrt{\tfrac{1}{(1-\lambda_1)}}x+\sqrt{(1-\lambda_1)}\left(\tfrac{\lambda_1}{1-\lambda_1}-\epsilon_y\right)\right)^2 && \text{(A.2.5)}\\
&= \left(f_1\left(x,\epsilon_y\right)\right)^2 && \text{(A.2.6)}\\
\beta\Delta V_0\left(x,\epsilon_y\right) &= \frac{\beta}{2}\left(\sqrt{\tfrac{1}{(1-\lambda_0)}}x-\sqrt{(1-\lambda_0)}\epsilon_y\right)^2 && \text{(A.2.7)}\\
&= \left(f_0\left(x,\epsilon_y\right)\right)^2 && \text{(A.2.8)}
\end{aligned}$$

with, provided conditions (A.2.1) and (A.2.2),

$$f_1\left(x,\epsilon_y\right)>0 \text{ and } f_0\left(x,\epsilon_y\right)<0. \tag{A.2.9}$$

For $\mathcal{Z}_1$, we rewrite the integral of (A.1.4) as:

$$\begin{aligned}
\int_l^{+\infty}\exp\left[-\beta\Delta V_1\left(x,\epsilon_y\right)\right]dx &= \int\limits_{f_1(x,\epsilon_y)}^{+\infty}\exp\left[-s^2\right]ds\\
&\leq \frac{1}{f_1\left(x,\epsilon_y\right)}\int\limits_{f_1(x,\epsilon_y)}^{+\infty}s\exp\left[-s^2\right]ds \text{ as } f_1\left(l,\epsilon_y\right)\geq 0 && \text{(A.2.10)}\\
&\leq \frac{1}{2\sqrt{\beta\Delta V_1\left(l,\epsilon_y\right)}}\exp\left[-\beta\Delta V_1\left(l,\epsilon_y\right)\right]
\end{aligned}$$

Therefore, the approximation (A.2.3) and (A.2.4) are valid if:

$$\frac{1}{\sqrt{2\pi\left(1-\lambda_1\right)\Delta V_1\left(l,\epsilon_y\right)}}\exp\left[-\beta\Delta V_1\left(l,\epsilon_y\right)\right]<\gamma \tag{A.2.11}$$

with γ an arbitrary small parameter. Similarly the criterion for $\mathcal{Z}_0$ is:

$$\frac{1}{\sqrt{2\pi\left(1-\lambda_0\right)\Delta V_0\left(l,\epsilon_y\right)}}\exp\left[-\beta\Delta V_0\left(l,\epsilon_y\right)\right]<\gamma. \tag{A.2.12}$$

If $\epsilon_y<\frac{l+\lambda_1}{1-\lambda_1}$ (resp. $\epsilon_y<\frac{l}{1-\lambda_0}$), $v(x)+1/2\left(\epsilon_y-x\right)^2$ has only one minimum in well 1 (resp. well0). In this case, we can neglect $\mathcal{Z}_0$ (resp. $\mathcal{Z}_1$) with the same conditions (A.2.11) (resp. A.2.12). We summarized the extended well approximation in table A.1.

A.2.3 Approximation of the partition function under extended wells asumption

Criteria on the internal degree of freedom ϵ_y

We want to replace $\mathcal{Z}_1$ and $\mathcal{Z}_0$ by their approximations in (A.1.11) and (A.1.12).

– In hard device, the term $e^{-\beta\frac{1}{2}N\lambda_f(\overline{\epsilon}-\epsilon_y)^2}$, is peaked at $\epsilon_y=\overline{\epsilon}$ while $\mathcal{Z}_1$ and $\mathcal{Z}_0$ are respectively peaked at -1 and 0, so we want the approximation we just derived for $\mathcal{Z}_1$ and $\mathcal{Z}_0$ to be valid in a certain interval around $\epsilon_y=\overline{\epsilon}$ where $e^{-\beta\frac{1}{2}N\lambda_f(\overline{\epsilon}-\epsilon_y)^2}$ is non vanishing. We have

$$\exp\left(-\beta\frac{1}{2}N\lambda_f\left(\overline{\epsilon}-\epsilon_y\right)^2\right)>\alpha \tag{A.2.13}$$

$\epsilon_y < \frac{l}{1-\lambda_0}$	$\frac{l}{1-\lambda_0} \leq \epsilon_y \leq \frac{l+\lambda_1}{1-\lambda_1}$	$\epsilon_y > \frac{l+\lambda_1}{1-\lambda_1}$
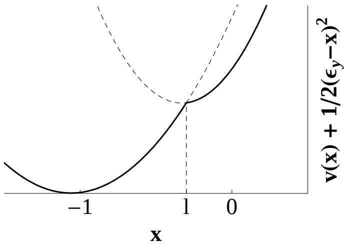	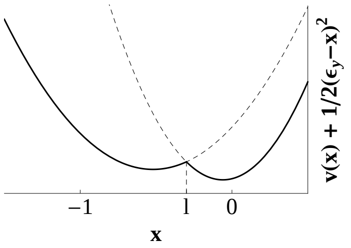	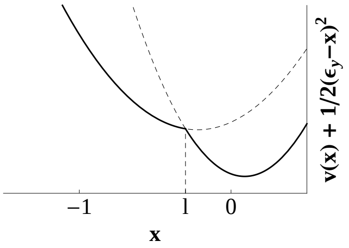
$\mathcal{Z}_0 \to 0$ if: $\frac{e^{-\beta\Delta V_1}}{\sqrt{2\pi(1-\lambda_1)\Delta V_1}} < \varepsilon$	extended wells if: $\frac{e^{-\beta\Delta V_i}}{\sqrt{2\pi(1-\lambda_i)\Delta V_i}} < \varepsilon$ with $i = 0, 1$	$\mathcal{Z}_1 \to 0$ if: $\frac{e^{-\beta\Delta V_0}}{\sqrt{2\pi(1-\lambda_0)\Delta V_0}} < \varepsilon.$

Tab. A.1 – **Extended wells approximation (EWA)**: criterion of validity depending on the value of ϵ_y. On the graphs, we show the form of the double well potential (thick lines) and its extensions (dashed lines). We distinguish 3 intervals of ϵ_y. First, if $\epsilon_y < \frac{l}{1-\lambda_0}$, the local minimum in well 0 disappears and one can neglect Z_0 provided that (A.2.12) is satisfied. Symetrically, one can neglect $\mathcal{Z}_1$ if $\epsilon_y > \frac{l+\lambda_1}{1-\lambda_1}$ and Eq. (A.2.12) is verified. For intermediate values of ϵ_y the approximation is valid provided criteria (A.2.12) and (A.2.11) are valid.

with α an arbitrarity small parameter determining non vanishing value of the exponential, for ϵ_y in:

$$\overline{\epsilon} - \sqrt{\frac{-2\ln(\alpha')}{\beta N\lambda_f}} < \epsilon_y < \overline{\epsilon} + \sqrt{\frac{-2\ln(\alpha)}{\beta N\lambda_f}} \tag{A.2.14}$$

- In soft device, $\exp(-\beta\sigma\epsilon_y) > \alpha$ if:

$$\begin{cases} \epsilon_y > \frac{\ln(\alpha)}{\beta\overline{\sigma}} & \text{if } \overline{\sigma} > 0 \\ \epsilon_y < \frac{\ln(\alpha)}{\beta\overline{\sigma}} & \text{if } \overline{\sigma} < 0. \end{cases} \tag{A.2.15}$$

As a conclusion, in hard device the criterions (A.2.11) and (A.2.12) have to be valid in the interval (A.2.14) and, in soft device, they have to be checked with (A.2.15).

Partition function as a sum over configurations

To perform the integration with respect to ϵ_y, we replace $\mathcal{Z}_1$ and $\mathcal{Z}_0$ by their approximations (A.2.3) and (A.2.4) in (A.1.11) and (A.1.12). The term $\left(\mathcal{Z}_1(\epsilon_y, \beta) + \mathcal{Z}_0(\epsilon_y, \beta)\right)^N$ is expanded using binomial coefficient and the integration can now be performed on ϵ_y. We obtain:

$$\mathcal{Z}_h(\overline{\epsilon}, \beta) \approx \left(\frac{2\pi}{\beta}\right)^{\frac{N+1}{2}} \sum_{k=0}^{N} \binom{N}{k} (q_h(k))^{\frac{1}{2}} \exp\left[-\beta\hat{V}\left(\overline{\epsilon}, \tfrac{k}{N}, 0, \tfrac{N-k}{N}\right)\right] \tag{A.2.16}$$

$$\mathcal{Z}_s(\overline{\sigma}, \beta) \approx \left(\frac{2\pi}{\beta}\right)^{\frac{N+2}{2}} \sum_{k=0}^{N} \binom{N}{k} (q_s(k))^{\frac{1}{2}} \exp\left[-\beta\hat{W}\left(\overline{\sigma}, \tfrac{k}{N}, 0, \tfrac{N-k}{N}\right)\right] \tag{A.2.17}$$

with

$$q_h(k) = \frac{(1-\lambda_1)^k (1-\lambda_0)^{N-k}}{N\lambda_f + k\lambda_1 + (N-k)\lambda_0} \tag{A.2.18}$$

$$q_s(k) = \frac{(1-\lambda_1)^k (1-\lambda_0)^{N-k}}{N\lambda_f (k\lambda_1 + (N-k)\lambda_0)}. \tag{A.2.19}$$

Hence, the partition functions Z_h and Z_s take the form of weigthed sums and in particular, the exponentials contain the energies of the system in the metastable states: $\hat{V}$ and $\hat{W}$, defined by the triplet $\left(\frac{k}{N}, 0, \frac{N-k}{N}\right)$ with $k = 0, 1, \ldots, N$ (see Eqs. 3.1.13 and 3.1.18). Hence, within extended well approximation, the partition function reduces to a sum of the contributions of all local minima.

Asymptotic branches

For large loading ($\overline{\epsilon} \to \pm\infty$ or $\overline{\sigma} \to \pm\infty$) the local minima disappear and the system ends up in the homogenous configurations $(1, 0, 0)$ or $(0, 0, 1)$. In those limits, we can obtain analytically the asymptotic expression of $\mathcal{Z}_h$ and $\mathcal{Z}_s$ by simply keeping only the terms $k = 1$ or $k = 0$ in Eq.(A.2.16) and (A.2.17). In hard device we obtain:

$$\begin{cases} \mathcal{Z}_h^-\left(\overline{\epsilon}, \beta\right) \approx \left(\frac{2\pi}{\beta}\right)^{\frac{N+1}{2}} \frac{\sqrt{1-\lambda_1}^N}{\sqrt{N\left(\lambda_1+\lambda_f\right)}} \exp\left[-\beta N \frac{1}{2} \frac{\lambda_1 \lambda_f}{\lambda_1+\lambda_f} \left(\overline{\epsilon}+1\right)^2\right] & \text{for } \overline{\epsilon} \to -\infty, \\ \mathcal{Z}_h^+\left(\overline{\epsilon}, \beta\right) \approx \left(\frac{2\pi}{\beta}\right)^{\frac{N+1}{2}} \frac{\sqrt{1-\lambda_0}^N}{\sqrt{N\left(\lambda_0+\lambda_f\right)}} \exp\left[-\beta N \left(\frac{1}{2} \frac{\lambda_0 \lambda_f}{\lambda_0+\lambda_f} \overline{\epsilon}^2 + v_0\right)\right] & \text{for } \overline{\epsilon} \to +\infty, \end{cases} \tag{A.2.20}$$

and in soft device:

$$\begin{cases} \mathcal{Z}_s^-\left(\overline{\epsilon}, \beta\right) \approx \left(\frac{2\pi}{\beta}\right)^{\frac{N+2}{2}} \frac{\sqrt{1-\lambda_1}^N}{\sqrt{\lambda_1 \lambda_f}} \frac{1}{N} \exp\left[-\beta N \left(-\frac{1}{2}\left(\frac{1}{\lambda_1}+\frac{1}{\lambda_f}\right)\left(\frac{\overline{\sigma}}{N}\right)^2 + \frac{\overline{\sigma}}{N}\right)\right] & \text{for } \overline{\epsilon} \to -\infty, \\ \mathcal{Z}_s^+\left(\overline{\epsilon}, \beta\right) \approx \left(\frac{2\pi}{\beta}\right)^{\frac{N+2}{2}} \frac{\sqrt{1-\lambda_0}^N}{\sqrt{\lambda_0 \lambda_f}} \frac{1}{N} \exp\left[-\beta N \left(-\frac{1}{2}\left(\frac{1}{\lambda_0}+\frac{1}{\lambda_f}\right)\left(\frac{\overline{\sigma}}{N}\right)^2 + v_0\right)\right] & \text{for } \overline{\epsilon} \to +\infty. \end{cases} \tag{A.2.21}$$

We recover, in the exponential, the expression of the global minimum (see Eq.(3.1.32) and (3.1.33)). Hence, in the limit of large loadings, the equilibrium probability becomes gaussian, centered at the global minimum.

Relation to Kramers approximation

The extended wells approximation we have derived here is similar to the Kramers approximation of chemical reactions where the transition rates over a potential barrier depends essentially on the size of the energy barrier at low temperature (see Sec.C.1.2). Within this scheme, one can describe the dynamics of the system by a set of ODE[1] on the population (or concentration) in each local minima (different chemical states, see Sec.C.2). For our system, a Kramers type approach is limited since a chemical state and the corresponding energy barrier, needed for Kramers definition of rate constant, exists only on a finite interval of the loading parameter (see Sec.3.1.2). Also, the extended wells is not working for intermediate values of β so we conclude that using Kramers approximation on our system is inadequate. In chemo-mechanical models (Huxley and Simmons, 1971; Piazzesi and Lombardi, 1995; Smith et al., 2008) (see Sec.2.4.4), the dynamics of the system is always described by the mean of rate constant defined following the Kramers approximation. Our model strongly departs from this approach: rate constants can only be defined on a very limited range of the applied loading.

A.3 Thermodynamic limit $N \to +\infty$

It is usually assumed in classical thermodynamics that the number of particles in the system is infinite ($N \sim 10^2 3$). In muscles, the number of cross-bridges is of the order

---

[1] ODE: Ordinary Differential Equations

of 100 (Piazzesi et al., 2007) which is finite but large enough to consider the asymptotic expressions of our system in the limit $N \to \infty$. We can study this limit combined or not with the extended wells approximation derived in the previous section.

First let's consider the case without extended well approximation. In Eqs.(4.2.11) and (4.2.12), when N is large, the probability distribution converges to a Dirac distribution at the minimum of F_y (resp. G_y). Hence, in the limit $N \to \infty$, we can apply Laplace method and obtain:

$$\lim_{N \to +\infty} \mathcal{Z}_h\left(\overline{\epsilon}, \beta\right) = \sqrt{2\pi} \frac{\exp\left[\beta F_y\left(\overline{\epsilon}, \epsilon_y^{\star,h}, \beta\right)\right]}{\sqrt{\beta \frac{\partial^2 F_y\left(\overline{\epsilon}, \epsilon_y^{\star,h}, \beta\right)}{\partial \epsilon_y^2}}} \tag{A.3.1}$$

$$\lim_{N \to +\infty} \mathcal{Z}_s\left(\overline{\epsilon}, \beta\right) = \sqrt{\frac{2\pi}{N\lambda_f \beta}} \sqrt{2\pi} \frac{\exp\left[-\beta G_y\left(\overline{\sigma}, \epsilon_y^{\star,s}, \beta\right)\right]}{\sqrt{\beta \frac{\partial^2 G_y\left(\overline{\sigma}, \epsilon_y^{\star,s}, \beta\right)}{\partial \epsilon_y^2}}} \tag{A.3.2}$$

where $\epsilon_y^{\star,h}$ and $\epsilon_y^{\star,s}$ are minima of F_y and G_y respectively. $\epsilon_y^{\star,h}$ and $\epsilon_y^{\star,s}$ have to be found numerically due to the presence of the erfc functions in the expression of $\mathcal{Z}_1$ and $\mathcal{Z}_0$.

Now, suppose the extended wells approximation is valid. We can similarly rewrite expressions (A.2.16) and (A.2.17) using Stirling equivalent for the binomial coefficient:

$$\mathcal{Z}_h(\varepsilon_t, \beta) \approx \left(\frac{\pi}{\beta}\right)^{\frac{N+1}{2}} \sqrt{\frac{1}{2\pi}\frac{1}{N}} \sum_{n_1=0}^{1} \psi_h(n_1) \exp\left[-N\varphi_h(n_1)\right] \tag{A.3.3}$$

$$\mathcal{Z}_s(\varepsilon_t, \beta) \approx \left(\frac{\pi}{\beta}\right)^{\frac{N}{2}+1} \sqrt{\frac{1}{2\pi N}\frac{1}{N}} \sum_{n_1=0}^{1} \psi_s(n_1) \exp\left[-N\varphi_s(n_1)\right] \tag{A.3.4}$$

with

$$\begin{aligned} \varphi_h(n_1, \overline{\epsilon}, \beta) = &- \frac{1}{2}\left(n_1 \ln(1-\lambda_1) + (1-n_1)\ln(1-\lambda_0)\right) \\ &+ n_1 \ln(n_1) + (1-n_1)\ln(1-n_1) \\ &+ \frac{\beta}{N} \hat{V}\left(\overline{\epsilon}, n_1, 0, 1-n_1\right), \end{aligned} \tag{A.3.5}$$

$$\begin{aligned} \varphi_s(n_1, \overline{\sigma}, \beta) = &- \frac{1}{2}\left(n_1 \ln(1-\lambda_1) + (1-n_1)\ln(1-\lambda_0)\right) \\ &+ n_1 \ln(n_1) + (1-n_1)\ln(1-n_1) \\ &+ \frac{\beta}{N} \hat{W}\left(\overline{\sigma}, n_1, 0, 1-n_1\right), \end{aligned} \tag{A.3.6}$$

and

$$\psi_h(n_1) = \left(n_1\left(1-n_1\right)\left(n_1\lambda_1 + \left(1-n_1\right)\lambda_0 + \lambda_f\right)\right)^{-\frac{1}{2}}, \tag{A.3.7}$$

$$\psi_s(n_1) = \left(n_1\left(1-n_1\right)\lambda_f\left(n_1\lambda_1 + \left(1-n_1\right)\lambda_0\right)\right)^{-\frac{1}{2}}. \tag{A.3.8}$$

The terms φ_h and φ_s contain explicitely the energies of the local minima $\hat{V}$ and $\hat{W}$ given by Eqs.(3.1.13) and (3.1.18). The other terms give information about the entropy of a given configuration and depend on the 'mixing rate' of the state (n_1) and the curvatures of the wells λ_1 and λ_0. In (A.3.3) and (A.3.4), we replace sums by integrals and obtain:

$$\mathcal{Z}_h(\varepsilon_t,\beta) \approx \left(\frac{\pi}{\beta}\right)^{\frac{N+1}{2}} \sqrt{\frac{1}{2\pi}} \int_0^1 \psi_h(n_1)\exp\left[-N\varphi_h(\overline{\epsilon},\beta,n_1)\right] dn_1,$$

$$\mathcal{Z}_s(\varepsilon_t,\beta) \approx \left(\frac{\pi}{\beta}\right)^{\frac{N+2}{2}} \sqrt{\frac{1}{2\pi N}} \int_0^1 \psi_s(n_1)\exp\left[-N\varphi_s(\overline{\sigma},\beta,n_1)\right] dn_1.$$

Finally, using Laplace method, we obtain:

$$\mathcal{Z}_h(\varepsilon_t,\beta) \approx \left(\frac{2\pi}{\beta}\right)^{\frac{N+1}{2}} \frac{\psi_h(n_1^{\star,h})\exp\left[-N\varphi_h(\overline{\epsilon},\beta,n_1^{\star,h})\right]}{\sqrt{N\left.\frac{\partial^2\varphi_h(\overline{\epsilon},\beta,n_1)}{\partial n_1^2}\right|_{n_1=n_1^{\star,h}}}} \tag{A.3.9}$$

$$\mathcal{Z}_s(\varepsilon_t,\beta) \approx \left(\frac{2\pi}{\beta}\right)^{\frac{N}{2}+1} N^{-\frac{1}{2}} \frac{\psi_s(n_1^{\star,s})\exp\left[-N\varphi_s(\overline{\epsilon},\beta,n_1^{\star,s})\right]}{\sqrt{N\left.\frac{\partial^2\varphi_s(\overline{\epsilon},\beta,n_1)}{\partial n_1^2}\right|_{n_1=n_1^{\star,s}}}} \tag{A.3.10}$$

where $n_1^{\star,h}$ and $n_1^{\star,s}$ are minima of φ_h and φ_s respectively, obtained by solving numerically the transcendental equations $\partial_{n_1}\varphi_{h,s} = 0$. For large $|\overline{\epsilon}|$ (resp. $|\overline{\sigma}|$), the minimum of φ_h (resp. φ_s) is either at $n_1 = 1$ or $n_1 = 0$ and we recover the asymptotic branches given by Eqs.(A.2.20) and (A.2.21).

A.3.1 Conclusion

In this section, we derived 4 different formulations of the partition function:

- An exact formula, that involves the use of special function to compute Z_1 and Z_0:

$$\mathcal{Z}_h\left(\overline{\epsilon},\beta\right) = \int_{\mathbb{R}} \exp\left(-\beta F_y\left(\overline{\epsilon},\epsilon_y,\beta\right)\right)\epsilon_y, \tag{4.2.11}$$

$$\mathcal{Z}_s\left(\overline{\sigma},\beta\right) = \sqrt{\tfrac{2\pi}{N\lambda_f\beta}} \int_{\mathbb{R}} \exp\left(-\beta G_y\left(\overline{\sigma},\epsilon_y,\beta\right)\right) d\epsilon_y \tag{4.2.12}$$

- Using the extended wells approximation, we could derive a first approximated formulas with finite N:

$$\mathcal{Z}_h\left(\overline{\epsilon},\beta\right) \approx \left(\frac{2\pi}{\beta}\right)^{\frac{N+1}{2}} \sum_{k=0}^{N} \binom{N}{k} \left(q_h\left(k\right)\right)^{\frac{1}{2}} \exp\left[-\beta\hat{V}\left(\overline{\epsilon},\tfrac{k}{N},0,\tfrac{N-k}{N}\right)\right] \tag{A.2.16}$$

$$\mathcal{Z}_s\left(\overline{\sigma},\beta\right) \approx \left(\frac{2\pi}{\beta}\right)^{\frac{N+2}{2}} \sum_{k=0}^{N} \binom{N}{k} \left(q_s\left(k\right)\right)^{\frac{1}{2}} \exp\left[-\beta\hat{W}\left(\overline{\sigma},\tfrac{k}{N},0,\tfrac{N-k}{N}\right)\right] \tag{A.2.17}$$

- Then if N is large, we can write, without extended wells approximation:

$$\lim_{N\to+\infty} \mathcal{Z}_h\left(\overline{\epsilon},\beta\right) = \sqrt{2\pi}\frac{\exp\left[\beta F_y\left(\overline{\epsilon},\epsilon_y^{\star,h},\beta\right)\right]}{\sqrt{\beta\frac{\partial^2 F_y\left(\overline{\epsilon},\epsilon_y^{\star,h},\beta\right)}{\partial\epsilon_y^2}}} \tag{A.3.1}$$

$$\lim_{N\to+\infty} \mathcal{Z}_s\left(\overline{\epsilon},\beta\right) = \sqrt{\tfrac{2\pi}{N\lambda_f\beta}}\sqrt{2\pi}\frac{\exp\left[-\beta G_y\left(\overline{\sigma},\epsilon_y^{\star,s},\beta\right)\right]}{\sqrt{\beta\frac{\partial^2 G_y\left(\overline{\sigma},\epsilon_y^{\star,s},\beta\right)}{\partial\epsilon_y^2}}} \tag{A.3.2}$$

where $\epsilon_y^{\star,h}$ and $\epsilon_y^{\star,s}$ are minima of F_y and G_y respectively.

– Finally, we can use both extended wells and large N approximation and use:

$$\mathcal{Z}_h(\varepsilon_t, \beta) \approx \left(\frac{2\pi}{\beta}\right)^{\frac{N+1}{2}} \frac{\psi_h(n_1^{\star,h}) \exp\left[-N\varphi_h(\overline{\epsilon}, \beta, n_1^{\star,h})\right]}{\sqrt{N \left.\frac{\partial^2 \varphi_h(\overline{\epsilon},\beta,n_1)}{\partial n_1^2}\right|_{n_1 = n_1^{\star,h}}}} \tag{A.3.9}$$

$$\mathcal{Z}_s(\varepsilon_t, \beta) \approx \left(\frac{2\pi}{\beta}\right)^{\frac{N}{2}+1} N^{-\frac{1}{2}} \frac{\psi_s(n_1^{\star,s}) \exp\left[-N\varphi_s(\overline{\epsilon}, \beta, n_1^{\star,s})\right]}{\sqrt{N \left.\frac{\partial^2 \varphi_s(\overline{\epsilon},\beta,n_1)}{\partial n_1^2}\right|_{n_1 = n_1^{\star,s}}}} \tag{A.3.10}$$

where $n_1^{\star,h}$ and $n_1^{\star,s}$ are minima of φ_h and φ_s respectively.

Those formula are still not fully explicit as the different minima have to be found numerically. In the next appendix, we apply the different approximations to the computation of isotherms.

Appendix B
Approximations of isotherms

B.1 Free energy

The free energies in hard and soft device are defined by Eqs.(4.1.5) and (4.1.6):

$$F(\overline{\epsilon},\beta) = -\frac{1}{\beta}\ln\mathcal{Z}_h\left(\overline{\epsilon},\beta\right), \tag{4.1.5}$$

$$G(\overline{\sigma},\beta) = -\frac{1}{\beta}\ln\mathcal{Z}_s\left(\overline{\sigma},\beta\right), \tag{4.1.6}$$

If we consider the limit $N \to \infty$, we derive Eqs.(A.3.1) and (A.3.2) with respect to $\overline{\epsilon}$ and $\overline{\sigma}$ and obtain:

$$F\left(\overline{\epsilon},\beta\right) \approx F_y\left(\overline{\epsilon},\epsilon_y^{\star,h},\beta\right) \tag{B.1.1}$$

$$G\left(\overline{\sigma},\beta\right) \approx G_y\left(\overline{\sigma},\epsilon_y^{\star,s},\beta\right) \tag{B.1.2}$$

Thus, in muscle, where we suppose this approximation is valid, the equilibrium free energy corresponds to the minimum of the non-equilibrium free energy landscapes F_y and G_y. Now if we use the extended wells approximation one can either compute the logarithm of Eq.(A.2.16) and Eq.(A.2.16) to obtain the free energy as a finite sum over configurations or consider also the limit $N \to \infty$. In this later case we obtain

$$\begin{aligned} F\left(\overline{\epsilon},\beta\right) \approx \hat{V}(\overline{\epsilon},n_1^{\star,h}) - \frac{1}{\beta}\Bigg(&\frac{N+1}{2}\ln\left(\frac{2\pi}{\beta}\right) - \ln\left(N(n_1^{\star,h}\lambda_1 + (1-n_1^{\star,h})\lambda_0 + \lambda_f)\right) \\ &+\frac{N}{2}\left(n_1^{\star,h}\ln\left(1-\lambda_1\right) + (1-n_1^{\star,h})\ln\left(1-\lambda_0\right)\right) \\ &-N\left(n_1^{\star,h}\ln(n_1^{\star,h}) + (1-n_1^{\star,h})\ln(1-n_1^{\star,h})\right)\Bigg) \end{aligned} \tag{B.1.3}$$

$$\begin{aligned} G\left(\overline{\sigma},\beta\right) \approx \hat{W}\left(\overline{\sigma},n_1^{\star,h}\right) - \frac{1}{\beta}\Bigg(&\frac{N+2}{2}\ln\left(\frac{2\pi}{\beta}\right) - \ln\left(N\right) - \ln(\lambda_f(n_1^{\star,h}\lambda_1 + (1-n_1^{\star,h})\lambda_0)) \\ &+\frac{N}{2}\left(n_1^{\star,h}\ln\left(1-\lambda_1\right) + (1-n_1^{\star,h})\ln\left(1-\lambda_0\right)\right) \\ &-N\left(n_1^{\star,h}\ln(n_1^{\star,h}) + (1-n_1^{\star,h})\ln(1-n_1^{\star,h})\right)\Bigg) \end{aligned} \tag{B.1.4}$$

When $\overline{\epsilon} \to \pm\infty$ (resp.$\overline{\sigma} \to \pm\infty$), we find the expression of the free energy by taking the logarithm of Eqs.(A.2.20) and (A.2.21). In hard device, we have:

$$\begin{cases} F^-(\overline{\epsilon},\beta) = N\frac{1}{2}\frac{\lambda_1\lambda_f}{\lambda_1+\lambda_f}(\overline{\epsilon}+1)^2 \\ \qquad -\frac{1}{\beta}\left(\frac{N+1}{2}\ln\left(\frac{2\pi}{\beta}\right)+\frac{N}{2}\ln(1-\lambda_1)\right. \\ \qquad \left. -\frac{1}{2}\ln\left(N(\lambda_1+\lambda_f)\right)\right) \text{ if } \overline{\epsilon} \to -\infty \\ F^+(\overline{\epsilon},\beta) = N\left(\frac{1}{2}\frac{\lambda_0\lambda_f}{\lambda_0+\lambda_f}\overline{\epsilon}^2+v_0\right) \\ \qquad -\frac{1}{\beta}\left(\frac{N+1}{2}\ln\left(\frac{2\pi}{\beta}\right)+\frac{N}{2}\ln(1-\lambda_0)\right. \\ \qquad \left. -\frac{1}{2}\ln\left(N(\lambda_0+\lambda_f)\right)\right) \text{ if } \overline{\epsilon} \to +\infty \end{cases} \tag{B.1.5}$$

and similarly in soft device:

$$\begin{cases} G^-(\overline{\sigma},\beta) = N\left(-\frac{1}{2}\left(\frac{1}{\lambda_1}+\frac{1}{\lambda_f}\right)\left(\frac{\overline{\sigma}}{N}\right)^2+\frac{\overline{\sigma}}{N}\right) \\ \qquad -\frac{1}{\beta}\left(\frac{N+2}{2}\ln\left(\frac{2\pi}{\beta}\right)+\frac{N}{2}\ln(1-\lambda_1)\right. \\ \qquad \left. -\ln(N)-\frac{1}{2}\ln(\lambda_1\lambda_f)\right) \text{ if } \overline{\sigma} \to -\infty \\ G^+(\overline{\sigma},\beta) = N\left(-\frac{1}{2}\left(\frac{1}{\lambda_0}+\frac{1}{\lambda_f}\right)\left(\frac{\overline{\sigma}}{N}\right)^2+v_0\right) \\ \qquad -\frac{1}{\beta}\left(\frac{N+2}{2}\ln\left(\frac{2\pi}{\beta}\right)+\frac{N}{2}\ln(1-\lambda_0)\right. \\ \qquad \left. -\ln(N)-\frac{1}{2}\ln(\lambda_0\lambda_f)\right) \text{ if } \overline{\sigma} \to +\infty \end{cases} \tag{B.1.6}$$

In these expressions, one recognizes the energy in the global minimum (given by Eqs.3.1.32 and 3.1.33) plus an entropic term, function of the elastic characteristics of the system. In the entropic part, the terms containing the filament elasticity λ_f are negligible compared to the other terms which are multiplied by N.

B.2 Equilibrium tensions and elongations

In the limit of large N, we apply Laplace method to Eqs.(4.2.16) and (4.2.18) to find that the mean values of ϵ_y in hard and soft devices correspond to the minima $\epsilon_y^{\star,h}$ and $\epsilon_y^{\star,s}$ of F_y and G_y that are found numerically. Thus we have, in the thermodunamic limit $N \to \infty$:

$$T_2(\overline{\epsilon},\beta) = N\lambda_f\left(\overline{\epsilon}-\epsilon_y^{\star,h}\right) \tag{B.2.1}$$

$$L_2(\overline{\sigma},\beta) = \frac{\overline{\sigma}}{N\lambda_f}+\epsilon_y^{\star,s} \tag{B.2.2}$$

If we use the extended wells approximation, we write:

$$
\begin{aligned}
T_2\left(\overline{\epsilon},\beta\right) &= -\frac{1}{\beta}\frac{\partial_{\overline{\epsilon}}\left(Z_h\left(\overline{\epsilon},\beta\right)\right)}{Z_h\left(\overline{\epsilon},\beta\right)} \quad \text{then with expression (A.2.16)} \\
&= \frac{\left(\frac{2\pi}{\beta}\right)^{\frac{N+1}{2}} \sum\limits_{k=0}^{N} \binom{N}{k} \hat{T}\left(\overline{\epsilon}, \frac{k}{N}, 0, \frac{N-k}{N}\right) \exp\left[-\beta \hat{V}\left(\overline{\epsilon}, \frac{k}{N}, 0, \frac{N-k}{N}\right)\right]}{Z_h\left(\overline{\epsilon},\beta\right)}
\end{aligned}
\tag{B.2.3}
$$

which we write as a balanced sum of the tension in each configuration $\left(\frac{k}{N}, 0, \frac{N-k}{N}\right)$:

$$
T_2\left(\overline{\epsilon},\beta\right) = \sum_{k=0}^{N} \hat{T}\left(\overline{\epsilon}, \tfrac{k}{N}, 0, \tfrac{N-k}{N}\right) \hat{p}_h\left(\overline{\epsilon}, k, \beta\right) \tag{B.2.4}
$$

where the coefficient $\hat{p}_h$ is given by:

$$
\hat{p}_h\left(\overline{\epsilon}, k, \beta\right) = \left(\frac{2\pi}{\beta}\right)^{\frac{N+1}{2}} \binom{N}{k} \frac{\left(q_h\left(k\right)\right)^{\frac{1}{2}}}{\mathcal{Z}_h\left(\overline{\epsilon},\beta\right)} \exp\left[-\beta \hat{V}\left(\overline{\epsilon}, \tfrac{k}{N}, 0, \tfrac{N-k}{N}\right)\right] \tag{B.2.5}
$$

with $q_h\left(k\right)$ defined by Eq.(A.2.18). We can also apply this computation to soft device case to find:

$$
L_2\left(\overline{\sigma},\beta\right) = \sum_{k=0}^{N} \hat{\epsilon}\left(\overline{\sigma}, \tfrac{k}{N}, 0, \tfrac{N-k}{N}\right) \hat{p}_s\left(\overline{\epsilon}, k, \beta\right) \tag{B.2.6}
$$

with:

$$
\hat{p}_s\left(\overline{\epsilon}, k, \beta\right) = \left(\frac{2\pi}{\beta}\right)^{\frac{N+2}{2}} \binom{N}{k} \frac{\left(q_s\left(k\right)\right)^{\frac{1}{2}}}{\mathcal{Z}_s\left(\overline{\sigma},\beta\right)} \exp\left[-\beta \hat{W}\left(\overline{\sigma}, \tfrac{k}{N}, 0, \tfrac{N-k}{N}\right)\right] \tag{B.2.7}
$$

and $q_s\left(k\right)$ from Eq.(A.2.19). Finally, the sum in Eq.(B.2.4) and Eq.(B.2.6) is transformed into an integral over $n_1 = \frac{k}{N}$ and this integral can be computed using Laplace method (see section A.3). If we apply this method to Eq.(B.2.4) and Eq.(B.2.6), the numerator and denominator cancel partially and the remaining terms are just:

$$
T_2\left(\overline{\epsilon},\beta\right) \approx \hat{T}(\overline{\epsilon}, n_1^{\star,h}, 0, 1-n_1^{\star,h}) \tag{B.2.8}
$$

$$
L_2\left(\overline{\sigma},\beta\right) \approx \hat{\epsilon_T}\left(\overline{\sigma}, n_1^{\star,s}, 0, 1-n_1^{\star,s}\right) \tag{B.2.9}
$$

where $n_1^{\star,h}$ and $n_1^{\star,s}$ are the minima of φ_h and φ_s. With this method, T_2 and L_2 appears to be a particular local minimum.

Figs.B.1 and B.2 show results given by the different methods in the simple case of symetric wells ($\lambda_1 = \lambda_0 = 0.5$, $l = -0.5$). (○) represents direct numerical computations using Eqs.(4.2.15) and (4.2.17). The solid line stands for the computation in the limit $N \to \infty$ without extended wells approximation. Dot-dashed line represents the case with extended wells approximation and finite N and dashed line represents the results with extended wells approximation and $N \to \infty$. The numerical integration and the computation of minima are done using Mathematica® dedicated functions.

Not surprisingly, all approximations are valid for $\beta \to \infty$, but for intermediate β, the extended wells approximation is not giving satisfactoty results (see our previous comments in Sec.A.2.3). Hence the use of extended wells approximation and by extrapolation, the Kramers approximation may lead to wrong results with this system.

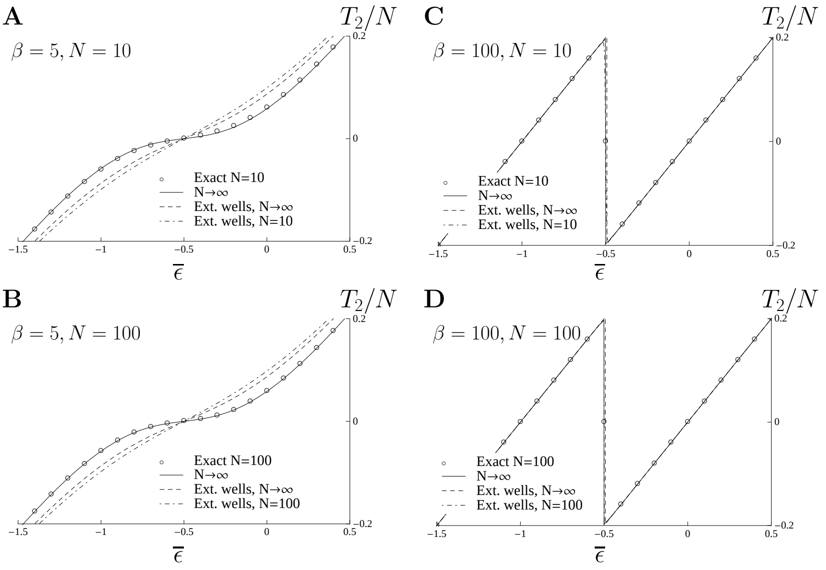

Fig. B.1 – **Thermal equilibrium tension in hard device** for $\lambda_1 = \lambda_0 = 0.5$, $l = -0.5$ and for different β and N. (**A**), $\beta = 5$, $N = 10$. (**B**), $\beta = 5$, $N = 100$. (**C**), $\beta = 100$, $N = 10$. (**A**), $\beta = 100$, $N = 100$. For each set of parameters, we computed the tension using exact direct numerical integration of Eq.(4.2.15) (○); $N \to \infty$ without extended wells approximation (EWA) (solid line); $N \to \infty$ with EWA (dashed line) and EWA with finite N (dot-dashed line).

The thermodynamic limit approximation gives satisfactory results (see solid lines) already from $N = 10$ in hard device (see Fig.B.1A). For soft device we found a good matching of the exact compuations from $N = 30$ (see Fig.B.2 A).

When $N \to \infty$ the negative slope remains in hard device. This behavior is different from classical distributed systems where it has been demonstrated in a general context that the free energy is convex and thus the stress-strain relation is monoton (Lebowitz and Lieb, 1969).

B.3 Entropy

We recall that:

$$S_h(\overline{\epsilon}, \beta) = \beta \left(\langle V \rangle_h (\overline{\epsilon}, \beta) - F(\overline{\epsilon}, \beta) \right) \tag{4.1.11}$$

$$S_s(\overline{\sigma}, \beta) = \beta \left(\langle W \rangle_s (\overline{\sigma}, \beta) - G(\overline{\sigma}, \beta) \right) \tag{4.1.12}$$

To avoid writing twice the same computations, we develop only the hard device case.

B.3.1 Computation of $\langle V \rangle_h$ without approximations

$$\langle V \rangle_h (\overline{\epsilon}, \beta) = \frac{1}{Z_h(\overline{\epsilon}, \beta)} \int V(\epsilon_1, \ldots, \epsilon_N, \epsilon_y, \overline{\epsilon}) \, e^{-\beta V(\epsilon_1, \ldots, \epsilon_N, \epsilon_y, \overline{\epsilon})} d\epsilon_1 \ldots d\epsilon_N d\epsilon_y \tag{B.3.1}$$

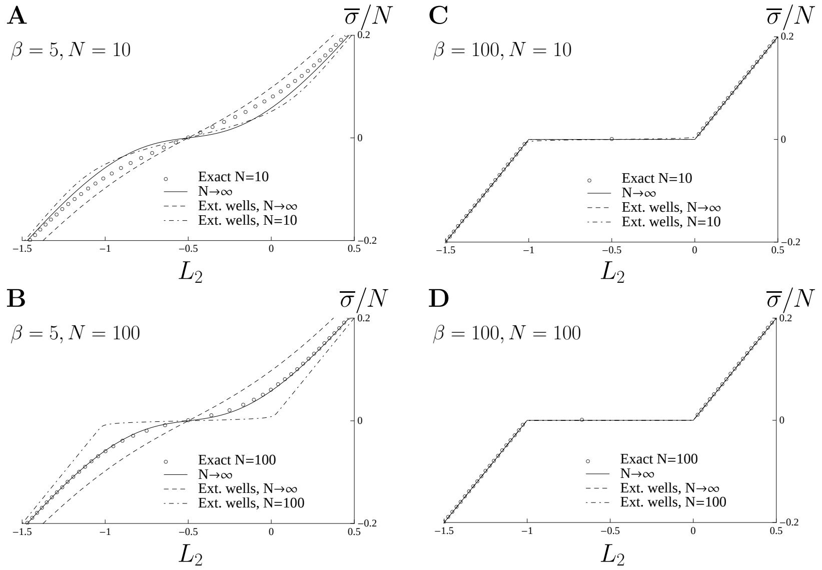

Fig. B.2 – **Thermal equilibrium elongation in soft device** for $\lambda_1 = \lambda_0 = 0.5$, $l = -0.5$ and for different β and N. (**A**), $\beta = 5$, $N = 10$. (**B**), $\beta = 5$, $N = 100$. (**C**), $\beta = 100$, $N = 10$. (**A**), $\beta = 100$, $N = 100$. For each set of parameters, we computed the tension using exact direct numerical integration of Eq.(4.2.17) (○); $N \to \infty$ without extended wells approximation (EWA) (solid line); $N \to \infty$ with EWA (dashed line) and EWA with finite N (dot-dashed line).

The integral in (B.3.1) can be split in a sum of N integrals concerning the cross-bridges part plus an integral over the filament part:

$$\langle V\rangle_h(\overline{\epsilon},\beta) = \frac{N}{Z_h(\overline{\epsilon},\beta)}\int\left(\frac{I(\epsilon_y,\beta)}{\mathcal{Z}_1(\epsilon_y,\beta)+\mathcal{Z}_0(\epsilon_y,\beta)} + \frac{1}{2}\lambda_f(\overline{\epsilon}-\epsilon_y)^2\right)\exp\left[-\beta F_y(\overline{\epsilon},\epsilon_y,\beta)\right]d\epsilon_y \quad \text{(B.3.2)}$$

with F_y defined by Eq.(4.2.13) and:

$$I(\epsilon_y,\beta) = \int_{-\infty}^{+\infty}\left(v(x)+\frac{1}{2}(\epsilon_y-x)^2\right)\exp\left[-\beta\left(v(x)+\frac{1}{2}(\epsilon_y-x)^2\right)\right]dx. \quad \text{(B.3.3)}$$

To compute I, we split the integral in two parts, I_1 and I_0 according to the shape of the double well potential v. I_1 and I_0 are troncated Gaussian integral. After some computations we obtain:

$$I_1(\epsilon_y,\beta) = \mathcal{Z}_0(\epsilon_y,\beta)\left(\tfrac{1}{2}\left(\lambda_0\epsilon_y^2+2v_0+\tfrac{1}{\beta}\right)+\frac{1}{\beta\sqrt{\pi}}\frac{f_0(\epsilon_y,\beta)\exp\left[-f_0^2(\epsilon_y,\beta)\right]}{\mathrm{erfc}\left(\mathrm{f_0}\left(\mathrm{\epsilon_y},\beta\right)\right)}\right) \quad \text{(B.3.4)}$$

$$I_1(\epsilon_y,\beta) = \mathcal{Z}_1(\epsilon_y,\beta)\left(\tfrac{1}{2}\left(\lambda_1(\epsilon_y+1)^2+\tfrac{1}{\beta}\right)-\frac{1}{\beta\sqrt{\pi}}\frac{f_1(\epsilon_y,\beta)\exp\left[-f_1^2(\epsilon_y,\beta)\right]}{\mathrm{erfc}\left(-\mathrm{f_1}\left(\mathrm{\epsilon_y},\beta\right)\right)}\right) \quad \text{(B.3.5)}$$

with f_1 and f_0 defined by Eqs.(4.2.9) and (4.2.10). Hence the mean energy is given by:

$$\langle V\rangle_h(\overline{\epsilon},\beta) = N\int_{-\infty}^{+\infty}\left(\frac{I_1(\epsilon_y,\beta)+I_0(\epsilon_y,\beta)}{\mathcal{Z}_1(\epsilon_y,\beta)+\mathcal{Z}_1(\epsilon_y,\beta)}+\frac{1}{2}\lambda_f(\overline{\epsilon}-\epsilon_y)^2\right)\frac{\exp\left[-\beta F_y(\overline{\epsilon},\epsilon_y,\beta)\right]}{\mathcal{Z}_h(\overline{\epsilon},\beta)}d\epsilon_y \quad \text{(B.3.6)}$$

With a similar approach, we find for the soft device:

$$\begin{aligned}\langle W\rangle_s\left(\overline{\sigma},\beta\right)=N\int\limits_{-\infty}^{+\infty}\Bigg(&\frac{I_1\left(\epsilon_y,\beta\right)+I_0\left(\epsilon_y,\beta\right)}{\mathcal{Z}_1\left(\epsilon_y,\beta\right)+\mathcal{Z}_1\left(\epsilon_y,\beta\right)}\\&-\frac{\overline{\sigma}}{N}\epsilon_y-\frac{\overline{\sigma}^2}{2N^2\lambda_f}+\frac{1}{2\beta N}\Bigg)\frac{\exp\left[-\beta G_y\left(\overline{\sigma},\epsilon_y,\beta\right)\right]}{\mathcal{Z}_s\left(\overline{\sigma},\beta\right)}d\epsilon_y.\end{aligned}\tag{B.3.7}$$

where the term $\frac{1}{2\beta N}$ comes from the integration with respect to ϵ and G_y is given by Eq.(4.2.14). We fially replace (B.3.6) and (B.3.7) in (4.1.11) and (4.1.12) together with expressions (4.1.5) and (4.1.6) of the Helmholtz and Gibbs free energies.

B.3.2 Approximations

The formula obtained for $\langle V\rangle_h$ and $\langle W\rangle_s$ can be simplified in the limit of large N as done before for T_2 and L_2. We obtain:

$$\langle V\rangle_h\left(\overline{\epsilon},\beta\right)\approx N\left(\frac{I_1\left(\epsilon_y^{\star,h},\beta\right)+I_0\left(\epsilon_y^{\star,h},\beta\right)}{\mathcal{Z}_1\left(\epsilon_y^{\star,h},\beta\right)+\mathcal{Z}_0\left(\epsilon_y^{\star,h},\beta\right)}+\frac{1}{2}\lambda_f\left(\overline{\epsilon}-\epsilon_y^{\star,h}\right)^2\right)\tag{B.3.8}$$

$$\langle W\rangle_s\left(\overline{\sigma},\beta\right)\approx N\left(\frac{I_1\left(\epsilon_y^{\star,s},\beta\right)+I_0\left(\epsilon_y^{\star,s},\beta\right)}{\mathcal{Z}_1\left(\epsilon_y^{\star,s},\beta\right)+\mathcal{Z}_0\left(\epsilon_y^{\star,s},\beta\right)}-\frac{\overline{\sigma}}{N}\epsilon_y^{\star,s}-\frac{\overline{\sigma}^2}{2N\lambda_f}+\frac{1}{2\beta N}\right)\tag{B.3.9}$$

On the other hand, when N is large, the free energies are given by (see Eqs.B.1.1 and B.1.2):

$$F\left(\overline{\epsilon},\beta\right)\approx N\left(\frac{1}{2}\lambda_f\left(\overline{\epsilon}-\epsilon_y^{\star,h}\right)^2-\frac{1}{\beta}\ln\left(\mathcal{Z}_1\left(\epsilon_y^{\star,h},\beta\right)+\mathcal{Z}_0\left(\epsilon_y^{\star,h},\beta\right)\right)\right),\tag{B.3.10}$$

$$G\left(\overline{\sigma},\beta\right)\approx N\left(-\frac{\overline{\sigma}}{N}\epsilon_y^{\star,s}-\frac{\overline{\sigma}^2}{2N\lambda_f}-\frac{1}{\beta}\ln\left(\mathcal{Z}_1\left(\epsilon_y^{\star,s},\beta\right)+\mathcal{Z}_0\left(\epsilon_y^{\star,s},\beta\right)\right)\right).\tag{B.3.11}$$

We then write that $S_h=\beta\left(\langle V\rangle_h-F\right)$ and $S_s=\beta\left(\langle W\rangle_s-G\right)$. The only remaining terms are those concerning the array of cross-bridges, $I_1, I_0, \mathcal{Z}_1$ and $\mathcal{Z}_0$. Hence:

$$S_h\left(\overline{\epsilon},\beta\right)\approx N\left(\beta\frac{I_1\left(\epsilon_y^{\star,h},\beta\right)+I_0\left(\epsilon_y^{\star,h},\beta\right)}{\mathcal{Z}_1\left(\epsilon_y^{\star,h},\beta\right)+\mathcal{Z}_0\left(\epsilon_y^{\star,h},\beta\right)}+\ln\left(\mathcal{Z}_1\left(\epsilon_y^{\star,h},\beta\right)+\mathcal{Z}_0\left(\epsilon_y^{\star,h},\beta\right)\right)\right)\tag{B.3.12}$$

$$S_s\left(\overline{\epsilon},\beta\right)\approx N\left(\beta\frac{I_1\left(\epsilon_y^{\star,s},\beta\right)+I_0\left(\epsilon_y^{\star,s},\beta\right)}{\mathcal{Z}_1\left(\epsilon_y^{\star,s},\beta\right)+\mathcal{Z}_0\left(\epsilon_y^{\star,s},\beta\right)}+\ln\left(\mathcal{Z}_1\left(\epsilon_y^{\star,s},\beta\right)+\mathcal{Z}_0\left(\epsilon_y^{\star,s},\beta\right)\right)\right)+\frac{1}{2}\tag{B.3.13}$$

where $n_1^{\star,h}$ and $n_1^{\star,s}$ are the minima of φ_h and φ_s respectivey (see Eqs.A.3.5 and A.3.6). The entropy does not depend on the filament stiffness λ_f. In the limit $\overline{\epsilon}\to\pm\infty$ (resp. $\overline{\sigma}\to\pm\infty$), the entropy becomes constant:

$$S_h^-\left(\overline{\epsilon},\beta\right)\approx\tfrac{N+1}{2}\left(1+\ln\left(\tfrac{2\pi}{\beta}\right)\right)-\tfrac{N}{2}\ln\left(1-\lambda_1\right)\ \text{ if }\overline{\epsilon}\to-\infty\tag{B.3.14}$$

$$S_h^+\left(\overline{\epsilon},\beta\right)\approx\tfrac{N+1}{2}\left(1+\ln\left(\tfrac{2\pi}{\beta}\right)\right)-\tfrac{N}{2}\ln\left(1-\lambda_0\right)\ \text{ if }\overline{\epsilon}\to+\infty\tag{B.3.15}$$

And similarly in soft device

$$S_s^-(\overline{\sigma},\beta) \approx \tfrac{N+2}{2}\left(1+\ln\left(\tfrac{2\pi}{\beta}\right)\right) - \tfrac{N}{2}\ln\left(1-\lambda_1\right) \text{ if } \overline{\sigma} \to -\infty \tag{B.3.16}$$

$$S_s^+(\overline{\sigma},\beta) \approx \tfrac{N+2}{2}\left(1+\ln\left(\tfrac{2\pi}{\beta}\right)\right) - \tfrac{N}{2}\ln\left(1-\lambda_0\right) \text{ if } \overline{\sigma} \to +\infty \tag{B.3.17}$$

We can also derive asymptotic formulas considering only the extended wells approximation. In this case, the above asymptotic formulas contains an additional term: $-\frac{1}{2}\ln\left(N\left(\lambda_{1,0}+\lambda_f\right)\right)$ in hard device and $-\ln\left(N\sqrt{\lambda_{1,0}\lambda_f}\right)$ in soft device. Thus, again the contribution of filament stiffness to the global entropy of the system is negligible compared to the contribution of the cross-bridges.

B.3.3 Temperature change during adiabatic loading

Let's denote β^0 a reference temperature, $S_h^0 = S_h\left(\beta^0, \overline{\epsilon}^0\right)$, the reference entropy in hard device and $S_s^0 = S_s\left(\beta^0, \overline{\sigma}^0\right)$, the reference entropy in soft device. During adiabatic loading, the entropy in conserved at the expense of a change in temperature β. To compute $\beta\left(\overline{\epsilon}\right)$ (or $\beta\left(\overline{\sigma}\right)$), one has to solve $S_h\left(\overline{\epsilon}, \beta\right) = S_h^0\left(\overline{\epsilon}^0, \beta^0\right)$ (or $\S_s\left(\overline{\sigma}, \beta\right) = S_h^0\left(\overline{\sigma}^0, \beta^0\right)$ in soft device). This operation is done numerically with extended well approximation or not. Nevertheless, we can compute the solution in the extreme cases $n_1^\star = 1$ or $n_1^\star = 0$, with extended wells approximation, corresponding to $\mathcal{Z}_0 = 0$ or $\mathcal{Z}_1 = 0$, without extended wells approximation.

When $n_1^\star = 1$, equation $S_h^0 = S\left(\beta^0, \overline{\epsilon}^0\right)$ and $S_s^0 = S\left(\beta^0, \overline{\sigma}^0\right)$ both reduce to:

$$\frac{S^0}{N} = \frac{1}{2} + \ln\left(\sqrt{\frac{2\pi\left(1-\lambda_1\right)}{\beta}}\right) \tag{B.3.18}$$

giving

$$\beta_1^\infty = 2\pi\left(1-\lambda_1\right)\exp\left[1 - 2\frac{S^0}{N}\right] \tag{B.3.19}$$

where S^0 is either S_h^0 or S_s^0 depending on the loading device, computed within the extended wells approximation.

Similarly, for $n_1^\star = 0$, we find:

$$\beta_0^\infty = 2\pi\left(1-\lambda_0\right)\exp\left[1 - 2\frac{S_0}{N}\right] \tag{B.3.20}$$

Without extended wells approximation, we find exatly the same results, given that for large loading, the extended wells is always valid. In the case of symetric wells, these extreme values of the temperature are equal: $\beta_1^\infty = \beta_0^\infty = \beta^\infty$.

B.4 Characteristic mean values

B.4.1 Fraction of population in well 1: $\langle n_1 \rangle$

We detail the hard device case. In steady state, the probability for cross-bridge 1 to be in well 1 is:

$$\langle n_1 \rangle_h\left(\overline{\epsilon}, \beta\right) = \int_{-\infty}^{l} p_1^h\left(\epsilon_1, \overline{\epsilon}, \beta\right) d\epsilon_1 \tag{B.4.1}$$

where p_1 is the marginal probability density for ϵ_1 defined by:

$$\begin{aligned} p_1^h\left(\epsilon_1, \overline{\epsilon}, \beta\right) &= \int p\left(\epsilon_1, \ldots, \epsilon_y, \overline{\epsilon}, \beta\right) d\epsilon_2, \ldots, d\epsilon_N, d\epsilon_y \\ &= \frac{1}{\mathcal{Z}_h\left(\overline{\epsilon}, \beta\right)} \int\limits_{-\infty}^{+\infty} \exp\left[-\beta\left(v\left(\epsilon_1\right) + \frac{1}{2}\left(\epsilon_y - \epsilon_1\right)^2 + N\lambda_f\left(\overline{\epsilon} - \epsilon_y\right)^2\right.\right. \\ &\qquad \left.\left. - \left(N-1\right)\log\left(\mathcal{Z}_1\left(\epsilon_y, \beta\right) + \mathcal{Z}_0\left(\epsilon_y, \beta\right)\right)\right)\right] d\epsilon_y \\ &= \frac{\int\limits_{-\infty}^{+\infty} \frac{\exp\left[-\beta\left(v(\epsilon_1) + \frac{1}{2}(\epsilon_y - \epsilon_1)^2\right)\right]}{\mathcal{Z}_1(\epsilon_y, \beta) + \mathcal{Z}_0(\epsilon_y, \beta)} \exp\left[-\beta F_y\left(\overline{\epsilon}, \epsilon_y, \beta\right)\right] d\epsilon_y}{\int\limits_{-\infty}^{+\infty} \exp\left[-\beta F_y\left(\overline{\epsilon}, \epsilon_y, \beta\right)\right] d\epsilon_y}. \end{aligned} \tag{B.4.2}$$

We see that the expression of p_1^h does not depend on the particular choice of the cross-bridge. Thus the exact expression of $\langle n_1 \rangle_h (\overline{\epsilon}, \beta)$:

$$\langle n_1 \rangle_h (\overline{\epsilon}, \beta) = \frac{\int\limits_{-\infty}^{+\infty} \frac{\mathcal{Z}_1(\epsilon_y,\beta)}{\mathcal{Z}_1(\epsilon_y,\beta)+\mathcal{Z}_0(\epsilon_y,\beta)} \exp\left[-\beta F_y\left(\overline{\epsilon}, \epsilon_y, \beta\right)\right] d\epsilon_y}{\int\limits_{-\infty}^{+\infty} \exp\left[-\beta F_y\left(\overline{\epsilon}, \epsilon_y, \beta\right)\right] d\epsilon_y}. \tag{B.4.3}$$

with F_y given by Eq.(4.2.13). A direct numerical integration is possible with the use of erfc functions. However, we apply Laplace method and it is straightforward to show that, in the limit$N \to \infty$:

$$\langle n_1 \rangle_h (\overline{\epsilon}, \beta) \overset{N \to \infty}{=} \frac{\mathcal{Z}_1(\epsilon_y^{\star,h}, \beta)}{\mathcal{Z}_1(\epsilon_y^{\star,h}, \beta) + \mathcal{Z}_0(\epsilon_y^{\star,h}, \beta)} \tag{B.4.4}$$

where, $\epsilon_y^{\star,h}$ is the minimum of F_y. Moreover, if we use the extended wells approximation, and the limit $N \to \infty$, we can rewrite:

$$p_1^h (\epsilon_1, \overline{\epsilon}, \beta) = \frac{1}{\mathcal{Z}_h (\overline{\epsilon}, \beta)} \int\limits_{-\infty}^{+\infty} \exp\left[-\beta\left(v\left(\epsilon_1\right) + \frac{1}{2}\left(\epsilon_y - \epsilon_1\right)^2 + N\lambda_f\left(\overline{\epsilon} - \epsilon_y\right)^2\right)\right]$$
$$\left(\mathcal{Z}_1\left(\epsilon_y, \beta\right) + \mathcal{Z}_0\left(\epsilon_y, \beta\right)\right)^{N-1} d\epsilon_y. \tag{B.4.5}$$

Now we integrate over $]-\infty, l]$ with respect to ϵ_1, then we apply the extended wells approximation (see Se.A.2) and develop the the term $\left(\mathcal{Z}_1 + \mathcal{Z}_0\right)^{N-1}$ using binomial coefficient:

$$\langle n_1 \rangle_h (\overline{\epsilon}, \beta) \approx \frac{\sum\limits_{k=0}^{N-1} \binom{N-1}{k} \frac{\sqrt{1-\lambda_0}^{N-(k+1)} \sqrt{1-\lambda_1}^{k+1}}{\sqrt{N\lambda_f+(k+1)\lambda_1+(N-(k+1))\lambda_0}} \exp\left[-\beta\hat{V}\left(\frac{k+1}{N}, 0, \frac{N-(k+1)}{N}\right)\right]}{\sum\limits_{k=0}^{N} \binom{N}{k} \frac{\sqrt{1-\lambda_0}^{N-k} \sqrt{-\lambda_1}^{k}}{\sqrt{N\lambda_f+k\lambda_1+(N-k)\lambda_0}} \exp\left[-\beta\hat{V}\left(\frac{k}{N}, 0, \frac{N-k}{N}\right)\right]} \tag{B.4.6}$$

and after rearanging the numerator we obtain with the extended approximation:

$$\langle n_1 \rangle_h (\overline{\epsilon}, \beta) \approx \sum_{k=0}^{N} \frac{k}{N} \hat{p}_h (\overline{\epsilon}, k, \beta) \tag{B.4.7}$$

with p_h given by Eq.(B.2.5).

Finally, after transforming the sum into integral, we apply Laplace method (the same type of computation has been done in Sec.B.2) and we find with extended wells approximation and in ther thermodynamic limit:

$$\langle n_1 \rangle_h (\overline{\epsilon}, \beta) \approx n_1^{\star,h} \tag{B.4.8}$$

$n_1^{\star,h}$ being the minimum of $\varphi_h (\overline{\epsilon}, \beta)$ defined by Eq.(A.3.5).

For soft device, the same type of computations give:

$$\langle n_1\rangle_s(\overline{\sigma},\beta) = \frac{\int\limits_{-\infty}^{+\infty} \frac{\mathcal{Z}_1(\epsilon_y,\beta)}{\mathcal{Z}_1(\epsilon_y,\beta)+\mathcal{Z}_0(\epsilon_y,\beta)} \exp\left[-\beta G_y(\overline{\sigma},\epsilon_y,\beta)\right] d\epsilon_y}{\int\limits_{-\infty}^{+\infty} \exp\left[-\beta G_y(\overline{\sigma},\epsilon_y,\beta)\right] d\epsilon_y} \quad \text{(exact)} \tag{B.4.9}$$

$$\langle n_1\rangle_s(\overline{\epsilon},\beta) \approx \sum_{k=0}^{N} \frac{k}{N}\hat{p}_s(\overline{\epsilon},k,\beta) \quad \text{(E.W.A with } p_s \text{ given by Eq.(B.2.7))} \tag{B.4.10}$$

$$\langle n_1\rangle_s(\overline{\sigma},\beta) \overset{N\to\infty}{=} \frac{\mathcal{Z}_1\left(\epsilon_y^{\star,s},\beta\right)}{\mathcal{Z}_1\left(\epsilon_y^{\star,s},\beta\right)+\mathcal{Z}_0\left(\epsilon_y^{\star,s},\beta\right)} \quad (N\to\infty) \tag{B.4.11}$$

$$\langle n_1\rangle_s(\overline{\sigma},\beta) = n_1^{\star,s} \quad (N\to\infty \text{ and E.W.A)} \tag{B.4.12}$$

where, $\epsilon_y^{\star,s}$ and $n_1^{\star,s}$ are the minima of G_y (see Eq.(4.2.14)) and φ_s (see Eq.(A.3.6)) respectively.

B.4.2 Mean position in the double well potential

The mean position in the double well potential can be used to compute the equilibrium tension (see Eq.(4.2.21)). Also this quantity is used to compute the size of the power-stroke in Sec.7.3. By definition we have in hard device:

$$\langle\epsilon_1\rangle_h(\overline{\epsilon},\beta) = \int\limits_{-\infty}^{+\infty} \epsilon_1 p_1^h(\epsilon_1,\overline{\epsilon},\beta)\, d\epsilon_1$$

where p_1^h is defined by Eq.(B.4.2). By integrating with respect to ϵ_1 we obtain:

$$\langle\epsilon_1\rangle_h(\overline{\epsilon},\beta) = \frac{1}{\mathcal{Z}_h(\overline{\epsilon},\beta)} \int\limits_{-\infty}^{+\infty} \frac{\mathcal{Z}_1(\epsilon_y,\beta)E_1(\epsilon_y,\beta)+\mathcal{Z}_0(\epsilon_y,\beta)E_0(\epsilon_y,\beta)}{\mathcal{Z}_1(\epsilon_y,\beta)+\mathcal{Z}_0(\epsilon_y,\beta)} \exp\left[-\beta F_y(\overline{\epsilon},\epsilon_y,\beta)\right] \delta\epsilon_y. \tag{B.4.13}$$

where:

$$E_1(\epsilon_y,\beta) = \frac{1}{\mathcal{Z}_1(\epsilon_y,\beta)} \int\limits_{-\infty}^{l} \epsilon_1 \exp\left[-\beta\left(\kappa_1(\epsilon_1+1)^2+(\epsilon_y-\epsilon_1)^2\right)\right] d\epsilon_1, \tag{B.4.14}$$

$$E_0(\epsilon_y,\beta) = \frac{1}{\mathcal{Z}_1(\epsilon_y,\beta)} \int\limits_{l}^{+\infty} \epsilon_1 \exp\left[-\beta\left(\kappa_0(\epsilon_1+1)^2+(\epsilon_y-\epsilon_1)^2\right)\right] d\epsilon_1. \tag{B.4.15}$$

which after some manipulations can be put rewritten as:

$$E_1(\epsilon_y,\beta) = (1-\lambda_1)\epsilon_y - \lambda_1 - \Delta_1(\epsilon_y,\beta) = \hat{\epsilon}_1(\epsilon_y) - \Delta_1(\epsilon_y,\beta) \tag{B.4.16}$$

$$E_0(\epsilon_y,\beta) = (1-\lambda_0)\epsilon_y + \Delta_0(\epsilon_y,\beta) = \hat{\epsilon}_0(\epsilon_y) + \Delta_0(\epsilon_y,\beta) \quad \text{with} \tag{B.4.17}$$

$$\Delta_1(\epsilon_y,\beta) = \sqrt{\frac{2(1-\lambda_1)}{\beta\pi}} \frac{\exp\left[-f_1^2(\epsilon_y,\beta)\right]}{\operatorname{erfc}(-f_1(\epsilon_y,\beta))}$$

$$\Delta_0(\varepsilon_t,\varepsilon_y) = \sqrt{\frac{2(1-\lambda_0)}{\beta\pi}} \frac{\exp\left[-f_0^2(\epsilon_y,\beta)\right]}{\operatorname{erfc}(f_0(\epsilon_y,\beta))}$$

Hence E_1 and E_0 appears as the position of the minimum inside each well (see Eqs.(3.1.4)), which does not depend on temperature, plus a correction term $\Delta_{1,0}$ that vanishes in the limit $\beta \to \infty$. Therefore, Eq.(B.4.13) appears as the sum of the two minima weighted by the mean population in each well: $\mathcal{Z}_1/(\mathcal{Z}_1+\mathcal{Z}_0)$ and $\mathcal{Z}_0/(\mathcal{Z}_1+\mathcal{Z}_0)$. The computation in soft device gives the same result with G_y instead of F_y in Eq.(B.4.13) and a multiplicative constant $\sqrt{\frac{2\pi}{N\lambda_f\beta}}$ that simplifies with Z_s in the denominator.

In we consider the thermodynamic limit ($N \to \infty$), Eq.(B.4.13) reduces to:

$$\langle \epsilon_1 \rangle_h (\overline{\epsilon}, \beta) \overset{N \to \infty}{=} \frac{\mathcal{Z}_1(\epsilon_y^{\star,h}, \beta) E_1(\epsilon_y^{\star,h}, \beta) + \mathcal{Z}_0(\epsilon_y^{\star,h}, \beta) E_0(\epsilon_y^{\star,h}, \beta)}{\mathcal{Z}_1(\epsilon_y^{\star,h}, \beta) + \mathcal{Z}_0(\epsilon_y^{\star,h}, \beta)} \tag{B.4.18}$$

and similarly in soft device with $\epsilon_y^{\star,s}$. $\epsilon_{y^{\star,h}}$ and $\epsilon_y^{\star,s}$ are the minima of F_y and G_y respectively. Now if we consider the extended wells approximation, the correction terms $\Delta_{1,0}$ in Eqs.(B.4.16) and (B.4.17) vanish and we are left with the following finite sum:

$$\langle \epsilon_1 \rangle_h (\overline{\epsilon}, \beta) \approx \sum_{k=0}^{N} \left(\frac{k}{N} \hat{\epsilon}_1 \left(\overline{\epsilon}, \frac{k}{N} \right) + \frac{N-k}{N} \hat{\epsilon}_0 \left(\overline{\epsilon}, \frac{k}{N} \right) \right) \hat{p}_h (\overline{\epsilon}, k, \beta) \tag{B.4.19}$$

with p_h given by Eq.(B.2.5) and $\hat{\epsilon}_{1,0}$ given by Eqs.(3.1.8) and (3.1.9). When considering also the thermodynamics limit ($N \to \infty$) we get:

$$\langle \epsilon_1 \rangle_h (\overline{\epsilon}, \beta) \approx n_1^{\star,h} \hat{\epsilon}_1(\overline{\epsilon}, n_1^{\star,h)}) + (1 - n_1^{\star,h}) \hat{\epsilon}_0(\overline{\epsilon}, n_1^{\star,h}) \tag{B.4.20}$$

with, $n_1^{\star,h}$ the minimum of φ_h (see Eq.(A.3.5)).

We find similar results in soft device:

$$\langle \epsilon_1 \rangle_s (\overline{\sigma}, \beta) = \frac{1}{\mathcal{Z}_s(\overline{\sigma}, \beta)} \int\limits_{-\infty}^{+\infty} \tfrac{\mathcal{Z}_1(\epsilon_y,\beta)E_1(\epsilon_y,\beta)+\mathcal{Z}_0(\epsilon_y,\beta)E_0(\epsilon_y,\beta)}{\mathcal{Z}_1(\epsilon_y,\beta)+\mathcal{Z}_0(\epsilon_y,\beta)} \exp\left[-\beta G_y(\overline{\sigma}, \epsilon_y, \beta)\right] d\epsilon_y. \text{ (exact)} \tag{B.4.21}$$

$$\langle \epsilon_1 \rangle_s (\overline{\sigma}, \beta) \approx \frac{\mathcal{Z}_1(\epsilon_y^{\star,s}, \beta) E_1(\epsilon_y^{\star,s}, \beta) + \mathcal{Z}_0(\epsilon_y^{\star,s}, \beta) E_0(\epsilon_y^{\star,s}, \beta)}{\mathcal{Z}_1(\epsilon_y^{\star,s}, \beta) + \mathcal{Z}_0(\epsilon_y^{\star,s}, \beta)} \ (N \to \infty) \tag{B.4.22}$$

$$\langle \epsilon_1 \rangle_s (\overline{\sigma}, \beta) \approx \sum_{k=0}^{N} \left(\tfrac{k}{N} \hat{\epsilon}_1 \left(\overline{\sigma}, \tfrac{k}{N} \right) + \tfrac{N-k}{N} \hat{\epsilon}_0 \left(\overline{\sigma}, \tfrac{k}{N} \right) \right) \hat{p}_s (\overline{\epsilon}, k, \beta) \ \text{(E.W.A with } p_s \text{ given by Eq.(B.2.7))} \tag{B.4.23}$$

$$\langle \epsilon_1 \rangle_s (\overline{\sigma}, \beta) \approx n_1^{\star,s} \hat{\epsilon}_1(\overline{\sigma}, n_1^{\star,s)}) + (1 - n_1^{\star,s}) \hat{\epsilon}_0(\overline{\sigma}, n_1^{\star,s}) \tag{B.4.24}$$

where, $\epsilon_y^{\star,s}$ and $n_1^{\star,s}$ are the minima of G_y (see Eq.(4.2.14)) and φ_s (see Eq.(A.3.6)) respectively.

APPENDIX C

First passage times

Consider a particle X undergoing a drift-diffusion motion in an energy landscape $V(X)$ inside an interval $[a,b]$. Suppose the particle is initially at $x_0 \in [a,b]$ at time t_0. We are interested in the case where the left boundary a is reflecting and the right boundary b is absorbing so that the particle can escape interval $[a,b]$ only through b. We would like to know: what is the average time before the particle reaches the boundary b of the interval $[a,b]$? The standard solution of this *escape time problem* in 1-D can be found in most textbooks on stochastic processes. Our analysis below is inspired by the books of C.W. Gardiner (Gardiner, 2004), R. Mahnke *et al.* (Mahnke et al., 2009) and Z. Schuss (Schuss, 2010).

C.1 First passage time

C.1.1 Elliptic equation for the mean passage time

In what follows, we use the notation $\mathbb{P}(X)$ for the probability of an event X. We denote $p(x,t|x_0,t_0)$, the conditional probability density of the random variable X^t for being at x at time t when starting at x_0 at time t_0. We define $\mathcal{G}(t,x_0,t_0)$, the probability of finding X^t starting from x_0 at time t_0 still in the interval $[a,b]$ at t:

$$\mathcal{G}(t,x_0,t_0) = \int_a^b p(x,t|x_0,t_0)\,dx \tag{C.1.1}$$

Let $\mathcal{T}(t_0,x_0 \to b)$ be the first passage time at $x=b$ from the position x_0 at time t_0: $\mathcal{T}(t_0,x_0 \to b) = \min\{t \geq t_0, x(t) = b\}$. From the definition of $\mathcal{G}$ (C.1.1), we see that $\mathbb{P}(\mathcal{T}(t_0,x_0 \to b) > t) = \mathcal{G}(t,x_0,t_0)$ (because a is a reflecting boundary), so the density $\mathcal{P}$ of $\mathcal{T}(t_0,x_0 \to b)$ is simply:

$$\mathcal{P}(t,x_0,t_0) = -\frac{\partial}{\partial t}\mathcal{G}(t,x_0,t_0).$$

For simplicity we will set $t_0=0$ and drop the dependence on t_0 in $\mathcal{G}$ and $\mathcal{T}$. The mean first passage time $\langle \mathcal{T}(x_0 \to b)\rangle$ [1] is the first moment of $\mathcal{T}(x_0 \to b)$:

$$\langle \mathcal{T}(x_0 \to b)\rangle = \int_0^\infty t\mathcal{P}(t,x_0)\,dt = -\int_0^\infty t\frac{\partial}{\partial t}\mathcal{G}(t,x_0)\,dt = \int_0^\infty \mathcal{G}(t,x_0)\,dt.$$

To compute $\langle \mathcal{T}(x_0 \to b)\rangle$, we first write that $p(x,t|x_0,t_0)$ is solution of the backward

---

[1] Here $\langle . \rangle$ must me understood as average over time, not over position.

Fokker–Planck Eq. where V is a generic energy landscape and β^{-1} is the diffusion coefficient:

$$\frac{\partial p\left(x,t|x_0,t_0\right)}{\partial t_0} = V'\left(x\right)\frac{\partial p\left(x,t|x_0,t_0\right)}{\partial x_0} - \beta^{-1}\frac{\partial^2 p\left(x,t|x_0,t_0\right)}{\partial x_0^2}. \tag{C.1.2}$$

Due to the reflecting boundary condition at $x_0 = a$ we must have[2]:

$$\left.\frac{\partial p\left(x,t|x_0,t_0\right)}{\partial x_0}\right|_{x_0=a} = 0$$

and due to the absorbing boundary condition at $x_0 = b$, we must require that

$$p\left(x,t|x_0 = b,t_0\right) = 0.$$

The initial condition for (C.1.2) is naturally: $p\left(x,t=t_0|x_0,t_0\right) = \delta\left(x-x_0\right)$.

As the drift term $-V'$ does not depend on time, the process is homogeneous in time which allows us to shift time derivative from t_0 to t and get:

$$\frac{\partial p\left(x,t|x_0,t_0\right)}{\partial t} = -V'\left(x\right)\frac{\partial p\left(x,t|x_0,t_0\right)}{\partial x_0} + \beta^{-1}\frac{\partial^2 p\left(x,t|x_0,t_0\right)}{\partial x_0^2}.$$

After integration over x, we obtain a partial differential equation on $\mathcal{G}$:

$$\frac{\partial}{\partial t}\mathcal{G}\left(t,x_0\right) = \left[-V'\left(x_0\right)\frac{\partial}{\partial x_0} + \beta^{-1}\frac{\partial^2}{\partial {x_0}^2}\right]\mathcal{G}\left(t,x_0\right) \tag{C.1.3}$$

with $\mathcal{G}\left(t=t_0,x_0\right) = 1$ and

$$\left.\frac{\partial}{\partial x_0}\mathcal{G}\left(t,x_0\right)\right|_{x_0=a} = 0; \quad \mathcal{G}\left(t,x_0=b\right) = 0.$$

After integration of Eq.(C.1.3) over t from 0 to $+\infty$, we obtain an elliptic equation for $\langle\mathcal{T}\rangle$:

$$\left[-V'\left(x\right)\frac{d}{dx_0} + \beta^{-1}\frac{d^2}{dx_0^2}\right]\langle\mathcal{T}\left(x_0\to b\right)\rangle = -1 \tag{C.1.4}$$

with the boundary conditions

$$\left.\frac{d}{dx_0}\langle\mathcal{T}\left(x_0\to b\right)\rangle\right|_{x_0=a} = 0; \quad \left.\langle\mathcal{T}\left(x_0\to b\right)\rangle\right|_{x_0=b} = 0. \tag{C.1.5}$$

This problem has an analytical solution. In the case of a passage to $x > \hat{x}_1$ (resp. to $x < \hat{x}_0$) considering a reflecting boundary condition at $-\infty$ (resp. $+\infty$) we find:

$$\begin{aligned}\langle\mathcal{T}\left(\hat{x}_1\to x\right)\rangle &= \beta\int_{\hat{x}_1}^{x}\exp\left[\beta V\left(s\right)\right]\left(\int_{-\infty}^{s}\exp\left[-\beta V\left(y\right)\right]dy\right)ds\\ \langle\mathcal{T}\left(\hat{x}_0\to x\right)\rangle &= \beta\int_{x}^{\hat{x}_0}\exp\left[\beta V\left(s\right)\right]\left(\int_{s}^{+\infty}\exp\left[-\beta V\left(y\right)\right]dy\right)ds.\end{aligned} \tag{C.1.6}$$

---

[2] The derivation of this boundary condition is not straightforward (see Mahnke et al. (2009) Sec. 4.2)

C.1.2 Kramers approximation

For convenience, we define V_1 and V_0 as the local expressions of V_{xb} for $\epsilon < l$ and $\epsilon \geq l$ respectively (see Eqs.4.2.5 and 4.2.6), and omit the dependence on ϵ_y to avoid excessive notations. We first split Eq.(C.1.6) as follows:

$$\begin{aligned}\left\langle \mathcal{T}\left(\hat{\epsilon}_1 \to \epsilon\right)\right\rangle = \beta \Bigg(\int_{\hat{\epsilon}_1}^{l} \exp\left[\beta V_1\left(s\right)\right] \left(\int_{-\infty}^{s} \exp\left[-\beta V\left(y\right)\right] dy \right) ds \\ + \int_{l}^{\epsilon} \exp\left[\beta V_0\left(s\right)\right] \left(\int_{-\infty}^{s} \exp\left[-\beta V\left(y\right)\right] dy \right) ds \Bigg)\end{aligned}$$

In both terms in the parenthesis, the inner integral is C^1 in s and is strictly positive. Therefore we can apply Laplace's Method on the outer integral, where both V_1 and V_0 have a single maximum at l. We obtain:

$$\begin{aligned}\left\langle \mathcal{T}\left(\hat{\epsilon}_1 \to \epsilon\right)\right\rangle &\sim \beta \left(\frac{e^{\beta V_1(l)}}{\beta a_1\left(l\right)} - \frac{\exp\left[\beta V_0\left(l\right)\right]}{\beta a_0\left(l\right)} \right) \int_{-\infty}^{l} \exp\left[-\beta V\left(y\right)\right] dy \\ a_1\left(l\right) &= \frac{1}{1-\lambda_1}\left(l+\lambda_1\right) - \epsilon_y \; ; \; a_0\left(l\right) = \frac{1}{1-\lambda_0} l - \epsilon_y\end{aligned}$$

In the remaining integral, V has only one minimum at $y = \hat{\epsilon}_1\left(\epsilon_y\right)$. By applying Laplace method for the second time and noting that $V_1\left(l\right) = V_0\left(l\right)$ we obtain in the limit $\beta \to \infty$:

$$\left\langle \mathcal{T}\left(\hat{\epsilon}_1 \to \epsilon\right)\right\rangle \sim \sqrt{\frac{2\pi\left(1-\lambda_1\right)}{\beta}} \exp\left[\beta\left(V_1\left(l\right) - V_1\left(\hat{\epsilon}_1\right)\right)\right] \left(\frac{1}{a_1\left(l\right)} - \frac{1}{a_0\left(l\right)} \right) \tag{C.1.7}$$

and similarly:

$$\left\langle \mathcal{T}\left(\hat{\epsilon}_0 \to \epsilon\right)\right\rangle \sim \sqrt{\frac{2\pi\left(1-\lambda_0\right)}{\beta}} \exp\left[\beta\left(V_0\left(l\right) - V_0\left(\hat{\epsilon}_0\right)\right)\right] \left(\frac{1}{a_1\left(l\right)} - \frac{1}{a_0\left(l\right)} \right). \tag{C.1.8}$$

C.2 Transition rates and equilibrium of population

C.2.1 Absorption rates

Consider again a generic double well potential V and an interval $[a, b]$ with an absorbing boundary at b and a reflecting boundary a a. The question we want to address now is the absorption rate at the boundary b of $[a, b]$. In other words, we deal with a steady state and ask how many trajectories escape the interval per unit of time ?

We have defined $\mathcal{G}$ (C.1.1), the probability to be still in interval $[a, b]$ at time t, having started at x_0 at time t_0 (see Eq.(C.1.1)). The absorption rate at time t for trajectories that started at x_0 at t_0 is defined by:

$$r\left(x_0, t\right) = -\frac{\dot{\mathcal{G}}\left(t, x_0\right)}{\mathcal{G}\left(t, x_0\right)}. \tag{C.2.1}$$

This expression can be read as the relative change of probability of being in the interval $[a, b]$ at time t. It can be shown that (Schuss, 2010), when $t \to \infty$, the steady state absorption rate $r\left(x_0\right)$ of trajectories starting at x_0 at time $t_0 = 0$ is equal to the inverse of the mean escape time and so not necessarily in the limit $\beta \to \infty$:

$$r\left(x_0\right) = \lim_{t \to +\infty} r\left(x_0, t\right) = \left\langle \mathcal{T}\left(x_0 \to b\right)\right\rangle^{-1}. \tag{C.2.2}$$

The proof is based on the development of $p\left(x,t|x_0,t_0\right)$ in eigenfunctions and eigenvalues of the Fokker–Planck operator. The steady state absorption rate at b is then equal to the principal eigenvalue μ_1 and the mean escape time to μ_1^{-1}. We can then compute the mean absorption rate r for the interval $[a,b]$ by using the formula:

$$r=\int_a^b r\left(x_0\right)f\left(x_0\right)dx_0=\int_a^b \left\langle \mathcal{T}\left(x_0\to b\right)\right\rangle^{-1} f\left(x_0\right)dx_0 \tag{C.2.3}$$

where $f\left(x\right)$ is the initial probability density of x at $t=t_0$ in $[a,b]$. In the cases we are interested in, the generic potential V has a single minimum at $\hat{x_0}$ in interval $[a,b]$ where a is a reflecting barrier. In the limit $\beta\to\infty$, the equilibrium density converges to $\delta\left(x-\hat{x}_0\right)$ so we have:

$$r\approx\left\langle \mathcal{T}\left(\hat{x}_0\to b\right)\right\rangle^{-1} \tag{C.2.4}$$

Appendix D

Equivalent model

D.1 Numerical scheme for the Fokker Planck equation

We present a stable and conservative numerical scheme to solve a particular Fokker-Planck equation. Precise hypothesis regarding regularity will not be discussed in this text.

Let d be the dimension of the space of configuration, Ω be the open set of $\mathbb{R}^d$ of configurations with a border $\partial\Omega$ regular enough, T be the final time.
We denote

$$b : \left| \begin{array}{rcl} \Omega \times [0,T] & \longrightarrow & \mathbb{R}^d \\ (x,t) & \longmapsto & b(x,t) \end{array} \right.$$

a sufficently regular function and $a > 0$ a strictly positive real number. The probability $p(x,t)$ to find the process in configuration $x \in \Omega$ at time $t \in [0,T]$ satisfies the following system of equations:

$$\left\{ \begin{array}{c} \partial_t p + \mathrm{div}(bp - a\nabla p) \text{ in } \Omega \times [0,T] \\ p(x,0) = p_0(x) \\ bp - a\nabla p \mid_{\partial\Omega\times[0,T]} = 0 \end{array} \right. \tag{D.1.1}$$

Where, p_0 is a given function that prescibes the initial probability distribution. The flux of probability $bp - a\nabla p$ is assumed to vanish on the boundary. By using the Green formula for the linear problem (D.1.1), one can find:

$$\int_\Omega p(x,t)dx = \int_\Omega p_0(x)dx = 1.$$

This is an important property of the probability density which we want we want to ensure in the numerical scheme.

D.2 Numerical resolution for $d = 1$

In the one dimensional case we denote $\Omega = [r,f]$ (with $r < f$). Then equation (D.1.1) takes the form:

$$\left\{ \begin{array}{c} \partial_t p + \partial_x(bp - a\partial_x p) \\ p(x,0) = p_0(x) \\ bp - a\partial_x p \mid_{(r,t)} = bp - a\partial_x p \mid_{(f,t)} = 0 \end{array} \right. \tag{D.2.1}$$

The numerical scheme will be based on the finite volume upwind method. Let us denote Z_d a linear mapping of $[r,f]$ with $N+1$ points. The spacing is then

$$dx = \frac{f-r}{N+1}$$

and we denote by Z the dual of this mapping on $[r + dx, f - dx]$. This is by itself a linear mapping of N points with the same spacing. We denote by the sequence x_j the points of both mappings

$$x_j = \frac{f - r}{N + 1}(j + \frac{1}{2}) + r.$$

Here, $j = -\frac{1}{2}, \frac{3}{2}, ..., \frac{2N-1}{2}, \frac{2N+1}{2}$ denotes the points of Z_d while $j = 1, 2, .., N-1, N$ denotes the points of Z.

By integrating (D.2.1)-(1) over a cell of Z_d we obtain:

$$\partial_t \int_{x_{j-\frac{1}{2}}}^{x_{j+\frac{1}{2}}} p(x,t)dx + F^{ex}_{j+\frac{1}{2}} - F^{ex}_{j-\frac{1}{2}} = 0$$

where $F^{ex}_{j+\frac{1}{2}}$ denotes the probability flux at $x_{j+\frac{1}{2}}$. We approximate this flux by its upwind approximation:$\forall j = 1, ..., N-1$,

$$F^{ex}_{j+\frac{1}{2}} \approx F_{j+\frac{1}{2}} = b(x_{j+\frac{1}{2}}, .)\frac{p(x_{j+1}, .) + p(x_j, .)}{2} - \left(|b(x_{j+\frac{1}{2}}, .)| + \frac{a}{dx}\right)\frac{p(x_{j+1}, .) - p(x_j, .)}{2}.$$

The two fluxes at the boundaries are set to 0 due to boundary conditions:

$$F_{-\frac{1}{2}} = F_{N+\frac{1}{2}} = 0$$

The term,

$$|b(x_{j+\frac{1}{2}}, .)|\frac{p(x_{j+1}, .) - p(x_j, .)}{2}$$

is numerical dissipation needed to stabilize the scheme. Now, to compute accurately the dissipation, we shall allways ensure that the estep dx is chosen in such a way that that:

$$dx \ll \frac{a}{Max(b(., t))}.$$

As we can see that very small noise a will requier a very small spacial step. To approximate the time derivative, we use an explicit scheme when the diffusion is not too small and an implicit scheme when the diffusion is very small.

More specifically, at each time step (we shall explain how it is chosen latter) we approximate the probability at a point x_j, $j = 1..N$ by its mean value over the cell $[x_{j-\frac{1}{2}}, x_{j+\frac{1}{2}}]$:

$$p^n_j = \frac{1}{dx}\int_{x_{j-\frac{1}{2}}}^{x_{j+\frac{1}{2}}} p(x,t)dx.$$

Then,

1. The explicit scheme gives the probability at the next step p^{n+1}_j based on the information from the previous step p^n_j as follows:

$$p^{n+1}_j = p^n_j - \frac{dt}{dx}\left(F^n_{j+\frac{1}{2}} - F^n_{j-\frac{1}{2}}\right)$$

2. The implict scheme computes the probability at the next step by solving at each time step, the following linear system:

$$p^{n+1}_j = p^n_j - \frac{dt}{dx}\left(F^{n+1}_{j+\frac{1}{2}} - F^{n+1}_{j-\frac{1}{2}}\right)$$

The stability of these linear schemes is covered by the Courant-Freidrich-Levy theorem. In the case of the explicit scheme the time step at each time should obey:

$$dt = \frac{\mathrm{CFL}dx}{\frac{2a}{dx} + Max(b(.,t))} \tag{CFL}$$

with,

$$\mathrm{CFL} < 1$$

We have seen that if the diffusion is very small, to capture it numerically dx must be very small ($dx = \epsilon \frac{a}{Max(b(.,t))}$, with $\epsilon \ll 1$) and hence in the case of the explicit scheme,

$$dt \sim \frac{\mathrm{CFL}}{2Max(b(.,t))^2} \epsilon dx$$

which is an order of magnitude smaller than a. In practice, such simulation is too long in practice even if each step takes a very short time. The implicit scheme is unconditionaly stable and no such condition on the time step arises. We shall use it when the diffusion is very small with recpect to drift.

In summary, both schemes are consitent and stable which implies that they converge to the exact solution when

$$dx \longrightarrow 0 \text{ and } dt \longrightarrow 0$$

given the (CFL) condition is satisfied in the explicit case. The order of the error is equal to one in both time and space.

D.3 Numerical resolution for $d = 2$ (and $d = 3$)

In the case $d = 2$ the domain is rectangular and we use a flux-vector-splitting method to compute numerically the solution of the Fokker–Planck equation:
Denote by H^j_{dt} the numerical scheme that advances the solution one time step dt ahead in the one dimensional (direction j) case :

$$\left\{p_j^{n+1}\right\}_{j=1..N} = H^j_{dt}(\{p_j^n\}_{j=1..N})$$

The Trotter-Katto formula justifies the use of the following scheme in a two dimensional case:

$$\left\{p_{i,j}^{n+1}\right\}_{i,j=1..N} = H^i_{\frac{dt}{2}}(H^j_{\frac{dt}{2}}(\{p_{i,j}^n\}_{i,j=1..N}))$$

In the explicit case, the stability of the scheme is still given by the a CFL condition:

$$dt = \mathrm{CFL}\ \mathrm{Min}\left(\frac{dx}{\frac{2a_x}{dx} + Max(b_x(.,.,t))}, \frac{dy}{\frac{2a_y}{dx} + Max(b_y(.,.,t))}\right)$$

In the implicit case, the scheme is still unconditionally stable. The order one in space and time is preserved.

D.4 Equivalent Fokker-Planck equation in soft device

D.4.1 Soft device experiment with a double well potential

The computations are very similar to the case of hard device

Complete set of Langevin's equations

In soft device the tension $\overline{\sigma}(t)$ is controled by the operator. The Gibbs energy is given by:

$$W(\epsilon_1, \ldots, \epsilon_y, \epsilon, \overline{\sigma}, t) = \sum_{i=1}^{N} \left(V_A(\epsilon_i) + \frac{1}{2}(\epsilon_y - \epsilon_i)^2 \right) + \frac{1}{2} N \lambda_f (\epsilon - \epsilon_y)^2 - \overline{\sigma}(t)\, \epsilon. \tag{D.4.1}$$

And the initial set of equations is

$$\begin{cases} d\epsilon_i^t = b\left(\epsilon_i^t, \epsilon_y^t\right) dt + \sqrt{2\beta^{-1}} dB_i^t, \text{ for } 1 \leq i \leq N & \text{(D.4.2a)} \\ \epsilon_y^t = \dfrac{\overline{\sigma}(t)}{N} + \dfrac{1}{N} \displaystyle\sum_{i=1}^{N} \epsilon_i^t & \text{(D.4.2b)} \end{cases}$$

where:

$$b(\epsilon_i, \epsilon_y) = -v'(\epsilon_i) + (\epsilon_y - \epsilon_i), \text{ for } 1 \leq i \leq N, \tag{D.4.3}$$

Ito calculus on ϵ_y^t

It follows from Eq.(6.2.5) that in the soft device:

$$h_i = \frac{1}{N}, \text{ for } 1 \leq i \leq N, \tag{D.4.4}$$

and obtain the following set of Langevin equation:

$$\begin{cases} d\epsilon_i^t = b\left(\epsilon_1^t, \ldots, \epsilon_N^t, t\right) dt + \sqrt{2\beta^{-1}} dB_t^i, \text{ for } 1 \leq i \leq N & \text{(D.4.5a)} \\ d\epsilon_y^t = b_y\left(\epsilon_1^t, \ldots, \epsilon_N^t, t\right) dt + \sqrt{2\beta^{-1}} \dfrac{1}{N} \displaystyle\sum_{i=1}^{N} dB_i^t & \text{(D.4.5b)} \end{cases}$$

with,

$$b_y(\epsilon_1, \ldots, \epsilon_N, t) = \frac{1}{N} \left(\overline{\sigma}'(t) + N\epsilon_y - \sum_{i=1}^{N} \left(v'(\epsilon_i) + \epsilon_i \right) \right) \tag{D.4.6}$$

here also we can replace the sum $\sum \epsilon_i$ using the equilibrium relation (D.4.2b) and obtain:

$$b_y(\epsilon_1, \ldots, \epsilon_N, t) = \frac{1}{N} \left(\overline{\sigma}'(t) + \overline{\sigma}(t) \right) - \frac{1}{N} \sum_{i=1}^{N} v'(\epsilon_i) \tag{D.4.7}$$

Equivalent set of Fokker-Planck equations

After integration, the drift of the one dimensional Fokker-Planck equation driving ϵ_y is given by:

$$\overline{b}_y(\epsilon_y, t) = \frac{1}{N} \left(\overline{\sigma}'(t) + \overline{\sigma}(t) \right) - \langle v'(x) \rangle_y \tag{6.4.10}$$

and the Fokker-Planck equation is:

$$\partial_t \overline{p}_y(\epsilon_y, t) = \partial_y \left(-\overline{b}_y(\epsilon_y, t)\, \overline{p}_y(\epsilon_y, t) \right) + \beta^{-1} \frac{1}{N} \partial_{yy} \overline{p}_y(\epsilon_y, t). \tag{6.4.10}$$

D.5 Weak coupling approximation: the stationary distribution

When $t \to \infty$, the probability density converges to the following Boltzmann distribution:

$$\overline{p}^{\infty}\left(\epsilon_1, g, \beta\right) = \frac{1}{\overline{\mathcal{Z}}\left(g, \overline{m}, \beta\right)} \exp\left[-\beta\left(v\left(\epsilon_1\right) - g\epsilon_1 - \overline{m}^{\infty}\epsilon_1 + \tfrac{1}{2}q\epsilon_1^2\right)\right] \tag{6.6.11}$$

Now the mean value of ϵ_1 is obtain from:

$$\left\langle\epsilon_1\right\rangle\left(g, \overline{m}\right) = m_1\left(\gamma, \overline{m}\right) + m_0\left(g, \overline{m}\right) \tag{D.5.1}$$

$$\text{with } m_1\left(\gamma, \overline{m}\right) = \int_{-\infty}^{l} x\overline{p}^{\infty}\left(x, g, \beta\right)dx \text{ and } m_0\left(\gamma, \overline{m}\right) = \int_{l}^{+\infty} x\overline{p}^{\infty}\left(x, g, \beta\right) \tag{D.5.2}$$

The computation of m_1 and m_0 is done in a similar way by a change of variable in the gaussian integral. We obtain:

$$m_1 = \overline{\mathcal{Z}}_1\left(g, \overline{m}, \beta\right)\left(\frac{g + \overline{m} - \frac{\lambda_1}{1-\lambda_1}}{q + \frac{\lambda_1}{1-\lambda_1}} - \sqrt{\frac{2}{\beta\pi\left(q + \frac{\lambda_1}{1-\lambda_1}\right)}}\frac{\exp\left[-h_1\left(g, \overline{m}\right)^2\right]}{\operatorname{erfc}\left(-h_1\left(g, \overline{m}\right)\right)}\right) \tag{D.5.3}$$

$$m_0 = \overline{\mathcal{Z}}_0\left(g, \overline{m}, \beta\right)\left(\frac{g + \overline{m}}{q + \frac{\lambda_0}{1-\lambda_0}} - \sqrt{\frac{2}{\beta\pi\left(q + \frac{\lambda_0}{1-\lambda_0}\right)}}\frac{\exp\left[-h_0\left(g, \overline{m}\right)^2\right]}{\operatorname{erfc}\left(h_0\left(g, \overline{m}\right)\right)}\right) \tag{D.5.4}$$

with

$$\overline{\mathcal{Z}}_1\left(g, \overline{m}, \beta\right) = \sqrt{\frac{2\pi}{\beta\left(q + \frac{\lambda_1}{1-\lambda_1}\right)}}\frac{1}{2}\operatorname{erfc}\left(-h_1\left(\gamma, \overline{m}\right)\right)e^{-\frac{\beta}{2}\left(\frac{\lambda_1}{1-\lambda_1} - \frac{\left(g+\overline{m}-\frac{\lambda_1}{1-\lambda_1}\right)^2}{q+\frac{\lambda_1}{1-\lambda_1}}\right)},$$

$$\overline{\mathcal{Z}}_0\left(g, \overline{m}, \beta\right) = \sqrt{\frac{2\pi}{\beta\left(q + \frac{\lambda_0}{1-\lambda_0}\right)}}\frac{1}{2}\operatorname{erfc}\left(h_0\left(\gamma, \overline{m}\right)\right)e^{-\frac{\beta}{2}\left(2v_0 - \frac{\left(g+\overline{m}\right)^2}{q+\frac{\lambda_0}{1-\lambda_0}}\right)},$$

$$h_1\left(g, \overline{m}\right) = \sqrt{\frac{\beta}{2}}\left(\sqrt{q + \frac{\lambda_1}{1-\lambda_1}}l - \frac{g + \overline{m} - \frac{\lambda_1}{1-\lambda_1}}{\sqrt{q + \frac{\lambda_1}{1-\lambda_1}}}\right),$$

$$h_0\left(g, \overline{m}\right) = \sqrt{\frac{\beta}{2}}\left(\sqrt{q + \frac{\lambda_0}{1-\lambda_0}}l - \frac{g + \overline{m}}{\sqrt{q + \frac{\lambda_0}{1-\lambda_0}}}\right).$$

The partition function $\overline{Z}$ in Eq.(6.6.11) is simply given by:

$$\overline{\mathcal{Z}}\left(g, \overline{m}, \beta\right) = \overline{\mathcal{Z}}_1\left(g, \overline{m}, \beta\right) + \overline{\mathcal{Z}}_0\left(g, \overline{m}, \beta\right). \tag{D.5.5}$$

Bibliography

Alberts, B., Johnson, A., Lewis, J., Raff, M., Roberts, K., and Walter, P. (2008). *Molecular biology of the cell.* Garland Science.

Allaire, G. (2007). *Analyse numérique et optimisation.* Les éditions de l'Ecole Polytechnique.

Ashkin, A. (1970). Acceleration anf trapping of particles by radiation pressure. *Phys. Rev. Lett*, 24(4):156–&.

Ashkin, A., Dziedzic, J., Bjorkholm, J., and Chu, S. (1986). Observation of a single-beam gradient force optical trap for dielectric particles. *Optical Letters*, 11(5):288–290.

Barclay, C. J., Woledge, R. C., and Curtin, N. A. (2010). Inferring crossbridge properties from skeletal muscle energetics. *Prog. Biopphys. Mol. Bio*, 102:53–71.

Bestel, J., Cément, F., and Sorine, M. (2001). A biomechanical model of muscle contraction. In Niessen, W. and Viergever, M., editors, *Medical Image Computing and Computer-Assisted Intervention – MICCAI 2001*, volume 2208 of *Lecture Notes in Computer Science*, pages 1159–1161. Springer Berlin / Heidelberg.

Bigland, B. and Lippold, O. (1954). The relation between force, velocity and integrated activity in human muscle. *Journal of Physiology-London*, 123(1):214–224.

Brandt, P., Cox, R., and Kawai, M. (1980). Can the binding of Ca^{2+} to 2 regulatory sites on troponin-c determine the steep pca -tension relationship of skeletal muscle ? *Proc. Natl. Acad. Sci. USA*, 77:4717–4720.

Brunello, E., Reconditi, M., Elangovan, R., Linari, M., Sun, Y., Narayanan, T., Panine, P., Piazzesi, G., Irving, M., and Lombardi, V. (2007). Skeletal muscle resists stretch by rapid binding of the second motor domain of myosin to actin. *Proc. Natl. Acad. Sci. USA*, 104(50):20114–20119.

Carbo, R. M., Smith, R. W. M., and Poese, M. E. (2010). Stability of the parametrically excited damped inverted pendulum: Theory and experiment. *J. ACM*, 128:1623–1631.

Cazorla, O., Freiburg, A., Helmes, M., Centner, T., McNabb, M., Wu, Y., Trombitas, K., Labeit, S., and Granzier, H. (2000). Differential expression of cardiac titin isoforms and modulation of cellular stiffness. *Circ. Res.*, 86(1):59–67.

Chapelle, D., Clément, F., Génot, F., Le Tallec, P., Sorine, M., and Urquiza, J. M. (2001). A physiologically-based model for the active cardiac muscle contraction. In Katila, T., Nenonen, J., Magnin, I., Clarysse, P., and Montagnat, J., editors, *Functional Imaging and Modeling of the Heart*, volume 2230 of *Lecture Notes in Computer Science*, pages 128–133. Springer Berlin / Heidelberg.

Chapelle, D., Le Tallec, P., Moireau, P., and Sorine, M. (2011). An energy-preserving muscle tissue model: formulation and compatible discretizations. *Int. J. Mult. Comp. Eng.* in Press.

Chauwin, J., Ajdari, A., and Prost, J. (1994). Force-free motion in asymmetric structures - a mechanism without diffusive steps. *Europhys. Lett.*, 27(6):421–426.

Chen, Y.-d. and Brenner, B. (1993). On the regeneration of the actin-myosin power stroke in contracting muscle. *Proc. Natl. Acad. Sci. USA*, 90(11):5148–5152.

Cooke, R. and Franks, K. (1980). All myosin heads form bonds with actin in rigor rabbit skeletal muscle. *Biochemistry*, 19(10):2265–2269.

Cordova, N., Ermentrout, B., and Oster, G. (1992). Dynamics of single-motor molecules - the thermal ratchet model. *Proc. Natl. Acad. Sci. USA*, 89(1):339–343.

Coupland, M., Puchert, E., and Ranatunga, K. (2001). Temperature dependence of active tension in mammalian (rabbit psoas) muscle fibres: effect of inorganic phosphate. *J. Physiol - London*, 536(3):879–891. Printed.

Craig, R. and Woodhead, J. (2006). Structure and function of myosin filaments. *Curr. Opin. Struct. Biol.*, 16(2):204–212.

Day, M. V. (1983). On the exponential exit law in the small parameter exit problem. *Stochastics*, 8:297–323.

De Gennes, P.-G. (2001). Maximum pull out force on DNA hybrids. *Cr. Acad. Sci. IV-Phys.*, 2:1505–1508.

Decostre, V., Bianco, P., Lombardi, V., and Piazzesi, G. (2005). Effect of temperature on the working stroke of muscle myosin. *Proc. Natl. Acad. Sci. USA*, 102(39):13927–13932.

Dobbie, I., Linari, M., Piazzesi, G., Reconditi, M., Koubassova, N., Ferenczi, M., Lombardi, V., and Irving, M. (1998). Elastic bending and active tilting of myosin heads during muscle contraction. *Nature*, 396(6709):383–387.

Dominguez, R., Freyzon, Y., Trybus, K. M., and Cohen, C. (1998). Crystal structure of a vertebrate smooth muscle myosin motor domain and its complex with the essential light chain: Visualization of the pre-power stroke state. *Cell*, 94(5):559–571.

Duke, T. A. J. (1999). Molecular model of muscle contraction. *Proc. Natl. Acad. Sci. USA*, 96(6):2770–2775.

Edman, K. (1988). Double hyperbolic force velocity relation in frog muscle fibers. *J. Physiol - London*, 404:301–321.

Edman, K. and Curtin, N. (2001). Synchronous oscillations of length and stiffness during loaded shortening of frog muscle fibres. *J. Physiol - London*, 534(265):553–563.

Edman, K., Reggiani, C., Schiaffino, S., and Tekronnie, G. (1988). Maximum velocity of shortening related to myosin isoforms composition in frog skeletal muscle fibers. *J. Physiol - London*, 395:679–694.

Efendiev, Y. R. and Truskinovsky, L. (2010). Thermalization of a driven bi-stable FPU chain. *Continuum Mech. Therm*, 22(6-8):679–698.

Eisenberg, E. and Hill, T. L. (1978). Cross-bridge model of muscl contraction. *Prog. Biopphys. Mol. Bio*, 33(1):55–82.

Eisenberg, E., Hill, T. L., and Chen, Y. (1980). Cross-bridge model of muscle contraction - quantitative analysis. *Biophys J.*, 29(2):195–227.

Fabiato, A. and Fabiato, F. (1978). Myofilament-generated tension oscillations during partial calcium activation and activation dependence of sarcomere length-tension relation of skinned cardiac cells. *J. Gen. Physiol.*, 72(5):667–699.

Finer, J., Simmons, R., and Spudish, J. (1994). Single myosin molecule mechanics - piconewton forces and nonometer steps. *Nature*, 368:113–119.

Ford, L., Huxley, A., and Simmons, R. (1977). Tension responses to sudden length change in stimulated frog muscle fibres near slack length. *J. Physiol - London*, 269:441–515.

Ford, L., Huxley, A., and Simmons, R. (1985). Tension transients during steady shortening of frog muscle fibers. *J. Physiol - London*, 361:131–150.

Ford, L. E., Huxley, A. F., and Simmons, R. M. (1981). The relation between stiffness and filament overlap in stimulated frog-muscle fibers. *J. Physiol - London*, 311:219–249.

Fortune, N., Geeves, M., and Ranatunga, K. (1991). Tension response to rapid pressure release in glycerinated rabbit muscle fibers. *Proc. Natl. Acad. Sci. USA*, 88:7323–7327.

Fusi, L., Reconditi, M., Linari, M., Brunello, E., Elangovan, R., Lombardi, V., and Piazzesi, G. (2010). The mechanism of the resistance to stretch of isometrically contracting single muscle fibres. *J. Physiol - London*, 588(3):495–510.

Gammaitoni, L., Hanggi, P., Jung, P., and Marchesoni, F. (1998). Stochastic resonance. *Rev. Mod. Phys.*, 70(1):223–287.

Gardiner, C. (2004). *Handbook of stochastic methods for physics chemistry and the natural sciences.* Springer, 3rd edition.

Geeves, M. and Holmes, K. (2005). The molecular mechanism of muscle contraction. In *Fibrous proteins: muscle and molecular motors*, volume 71 of *Advances in Protein Chemistry*, pages 161–193.

Gorban, A. A. and Karlin, I. V. (2004). *Invariant Manifolds for Physical and Chemical Kinetics*, volume 660 of *Lect. Notes Phys.* Springer.

Graham, C. and Talay, D. (2010). *Simulation Stochastique et Méthodes de Monte-Carlo.* Editions de l'Ecole Polytechnique.

Granzier, H., mattiazzi, A., and Pollack, G. (1990). Sarcomere dynamics during isotonic velocity transients in single frog-muscle fibers. *Am. J. Physiol.*, 259(2, Part 1):C266–C278.

Grill, S., Kruse, K., and Julicher, F. (2005). Theory of mitotic spindle oscillations. *Phys. Rev. Lett*, 94(10).

Grossmann, F., Dittrich, T., Jung, P., and Hanggi, P. (1993). Coherent transport in periodically driven bistable system. *J. Stat. Phys.*, 70(1-2):229–245.

Guerin, T., Prost, J., and Joanny, J. F. (2010a). Dynamic instabilities in assemblies of molecular motors with finite stiffness. *Phys. Rev. Lett*, 104(24).

Guerin, T., Prost, J., Martin, P., and Joanny, J.-F. (2010b). Coordination and collective properties of molecular motors: theory. *Curr. Opin. Cell Biol.*, 22(1):14–20.

Günther, S. and Kruse, K. (2007). Spontaneous waves in muscle fibres. *New J. Phys.*, 9.

Hanggi, P., Talkner, P., and Borkovec, M. (1990). Reaction-rate theory - 50 years after kramers. *Reviews of Modern Physics*, 62(2):251–341.

Hanson, J. and Huxley, H. (1953). Structural basis of the cross-striations in muscle. *Nature*, 172:530–532.

Hill, A. V. (1938). The heat of shortening and the dynamic constants of muscle. *P Roy. Soc. Lond. B Bio.*, 126(843):136–195.

Hill, T. (1964). *Thermodynamics of small systems.* Dover Publications, Inc.

Hill, T. L. and Chen, Y.-d. (1974). Further analysis of simple prototypal muscle model near and far from equilibrium. *Proc. Natl. Acad. Sci. USA*, 71(3):2478–2481.

Holmes, K. and Geeves, M. (2000). The structural basis of muscle contraction. *Philos. T. Roy. Soc. B*, 355(1396):419–431.

Howard, J. (1997). Molecular motors: structural adaptations to cellular functions. *Nature*, 389(9):561–567.

Howard, J. (2001). *Mechanics of motor proteins and the cytoskeleton*. Sinauer.

Huxley, A. (1998). How molecular motors work in muscle. *Nature*, 391:239.

Huxley, A., Lombardi, V., and Peachey, L. (1981). A system for a fast recording of longitudinal displacement of a striated-muscle fiber. *Journal of Physiology-London*, 317:12–13.

Huxley, A. and Niedergerke, R. (1954). Structural changes in muscle during contraction - interference microscopy of living muscle fibres. *Nature*, 173:971–973.

Huxley, A. F. (1957). Muscle structure and theories of contraction. *Prog. Biophys. Mol. Bio.*, 7:258–318.

Huxley, A. F. and Simmons, R. M. (1971). Proposed mechanism of force generation in striated muscle. *Nature*, 233:533–538.

Huxley, A. F. and Tideswell, S. (1996). Filament compliance and tension transients in muscle. *J. Muscle Re. Cell M.*, 17:507–511.

Huxley, H. (1953). Electron microscope studies of the organisation of the filaments in striated muscle. *Biochim. Biophys. Acta*, 12:387–400.

Huxley, H. E. (1969). Mechanism of muscular contraction. *Science*, 164:1356–&.

Huxley, H. E., Stewart, A., Sosa, H., and Irving, T. (1994). X-ray diffraction measurements of the extensibility of actin and myosin filaments in contracting muscle. *Biophys J.*, 67:2411–2421.

Irving, M., Piazzesi, G., Lucii, L., Sun, Y., Harford, J., Dobbie, I., Ferenczi, M., Reconditi, M., and Lombardi, V. (2000). Conformation of the myosin motor during force generation in skeletal muscle. *Nature structural biology*, 7(6):482–485. Demande a la bibliotheque.

Ishijima, A., Kojima, H., Higuchi, H., Harada, Y., Funatsu, T., and Yanagida, T. (1996). Multiple- and single-molecule analysis of the actomyosin motor by nanometer piconewton manipulation with a microneedle: Unitary steps and forces. *Biophys J.*, 70(1):383–400.

Ishiwata, S., Shimamoto, Y., and Fukuda, N. (2011). Contractile system of muscle as an auto-oscillator. *Prog. Biopphys. Mol. Bio*, 105(3, SI):187–198.

Jarzynski, C. (1997). Nonequilibrium equality for free energy differences. *Phys. Rev. Lett*, 78(14):2690–2693.

Jung, P. (1993). Periodically driven stochastic-systems. *Phys. Rep.*, 234(4-5):175–295.

Jülicher, F., Ajdari, A., and Prost, J. (1997). Modeling molecular motors. *Reviews of Modern Physics*, 69(4):1269–1281.

Jülicher, F. and Prost, J. (1997). Spontaneous oscillations of collective molecular motors. *Phys. Rev. Lett*, 78(23):4510–4513.

Katz, B. (1939). The relation between force and speed in muscular contraction. *Journal of Physiology*, 96:45–64.

Kawai, M. and Halvorson, H. (1991). 2 step mechanism of phosphate release and the mechanism of force generation in chemically skinned fibers of rabbit psoas muscle. *Biophys. J.*, 59(2):329–342.

Kaya, M. and Higuchi, H. (2010). Nonlinear elasticity and an 8-nm working stroke of single myosin molecules in myofilaments. *Science*, 329:686–689.

Kitamura, K., Tokunaga, M., Iwane, A., and Yanagida, T. (1999). A single myosin head moves along an actin filament with regular steps of 5.3 nanometres. *Nature*, 397:129–134.

Kloeden, P. E. and Platen, E. (1999). *Numerical Solution of Stochastic Differential Equations*. Springer.

Knight, A., Veigel, C., Chambers, C., and Molloy, J. (2001). Analysis of single-molecule mechanical recordings: application to acto-myosin interactions. *Prog. Biophys. Mol. Bio.*, 77(1):45–72.

Knight, K. (2001). Structural phase transition, oxygen vacancy ordering and protonation in doped baceo$_3$:results from time of flight neutron powder diffraction investigation. *Solid State Ionics*, 145:275–294.

Kojima, H., Ishuima, A., and Yanagida, T. (1994). Direct measurement of stiffness of single actin filaments with and without tropomyosin by in vitro nanomanipulation. *Proc. Natl. Acad. Sci. USA*, 91(12):12962–12966.

Kramers, H. (1940). Brownian motion in a field of force and the diffusion model of chemical reactions. *Physica*, 7:284–304.

Kruse, K. and Jülicher, F. (2005). Oscillations in cell biology. *Curr. Opin. Cell Biol.*, 17(1):20–26.

Kurtz, T. (1971). Limit theorems for sequences of jump markov processes approximating ordinary differential processes. *J. Appl. Probab.*, 8(2):344–356.

Kurtz, T. (1972). Relationship between stochastic and deterministic models for chemical reactions. *J. Chem. Phys.*, 57(7):2976–1278.

Kurtz, T. G. (1970). Solutions of ordinary differential equations as limits of pure jump markov processes. *J. Appl. Probab.*, 7(1):49.

Lebowitz, J. L. and Lieb, E. H. (1969). Existence of thermodynamics for real matter with Coulomb forces. *Phys. Rev. Lett*, 22(13):631–&.

Lelièvre, T., Rousset, M., and Stoltz, G. (2010). *Free Energy Computations, A mathematical perspective*. Imperial College Press.

Leonard, T. R., Joumaa, V., and Herzog, W. (2010). An activatable molecular spring reduces muscle tearing during extreme stretching. *J. Biomech.*, 43(15):3063–3066.

Lewalle, A. (2008). Single-molecule measurement of the stiffness of the rigor myosin head. *Biophys J.*, 94:2160–2169.

Linari, M., Bottinelli, R., Pellegrino, M., Reconditi, M., Reggiani, C., and Lombardi, V. (2004). The mechanism of the force response to stretch in human skinned muscle fibres with different myosin isoforms (vol, 554, pg 335, 2004). *J. Physiol - London*, 555:851. Printed.

Linari, M., Caremani, M., and Lombardi, V. (2010). A kinetic model that explains the effect of inorganic phosphate on the mechanics and energetics of isometric contraction of fast skeletal muscle. *P Roy. Soc. Lond. B Bio.*, 277(270):19–27.

Linari, M., Caremani, M., Piperio, C., Brandt, P., and Lombardi, V. (2007). Stiffness and fraction of myosin motors responsible for active force in permeabilized muscle fibers from rabbit psoas. *Biophys. J.*, 92:2476–2490. Printed.

Linari, M., Dobbie, I., Reconditi, M., Koubassova, N., Irving, M., Piazzesi, G., and Lombardi, V. (1998). The stiffness of skeletal muscle in isometric contraction and rigor: The fraction of myosin heads bound to actin. *Biophys J.*, 74(5):2459–2473.

Linari, M. and Lombardi, V. (2010). Mechanics and kinetics of skeletal muscle myosin studied in single demembranated fibres. Number 262.

Linari, M., Lombardi, V., and Piazzesi, G. (1997). Cross-bridge kinetics studied with staircase shortening in single fibres from frog skeletal muscle. *J. Muscle Re. Cell M.*, 18(1):91–101.

Linari, M., Piazzesi, G., and Lombardi, V. (2009). The effect of myofilament compliance on kinetics of force generation by myosin motors in muscle. *Biophys J.*, 96(2):583–592.

Lindstedt, S., LaStayo, P., and Reich, T. (2001). When active muscles lengthen: Properties and consequences of eccentric contractions. *News Physiol. Sci.*, 16:256–261.

Linke, W., Ivemeyer, M., Labeit, S., Hinssen, H., Ruegg, J., and Gautel, M. (1997). Actin-titin interaction in cardiac myofibrils: Probing a physiological role. *Biophys. J.*, 73(2):905–919.

Lombardi, V. and Piazzesi, G. (1990). The contractile response during steady lengthening of stimulated frog muscle fibers. *Journal of physiology-London*, 431:141–171.

Lombardi, V., Piazzesi, G., Ferenczi, M., Thirlwell, H., Dobbie, I., and Irving, M. (1995). Elastic distortion of myosin heads and repriming of the working stroke in muscle. *Nature*, 374:553–555.

Lombardi, V., Piazzesi, G., and Linari, M. (1992). Rapid regeneration of the actin myosin power stroke in contracting muscle. *Nature*, 355(6361):638–641.

Lymn, R. and Taylor, E. (1971). Mechanism of adenosine triphosphate hydrolysis by actomyosin. *Biochemistry*, 10(25):4617–&.

Magnasco, M. (1993). Forced thermal ratchets. *Phys. Rev. Lett*, 71(10):1477–1481.

Mahnke, R., Kaupužs, J., and Lubashevsky, I. (2009). *Physics of stochastic processes-How randomness acts in time*. Wiley-VCH.

Marcucci, L. and Truskinovsky, L. (2010). Mechanics of the power stroke in myosin II. *Phys. Rev. E*, 81(051915).

Martin, P., Mehta, A., and Hudspeth, A. (2000). Negative hair-bundle stiffness betrays a mechanism for mechanical amplification by the hair cell. *Proc. Natl. Acad. Sci. USA*, 97(22):12026–12031.

Martyn, D., Chase, P., Regnier, M., and Gordon, A. (2002). A simple model with myofilament compliance predicts activation-dependent crossbridge kinetics in skinned skeletal fibers. *Biophys. J.*, 83(6):3425–3434.

Meacci, G. and Kruse, K. (2005). Min-oscillations in escherichia coli induced by interactions of membrane-bound proteins. *Phys. Biol.*, 2(2):89–97.

Mehta, A., Finer, J., and Spudich, J. (1997). Detection of single-molecule interactions using correlated thermal diffusion. *Proc. Natl. Acad. Sci. USA*, 94(15):7927–7931. Colloquium on Genetics and the Origin of Species, Irvine, CA, Jan 30-Feb 01, 1997.

Mijailovich, S., Fredberg, J., and Butler, J. (1996). On the theory of muscle contraction: Filament extensibility and the development of isometric force and stiffness. *Biophys. J.*, 71:1475–1484.

Mitrossilis, D., Fouchard, J., Guiroy, A., Desprat, N., Rodriguez, N., Fabry, B., and Asnacios, A. (2009). Single-cell response to stiffness exhibits muscle-like behavior. *Proc. Natl. Acad. Sci. USA*, 106(43):18243–18248.

Molloy, J., Burns, J., Kendrickjones, J., Tregear, R., and White, D. (1995). Movement and force produced by a single myosin head. *Nature*, 378(6553):209–212.

Novak, I. and Truskinovsky, L. (2002). *Mechanics of muscle fibers.* PhD thesis, University of Minnesota.

Offer, G. and Ranatunga, K. W. (2010). Crossbridge and filament compliance in muscle: implications for tension generation and lever arm swing. *J. Muscle Re. Cell M.*, 31(4):245–265.

Piazzesi, G., Francini, F., Linari, M., and Lombardi, V. (1992). Tension transients during steady lengthening of tetanized muscle-fibers of the frog. *J. Physiol - London*, 445:659–711.

Piazzesi, G., Linari, M., Reconditi, M., Vanzi, F., and Lombardi, V. (1997). Cross-bridge detachment and attachment following a step stretch imposed on active single frog muscle fibres. *J. Physiol - London*, 498(1):3–15.

Piazzesi, G. and Lombardi, V. (1995). A cross-bridge model that is able to explain mechanical and energetic properties of shortening muscle. *Biophys J.*, 68(5):1966–1979.

Piazzesi, G., Lucii, L., and Lombardi, V. (2002a). The size and the speed of the working stroke of muscle myosin and its dependence on the force. *J. Physiol - London*, 545:145–151.

Piazzesi, G., Reconditi, M., Linari, M., Lucii, L., Bianco, P., Brunello, E., Decostre, V., Stewart, A., Gore, D. B., Irving, T. C., Irving, M., and Lombardi, V. (2007). Skeletal muscle performance determined by modulation of number of myosin motors rather than motor force or stroke size. *Cell*, 131(4):784–795.

Piazzesi, G., Reconditi, M., Linari, M., Lucii, L., Sun, Y., Narayanan, T., Boesecke, P., Lombardi, V., and Irving, M. (2002b). Mechanism of force generation by myosin heads in skeletal muscle. *Nature*, 415(19):659–662.

Placais, P., Balland, M., Guerin, T., Joanny, J., and Martin, P. (2009). Spontaneous oscillations of a minimal actomyosin system under elastic loading. *Phys. Rev. Lett*, 103(15).

Prost, J., Chauwin, J., Peliti, L., and Ajdari, A. (1994). Asymmetric pumping of particles. *Phys. Rev. Lett*, 72(16):2652–2655.

Puglisi, G. and Truskinovsky, L. (2000). Mechanics of a discrete chain with bi-stable elements. *Journal of the mechanics and physics of solids*, 48:1–27.

Ranatunga, K. W., Moira, E., Coupland, M. E., and Mutungi, G. (2002). An asymetry in the phosphate dependence of tension transients induced by length perturbation in mammalian (rabbit psoas) muscle fibres. *J. Physiol - London*, 542:899–910.

Rassier, D. and Herzog, W. (2005). Relationship between force and stiffness in muscle fibers after stretch. *J. Appl. Physiol.*, 99(5):1769–1775.

Rassier, D., Herzog, W., and Pollack, G. (2003a). Dynamics of individual sarcomeres during and after stretch in activated single myofibrils. *Proc. Natl. Acad. Sci. USA*, 270(1525):1735–1740.

Rassier, D., Herzog, W., Wakeling, J., and Syme, D. (2003b). Stretch-induced, steady-state force enhancement in single skeletal muscle fibers exceeds the isometric force at optimum fiber length. *J. Biomech.*, 36(9):1309–1316.

Rassier, D. E. and Pavlov, I. (2010). Contractile Characteristics of Sarcomeres Arranged in Series or Mechanically Isolated from Myofibrils. In Rassier, DE, editor, *Muscle* *biophysics: from molecules to cells*, volume 682 of *Advances in Experimental Medicine and Biology*, pages 123–140.

Rayment, I., Holden, H., Whittaker, M., Yohn, C., Lorenz, M., Holmes, K., and Milligan, R. (1993). Structure of the actin-myosin complex and its implications for muscle contraction. *Science*, 261(5117):58–65.

Reconditi, M. (2006). Recent improvements in small angle x-ray diffraction for the study of muscle physiology. *Rep. Prog. Phys.*, 69(23):2709–2759.

Reconditi, M., Koubassova, N., Linari, M., Dobbie, I., Narayanan, T., Diat, O., Piazzesi, G., Lombardi, V., and Irving, M. (2003). The conformation of myosin head domains in rigor muscle determined by x-ray interference. *Biophys J.*, 85(2):1098–1110.

Reconditi, M., Linari, M., Lucii, L., Stewart, A., Sun, Y., Boesecke, P., Narayanan, T., Fischetti, R., Irving, T., Piazzesi, G., Irving, M., and Lombardi, V. (2004). The myosin motor in muscle generates a smaller and slower working stroke at higher load. *Nature*, 428(6982):578–581.

Risken, H. (1988). *The Fokker-Planck equation Methods of solution and application.* Springer.

Rogers, R. and Truskinovsky, L. (1997). Discretization and hysteresis. *Physica B*, 233(4):370–375. Workshop on Hysteresis Modeling and Micromagnetism, George Washington Univ., Ashburn, VA, May 20-22, 1996.

Roots, H., Offer, G. W., and Ranatunga, K. W. (2007). Comparison of the tension responses to ramp shortening and lengthening in intact mammalian muscle fibres: crossbridge and non-crossbridge contributions. *J. Muscle Re. Cell M.*, 28(2-3):123–139. Printed.

Sasaki, D., Fujita, H., Fukuda, N., Kurihara, S., and Ishiwata, S. (2005). Auto-oscillations of skinned myocardium correlating with heartbeat. *J. Muscle Re. Cell M.*, 26(2-3):93–101.

Sasaki, D., Fukuda, N., and Ishiwata, S. (2006). Myocardial sarcomeres spontaneously oscillate with the period of heartbeat under physiological conditions. *Biochem. Bioph. Res. Co.*, 343(4):1146–1152.

Sato, K., Ohtaki, M., Shimamoto, Y., and Ishiwata, S. (2011). A theory on auto-oscillation and contraction in striated muscle. *Prog. Biopphys. Mol. Bio*, 105(3, SI):199–207. 36th International Congress of Physiological Sciences (IUPS2009), Kyoto, JAPAN, JUL 27-AUG 01, 2009.

Schuss, Z. (2010). *Theory and application of stochastic processes: an analytical approach.* Springer.

Sekimoto, K. (2010). *Stochastic Energetics.* Lect. Notes Phys. 799.

Shimamoto, Y., Suzuki, M., Mikhailenko, S. V., Yasuda, K., and Ishiwata, S. (2009). Intersarcomere coordination in muscle revealed through individual sarcomere response to quick stretch. *Proc. Natl. Acad. Sci. USA*, 106(29):11954–11959.

Smith, D., Geeves, M., Sleep, J., and Mijailovich, S. (2008). Towards a unified theory of muscle contraction. 1: Foundations. *Ann. Biomed. Eng.*, 36:1624–1640.

Smith, D. and Sleep, J. (2004). Mechanokinetics of rapid tension recovery in muscle: The myosin working stroke is followed by a slower release of phosphate. *Biophys. J.*, 87:442–456.

Smith, D. and S.M., M. (2008). Towards a unified theory of muscle contraction. 2: Predictions with the mean-field approximation. *Ann. Biomed. Eng.*, 36:1353–1371.

Smith, S., Cui, Y., and Bustamante, C. (1996). Overstretching b-dna: The elastic response of individual double-stranded and single-stranded dna molecules. *Science*, 271(5250):795–799.

Sugi, H. and Tsuchiya, T. (1981). Isotonic velocity transients in frog muscle fibers following quick changes in load. *Journal of physiology-London*, 319(OCT):219–238.

Telley, I., Denoth, J., Stussi, E., Pfitzer, G., and Stehle, R. (2006a). Half-sarcomere dynamics in myofibrils during activation and relaxation studied by tracking fluorescent markers. *Biophys. J.*, 90(2):514–530.

Telley, I. A., Stussi, E., Denoth, J., Stehle, R., Pfitzer, G., and Ranatunga, K. W. (2006b). Sarcomere popping requires stretch over a range where total tension decreases with length - reply from i. a. telley, r. stehle, k. w. ranatunga, g. pfitzer, e. stussi and j. denoth. *J. Physiol - London*, 574(2):629–630. Printed.

Tortora, G. J. and Derrikson, B. (2009). *Principles of Anatomy and Physiology.* John Wiley & Sons, Inc, 12 edition.

Tyska, M. and Warshaw, D. (2002). The myosin power stroke. *Cell Motil. Cytoskel.*, 51(1):1–15.

U.S. Departement of Energy (2011). Energy technologies and energy efficiency. http://www.fueleconomy.gov/FEG/atv.shtml.

Veigel, C., Bartoo, M., White, D., Sparrow, J., and Molloy, J. (1998). The stiffness of rabbit skeletal actomyosin cross-bridges determined with an optical tweezers transducer. *Biophys. J.*, 75(3):1424–1438.

Vilfan, A. and Duke, T. (2003). Instabilities in the transient response of muscle. *Biophys J.*, 85(2):818–827.

Vilfan, A. and Frey, E. (2005). Oscillations in molecular motor assemblies. *J. Phys.: Condens. Matter*, 17:S3901–S3911.

Wakabayashi, K., Sugimoto, Y., Tanake, H., Ueno, Y., Takezawa, Y., and Amemiya, Y. (1994). X-ray-diffraction evidence for the extensibility of actin and myosin filaments during muscle contraction. *Biophys. J.*, 67(6):2422–2435.

Walcott, S. and Herzog, W. (2008). Modeling residual force enhancement with generic cross-bridge models. *Math. Biosci.*, 216:172–186.

Wang, H. and Oster, G. (2002). Ratchets, power strokes, and molecular motors. *Appl. Phys. A-Mater.*, 75(2):315–323.

White, H. and Taylor, E. (1976). Energetics and mechanism of actomyosin adenosinetriphosphate. *Biochemistry*, 15(26):5818–5826.

Yanagida, T. and Ishijima, A. (1995). Forces and steps generated by single myosin molecules. *Biophys J.*, 68(4, Suppl. S):S312–S320. 7th Biophysical Discussions on Molecular Motors - Structure, Mechanics and Energy Transduction, AIRLIE, VA, OCT 21-23, 1994.

Yanagida, T., Kitamura, K., Tanaka, H., Iwane, A., and Esaki, S. (2000). Single molecule analysis of the actomyosin motor. *Curr. Opin. Cell Biol.*, 12(1):20–25.

Résumé :

Mécanique de la récupération rapide de force des muscles striés
Cette thèse est consacrée à la modélisation de la réponse transitoire d'une fibre musculaire squelettique soumise à des sollicitations mécaniques rapides. A l'échelle du nanomètre, la fibre musculaire contient des filaments d'actine et de myosine regroupés en unités contractiles appelées "sarcomères". Le filament de myosine est un assemblage de moteurs moléculaires qui, en présence d'ATP, s'attachent et se détachent périodiquement au filament d'actine. Au cours de ce processus d'attachement-détachement, la myosine génère une force lors d'un changement de conformation appelé "power-stroke". Ses caractéristiques peuvent être étudiées lors de la réponse transitoire de la fibre soumise à des sollicitations mécaniques rapides. Nous proposons un modèle mécanique innovant du demi-sarcomere permettant de relier les caractéristiques de la myosine à la réponse de la fibre complète. A la différence des modèles existants, privilégiant une approche discrète, ce modèle s'appuie sur la définition d'un potentiel d'énergie continu qui prend en compte une interaction de champ moyen entre les moteurs moléculaires. Ce système présente des réponses radicallement différentes à longueur imposée et à force imposée. Nous proposons en particulier une explication à la différence de cinétique observée expérimentalement. Nous montrons également que le demi-sarcomere est mécaniquement instable ce qui explique les inhomogénéités de longueurs observées dans une myofibrille.

Abstract:

Mechanics of fast force recovery in striated muscles
This thesis is devoted to the modelling of transient response of muscle fibers submitted to fast mechanical loadings. At the nanometer scale, the muscle fiber contains actin and myosin filaments grouped to form contracile units called 'sarcomeres'. Myosin filament is an assembly of molecular motors that periodically attach and detach to the actin filament in presence of ATP. During this attachement-detachement process, myosin undergoes a force generating conformational change called the 'power-stroke' whose characteristics can be revealed by the transient responses following fast mechanical loadings. We propose an innovative mechanical model of a half sarcomere that links the characteristics of myosin to the response of the whole fiber. Unlike existing models, using a discrete approach, this model is based on the definition of a continuous energy landscape that takes into account a mean field interaction between the molecular motors. This system presents radically different responses under imposed length and imposed force conditions. We particularly emphasize a difference in the kinetics, also observed experimentally. We show that the half-sarcomere is inherently unstable which explains the sarcomere length inhomogeneities observed recently on myofibrils.